PNNL-13501

Pacific Northwest
National Laboratory
Operated by Battelle for the
U.S. Department of Energy

Laboratory Directed Research and Development Annual Report - Fiscal Year 2000

April 2001

Prepared for the U.S. Department of Energy
under Contract DE-AC06-76RL01830

DISCLAIMER

PACIFIC NORTHWEST NATIONAL LABORATORY
operated by
BATTELLE
for the
UNITED STATES DEPARTMENT OF ENERGY
under Contract DE-AC06-76RL01830

Printed in the United States of America

Available to DOE and DOE contractors from the
Office of Scientific and Technical Information,
P.O. Box 62, Oak Ridge, TN 37831-0062;
ph: (865) 576-8401
fax: (865) 576-5728
email: reports@adonis.osti.gov

Available to the public from the National Technical Information Service,
U.S. Department of Commerce, 5285 Port Royal Rd., Springfield, VA 22161
ph: (800) 553-6847
fax: (703) 605-6900
email: orders@ntis.fedworld.gov
online ordering: http://www.ntis.gov/ordering.htm


This document was printed on recycled paper.

(8/00)

PNNL-13501

Laboratory Directed Research and Development Annual Report

Fiscal Year 2000

April 2001

Prepared for the U.S. Department of Energy
under Contract DE-AC06-76RL01830

Pacific Northwest National Laboratory
Operated by Battelle for the U.S. Department of Energy

Contents

Computational Science and Engineering

Computer Science and Information Technology

Design and Manufacturing Engineering

Earth System Science

Director's Statement

I am pleased to present the FY 2000 Annual Report on Laboratory Directed Research and Development (LDRD) at the Pacific Northwest National Laboratory. From our LDRD program springs a renewed vitality of science and technology, a test bed for promising research, and most importantly, a strengthened ability to address complex problems of national importance.

The LDRD program provides an opportunity for our staff to conduct experimental research on advanced scientific areas that have the potential for important new discoveries and innovative solutions to difficult technical problems. These projects span a broad range of topics—from subsurface microbes to atmospheric processes, and from nanoscale atom clusters to geologic oil reserves.

Perhaps one of the most exciting LDRD projects described in this year's report is one in the life sciences where we have extended previous work in genomics into the new frontier area of proteomics. Using mass spectrometry to catalogue and characterize proteins on a large scale, we can now rapidly identify proteins that are made in response to a change in the cellular environment. Many of these proteins have never been described. This advance in fundamental biology could greatly improve our understanding of how cells respond to toxic insults and could lead to new techniques for bioremediation and environmental cleanup as well as early diagnosis and treatment of diseases.

As we head into the next century, we will be relying on the LDRD program to form the foundation for a new generation of products and processes that will benefit the U.S. Department of Energy, the nation, and the tax-payers. For example, LDRD-funded research on fuel cells promises to yield important new advances in powering energy-efficient, low-polluting automobiles and trucks. The increasing importance of computer information and network security also is being addressed through LDRD research, where we are developing technologies that could prevent destructive intrusions on national energy, transportation, and communication centers.

Keeping us at the cutting edge of science and technology, the LDRD program fosters an innovative work environment that helps us recruit and retain the best and brightest staff. Here, our scientists and engineers are encouraged to turn their discoveries into practical solutions.

The LDRD program has proven essential to the outstanding record of achievement at Pacific Northwest National Laboratory, and we expect it to remain a cornerstone of our success in the 21st century.

Lura J. Powell, Ph.D.
Laboratory Director

Introduction

Department of Energy Order 413.2A sets forth DOE's policy and guidelines for Laboratory Directed Research and Development (LDRD) at its multiprogram laboratories. As described in 413.2A, LDRD is "research and development of a creative and innovative nature that is selected by the Laboratory Director or his or her designee for the purpose of maintaining the scientific and technological vitality of the Laboratory and to respond to scientific and technological opportunities in conformance with the guidelines in this Order." DOE Order 413.2A requires that each laboratory submit an annual report on its LDRD activities to the Cognizant Secretarial Officer. This document is our report of LDRD research at Pacific Northwest National Laboratory for fiscal year 2000.

The Laboratory supported 144 LDRD projects in 2000. The total funding allocated to these projects was approximately $12.3 million. This amount represented about 3 percent of the Laboratory's operating budget. The maximum allowed by Congress in fiscal year 2000 was 4 percent, excluding Environmental Management funds.

The Laboratory focused its LDRD research on well-defined missions and scientific assets, and developed new and innovative approaches that supported our core technical capabilities. The Laboratory's core technical capabilities, reflected by our 15 technical networks in 2000, were

- Analytical and Physical Chemistry
- Biosciences and Biotechnology
- Computational Science and Engineering
- Computer Science and Information Technology
- Design and Manufacturing Engineering
- Earth System Science
- Energy Technology and Management
- Human Health and Safety
- Materials Science and Technology
- Micro/Nano Technology
- Nuclear Science and Engineering
- Policy and Management Sciences
- Sensors and Electronics
- Separations and Conversion
- Statistics.

In accordance with DOE guidelines, this report provides a Director's statement, an overview of the Laboratory's management and self-assessment processes, a 5-year project funding table, project summaries for each LDRD project (organized by technical capability area), and brief descriptions and funding profiles for each new project started in fiscal year 2001.

LDRD Program Management

Pacific Northwest National Laboratory manages its LDRD program to ensure compliance with DOE Order 413.2A. The Laboratory has established criteria for selecting projects, evaluating the quality of science and technology through Laboratory-level technical reviews and division reviews, and gathering data on project progress. Our goal is to achieve a high level of scientific return on investment. Our program emphasizes excellence and innovation, so that capabilities developed with LDRD funds will effectively support DOE's and the Laboratory's missions.

The LDRD program makes it possible for our Laboratory to apply science and technology to meet critical national needs. The increasing complexity of these needs requires innovative and creative technology solutions. Since the demand for solutions frequently occurs at a faster pace than can be anticipated or adopted in the federal budget process, we strive to maintain an environment in which creativity and innovation are encouraged and supported. The LDRD program is the support mechanism by which we formulate new theories, hypotheses, and approaches; build new scientific capabilities; and identify and develop technology solutions. The principal goals of the LDRD program are to

- maintain the scientific and technical vitality of the Laboratory
- enhance the Laboratory's ability to address future DOE missions
- foster an environment that encourages creativity and innovation
- provide opportunities for developing and testing new research concepts
- support new ideas that have exceptional scientific and technical merit.

LDRD Program Benefits

The LDRD program strengthens the Laboratory's fundamental research component, supports our applied research and development programs, and provides capabilities for integrating scientific discovery with technology applications. Specific examples of direct applications of LDRD research to technology solutions are described in the many project reports that compose this document.

LDRD Program Management Process and Timeline

The Director of Strategic Planning is responsible for oversight and management of the LDRD program. Our LDRD program is funded through a Laboratory overhead account that is applied to the value-added base on all 1830 contract accounts. The Director of Finance ensures that these funds are accumulated and accounted for in the appropriate manner. The Laboratory Director and the Strategy Council (which includes the Associate Laboratory Directors) approve the funding levels for the LDRD accounts. The Technical Council (comprising senior research staff) and the Business Council (comprising managers of major DOE programs) develop recommendations to the Director for allocating funds among projects.

The major sequential steps governing Pacific Northwest National Laboratory's LDRD management process are

1. The Director of Strategic Planning issues a formal schedule for research proposals, proposal review, and project reporting. Guidance for this process is prepared and issued annually *(April-May).*

2. The LDRD Program Office within Strategic Planning prepares a Laboratory-wide call for LDRD proposals. Initiative and division managers solicit LDRD proposals from research staff and forward selected projects to Strategic Planning as candidates for potential funding *(May-June).*

3. The LDRD Program Office prepares and submits an annual LDRD Program Plan to DOE. The Laboratory Director approves initial funding for the LDRD accounts *(July).*

4. The Laboratory's Technical Council and Business Council conduct reviews of proposed LDRD projects for Laboratory-level investments. Further, technical divisions review division-level projects *(July-August).*

5. After reviews by the Technical and Business Councils are complete for Laboratory-level investments, and by the technical divisions for division-level investments, the recommendations are forwarded to the Strategy Council for approval *(September).*

6. Principal investigators submit approved LDRD project proposals to the LDRD Program Office for review and compliance with DOE requirements. All project documents for compliance with National Environmental Policy Act and other environmental, safety, and health requirements also are submitted *(October-November).*

7. The Budget and Analysis Office establishes six-digit work breakdown structure codes for each of the LDRD accounts. Approved projects are authorized to start after the LDRD Program Office assigns a specific work breakdown structure number to the LDRD project.

The Laboratory's *Guide to Laboratory Directed Research and Development* is a brochure that provides guidance to help all Laboratory staff comply with the requirements of DOE Order 413.2A. This guide, which is also available electronically on the LDRD internal home page, describes accountability and reporting requirements for LDRD projects and the proper use of LDRD funds. The LDRD Program Office conducts reviews to ensure compliance with these criteria.

Individual LDRD projects are limited to a maximum $500K per fiscal year and to a maximum of $1 million over the lifetime of the project (unless exceptions are approved by the Director of Strategic Planning). The majority of the Laboratory's LDRD projects are funded well below these levels.

Peer Review and Self-Assessment

Introduction

Pacific Northwest National Laboratory assesses the performance of its Laboratory Directed Research and Development (LDRD) program to ensure that the program is compliant with DOE Order 413.2A (i.e., that projects represent innovative and creative science and contribute to the Laboratory's pursuit of excellence in science and technology). Peer review is a key facet of our self-assessment program. This section of the annual report outlines the Laboratory's peer review process for LDRD projects, as well as how the program ties into the Laboratory's overall process for self-assessment. The Director of Strategic Planning and the LDRD Program Office monitor the process of peer review as a part of our self-assessment for each phase of proposal submission, review, selection, and project funding.

The technical quality of LDRD research at the Laboratory is measured primarily by

- peer review
- analysis of technical accomplishments as judged by tangible output metrics for Laboratory-level and division-level LDRD projects.

Excellent scientific and technical quality and a high level of productivity are the major goals of the LDRD program and of all the Laboratory's research programs. Research quality and the potential for research that leads to important scientific developments are best evaluated by peer reviews employing respected subject matter experts and professionals. Project performance with demonstrated measures and outcomes also is reviewed through self-assessment to ensure progress toward strategic goals.

Peer Review

Pacific Northwest National Laboratory uses peer review to evaluate the quality, relevance, and performance of our scientific research. Peer review is the universally accepted process for determining the direction of and setting standards for scientific, engineering, and technology research and development. Our formal peer review process ensures the technical integrity of our work, enhances our stature within the scientific community, and ensures that our products and services meet our customers' needs. A quality peer review process is an acknowledged good management practice and a primary element of our self-assessment program.

Self-Assessment

We assess our LDRD program performance by evaluating the scientific excellence of our projects, the quality of our planning, and our progress and accomplishments.

Self-assessment on scientific excellence is based primarily on the results of peer reviews of the Laboratory's science and technology programs by the Division Review Committees, external peer review panels, technical and business reviews, and compliance reviews.

The LDRD Review Process

The Laboratory Director and Strategy Council commission technical and business reviews of proposed LDRD projects as part of the annual business planning process. The following steps are involved in this review process.

Laboratory-Level Projects

All Laboratory-level technical proposals are submitted to Strategic Planning. The proposals are then forwarded to the Technical Council and to the Business Council for review.

- The Technical Council peer reviews individual LDRD project proposals for scientific and technical quality using internal and external reviewers. The five criteria used for rating the technical quality of proposals are

  - Technical Significance. The project needs to address an important technical problem, advance the state of the art in a capability or technology area, and distinguish the Laboratory from what other institutions are doing.

  - Technical Approach. Projects must have a technical strategy and plan that are well integrated, well developed, conceptually sound, and that show achievable endpoints.

  - Technical Innovation. Projects should develop novel technical concepts, approaches, and methods that create intellectual value, challenge existing paradigms, and develop new capabilities.

  - Technical Staff. Projects need to have investigators with a balanced mix of technical training and experience, and with a proven record of technical accomplishment.

  - Technical Environment. Projects must aggressively track relevant technical activities to manage the technical direction of the investment. Projects must actively seek external technical expertise to strengthen investments, as appropriate (such as collaborations and new hires).

The Technical Council members rate each proposal and provide a funding recommendation to the Laboratory Director and the Strategy Council.

- The Laboratory Director and the Strategy Council commission the Business Council to review each technical focus area to ensure that Laboratory thrusts are applicable to DOE missions and needs. The five criteria used for rating technical focus areas are

  - Enduring Benefit to the Laboratory. Projects should focus on developing our staff resources, analytical tools and equipment, and new technical capabilities.

  - Market Attractiveness. Projects must be relevant to DOE missions and the likelihood of new programs, if successful outcomes are achieved.

  - Ability to Compete. Projects should match Laboratory capabilities to mission roles and should identify a clear distinction from the work of others.

  - Financial. Projects should ensure that the expected results are commensurate with available funding.

  - Planning and Execution. For continuing projects, the proposals are rated for technical quality and the project managers are rated on performance ability.

The Business Council forwards its recommendations as a part of the decision package to the Laboratory Director and Strategy Council.

The Laboratory Director and Strategy Council approve the proposal recommendations and allocate funding and other resources to proposed projects according to strategic goals and priorities of the Laboratory. The principal investigators and the Laboratory staff are then notified of these funding decisions.

The Technical Council and the Strategy Council are responsible for monitoring and reviewing Laboratory-level LDRD projects throughout the fiscal year to ensure that the projects are making appropriate technical progress.

Division-Level Projects

Each research division at the Laboratory undertakes a similar review and evaluation process for proposed projects that address the division's strategic objectives. The Associate Laboratory Director for each division appoints an internal

committee to evaluate and recommend projects for funding. These internal review committees are also responsible for monitoring project progress and for ensuring that appropriate technical progress is being made. The LDRD Program Office also reviews division-level projects. In addition, the Division Review Committees review selected LDRD projects as part of the division's peer review/self-assessment process.

Division Review committees for each research division are appointed by the Laboratory Director. The Committees review Division activities on a 3-year, rotating basis so that all work is reviewed at least once every 3 years. The Committees evaluate the science and engineering activities based on the following four criteria:

- quality of science and engineering
- relevance to DOE missions or national needs
- success in construction and operation of major facilities
- effective and efficient program management.

Compliance Review

The oversight and reporting structure for the LDRD program is the responsibility of the LDRD Program Office, reporting to the Director of Strategic Planning. This office reviews projects for compliance with DOE Order 413.2A.

In addition, the Director of Strategic Planning and the LDRD Program Office monitor the process of peer review and self-assessment for each phase of proposal submission, review, selection, and project funding. Each project is evaluated for mission relevance, scientific quality, and progress toward objectives using an integrated planning and review process. Midyear and annual summaries of project performance are analyzed and linked to Laboratory critical outcomes. Copies of the "prep and risk analysis" for each proposal are provided to the LDRD Program Office. Project costs and spending rates are tracked in the Laboratory's financial system. Annual reports of technical progress are obtained from the principal investigators for annual reporting. Tangible output metrics are obtained by an annual survey from each principal investigator.

Analysis of Performance and Return on Investment

Among the principal objectives of the LDRD program are to maintain the scientific and technical viability of the Laboratory and to enhance the Laboratory's ability to address future DOE missions. The LDRD program at Pacific Northwest National Laboratory is aligned with the priorities identified in DOE's strategic plan and its research and development portfolio for science, environmental quality, energy resources, and national security. Our LDRD projects support new and innovative science and address most of the Laboratory's core technical capabilities.

Institutional and Mission Areas of Emphasis

Institutional mission areas of emphasis are highlighted below. Advanced scientific research in the **biological and environmental sciences** continues to be a major thrust of our LDRD program. The Laboratory's investments in molecular biology and biochemistry are being integrated with related efforts in physics, imaging, and computation to substantially advance the capabilities needed to identify, understand, and mitigate the consequences of environmental pollutants. Our multidisciplinary research efforts apply instrumentation and computation to visualize cellular and molecular processes, and to study the complex cell-signaling networks responsible for biological function. We are studying gene products using techniques to resolve, quantify, identify, and characterize proteins and protein interactions. This information is synthesized into an integrated cellular context using computation and modeling.

Research and application of **advanced computational modeling and simulation** is a growing area of investment within the Laboratory's LDRD program. Research is focused on developing high-performance algorithms, software suites, and collaborative problem-solving environments, and delivery of significant new scientific analyses of complex issues facing DOE's energy, environmental, and national security missions. The overarching scientific theme of current investments is the development of methods and tools that enable researchers to bridge the range of temporal and spatial scales from the atomic to field scale. The technical areas being targeted include atmospheric chemistry and transport, computational chemistry

methods applicable to combustion, subsurface chemistry and modeling, engineering simulation of materials and associated manufacturing processes, and computational science infrastructure. Results include significantly enhanced subsurface fate and transport models that are being applied to DOE environmental problems, flexible problem-solving environments, and many technical publications.

Laboratory research in **computer science and information technology** is developing innovative approaches and new software packages to analyze and display large and diverse data sets and to protect valuable or sensitive computer systems from attack or compromise. The primary target for both focus areas is national security applications, but the tools for managing the large data sets have applications to other DOE missions.

In the area of **advanced scientific instrumentation,** new techniques are being developed to measure and characterize environmental contaminants and chemicals. An expanding area of investigation is the infrared detection of chemicals in the atmosphere and on surfaces under a wide variety of conditions. These efforts primarily support the national security and environmental missions.

Research in **process science and technology** is directed toward developing new materials and technologies for a variety of chemical processes with the intent of increased efficiency, reduced pollution, or performing novel functions. The focus of our efforts is on extending fundamental scientific developments in chemistry and materials to new microscale and conventional-scale systems. Results have application to waste management, environmental cleanup, carbon management as it affects global climate changes, and processes for energy-intensive industries.

Projects in **material science, nanostructures, and nanomaterials** technology involve development and testing of a wide range of materials for special applications. Recent studies focus on fundamental studies of the extraordinary properties of molecular clusters and on self-assembled monolayers on mesoporous supports. The applications include nanomaterials for removal of contaminants from the environment, ceramics for fuel cells, and lightweight materials for cars and trucks. These projects primarily support DOE's science and energy missions.

In the area of **thermal and energy systems,** our research is focused on advanced power systems using solid-oxide fuel cell technology for widespread applications in vehicles and buildings. This research seeks to overcome the limitations of high-temperature operations, improved component manufacturing, and improved system performance. Our work on microtechnology devices seeks the development of miniature devices for heating and cooling applications and chemical processing.

There are a number of noteworthy accomplishments on specific LDRD projects, highlighted below. These projects can be mapped to specific mission areas above.

- **Combination Microscopy.** We combined fluorescent optical microscopy with magnetic resonance imaging and obtained the first simultaneous images of living cells and cellular processes. The coupling of confocal microscopy with nuclear magnetic resonance (NMR) spectrometry allows simultaneous, noninvasive analysis of single cells or three-dimensional cell clusters.

- **Cell Signaling.** We developed a technique for studying ion flux across cell membranes in living cells to determine how cells respond to their environment. From these results, we formulated predictive models of cell-signaling pathways and networks to better understand intracellular function and responses to external stimuli.

- **Proteomics.** We used advanced separation-sciences techniques involving protein arrays and high-resolution chromatography, combined with mass spectrometry, to show how proteins are organized into pathways and networks, and how proteins interact to form functional complexes. We applied this technology to identify unique biological warfare agent protein signatures.

- **Protein Structure.** We developed methods using NMR spectrometry to determine the structure and functional class of proteins.

- **DNA Fingerprinting.** We developed automated DNA microarrays for detecting and characterizing environmental microorganisms.

- **Carbon Sequestration.** We identified methods for deep ocean sequestration of carbon dioxide, methods for injecting carbon dioxide into deep geologic formations, and computational tools for analyzing carbon distributions in the atmosphere.

- **Scalable Computer Algorithms.** We developed high-performance, scalable computer algorithms for analyzing multiphase atmospheric processes. We also developed mathematical techniques for large-scale data archive and scientific data management.

- **Aerosol Analysis Mass Spectrometry.** We modified a conventional laser desorption ion trap mass spectrometer for chemical analysis of aerosol particles. This system is being tested at the Hanford Site as a method to analyze samples and detect potential tank leaks more quickly and at lower cost.

- **Solid-Oxide Fuel Cells Improvements.** Our scientists are improving the chemical, thermal, mechanical, and electro-chemical processes in solid-oxide fuel cells. These advances are needed to improve performance and to reduce the costs of producing power for both stationary and mobile systems. We are optimizing fuel cell stack design to minimize the thermo-mechanical stress within ceramic components. We are also developing, fabricating, and testing a thick, porous anode that is compatible with other solid-oxide fuel cell components.

- **Nano-Scale Materials Technology.** We discovered and characterized new nanocrystalline metal oxide materials. We developed and tested novel photocatalysts grown as copper oxide quantum dots on anatase substrates for applications such as hydrogen production. We produced molecular beams to synthesize and characterize nanoporous magnesium oxide thin films with high surface areas.

- **Remote Surveillance of Weapons of Mass Destruction.** We developed agent technologies for registering and calibrating satellite surveillance photos to extract new information from surveillance photography. We also developed infrared sensing, matrix-assisted laser desorption ionization with time-of-flight spectroscopy, and software tools for correlating remote measurements of chemical releases from weapons facilities with other intelligence data to identify and monitor weapons production activities.

Project Metrics

Another way that the Laboratory evaluates LDRD productivity is through analyzing project accomplishments. The output metrics collected include the following:

Metric	Number	Value
Client Follow-on Funding	$26.5M	This metric demonstrates the relevance of projects to Department of Energy missions and priorities.
Awards	1	This indicator helps determine the strength in developing and transferring relevant technologies that are valued by the technical community.
Publications	131	Publication in the open scientific literature is an indicator of scientific productivity and quality as well as external recognition.
New Hires and Post-Doctoral Fellows	129	This metric is an indicator that the Laboratory is building its capabilities and is expanding its staff resources.
Copyrights, Inventions, and Patents Filed or Granted	82	These metrics indicate progress, innovation, and leading-edge development in science and technology. The protection of intellectual property provides the opportunity for technology developed at the Laboratory to be used by the Department.

Summary

Each national laboratory must ensure that its LDRD program provides outstanding value and return on investment. Performance reviews ensure that research funds are used for their intended purposes and result in value to the Laboratory, to the Department of Energy, and the nation.

Peer review and other components of our self-assessment processes help the Laboratory measure the performance of the LDRD program. Through self-assessment, the Laboratory can manage the program effectively and implement lessons learned where improvements are needed. We analyze our performance and return on investment by tracking and analyzing tangible measures of accomplishment.

Analytical and Physical Chemistry

Advanced Methodology for the Analysis of Organic Components

James A. Campbell, Eric W. Hoppe, Joe W. Brothers

Study Control Number: PN0004/1411

Faster and cheaper methods for the analysis of organic components in tank wastes and other environmental samples are required for cleanup efforts at DOE sites. Matrix-assisted laser desorption ionization/time-of-flight mass spectrometry is a promising technique that requires minimal sample preparation, provides rapid analysis, reduces personnel exposure, and minimizes waste.

Project Description

Analytical techniques for the analysis of chelators, chelator fragments, and organic acids in radioactive wastes typically involve derivatization and gas chromatography/mass spectrometry, which is a time-consuming and labor-intensive approach. Derivatization techniques also produce artifacts related to production of nitroso compounds. Alternatively, liquid chromatography has been used for analyis of these constituents in radioactive wastes but chromatography is hindered by additional waste generation and by co-elution problems in complex matrices. In addition, the analytical procedures for regulatory compounds (semivolatiles, polychlorinated biphenyls, pesticides) are time-consuming and require considerable sample preparation methodologies.

The matrix-assisted laser desorption ionization (MALDI) technique, in combination with time-of-flight mass spectrometry (TOFMS) allows an entire mass spectrum to be measured in a single analytical step. Since the MALDI process produces positive and negative ions directly with very little sample, MALDI is an efficient micro-sampling technique that requires minimal sample preparation. MALDI offers additional advantages including reduced personnel radiation exposure and minimal waste production.

We have used MALDI/TOF to examine anions, organic acids, and chelators that are known to be present in storage tank wastes. Samples of ethylenediaminetetra-cetic acid, N-(2-hydroxyethyl)ethylenediametriacetic acid, citric acid, nitrilotriacetic acid, and several inorganic anions including sulfate, nitrate, and nitrite (Goheen et al. 1997) were analyzed using MALDI/TOF. This project focused on developing MALDI/TOF as a quantitative tool for analyzing organic components of regulatory interest. Mixtures of analytes also were analyzed. This research provides a method that reduces the cost and time required to perform chemical analyses.

Introduction

We developed analytical techniques for organic constituents, including phosphate-related components (tributyl phosphate, dibutyl butyl phosphonate, and bis-(2-ethylhexyl)phosphoric acid) and chelators in tank waste. These techniques involve derivatization gas chromatography/mass spectrometry for the analysis of chelators and chelator fragments. We also developed ion chromatography for low molecular weight acids, such as oxalate, formate, and acetate. With these and other analytical techniques, we were able to account for 80% to 95% of the total organic carbon in most tank waste samples.

The above techniques, although providing important analytical data, are labor-intensive and time-consuming. We have shown that MALDI/TOF can identify low molecular mass solids including chelators, low molecular weight acids, and nitrites. Mass spectra were observed for the chelator compounds in the positive ion mode and for the low molecular weight acids in the negative ion mode. Because of its inherent advantages of limited sample preparation and minimal waste production, MALDI/TOF represents an attractive technique for the analysis of organics in tank waste matrices. The results of this study will provide the opportunity for a substantial savings in the cost and time required to perform chemical analyses.

Approach

Standard solutions of phosphate-related compounds known to be present in Hanford tank wastes were analyzed using MALDI/TOFMS. Standard solutions of the regulatory compounds were also analyzed using MALDI. We evaluated the efficiency and cost-effectiveness of the MALDI/TOFMS technique for analyzing these solutions.

Results and Accomplishments

We successfully applied MALDI/TOFMS for the analysis of phosphate-related components known to be present in Hanford tank wastes. Figure 1 is a positive ion MALDI spectrum of dihydroxybenzoic acid, the matrix material. Figures 2a, b, and c show the positive ion MALDI spectra of phosphates. The spectra for tributyl phosphate and dibutyl butyl phosphate show protonated $[M+H]^+$ and sodium-adduct $[M+Na]^+$ peaks. The letter M designates the parent compound. The spectrum of bis-(2-ethylhexyl) phosphoric acid shows a sodium-adduct ion at m/z 346. Previous studies of chelators (Goheen et al. 1997) showed the presence of strong base peaks that indicated protonated and sodium-adduct intact molecules. Table 1 lists the observed ions with dihydroxybenzoic acid as the matrix for the chelators, organic acids, and phosphates.

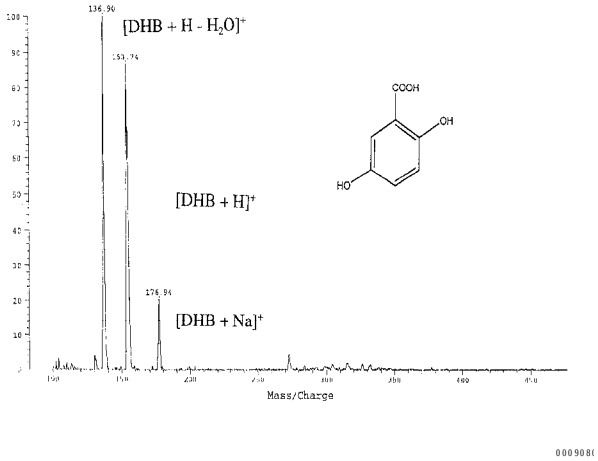

Figure 1. Positive ion MALDI spectrum of dihydroxybenzoic acid

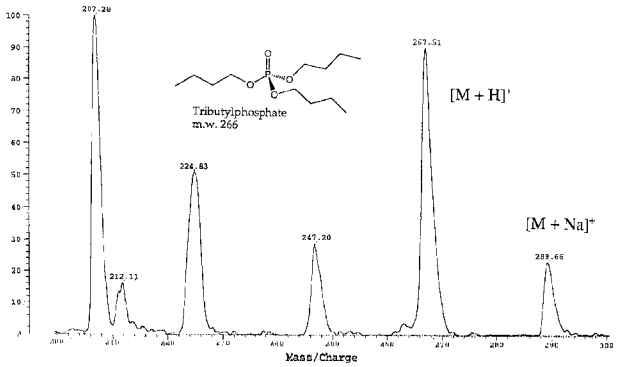

Figure 2a. Positive ion MALDI spectrum of tributyl phosphate

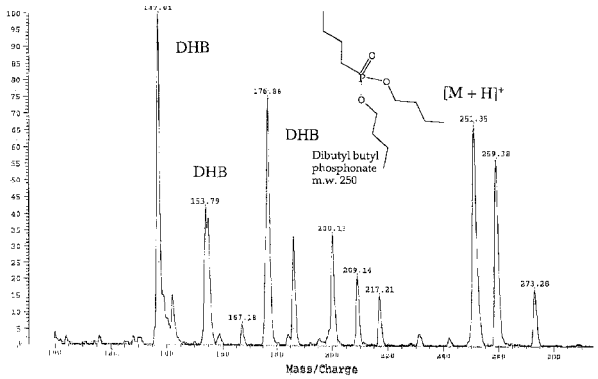

Figure 2b. Positive ion MALDI spectrum of dibutyl butyl phosphonate

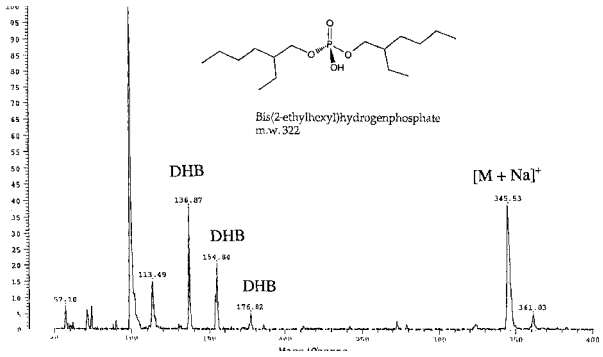

Figure 2c. Positive ion MALDI spectrum of bis-(2-ethylhexyl) phosphoric acid

The Regulatory Data Quality Objective lists approximately 125 compounds that require analysis in tank wastes (Weimers et al. 1998). Many of these compounds (nitrosodiphenylamine, pentachlorophenol, phenol, nitrobenzenes, triphenylamine) were examined using MALDI. Most of the compounds examined exhibited either positive ion or negative ion spectra.

Summary and Conclusions

Matrix-assisted laser desorption ionization/time-of-flight mass spectrometry was used successfully for analyzing phosphate-related components of tank wastes. MALDI was used successfully for many of the regulatory organic components. We found that MALDI is an attractive alternative to present analysis methods that are expensive,

Table 1. Positive and negative ions observed by MALDI-TOFMS with dihydroxybenzoic acid

Analyte	Molecular Weight	Ions Observed (m/z)	
		(-)	(+)
Sodium Nitrate	85	62 [NO_3^-]	
Sodium Nitrite	69	46 [NO_2^-]	
Oxalic Acid	90	89 [M-H]$^-$	
Fumaric Acid	116	115 [M-H]$^-$	
Maleic Acid	116	115 [M-H]$^-$	
Succinic Acid	118	117 [M-H]$^-$	
Ammonium Sulfate	132	97 [HSO_4^-]	
Citric Acid	192	191 [M-H]$^-$	
Iminodiacetic Acid	134		157 [M+Na]$^+$173 [M+K]$^+$
N-(2-hydroxyethyl)-ethylene diametriacetic Acid	278		279 [M+H]$^+$301 [M+Na]$^+$
Ethylenediamediacetic Acid	176		177 [M+H]$^+$199 [M+Na]$^+$
Nitrilotriacetic Acid	191		192 [M+H]$^+$214 [M+Na]$^+$
Ethylenediaminetetra-acetic Acid	336		315 [Na_2EDTA-Na+2H]$^+$
			337 [Na_2EDTA+H]$^+$
Ethylenediaminetetra-acetic Acid	336		359 [Na_2EDTA+Na-H]$^+$
PHOSPHATES			
Tributyl phosphate	266		267 [M+H]$^+$
Bis-(2-ethylhexyl) phosphoric Acid	322		346 [M+Na]$^+$
Dibutyl butyl phosphonate	250		251 [M+H]$^+$
Bis-(2-ethylhexyl) phosphite	306		329 [M+Na]$^+$

time-consuming, and labor-intensive. Other advantages of MALDI/TOFMS include the following:

- produces both positive and negative ion signals
- little sample is required
- efficient micro-sampling
- minimizes radiation exposure, sample preparation, and hazardous waste production
- lower cost of analysis (perhaps by a factor of 10 over present methods) for certain organic analytes.

References

Goheen SC, KL Wahl, JA Campbell, and WP Hess. 1997. "Mass spectrometry of low molecular mass solids by matrix-assisted laser desorption/ionization." *J. of Mass Spectrometry*, 32:820-828.

Weimers KD, KL Lerchen, M Miller, and K Meier. 1998. *Regulatory Data Quality Objectives Supporting Tank Waste Remediation System Privatization Project.* PNNL-12040, Pacific Northwest National Laboratory, Richland, Washington.

Publications

Campbell JA, WP Hess, JR Lohman, SC Goheen. "Analysis of Hanford-related organics using matrix-assisted laser desorption ionization/time-of-flight mass spectrometry (MALDI/TOFMS). *Journal of Radioanalytical and Nuclear Chemistry* (in press).

Campbell JA and JR Lohman. "Analysis of regulatory organic compounds using MALDI/TOFMS." (in preparation).

Complex Mixture Modeling for Occupation Exposure Assessment

James A. Campbell, Charles Timchalk

Study Control Number: PN00022/1429

Occupational exposure to complex chemical mixtures is a major health concern in both DOE and the National Institute of Occupational Safety and Health. This research represents a novel strategy for addressing health concerns of exposure to complex mixtures. This project represents an important linkage between exposure, dose, and biological response.

Project Description

Occupational exposures to chemicals usually involves mixtures of agents. The human health effects of mixed chemical exposures are difficult to assess. A comprehensive toxicological evaluation of chemical mixtures is rarely feasible. Nonetheless, strategies may be developed for assessing classes of chemical agents with similar metabolism and toxicity profiles. To address this chemical mixture issue, we applied physiologically based pharmacokinetic/pharmacodynamic (PBPK/PD) modeling to in vivo and in vitro toxicology studies. Our PBPK/PD model was linked to the target tissue dosimetry with the observed biological response (esterase inhibition) for two important organophosphate chemicals: chlorpyrifos and diazinon. These chemical agents were chosen because we have extensive toxicological and pharmacokinetic databases for these materials. Chlorpyrifos and diazinon are similar in chemical structure, mechanism of action, metabolic pathways, and the potential for occupational exposure to mixtures of the agents. This project focused on demonstrating the capability to identify and quantify metabolites in a mixture.

Introduction

The health implications of mixed chemical exposures are poorly understood because the toxicology of such mixtures is difficult to characterize. Organophosphate pesticides are used in a variety of agricultural settings, and workers are at substantial risk for occupational and environmental exposure to these toxins.

The potential for organophosphate interactions has been well understood for some time. Early studies demonstrated the acute, synergistic, toxicological interactions between malathion and ethyl-*p*-nitrophenyl phenylphosphonothionate. These studies suggested that malathion and ethyl-*p*-nitrophenyl phenylphosphonothionate complete as inhibitors of each other's hepatic metabolism (both activation and detoxification). We assumed from studies of chlorpyrifos and parathion that chlorpyrifos and diazinon may behave similarly. In vitro kinetic analysis in rats are required to adequately define metabolic parameters in vivo for chlorpyrifos and diazinon interactions.

Approach

We initiated studies to demonstrate the ability to quantitate chlorpyrifos, chlorpyrifos-oxon, diazinon, diazinon-oxon, and their major metabolites, trichloropyridinol and 2-isopropyl-4-methyl-6-hydroxyprimidine, respectively. We used analytical methods, such as gas chromatography/electron ionization mass spectrometry.

A limited in vitro metabolism study was conducted with rat hepatic microsomes. The studies entailed co-exposure to both chlorpyrifos and diazinon, and focused on the capability to quantitate the critical metabolites and provide a limited demonstration of chlorpyrifos and diazinon interactions.

Results and Accomplishments

We obtained full scan electron ionization mass spectra for 1) chlorpyrifos, 2) silylated derivative of 2-isopropyl-4-methyl-6-hydroxypyrimidine, 3) silylated derivative of trichloropyridinol, 4) diazinon, 5) chlorpyrifos-oxon, and 6) diazinon-oxon. We used chemical ionization mass spectrometry to confirm the compound identity and molecular weight. The relative retention times were determined for all six compounds listed above. Figure 1 is the mass spectrum of silylated-trichloropyridinol, and Figure 2 is the mass spectrum of silylated-2-isopropyl-4-methyl-6-hydroxypyrimidine. The ions highlighted indicate the ions used in the selected ion-monitoring mode for detection and quantification. The ions monitored for chlorpyrifos were m/z 314, 316, for silylated-2-isopropyl-4-methyl-6-hydroxypyrimidine m/z 209, 210, silylated-trichloropyridinol m/z 254, 256, diazinon m/z 304, 305, chlorpyrifos-oxon m/z 298, 299, and m/z 273, 274 for diazinon-oxon.

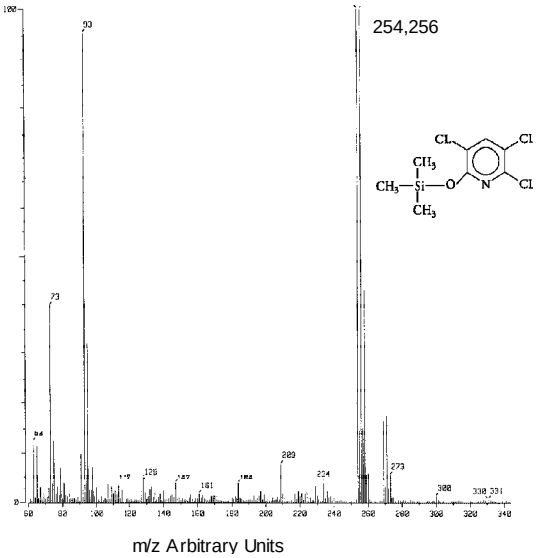

Figure 1. Mass spectrum of silylated-trichloropyridinol

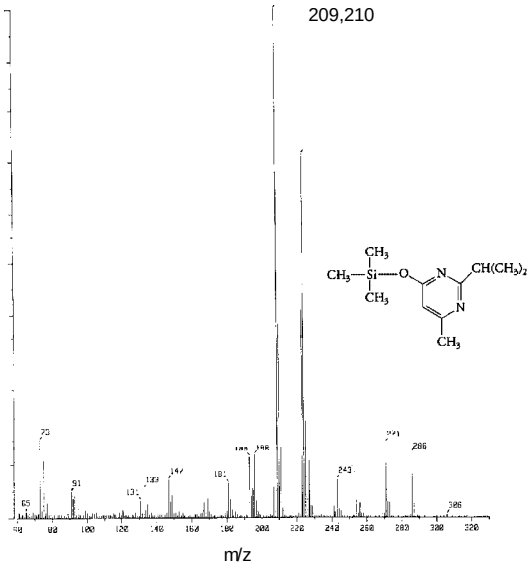

Figure 2. Mass Spectrum of silylated-2-isopropyl-4-methyl-6-hydroxypyrimidine

One-half of a solution of metabolized chlorpyrifos was extracted and derivatized for trichloropyridinol. The resulting concentration was approximately 2 ppm and the oxon was not detected. Another sample containing equal concentrations of chlorpyrifos and diazinon was extracted and derivatized for trichloropyridinol. The concentration for trichloropyridinol was 2 ppm. The results indicated good reproducibility. Concentrations were based on the response of a standard. A duplicate sample was extracted and analyzed for chlorpyrifos and chlorpyrifos-oxon, but no peaks were detected. These preliminary results suggested, under these reaction conditions and concentrations of analytes, that the metabolism of chlorpyrifos was not inhibited by the presence of diazinon. These results also indicated complete metabolism of chlorpyrifos to trichloropyridinol.

Summary and Conclusions

We developed analytical methods for analyzing chlorpyrifos, diazinon, associated oxons, and metabolites and concluded that

- the components can be extracted and analyzed at low concentrations with very good reproducibility
- electron ionization with selected ion monitoring may not be the most sensitive method for detection (negative ion electrospray ionization mass spectrometry may be better)
- the metabolism of chlorpyrifos was not inhibited by the presence of diazinon under test conditions and concentrations
- further studies will be needed at lower concentrations to verify lack of inhibition.

Publication and Presentation

Campbell, JA, TS Poet, GM Mong, and C. Timchalk. June 2000. "In vitro metabolism study with a mixture of the organophosphate insecticides chlorpyrifos and diazinon." Presented at the 48th ASMS Conference on Mass Spectrometry and Allied Topics, Long Beach, California. In *Proceedings of 48th ASMS Conference on Mass Spectrometry and Allied Topics* (in press).

Development of New Laser-Mass Spectrometric Method for the Detection of Low Volatility Compounds in Particulate Matter

Michael Alexander, Chris Aardahl

Study Control Number: PN00035/1442

Understanding the composition and chemistry of particulate matter is important to DOE in a variety of areas, from national security to health effects and atmospheric chemistry. Current methods for analyzing low-volatility components of particulate matter require sampling and subsequent laboratory analysis. The technology developed by this project will provide a significant advancement in the development of portable instrumentation capable of making real-time measurements for the field analysis of samples important to DOE projects. These include explosive and chemical warfare agent monitoring, cleanup activities, and particulate emissions monitoring.

Project Description

We began an investigation on the use of laser desorption of solid samples combined with direct air sampling mass spectroscopy for analyzing semivolatile and nonvolatile components of particulate matter. Although instrumentation based on the results of this project can potentially be applied to the analysis of any solid sample, we focused on the measurement of low-volatility compounds in particulate matter. Our device uses a semipermeable membrane as a direct interface to an ion trap mass spectrometer to provide high selectivity as well as sensitivity close to 100 parts per trillion for volatile species. The membrane interface ion trap mass spectrometer was used in combination with existing pulsed lasers available at the EMSL facility to illuminate the basic processes of laser desorption of low-volatility species into the gas phase and transport of these molecular species across the membrane interface. A successful demonstration of the basic method led to follow-on research for field collection of aerosol samples on filters in Houston as part of the Texas 2000 Air Quality Study (TX2000ARQ). Filter samples were collected with 4-hour time resolution over a period of 5 days. Real-time membrane introduction ion trap mass spectroscopy was used to monitor the volatile organics present in the gas phase that corresponded to the filter samples.

Introduction

Research in the area of atmospheric particulate matter has increased significantly in recent years. The motivation for this is largely due to new mandates from the Environmental Protection Agency regarding PM2.5 and potentially PM1.0 in coming years. Chemical analysis of aerosols becomes quite difficult at small sizes because the mass of material available for analysis decreases dramatically with size. Generally, particulate matter is collected on filters and analyzed using wet chemistry techniques that are costly and do not provide composition data in reasonable time frames for many applications. In addition, it is plausible that mixing and coalescence of particles during collection can change their chemical composition. To date, in situ techniques have been developed for small particles (down to 150 nm) based on ultraviolet laser ionization-mass spectrometry; however, laser ionization usually degrades the organic fraction in particles to the point where reconstitution of the chemical species is tenuous at best. These methods also are limited by low throughput, and the instrumentation required is large and expensive.

This project is an outgrowth of our research on membrane introduction ion trap mass spectroscopy and laser desorption. The previous work includes the development of an in situ method for the detection of iodine species in the atmosphere at concentrations of less than 1 ppb. The membrane provides an enhancement of 100 to 1000 in the ratio of the sample to atmospheric gases such as nitrogen, oxygen, and water vapor. The device was set up at our wind tunnel facility where it was used to study the fate and transport of iodine species in the atmosphere as part of DOE's nuclear nonproliferation program.

Although the use of membranes as a method for introducing samples into a mass spectrometer is not new, the application to sampling volatile and semivolatile inorganic species in situ was a novel approach. The ability of the membrane ion trap mass spectrometric method to detect semivolatile inorganic species in situ suggested the possibility of using laser desorption to

introduce low-volatility compounds into the gas phase for transport across the membrane to the mass spectrometer.

Results and Accomplishments

- We successfully demonstrated laser desorption membrane introduction ion trap mass spectroscopy using polyaromatic hydrocarbons.
- Constructed a semiautomated field device for acquiring filter samples.
- Adapted the membrane introduction ion trap mass spectroscopy device for field deployment in Houston.
- Deployed the combined filter and real-time gas-phase membrane introduction ion trap mass spectroscopy at TX2000AQS in Houston.

A schematic of the membrane introduction ion trap mass spectroscopy device for analysis of samples is shown in Figure 1. Semivolatile organics, such as polyaromatic hydrocarbons are placed into the gas phase by the laser pulse, pass through the membrane, and are carried into the mass spectrometer by a flow of helium. The instrument deployed in Houston collected the particulates on a filter for subsequent laboratory analysis. Three filter combinations were used in order to check for volatilization artifacts: Teflon, quartz, and Teflon followed by quartz. Each filter configuration was exposed to sample air alternately for 10-minute intervals over 4 hours. The air samples were passed directly through the membrane for real-time analysis of the gas-phase organics. The semiautomated field device is shown in Figure 2. A sample mass spectrum from Houston air is shown in Figure 3. The major components were found to be alkanes and alkenes by using the sequential mass spectrum capabilities of the ion trap system. These MS-MS scans also showed the presence of acetaldehyde. The higher weight compounds were not conclusively identified.

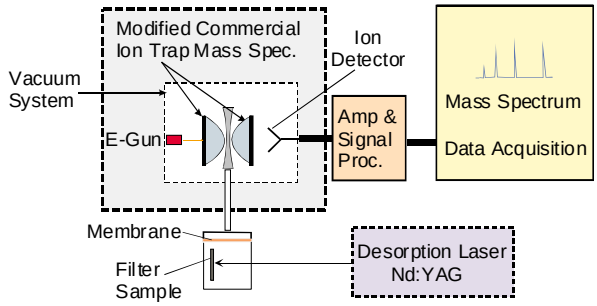

Figure 1. Schematic diagram of laser desorption membrane ion trap mass system

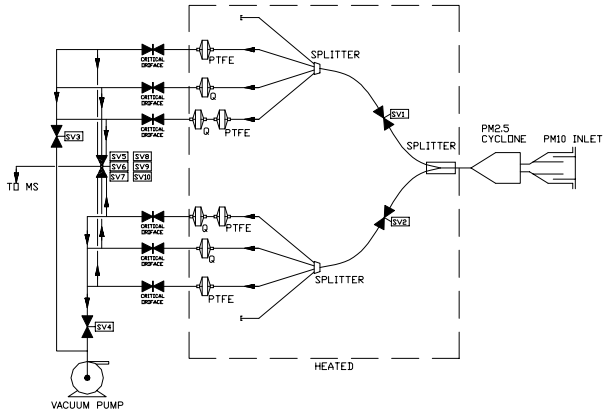

Figure 2. Schematic diagram of automated filter collection system deployed in Houston

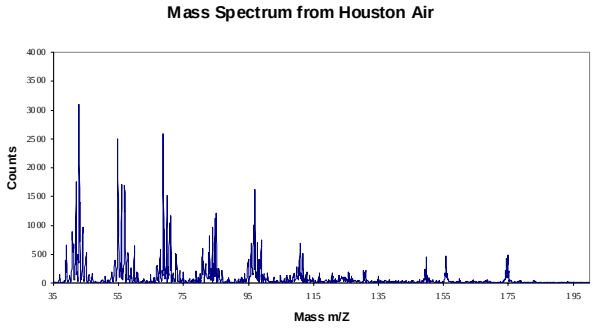

Figure 3. Sample mass spectrum of Houston air

Dynamics Studies of Surface-Induced Dissociation Processes

Anil K. Shukla, Jean H. Futrell

Study Control Number: PN00037/1444

The use of mass spectrometry for analyses of high mass ions is an area of increasing emphasis in analytical research due to the importance of high mass ions to such research areas as proteomics. However, the successful use of mass spectrometry to analyze high mass ions requires the development of new approaches and techniques. The purpose of this project is to gain a fundamental understanding of one such technique—surface collision-induced dissociation.

Project Description

Ion-surface collisions have long been used for characterizing and modifying surfaces. In recent years, with the introduction of new soft ionization techniques of electrospray and matrix assisted laser desorption, widely used techniques of collision-induced dissociation (ion-neutral gas collisions) do not appear to be efficient in dissociating very high mass ions. Several laboratories have demonstrated that ion-surface collisions can be used more efficiently than gas-phase collisions to dissociate impacting ions of high masses. Unfortunately, the basic understanding of the ion-surface collision phenomenon, especially of processes leading to dissociation of polyatomic ions of even low masses is not well understood. Questions remain regarding the role of the surface and its characteristics, ion characteristics, and physical phenomena, such as image-charge interaction potential, that must be answered before the technique can be universally applied on a routine basis. We are, therefore, building a prototype system where we will use well-defined ion beams (mass, energy, intensity, divergence, surface impact angle) and surfaces (tailored, self-assembled monolayers) for collisions and to monitor the mass, scattering, and energy of product ions from their reactions. We hope to determine, not only the necessary parameters, but also the mechanisms of energy transfer and dissociation phenomena in ion-surface collisions.

Results and Accomplishments

The unique instrument under development for the proposed research on the dynamics of surface-induced dissociation processes is shown schematically in Figure 1. The design of the instrument has been finalized and construction and assembly of the components inside the collision chamber are nearing completion. The first-stage mass spectrometer (JEOL, GCmate) for use as the mass and energy analyzed ion beam source for surface-induced dissociation experiments in the collision chamber was tested using a set of ions that are of interest for further studies. It is now being modified to interface with the collision chamber, and necessary ion optics to decelerate the ion beam to the desired lower collision energy have been constructed. An energy analyzer and quadrupole mass filter will be mounted on a rotator for angle- and energy-distribution measurements of secondary ions. Necessary electronics for the control of the experiment and data collection are being acquired.

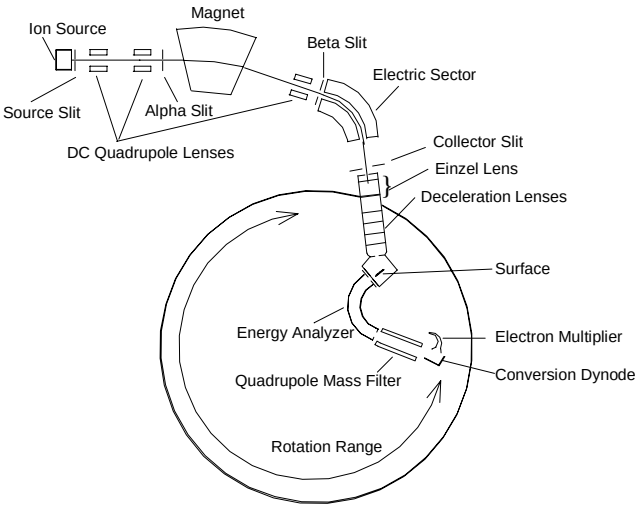

Figure 1. Ion-surface collision instrument

Tandem Mass Spectrometry of Nitrobenzyl Alcohols

The performance of the first-stage mass spectrometer was evaluated for stability and ion beam characteristics using isomers of nitrobenzyl alcohol. Using linked scans to determine their dissociation pathways, we observed that the nitro-nitrite rearrangement leading to the loss of nitrous oxide from the molecular ion is almost completely suppressed in ortho-nitrobenzyl alcohol. In meta- and para-nitrobenzyl alcohol, there is some evidence for this

arrangement, but the charge is retained by the breakaway nitrous oxide moity rather than the ring as normally observed in nitroaromatic ions. The dissociation pathways, determined using linked scans, show very different dissociation pathways for the three isomers.

Publications and Presentations

Shukla AK and JH Futrell. 2000. "Tandem mass spectrometry: Dissociation of ions by collisional activation." *J. Mass Spectrom*. 35:1069-1090.

Shukla AK, AD Sen, and JH Futrell. August 2000. "Surface-induced dissociation of ion: Bridging the gap between surface science and analytical mass spectrometry." 15th International Mass Spectrometry Conference, Barcelona.

Acknowledgment

We thank Julia Laskin for suggestions and helpful discussions, Mark Townsend for contribution to the ion optics components and thank John Price, Jim Follansbee, Jim Ikes for design and fabrication of the electronics components and data acquiring system. Support of David Lindgren as a summer intern under the Community College Initiative is gratefully acknowledged.

High Efficiency Chromatographic Separations for Support of Biological Warfare Threats for Law Enforcement Agencies

Jon H. Wahl, Bob W. Wright, Karen L. Wahl

Study Control Number: PN00049/1456

Biological warfare threats are of major concern to law enforcement agencies. MALDI-MS is emerging as a powerful tool for rapid fingerprinting and identification of bacteria. However, the actual individual components of bacteria, such as proteins that create these fingerprints, are typically unknown. Individual component identity is required for many reasons such as justifying fingerprint uniqueness or gaining a greater understanding of these threats. No single technique is capable of analyzing the range of proteins that are present in a typical biological warfare agent. Consequently, powerful new separation methods are required for their determination.

Project Description

The goal of this project is to develop high-efficiency separation instrumentation and methods required for the automated analysis and characterization of components comprising these biological fingerprints. This research involves development of multidimensional separation techniques to automatically separate, isolate, and identify proteins or peptides that are present in complex biological samples. The novelty of the proposed research involves the investigation and use of multidimensional separation strategies to increase the overall separation power that is required for the difficult and complex samples of biological warfare threats.

Introduction

At present, there is no one single experimental technique that is capable of analyzing the range of proteins that are present in a typical biological warfare agent (i.e., a single-cell bacterium). Bacterial proteins range in size between ~3000 Da and ~100 kDa, have differing hydrophobic and hydrophilic character, and vary in concentration. Consequently, the complete analysis of a very complex biological sample will require general methods with a different approach for specific questions. Presently, protein identification involves the separate, offline extraction and analysis of an individual solute "spot" using two-dimensional polyacrylamide gel electrophoresis (2-D PAGE), which is slow, cumbersome, and labor intensive. In many of these approaches, proteins are lost due to the lack of sensitivity to detect proteins in the lower concentration. Typically, 20% or more of the proteins are not observed. The difference between the most and least concentrated protein in a cell is approximately six orders of magnitude. Moreover, 2-D PAGE results from different labs are difficult to compare and sensitivity is limited by the amount of a protein needed to visualize a spot (typically ~10 femtomoles). Technology for rapid protein identification involves digestion of a protein mixture with subsequent mass spectral analysis of the peptide mixture (Burlingame and Carr 1996). From the obtained mass spectral data, a few unique ions are then cross-referenced to present-day protein library databases for possible matches. This approach works well for predicted or known proteins within the database, which may be problematic for biological warfare agents. However, if the desired protein is one that was not predicted, then an indepth and comprehensive analysis of the protein is required. Consequently, the individual protein or proteins must be separated to obtain accurate and reliable data.

Currently, multidimensional separations have the following advantages to address these issues: 1) multi-dimensional separations can be tailored to specific problems of complex sample analysis, 2) multi-dimensional separations provide the only means of obtaining adequate separation power to resolve the proteins from complex mixtures, 3) analyte funneling is possible where high analyte loading levels can be used to ensure that adequate levels of individual proteins reach the detector, 4) online multidimensional separations allow virtually 100% transfer of analyte from one stage to the next, and 5) multidimensional separations allow implementation of parallel separation stages for greater throughput.

Results and Accomplishments

Research efforts this year focused on installing and evaluating various separation configurations. Explicitly,

two liquid chromatographic gradient systems were purchased and installed. With these gradient systems, various multidimensional strategies and layouts were examined and "valved" together, including a two-column, two-valve and a single-column, single-valve approach for interfacing to the second-dimension separation. The single-column approach was chosen as the final configuration because of the greater reproducibility of the separations. Preliminary separations during this initial system evaluation included lysed *Bacillus subtilis* cells and the supernate from *Escherichia coli* cells that were soaked in 0.1% trifluoroacetic acid to release various proteins. These separations involved two-dimensional comprehensive assays of anion exchange chromatography times reversed-phase liquid chromatography. From this initial work, a breadboard multidimensional system was configured. Using this configured multidimensional chromatographic system, hydrophobic interaction chromatography was investigated as an option for one of the preliminary dimensions prior to reversed-phase liquid chromatography. Multidimensional separations were performed for *E. coli, B. atrophaeus B. subtilis var niger* cell lysates.

Figure 1 illustrates a typical two-dimensional separation obtained for lysed *E. coli* cells. The individual spots represent separated proteins. In comparison to Figure 2, which is a one-dimensional separation of the same *E. coli* sample, the separation from the two-dimensional approach is much more complete. This overall system includes the two gradient liquid chromatographic pumps, the valving system for the separations within a heated zone, dual fraction collectors for MALDI-MS detection, ultraviolet, and visible light detection, and integrated computer control of the separation system and data acquisition.

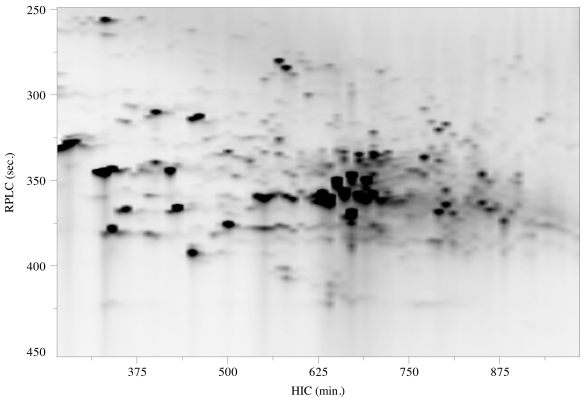

Figure 1. Two-dimensional chromatogram of *E. coli* lysate. First dimension was hydrophobic interaction chromatography, second dimension was reversed-phase liquid chromatography.

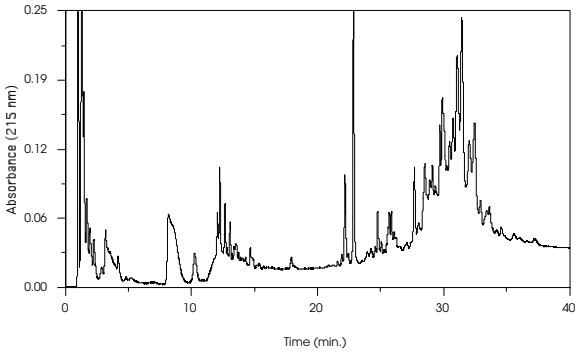

Figure 2. One-dimensional reversed-phase liquid chromatography chromatogram of *E. coli* lysate

To decrease the sample complexity and to facilitate interfacing to the MALDI-MS, an additional liquid chromatographic system was set up. This system is capable of gradient elution and on-line fraction collection directly onto a MALDI plate. The liquid chromatographic system is computer controlled and is programmed for automated sample collection directly onto a MALDI plate. This system is used to examine the various proteins that are released into the supernate from *E. coli, B. atrophaeus B. subtilis var niger* cells that were soaked in 0.1% trifluoroacetic acid (Figures 3 and 4). Figure 3 illustrates the reduced sample complexity that is obtained when whole cells are soaked in the 0.1% trifluoroacetic acid solution compared to Figure 2. Although the number of proteins that are released is fewer compared to a lysed sample, biomarkers that are unique to the MALDI fingerprinting are obtained as shown in Figure 4. During these experiments, the operation of the MALDI mass spectrometer was automated for data collection. This allows unattended data collection of 100 samples overnight.

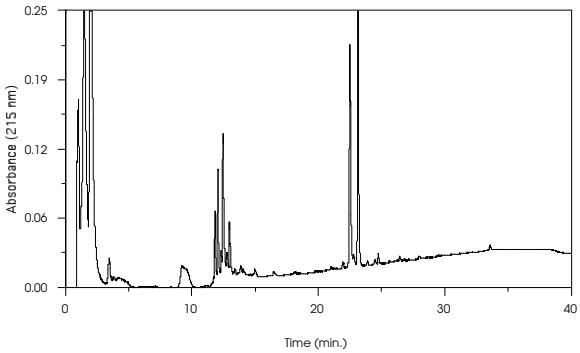

Figure 3. One-dimensional reversed-phase liquid chromatography chromatogram of supernate from *E. coli*, cells that were soaked in 0.1% trifluoroacetic acid

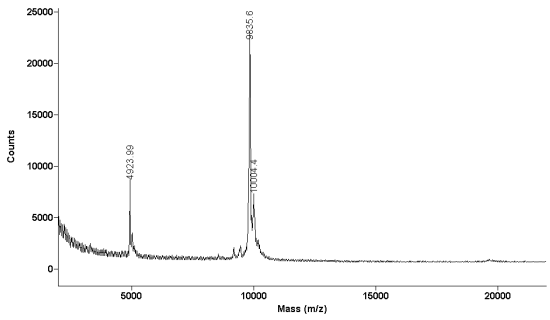

Figure 4. MALDI mass spectra obtained from chromatogram shown in Figure 3

Summary and Conclusions

The results shown and discussed in this report demonstrate important findings. Multidimensional separations are clearly an ideal method to provide the sample capacity that is required for performing both trace and percent level concentration separations, while providing the required peak capacity. Work is under way to increase the throughput using parallel separation strategies. These results represent encouraging progress toward the goal of achieving a completely on-line and automatic multidimensional system for the comprehensive analysis of complex protein mixtures identical to those produced from cell lysates.

Reference

Burlingame AL and SA Carr, Eds. 1996. *Mass spectrometry in the biological sciences.* Humana Press, Totoua, New Jersey.

Integrated Microfabricated Devices for Rapid and Automated Identification of Biological Agents

Yuehe Lin, Keqi Tang, Richard D. Smith, Dean W. Matson

Study Control Number: PN98039/1285

There is an enormous need for highly rapid and sensitive identification of microorganisms across a spectrum of research areas, as well as in medicine and in clinical applications where there often is no available technological solutions to provide the desired speed and reliability. The new technology developed from this project would find broad applications in biological and medical research, as well as forensic and clinical applications, pathogen detection, and would also advance DOE's interest in biological research and bioremediation.

Project Description

This project involves the development and evaluation of novel integrated microfabricated devices for the rapid and automated identification of biological agents (pathogens) and other medical and biological applications. Microfabricated devices were developed for the rapid fractionation and processing of small biological samples (micro-biopsies). These integrated devices were interfaced directly with mass spectrometers for analysis of cellular components from complex matrices (cell lysates) for identification of biological agents based upon the detection of specific constituents ("biomarkers"). This work will develop PNNL's capability in the Bio-MEMS area and provide a powerful tool for environmental health research at the molecular level.

Introduction

During fiscal year 1998 and fiscal year 1999, we successfully demonstrated on-line sample cleanup, separation, and concentration of complex biological samples (cell lysates) using microfabricated dual-dialysis and isoelectric focusing devices. In fiscal year 2000, we continued to modify and improve the design of these components. The microfabricated dual-dialysis device, combined with global ESI-MS/MS, was tested for use in the characterization of microorganisms and biomarkers. Specifically, the application of this method for detecting the bacteriophage MS2 in the presence of a large excess of *E. coli* was successfully demonstrated.

Results and Accomplishments

To expand the capability of microfabricated analytical devices and allow for high-throughput parallel sample processing, plastic microchips containing arrays of laser-micromachined electrospray nozzles were developed. These micronozzle arrays will be key components for directly interfacing microfluidic sample separation and cleanup devices with mass spectrometers.

The micronozzle arrays were fabricated from 1-mm thick polycarbonate sheet material using PNNL's Resonetics Maestro UV excimer laser micromachining station. All machining was performed using a Lumonics 848 excimer laser operating at 248 nm. Through-holes were first machined at a high demagnification factor (~35 times) using a small circular mask in the laser beam. The laser demagnification was then reduced to approximately five times and a well was machined around the nozzle outlet. Because of the inherent taper of the laser at low demagnification factors, the nozzle tips produced by this method had a conical cross section recessed into the end of the chip. The openings of these micromachined nozzles were flush with the end of the polycarbonate chips, thereby reducing susceptibility to breakage or other damage.

When the laser-machined micronozzle arrays were tested for electrospray formation and stability, it was observed that under a variety of conditions the solution exiting the hole rapidly moistened the edge surface of the nozzle. This wetting prevented the formation of a well-focused electric field essential for the generation of a stable electrospray. To inhibit the wetting process, the surfaces of the polycarbonate microchips were treated with CF_4 RF plasma. After this plasma treatment, the surface property of polycarbonate chip was changed from hydrophilic to hydrophobic. The increased hydrophobicity of the treated polycarbonate surface prevented the sample solution from spreading over the edge surfaces of the nozzles and helped to focus the electric field at the surface of the liquid exiting the channel. Stable electrospray was

directly generated from the microchip without the use of a nebulizing gas. The microelectrospray nozzle array provides a reproducible, controllable, and robust means of producing electrospray of a liquid sample from a plastic microchip.

One application of microfabricated multi-electrospray arrays is to enhance the sensitivity of mass spectrometry. A microfabricated electrospray array was used as an ionization source and was interfaced with a heated multicapillary inlet and an electrodynamic ion funnel. The inlet was constructed from an array of seven thin-wall stainless steel tubes soldered into a central hole of a cylindrical heating block. An electrodynamic ion funnel was used in the interface region to more effectively capture, focus, and transmit ions from the multicapillary inlet. As indicated in Figure 1, the multi-microelectrospray arrays generated higher ion density compared with single electrospray generated from a fused silica capillary.

Microfabricated capillary electrophoresis devices were also fabricated on polycarbonate substrates. A microelectrospray nozzle was laser-machined from the exit of the separation microchannel. This design simplifies the fabrication of capillary electrophoresis chips and eliminates the dead-volume between the microchip and a mass spectrometer.

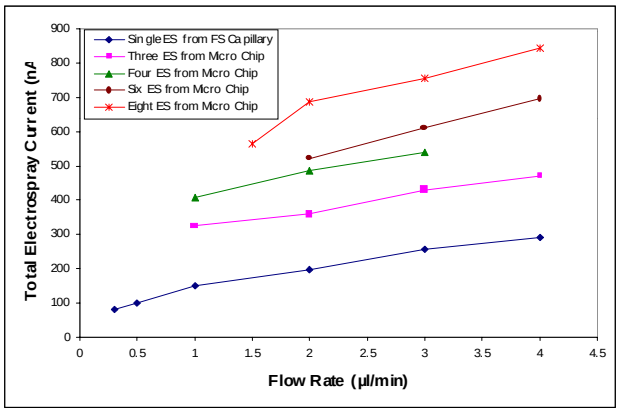

Figure 1. Total spray current versus liquid flow rate for multi-electrosprays generated from microfabricated nozzle arrays using 50:50 methanol : water + 1% acetic acid

Future developments include coupling microchip-based sample cleanup and separations using the laser-micromachined microchips to provide high-throughput sample processing/mass spectrometric characterization of microorganisms.

Publications and Presentations

Lin Y, DW Matson, DE Kurath, J Wen, F Xiang, WD Bennett, PM Martin, and RD Smith. 2000. "Microfluidic devices on polymer substrates for bioanalytical applications" in: *Microreaction Technology:Industrial Prospects*. W. Ehrfeld, ed., pp. 451-460. Springer-Verlag.

Wen J, Y Lin, F Xiang, D Matson, and RD Smith. 2000. "Direct electrospray from microfabricated isoelectric focusing devices for ESI mass spectrometry." *Electrophoresis,* 21:191-197.

Xiang F, GA Anderson, TD Veenstra, MS Lipton, and RD Smith. 2000. "Characterization of microorganisms and biomarker development from global ESI-MS/MS analyses of cell lysates." *Analytical Chemistry*, 72:2475-2481.

Tang K, Y Lin, DW Matson, T Kim, and RD Smith. "Generation of multiple electrosprays using micro fabricated emitter arrays for improved mass spectrometric sensitivity." *Analytical Chemistry* (submitted).

Lin Y, K Tang, D Matson, and RD Smith. May 2000. "Integrated microfluidic device for rapid identification of microorganisms." The First DOE Biomedical Engineering Meeting, Albuquerque, New Mexico (invited presentation).

Lin Y. August 2000. "Microfabricated devices for bioanalytical applications." University of Idaho, Moscow (invited presentation).

Lin Y, K Tang, P Martin, DW Matson, and RD Smith. September 2000. "Microfluidic devices for rapid sample processing/mass spectrometric characterization of proteins." BioMEMS & Biomedical Nanotechnology World 2000, Columbus, Ohio.

Matrix Assisted Laser Desorption/Ionization Using Resonant Laser Ablation

Gregory C. Eiden

Study Control Number: PN98046/1292

Matrix assisted laser desorption/ionization (MALDI) provides an unparalleled capability to characterize large molecules, both naturally occurring and synthetic, and has found widespread application in the life sciences and materials analysis. Our work has pointed the way to a new approach in MALDI that will enable the characterization of materials that could not previously be detected by MALDI, as well as a new way to characterize the mechanistic components of MALDI ion formation processes.

Project Description

We have developed a new approach to generating matrix assisted laser desorption/ionization (MALDI) mass spectra of large molecules, especially those that have traditionally been difficult to observe by MALDI. While the focus has been MALDI detection of synthetic polymers, this work will impact MALDI more broadly by enabling polypeptide and nucleic acid MALDI. Our short-term interest has been in improving MALDI by making the ionization of analyte molecules more selective and efficient using resonant ionization of selected elements in the prepared sample. This is in contrast to the conventional non-resonant MALDI process using fixed wavelength lasers, typically the 337 nm nitrogen laser. The cations formed are chosen for the specificity of their gas-phase reactivity with the analytes of interest. The desired reactivity can be simple adduct formation when a spectrum of parent molecules is needed (weight distribution measurement of a polymer) or fragmentation when structural information is needed. Using resonant ionization, the ion yield is controllable independently of the ablation yield. By choosing different metal cations, different gas-phase reactions are selected. We thus gain independent control over the plume density (via the ablation rate), the reagent (metal) ion density, and the gas-phase chemistry. By controlling these factors, most of the processes leading to ion formation can be controlled or at least manipulated. Our longer-term interests focus on understanding the ionization mechanism in MALDI experiments other than synthetic polymers.

Introduction

Measurements of metal cation reactivity are conveniently made using a plasma source-ion trap mass spectrometer. Reaction conditions in the trap are drastically different from those in the laser plume—ion and neutral temperatures differ, as well as number density, collision rates, and other factors—however, the reactivity trends established from ion trap data are useful in guiding the choice of metal species in the resonant laser ablation MALDI experiments.

This project is being conducted in collaboration with a team external to PNNL. Those members of the team are Dr. Kevin G. Owens of Drexel University (Philadelphia, Pennsylvania), Dr. Scott D. Hanton of Air Products and Chemicals, Inc. (Allentown, Pennsylvania), and Dr. Robert J. Noll of Lawrence University (Appleton, Wisconsin).

Results and Accomplishments

At Drexel University, we successfully demonstrated several combinations of polymer and metal salts that yield MALDI or laser desorption mass spectra using a single tunable dye laser pulse for both matrix desorption and metal ionization. Examples include copper with polystyrene-2450 and silver with polystyrene-1250. Although we have observed resonance effects (stronger MALDI adduct signals with the laser tuned to the metal atomic resonance), the highly variable nature of MALDI ion signals makes it difficult to quantify the degree of resonance enhancement.

At PNNL, ion trap reaction studies were made for numerous metal cations reacting with selected small organic molecules. We compared the reactivity of n-octane versus 2,2,4-trimethylpentane with the following metal cations: Sc^+, Ti^+, V^+, Cr^+, Mn^+, Ni^+, Co^+, Cu^+, Zn^+, Y^+, Zr^+, Mo^+, Ag^+, and U^+. Some of these choices were dictated by prior knowledge of metal cation reactivity in beam studies, e.g., propane + Ni^+ reactivity, or from prior work where certain metals were reported to enhance adduct formation in polymer MALDI (polystyrene +

Ag^+). We measured ratios of adduct ion intensity to elimination product ion intensity. In this way, we have been able to identify promising candidates for measurement of parent ion spectra using adduct forming ions versus candidates for fragmentation studies using cations whose reactions involve extensive elimination. We have made similar measurements for n-decane, but we cannot presently measure reagent gas pressure accurately in the ion trap used, so that only a qualitative comparison of the trimethylpentane and n-decane data can be made. Comparisons of metal cation reactivity with a given reagent gas are much more reliable. Thus, for example, we observe nearly identical (and extensive) fragmentation patterns for Ni^+ and Co^+ reacting with either of the organic reagents. Based on our observations, we chose V, Cu, and Ag as metals most likely to result in formation of a polymer-metal ion adduct, rather than an extensively fragmented product ion. For reasons that are as yet not understood, only the Ag was successful in yielding useful adduct signal in the resonant laser ablation MALDI experiments. One possible explanation for the failure of V and Cu might be in the resonant laser ablation cation yield from the metal compounds used (VAcAc and CuTFA), n.b., resonant laser ablation yields depend on the chemical state of the metal and obviously so, since the resonant laser ablation process seeks to excite ground state, gas-phase atoms. Experiments to address this issue have been identified and will be pursued. We will also measure absolute reaction rates for each of these reagents with various cations and thereby obtain an absolute basis for comparison not only among various ion trap experiments, but also with resonant laser ablation MALDI data.

In our work, combining resonant laser ablation with an otherwise conventional MALDI experiment, we have partially characterized the wavelength and extraction delay dependence of the observed signal. When the ions are extracted from the time-of-flight source region immediately (<50 nsec) after the laser fires, there is insufficient time for extensive reaction of the ions with neutrals in the plume. If the delay is too long, ions will drift out of the source region due to their nascent kinetic energy and possibly due as well to weak fields leaking from the second acceleration zone. In addition to this reaction time effect, the resolution of the time-of-flight depends on the extraction delay. However, over a reasonably broad range of delay times, the ion collection efficiency and thus peak areas are sensibly constant. Most of the change in the observed peak areas can be ascribed to reaction time rather than ion collection efficiency. Given the modest range of reaction times that we can access in the resonant laser ablation MALDI experiment while retaining useful signal, this parameter is most likely to be used primarily to aid mass spectral peak assignment, rather than as a means for improving the analytical utility of the method.

MALDI Ionization Fundamentals

Obviously, a key element of the MALDI experiment is the ionization step. Unfortunately, little detailed investigation of the ionization mechanism has been reported and explanations for the successes and failures of MALDI are typically phenomenological. Ionization in MALDI has been ascribed to direct ion and excited species production from the surface of the sample, to photoexcitation or photoionization processes in the desorbed plume, and to various energy, charge, and atom transfer processes occurring in the desorbed plume. Different analytes containing different functional groups are amenable to different ionization pathways. In polymer MALDI, analyte ions are thought to be created through cationization reactions in the desorption plume shortly after the laser beam strikes the target. These cationization reactions commonly include alkali cations associating with oxygen functional groups, protons associating with more basic nitrogen functional groups, and various transition metal ions such as copper (I) and silver (I) associating with the double bonds in unsaturated hydrocarbon analytes. The simple inclusion of the appropriate metal species in the sample usually suffices to effect cationization. However, in nearly all cases, the mechanisms proposed have been established or suggested using circumstantial evidence and sometimes ignoring important features of the observations. An example of the latter is the early observation of a very high order dependence of the MALDI ion signal on laser intensity, suggesting a highly nonlinear process (or coupled processes) leading to ionization. However, nearly all subsequent work seeks to explain the photon dependence of the MALDI ionization process in terms of single-photon or two-photon excitation processes.

Molecular Beam Synthesis and Characterization of Nanoporous Catalytic Materials

Greg A. Kimmel, R. Scott Smith, Bruce D. Kay

Study Control Number: PN00070/1477

Materials with properties tailored to meet specific requirements are increasingly important in the development and refinement of new technologies. For the successful development of new materials for chemical applications, characterization of the uptake, reactivity, and release of gases by new materials is essential. We have used molecular beam techniques to grow and characterize complex materials with unique properties for chemical applications.

Project Description

We have used the state-of-the-art molecular beam capabilities in the EMSL to synthesize and characterize nanoporous films, a class of very high-surface-area materials with important potential applications in chemical sensors, catalysis, and hydrogen storage. Typically, molecular beam technology has been used to produce thin, layered structures in two-dimensional films. Three-dimensional structures are then fabricated by lithography (for example). We used molecular beam techniques to grow and characterize complex materials with unique properties for chemical applications. Recent work in several laboratories, including our own, has demonstrated that the morphology of thin films grown by vapor deposition depends strongly on the angular distribution of the molecules incident from the gas phase. While a broad class of nanoporous materials has been synthesized using this method, the rational design of these materials for specific applications is in its infancy. Furthermore, beyond examining the structure, very little work has been done to characterize the physical and chemical properties of these novel materials. Specifically, virtually nothing is known about the rates and mechanisms of adsorption, diffusion, and reaction of gases in these materials. Research in this area is germane to DOE initiatives, such as nanotechnology and carbon management. This project has demonstrated our proof-of-principle capability in nanoporous catalyst synthesis and characterization.

Introduction

The physical and chemical properties of many technologically relevant materials, such as surface area, porosity, thermal conductivity, refractive index, and catalytic activity, are intimately related to the morphology (structure) on a nanometer scale, so controlling the morphology of materials on this scale has important implications for many technologies. In the past few years, it has been demonstrated that the nanometer scale morphology of a number of materials grown by vapor deposition depends strongly on the angular distribution of the incident molecules. Recently, we have shown that even the morphology of low melting point molecular solids such as amorphous water ice can be controlled in this fashion (Stevenson et al. 1999). In this project, we used a collimated beam to grow nonporous to highly porous amorphous materials. We were able to grow porous amorphous solid water with very high surface areas. Collectively, these findings show that our process can be used to control the morphology of a wide range of materials classes including metals, semiconductors, oxides, fluorides, and molecular solids.

A simple physical mechanism, ballistic deposition, can be used to understand our project results. The basic premise of ballistic deposition is that molecules incident from the gas phase stick at the first site they encounter at the surface of the solid without subsequent diffusion. Therefore, by controlling the process we can control the morphology of the film. To make a useful catalytic material, the chemical composition of the nanoporous material must also be controlled. For example, one could potentially simultaneously control the oxide pore structure and the location of the catalytically active metal site during synthesis.

The interaction of gases and fluids with these nanoscale films forms the basis for a variety of useful applications of these materials. For example, the rates of uptake, sequestration, reaction, and release of gases in these materials often determines their performance characteristics in devices such as catalysts and chemical sensors. A detailed understanding of the relationship between these kinetic processes and the morphology of the material is lacking. For these materials, the transport

of reagents through the pores and the catalytic reactions are intimately coupled. Molecular beams have historically been used to study heterogeneous kinetic processes on nonporous materials. However, molecular beam techniques are also ideally suited to study the coupled transport/reaction processes occurring in nanoporous materials. Understanding these processes is essential for the rational design and synthesis of materials for particular applications.

Results and Accomplishments

The morphology of thin nanoporous magnesium oxide (MgO) films, deposited under ballistic deposition conditions, was characterized using scanning electron microscopy (SEM). The SEM micrographs of films grown at room temperature on a Si(100) substrate using a directed beam of Mg in a background pressure of O_2 ($\sim 1\times10^{-5}$ torr) are shown in Figure 1. Rather compact films with small pores are shown in Figure 1a. This sharply contrasts with the films shown in Figure 1b where the individual MgO filaments are separated by large voids. These two images demonstrate the ability of our process to control film morphology and confirm the conclusions from our previous study of the porosity of amorphous solid water films (Stevenson et al. 1999). We have also shown that the growth morphology of MgO thin films is very similar on other substrates such as Si(111) and glass.

For the purposes of chemical characterization, we have grown thin (< 50 nm) MgO films on an atomically clean Mo(100) substrate in our ultrahigh vacuum molecular beam scattering apparatus. The films were deposited under conditions analogous to those shown in Figure 1. The surface area and the surface adsorption energies were characterized using the adsorption of N_2 monolayers. The physisorbed N_2 monolayer is desorbed by linearly increasing the substrate temperature as shown in Figure 2. The desorption spectra obtained from a porous MgO film grown at a deposition angle of 85 degrees and substrate temperature of 200 K is shown with a solid line. The area under the desorption curve is a measure of surface area and can be directly compared with the curve corresponding to the N_2 adsorbed on flat, highly ordered MgO(100) film (thin solid line). This comparison yields a surface area that is substantially higher than the surface areas of traditional catalytic materials. The broad

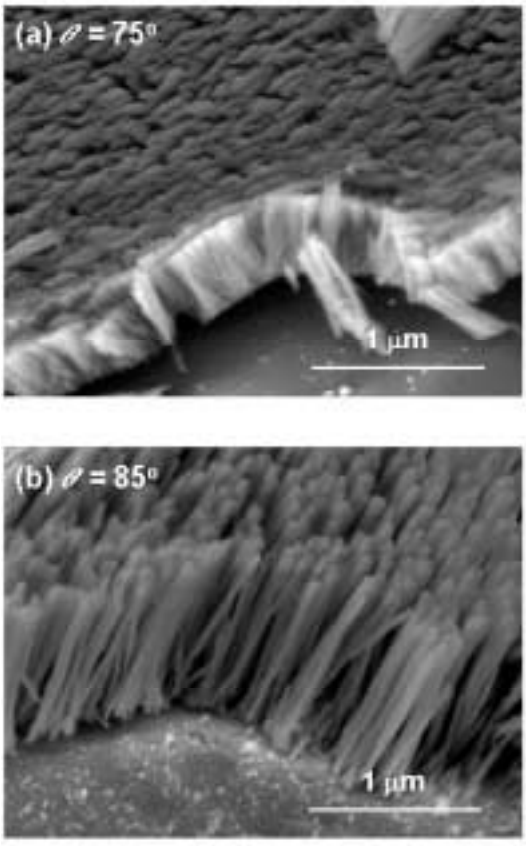

Figure 1. SEM images of nanoporous MgO films deposited on a Si(100) substrate at 300 K. The deposition angle of Mg beam with respect to the substrate normal is 75° and 85° for Figures 1a and 1b, respectively.

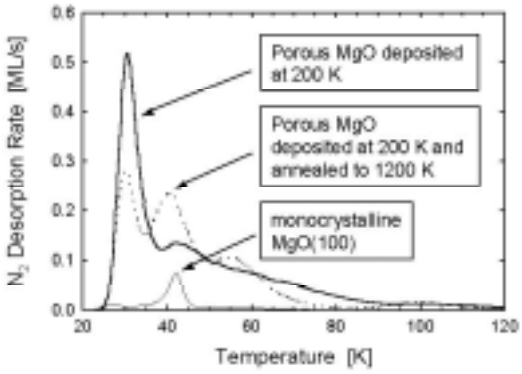

Figure 2. Temperature programmed desorption of N_2 monolayer from 25 mL thick MgO films. Solid line—nanoporous film grown at deposition angle of 85° and temperature of 200 K, dotted line—same film after further annealing at 1200 K, thin solid line—dense monocrystaline film grown at 0° and 600 K.

temperature distribution of the desorption states indicates a wide range of different surface binding sites. The dotted line shows the N_2 desorption from the same film after annealing. The area under the desorption curve is comparable to that of the as-grown film showing that the annealing did not cause substantial loss of the film surface area. The high temperature annealing changes the ordering and the binding properties of the surfaces.

Summary and Conclusions

We have demonstrated the capability to grow thin nanoporous MgO films with high surface areas. The morphology of the films can be controlled by varying the preparation parameters. Prepared films are thermally stable upon annealing. At high temperatures, changes in the ordering and binding properties of the surfaces occur.

Reference

Stevenson KP, GA Kimmel, Z Dohnálek, RS Smith, and BD Kay. 1999. "Controlling the morphology of amorphous solid water." *Science* 283, 1505.

Native Aerosols: Their Composition, Distribution, Reactivity, and Coupling to Tropospheric Chemistry

Alexander Laskin, James P. Cowin

Study Control Number: PN99051/1379

Atmospheric particles are increasingly cited as being potentially harmful to human health and as playing a major role in the regional pollution chemistry of gases like ozone. In this project, we field-deployed a new device to better characterize these particles and track their sources.

Project Description

Atmospheric particles, whether the result of regional pollution, crop burning, distant dust storms, or local activities like tank maneuvers at an army base, have air chemistry and health implications that depend on the particular mix of particle compositions present. Most existing methods of particle analysis are too poorly time-resolved (hours or days) to follow the evolution of these mixtures, and give typically only gross average particle composition. The Laboratory developed a novel automated Time-Tagged Particle Sampler that can take thousands of samples of particles in the field and preserve this archive for intensive, single-particle analysis in the lab.[(a)] The purpose of this project was to prepare the lab-prototype for actual field work, and then to demonstrate its utility by successfully carrying out a significant field study. We have, to date, made the device field-portable, tested it as a mobile analyzer (sampling from a moving automobile), and most notably, have used it to take thousands of samples as part of the extensive Texas 2000 Air Quality Study (August 15 through September 15, 2000) in Houston. These samples are currently being analyzed.

Introduction

Typical atmospheric particles span the size range from 0 to several microns, with a preponderance (area or mass weighted) between 0.1 and 1 micron. The particles present are almost always a heterogeneous group, including (often simultaneously) many minerals from soil dust; tire wear dust; ash from distant burning; fly-ash; soot from diesel exhaust; sea salt from wave spray; industrial dust from processing, grinding, and wear; and particles derived from atmospheric gases (or coated by them) such as ammonium nitrate, ammonium sulphate, sulfuric acid droplets, and photochemical smog tars. At a fixed site, the number and composition of aerosols can vary rapidly on the scale of 10 minutes (see Figure 1), while air sampled from a moving airplane can vary on the 1-minute time frame or less. Because the health or regional pollution chemistry effects are nonlinear functions of concentration and particle types, composition averaged over long times or over all particles is not adequate to predict the particles health or pollution chemistry. Existing methods are not satisfactory (McMurry 2000; Chow 1998), and new approaches are needed. Time-resolved single particle analysis in the field using a mass spectrometer with an aerosol inlet is one such new development (Seuss 1999), but these "field instruments" are very large, expensive, and difficult to operate.

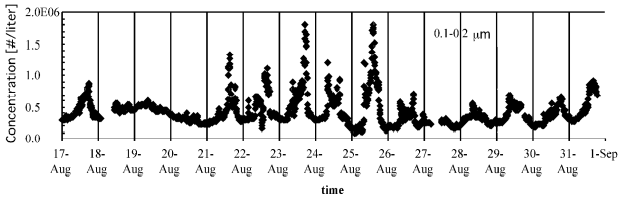

Figure 1. Particle concentration measured during first 2 weeks of Texas 2000 study (Houston), in 0.1 to 0.2 micron size range by optical particle counter. Vertical lines mark each midnight, each dot is 10-minute average, 1960 points shown.

We chose instead to refine field-sampling approaches and optimize single particle analysis in the lab. The new aerosol characterization technology allows field collection and analysis of aerosol properties with unprecedented time resolution (1 minute) and the ability (through automated individual particle analysis) to determine the specific mix of materials making up the particles. This will much better determine the source of the particles and allow better prediction of their chemistry and health effects. These are revolutionary capabilities that are

(a) See related article on "Ultrasensitive Studies of Reactive Aerosols," James Cowin, Stephen Joyce, and Stephen Barlow, in this annual report.

expected to result in significant advances in our ability to develop predictive tropospheric air quality models.

Approach

The particle collector was largely developed under another LDRD project (Cowin et al. LDRD program in Ultrasensitive Studies of Reactive Aerosols, 1999-2000), and is only briefly described here. Figure 2 shows it in its present form. Air at 1 liter per minute is pumped through a nozzle, which deposits on substrates most of the particles larger than 0.25 micron, and a useful fraction of those down to 0.1 micron. The substrate tray shown holds 177 samples. The tray is scanned by a laptop computer-controlled drive at preplanned intervals. When deployed, we typically run a commercial laser-particle counter in parallel with it, to help recognize priority times to analyze.

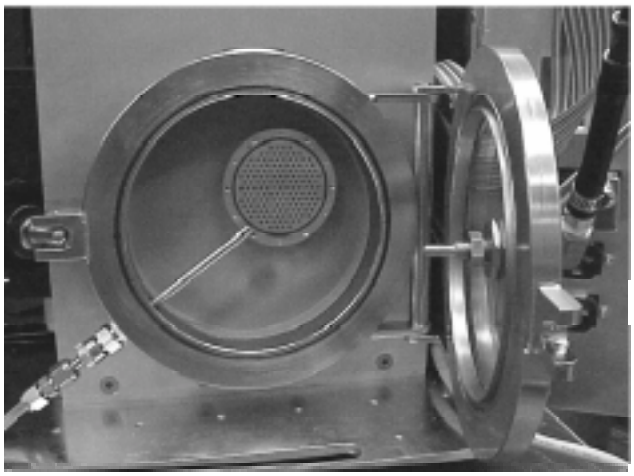

Figure 2. Time-tagged particle collector, shown with chamber open. In the chamber is a sample tray with 177 samples, in the door at left is a particle deposition nozzle.

Results and Accomplishments

Automated Analysis

Many thousands of particles need be examined. For this we installed commercial software (DiskInspector for Oxford Instruments) to run a scanning electron microscope. This permits fully automated analysis of about 10,000 particles every 24 hours. Typically this kind of analysis has been considered feasible only for the largest particles (> 1 micron). Through various innovations, we are able to achieve excellent results down to 0.2 micron, and useful results to 0.1 micron. A typical x-ray analysis of a small particle from our automated analysis is shown in Figure 3.

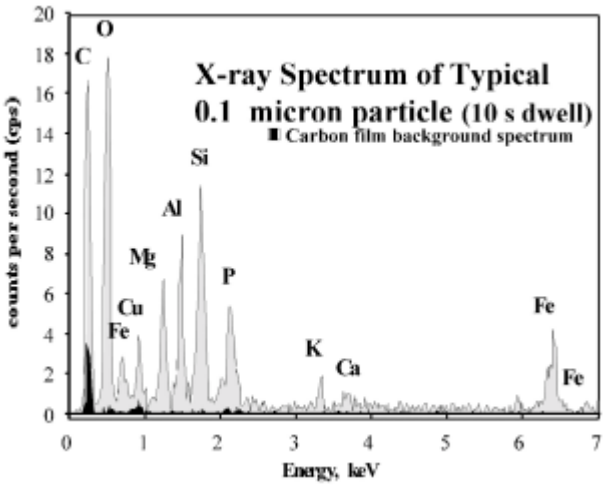

Figure 3. Typical x-ray of small atmospheric particle, showing excellent elemental analytical results and small background

Validation of Analysis

We demonstrated the validity of the analysis by examining a dozen or so different kinds of laboratory generated aerosols of known composition. Figure 4 shows results for a particular sulfur containing organic aerosol. Generally the results are excellent down to 0.2 micron and useful to 0.1 micron (Laskin 2000).

Mobile Platform

To demonstrate the mobility of our collector, we made two, 3-hour field trips with the collector mounted in a standard car, powered from the cigarette lighter outlet, taking samples every 2 minutes. We drove on exceedingly rough dirt roads, on highways, and up mountains, and found the device adequate to the task. The collector also can be flown in an airplane.

Houston Field Study

A large atmospheric pollution study was conducted from August 15 to September 15, in Houston, Texas. This Texas 2000 Air Quality Study was an excellent opportunity to test the device and allow for comparisons against other particle methods. We collected over 3000 samples at the William's Tower site.

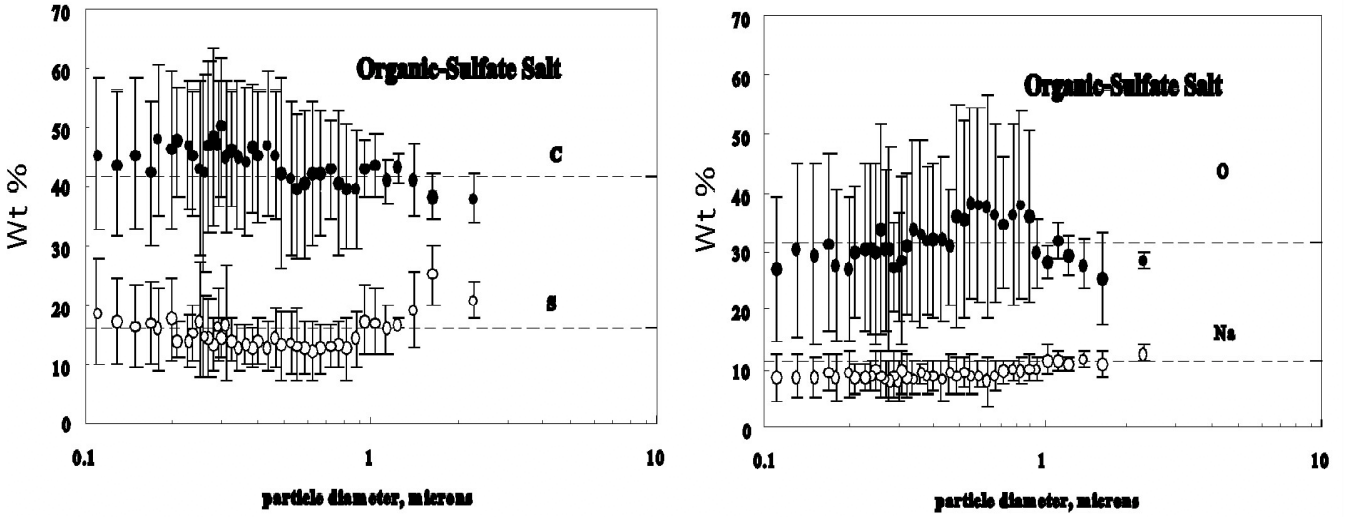

Figure 4. Automated analysis results for a semivolatile organic. The substance is anthraquinone-2,6-disulfonic acid disodium salt, which contains C, S, O, and Na. Plotted is the average composition for each particle bin, binned after individual analysis, compared to the nominal values (dashed lines). These organic particles are considered difficult to analyze due to their susceptibility to beam damage, low contrast in the SEM images, and low atomic mass, yet the analyses we achieve are semiquantitatively (±15 % units of scatter) useful down to about 0.1 micron, even for C and O.

Summary and Conclusions

The particle sampler was successfully turned into a field device. Its analytical validity was tested through laboratory analyses of many particle samples. It was successfully deployed in a major field study.

We plan to continue to analyze and publish results from the Houston field study. Other field studies also will be pursued.

References

Chow JC and JG Watson. 1998. *Guideline for speciated particle monitoring*, esp. Chapter 5, "Measurement Artifacts and Interferences." U.S. Air Quality Planning and Standards Report, U.S. Environmental Protection Agency, Washington, D.C.

McMurry PH. 2000. "A review of atmospheric aerosol measurements." *Atm. Envir.* 34:1959-1999.

Seuss DT and KA Prather. 1999. "Mass spectrometry of aerosols." *Chem. Rev.* 99:3007-3035.

Publication

Laskin A and JP Cowin. "Automated single particle scanning-electron-microscopy/energy-dispersed-x-ray analysis of submicron particles down to 0.1 micron." *Analytical Chemistry* (submitted).

Surface-Induced Dissociation of Polyatomic Cations

Anil K. Shukla, Julia Laskin, Eduard V. Denisov, Jean H. Futrell

Study Control Number: PN99069/1397

Mass spectrometry for analyses of high mass ions is an area of increasing emphasis in analytical research because of the importance of high mass ions to such research areas as proteomics. Ion cyclotron resonance mass spectrometers have particular relevance to these analyses because of their unique capability to collect all the ions up to high masses at extremely high resolution and quantitatively monitor reactions over the time range from microseconds to seconds. The purpose of this project is to develop a novel optimized surface collision activation ion cyclotron resonance prototype that will provide information on the reactivity and thermochemistry of high mass ions.

Project Description

A number of studies have shown the applicability of ion-surface collisions leading to the dissociation of ions as an efficient and attractive alternative to normally used ion-neutral gas collisions in analysis and structural characterizations. Most of these studies have used sector and quadrupole mass analyzers for this purpose, where scattering losses and slower dissociation (~10 to 50 microseconds) contribute significant uncertainties in the intensity measurements. Ion cyclotron resonance mass spectrometers have the unique capability of collecting all the ions up to very high masses at extremely high resolution and quantitatively monitoring reactions over the time range from microseconds to seconds. Since the resolution in ion cyclotron resonance is directly related to the background pressure, gas phase collisions drop the effective mass resolution by several orders of magnitude. This complication is bypassed with surface rather than neutral collisions. Development of an optimized ion cyclotron resonance surface collision activation instrument, therefore, enables the determination of complete activation and dissociation processes including step-wise ion dissociation. We propose to build an ion cyclotron resonance system using a 7-tesla superconducting magnet with capabilities to introduce mass-selected, energy-relaxed ion beams inside the ion cyclotron resonance cell, where it can be reacted with a well-defined surface to determine all fragmentation processes simultaneously. We have developed procedures to determine kinetic energy of ions and model ion intensity distributions to estimate internal energy distributions of all fragment ions. We hope that a combination of all these techniques, if successful, will provide us additional information on the reactivity and thermochemistry of high mass ions.

Results and Accomplishments

The instrumentation for Fourier transform ion-cyclotron resonance mass spectrometer using a 7-tesla superconducting magnet was developed. The vacuum chambers, electrospray source with a hydrodynamic ion funnel, mass selection by radio frequency direct current quadrupole, thermalization of ions in a radio frequency-only quadrupole, and necessary ion optics for the transfer of ions into the cell inside the magnetic field have been constructed. A load-lock system for the introduction and easy replacement of a surface is under construction. The system is being tested under vacuum for ion formation, their transmission characteristics, and various parameters to optimize experimental conditions. A schematic view of the instrument is shown in Figure 1. The data system for the instrument and necessary electronics for the radio frequency and direct current supplies have been built, and delivery of the 7-tesla magnet is anticipated in October 2000.

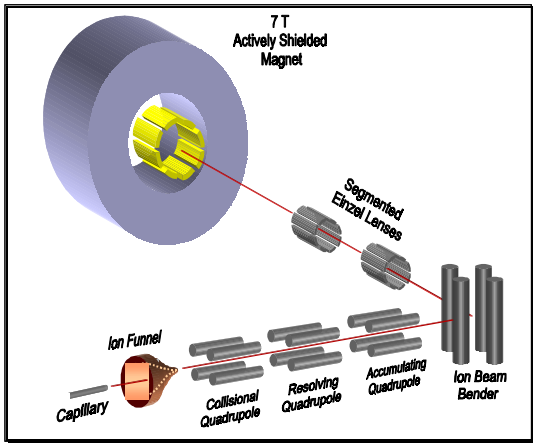

Figure 1. A schematic view of the instrument with 7-tesla superconducting magnet

Acknowledgments

We thank Mathew Covert for making necessary drawings, Mark Townsend and Joe Killinger for constructing ion optics components, Jim Follansbee, Jim Ikes, Beverley Taylor, and David Prior for the electronics components, and Gordon Anderson for design and fabrication of the data system and associated electronics.

Ultrasensitive Studies of Reactive Aerosols

James P. Cowin, Stephen A. Joyce

Study Control Number: PN99073/1401

Atmospheric particles are potentially harmful to human health, and to play a major role in the regional pollution chemistry of gases like ozone. In this project, we developed a field device to better collect, characterize, and maintain these particles and track their sources. Three laboratory methods for analyzing the collected particles with single aerosol particle sensitivity were also refined and improved.

Project Description

Reactive aerosols, particles ranging from 0.01 micron to 5 microns in diameter, are important in the atmosphere, in nanoparticle composite materials, in medicine, and in chemical processes. Characterizing their composition and reactivity is very difficult for several reasons: 1) their heterogeneity requires studying the individual reactivity of many classes of particles; 2) the samples can be too sparse for most analytical methods to deal with (a few thousand 0.25 micron particles, for example, for time-resolved, field-collected atmospheric samples); 3) usable analytical methods need automation to examine thousands of individual particles; and 4) reactive aerosols are not sufficiently protected between collection and analysis. To address these needs, we developed a new field collector for particles, the "Time-Tagged Particle Sampler," that can take thousands of samples of particles in the field, and preserve this archive for intensive, single-particle analysis in the laboratory. We also further developed three methods for conducting such laboratory analyses as follows:

- Automated analysis of particles via EDAX (energy dispersed analysis of x-rays) using a scanning electron microscope was developed, so that we could examine 10,000 particles per day in particles ranging from 0.1 to 5 microns for elemental composition (carbon and beyond in the periodic table).

- The "Enviroscan" environmental microscope at EMSL was used to study hydration properties of laboratory-generated NaCl/NaBr mixed aerosols, in which a surface film of dissolved NaBr composition was formed over a wide range of humidities. This microscope will also be used to study hydration properties of field-collected aerosols.

- We demonstrated the utility of time-of-flight secondary ion mass spectrometry to study the molecular speciation of field aerosols, both at the surface and as a depth profile.

Introduction

Existing methods to collect and analyze atmospheric particles are not satisfactory (McMurry 2000; Chow 1998), because the information typically is obtained on too coarse a time frame, and is usually an average composition of all the particles present. This deficiency has spurred many recent new approaches. Time-resolved single particle analysis in the field using a mass spectrometer with an aerosol inlet is one such new development (Seuss 1999), but these "field instruments" are relatively large, expensive, and difficult to operate.

We chose instead to attempt to refine field-sampling approaches and optimize single particle analysis in the laboratory. The new aerosol characterization technology developed in this project allows field collection and analysis of aerosol properties with unprecedented time resolution (1 minute) and the ability (through individual particle analysis) to determine the specific mix of materials making up the particles. This new approach will better determine the source of the particle, and allow better prediction of their chemistry and health effects. These are revolutionary capabilities that are expected to result in significant advances in our ability to develop predictive tropospheric air quality models.

Results and Accomplishments

Field Portable Instrument. The laboratory prototype unit was repackaged and redesigned to make a field portable unit as shown in Figure 1. It weighs about 50 kg, and is about 20 x 20 x 16 inches, although it could be built much

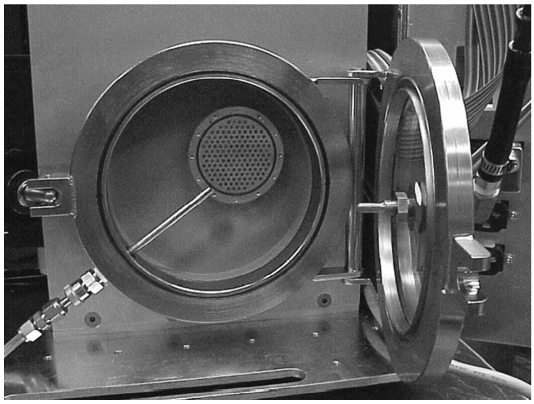

Figure 1. Time-tagged particle collector, shown with chamber open. In chamber is sample tray with 151 samples, in door at left is particle deposition nozzle.

smaller. The unit requires 200 watts of power. The sample tray holds 177 samples, and at 10 minutes/sample, will last for nearly 30 hours before a new tray must be inserted. For 1-minute samples, the unit will collect samples for nearly 3 hours, which is adequate for many air-flight studies.

Individual Particle Hydration Studies. We conducted a systematic study of mixed composition micron-sized particles of NaCl and NaBr. This study was relevant to sea salt aerosol generated from wave action and related to unsolved processes whereby Br is released to the atmosphere. We found that over a wide range of average compositions of the mixed salts, a pure-phase surface film of NaBr/NaCl liquid exists on top of undissolved particles.

Time-of-Flight Secondary in Mass Spectrometer Studies of Individual Particles. Our facility has an excellent customized version of a physical electronic time-of-flight secondary in mass spectrometer. It scans a 50-nanometer ion beam over a sample and examines the coincidentally ejected ions mass spectrometrically. Figure 2 shows the high resolution results for collected atmospheric particles. At the top, we see how an organic film coats the particles, and when ion sputtering is used to remove the outer few nanometers of the particles, the inorganic particle cores are revealed. We also have spatially mapped individual aerosol molecular composition with 200 nm resolution.

Summary and Conclusions

- The time-tagged particle collector was successfully developed and is currently being deployed in the field.

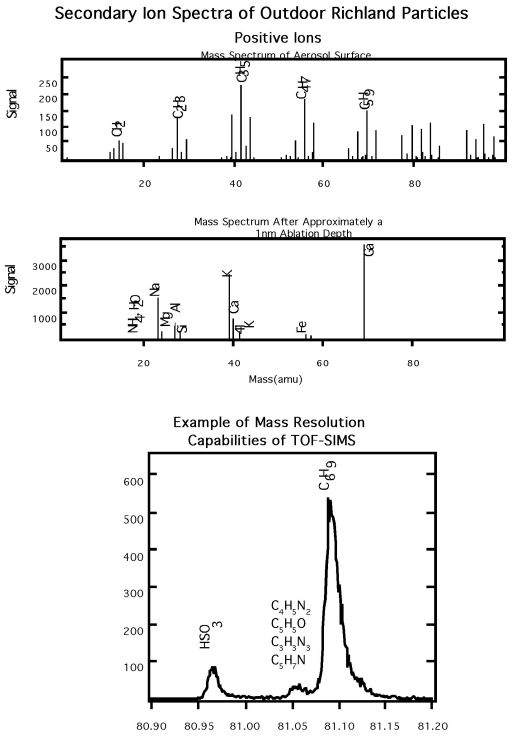

Figure 2. TOF-SIMS analysis of individual atmospheric particles, showing at top, how outer nanometer is largely organics. After removal, the particle core is clearly inorganic. Bottom shows how extremely high mass resolution of the TOF-SIMS makes chemical analysis of complex species feasible.

- Fully automated particle analysis by scanning electron microscopy and x-ray analysis was demonstrated, with capabilities beyond current standard practice.

- Single particle hydration studies using a scanning electron microscope were developed and applied to sea-salt aerosol problems.

- Secondary ion studies of organic coatings on atmospheric particles were demonstrated.

References

Chow JC and JG Watson. 1998. Guideline for speciated particle monitoring. esp. Chapter 5, "Measurement Artifacts and Interferences." *U.S. Air Quality Planning and Standards Report,* U.S. Environmental Protection Agency, Washington, D.C.

McMurry PH. 2000. "A review of atmospheric aerosol measurements." *Atm. Envir*. 34, 1959-1999.

Seuss DT and KA Prather. 1999. "Mass spectrometry of aerosols." *Chem. Rev*. 99, 3007-3035.

Publication

Laskin A and JP Cowin. 2000. "Automated single particle scanning-electron-microscopy/energy-dispersed-x-ray analysis of submicron particles down to 0.1 micron." *Analytical Chemistry* (submitted).

Biosciences and Biotechnology

Analysis of Receptor-Modulated Ion Channel Signaling by Confocal Optical/Patch-Clamp Microscopy

H. Peter Lu, Brian D. Thrall, Steven D. Colson

Study Control Number: PN00010/1417

Regulated ion flux across cell membranes plays a fundamental and crucial role in live cells. Ion channels control and regulate the ion current flux and therefore play a key role in regulating how cells respond to their changing environment. The purpose of this research project is to develop a unique technology, by combining our extensive imaging capabilities, a confocal scanning linear/nonlinear optical microscope, with state-of-the-art patch-clamp technologies. Application of this unique instrumentation will present an unprecedented opportunity of seeking mechanistic and dynamic understanding of ion channel functions and structures in living cells.

Project Description

This research project will develop a unique technology, by combining a confocal scanning linear/nonlinear optical microscope (see Figure 1) with state-of -the-art patch-clamp technologies, which will significantly enhance the diagnostic and investigative capabilities of both methods by combining real-time fluorescence measurements with real-time single-channel current measurements in a living cell. To illustrate the power of this approach in cell signaling research, this technology will be used to gain an understanding of how ion channel activities are regulated by conformational change dynamics and channel formation mechanisms using the gramicidin ion channels.

We designed, developed, and assembled an instrument combining patch-clamp measurements with a real-time scanning confocal microscope. We achieved recording single-ion channel (gramicidin dimers) current (on-off) trajectories with high sensitivity and established computational data analysis of single-ion channel stochastic time trajectories (Figures 2 and 3). In combining single-molecule spectroscopy and optical imaging, we have moved significantly forward in obtaining fluorescence images of single-dansyl gramicidin molecules and their dimers in lipid bilayers. By combining the patch-clamp technique and confocal fluorescence microscopy, it will become feasible to study ligand binding and dissociation, ligand binding cooperativity, ion channel activation and desensitization, and ion channel protein conformational changes in an intact cell in real-time. The measurements of ion channel protein conformational changes correlated with ion channel current trajectories have never been achieved before, and they are essential for the understanding of

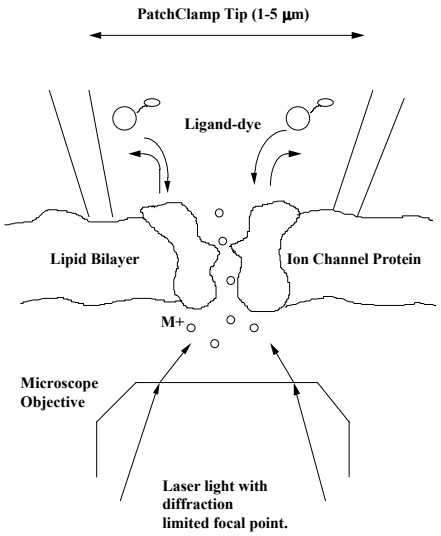

Figure 1. We combine laser scanning confocal optical microscopy with patch-clamp technique to study the ion channel conformational dynamics and mechanism of the single-ion channels. Single ligand-gated channel protein conformational change dynamics can be studied by monitoring fluorescence spectral fluctuations. Ligand binding/unbinding motion and ion-channel conformational changes are probed by two-photon confocal microscope and ion channel open/close states are monitored by patch-clamp ion channel current measurement. Dye-labeled ligands in nanomolar concentrations can be introduced to a receptor from the patch-clamp micropipette.

ion channel molecular dynamics and ion channel mechanisms. Understanding the correlated conformational dynamics of a single ion channel will be a significant step in deciphering the molecular mechanisms of ion channel functions.

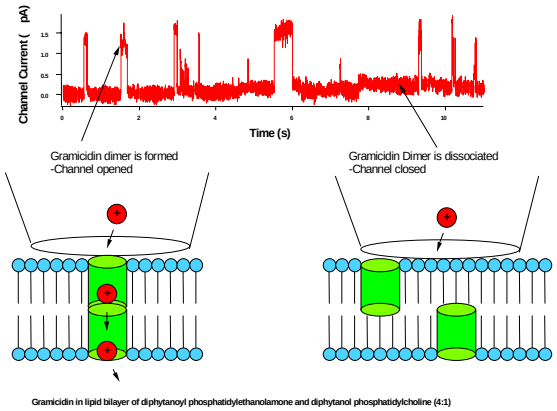

Figure 2. Patch-clamp single-ion channel study of ion channel kinetics induced by diffusion controlled spontaneous dimerization of gramicidin A. A single-ion channel current trajectory of gramicidin A in a lipid bilayer of diphytanol phosphatidylethanolamone and diphytanol phosphatidylcholine (4:1). Gramicidin dimer formation and dissociation results in opening and closing of a single ion channel, respectively. A high signal-to-noise ratio (noise less than 0.5 pA) has been achieved in our current experimental setup. A 1-µm diameter patch-clamp pipette tip was used to record this trajectory.

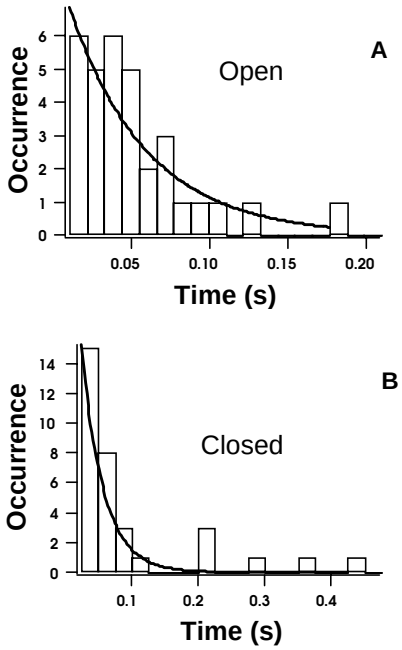

Figure 3. Dansyl gramicidin C dimerization kinetics calculated from channel open and close time distributions deduced from a long trajectory shown. Each on-off cycle corresponds to a single dimer formation and dissociation. The on-time and off-time correspond to the "waiting time" (an activation process) for gramicidin to form a dimer and the subsequent dissociation of the dimer. A single-exponential dimerization rate of 14.3 s^{-1} was observed for this system. The dimer dissociation kinetics cannot be fit well with a single-exponential decay, which indicates the possibility that at least two types of local environments or dimers exist.

Introduction

Tight regulation of ion flux across cell membranes is a fundamental and universal mechanism by which eukaryotic cells respond to their changing environment. Ion channels are critical in basic physiological processes and in higher functions. For example, receptor-operated Ca^{++} channels including the glutamate channels are thought to regulate critical physiological processes such as insulin secretion, bone resorption, and histamine secretion associated with inflammatory responses. Thus, the molecular determinants of ion channel regulation impact a wide range of cell signaling activities that are critical to both normal organ function as well as disease etiology. Nonetheless, the mechanisms by which these channels maintain a high degree of specificity for Na^{+}, K^{+} or Ca^{++} are still poorly understood (reviewed in Dingledine et al. 1999). Site-directed mutagenesis studies indicate that the specificity of a channel is not simply due to pore size, since even subtle ionic changes in channel subunits have dramatic effects on ion permeability (Ferrer-Montiel et al. 1996). Thus, subtle structural dynamics of ion channels likely play an important role in regulating channel function and selectivity. Although crystal and solution structure data (Armstrong et al. 1998) have provided insight into the functional properties of ion channels, inferences must be made from these in vitro studies to the structure-function relationships within the living cell. The correlation of patch-clamp recording of single-ion channel current trajectories with optical recording of the ion channel localization and conformational changes within a living cell could provide direct insights to these issues. The combined use of single molecule spectroscopy with patch-clamp technology would provide a technology that, when applied to living cells, would significantly change the landscape of the current fields of ion channel pharmacology and dynamics.

Approach

Sakmann and Neher received the Nobel Prize in Medicine in 1991 for the development of the patch-clamp technique (Sakmann and Neher 1995). Using this technique, a micropipette (0.5-µm to 10-µm diameter) is attached to the cell surface allowing the recording of whole-cell or single-channel ion currents flowing across biological membranes through ion channel proteins. It has had a major impact on the understanding of cell activities, cell signaling processes, and other cell functions. Our

laboratory (Lu and Xie 1997; Lu et al. 1998; Xie and Lu 1999) and others (Xie and Trautman 1998) demonstrated that single-molecule fluorescence spectrum and lifetime typically fluctuate as the changes of local environment and internal or external conformations of proteins.

Using a fast, high-sensitivity, intensified charge coupled device camera and our time-correlated single-photon counting trajectory device, we can record the spectral and fluorescence lifetime fluctuation trajectories. These reveal intrinsic single-molecule conformational dynamics and environmental change dynamics by calculating first and higher order autocorrelation functions from the trajectories. Single-pair fluorescence resonant energy transfer measures the distance change with angstrom-level sensitivity between a single donor/acceptor pair in a single-protein or single-complex. Molecule conformational changes, protein motions, ligand-protein and protein-protein interactions can be monitored by exciting the donor and monitoring either the donor's and acceptor's intensity trajectories or both, but separately.

Gramicidin channels (Figure 2) are chosen as a model ion channel for the system development because of their known structure, well-defined function, ease of preparation, and commercial availability. A gramicidin channel is a dimer of two 15-amino acid units that meet head-to-head in the interior of the membrane bilayer. Cations, but not anions, permeate through the resulting structure. There is a wealth of single-channel electrophysiological data for permeation through the channel in different lipid types and with different salt concentrations. However, single-gramicidin-channel conformational changes, correlated with ion channel current trajectories, have never been recorded. The knowledge of how the channels work in real-time is absent.

Results and Accomplishments

We have designed, developed, and installed a patch-clamp instrumental component coupled with a real-time scanning confocal microscope, establishing a formal procedure to make the patch-clamp pipette tips. Single-peptide ion channel current trajectories at the picoampere level were recorded with low noise (less than 0.5 picoampere), and statistical analysis programs were developed to analyze the stochastic ion channel open-close kinetics. The dimerization dynamics of single-peptide ion channels, gramicidin A and dansyl gramicidin C, were probed by monitoring single-ion channel current on and off trajectories, and the dynamics were found to be inhomogeneous due to different local environments around the single-dimers and monomers. Extensive exploratory experiments have been carried out in order to obtain fluorescence single-ion channel imaging and correlate dimerization dynamics measurements from both fluorescence trajectories and ion current trajectories using the combined patch-clamp confocal microscope. These results may be summarized as follows:

1. We designed, developed, and installed a patch-clamp instrumental component coupled with a real-time scanning confocal microscope.

2. We developed and improved the procedures of preparing patch-clamp micropipette tips with defined aperture sizes (5-μm to 500-nm in diameter).

3. We developed and improved the technical methods of preparing stable lipid vesicles and lipid bilayers formed at the patch-clamp pipette tips.

4. We achieved measurements of single-ion channel (gramicidin dimers) current (on-off) trajectories with a high sensitivity (pA) (Figure 2).

5. We established computational data analysis of single-ion channel stochastic time trajectories (Figure 3).

6. We designed, developed, and installed a single-molecule optical imaging instrumental component coupled with the real-time scanning confocal microscope and the patch-clamp instrument. Using a galvo-mirror two-dimensional scanning mechanism, we were able to scan a laser diffraction-limited focused spot using either cw laser excitation for linear fluorescence imaging and femtosecond pulse laser for two-photon fluorescence imaging. Two-photon fluorescence imaging gives high spatial resolution (beyond diffraction limit) and low autofluorescence background.

7. We installed and tested an intensified change coupled device camera that has single-photon counting sensitivity and video-rate imaging collection speed. Installed computer-controlled two-dimensional electropiezo close-loop scanning stage with nm-precision to facilitate focusing laser on a selected single-ion channel protein under a patch-clamp pipette aperture.

8. We conducted extensive single-molecule imaging exploratory experiments.

Summary and Conclusions

The combined patch-clamp confocal microscope was successfully designed, developed, and assembled. We had demonstrated the potential of the microscope using gramicidin A and dansyl gramicidin C (fluorescent analog of gramicidin A) as a model system: single gramicidin dimerization and dimer dissociation by simultaneously recording stochastic on-off trajectories for ion channel current and single channel (channel-ligand) conformational change dynamics. This project will continue during the second year to further refine the confocal microscope to enhance the capability of combined two-photon fluorescence imaging and single-ion channel current measurements. The mechanism and dynamics of single-glutamate receptor ion channel proteins in live cells will be studied using the confocal microscope.

References

Armstrong N, Y Sun, G Chen, and E Gouaux. 1998. "Structure of a glutamate-receptor ligand binding core in complex with kainate." *Nature* 395:913-917.

Dingledine R, K Borges, D Bowie, and SF Traynelis. 1999. "The glutamate receptor ion channels." *Pharmacological Reviews* 51:7-61.

Ferrer-Montiel A, W Sun, and M Montal. 1996. "A single tryptophan on M2 of glutamate receptor channels confers high permeability to divalent cations." *Biophys J.* 71:749-758.

Lu HP and XS Xie. 1997. "Single-molecule spectral fluctuations at room temperature." *Nature* 385:143-146.

Lu HP, L Xun, and XS Xie. 1998. "Single-molecule enzymatic dynamics." *Science* 282:1877-1882.

Sakmann B and E Neher. 1995. *Single-Channel Recording*. Eds. B Sakmann and E Neher, Plenum Press, New York.

Xie XS and HP Lu. 1999. "Single-molecule enzymology." *J. Bio. Chem*. 274:15967-15970.

Xie XS and JK Trautman. 1998. "Optical studies of single molecules at room temperature." *Annu. Rev. Phys. Chem.* 49:441-480.

Automated DNA Fingerprinting Microarrays for Environmental Epidemiology of Pathogenic Microorganisms

Darrell P. Chandler, Douglas R. Call, Cynthia J. Bruckner-Lea

Study Control Number: PN00011/1418

If we are to successfully develop and apply diagnostic instruments in environmental sciences, we will need to more capably discriminate between closely related microorganisms. Such instruments must be rapid, easy-to-use, and conducive to automation; capable of producing statistically rigorous data with relative ease; and highly reproducible. The objective of this work is to develop new instruments for discriminating between microorganisms based on their DNA fingerprints.

Project Description

The objective of this project is to develop an integrated DNA fingerprinting microarray system for the identification, characterization, location, and tracking of pathogenic microorganisms in environmental systems and non-human vectors. Nonamer- and decamer-oligonucleotide arrays were constructed and used to interrogate repetitive-DNA polymerase chain reaction (PCR) products from closely related *E. coli* and *Xanthomonas* isolates. Seven unique microarray fingerprints were obtained with a simple five-probe nonamer array, where gel electrophoresis of polymerase chain reaction products showed no genetic discrimination. A 50-probe nonamer array was subsequently constructed and is being used to investigate signal variation due to polymerase chain reaction, hybridization, and signal generation. The 50-probe array is now being used to fingerprint 50 to 100 different strains of *E. coli* and *Xanthamonas*, respectively.

Introduction

Current epidemiological investigations of pathogenic microorganisms use fairly standard techniques for DNA "fingerprinting," or discriminating between closely related isolates. These include pulsed field gel electrophoresis, variations on southern hybridization or polymerase chain reaction-based techniques such as randomly amplified polymorphic DNA typing, restriction fragment length polymorphism, single-stranded conformation polymorphism, denaturing gradient gel electrophoresis, or combinations thereof. In all cases, these typing methods access a limited complement of genetic information, the analytical method is technically challenging and time-consuming, and parallel processing with many independent restriction enzymes or probes is required to achieve statistical rigor and confidence in the resulting pattern of DNA fragments. Still, standard fingerprinting techniques fail to answer fundamental epidemiological questions. For example, Hancock et al. (1998) identified multiple sources of *E. coli* O157:H7 in feedlots and dairy farms, but were unable to discriminate between isolates. In the absence of adequate resolving power, it is not possible to determine how pathogens disseminate in the environment, enter into and distribute between environmental reservoirs, or impact human health. Similar limitations persist for most other epidemiological studies of pathogenic (and non-pathogenic) microorganisms.

The objective of this research is to develop and demonstrate DNA fingerprinting microarrays for epidemiological identification and discrimination of closely related microorganisms, focusing on the occurrence, distribution, and transmission of *E. coli* O157:H7 found in cattle, dairy farms, and feedlots. The scope of the work involves the development of novel hybridization conditions and procedures for decamer probes (DNA or polynuclear aromatic hydrocarbons) attached to a two-dimensional support and genetic discrimination between clonal isolates of *E. coli* O157:H7 and/or *Xanthomonas*. The expected results of this research include immediate application of the fingerprint array to better understand the dissemination of *E. coli* O157:H7 (and other microorganisms) within and between environmental reservoirs.

Results and Accomplishments

Initial experiments focused on reproducible printing and hybridization of decamer probes to polymerase chain reaction-amplified DNA targets. Biotinylated repetitive DNA primers (REP, ERIC) were used to prime a

polymerase chain reaction from genomic DNA from eight strains of *E. coli*. Polymerase chain reaction products were then hybridized to a low-density microarray consisting of five random decamer probes. The ERIC polymerase chain reaction primer generated distinguishable agarose gel fingerprints for the eight isolates; hybridization of ERIC-polymerase chain reaction fragments to a random five-probe decamer array generated reproducible and distinct DNA fingerprints for three of the eight isolates. More exciting results are shown in Figure 1, where the REP polymerase chain reaction primers showed no variability in agarose gel fingerprint profiles, but the five-probe decamer array was able to identify at least three unique fingerprints among the isolates. We have improved hybridization buffers and procedures and investigated the printing, binding, and hybridization properties of nine-mer probes in this context. Overcoming probe cross-contamination during printing was a significant technical obstacle that is now resolved. We verified that nonamer probes can be successfully printed and hybridized to REP/ERIC polymerase chain reaction products, which provides approximately five times greater sampling of the *E. coli* genome and polymerase chain reaction products than does an array of 10-mer probes. Using nine-mer capture probes, the REP fingerprinting array generated seven unique fingerprint profiles from the eight strains of *E. coli*.

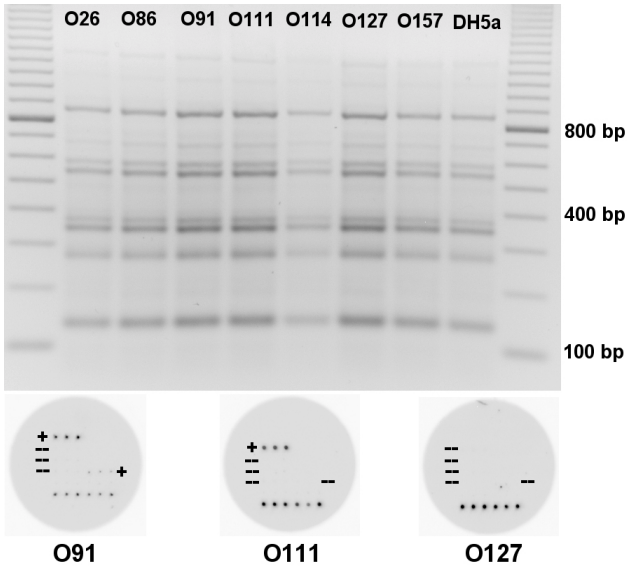

Figure 1. REP polymerase chain reaction DNA fingerprinting by agarose gel electrophoresis (top) and random DNA fingerprinting array (bottom). This microarray/polymerase chain reaction primer combination generated three unique profiles where gel electrophoresis was ineffective in genetic discrimination. Switching to a random nonamer array resulted in seven unique array profiles.

Based on these results, we constructed a 50-probe nonamer fingerprinting array. Initial hybridization results with *E. coli* REP polymerase chain reaction products illustrate the need for improved image analysis and statistical capabilities for routine implementation of microarrays in epidemiological investigations. Even with four replicate arrays in two independent hybridization chambers, there was sufficient signal variation at certain probe spots (Figure 2, squares) to question their assignment as "positive" or "negative" signals. Phoretix image analysis software allowed us to assign an arbitrary threshold for positive signal and scoring purposes. This procedure was used to fingerprint a small set of *Xanthomonas* isolates (Figure 3) and demonstrated that unambiguous identification of closely related isolates can be obtained with a DNA fingerprinting microarray. Current research is focused on a more comprehensive fingerprinting analysis of *Xanthomonas* isolates.

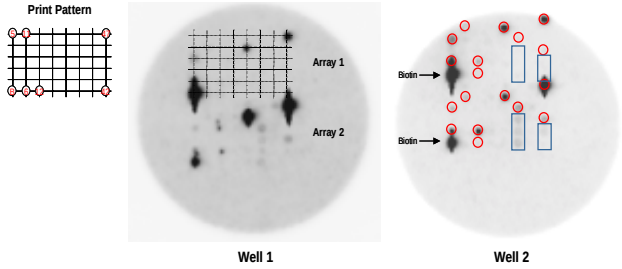

Figure 2. 50-probe random nonamer array hybridized to *E. coli* REP polymerase chain reaction products. Four independent arrays were printed in two hybridization wells. Circles indicate hybridization signals easily visible to the unaided eye. Rectangles highlight regions of signal variability at identical probe locations.

Summary and Conclusions

We have demonstrated that random DNA fingerprinting arrays can be successfully used to identify closely related microorganisms. Improved statistical techniques will be required to assess variability in signal intensity at individual spots and compare profiles between organisms.

Reference

Hancock DD, TE Besser, DH Rice, ED Ebel, DE Herriott, and LV Carpenter. 1998. "Multiple sources of Escherichia coli 0157 in feedlots and dairy farms in the northwestern USA." *Prev. Vet. Med*. 35:11-19.

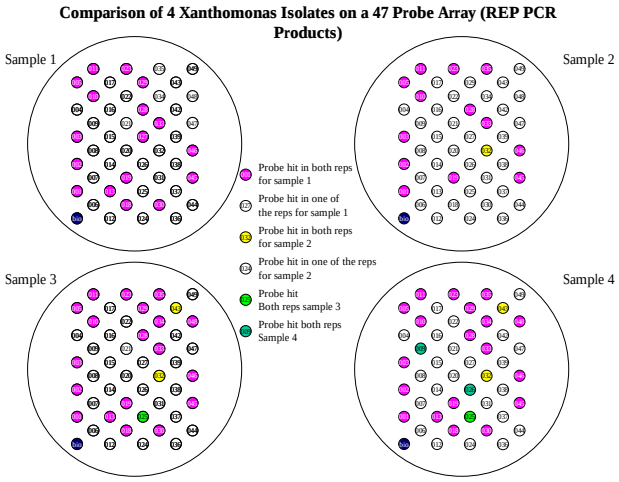

Figure 3. Microarray fingerprints of four *Xanthamonas* isolates, color-coded to highlight similarities and differences in the respective profiles. Positive hybridization was determined by arbitrary threshold values within the Phoretix software package. Hatched spots represent probes that were only scored positive by Phoretix in one of two replicate hybridizations.

Publications

Call DR., FJ Brockman, and DP Chandler. 2000. "Genotyping Escherichia coli O157:H7 using multiplexed PCR and low-density microarrays." *Int. J. Food Microbiol*. (in press).

Call DR, DP Chandler, and FJ Brockman. "Fabrication of DNA microarrays using unmodified oligomer probes." *BioTechniques* (submitted).

Biologically-Based Dose-Response Models for Low Dose Exposures to Chemicals and Radionuclide Mixtures

Charles Timchalk, William B. Chrisler, Richard Corley

Study Control Number: PN00016/1423

A challenge associated with DOE's massive cleanup efforts is understanding the impact of concurrent exposures to, or mixtures of, radionuclides and toxic chemicals. Current human health risk assessment procedures are cumbersome, address one chemical or radionuclide at a time, and are oftentimes overly conservative. This research looks at methods to assess health risks from mixtures of chemicals and radionuclides.

Project Description

In recent years, advances in biologically based models of internal radiation dosimetry and response modeling have provided unique opportunities to understand and predict the human health risks associated with mixed exposures. In a previous study, a representative chemical (benzene that is toxic to the bone marrow) and a bone-seeking radionuclide (yttrium-90 that is capable of irradiating bone marrow and thus causing toxicity), were evaluated for toxicological interactions in the CBA/Ca mouse model (a strain of inbred mice) (Timchalk et al. 2000). The results from these in vivo studies were consistent with previously published reports where benzene and radiation both independently target hematopoiesis. However, the overall biological responses following a co-exposure were complex since benzene and radiation appeared to cause different shifts in the myeloid and erythroid cell populations.

A pharmacodynamic model was developed to describe cytotoxicity and cell kinetics following benzene exposure in mice (Scheding et al. 1992; Cox 1996). The model will eventually be adapted to quantitatively evaluate the biological response from a co-exposure to benzene and radiation. Since benzene and radiation share a common target tissue (bone marrow) and toxicological response (hematotoxicity, acute myelogenous leukemia), it is reasonable to anticipate that these two agents, in collaboration, are capable of producing a dose-dependent hematotoxic interaction. The model as described by Scheding et al. (1992) consists of a set of compartments representing specific cell populations including: CFU-S, CFU-E, CFU-GM, and mature erythrocytes and granulocyte/macrophage cells. As depicted in Figure 1, the erythrocytic (CFU-E) and granulocytic (CFU-GM) cell lineage descend from a common progenitor stem cell (CFU-S) and the hematopoiesis process (cell differentiation/proliferation) is under feedback control (I). CFU-S stem cells are self-renewing and capable of differentiating into CFU-E or CFU-GM. In addition, CFU-GM and CFU-E progenitors are under feedback control (II) from erythro- and granulopoietic bone marrow cells, respectively. Benzene and radiation are believed to act on all proliferating cell stages and the loss coefficients (KH_1, KH_2, KG_1, KG_2, KE_1, KE_2) will be used to quantify the extent of damage to the various precursor cell populations.

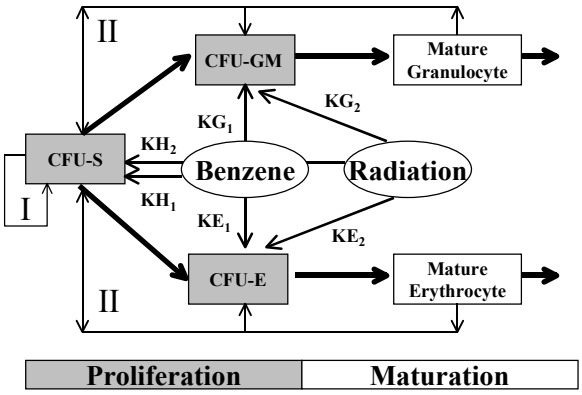

Figure 1. Structure of the pharmacodynamic model for benzene/radiation interaction on hematopoiesis. The model incorporates feedback regulation (I and II) for self-renewal, differentiation, and proliferation. Benzene metabolites and radiation are both assumed to act on proliferating cell stages. Model adapted from Scheding et al. (1992).

The focus of this project was to develop an in vitro stem cell culture using bone marrow cells obtained from CBA/Ca mice to evaluate the toxicological response following benzene metabolite and radiation exposures. Development of this in vitro stem cell culture system is needed to experimentally develop and validate pharmacodynamic models of cell injury.

Approach

Hematopoietic (bone marrow) progenitor cell populations will be cultured from CBA/Ca mice according to Farris et al. (1997) and Green et al. (1981). The CBA/Ca mouse was chosen since it is a useful model for benzene-induced leukemia and will be of relevance for understanding the human disease process.

In brief, the CFU-S were cultured in conditioned semisolid agar media containing macrophage-colony stimulating factor, interleukin 3, and incubated for up to 12 days at 37°C with various combinations of benzene metabolites (phenol and hydroquinone). At approximately 12 hours prior to counting, the cells were overlaid with a solution of 2-(4-iodophenyl)-3-(4-nitrophenyl)-5-phenyltetrazolium chloride) that is metabolized by viable cells forming a red color for macroscopic quantitation. The CFU-E progenitor cells were cultured in a methycellulose semisolid medium containing 30% fetal bovine serum, 1% bovine serum albumin, and colony stimulating factors erythropoietin as previously described (Farris et al. 1997). Cultures were incubated at 37°C for about 2.5 days and examined by light microscopy, and cell aggregates were scored as colonies. The CFU-GM assay was conducted using the agar culture technique described by Farris and Benjamin (1993). Cultures were incubated for up to 7 days at 37°C with various combinations of benzene metabolites and on day 6, 2-(4-iodophenyl)-3-(4-nitrophenyl)-5-phenyltetrazolium chloride was added to the colonies as previously described for the CFU-S assay and colonies were scored. The results of these studies were expressed as number of colonies formed per two femurs and were compared to the response from nontreated cultures. The results were expressed as a percent of control.

Similar studies were conducted by exposing stem cells to the ^{60}Co source available at our Laboratory. This gamma radiation source provides an efficient technique for exposing cells at a known radiation dose and dose rate. Studies were also conducted with radiation in combination with benzene metabolites to generate preliminary data on potential interactions in these specific cell types important to the development of both radiation and benzene-induced leukemia.

Results and Accomplishments

Initial efforts primarily focused on optimizing experimental conditions for isolation and culturing of the bone marrow stem (CFU-S) and progenitor cells (CFU-E and CFU-GM) obtained from naïve mice. Once conditions were optimized, experiments with radiation or benzene metabolites were conducted. The preliminary experiments were designed to determine the dose-response for bone marrow cell proliferation following exposure to gamma radiation (^{60}Co) and are presented in Figure 2. Cells were exposed to a dose range from 0.01 to 10 Gy. For all three cell populations, a clear dose-response relationship was established. However, doses greater than 1 Gy decreased colony formation to 11 to 16% of the control response. Based on these results, the radiation doses for the mixed exposures were set at 0.01, 0.1, and 1 Gy.

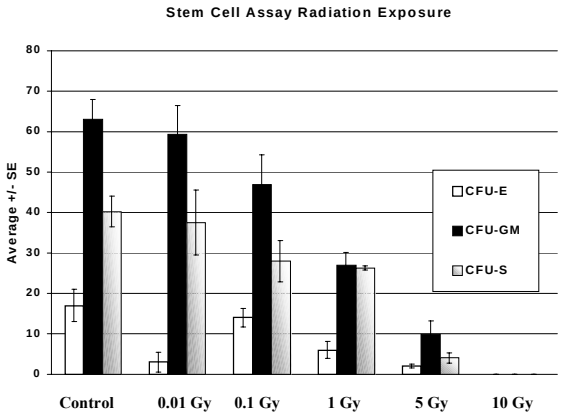

Figure 2. Colony formation dose-response for CFU-E, CFU-GM, and CFU-S cells following in vitro exposure to radiation ranging from 0 to 10 Gy from an external ^{60}Co source

The selection of phenol and hydroquinone concentrations for in vitro evaluation in the stem cell assay were based on the results seen in bone marrow cells obtained from Swiss Webster mice (Corti and Snyder 1998). The results obtained with the CFU-S cells following exposure to phenol and HQ at concentrations of 0, 10, 20, and 40 μM and to a mixture of phenol (40 μM) + HQ (10 μM) are presented in Figure 3. These results in CFU-S cells are consistent with the response reported by Corti and Snyder (1998) with CFU-E cells indicating that hydroquinone is more cytotoxic than phenol and that the combined response of hydroquinone and phenol, on CUF-S cells is significantly greater that additive. However, the combined response was not seen with the CFU-GM or CFU-E progenitor cells.

The CFU-S cell response to a combined exposure to both radiation and benzene metabolites is presented in Figure 4. Again, the radiation exposure produced a similar dose-response as seen with the preliminary radiation studies, although the inhibition at 1 Gy was less that previously observed. In the absence of radiation treatment, hydroquinone, phenol, and hydroquinone plus

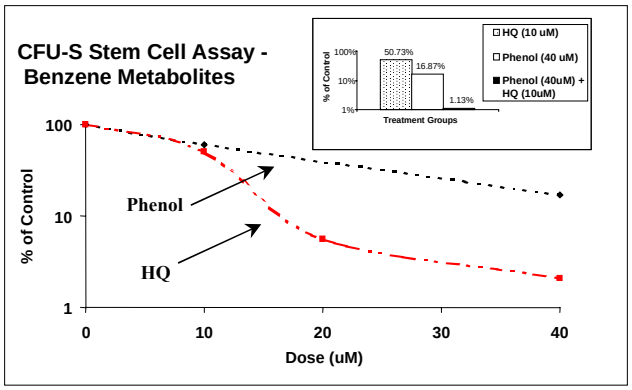

Figure 3. CFU-S cell colony formation response following in vitro exposure to phenol, hydroquinone, and phenol plus hydroquinone

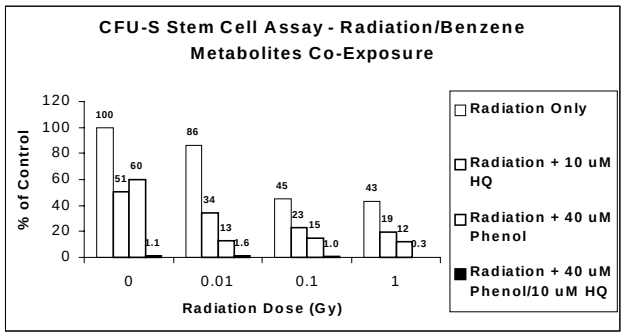

Figure 4. CFU-S cell colony formation response following in vitro exposure to both radiation (0 to 1 Gy) and phenol, hydroquinone, and phenol plus hydroquinone. Percent of control values for each treatment are presented over the bar graphs.

phenol treatments were 51, 60, and about 1% of control, respectively. However, the chemical treatments of CFU-S cells in the presence of the radiation did not appear to shift the dose-response beyond what the chemicals accomplished by themselves. These preliminary in vitro studies suggest that the cytotoxic effects of benzene metabolites and radiation on bone marrow stem progenitor cells may be independent. Future studies are needed to determine if a similar response is seen following in vivo exposure to benzene and radiation.

Summary and Conclusions

An in vitro bone marrow stem cell culture assay for evaluation of chemical and radionuclide interactions was established. Preliminary experiments demonstrated that the colony-forming assay was sensitive to dose-dependent radiation effects. The benzene metabolites phenol and hydroquinone produced a dose-dependent inhibition of stem cell colony formation (CFU-S). The metabolite combination effect was multiplicative (greater than additive). Under in vitro exposure conditions, radiation did not shift the dose-response beyond what the benzene metabolites could accomplish independent of radiation. Future studies will determine if a similar response is obtained in mice following in vivo mixed chemical and radiation exposures. The approaches developed in this project will form the experimental cornerstone for pharmacodynamic model development for chemical and radiation interactions on bone marrow cells.

References

Corti M and CA Snyder. 1998. "Gender- and age-specific cytotoxic susceptibility to benzene metabolites in vitro." *Tox. Sci.* 41:42-43.

Cox, Jr. LA. 1996. "Reassessing benzene risks using internal doses and Monte-Carlo uncertainty analysis." *Environ. Health Perspect.* 104 (Suppl. 6):1413-1429.

Farris G M and SA Benjamin. 1993. "Inhibition of myelopoiesis by conditioned medium from cultured canine thymic cells exposed to estrogen." *Am. J. Vet Res.* 54:1366-1373.

Farris GM, SN Robinson, KW Gaido, BA Wong, VA Wong, WP Hahn, and RS Shah. 1997. "Benzene-induced hematotoxicity and bone marrow compensation in B6C3F1 mice." *Fundam. Appl. Toxicol.* 36:119-129.

Green JD, CA Snyder, J LoBue, BD Goldstein, and RE Albert. 1981. "Acute and chronic dose/response effects of inhaled benzene on multipotential hematopoietic stem (CFU-S) and granulocyte/macrophage progenitor (GM-CFU-C) cells in CD-1 mice." *Toxicol. Appl. Pharmacol.* 58:492-503.

Scheding S, M Loeffler, S Schmitz, HJ Seidel, and HE Wichmann. 1992. "Hematotoxic effects of benzene analysed by mathematical modeling." *Toxicol.* 72:265-279.

Timchalk C, JE Morris, and RA Corley. 2000. "Effects of co-exposure of benzene and radiation (Yttrium-90) on hematopoiesis in CBA/CA mice." *Tox Sci.* 54(1):1649.

Publication

Timchalk C, JE Morris, and RA Corley. 2000. "Effects of co-exposure of benzene and radiation (Yttrium-90) on hematopoiesis in CBA/CA mice." *Tox Sci.* 54(1):1649.

Biomolecular Interaction Assay System

Jay W. Grate, Cynthia Bruckner-Lea

Study Control Number: PN99005/1333

Understanding protein-protein and protein-DNA interactions is integral to understanding the function of living organisms and how organisms respond to insults such as environmental exposure to chemicals and radiation. Methods are being developed on this project to rapidly measure the interactions between these biomolecules.

Project Description

The purpose of this project was to build and test a device for rapidly measuring the interactions between biomolecules (proteins and DNA) and multiple protein complexes. We constructed two different renewable microcolumn devices with on-column optical detection, and wrote computer control programs to automate the experimental systems. The renewable microcolumn systems were then used to monitor the binding of several model proteins (antibodies) and measure the interaction between proteins and DNA fragments. This project advances our ability to rapidly measure biomolecular interactions and therefore understand biological systems.

Introduction

A number of sensor technologies have been adapted to monitoring biomolecular interactions. Acoustic wave devices such as flexural plate wave devices, surface transverse waves, and quartz crystal microbalances detect the mass increase observed upon binding of a solution biomolecule to a surface bound biomolecule. However, these devices also respond to changes in viscosity, temperature, liquid density, and viscoelastic effects, which may confound the interpretation of observed signals. In addition, nonspecific binding is often indistinguishable from specific binding. Several techniques for refractive index sensing, such as planar wave guides and surface plasmon resonance, can also be used to observe biomolecular interactions localized at a surface. Again, nonspecific binding is indistinguishable from specific binding, and the derivatized surface must be very thin and uniform to obtain adequate sensitivity and reproducibility. All of these techniques use planar surfaces that must be derivatized with the first biomolecule. These surfaces are difficult to prepare and characterize, and must be prepared fresh for each assay. In addition, these techniques cannot measure the binding of multiple proteins to form large protein complexes. Therefore, there is the need for the development of new techniques for conducting many rapid, automated measurements of biomolecular binding events, including the formation of multiple protein complexes.

Approach

This project will develop renewable surface sensing techniques for monitoring biomolecule binding events. In this approach, a suspension of surface derivatized beads is introduced into a flow system and then automatically trapped by a barrier that stops the beads but allows the fluid to proceed (Bruckner-Lea et al. 1999, 2000; Chandler et al. 1999, 2000; Ruzicka and Hansen 2000; Ruzicka and Scampavia 1999; Ruzicka 1998). This produces a small microcolumn of beads (only about a microliter in volume) in a location for observation. The beads can then be automatically perfused with reagent or sample solutions to perform separations or surface reactions. Detection methods can be used to observe optical changes (absorbance or fluorescence) on the bead surfaces. At the completion of the observation, the beads can be flushed from the observation area and disposed. A new bed of beads can then be packed for the next assay. This new bead bed has a fresh surface, hence the name renewable surface sensing.

The renewable surface approach has a number of advantages over planar formats, and over the surface plasmon resonance method. The flow injection system is far more flexible for delivering solutions to the observation area. This feature may become particularly important when attempting to create and observe assemblies of more than two components. The spectral detection, as opposed to a single refractive index change, provides more selective detection by providing more information for observing particular species and zeroing out undesirable contributions to signals. In addition, the column format is compatible with typical measurements by affinity chromatography for obtaining thermodynamic

information on binding. The real-time observation under controlled solution conditions will provide kinetic information. The renewable surface approach also permits a wide latitude in selection of surfaces for biomolecular binding (surface plasmon resonance requires a metal surface as part of the transduction mechanism). Finally, the bead format provides a large surface area sample that can be characterized by a variety of techniques. In addition, beads with many chemical functional groups for attaching proteins or DNA are already commercially available and can serve as the foundation for creating biomolecular assemblies.

Results and Accomplishments

Renewable Microcolumn System Design

Two custom renewable microcolumn flow cells were designed and evaluated: a piston flow cell and a rotating rod flow cell (Figure 1). Both flow cells include a microcolumn volume of about 1 μL and a path length of 1 mm. The fluidic system allows automated packing of a microcolumn from a stirred slurry, followed by perfusion of the column with various sample and wash solutions (all automated). Optical fibers leading to the flow cell were used to monitor the microcolumn absorbance during column delivery and protein binding to the microcolumn during sample perfusion. Reproducibility of column packing and absorbance baseline noise was identical for both devices. However, the rotating rod design (Figure 1b) was more reliable and rugged over many months of use.

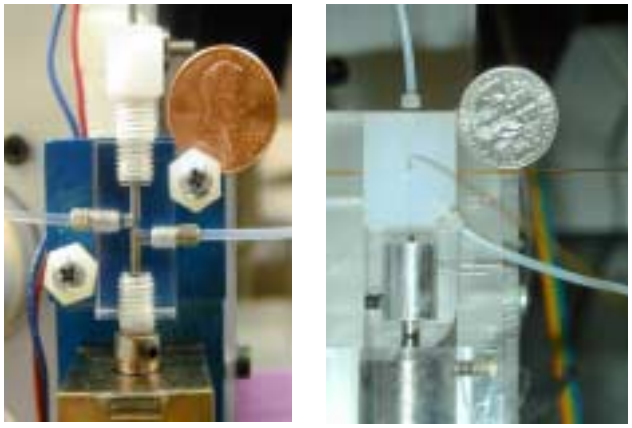

(a) (b)

Figure 1. Renewable microcolumn flow cells for automated protein binding studies. (a) Moving piston flow cell; (b) rotating rod flow cell. Both designs monitor the UV-VIS absorbance through microcolumns with a 1-mm path length and 1-μL microcolumn volume.

Measurement of Protein-Protein Interactions

The detection of the binding of multiple proteins was demonstrated using the renewable microcolumn system. Microcolumns that are 1 μL in volume were automatically formed from a slurry of Sepharose beads. Sepharose beads were derivatized with Protein G, and absorbance spectra were collected during in situ binding of human IgG and goat anti-human-IgG. The human IgG and the anti-IgG were labeled with different fluorescent dyes. Chicken IgG which will not bind to the Protein G beads was used as a control to see if nonspecific binding occurs (no nonspecific binding was observed). The absorbance spectra were collected over time and showed that the ultraviolet absorbance (280 nm) corresponded to the dye absorbance (496 or 557 nm) expected upon protein binding (Figure 2). The proteins were removed by perfusion with 0.1 M HCl. The data showed that the renewable microcolumn system can detect in situ binding of multiple proteins. We monitored the binding of three protein complexes, and expect that the system would be suitable for investigating complexes containing up to 15 to 20 proteins. The detection limit of the renewable microcolumn system that included a 1-mm path length and Sepharose 4B beads (Zymed) was estimated to be 0.005 μg protein bound to the beads (as measured using commercial IgG antibody proteins). However, fluorescence detection (rather than absorbance) will be necessary in some cases for increasing sensitivity to allow detection of proteins with low absorbance. In the next year of this project, we will incorporate on-column fluorescence detection.

Measurement of DNA-Protein Interactions

Initial experiments were also conducted to demonstrate that the renewable microcolumn system can be used to measure the binding of nucleotide excision repair proteins (RPA and XPA) onto DNA fragments. These proteins are part of a complex set of proteins that are involved in repairing damaged DNA, an important biological process in which the details of the formation are not well understood. Sepharose beads were derivatized with fluorescently labeled single-stranded DNA fragments, and absorbance measurements were collected during in situ binding of RPA protein and XPA protein perfused sequentially over the microcolumn. The proteins were removed by washing with 0.1 M HCl, and the labeled oligonucleotide remained attached to the beads. Initial results show that both RPA and XPA bind to the single-stranded DNA. We are continuing these studies to investigate protein binding onto both single-stranded and double-stranded DNA that is immobilized onto beads.

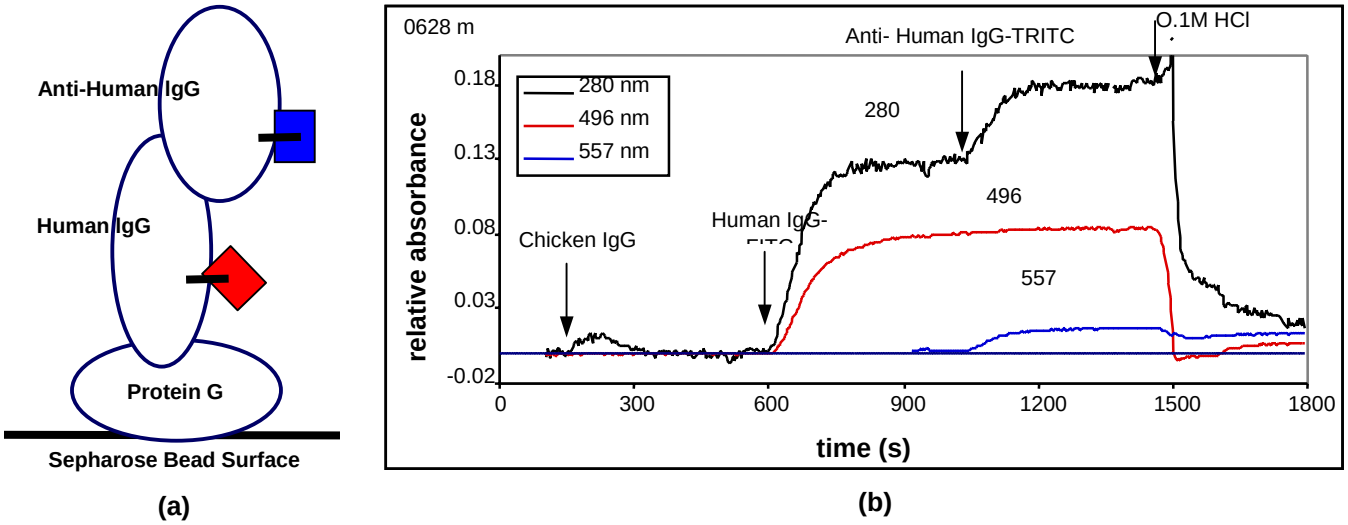

Figure 2. Automated protein binding experiments demonstrating the selective binding of multiple proteins onto a renewable microcolumn. The system is shown schematically in (a) and on-column absorbance data at three wavelengths are shown in (b). The column is perfused at 0.5 µL/s with three proteins (40 µg/mL, 50 µL). Each injection is followed by 150 µL phosphate buffered saline (0.5M HCl, pH 7.4). Chicken IgG does not bind to the protein G Sepharose beads (demonstrates negligible nonspecific protein binding), but subsequent injections of human IgG and goat anti-human IgG bind to the microcolumn. The protein binding can be monitored in the UV region (due to aromatic amino acids) and also at the wavelengths of specific labels on the proteins (fluorescein=496 nm and tetramethylrhodamine=557 nm).

The renewable microcolumn format allows rapid, automated testing of many experimental parameters such as solution concentrations, bead surface chemistries, and the order of perfusion events.

Binding Kinetics

We evaluated kinetic models for modeling protein binding within the renewable microcolumn system in order to use the system to obtain quantitative kinetic information. The CLAMP computer program (University of Utah) for bimolecular interaction analysis was used to estimate the kinetic constants that can be investigated using the renewable microcolumn system. This analysis indicated that the renewable microcolumn system could be used to investigate binding reactions with equilibrium constants ranging from 10^6 to 10^{12}, which covers many biomolecular interactions of interest.

Summary and Conclusions

Two automated renewable microcolumn systems with on-column absorbance detection were successfully designed, assembled, and tested. The automated systems were used to detect multiple protein binding events and also DNA-protein interactions. The advantages of this approach for studying biomolecular interactions are

1. automated renewal of the sensing surface eliminates problems with surface fouling

2. the renewable microcolumn format and automated fluidics allow rapid, automated testing of many experimental parameters such as solution concentrations, bead surface chemistries, and the order of protein binding events

3. the formation of large protein complexes could be investigated using this technique

4. fluorescence detection and protein labeling will be needed for studying small proteins using this technique.

This project will continue into fiscal year 2001 to develop methods for obtaining quantitative protein binding data for biologically important protein systems, and also incorporate on-column fluorescence detection to allow the detection of small proteins.

References

Bruckner-Lea CJ, DA Holman, BL Schuck, FJ Brockman, and DP Chandler. 1999. "Strategies for automated sample preparation, nucleic acid purification, and concentration of low target number nucleic acids in environmental and food processing samples." *In SPIE Proceedings 1999*, 3544:63-71.

Bruckner-Lea CJ, MS Stottlemyre, JW Grate, DA Holman, FJ Brockman, and DP Chandler. 2000. "Rotating rod renewable microcolumns for automated, solid-phase DNA hybridization studies." *Anal. Chem*. 72:4135-4141.

Chandler DP, FJ Brockman, DA Holman, JW Grate, and CJ Bruckner-Lea. 2000. "Renewable microcolumns for solid-phase nucleic acid separations and analysis from environmental samples." *Trends Anal. Chem*. 19:314-321.

Chandler DP, BL Schuck, FJ Brockman, and CJ Bruckner-Lea. 1999. "Automated nucleic acid isolation and purification from soil extracts using renewable affinity microcolumns in a sequential injection system." *Talanta* 49:969-983.

Ruzicka J. 1998. "Bioligand interaction assay by flow injection absorptiometry using a renewable biosensor system enhanced by spectral resolution." *Analyst* 123:1617-1623.

Ruzicka J and EH Hansen. 2000. "Flow injection: from beaker to microfluidics." *Anal. Chem*. 72:212A-217A.

Ruzicka J and L Scampavia. 1999. "From flow injection to bead injection." *Anal. Chem*. 71:257A-263A.

Publications and Presentations

Bruckner-Lea CJ, MS Stottlemyre, DA Holman, JW Grate, FJ Brockman, and DP Chandler. 2000. "Rotating rod renewable microcolumns for automated, solid-phase DNA hybridization studies." *Anal. Chem.* 72:4135-4141.

Chandler DP, DA Holman, FJ Brockman, JW Grate, and CJ Bruckner-Lea. 2000. "Renewable microcolumns for solid-phase nucleic acid separations and analysis from environmental samples." *Trends in Analytical Chemistry* 19(5):314-321.

Grate JW, OB Egorov, and CJ Bruckner-Lea. 1999. "Renewable surfaces for separation and sensing." *Proceedings of Photonics East, SPIE International Symposium on Environmental and Industrial Sensing* 3857:70-73.

Bruckner-Lea CJ, DA Holman, M Stottlemyre, P Rieke, FJ Brockman, JW Grate, and DP Chandler. October 1999. "Renewable surface biosensors." Presented at the Biosensors and Biomolecular Electronics Session of the 196th Meeting of the Electrochemical Society, Honolulu, Hawaii.

Bruckner-Lea CJ, D Chandler, L Olson, D Holman, and J Grate. May 1999. "Renewable surface biosensors." Poster presentation, IBC's 2nd Annual International Conference on Biosensor Technologies, San Diego, California.

Characterization of Global Gene Regulation by Tumor Necrosis Factor Alpha in Genetically Defined Mice

Brian D. Thrall, Kwong-Kwok Wong

Study Control Number: PN00019/1426

The scientific goal of this project is to characterize gene regulation mediated by cell signaling pathways of broad applicability to human biology and environmental health. This project will serve as a means to implement and focus the Laboratory's capabilities in mouse genomics (cDNA arrays and informatics), provide a focus and direction for the integration of genomics and bioinformatics capabilities at the Laboratory, and build capabilities in support of our biological sciences program.

Project Description

The cytokine tumor necrosis factor alpha (TNFα) mediates a diverse range of cellular responses induced by environmental agents, including apoptosis, cell proliferation, and differentiation. TNFα-mediated signaling pathways are known to be stimulated by a broad range of environmental agents, including radiation, chemicals, and pathogenic microbes. The cellular responses to TNFα are tissue-specific, a reflection of cell-specific patterns of genes regulated by the signaling pathways stimulated by TNFα. This project will create a mouse-specific cDNA microarray which will then be used to globally assess these gene expression patterns regulated by TNFα in isolated cells and in the whole animal. By understanding these global patterns, tissue-specific differences in gene regulation will be identified that will help integrate the key signaling pathways that govern the cell-specific responses to TNFα, in the context of the whole animal. This information can then be extended to identify the key molecular pathways that govern cell-specific responses mediated by TNFα in response to exposure to environmental contaminants such as radiation and chemicals.

Introduction

Among the cytokines that contribute to immune responses, tumor necrosis factor alpha (TNFα) plays both a major and early role in the inflammatory response. In addition to a physiological role in immune function, TNFα can also mediate direct cellular effects, including apoptosis and mitogenesis, as well as promote differentiation in a cell type-specific manner. Disruption of the normal signaling pathways associated with abnormal release and/or synthesis of TNFα is hypothesized to contribute to a wide range of disease states (reviewed in Luster et al. 1999). For example, an essential role for TNFα in promotion of mouse skin tumors has been independently demonstrated by two studies (Saganuma et al. 1999; Moore et al. 1999). Although the mechanisms for this are not understood, the stimulation of clonal growth of initiated cells by TNFα (secreted by tissue macrophages) is hypothesized. This hypothesis is supported by in vitro studies that demonstrate a promoting role of TNFα in mouse JB6 cells. Other pathological states linked to TNFα release or deregulation include pathologies involving the immune system, including autoimmune diseases, arthritis, multiple schlerosis, and inflammatory bowel disease (Kollias et al. 1999). Evidence for a causative role of TNFα in the etiology of lung fibrosis is particularly strong. For example, TNFα released by phagocytic lung macrophages may be responsible for a local induction of apoptosis after exposure to particulate matter associated with air pollution associated with energy-related facilities (Chin et al. 1998). Stimulation of collagen and fibrinogen synthesis in endothelial cells by TNFα is likely the initial signal that leads to lung fibrosis after prolonged exposure to particulate matter. Exposure to ionizing radiation also stimulates TNFα release in lung cells. For example, TNFα is a central mediator of the events leading to radiation-induced lung fibrosis. Interestingly however, low dose total body irradiation (0.2 Gy) has also been associated with beneficial effects of TNFα, such as inhibition of tumor cell metastasis (Hashimoto et al. 1999). The reasons for the pleitropic responses to TNFα are unclear, but most likely reflect differences in the signaling pathways induced and the global patterns of genes regulated by TNFα in different cell types. Thus, to understand the underlying basis for TNFα-mediated effects, we need to evaluate the gene networks regulated by TNFα in a global manner.

Results and Accomplishments

High Throughput PCR Amplification of cDNA from Bacterial Culture

We successfully completed the amplification of 2000 mouse cDNA by PCR. PCRs were performed in 96-wells format directly from bacterial lysate, and products were purified subsequently (see Figure 1).

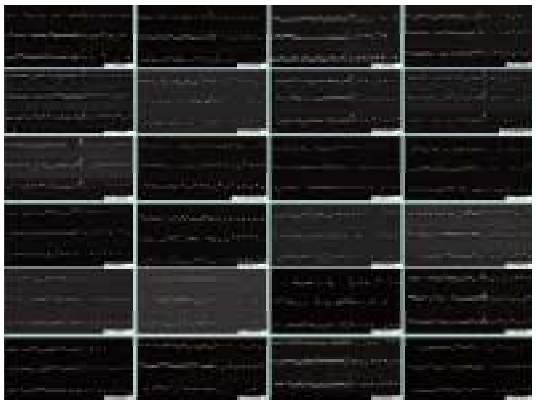

Figure 1. PCR products derived from 2304 mouse cDNA clones

Construction of Control RNA and DNA Fragment

Two control genes have been constructed from the kanamycin and ampicillin genes by adding a T7 promoter and a polyA tail to the each of the DNA fragments. A few hundred micrograms of RNA transcripts have been produced to be used as internal controls for balancing signals. Control RNA was successfully labeled with Cy3 and hybridized with a testing slide with the control cDNA spotted a hundred times (Figure 2).

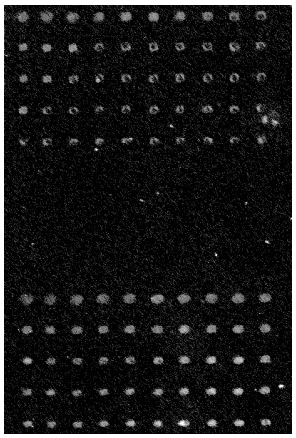

Figure 2. Hybridization of Cy3-labeled control RNA (kanamycin gene) with control PCR fragments on glass slide. Control PCR fragments were spotted 50 times at two concentrations on aldehyde treated slide.

Fabrication of cDNA Microarray

A program has been written with software AxSys^{TM} and has been used to control the arrayer in spotting approximately 2000 cDNA on a single glass slide. Spotted cDNA was cross-linked on a chemically treated surface. We have successfully cross-linked cDNA on aldehyde or polylysine coated glass surface (Figure 3).

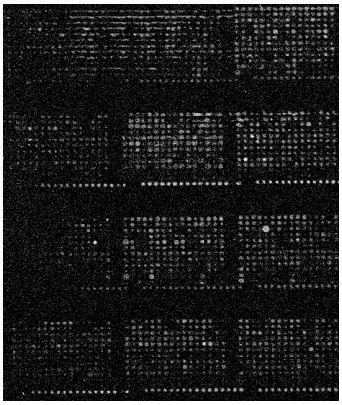

Figure 3. Visualization of immobilized 1920 unique PCR fragments using Cy3-labeled control RNA by hybridization at low stringency

Establishing cDNA Labeling Methods

Two cDNA labeling methods have been shown to be effective in labeling target total RNA (Figure 4). Reagents from Genisphere Inc. that use capturing oligos to capture a three-dimensionally linked Cy3 or Cy5 molecules for signaling amplification seems more cost-effective.

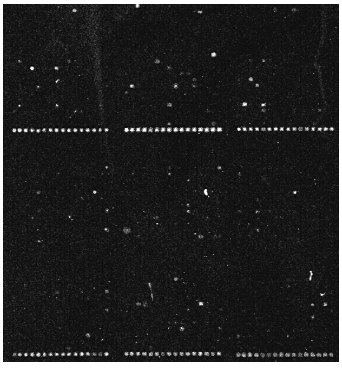

Figure 4. Analysis of gene expression profile of murine macrophage after infected with *Salmonella* for 19 hours

Summary and Conclusions

The process to fabricate mouse cDNA microarrays has been established. The ability to amplify cDNA from bacterial culture lysate allows us to generate thousands of

PCR products for immobilization on chemically treated glass surface in a few months. The Genisphere labeling method is efficient in generating highly fluorescent probes from a few micrograms of total RNA. We concluded that the

- good quality PCR products can be obtained from bacterial culture lysate for cDNA microarray fabrication
- kanamycin and ampicilin genes can be used as internal control genes
- a few micrograms of total RNA are sufficient to generate probes for hybridization using cDNA microarray.

This project will continue during the next year to amplify more cDNA clones that will include most of the TNFα related clones and unknown EST clones. Mouse cDNA microarrays fabricated will be used to characterize the global gene expression profile affected by TNFα.

References

Chin, BY, ME Choi, MD Burdick, RM Strieter, TH Risby, and AMK Choi. 1998. *Am. J. Physiol.* 275:L942-L949.

Hashimoto S, H Shirato, M Hosokawa M. et al. 1999. *Radiat Res* 151:717-724.

Kollias G, E Douni, G Kassiotis, D Kontoyiannis. 1999. *Immunol Rev* 169:175-194.

Luster MI, PP Simeonova, R Galluci, J Matheson. 1999. *Crit Rev Toxicol* 29:491-511.

Moore RJ, DM Owens, G Stamp, et al. 1999. *Nature Med* 5:828-831.

Suganuma M., S Okabe, MW Marino, et al. 1999. *Cancer Res* 59:4516-4518.

Publications and Presentations

Wong KK. "Identification of differentially over expressed genes in ovarian cancer by Micromax cDNA microarray." *Biotechniques*. (in press).

Wong KK. September 2000. "Identification of differentially expressed genes in ovarian cancer by cDNA microarray." Invited presentation, Northwest Conference on Microarrays, Seattle, Washington.

Characterization of Nodes in Cell-Signaling Pathways Using High-Throughput Array Technologies

David L. Springer, Kwong Kwok Wong, Richard C. Zangar, Susan M. Varnum, John H. Miller, Catherine E. Petersen, Karen L. Wahl, Karin D. Rodland

Study Control Number: PN99007/13335

This project is developing new technologies to address broad issues of gene expression and protomics. Our ultimate goal is to understand cell signaling pathways and networks and determine how they are regulated. Identification and characterization of proteins involved in cell signaling events and how they are altered by environmental exposures will provide critical information regarding the onset and progression of human disease.

Project Description

Scientific studies of gene expression and proteomics use information from cDNA arrays to identify genes whose expression is altered by environmental stresses and disease states. In addition, antibody arrays are being developed to selectively and quantitatively capture specific proteins from cellular preparations. Once captured, the proteins are identified using advanced mass spectrometric techniques, and their post-translational modification status is determined. Changes in cellular proteins will then be related to cell function. These new approaches will enhance our understanding of how changes in the proteome in response to environmental agents contribute to the onset and progression of human diseases.

Introduction

To better understand the disease process, it is necessary to understand both normal and abnormal signaling. A major function of proliferation-associated signal transduction pathways is regulation of the cell's decision to proliferate or not, based on the integration of numerous extracellular (and therefore environmental) stimuli. Among those extracellular molecules capable of modifying cellular behavior, calcium and other multivalent cations including cadmium and gadolinium have recently been identified as key mediators of the balance between proliferation and differentiation. In mammalian cells, a recently cloned G-protein coupled receptor, the calcium-sensing receptor (CaR), has been shown to be the key player in sensing changes in these small molecules and translating them into proliferative responses. One disease in which the CaR appears to play an essential role is ovarian cancer, and we have selected this disease as a test bed for development of new high-throughput technologies. Professor Rodland's laboratory at Oregon Health Sciences University, Portland, has demonstrated that the cell type responsible for human ovarian cancer, the ovarian surface epithelial cell, is critically dependent on relatively high levels of extracellular calcium for proliferation, and the CaR is the molecule responsible for initiating this response (McNeil et al. 1998; Hobson et al. 2000). The presence of an aberrant truncated version of the CaR in 75% of highly malignant ovarian tumors (stages III and IV) was characterized by Rodland. The major focus of this project is to delineate the precise pathways by which normal CaR modulates the proliferation of ovarian surface epithelial cells to define how these pathways are disrupted by the aberrant receptor in the process of ovarian carcinogenesis.

Approach

Traditional approaches to the study of signaling pathways, such as those based on co-immunoprecipitation, affinity chromatography, 2D-PAGE, and in vitro kinase assays, have established that signaling pathways involve the concerted interaction of multiple proteins in series and in parallel, and that these interactions most frequently involve specific post-translational modifications which serve as the activating step for the next round of signaling. Despite the considerable advances in knowledge provided by these older technologies, they have serious shortcomings that limit our ability to fully comprehend signaling processes. Traditional biochemical approaches are limited to interactions between known proteins with high affinity for each other and that are present at relatively abundant levels. In this project, we are applying state-of-the-art technologies dependent on antibody technology coupled to mass spectroscopy to

identify novel proteins of importance in signal transduction and to more fully characterize interactions among proteins expressed at low levels and, therefore, most likely to be rate-limiting and critical to the disease process. Ultimately these analytical approaches will be coupled with sophisticated mathematical modeling techniques to both guide and refine the developing picture of intracellular signaling.

Results and Accomplishments

cDNA Arrays

The ability to simultaneously measure the expression level of thousands of genes allows us to identify differentially expressed genes in a relative short time. In the past year, we have established the capability to fabricate cDNA microarrays and to analyze data generated from these cDNA microarrays. To establish this capability, we acquired a robotic arrayer from Cartesian Technologies for fabricating cDNA microarrays, and a dual laser scanner to acquire and analyze the expression signals. Furthermore, software, Imagene™ 3.0 (Figure 1) and OmniViz™, is being evaluated for data mining and clustering analysis.

To establish the process of fabricating mouse cDNA microarray, we acquired 23,000 unique mouse cDNA clones from Research Genetics and National Institute of Aging. High-throughput polymerase chain reaction (PCR) amplification of cDNA clones, robotic arraying, cross-linking of PCR products on chemically treated slides, labeling of target RNA, hybridization, and signal analysis have been optimized (Figure 2). Applications of these cDNA microarrays will be developed in the coming years. We have also used a few commercial cDNA microarrays to establish the protocols and to identify differentially expressed genes in ovarian cancer. From the cDNA microarray experiment, we were able to identify 47 genes that are over expressed in ovarian cancer (Wong et al. 2000). A patent has been filed for detection of ovarian cancer using the identified genes.

Characterization of Proteins by Mass Spectrometry

We have developed matrix assisted laser desorption ionization mass spectrometry (MALDI-MS) techniques for identifying unknown proteins and for determining structural modifications to these proteins. Using these approaches, we have demonstrated the ability to identify both known and unknown proteins in partially purified protein fractions. Using antibodies to immunoprecipitate tyrosine phosphorylated proteins coupled with separation on 1D-PAGE gels, we have identified several phosphorylated proteins associated with malignant transformation in an ovarian cancer model (Figure 3).

While we have shown that current procedures are adequate for identifying proteins, these methods typically provide less than 50% coverage of the peptide fragments contained in a single protein. Identification of protein variations associated with covalent modifications such as phosphorylation, mRNA splicing, or proteolysis requires

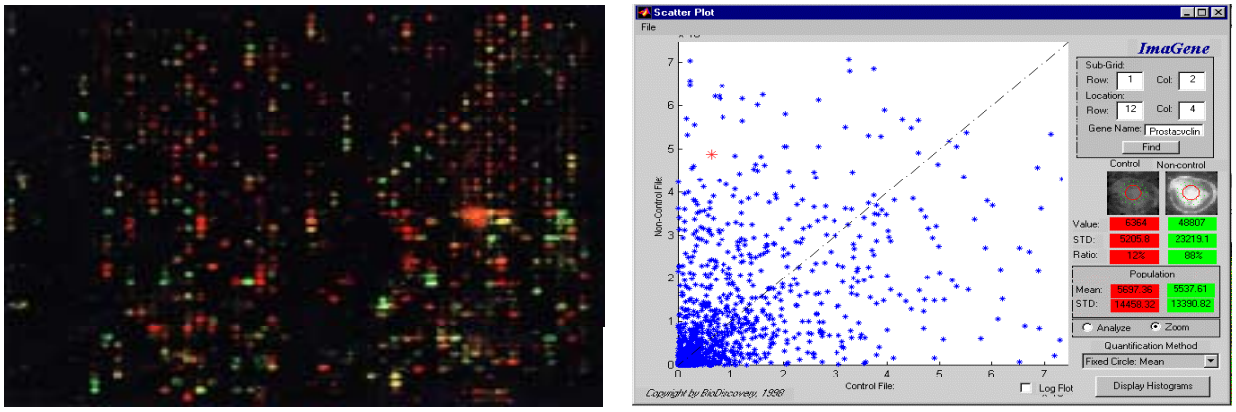

Figure 1. Data mining of differentially expressed genes in ovarian cancer using software Imagene 3.0. 1a. Differentially expressed gene analysis on three pooled normal HOSE cultures (HOSE17, HOSE636, and HOSE642) and three pooled ovarian cancer cell lines (OVCA420, OVCA433, and SKOV3) using a commercially available cDNA microarray containing 2400 human cDNA. Probes derived from cancer cell lines and normal HOSE cells were fluorescently labeled with cy3 (green) and cy5 (red) respectively. 1b. Scatter plot analysis of a single microarray experiment using Imagene software. The control is the relative expression level of genes in HOSE cells, and the non-control is the relative gene expression level of genes in ovarian cancer cell lines. When a dot is highlighted, the name of the gene, the flourescent intensity, and actual spot image will be shown in the right side panel and directly linked to Medline and GenBank databases.

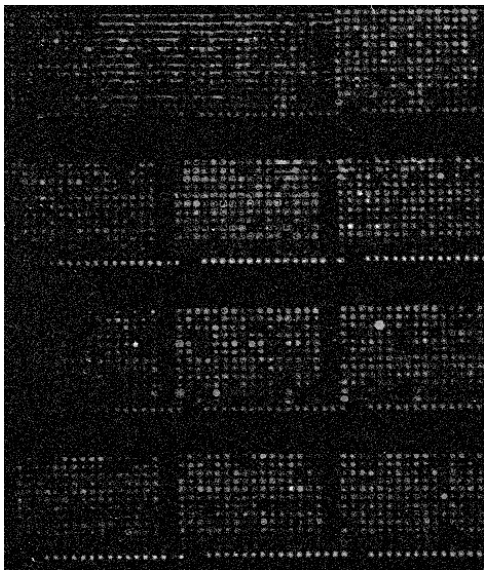

Figure 2. Hybridization of a cy3-labeled control RNA to a microarray with 1920 cDNA fragment to reveal immobilized polymerase chain reaction product

analysis of peptide fragments that are representative of the complete protein sequence. To improve these methods, we developed a combination of protein digestion and gel extraction procedures that provide >95% coverage of a test protein. These procedures should be suitable for determining protein modifications with a high degree of confidence.

Protein Arrays

A major goal of this task is the development of protein arrays that will allow for the rapid identification and characterization of a large number of proteins involved in cell signaling pathways important in the genesis of ovarian cancer. In order to accomplish this, we are developing arrays of antibodies that will selectively bind cell-signaling proteins. Bound proteins will be evaluated using sophisticated mass spectrometric methods. This coupling of protein array technology with advanced mass spectrometric detection provides a high-throughput approach and a means to identify and characterize biologically important changes in the proteome (Figure 4).

We have developed the initial methodologies necessary for the attachment of antibodies to a solid support that are compatible with mass spectrometry. Currently two different attachment chemistries have been employed. In both cases, a self-assembled monolayer is generated on gold, a surface that is preferred for MALDI-MS. The antibody is then covalently attached to the self-assembled monolayer. The first self-assembled monolayer we tried, dithiobis(succinimidyl propionate), is an amine-reactive, homobifunctional cross-linker that covalently attaches the antibodies to the gold surface. We have also achieved good protein attachment using an alkanethiolated self-assembled monolayer. For this attachment strategy, a zero-length carbodiimide linker is employed to covalently link the terminal carboxylic acid group of the self-assembled monolayer with a primary amine from the protein. Additionally, we developed the necessary methods to analyze the different attachment chemistries both to monitor the attachment of the self-assembled monolayer and antibody and to address the functionality of the immobilized antibody. We are currently using these methods to optimize and extend our attachment strategies.

Summary and Conclusions

Technologies to characterize the relationship between signal transduction, environmental exposures, and human diseases are being implemented. These include

- cDNA microarrays
- antibodies to capture specific proteins
- protein characterization by mass spectrometry
- protein identification using bioinformatics programs.

References

Hobson et al. 2000. "Signal transduction mechanisms linking increased extracellular calcium to proliferation in ovarian surface epithelial cells." *Exp. Cell Res.* 258:1-11.

McNeil et al. 1998. "Functional calcium-sensing receptor expression in ovarian surface epithelial cells." *Amer. J. Obstet. Gynec.* 178:305-313.

Wong KK, RS Cheng, and SC Mok. "Identification of differentially over expressed genes in ovarian cancer cells by MICROMAX cDNA microarray." *BioTechniques* (in press).

Publications and Presentations

Wong KK, RS Cheng, and SC Mok. "Identification of differentially over expressed genes in ovarian cancer cells by MICROMAX cDNA microarray." *BioTechniques* (in press).

Zangar RC, KL Wahl, CE Petersen, RD Rodland, DL Springer. 2000. "Protein primary structure determined by protease digestion and MALDI-MS peptide analysis." To be presented at Hanford Symposium, Richland, Washington.

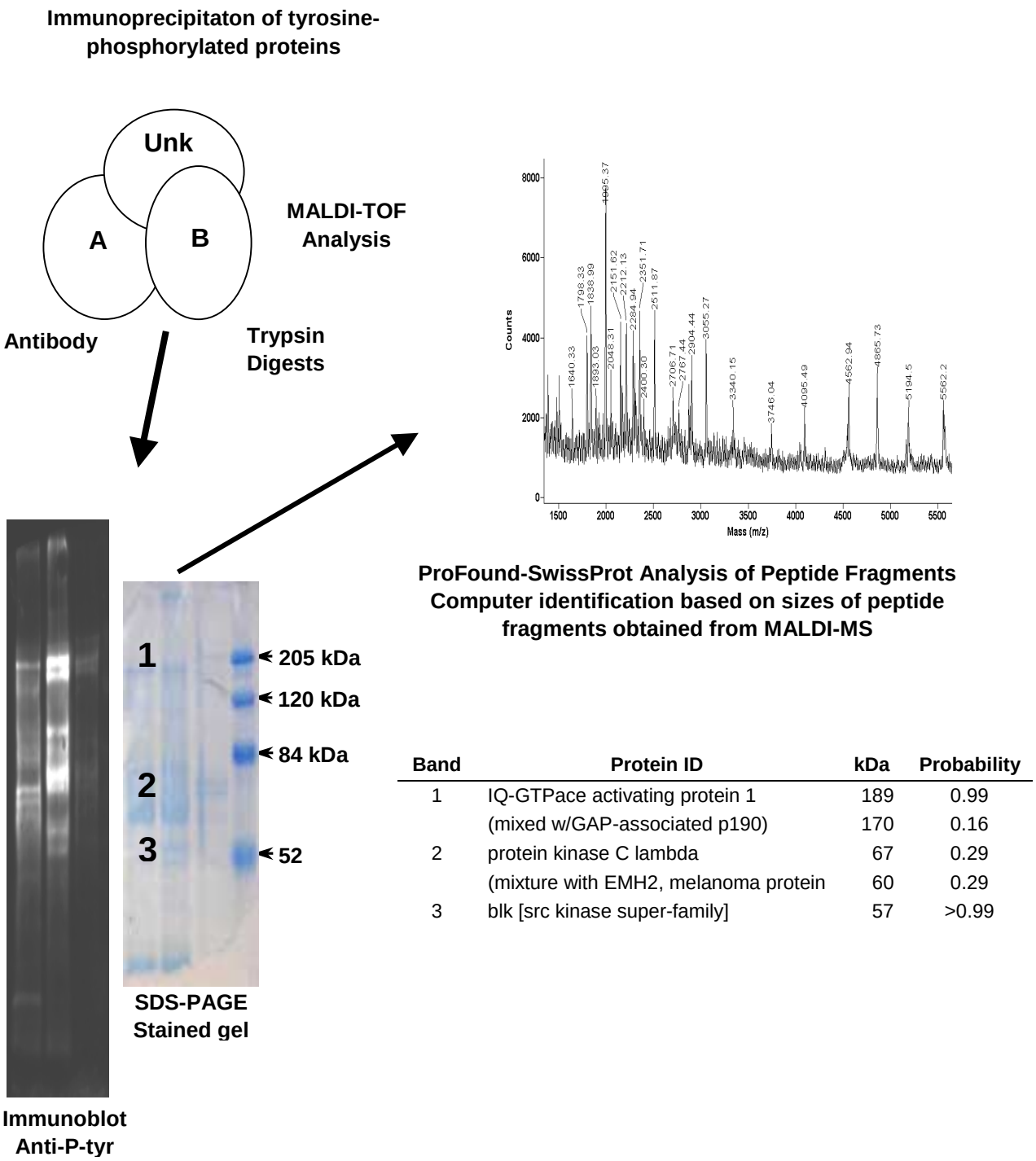

Band	Protein ID	kDa	Probability
1	IQ-GTPace activating protein 1	189	0.99
	(mixed w/GAP-associated p190)	170	0.16
2	protein kinase C lambda	67	0.29
	(mixture with EMH2, melanoma protein	60	0.29
3	blk [src kinase super-family]	57	>0.99

Figure 3. Identification of tyr-phosphorylated proteins using immunoprecipitation, gel separation, trypsin digestion and MALDI-MS

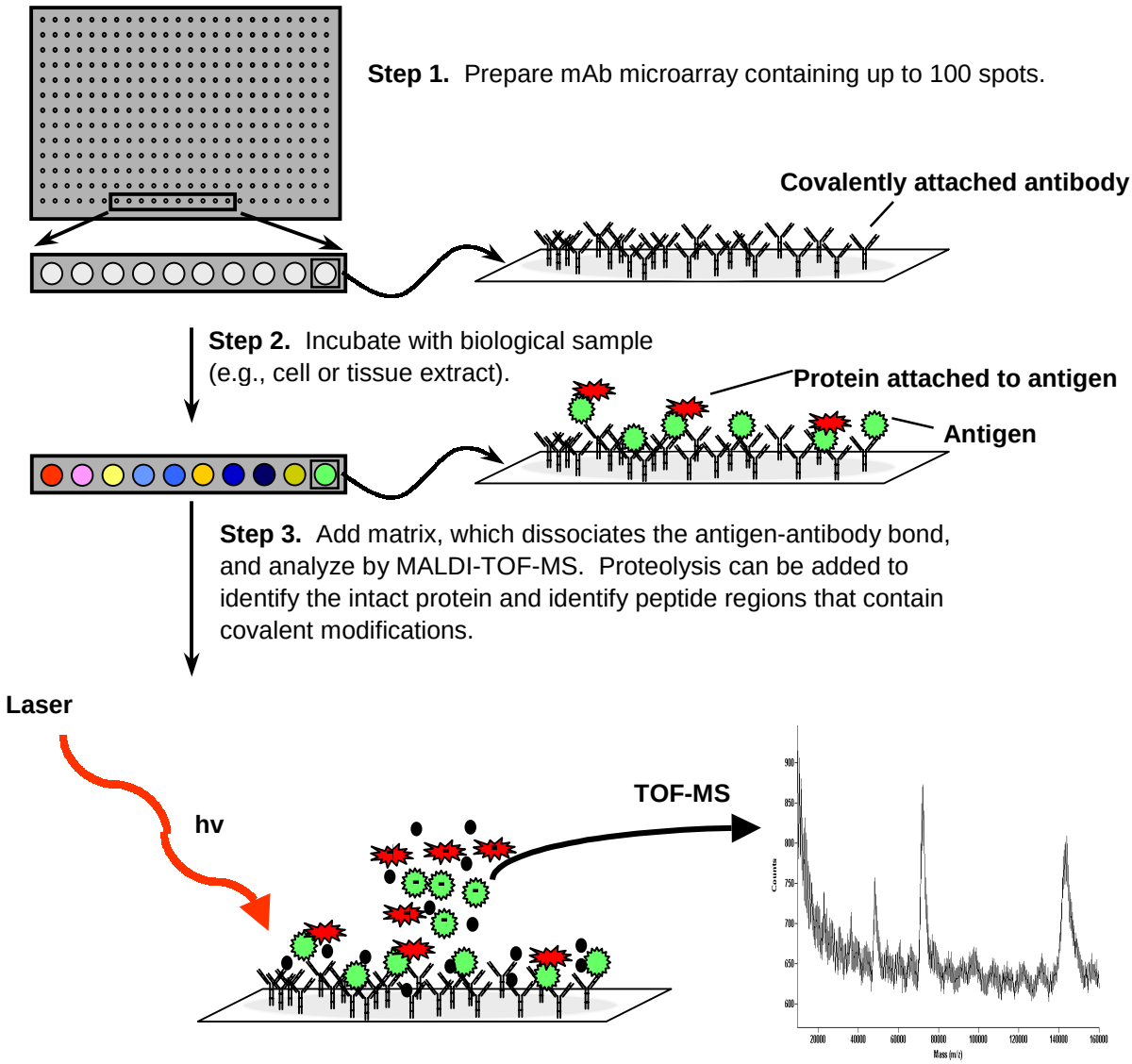

Figure 4. Microarray procedures for protein analysis

Coupled NMR and Confocal Microscopy for In Situ, Real Time Cellular Measurement Capabilities

Steven D. Colson, Paul D. Ellis, Robert A. Wind, Eric J. Ackerman, Don S. Daly, Gary R. Holtom, Paul D. Majors, Kevin R. Minard, John M. Price

Study Control Number: PN99009/1337

The purpose of this project is to develop an instrument that integrates magnetic resonance microscopy (MRM) and confocal optical microscopy (OM) so both can be exploited simultaneously for noninvasive analysis of live, large single cells or three-dimensional cell systems. This instrument may be considered as the next generation instrument for biochemical and biomedical research on a cellular level.

Project Description

A multidisciplinary research team is carrying out a project that will generate a novel microscope specifically designed for cellular research. The instrument will integrate magnetic resonance microscopy and confocal optical microscopy so both can be exploited simultaneously for noninvasive analysis of live, large single cells or three-dimensional cell systems. The work performed included 1) constructing, calibrating, and testing the optical and magnetic resonance components of the microscope; 2) developing software to operate the confocal microscope; 3) developing statistical and image processing methods to improve the information obtained with magnetic resonance microscopy; and 4) bench-marking magnetic resonance microscopy-only and optical microscopy-only activities to establish the state of the art in each imaging modality. The first combined images have been obtained of individual *Xenopus laevis* oocytes. These high-resolution optical images have been used to increase the spatial resolution and the contrast near the cell boundaries in the magnetic resonance images.

Introduction

Both magnetic resonance microscopy and confocal optical microscopy each have their unique advantages and disadvantages when applied to studies of live cells (Blümler et al. 1998; Aiken et al. 1995; Pawley 1995). For example, while optical images can be acquired with a high spatial and temporal resolution, the application of optical microscopy is largely limited to transparent and stained samples. Conversely, while magnetic resonance microscopy is well suited for optically opaque samples and generally requires no exogenous contrast agents, the method is sensitivity limited. Despite these shortcomings, however, magnetic resonance microscopy is extremely useful as it can provide both biophysical and biochemical information that cannot be obtained with optical microscopy, and that is particularly useful for understanding health and disease at a cellular level. Therefore, correlating the optical microscopy and magnetic resonance microscopy data provides significant advantages over each of the methodologies individually.

The specific aim of this project is to construct a microscope that will make it possible to study cells simultaneously with optical microscopy and magnetic resonance microscopy. Then the data obtained with one technique will be used to guide and optimize measurements with the other methodology. For example, the high-resolution optical images can be used to select volumes of interest on which to perform local magnetic resonance spectroscopy and to increase the resolution and contrast in the magnetic resonance images. On the other hand, magnetic resonance microscopy can provide complementary information in opaque or partially opaque cell systems, where optical microscopy is of only limited use. Moreover, the combined microscope will provide simultaneous optical/magnetic resonance information about cellular events, thus correlating the optical and magnetic resonance data. Therefore, the integrated optical microscopy/magnetic resonance microscope will significantly improve the capabilities of both methodologies for cellular research.

Results and Accomplishments

Magnetic Resonance Microscopy

We tested the performance of the magnetic resonance part of the compound microscope, and found that the magnetic

resonance sensitivity is about a factor 2 below its theoretical maximum. This is due to the thin wire used for the magnetic resonance solenoid, which we applied to create relatively large optical windows between the coil turns. Investigations are continuing to improve this situation. Also, magnetic resonance microscopy-only studies were continued of single *Xenopus laevis* oocytes undergoing heat stress. Several interesting features were observed: the volume increased by 8 to 10% upon heating, the images show a formation of T_1-enhanced, diffusion-limited water layers adjacent to the plasma membrane and inside the nuclear membrane, the lipid lines in the spectra were narrowed by 30%, and some intensity changes occurred in the spectral lines of other metabolites. We have not yet been able to interpret these changes, which are in part irreversible, in terms of cellular activities occurring during heat shock.

Optical Microscopy

The optical system was tested, and it was found that after careful alignment of all the optical components, the point-spread functions of our microscope in the x-, y-, and z-direction are about 85% of that of a commercial (Sarastro) confocal microscope, with the same numerical aperture. This slightly reduced image quality is probably a result of the fact that our confocal microscope is a more complex system than usual.

Software Developments for Confocal Microscopy and Image Analysis

Work on the combined optical microscopy/magnetic resonance microscopy system developed in the Environmental Molecular Sciences Laboratory (EMSL) yielded the first release of a distributed software system for remote confocal microscopy control, collaborative image analysis, and network data file management. A front-end software package, EMSL Scientific Imaging, provides a cross-platform (PC/UNIX) interface for the acquisition, visualization, and storage of information from network archives of magnetic resonance microscopy and optical microscopy data and from Internet-accessible microscope systems. EMSL Scientific Imaging communicates with the EMSL 3-D Image Server (3DIS) that supports secure, remote acquisition and control of the microscope hardware. Together, these pieces form a complete system for remote microscopy experiments. EMSL Scientific Imaging and 3DIS form the foundation for the combined instrument system that will support simultaneous acquisition from both microscopes simultaneously.

Combined Optical Microscopy/Magnetic Resonance Microscopy

Confocal fluorescence images and magnetic resonance water and lipid images were obtained on *Xenopus laevis* oocytes of different growth stages. Prior to the image experiments, the oocytes and their surrounding follicle particles were stained with rhodamine-123, a nontoxic fluorescent dye selective for active mitochondria. Then the stained oocytes were injected into the perfusion system, filled with Barth's medium, and the flowing medium transported the oocytes into the sample chamber and pressed them against the constriction in the perfusion tube. In order to register and calibrate the optical microscopy and magnetic resonance microscopy image spaces, a 0.53-mm translucent polystyrene bead was injected prior to the insertion of the oocyte cells. In Figure 1, two-dimensional optical microscopy and magnetic resonance microscopy images of a same plane through the bead and a 0.62-diameter stage-3 oocyte are shown. With magnetic resonance microscopy, the distribution of both water and mobile lipids were imaged.

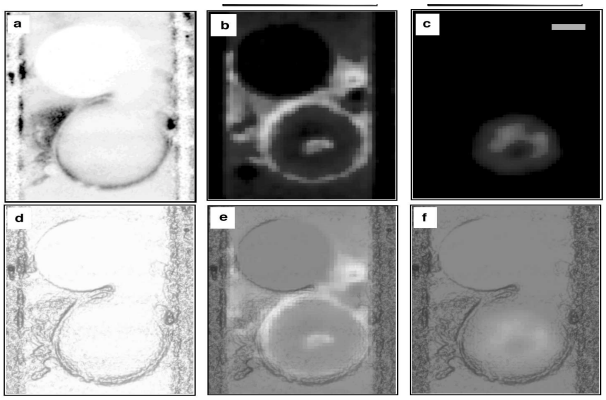

Figure 1. Two-dimensional combined optical microscopy and magnetic resonance microscopy images of a 0.53-mm-diameter polystyrene bead (top object) and a 0.62-mm-diameter stage-3 *Xenopus laevis* oocyte (bottom object) in a 0.82 mm inside diameter glass capillary tube. (a) an optical microscopy image; (b) a water-selective magnetic resonance image; (c) a lipid-selective magnetic resonance image; (d) an optical microscopy relief contour image, obtained from image (a); (e) an overlay of the water magnetic resonance image with the optical microscopy relief image; and (f) an overlay of the lipid magnetic resonance image with the optical microscopy relief image. The scale bar shown in (c) is 0.2 mm in length.

In the optical microscopy image, the right side of the bead and the top right side of the oocyte are poorly defined. This is due to the presence of three small oocytes in the optical path and below the optical microscopy plane, which produce shadows in the plane of interest. The high optical microscopy intensity at the oocyte boundary is believed to arise from the mitochondria in the surrounding follicle cell layer, while the interior is optically opaque. Additional features include stained connective tissue near the oocyte and a fluorescing layer along the inner wall of the sample tube. We conclude that excellent image registration of both images is obtained. Figure 2 shows similar confocal and magnetic resonance images obtained on a smaller stage-2 (0.38-mm-diameter) transparent oocyte. In contrast to results obtained on the larger oocyte, the confocal image clearly shows the mitochondrial cloud, whereas in the water magnetic resonance image, only an inside layer of enhanced water intensity is detected. The results clearly illustrate that combined microscopy provides significantly more information than obtained with each of the techniques individually. The magnetic resonance images provide detailed information about the intra-cellular structure of the larger opaque oocyte that is not observed with optical microscopy. On the other hand, in the smaller transparent oocytes, the high-resolution optical images can be used to complement the relatively low-resolution magnetic resonance images.

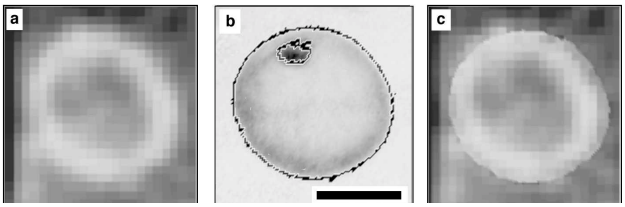

Figure 2. Application of confocal image data to enhance the resolution and contrast of magnetic resonance images at object boundaries. (a) magnetic resonance water image of the stage-2 oocyte; (b) optical microscopy image of the same oocyte, and the contour plot, obtained from this image; (c) magnetic resonance image with enhanced resolution and contrast near the contour boundaries. Enhancement was achieved by overlaying the image (a) and the contour plot (b) to distinguish magnetic resonance image pixels containing the boundaries between the cell and the surrounding medium. Next, the average magnetic resonance intensities in these pixels were redistributed using the confocal boundaries. The scale bar shown in (b) is 0.2 mm in length.

First Optical Microscopy/Magnetic Resonance Microscopy Application: Sharpening of the Magnetic Resonance Images

The a priori knowledge provided by the confocal image can be used to improve the boundary resolution and the contrast in the magnetic resonance images. This is illustrated in Figure 2 as well. By overlaying the high-resolution optical contour plot, given in Figure 2b, with the relatively low-resolution magnetic resonance image shown in Figure 2a, image pixels can be identified in the magnetic resonance image containing the boundary between the oocyte and the surrounding medium. Then the average intensity in each of these pixels can be redistributed into each compartment inside these pixels. Figure 2c shows the resulting magnetic resonance image. It follows that both the boundary resolution and contrast are significantly enhanced. Hence integrated optical microscopy/magnetic resonance microscopy can be used to produce images in which the optical spatial resolution is combined with the magnetic resonance contrast, which could be important for a variety of applications, including the diagnosis of diseased cells.

Statistical Analysis

The research and development of algorithms to analyze the combined measurement sets from the magnetic resonance and optical microscopes focused on three problems: 1) image and spectrum enhancement, 2) image registration (alignment of data spaces), and 3) spectral unmixing/spectral sharpening. The first problem involves the elimination or minimization of measuring artifacts. The second problem is due to differences in physical alignment, resolution, and measuring mode of the two distinct instruments. The third problem is about capitalizing on the complementary, but distinct, information provided by two distinct instruments simultaneously measuring the same sample. Solutions to these problems using existing software such as Image-J by NIH and IBM's OpenDX melded with custom components are being explored. At this time, we have identified the necessary operations (deconvolution, image warping, spectral unmixing); we have derived preliminary algorithms, and have developed prototype subroutines. We have not, as yet, developed a refined and integrated analysis package.

Summary and Conclusions

The first optical microscopy/magnetic resonance microscopy microscope was successfully assembled and tested, and the first combined images have been obtained of *Xenopus laevis* oocytes. We anticipate that a complete integration of optical and magnetic resonance microscopy could result in a variety of new applications for cellular research.

- The high-resolution optical images can be used to increase the spatial resolution and contrast in the magnetic resonance images.
- Boundaries of organelles in large cells or specific areas in cell agglomerates observed in optical images can be used to guide and optimize volume-selective magnetic resonance microscopy experiments to obtain magnetic resonance spectra of identified regions.
- In (partially) opaque samples, the magnetic resonance images can be used to complement the optical contour images.
- The microscope provides real-time correlation between the optical and magnetic resonance data.
- The microscope makes it possible to study dynamic events in live cells simultaneously with both techniques.
- The optical information can be used to separate magnetic resonance data of different cell populations in heterogeneous cell systems.

The project will continue during fiscal year 2001, further optimizing the system and exploring the applications mentioned above on single *Xenopus oocytes* and model tumor spheroids.

References

Aiken NR, EW Hsu, and SJ Blackband. 1995. "A review of NMR microimaging studies of single cells." *J. Magn. Reson. Anal.* 1:41.

Blümler P, PB Blümich, RE Botto, E Fukushima, Eds. 1998. "Spatially resolved magnetic resonance." Wiley-VCH, Weinheim.

Pawley JB, Ed. 1995. *Handbook of biological confocal microscopy*. Plenum, New York.

Publications and Presentations

Wind RA, KR Minard, GR Holtom, PD Majors, EJ Ackerman, SD Colson, DG Cory, DS Daly, PD Ellis, NF Metting, CI Parkinson, JM Price, and X-W Tang. "An integrated confocal and magnetic resonance microscope for cellular research." *J. Magn. Reson.* (in press).

Wind RA. November 1999. "Recent developments in magnetic resonance microscopy at PNNL." Washington University, St Louis, Missouri.

Wind RA, EJ Ackerman, DG Cory, GR Holtom, PD Majors, KR Minard, and X-W Tang. April 2000. "Integrated optical and magnetic resonance microscopy for cellular research." 41th ENC, Asilomar, California.

Wind RA, KR Minard, and PD Majors. April 2000. "Magnetic resonance microscopy at PNNL." Oregon Health Sciences University, Portland, Oregon.

Wind RA, KR Minard, and PD Majors. May 2000. "In vivo and in vitro magnetic resonance microscopy at PNNL." DOE Biomedical Engineering Contractors Meeting, Albuquerque, New Mexico.

Wind RA, GR Holtom, KR Minard, and BD Thrall. July 2000. "Integrated optical/magnetic resonance microscopy for cellular research." NCI Meeting about the Innovative Molecular Analysis Technologies Programs, Chantilly, Virginia.

Majors PD, EJ Ackerman, GR Holtom, LM Iakoucheva, NF Metting, KR Minard, and RA Wind. August 2000. "Combined, noninvasive confocal and magnetic resonance microscopy of live *Xenopus oocytes*." 8th International *Xenopus* Conference, YMCA of the Rockies, Estes Park, Colorado.

Acknowledgment

The gradient coil system used in the magnetic resonance microscope was designed in collaboration with Dr. David Cory at the Massachusetts Institute of Technology, and constructed by Cory and coworkers.

Development and Applications of a Multifunctional Optical Microscope for Mapping Cellular Signaling Pathways

Gary R. Holtom, Brian D. Thrall, Thomas J. Weber, Steven D. Colson, Noelle F. Metting

Study Control Number: PN00026/1433

Microscopy using molecular vibrations as an agent for image contrast provides opportunities for visualizing cellular components that are not visible by fluorescence microscopy. We extend fluorescence microscopy by adding simultaneous Coherent Anti-Stokes Raman Scattering vibrational microscopy, thereby increasing the range and nature of data recorded during research on individual live cells.

Project Description

The first year goal was to simplify and improve the apparatus previously used to demonstrate feasibility. We now have a second, complementary data channel, a versatile data acquisition system, improved sample handling, and a greatly simplified, yet more flexible laser source that permits rapid changes in the Raman frequency. These modifications enable us to conduct useful biological experiments in a routine fashion.

Introduction

The older, one-of-a-kind laser system, which required an experienced operator, was replaced with a commercial unit that is simpler, more reliable, and provides access to a wide range of molecular frequencies. Electronics and computer controls were improved so that high-quality images can be obtained quickly enough to be useful in live biological experiments. In addition, the new capability for simultaneous collection of fluorescence images provides useful complementary information for benchmarking purposes. Sample handling was greatly improved so that a tissue culture may be studied under controlled perfusion and temperature conditions.

Preliminary survey work conducted at different Raman frequencies shows changes in contrast as various molecular vibrations are enhanced. High signal-to-noise ratio data sets are obtained on a time scale of 2 minutes per image at a resolution of 200 by 200 pixels, with a diffraction limited spot size of 300 nm. The average laser powers are low enough (sub-mW) that live cells are still viable after scanning 15 images over a period of 4 hours; the duration of the test. Since no dyes are required for coherent anti-stokes Raman scattering imaging, photo-bleaching is not a problem. In addition, the same z-sectioning capability made possible by two-photon confocal microscopy is realized, permitting full three-dimension data sets to be obtained with complementary contrast mechanisms.

Results and Accomplishments

The most important equipment change was installation of a tunable laser system that replaced the one-of-a-kind apparatus of our own construction. We modified the source to reduce the laser line width to 100 cm^{-1} and to also permit tuning over the range of 0 to 4000 cm^{-1}, a significant improvement over the configuration as delivered. A number of optical filter combinations were tested for the required spectral properties and we now have access to Raman frequencies from 800 to 3600 cm^{-1} with essentially no background signal. In addition, we have dual-channel detection capability for isolating the anti-stokes Raman channel (wavelengths above 700 nm) from fluorescence signals (650 nm or shorter), allowing us to use a wide range of dyes for marking specific cellular components.

Sample handling was improved by a number of measures. The microscope is now enclosed in a light-tight temperature-regulated box so that the sample is maintained at 37°C. Tissues are cultured in 35 mm diameter petri dishes with cover-slip bottoms. The coherent anti-stokes Raman scattering signal, which emerges from the top of the dish, is collected by dipping a high numerical-aperture condenser in the culture medium and is directed to a filter assembly enclosing the pair of photomultiplier tubes. A video camera and frame-grabber are available for recording a transmitted light image of the sample.

The detection channels use photomultiplier tubes with very high gain and excellent sensitivity at long

wavelength. Dark noise is substantially eliminated with a gated sample/hold amplifier that is time-gated to the laser pulse. By using analog detection, we are now able to take advantage of modestly increased laser power (from about 10^{-4} to 10^{-3} W) to increase the detected signal by a factor of 10^3, with no increase in background signal. A new computer interface and control program record the signal for each laser shot for optimal averaging, and allow complete control over scan speed and image resolution, limited only by the mechanical capabilities of the scanning stage.

Biological samples with green fluorescent protein provide localized fluorescent signals when specific cellular metabolic pathways become active. A number of fluorescent dyes have been tested, the most useful to date being Mitotracker Green and Syto-13, a DNA/RNA stain. Fluorescence from the protein and these dyes is green, so that it does not interfere with the coherent anti-stokes raman scattering detection channel. Figure 1 shows an image pair from Hepa cells. The lipid rich small spots seen in the coherent anti-stokes raman scattering image at 2900 cm^{-1} (top) are correlated with the Mitotracker Green labels (bottom).

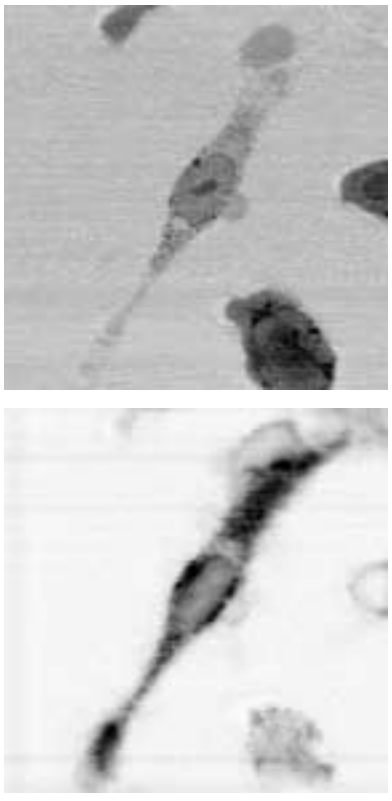

Figure 1. Hepa cells showing lipid-rich structures marked by coherent anti-stokes Raman scattering at 2900 cm^{-1} (top panel) and by Mitotracker Green (bottom panel)

Figure 2 shows an image pair of hepatocytes that have a defective lipid metabolism, resulting in large lipid vesicles. Conventional microscopy does not reveal the chemical nature of the vesicles, but the great intensity enhancement at a Raman frequency of 2900 cm^{-1} clearly identifies them as very high in lipid content. Repeating the image at a Raman frequency of 2200 cm^{-1}, which is off-resonance for hydrocarbons, shows a weaker enhancement and a reversal in image contrast.

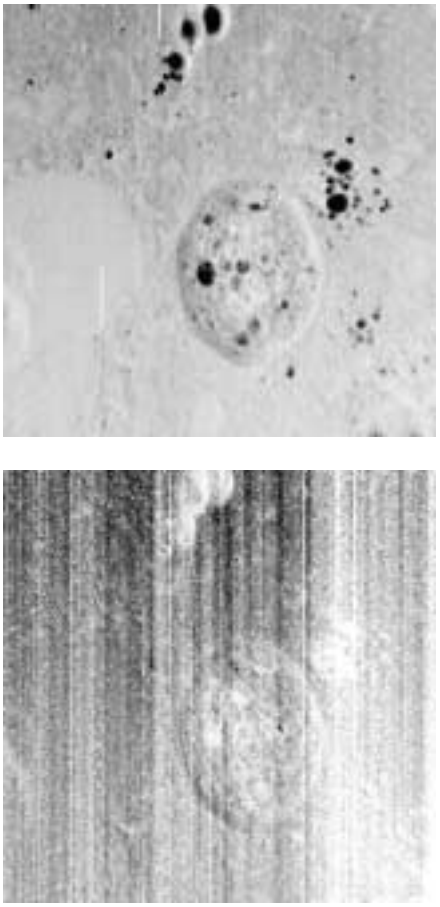

Figure 2. Hepatocytes with large lipid vesicles, showing the change in image contrast and intensity going from a coherent anti-stokes Raman scattering frequency of 2900 cm^{-2} (top) to 2200 cm^{-1} (bottom)

Figure 3 shows Hepa-1 cells undergoing apoptosis. The contrast provided by the Raman band at 2900 cm^{-1} is clearly different from the contrast due to Syto-13 nuclear stain.

Figure 4 shows D2XR11 cells undergoing apoptosis. The top panel is 120 minutes after treatment with TNFα and the bottom panel is after 160 minutes, showing detachment from the cover slip.

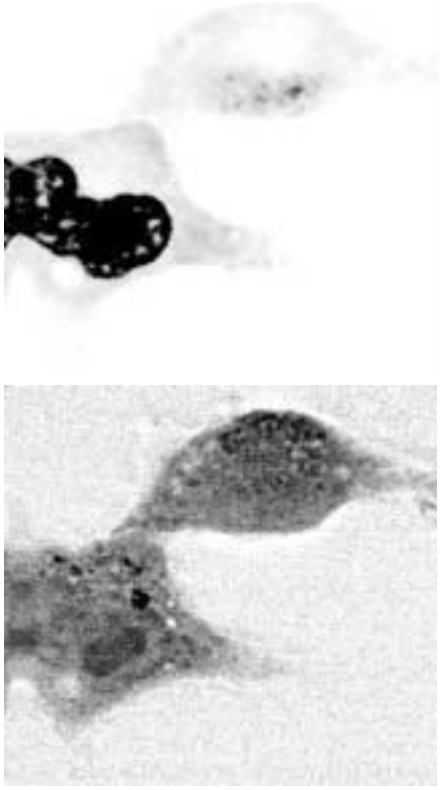

Figure 3. Hepa-1 cells undergoing apoptosis. Top panel: coherent anti-stokes Raman scattering image at 2900 cm^{-1}, showing lipid concentration. Bottom panel: Syto-13 stain for DNA/RA. Image scale is 47 by 47 microns.

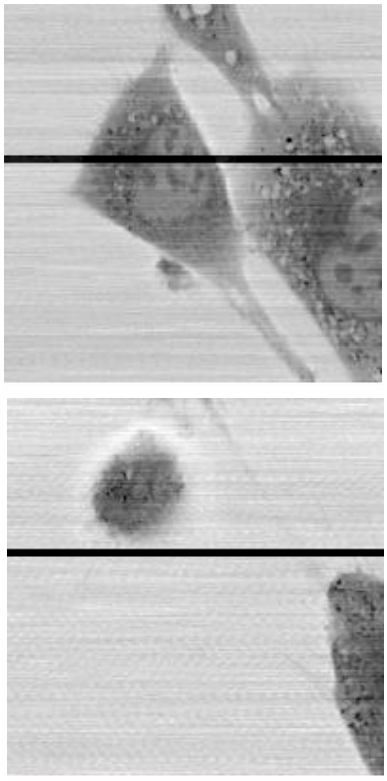

Figure 4. D2XRII undergoing apoptosis using the Raman frequency of 2900 cm^{-1}. The top panel is 120 minutes after treatment with TNFα and the bottom panel is after 160 minutes, showing detachment. The black streak is a data artifact.

Two experimental problems have been clearly identified and solutions for them are in progress. The first problem is the reduction of the laser line width from 100 cm^{-1} to about 35 cm^{-1}, close to the natural line width of many Raman peaks. A simple interference filter is convenient for reducing the line width of the fixed-frequency Ti:sapphire laser but this is not a useful solution for the tunable OPA, which produces the Stokes-shifted Raman frequency. A special thin etalon is under construction and is expected to produce a substantial increase in image contrast resulting from the reduced spectral line width.

The other outstanding problem is the chromatic aberration of the microscope objective. Visible aberrations are insignificant in modern high numerical opertune lenses, but there is a large focal plane shift between the pump laser at 810 nm and the Raman-shifted laser at 900 to 1070 nm, resulting in a broadening in the z-axis resolution from an expected 0.6 to about 2 microns. A custom lens is expected to solve this problem and also permit the use of thick samples by using water instead of oil as an immersion medium.

Summary and Conclusions

We learned that biological samples can tolerate sufficiently high pulse energy to make a coherent anti-stokes Raman scattering signal of many photons per laser pulse, and long-term experiments are tolerated by live tissue cultures. A number of dyes, both green fluorescent protein and fluorescent stains, provide useful identification of cellular features. The contrast of the sample changes dramatically with Raman frequency. Three-dimensional sample imaging and long duration movies of tissue cultures are obtained routinely.

Solutions for the two remaining technical challenges will be made in the next year of this study. We will then continue with the primary activity of the project, providing a molecular basis for features observed in cell images, and then apply this knowledge to relating molecular signatures and cellular signaling pathways. We expect to move from monolayer cell cultures to thick (100 micron) tissue samples with improvements in the objective lens design, which will make new experiments possible.

Development of a New High-Throughput Technology and Data Analysis Capabilities for Proteomics[(a)]

Richard D. Smith, Gordon A. Anderson, Tim D. Veenstra, Mary S. Lipton, Ljiljana Pasa-Tolic

Study Control Number: PN99068/1396

Proteomic analysis provides the key to understanding how cellular processes function in concert. The development of high throughput methods for proteomic studies will allow the effects of a variety of agents, including low-dose radiation exposure on organisms to be discerned in a rapid and global manner.

Project Description

This project is developing powerful new tools for broad evaluation and quantitation of protein expression. We will develop and demonstrate new approaches for proteome surveys that include the simultaneous capabilities for global 1) protein identification, and 2) precise determination of relative expression levels simultaneously for many proteins as a result of an environmental perturbation. The approach will be orders of magnitude more sensitive, faster, and informative than existing methodologies, including unmatched quantitative expression data. This project is also aimed at the development of new capabilities for data analysis that will "mine" these proteomic data and enable improved understanding of complex cellular signaling networks and pathways involving large numbers of proteins expressed by an organism. These capabilities will provide a basis for studying and understanding the subtle differences in the expressed proteome of an organism as the result of an environmental perturbation, such as in response to a chemical or radiation exposure, or differences arising from disease state(s), position in the cell cycle, or between different cell or tissue types. This new approach will enable systems-level views of differential protein expression so as to enable a global understanding of gene function and provide an enhanced view of systems-level cellular operations.

Introduction

As biological research moves increasingly toward the study of complex systems (consisting of networks of networks), the so-called "post genomics era," there is a clearer recognition of the complexity of cellular systems, and the growing optimism that the complexity of these systems is not intractable to understanding. In this new paradigm, whole cellular systems will be studied and modeled, and new understandings gained regarding their systems-level behavior and emergent properties arising from their complex nature.

Understanding complex cellular systems challenges the capabilities of all present approaches and research technologies, particularly since (to be most useful) understanding must be gained at a level of detail that provides insights into the various roles of the dominant chemically active class of cellular components—proteins. Proteins are, by far, the most important class of biochemically active molecules in cells, and they are also the most common target for drug development and manipulation. Thus, systems-level studies are most effective when they provide insights into the functional roles of individual proteins in the context of the complete system. A key desired goal is the ability to predict cellular and organism-level responses to environmental perturbations, which would then provide a basis for predicting low dose responses to chemical or radiation exposures and developing much more effective drugs that can also be tailored to an individual.

While the availability of complete genome sequences opens the door to important biological advances, much of the real understanding in cellular systems and the roles of its constituents will be based upon proteomics (which we define here as the study of how the proteome responds to its environment). The proteome may be defined as the entire complement of proteins expressed by a particular cell, organism, or tissue at a given time or under a specific set of environmental conditions. Surveys at the mRNA level do not provide exact information regarding the levels of proteins actually expressed or their subsequent

(a) Project started as a task under project, "Simultaneous Virtual Gel and Differential Display" in FY 1999. Subsequent tasks were added to this project in FY 2000.

cellular processing (such as post-translational modifications). Protein modifications, such as phosphorylation, can modulate protein function and are essential to the understanding of regulatory mechanisms. Changes in the proteome occur, for example, when environmental conditions change, upon exposure to different chemicals and ionizing radiation, during the cell cycle, with the onset of disease states and in the "normal" aging process. The biological processes involved in cell signaling, transcription, regulation, responses to stresses, etc., are elements of the complex linkages that determine system properties. The capability to measure such changes in the proteome with good precision is important for understanding these complex systems and the functions of their individual components.

At present, no rapid and sensitive technique exists for large-scale proteome studies. The study of proteins on a one-at-a-time basis, as conventionally practiced, provides an implausibly slow route to understanding cellular processes dictated by the expected 50,000 to 100,000 gene products expected from the human genome, and the additional 10- to 100-fold complexity introduced by their various modified forms. Beyond such considerations, it is generally accepted that such reductionist approaches are unlikely to provide insights into systems-level properties. The closest comparable technology, two-dimensional polyacrylamide gel electrophoresis (2-D PAGE), is a slow, labor intensive, and cumbersome technology.

The most common mechanism by which cells propagate signals via protein pathways and networks is phosphorylation. Studies estimate that as many as one-third of all cellular proteins derived from mammalian cells are phosphorylated. Cellular processes ranging from differentiation, development, cell division, peptide hormone response, and protein kinase activation are all regulated via phosphorylation. The large number of phosphorylated proteins requires methods that are able to rapidly identify proteins that undergo phosphorylation. The predominant method of studying protein phosphorylation is to label the proteins using radioactive phosphorous-32-labeled inorganic phosphate. The use of 32P (inorganic) to label proteins does not lend itself to high-throughput proteome-wide analysis due to the problems associated with the handling of radioactive compounds and the radioactive contamination of instrumentation. In addition, while immuno- and metal-affinity columns have been used to enrich mixtures for phosphopeptides, these strategies result in the isolation of many non-phosphorylated peptides through non-specific interactions complicating the analysis by introducing uncertainty about the nature of each peptide.

Approach

One objective of this project is to demonstrate the detection and identification of large numbers of proteins from yeast (or other organisms for which a full genomic sequence is available) and new stable isotope labeling methods to provide precise levels of expression of all proteins for eukaryotic proteomes. This approach will provide a systems-level view, with greatly improved sensitivity and high-precision quantitation of protein expression in cells, and the basis for new understandings in cell signaling and protein function. The information obtained would also provide essential input for modeling studies aimed at simulations of cells. In the second year of this project, we will continue development of the new proteome expression measurement technology described below and undertake the initial developments necessary for its extension and application to mammalian tissues. We will use these approaches to demonstrate new methods for 1) the proteome-wide identification and quantitation of phosphorylated proteins (highly relevant to signal transduction), and 2) for the determination of protein-protein interactions. The project efforts will also include the visualization tools necessary to display and interpret the extremely large and complicated data sets, so as to enable the study and understanding of complex networks and pathways associated with cellular responses at the systems level. An essential part of the data analysis tools to be developed will be those necessary for mining the data to extract information on protein modifications, unexpected modes of protein expression (recoding) and sequence frame shifts and other biological insights.

Our Laboratory is presently developing new experimental capabilities that provide major advances for proteomics. This new technology is based upon capillary electrophoresis separations in conjunction with direct mass spectrometric analysis and thus, avoids the labor-intensive process of individual spot excision and analysis as well as the time-consuming gel-based separation. Unlike 2-D PAGE separations that yield protein "spots" that must still be individually analyzed, our approach provides simultaneous information on expression level, protein identification, and protein modifications. However, new challenges for effective data analysis arise due to the quantity of information from each proteome measurement. Data analysis and effective use of the information presently constitutes an enormous bottleneck to the use of the "flood of data" that can now be generated. A complete two-dimensional capillary electrophoresis Fourier-transform ion cycloton resonance proteome analysis is projected to include a total of perhaps 1,000 mass spectra having generally high complexity, and amounting to approximately 1 to 10

Gbyte of raw data. Software tools required to address these large data sets are essential and do not presently exist. Visualization of the data is only the first step for its effective use.

We are developing capillary high-performance liquid chromatography separations combined with electrospray ionization-Fourier-transform ion cyclotron resonance (ESI-FTICR) mass spectrometry for the rapid and ultrasensitive analysis of the array of proteins expressed by cells. The approach involves the use of two separation stages and an intermediate enzymatic digestion step. In addition we are developing methods for the identification of large numbers of proteins from genomic databases based upon the use of "accurate mass tags" obtained from the high mass measurement accuracy provided by Fourier-transform ion cyclotron resonance. The approach to be taken will avoid the complexities of routine use of tandem mass spectrometry (MS/MS) for identification, will allow many proteins to be identified simultaneously and with much greater sensitivity than present methods, and will be orders of magnitude faster than methods based upon conventional 2-D PAGE. The technology will be developed and initially demonstrated for the eukaryote Saccharomyces cerevisiae (yeast).

The new instrumental approaches are orders of magnitude more rapid and sensitive than existing technology. The accuracy of Fourier-transform ion cyclotron resonance mass measurements opens the use of "accurate mass tags" for protein identification, and also the use of new multiplexed-MS/MS methods for the high throughput characterization of protein modifications (phosphorylations crucial to signal transduction).

An aspect of this research involves the development of methods for precise determination of relative levels of protein expression for all proteins from the same measurement used for identification. This new approach uses isotopically labeled media so as to provide effective internal standards for all proteins, and thus the basis for precise quantitation of expression levels based upon mass spectrometric methods. This approach is expected to allow the basis for highly effective differential analyses that will immediately highlight differences in expression levels. The instrumental approach to be developed in this the phase of the project will enable proteome visualization and characterization with much greater speed and sensitivity than previously possible. It would provide the basis for differential displays to determine the precise systems level changes in the proteome upon modification of an organism's environment or disease state. The specific objectives involve demonstration of the capability for detection and identification of large numbers of proteins from yeast (or other organisms for which a full genomic sequence is available) and to simultaneously apply stable-isotopic labeling methods (using organisms grown in $^{12}C/^{13}C$ isotopically enriched/depleted media) to obtain information on the precise levels of expression of all detected proteins.

Results and Accomplishments

1. High-resolution capillary isoelectric focusing separations of whole cell protein extracts have been achieved based upon the development of new covalently bonded hydroxy propyl cellulose capillary columns. The peak capacities demonstrated by these high-resolution separations for protein extracts have been >600. (The peak capacity is a measure of the number of peaks that can theoretically be resolved in a separation; typical peak capacities for high-performance liquid chromatography separations are <50.)

2. Capillary isoelectric focusing separations have been implemented with robotic fraction collection.

3. Initial conditions for enzymatic digestion of high-resolution protein fractions have been established. Further refinement is required to achieve more complete and uniform protein digestion for the array of fractions.

4. Initial results have been achieved demonstrating the high mass measurement accuracy that can be achieved using Fourier-transform ion cyclotron resonance mass spectrometry. The level of 0.75 ppm was achieved for peptides. At this level, calculations show that many peptides can function as accurate mass tags for protein identification.

5. The concept of using stable isotope labeling has been demonstrated for precise quantitation of protein expression levels.

6. A novel approach for multiplexed MS/MS (tandem mass spectrometry) has been developed and demonstrated that exploits the high mass measurement accuracy of Fourier-transform ion cyclotron resonance and allows multiple proteins to de dissociated for identification of proteins and for studies of modifications.

7. Conditions for yeast culturing in stable isotope labeled media have been developed.

8. Initial demonstration of an off-line approach for two-dimensional capillary isoelectric focusing and capillary high-performance liquid chromatography separations combined with ESI-FTICR mass spectrometry for the rapid and ultrasensitive analysis of the array of proteins expressed by cells.

9. Demonstration of methods for the identification of large numbers of proteins from genomic databases based upon the use of accurate mass tags obtained from the high mass measurement accuracy provided by Fourier-transform ion cyclotron resonance.

10. Demonstration of methods for precise determination of relative levels of protein expression for all proteins from the same measurement used for identification.

The project also includes the development of visualization tools for effectively displaying multiple, hyper-dimensional, feature-rich data sets to allow one to rapidly derive meaning from the often small differences in expressed proteomes that are the result of environmental perturbations. Significant developments have been made in many areas needed to visualize and present the data, but constant development is needed to keep pace with the ever growing field on bioinformatics. We have and are continuing to develop the tools to link that information to repositories of biological data for deriving information related to the function(s) of specific proteins. Developments to aid data analysis have included methods for visualization of relative protein expression rates (systems-wide differential or comparative displays of the results from perturbed proteomes). Important also to future efforts will be the automation of protein identification and the linkage to web databases that will provide information on the function of known proteins. Thus, the linkages we envision will provide the basis for gleaning biological function of new genes and for providing greatly improved understanding of the complex networks and pathways that constitute cellular systems.

Summary and Conclusions

The ability to make high-throughput measurements of proteomes will have enormous and immediate impacts on broad areas of biological and biomedical research. One of the key proteomic technologies will be the capability to study entire proteomes and to directly probe the effects of environmental perturbations and disease states, providing the basis for inference of function of individual proteins as well as new systems-level understandings.

Publications

Belov ME, MV Gorshkov, HR Udseth, GA Anderson, and RD Smith. 2000. "Zeptomole-sensitivity electrospray ionization Fourier transform ion cyclotron resonance mass spectrometry of proteins." *Anal. Chem.* 72:2271-2279.

Bruce JE, GA Anderson, MD Brands, L Pasa-Tolic, and RD Smith. 2000. "Obtaining more accurate FTICR mass measurements without internal standards using multiply charged ions." *J. Amer. Soc. Mass Spectrom.* 11:416-421.

Conrads TP, GA Anderson, TD Veenstra, L Pasa-Tolic, and RD Smith. 2000. "Utility of accurate mass tags for proteome-wide protein identification." *Anal. Chem.* 72:3349-3354.

Gao H, Y Shen, TD Veenstra, R Harkewicz, GA Anderson, JE Bruce, L Pasa-Tolic, and RD Smith. 2000. "Two dimensional electrophoretic/chromatographic separations combined with electrospray ionization-FTICR mass spectrometry for high throughput proteome analysis." *J. Microcolumn Separations* 12:383-390.

Masselon C, GA Anderson, R Harkewicz, JE Bruce, L Pasa-Tolic, and RD Smith. 2000. "Accurate mass multiplexed tandem mass spectrometry for high-throughput polypeptide identification from mixtures." *Anal. Chem.* 72:1918-1924.

Shen Y and RD Smith. 2000. "High-resolution capillary isoelectric focusing of proteins using highly hydrophilic-substituted cellulose-coated capillaries." *J. Microcolumn Separations* 12:135-141.

Shen Y, SJ Berger, GA Anderson, and RD Smith. 2000. "High-efficiency capillary isoelectric focusing of peptides." *Anal. Chem.* 72:2154-2159.

Shen Y, SJ Berger, and RD Smith. "Capillary isoelectric focusing of yeast cells." *Anal. Chem.* (in press).

Zhang C-X, F Xiang, L Pasa-Tolic, GA Anderson, TD Veenstra, and RD Smith. 2000. "Stepwise mobilization of focused proteins in capillary isoelectric focusing mass spectrometry." *Anal. Chem*. 72:1462-1468.

Development of the Recombinant Protein Expression Laboratory

Eric J. Ackerman, Karen Wahl, John Wahl

Study Control Number: PN99022/1350

The post-genomic sequencing era will involve understanding proteins. This effort will require production of active proteins in sufficient quantity for structural and functional studies. This project seeks to develop the capability for producing recombinant proteins that are of particular relevance for the Biomolecular Networks initiative[(a)]. Furthermore, this project developed methods to analyze protein activity using fluorescence methods as well as to map flexible or unstructured regions of proteins.

Project Description

Creating libraries of protein expression vectors, proteins, and antibodies will be valuable national assets. Producing milligram quantities of nearly all proteins in active form from any desired species whose genome sequence is available is the goal of this project. The protein factory will also produce affinity-purified antibodies of high specificity. Each individual protein successfully expressed by the protein factory represents potential new research and funding opportunities for determining the structures and functions of important biomolecules. The collection of proteins expressed by the protein factory represents a unique research opportunity to study interactions amongst a library of proteins.

Cell-signaling research within the Biomolecular Networks initiative relies on the availability of active proteins and specific antibodies to support molecular understanding of environmental stress responses and several non-signaling projects in structural biology, nanotechnology, biomaterials, and health products. Sufficient proteins and antibodies will be available to construct large arrays for high throughput identification of interactions and functional assignment. Initial goals are production of modest numbers of critical proteins and antibodies involved in environmental cell signaling. These reagents will hasten development of separation methodologies enabling sensitive mass spectrometry analysis of a diagnostic subset of the proteome responding to environmental stress.

Introduction

In the absence of proteins, the experiments to explain biological phenomena are often indirect and do not yield sufficient data for reliable modeling. Once proteins are available, important mechanistic understandings will emerge leading to predictions requiring even more proteins, thus driving further discoveries. Non-protein-based research approaches will continue to yield important contributions, but it is only now feasible to attack biological problems from a comprehensive, protein-based approach by the following generalized strategy. Protein preparation requires obtaining the protein-coding genes, placing genes in expression vectors, expressing the protein, and purifying the active protein. The functions of most proteins are unknown; therefore, their activity cannot be measured. Nonetheless, if a protein is expressed and purified in soluble form at high concentrations, it will more than likely be active. The above description is equally valid for individual proteins or groups of proteins. This project seeks to initially purify proteins that are crucial in cell-signaling events related to stress responses, DNA repair-related signaling, and apoptosis.

Approach

The initial aim of this research is to optimize our expression/purification efforts by making proteins useful for many aspects of environmental signaling problems. It is essential to identify appropriate expression systems and vectors for expression in *E. coli*, pichia, and insect cells. Some proteins can be made only by expression in mammalian cells. Nonetheless, our initial efforts are limited to non-mammalian expression systems because 1) retrofitting our existing building with the appropriate filtration, water, air-locks, etc., is not cost-effective; 2) many interesting proteins can be expressed in microbes, thus avoiding the need for mammalian

(a) Formerly the Environmental Health initiative

expression systems for several years; and 3) the cost of a mammalian expression protein factory is too costly at the present time.

Results and Accomplishments

Several proteins were successfully produced in active form. One of these proteins, XPA, has been used successfully in several projects.

1. Single-molecule XPA-DNA binding measurements. This is the first demonstration of a DNA binding protein to be bound to a bona fide damaging lesion. Manuscripts for this single-molecule XPA work and our conventional spectrofluorimetry studies are in preparation. The underlying work demonstrates the proteins and DNA substrates are functionally active.

2. We have provided DNA substrate, XPA, and RPA to Biomolecular Interaction. Active DNA repair proteins provide an attractive test system for this project, especially because results can be compared to the single-molecule and conventional spectroscopy studies.

3. Partial proteolysis and domain mapping were successful. We demonstrated that partial proteolysis fragments of XPA can be quickly and accurately characterized at both N- and C- termini by mass spectrometry, eliminating the need for N-terminal sequencing. The underlying scientific assumption is that regions readily cleaved by partial proteolysis are accessible and/or potentially disordered. Our results agree with fragmentary nuclear magnetic resonance structural information on XPA. Potentially, all future proteins prepared in the Protein Factory could be proteolytically mapped by the methods we developed for XPA and tested by the program PONDR (under refinement at Washington State University).

4. A shorter version of the XPA protein was also successfully expressed and purified. This fragment is larger than the ~1/3 of XPA whose NMR structure was determined independently by Japanese investigators and Mike Kennedy. This new XPA protein has not yet been characterized for DNA binding, spectrofluorimetry, or single-molecule work. These studies may provide new insights into the damage recognition problem by demonstrating functions or lack of functions of the missing regions.

5. Careful spectrofluoremetric equilibrium and kinetic measurements of XPA binding fluorescently labeled oligonucleotides were made.

6. Remaining stocks of poly (AOP-ribose) polymerase are being studied in Sam Wilson's laboratory at the National Institute of Environmental Health Sciences for a role in base excision repair. A manuscript is in preparation.

Summary and Conclusions

We demonstrated the necessary capabilities to clone, express, purify, and characterize recombinant proteins. The combination of partial proteolysis, mass spectrometry, and a program that predicts protein flexibility or disorder offers an important characterization tool to map unstructured regions of proteins. Development of fluorescent spectroscopy capabilities with a DNA repair protein offers an alternative characterization technology widely applicable to other proteins and complexes.

Publications

Brooks PJ, DS Wise, DA Berry, JV Kosmoski, MJ Smerdon, RL Somers, H Mackie, AY Spoonde, EJ Ackerman, K Coleman, RE Tarone, and JH Robbins. 2000. "The oxidative DNA lesion 8,5'-cyclo-2'-deoxyadenosine is repaired by the nucleotide excision repair pathway and blocks gene expression in mammalian cells." *J. Biol. Chem.* 275:22355-62.

Iakoucheva IM, AM Kimzey, CD Masselon, JE Bruce, EC Garner, CJ Brown, AK Dunker, RD Smith, and EJ Ackerman. 2000. "Identification of intrinsic order and disorder in the DNA damage-recognition protein XPA by time-resolved proteolysis and Fourier transform ion cyclotron resonance mass spectrometry." *Protein Sci.* (submitted).

Discovery, Isolation, and Characterization of Strong Plant Promoters

Brian Hooker, Ziyu Dai

Study Control Number: PN98024/1270

This project was initiated to develop the molecular biology capabilities needed for analysis of higher plant gene expression under post-harvest and senescence conditions and the subsequent isolation of novel promoters related to these plant life stages. These new capabilities provide the scientific foundation for engineering senescence and stress-induced responses in specific crop plants. Potential applications could impact the productivity of plants grown for food, fiber, energy, or other applications, while reducing the environmental impacts of agricultural production.

Project Description

The focus of this project was to isolate and characterize novel plant promoters and promoter regulatory elements that might be applied to improve heterogeneous gene expression in higher plants. Various regulatory (promoter) sequences can potentially control gene expression in transgenic plants to achieve different expression systems and targets related to temporal or spatial expression, or create inducible systems that are responsive to different external factors and chemicals, etc. Further characterization of novel promoters and their associated regulatory elements also provides greater understanding of regulatory mechanisms for gene expression in higher plants.

Introduction

The introduction of new traits into crop plants through molecular biology techniques is beginning to play an important role in maintaining and improving agricultural productivity. The discovery and development of novel, efficient promoters and expression systems is very attractive for the genetic engineering of any organisms. A promoter is defined as the region of DNA that RNA polymerase binds to, initiating transcription. In its most minimal form the promoter typically includes a TATA box, which is located about 20 to 30 base pairs upstream of the transcription start site, and a CAAT box. In the upstream promoter region of the TATA box and CAAT box, there exist other regions that influence transcription. These regions are called *cis*-acting elements, which can regulate transcription strength as a function of temporal or spatial conditions and/or in response to external stimuli.

Promoters directly control the initiation of transcription and the subsequent expression level of the gene of interest, as well as the plant portion in which the encoded protein is produced. Promoters may initiate gene expression throughout the entire plant (the cauliflower mosaic virus 35S promoter) or only in specific tissues, such as green portions (the chlorophyll a/b binding protein promoter). In addition, the activity of some promoters may be induced by certain stresses or chemical stimuli (pathogenesis related protein promoters).

Protein synthesis in ribosomes occurs in all known organisms. Cytoplasmic ribosomal protein genes have been studied in animals and yeast, but there is little information on the regulatory elements of these ribosomal protein genes for plant systems (Dai et al. 1996). Two cytoplasmic ribosomal protein genes (rpL25 and rpL34) were previously isolated from tobacco NT1 suspension cells at the stage of cell rapid division (Gao et al. 1994). The rpL34 promoter was identified and functional analysis was completed using the *cat* reporter gene (Dai et al. 1996).

Plant senescence-associated genes are important targets for the development of new plant traits. For example, the cytokinin biosynthesis gene was linked with an *Arabidopsis* senescence-specific promoter, resulting in senescence-resistant tobacco plants (Gan and Amasino 1995). In addition, senescence-specific promoters may comprise good targets for "post-harvest" foreign protein production in plant bioreactors (Cramer et al. 1997). The senescence of plant tissues may be artificially triggered through application of chemical stimuli such as abscisic acid, ethylene, or methyl jasmonate (Park et al. 1998), or through harvest from intact plants. The carbon and nitrogen sources of senescence tissues can then be partitioned into new products (proteins or other chemicals) in targeted plant portions (non-food portions). For example, related research at our Laboratory showed

accumulation of protein products, including CBHI and E1 cellulases, under senescence conditions in tobacco leaves (Dai et al. 2000).

Approach

Research focused on following areas: 1) isolating and characterizing senescence and abscission related promoters in potato and corn, 2) characterizing cis-acting regulatory elements of ribosomal protein gene L34 (rpL34) promoter, and 3) isolating ribosomal protein gene L25 (rpL25) promoter and testing its function. Two different approaches were used for isolation of senescence-associated genes in potato and corn.
For potato, the novel cDNA clones were isolated via the differential hybridization screening method. A cDNA library was constructed from poly $(A)^+$ RNA isolated from the dark-treated, excised potato leaf tissues with ZAP cDNA synthesis kit (Stratagene). About 60,000 plaques from the cDNA library were plated, transferred onto duplicate nitrocellulose filters, hybridized with radio-labeled cDNA probes synthesized independently from 1 μg poly $(A)^+$ RNA of healthy untreated leaf tissue and dark-treated tissues. The plaques that displayed different signal intensity between the two probes were collected, re-plated, and screened again using newly synthesized cDNA probes. A single, pure plaque from each of these clones still demonstrating the differential hybridization signal intensity was collected, and the pBluescript phagemid containing the cDNA insert was excised from the UniZAP vector as the described by the manufacturer (Stratagene, California, USA). The nucleotide sequences were determined by automated sequencing and the searches of the Genbank databases were performed with BLASTN.

For corn, the novel cDNA clones were isolated with suppressive subtractive hybridization methods as described by the manufacturer (CLONTECH, California, USA). A series of novel cDNA clones that carry partial cDNA fragments were isolated. The 5'-end and 3'-end cDNA fragments were further isolated with a Marathon cDNA amplification kit (CLONTECH, California, USA) and the cDNA clones were confirmed by DNA sequencing. The DNA sequences were analyzed via BLASTN data searches.

The *cis*-acting elements of rpL-34 promoter were identified and characterized by the loss-of-function (internal deletion) and the gain-of-function (multimers of cis-acting elements with mini-promoter). The effects of these cis-acting elements on the promoter activity were determined by *GUS* reporter gene (its activity and histochemical staining in different tissues and developmental stages) in transgenic plants. The *rpL25* promoter was isolated with the inverse PCR method. Briefly, the genomic DNA fragments were first circled by DNA ligation. Then two DNA primers, which were complementary to the 3'-end and 5'-end of DNA sequences of *rpL25* cDNA clone, were used for genomic PCR. The PCR products were confirmed by DNA sequence. The functions of promoter were determined with *GUS* reporter gene by transient and *Agrobacterium*-mediated stable transformation.

Results and Accomplishments

The function of two important regulatory elements within the rpL34 promoter region was determined by gain-of-function analysis using tandem repeats of each element in a variety of arrangements. Screening and characterization of these elements in transient assay has been completed. In addition, stably transformed tobacco lines have been produced for further characterization of gain-of-function. In addition, hybrid L34/35S promoters have been tested in transient assays.

The rpL25 promoter was isolated and tested in transient assay as well as in stable transformants. The expression pattern of the L34 and L25 promoters are compared in young seedlings in Figure 1. Although both promoters appear to express preferentially in meristematic tissues, the L25 shows strong expression only during seed germination and early seedling growth stages.

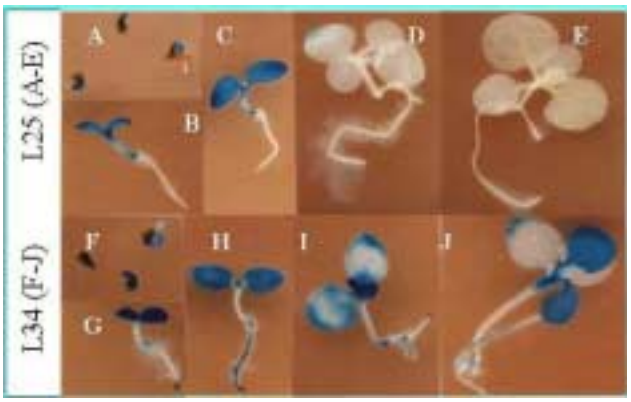

Figure 1. Transgenic seedlings bearing a B-glucoronidase (GUS) gene flanking either the L25 (Panels A-E) and L34 (Panels F-J) promoters. Seedlings were stained for GUS detection at increasing age (A and F, 0 days post-imbibition; B and G, 3 days; C and H, 6 days; D and I, 9 days; E and J, 16 days).

Senescence cDNA libraries were developed for both potato (*Solanum tuberosum*) and corn (*Zea mays*). When these libraries were screened with a differential hybridization method, over 50 different clones, which are

putatively induced by artificial senescence conditions, were identified and sequenced. Similarly, more than 20 novel clones were isolated from corn suppressive subtractive cDNA library. When compared to other known sequences via homology screening, gene candidates putatively encode the following functionalities, among others: photosynthesis, photorespiration, carbon metabolism, nitrogen metabolism, proteases and protease inhibitors, and aminotransferases.

Senescence-related responses were assessed by completing Northern-blot assays on newly discovered clones. Senescence conditions were simulated by cutting leaf tissues from intact normal plants, then incubating cuttings in DI water in the dark for up to 4 days. A variety of responses were observed with the onset of artificial senescence conditions, ranging from a rapid accumulation of mRNA upon dark treatment to a gradual accumulation of mRNA over the 4-day incubation (Figure 2). Promoters from three separate potato clones PSEN1, PSEN2, and PSEN3 were subsequently isolated and sequenced.

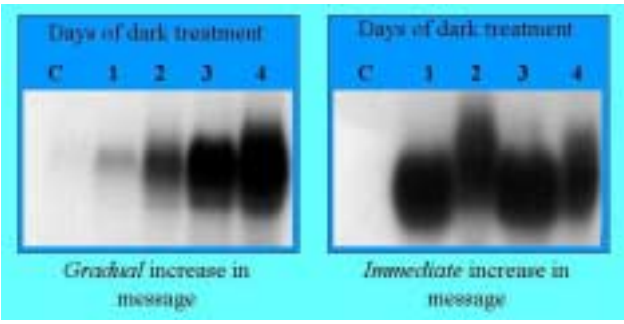

Figure 2. Contrasting Northern blot assays completed using senescence-active cDNA isolated from potato as probes. Each lane corresponds to results seen at increasing days of dark treatment post-abscission of potato leaves.

Summary and Conclusions

In this project, we isolated more than 50 unique gene clones and 4 promoters, and provided detailed characterization of the rpL34 promoter. The resulting molecular genetics knowledge will enable the characterization of both meristematic as well as senescence processes in relevant crop plants. These advances may enable development of alternative uses of high volume crops for renewable production of fuels and chemicals, as well as the efficient sequestration of airborne carbon in terrestrial plants.

References

Gao et al. 1994. *Plant Mol Biol.* 25:761-770.

Dai et al. 1996. *Plant Mol Biol.* 32:1055-1065.

Gan and Amasino 1995. *Science.* 270:1966.

Cramer et al. 1997. U.S. Patent 5689056.

Park et al. 1998. *Plant Mol Biol* 37:445.

Dai Z, B Hooker, R Quesenberry, DB Anderson, and SR Thomas. 2000. *Plant Mol Biol.* (submitted).

Presentations

Shi L, Hooker BS, Quesenberry RD, An G, Dai Z. July 1999. "Functional analysis of promoter elements controlling developmental and environmental regulation of a tobacco ribosomal protein gene *L34*." Presented at the 1999 American Society of Plant Physiologists Annual Meeting, Baltimore, Maryland.

Shi L, Hooker BS, Gao J, and Dai Z. July 2000. "Isolation and Characterization of the Genomic DNA Clones of Ribosomal Protein Gene L25 in Tobacco." Presented at the 2000 American Society of Plant Physiologists Annual Meeting, San Diego, California.

Endocrine Disruption in the Built Environment

Larry E. Anderson, James E. Morris, Lyle B. Sasser

Study Control Number: PN00039/1446

Spectrum restricted and daylight/night lighting in the built environment may alter natural neuroendocrine rhythms and developmental processes. This project is designed to address the issue of possible endocrine disruption and changes in long-term health by evaluating the influence of lighting changes on the endocrine system.

Project Description

Differences in spectral irradiance and intensity are known to affect circadian response in humans in a laboratory. Preliminary data from our laboratory suggests that altered lighting may have more serious consequences. Continuous light was observed to greatly accelerate development of mammary tissue in rats. The potential for environmental pollutants to alter endocrine function, resulting in a variety of adverse health effects, has become a high visibility environmental issue. This project was devoted to investigating changes in tissue morphology and in hormone levels, associated with mammary tissue development, from altered timing of light exposure. The expected outcome of this project was focused on the effects of light on the endocrine system, specifically, the effects of altered light (timing) on hormone levels in an animal model.

Introduction

Life in industrialized societies is primarily life inside buildings. Lighting in the built environment is quite different from sunlight in intensity, spectral content, and timing over the 24-hour daily period. Sunlight maintains a 24-hour rhythm of endocrine function, including melatonin release, as well as a host of other physiological rhythms that are essential in the developmental processes. Whether changes in the lighting environment have an impact on environmental health issues, such as the rise in breast and prostate cancer incidence, or altered childhood development, is not known. However, a biological rationale exists for potential endocrine disruptive effects on disease through, for example, changes in melatonin and impacts on estrogen homeostasis.

Approach

This study was designed to investigate the effects of light exposure (constant, 24 hours per day) on mammary tissue development. Experiments in rats were conducted to examine both the endocrine (hormonal) responses and morphological alterations in development. Normally, under a 12:12 light-dark cycle, female rats first begin estrus at 32 to 35 days of age. As the mammary gland develops, terminal end buds begin to appear and subsequently evolve into alveolar buds and eventually into terminal ducts. This occurs from 40 to 60 days of age, with maximum development activity at ages 40 to 46 days. The alveolar buds evolve into lobules of type 1, which are more highly differentiated structures than terminal end buds, terminal ducts, or alreolor buds, but do not produce milk. Based on early work, we anticipate profound changes in development of the mammary epithelial tissue in the direction of a more rapid development under constant lighting. In follow-up, we determined levels of a key hormone (prolactin) in the mammary tissue as well as the morphological staging of development under the altered lighting scheme.

Results and Accomplishments

The proposed study was conducted where animals were either exposed to a normal light cycle (12:12 light/dark) or constant light (24 hour light) during the day. The exposures occurred from birth through young adulthood (approximately 60 days of age). Preliminary evidence indicated a pronounced enhancement of mammary tissue development in constant light-exposed rats; even to the production of lactation in non-pregnant animals. The main experiment was delayed until late in the fiscal year. Tissues were sent to Dr. Irma Russo, Chief of Molecular Endrocrinology, at the Fox Chase Cancer Center (Philadelphia) where the morphology of the mammary tissue is being examined and quantified. Prolactin levels in the various tissues are also in the process of being measured in our laboratory. To date, the exposure code has not been broken, so specific results cannot be presented until the assays are completed. In all, approximately 50 animals per lighted condition were used in the study and tissues from the animals were examined at 3 different time points throughout early development.

Publication

Anderson LE, JE Morris, LB Sasser, and RG Stevens. 2000. "Effect of constant light on DMBA mammary tumorigenesis in rats." *Cancer Letters* 148:121-126.

Fungal Conversion of Agricultural Waste Glucose/Cellulose Materials to Malonic Acid

Susan A. Thomas, Margaret R. Pinza, Peter Becker

Study Control Number: PN00048/1454

Low-cost products derived from readily available, renewable agricultural resources (such as glucose, cellulose) may be converted into useful and marketable products, replacing hydrocarbon feedstocks. For example, 3- to 6-carbon chain-length organic acids can be used as feedstocks for producing industrial chemicals and materials. We are developing new, cost-competitive processes that use renewable feedstocks to produce compounds that are of value to industry, reduce the use of petroleum, provide substantial energy savings, and afford significant market penetration for the burgeoning bio-products industry.

Project Description

The objectives of this project were 1) to verify microbial production of malonic acid, as indicated during prior fungal collection screening experiments, 2) to quantify malonic acid yield and fungal biomass production, and 3) to compare two different fermentation methods for effect upon malonic acid production. Four sets of experiments were conducted using approximately 20 different fungal strains. All experiments were conducted over a 7-day period and chemical and biomass data were collected throughout testing. Malonic acid production by 20 fungal strains was quantified.

Introduction

In previous studies, researchers developed a collection of filamentous fungi and conducted screening studies to identify strains with novel traits (such as pH tolerance) and to identify metabolic products of interest (enzymes). These discoveries primarily were applied to remediation of contaminants. We have a patent pending for a method of preconditioning strains to degrade or fully remediate contaminated substrates. Recent Laboratory experiments indicated that similar approaches can be used to develop novel fermentation organisms for production of organic acids, which can then be catalytically converted to higher-value chemicals, forming a renewable route for production of industrial chemicals. Specifically, several strains indicated production of malonic acid, a dicarboxylic acid with molecular structure very suitable to catalytic conversion and synthesis to molecules of industrial interest.

This project was planned to confirm production of malonic acid and to better understand the major parameters associated with malonic acid production by filamentous fungi. This knowledge, in conjunction with other technologies, such as condensed phase catalysis, provides an integral piece of the Laboratory's capability to create valuable chemical precursors and novel products from agricultural biomass using a series of novel biological and chemical processes.

Approach

We screened 20 fungal strains initially grown on malt extract agar and subsequently transferred to malt extract broth. Two fermentation methods were compared using 10% glucose medium and 4-day test duration. The first method used 500 mL Erlenmeyer flasks containing 250 mL of glucose and fungal inoculums. Aeration and agitation were accomplished by bubbling filtered air through the liquid medium (Figure 1). The test design called for daily sampling for chemical analysis and 48-hour sampling for biomass. The second method used 250 mL baffled flasks containing 40 mL of glucose and fungal inoculums, with an orbital shaker used for aeration/agitation. Chemical and biomass sampling occurred on days 0 and 4.

Results and Accomplishments

Results of the two fermentation methods were compared using biomass and analytical data. To date, biomass gain has been measured and analyzed for most of the experiments. These results show that all but two strains had an increase in biomass when the baffled shaker flasks were used. Figure 2 compares biomass gain for fungal strain 13 using both fermentation methods. The same fungal strain grown by baffled flask fermentation method had a biomass gain of 0.0033 g/mL/day and by the bubbler flask method, approximately 0.0025 g/mL/day.

Figure 1. Two different glucose fermentation setups for aeration/agitation: 500-mL blubbler flasks (top), and 250-mL baffled shaker flasks (bottom)

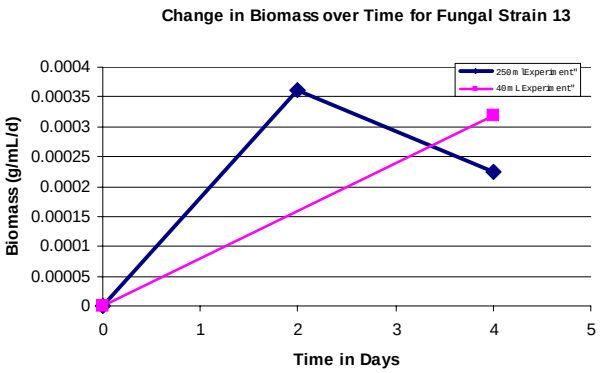

Figure 2. Comparison of biomass for fungal strain 13 using two different fermentation methods

The relative quantity of malonic acid in the cell-free extract of all fungal strains tested was variable between the two fermentation methods. Some cell-free extracts had increased quantities of malonic acid when the baffled flask was used, whereas other extracts showed increased malonic acid levels when bubbler flask was used. Table 1 is a summary of relative malonic acid yield by both fermentation methods. The yields in cultures by both methods were low with respect to the amount of glucose present. Therefore, estimates of malonic acid yield in grams per liter could not be determined.

Table 1. Summary of malonic acid presence in cell-free extract of selected fungal strains

	Species	Shaker (40 mL)	Bubbler (250 mL)
Week 1	H7	0	1
	F	3	3
	V	3	1,3
	C	0	1
	13	0	1,2
	Control	NM	NM
Week 3	CV	0	1
	X	0	1
	Control	0	1
Week 4	CC-2	0	0
	I	0	0
	M	0	0
	O	0	0
	NAM	0	0
	Control	0	0
Week 5	ZZZZ	0	0
	HC	0	0
	V8	0	0
	Z	0	0
	Control	0	0
Week 6	Y	0	0
	V	0	0
	Control	0	0
Week 7	Lp	0	0
	K	0	0
	Control	0	0

0 = nondetect
1 = S (spike)
2 = SP (spike/peak)
3 = P (peak)
NM = not measured

Summary and Conclusions

The relative amount of malonic acid was estimated for 20 fungal strains. The levels of malonic acid were relatively small, typically less than 0.1 g/L. From this data set, it does not appear that one fermentation method is more effective than the other for increasing the yield of malonic acid. However, overall biomass gain was slightly higher when the baffled flasks were used. Future work will apply methods to increase the yield of malonic acid and may involve preconditioning of strains on glucose and the addition of macro-and/or micronutrients to increase the robustness of the fungal strains. The results will form the basis for creating a process to produce malonic acid on larger scales with significant energy savings over those of current practices.

Fungal Conversion of Waste Glucose/Cellulose Materials: Organic Solvents/Organic Acids

Susan A. Thomas, Margaret R. Pinza, Peter Becker

Study Control Number: PN00048/1455

Agricultural wastes such as corn fiber or other cellulose- or glucose-containing material into useful and marketable products. Examples include 3- to 6-carbon chain length organic acids and solvents that can be used as industrial chemical precursors.

Project Description

The experimental design included screening 46 fungal strains for chemical byproduction on processed corn glucose material in liquid culture. Specifically, the liquid exudates were analyzed by liquid chromatography for the presence and relative quantities of organic alcohols and acids. Approximately 20 strains were selected as candidates for further study based on the production of some organic acids or alcohols and for growth on a 10% glucose medium.

Background

The current use for corn glucose waste is conversion to low-value animal feed, which is sold at or near cost to European markets. The use of fungus and their enzymes to convert spent corn glucose waste into useful organic acids and solvents has the advantages of providing value-added domestic products and high-protein residue for animal feed and reducing transportation costs and energy use for production.

Introduction

The goal of this study was to prove the concept that higher filamentous fungi can be used to produce desirable organic acids and solvents in liquid fermentation with processed corn glucose. Fungal biotechnology is the application of fungi or their subcellular components in the context of associated process-technology for manufacturing service industries and for environmental management (Arora et al. 1992). Typically, fungi are employed to produce biomass, to produce or to catalyze the production of useful end products, or to degrade biological and chemical wastes and contaminants.

We have a patent pending on the method of preconditioning fungal strains to contaminants of interest and then using the preconditioned strains to remove or degrade contaminants. This method results in proprietary strains that are specifically adapted to more efficiently remediate contaminants of interest under prescribed environmental conditions. Our mycoremediation study began in 1996, and since that time a variety of contaminants have been addressed: organophosphates, petroleum hydrocarbons, endocrine disrupters, pesticides, fertilizers, alkaloids, and several strains of bacteria. We expect that if preconditioned strains of fungus are used to degrade processed corn glucose, then greater quantities of acids or solvents could be produced.

Current industry practices use bacterial systems to perform the conversion of glucose waste to lactic acid. This practice is limited in the ability to convert commercial quantities both at a competitive cost and without generating a waste stream (T Werpy, Pacific Northwest National Laboratory, personal communication, September 1999). The advantage of filamentous fungi for the byproduction of organic acids and solvents is the efficiency and low cost of the method. For example, use of the fungal systems should eliminate certain steps required in the bacterial approach because of the tolerance of low pH and high salinity of the fungal strains we use. The bacterial approach requires neutralization of the fermentation process with compounds such as calcium hydroxide, the subsequent recovery of the desired product (lactic acid) by addition of gypsum or similar compounds, and the consequent need to treat the waste streams generated by these steps.

Approach

We screened a total of 46 species. The cultures were all grown initially on Difco malt extract agar, and were then converted to malt extract broth culture by homogenizing the malt extract agar plates with 50 mL to 100 mL sterile malt extract broth and decanting the homogenate into sterile 500-mL Erlenmeyer fermentation flasks with bubbler tubes and vented stoppers containing 250 mL to 400 mL sterile malt extract broth. Filtered air from the laminar flow hood was supplied to stir the flask contents by bubbling the air from near the bottom of the flask through a cotton-plugged, sterile 1-mL pipette (Figure 1).

Malt extract broth cultures were allowed to grow 3 days before an aliquot of each was used to inoculate 200 mL to 300 mL 10% glucose solution (Sigma #G-8270 D + Glucose [Dextrose; corn sugar, minimum 99.5%]).

Figure 1. Glucose fermentation setup for 250 mL bubbler flasks: spherical growth (top); bubbler flask setup in the laminar flow hood

Glucose cultures were sampled starting at 4 days after inoculation and at ~2- to 3-day intervals thereafter for a total of 21 to 28 days. Sampling consisted of removal of 1.5 mL aliquots under sterile conditions in a laminar flow hood using the bubbler pipette as the transfer pipette. The aliquots were centrifuged at 5585g for 5 minutes to provide cell-free extract. Subsequently, each 1 mL supernatant was decanted into a labeled 1.5 mL polypropylene centrifuge tube. The samples were frozen and stored until analysis by liquid chromatography at our Laboratory. The remaining 0.5 mL of each aliquot was used for pH measurement.

Results and Accomplishments

Table 1 is a summary of the production of organic acids and solvents by 45 fungal strains (one strain lost due to contamination). Approximately 24 fungal strains produced malonic acid; of these, 20 met criteria of increasing or high-peak yield of malonic acid and were then selected for follow-on studies.

Acidity and alkalinity measurements were taken on all liquid fungal cultures used in the screening study. The

Table 1. Summary of organic byproducts of fungal fermentation of glucose (g/L)

Species Name	Oxalate	Citrate	Malonic	Sorbitol	Glycerol
D	2.5 – 2.6		0.30		
E	2.2 – 2.9	3.35	0.3 – 0.9	0.20	
F		1.50			
J	1.0 – 1.1		0.50		
Y	1.7 – 2.6	1.30	0.4 – 0.5	0.40	
Po	1.4 – 13.2			0.30	
V	0.20 – 0.32		0.3 – 1.5	1.20	
ZZ		0.20	0.90		
13	0.1 – 4.0	0.7 – 2.5	1.1 - 2.1	1.00	0.7 – 1.7
I	2.4 – 3.2	1.3 – 2.8	1.3 – 2.5	2.40	1.70
A	0.2 – 2.3	1.1 – 1.5			
K	2.3 – 2.8	0.2 – 2.2	1.90		0.20
Gf	2.2 – 2.7	1.0 – 1.5			0.10
M	1.9 – 3.1	1.6 – 3.5	1.70	1.00	1.1 – 2.9
O	1.8 – 2.4	1.0 – 1.8	2.0 – 2.6		
P	1.9 – 2.6	1.2 – 1.8			
ZZZ	2.3 – 3.2	1.2 – 2.1			0.20
R	2.1 – 2.7	1.3 – 3.1			
8	1.7 – 2.8	1.5 – 1.9		2.10	
20	0.1 – 2.7				
H	2.3 – 3.1		1.00	0.6 – 1.0	
N	2..5 – 3.0				
Q	2.5 – 3.0		2.00	1.60	
S	2.1 – 2.8	1.0	1.9 – 2.1	3.40	
W	2.1 – 2.9			0.70	
Z	2.1 – 2.6	1.5 – 2.3	1.30		
ZZZZ	2.0 – 3.1	0.8 – 1.1	1.50		0.2 – 3.3
ZZZZZZ	2.4 – 3.2			1.40	
3	0.1 – 2.8			0.40	
10	0.3 – 3.2			0.4 – 1.8	
Ab1	0.1 – 3.2		0.3 – 0.4	0.20	
CC2	0.2 – 3.2		0.40	0.10	0.40
CV	0.1 – 3.7		0.3 – 0.4	0.70	
FV	0.2 – 2.4			0.3 – 0.7	0.20
GFO	0.1 – 3.5			0.60	

results showed that at least 11 strains were growing at or below pH 4 by day 15 of testing. The fungal strains that performed on low pH conditions (<4) were screened for enzyme activity using the standard API-Zym screening tests. For some strains, significant levels (between 1 and 40 nanomoles per 65 µL sample) of acid phosphatase and napthol-AS-BI-phospholydrolase were indicated by the test. Other enzyme activity was found in lower amounts and included esterase lipase, N-acetyl- ß -glucosaminidase, ß-glucuronidase, α-mannosidase, and α-fructosidase.

Summary and Conclusions

We demonstrated that higher filamentous fungi can produce organic acids and solvents from corn glucose. Half of the strains tested produced organic acids and solvents and can grow in low pH environments (some as low as 2 or 3).

Most of the cultures screened reached a stable pH value by day 15 of testing. Measurable levels of desired acids and solvents are present by the midpoint of testing, and the pattern of increased production, decreased production, or no change in production varied among the different fungal strains tested. The fungal strains used for this screening were naive regarding conditioning to higher levels of glucose. Past studies have shown that preconditioning of fungal strains to the contaminant of interest can increase their efficiency in degrading the contaminant. Therefore, preconditioning to higher concentrations of glucose could increase production of desired compounds.

Reference

Arora DK, RP Elander, and KG Mukerj, Eds. 1992. *Fungal Biotechnology*. Marcel Dekker, New York.

Fungal Molecular Biology: Promoter Isolation and Characterization

Johnway Gao, Todd O. Stevens, Fred J. Brockman

Study Control Number: PN99028/1356

The capability to discover, isolate, and characterize novel genetic regulatory elements and to develop transformation systems for industrially viable fungus strains is a vital part of creating new processes for efficient conversion of plant materials (cellulose, hemicellulose, starch, and sugars), and to useful products, such as biocatalysts (foreign protein expression) and bio-based fuels and chemicals (pathway engineering).

Project Description

The genetic regulatory patterns of native *R. oryzae* (ATCC9363) promoters associated with the phosphoglycerate kinase (*pgk*) and glucoamylase genes were characterized by Northern blot analysis in various growth environments containing starch, hexoses, and pentoses. Chromosomal integration vectors were designed and constructed for genetic transformation of *R. oryzae*. Chromosomal integration vectors were constructed using the phosphoglycerate kinase 1 (*pgk1*) promoter to direct the expression of an antibiotic resistance gene and a marker gene coding for a green fluorescent protein (*gfp*). *R. oryzae* spores were transformed with the integrating vector using an electroporation method. The project also tested the possibility to convert multi-nucleate spores of *R. oryzae* to single-nucleate lineages using laser micromanipulation and microsurgery techniques.

Introduction

To date, there are only a limited number of fungal strains and expression systems available in the public domain. The available expression systems include various species of *Aspergillus* and the yeasts *Saccharomyces cerevisiae* and *Pichia pastoris*. However, these strains represent only a small sample of this diverse microbial community, and they are not necessarily optimal for converting plant material into useful products. For example, neither *Saccharomyces cerevisiae* nor *Pichia pastoris* can grow directly on plant materials, but require refined substrates such as glucose, galactose, and methanol. The ability to genetically harness other fungi requires a fundamental understanding of gene regulation and its application to product biosynthesis. The objective of the project was to develop this expertise and to create a new capability in fungal molecular biology. This was accomplished by elucidating gene regulatory mechanisms and developing transformation vector system in a model filamentous fungus with known utility (*R. oryzae*, capable of degrading plant materials and producing lactic acid) (Soccol et al. 1995; Yin et al. 1997).

Approach

The current project focused on the development of a transformation system for the model filamentous fungi, *R. oryzae*, as a viable platform that can be used in biotechnology applications. The development of a transformation system of *R. oryzae* requires a fundamental understanding of important gene regulatory characteristics under various environmental conditions as well as the development of transformation and expression vector. In addition, the characterization of multi-nuclei in different growth stages of *R. oryzae* is also essential to determine the feasibility to convert multi-nucleate fungal spores to single-nucleate spores.

Results and Accomplishments

This project involved four principal efforts: 1) promoter regulatory pattern characterization, 2) design and construction of chromosomal integrating vector, 3) system transformation experiments, and 4) feasibility of converting multi-nucleate fungal spores to single-nucleate spores.

Promoter Regulatory Pattern Characterization

To characterize the regulatory patterns of the *pgk1* promoter and glucoamylase promoter, *R. oryzae* was grown in different culture media containing glucose, starch, xylose, mannose, galactose, and arabinose, respectively. Total RNA samples were isolated from the mycelia biomass, separated in formaldehyde-agarose gel, and subsequently capillary-blotted onto Zeta-Probe membrane. Northern blots were hybridized with an α^{32}P-dCTP labeled *pgk1* gene probe and glucoamylase gene probe, respectively. The Northern-blot analysis results

are shown in Figure 1(a) and 1(b), indicating that *pgk1* promoter can regulate gene expression in all the conditions tested while the glucoamylase promoter only regulate gene expression in the conditions of glucose, starch, xylose, and galactose, but not in mannose and arabinose conditions. Therefore, *pgk1* promoter is a constitutive promoter while glucoamylase promoter is an inducible promoter.

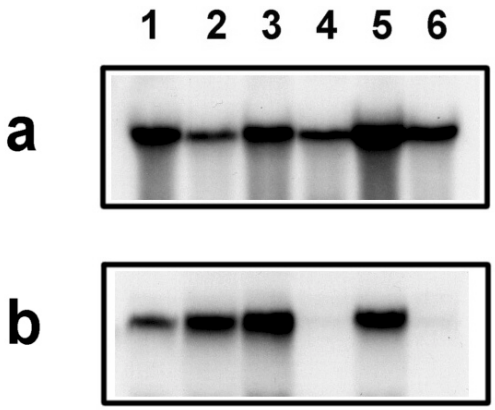

Figure 1. Genetic regulatory patterns of *R. oryzae pgk1* promoter (a) and glucoamylase promoter (b). Lanes 1, 2, 3, 4, 5, and 6 are total RNA samples prepared from *R. oryzae* cultures grown in the medium with glucose, potato starch, xylose, mannose, galactose, and arabinose, respectively.

Design and Construction of Chromosomal Integrating Vector System

A chromosomal integrating vector was designed as shown in Figure 2, primarily containing two fungal expression cassettes, one of which is an antibiotic resistance (geneticin or sulfanilamide) gene and the other *gfp* marker gene expression cassette. Both the expression cassettes are under the control of the constitutive *pgk1* promoter and terminated by a fungal terminator Taox1. The *gfp* gene expression cassette is flanked by a native *R. oryzae* gene to serve as the chromosomal integrating element for foreign gene insertion into the fungal host during transformation. The antibiotic resistance gene expression cassette is used to select transformant candidates after transformation. The chromosomal integrating vectors were constructed through a series of vector cloning efforts, and used for the following transformation test.

Transformation Experiments

Germinated and enzyme-digested *R. oryzae* spores were transformed with the constructed chromosomal integrating vector using electroporation method. After transformation, transformants were screened in selective culture medium containing antibiotic geneticin. Potential

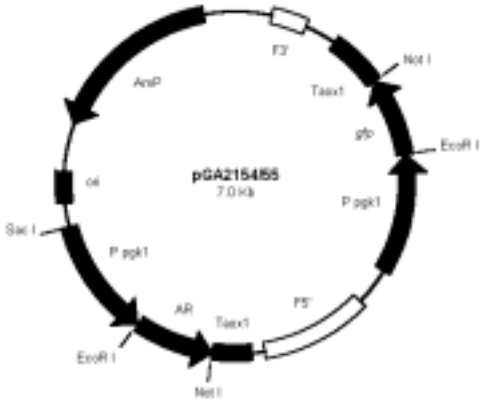

Figure 2. Plasmid map of a chromosomal integrating vector for *R. oryzae* transformation. Amp, ampicillin resistance gene; AR, antibiotic resistance gene; F5'and F3', chromosomal integrating element 5' and 3' end regions, respectively; ori, plasmid replication origin; P pgk1, phosphoglycerate kinase 1 promoter.

transformants were sub-cultured onto fresh selective culture medium for further screening. Based on the experiment, the transformation frequency was low, about three to four transformants per μg DNA. After sporulation, spores of transformed candidates were collected and germinated in a culture medium containing antibiotics. Genomic DNA samples were then prepared for a gene insertion test using polymer chain reaction. Results show that some of the transformed candidates have the *gfp* marker gene insertion.

Feasibility of Converting Multi-Nucleate Fungal Spores to Single-Nucleate Spores

Rhizopus was found to have an extremely large number of nuclei for a given cell volume. In ungerminated spores, individual nuclei could not be distinguished, probably because of both close packing and inherent fluorescence of the spore. In freshly germinated cells, 10 to 20 nuclei are visible, and within a few hours of germination, a growing mycelium usually contains nearly 100 nuclei as shown in Figure 3. Because genetic manipulation of *Rhizopus* is likely to affect only a fraction of the nuclei present, the effects of such manipulations are likely to become diluted in subsequent generations. If the non-transformed nuclei can be identified and eliminated by laser micromanipulation and microsurgery, then strains of *Rhizopus,* which contain only transformed genomes, might be obtained. Studies show that spores were resistant to the cutting laser, while mycelia could readily be ablated with the cutting laser on high power. However, methods will need to be developed to differentiate the transformed nuclei from untransformed ones.

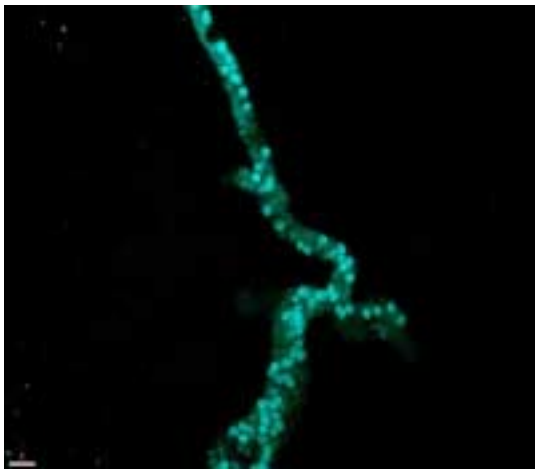

Figure 3. Microscopy image of a growing mycelium containing multi-nuclei (bright dots). Nuclei were stained with SYTO11 dye and imaged by confocal laser scanning microscopy.

Summary and Conclusions

The native *R. oryzae* promoters have been characterized for their regulatory patterns in various culture environments. The phosphoglycerate kinase 1 promoter can effectively and constitutively regulate gene expression while the glucoamylase promoter regulates gene expression under limited conditions. A chromosomal integrating vector system has been designed and constructed, and can be used for *R. oryzae* transformation study. Efforts were also dedicated for the feasibility of converting multi-nucleate spores to single-nucleate spores. The *R. oryzae* promoters isolated in this project may also be used to direct foreign gene expression in other fungal species. The fungal vector design strategies and fungal transformation protocols developed in this project will also be applied to genetically engineer filamentous fungi for biotechnology applications.

References

Soccol CR, VI Stonoga, and M Raimbault. 1995. "Production of L-lactic acid by *Rhizopus* species." *World Journal of Microbiology & Biotechnology* 10:433-435.

Yin P, N Nishina, Y Kosakai, K Yahiro, Y Park, and M Okabe. 1997. "Enhanced production of L(+)-lactic acid from corn starch in a culture of *Rhizopus oryzae* using an air-lift bioreactor." *Journal of Fermentation and Bioengineering* 84(3):249-253.

Publications and Presentations

Gao J, BS Hooker, RS Skeen, DB Anderson. 2000. "Direct starch conversion to industrial biocatalysts using transgenic fungal system under control of inducible and constitutive promoters." ACS Volume based on Advancing Sustainability through Green Chemistry (submitted).

Gao J, RS Skeen, and R Quesenberry. May 2000. "Nutritional effects on lactic acid production without addition of a neutralizer in the Rhizopus oryzae." Presented to 22nd Symposium on Biotechnology for Fuels and Chemicals, Gatlinburg, Tennessee.

Improving H_2 Production by Rational Enzyme Redesign

Rick Ornstein

Study Control Number: PN99029/1357

Because of the large potential for use of H_2 as a clean fuel and alternative energy source, considerable recent effort has been directed to improve the efficiency of hydrogenase mediated H_2 production. Our focus is to develop the necessary background capability to apply a rational enzyme redesign approach to increase the efficiency of this enzyme. Hydrogenases can oxidize H_2 to provide a microorganism with a source of strong reductants or generate hydrogen as sinks of excess electrons. For example, anaerobic sulfate-reducing bacteria can grow on H_2 as an electron donor with sulfate and thiosulfate as terminal electron acceptors. Conversely, these same bacteria produce hydrogen upon fermentative growth on pyruvate in the absence of sulfate.

Project Description

Although a growing number of three-dimensional x-ray structures of hydrogenases have been solved by high resolution, important ambiguities exist about the active site structural details and much is unknown about the fundamental mechanism of action(s). We employed state-of-the-art computational and theoretical methods to begin to resolve these ambiguities.

Introduction

Hydrogenase from *Desulfovibrio gigas* (*D. gigas*) has been characterized by determining the crystal structure and by a variety of spectral methods. The crystallographic analysis of the enzyme has shown that the active site is a bimetallic center that is attached to the protein via four thiolates from cysteine residues. The bimetallic center is known to be Ni-Fe. The Fe center is also coordinated to three nonprotein ligands, two CN and one CO (Scheme 1). The electronic and steric properties of the bimetallic center and the attached nonprotein ligands crucially influence enzymatic H_2 heterolytic bond cleavage, and remain uncertain. We employed state-of-the-art computation chemistry methods to address this question.

Approach

The electronic and steric effects of the cysteines and protein backbone were determined by density functional theory calculations on a series of the model complexes:

$(CO)(CN)_2Fe(SR)_2Ni(SR)_2^-$,
$(CO)(CN)(CNH)Fe(SR)_2Ni(SR)_2$,
$X\cdots(CO)(CN)_2Fe(SR)_2Ni(SR)_2^-$, and
$X\cdots(CO)(CN)(CNH)Fe(SR)_2Ni(SR)_2$ (R_1, R_2 = H, CH_3; X = H_2O, NH_3). Additional details are described in Nui and Ornstein (submitted).

Results and Accomplishments

For the first model complex, the following SR combinations were examined:

- all SCH_3
- all SH
- $Fe(SCH_3)_2Ni(SH)_2$
- $Fe(SH)_2Ni(SCH_3)_2$.

The atomic spin density, charge, and total energy of each structure were determined (see Table 1, Nui and Ornstein). Our calculations indicate:

- The SH model for the cysteines in the actual [NiFe] *D. gigas* hydrogenase is acceptable for an initial investigation of the structures and reaction mechanisms of the active sites, $(CO)(CN)_2Fe(SR)_2Ni(SR)_2$, although this simplified model might underestimate the reactivity of the active site of the [NiFe] hydrogenase.

- The protein backbone may contribute significantly to the structural and electronic properties of the bimetallic cluster of the active sites. However, these steric distortions by the twist of the terminal cysteines and the folding of the Ni-Fe cluster only lead to a small destabilization of the Ni-Fe cluster, and have no significant influence on the nonprotein ligands, CO and CN.

- The CO and CN stretching frequencies seem to be sensitive to the electronic effects of the thiolate substituent and protein backbone.

These results can be used to understand CN and CO vibrational frequency changes upon protonation and hydrogen bonding interaction and upon conformational variations of in the hydrogenase active sites.

Reference

Nui S and RL Ornstein. "The influences of the protein residues, protein backbone, and protonation on the active site models in the nickel-iron hydrogenase of *Desulfovibrio gigas*. A density functional theory investigation." *Journal of Physical Chemistry* (submitted).

Isoprostane-Mediated Tumor Promotion

Thomas J. Weber

Study Control Number: PN99036/1364

Exposure to radiation has been associated with life-span shortening and cancer. The response of a living organism to radiation can be modified by many factors. The toxic response to ionizing radiation, as well as to numerous chemical contaminants at DOE sites, is associated with the generation of an oxidative stress. However, the cellular and molecular mechanisms underlying the carcinogenic response to reactive oxygen species is not known.

Project Description

The toxic response to ionizing radiation, as well as numerous contaminants identified on DOE sites, is consistently associated with the generation of an oxidative stress. Thus, defining the effects of oxidative stress in mammalian systems is of central interest to DOE. Oxidative stress is known to play a role in physiologic and pathophysiologic processes such as cancer, aging, and neuronal degeneration. It is not clear whether low-level environmental exposure to radiation sources, or toxicants whose mechanism of action includes an oxidative stress component, will increase the risk of cancer.

In the present study, we have investigated whether prototypical isoprostanes modulate anchorage-dependent and -independent growth of several in vitro model systems as an index of tumor promoting activity. We have found that the isoprostanes modulate anchorage-dependent and -independent growth at extremely low concentrations (pM-nM), suggesting the biological activity of these compounds is physiologically relevant.

Introduction

Oxygen free radicals have been implicated in the pathophysiology of a number of human diseases, including cancer, atherosclerosis, neurodegenerative disorders, and aging. Oxidative stress is also central to the adverse effects of ionizing radiation. Recent experimental evidence indicates that arachidonic acid may be converted by reactive oxygen species into a new class of oxidized lipid metabolites, termed the isoprostanes. In several model systems, the isoprostanes have been shown to be biologically active and coupled to signal transduction pathways associated with carcinogenic processes. Therefore, it will be important to determine whether the formation of isoprostanes in response to ionizing radiation and other environmental associated toxic insults may increase cancer risk.

The isoprostanes have been shown to signal through the inositol phospholipid/protein kinase C pathway, which in turn, is widely implicated in carcinogenic processes. Thus, the isoprostanes may represent a novel class of physiologically relevant tumor promoters.

To test this hypothesis, we conducted preliminary studies to determine whether isoprostanes exhibit tumor promoting activity using an in vitro model of tumor promotion (JB6 cell). In addition, we have investigated whether prototypical isoprostanes modulate anchorage-dependent and -independent growth of several in vitro model systems as an index of tumor promoting activity. We have found that the isoprostanes modulate anchorage-dependent and -independent growth at extremely low concentrations (pM-nM), suggesting the biological activity of these compounds is physiologically relevant.

Results and Accomplishments

We previously showed that 8-iso-$PGF_{2\alpha}$ increased the anchorage-independent growth of JB6 cells. We have extended our investigation to several other in vitro model systems and a second prototypical isoprostane (8-iso-PGE_2) to determine whether the biological activity of the isoprostanes was generalizable. Increasing experimental evidence indicates that vascular smooth muscle cells are responsive to isoprostanes, and the biological response isoprostanes may be mediated by a thromboxane A_2 (TXA_2) receptor (TP), or a putative novel isoprostane receptor. Studies were conducted to determine whether 8-iso-$PGF_{2\alpha}$ and DDM-PGE_2 modulate the proliferation of smooth muscle cells in vitro. Rat aortic smooth muscle cells were treated with a range of prostanoid concentrations and cell proliferation determined using a picogreen DNA quantitation assay and multiwell fluorescent plate reader (Cytofluor 4000) according to manufacturer's directions. DNA synthesis was increased in a concentration-dependent fashion by 8-iso-$PGF_{2\alpha}$, but

not DDM-PGE_2 (Figure 1). The lack of correlation with a TP receptor agonist suggests that the proliferative response to 8-iso-$PGF_{2\alpha}$ is unrelated to the endothelial type TP receptor, and is consistent with evidence suggesting smooth muscle cells may express a unique isoprostane receptor. Of particular interest is the proliferative response to 8-iso-$PGF_{2\alpha}$, which was apparent at extremely low concentration (100 pM). In a separate study, non-LDRD the proliferative response of smooth muscle cells to 8-iso-PGE_2 was investigated. 8-iso-PGE_2 (0.1-100 nM) did not modulate smooth muscle cells proliferation (data not shown).

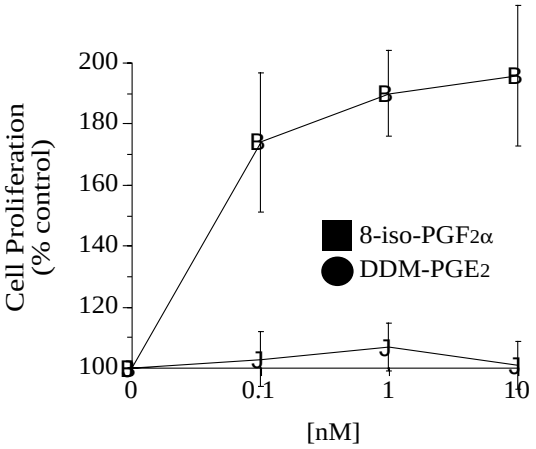

Figure 1. Proliferative response of smooth muscle cells to 8-iso-$PGF_{2\alpha}$, but not DDM-PGE_2

In the absence of enzymatic activity, 8-iso-$PGF_{2\alpha}$ is the dominant isoprostane generated by the oxygen free radical catalyzed peroxidation of arachidonic acid. However, experimental evidence suggests that 8-iso-PGE_2 is the major isoprostane product formed in the liver, indicating that prostanoid biosynthetic pathways may influence the class of isoprostane generated in an organ-specific manner. This observation is relevant to the response of primary hepatocytes to prototypical isoprostanes. Hepatocytes were isolated from male B6C3F1 mice using a standard collagenase digestion and percoll gradient purification. Hepatocytes were incubated in attachment medium for 4 hours, and subsequently treated with epidermal growth factor (1 to 10 ng/mL), 10 nM 8-iso-$PGF_{2\alpha}$, 10 nM 8-iso-PGE_2, or epidermal growth factor + isoprostane for 48 hours in the presence of 50 μM 5-bromo-2'-deoxyuridine in defined mitogen restricted media. Cell proliferation was determined using an anti-BrdU antibody, horse radish peroxidase conjugated secondary antibody, and colorimetric detection (and quantifying labeled nuclei). Epidermal growth factor increased proliferation in a dose-dependent fashion, while isoprostanes alone were without effect (Figure 2; 8-iso-$PGF_{2\alpha}$ not shown). However, cotreatment of cells with 1 ng/mL epidermal growth factor and 10 nM 8-iso-PGE_2 resulted in a proliferative response comparable to a 10 ng/mL epidermal growth factor concentration, despite the lack of effect of 8-iso-PGE_2 alone. In contrast, 8-iso-PGF_{2a} as a cotreatment was without effect. Therefore, cultured hepatocytes are responsive to the major class of isoprostane (8-iso-PGE_2) observed in vivo, but not to the major class predicted in the absence of enzymatic activity (8-iso-PGF_{2a}). Further, the lack of effect of 8-iso-PGE_2 alone raises the possibility that the cotreatment effect with epidermal growth factor on cell proliferation may be synergistic.

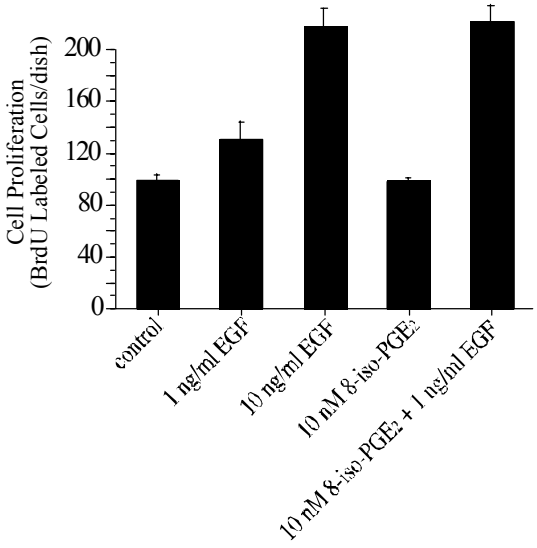

Figure 2. 8-iso-PGE_2 modulates epidermal growth factor-dependent proliferation in primary hepatocytes isolated from male B6C3F1 mice

The effect of 8-iso-$PGF_{2\alpha}$ on the growth of human breast cancer cell line (MCF-7) was investigated. Cell proliferation was determined using the picogreen assay. Under anchorage-dependent conditions, 8-iso-$PGF_{2\alpha}$ did not modulate MCF-7 proliferation (data not shown). In contrast, under anchorage-independent conditions (growth on soft agar), 10 nM 8-iso-$PGF_{2\alpha}$ increased MCF-7 proliferation as determined by an increase of DNA/dish (Figure 3). Epidermal growth factor was included as a positive control and to investigate cotreatment effects. However, in contrast to the hepatocyte model, cotreatment of cells with epidermal growth factor and 8-iso-$PGF_{2\alpha}$ resulted in a proliferative response that was additive.

We next investigated whether prototypical isoprostanes modulated the proliferation of human renal epithelial cells (HK-2). HK-2 cells were treated with 0.1 to 100 nM 8-iso-PGE_2 and 8-iso-$PGF_{2\alpha}$ for 3 days and cell proliferation determined by quantifying DNA/dish.

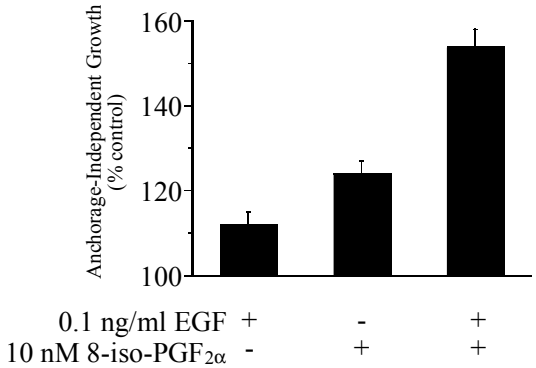

Figure 3. 8-iso-PGF$_{2\alpha}$ increases anchorage-independent, but -dependent growth of the MCF-7 human breast cancer cell line

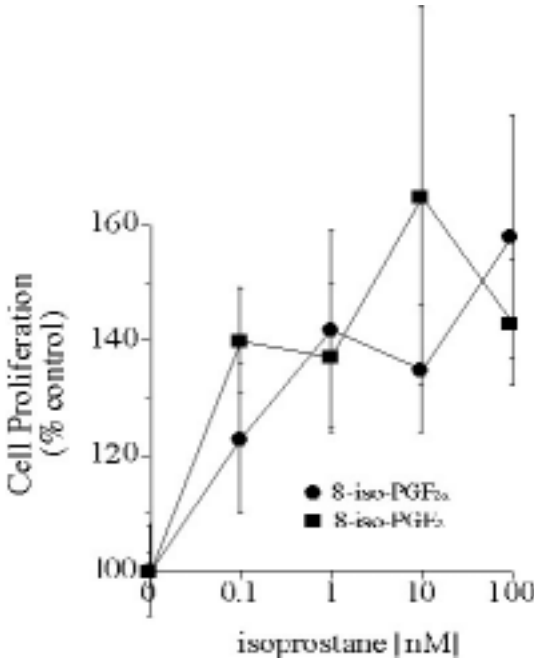

Figure 4. Modulation of human renal epithelial proliferation (HK-2) by prototypical isoprostanes

8-iso-PGE$_2$ and 8-iso-PGF$_{2\alpha}$ increased proliferation in a concentration-dependent fashion (Figure 4). Importantly, the proliferative response was apparent at pM-nM concentrations.

Summary and Conclusions

Prototypical isoprostanes modulate anchorage-dependent and anchorage-independent growth of several in vitro model systems derived from experimental animal models (JB6, rat aortic SMCs, B6C3F1 mouse) and of human origin (HK-2, MCF-7). Importantly, the cellular response to prototypical isoprostanes was apparent at extremely low concentration (pM-nM) in all model systems, suggesting the biological activity of the isoprostanes is physiologically relevant. We looked to correlate isoprostane responsiveness with known prostanoid receptor pharmacology, however, we found no clear correlation. Further complicating the interpretation of our results was the differential responsiveness of model systems to isoprostanes under anchorage-dependent and -independent conditions, as well as potential differences in signal transduction crosstalk with epidermal growth factor-dependent signaling. Therefore, the role of isoprostanes in physiology and pathophysiology must be determined in a cell type and organ specific fashion.

Presentation

A seminar entitled “Cellular transformation by prostanoids and isoprostanes: linking response to G-protein coupled receptors” was presented at the National Institutes of Health, National Cancer Institute, Frederick, Maryland, November 1999.

Microbial Siderophore Role in Metal Uptake by Oats and Crested Wheatgrass

Robert J. Fellows, Zheming Wang, Calvin C. Ainsworth

Study Control Number: PN99042/1370

An improved understanding of the impacts on metal uptake due to fundamental microbial/root processes in the rhizosphere is important to DOE research programs associated with environmental remediation, ecological health and risk assessment, and development of energy biomass crops.

Project Description

The objective of this project was to develop a method for studying the fundamental microbial/root processes in the rhizosphere. This methodology may be applied to understand metal and radionuclide movement in terrestrial and agricultural ecosystems, an area that is not well understood and has not been studied in vivo. The effort investigated metal [Eu(III)] and microbial siderophore (MS) transport into roots and root cells of oats (*Avena sativa*, var. Coker 227), and crested wheat grass (*Agropyron cristatum*, var.Hycrest). It utilized the spectroscopic capability of the Environmental Molecular Sciences Laboratory, combined with axenic plant culture and confocal laser microscopy, to follow metal uptake and partitioning into intact, functioning plant roots and the individual tissues and cell types composing roots.

The results demonstrated that Eu(III) was preferentially accumulated within the meristematic region of the root tip. In this region, and in the maturing portions of the root, the majority of the metal was found within the stele, specifically in the parenchymal cells and the developing phloem. The technique developed and demonstrated in this study is important in that it affords a means to resolve in vivo and in real-time, metal accumulation by a functioning, intact plant root.

Introduction

Plant mineral nutrition, and metal or radionuclide uptake, may be modified by a number of external rhizosphere factors, including the chemical form and valence state of the metals, soil media influences, and microbial factors, including the production and activity of siderophores. While current knowledge of metal uptake places the defining step as transport across an intact cell membrane into the symplasm, or living portion of the plant root (Marschner 1995), the underlying mechanisms which may affect this process are not known, including extracellular factors such as rhizosphere microorganisms and their metabolites (such as siderophores).

Europium, although not a required plant nutrient, is accumulated by plants. It is important as both a macronutrient (Ca) (Horrocks and Albin 1987), and nonradioactive trivalent actinide [e.g. Americium (III)] (Ke et al. 1993) analog. It also possesses differing fluorescence characteristics in the bound and unbound state permitting confirmation of root uptake and accumulation or complexation with rhizosphere components such as siderophores. Calcium is a critical cation within the root for metabolism, ion balance, and cell elongation (root growth). Burda et al. (1995) have previously shown that europium is an effective calcium probe in isolated chloroplasts. Kelly et al. (1999) reported that europium (III) binds to the outer surface of roots of water hyacinth (*Eichhornia crassipes*), an aquatic plant known to rapidly accumulate radionuclides. Unfortunately, these and all other studies to date have required in vitro or post-mortem analysis of the tissues. The results of this effort have produced a means of following in vivo, real-time metal accumulation by a functioning intact plant root and a technique to assess those external factors (e.g., siderophores) which may affect these processes.

Approach

Two chemically pure synthetic siderophores were obtained from Sigma Chemical Co. (St. Louis, Missouri), Desferrol (Desferroxamine), and Ferrichrome, both are commercial pharmaceuticals that possess fluorescent properties when complexed with metals. Oats (*Avena sativa*, var. Coker 227), and crested wheat grass (*Agropyron cristatum*, var.Hycrest) were obtained locally and from sources within the U.S. Department of Agriculture (in Texas and Utah). The plants were cultured axenically. This included aseptic separation of the embryo from the seed coat, surface sterilization with sodium hypochlorite, germination on nutrient agar,

selection of seedlings demonstrating no contamination, and aseptic transfer to sterile nutrient solution (tenth-strength Hoagland's) oxygenated with 0.22 µ filtered air. Growth conditions included a light intensity of 300 µE m^{-2} sec^{-1}, (fluorescent/incandescent mix), 18 to 23°C day/night temperatures, and 60% R.H. Continual sterility checks were performed on the roots and nutrient solution.

The microscope for observing siderophore uptake was assembled along with a newly designed and constructed plant holder, consisting of a Nikon TE-300 inverted optical microscope with CFI60 infinity optics, fitted with Toshiba Tu40A 3-chip color CCD camera, Scion CG7 color frame grabber, imaging software, a Nikon optical camera, a thermoelectrically cooled Hamamatsu 4220p photon counting photomultiplier tube, a Stanford Research SR400 two-channel gated photon counter, and a Ludl LEP Biopoint computer controlled multi-axis translation stage. A specially made sample holder was attached to the sample translation stage permitting direct observation and laser induced fluorescence imaging of a live plant root in its growth media.

Results and Accomplishments

Critical to the study was the requirement that there be no interference from the native fluorescence of plant tissues or extracellular siderophores on the resolution of europium in and out of the plant and the confirmation of spectral changes following uptake and complexation within the plant. The spectra, shown in Figure 1, demonstrated that both the oat and grass roots will not interfere with that of the europium. The characteristic emissions in the 590 to 620 nm range are plainly evident in this system. Shifts in the two emission peaks are characteristic of europium binding. Figure 2 shows that there is a shift between the uncomplexed supplied Eu(III) media (both with and without nutrient solution) and that observed in the root and leaf tissue. Figure 2 also demonstrates that the Eu is transported to the leaves (shoot) of the plants. In fact Eu accumulation in the roots and shoot was nearly linear even over 5 days (data not shown). The siderophores available during the study, Desferrol and Ferrichrome, were unable to be resolved in the system either alone or complexed with Eu(III). Following several unsuccessful attempts, it was decided to pursue actual uptake and distribution of the metal itself.

Fluorescence changes within individual tissues and cell types along developing primary and secondary roots of oats immersed in nutrient solution containing 10 mM europium (III) were followed with the confocal scanning laser microscope. Distribution of the europium was observed to decrease basipetally along the root axis with

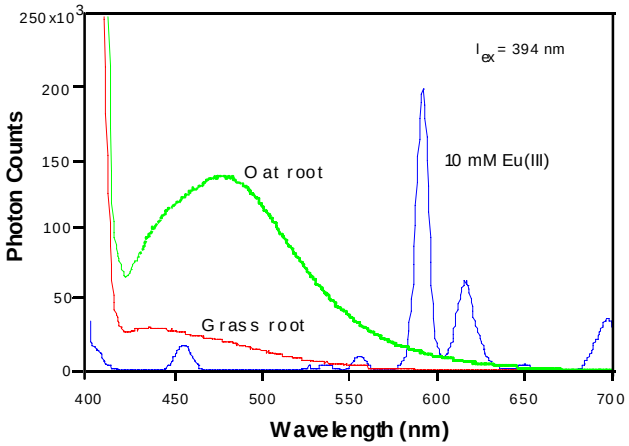

Figure 1. Fluorescence spectra at 394 nm for 10 mM $EuCl_2 \cdot 6H_2O$ solution, 21-day-old oat root and 28-day-old grass root demonstrating that plant root fluorescence does not conflict with europium signature

the highest concentrations consistently found in the meristematic tissue below the root cap at the tip and up to 300 to 500 µm back (Figure 3). Here, and for up to 2000 to 3000 µm back from the tip, concentations were highest after 48 to 72 hours after exposure. Transverse scans were made across the intact roots where a rapid rise in fluorescence at the epidermis followed by a slight decline throughout the cortex and another rise through the stele was observed. Freehand cross sections approximately 300 to 500 µm thick were taken and scanned to precisely identify the tissue types involved in the fluorescence patterns. The sections were subsequently stained with 0.1% (w/v) toluidine-o blue dye, rinsed in distilled H_2O, and photographed. The results for individual cell types are shown in Figure 4. Here the relative fluorescence shows that the stele contains the highest concentration of europium and that the xylem parenchyma, known to control composition of the transpiration stream (Boer and Wegner 1997), and the sieve element-companion cell complexes of the phloem were the highest within this structure.

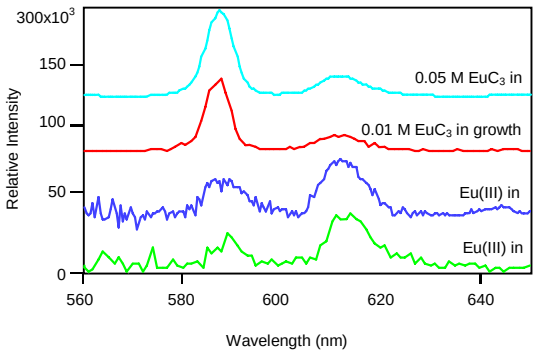

Figure 2. Fluorescence spectra at 394 nm for a 10 mM europium (III) solution in H_2O, 10 mM europium (III) in nutrient solution, oat root, and oat leaf following a 48-hour exposure period

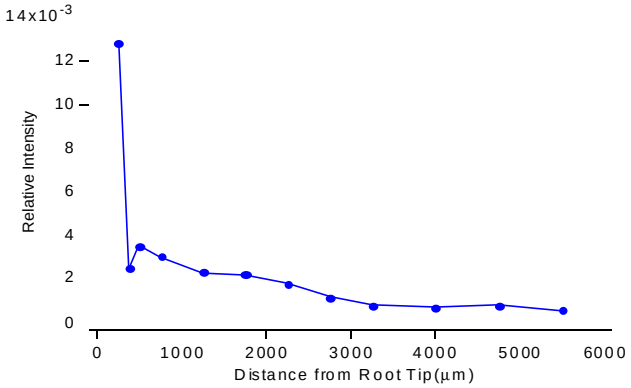

Figure 3. Fluorescence levels at 394 nm along longitudinal axis of oat root immersed in 10 mM europium (III) for 48 hours

Observations also indicate a preferential abaxial distribution of the europium (III) parallel to the plane of gravity. This may indicate regions where there are high extracellular fluxes of Ca^{+3} in response to gravitropic stimulation. Calcium fluxes are important to nutrition and other metabolic activities. If europium (III) is an effective calcium probe, possible in vivo observations of plant nutrition activities are possible. Also europium (III) fluorescence was often higher in cells with dense cytoplasm and high nucleic acid to cytoplasm ratios (meristematic and phloem cells). Uranium, another actinide, is often used as a nucleic acid stain in electron microscopy. Europium interaction with similar material may permit real-time analysis of the effects of the actinides on cellular metabolism.

Summary and Conclusions

The results of this work show a new technique for the in vivo, real-time study of metal europium (III) accumulation by a functioning intact plant root. Highest concentations were observed in the stele of the root, specifically in the xylem parenchyma and phloem. This approach can prove valuable for basic and applied studies in plant nutrition and environmental uptake of actinide radionuclides, as well as micronutrient metals.

References

deBoer AH, and LH Wegner. 1997. "Regulatory mechanisms of ion channels in xylem parenchyma." *J. Exptl. Bot.* 48:441-449.

Burda K, K Strzalka, and GH Schmid. 1995. "Europium- and dysprosium-ions as probes for the study of calcium binding sites in photosystem II." Zeitschrift fuer Naturforschung, Section C, *Biosciences* 50(3-4):220-230.

De Horrocks W Jr., and M Albin. 1987. "Lantanide ion luminescence." pp. 1-103. In: S.J. Lippard, ed. *Progress in Inorganic Chemistry.* Vol 31. J. Wiley & Sons, NY.

Ke HYD; GD Rayson, and PJ Jackson. 1993. "Luminescence study of Eu(3+) binding to immobilized *Datura innoxia* biomaterial." *Environ. Sci. Technol.* 27(12):2466-2471.

Kelly C, RE Mielke, D Dimaqibo, AJ Curtis, and JG Dewitt. 1999. "Absorption of Eu(III) onto roots of water hyacinth." *Environ. Sci. Technol.* 33:1439-1443.

Marschner H. 1995. *Mineral nutrition of higher plants.* 2nd ed. Academic Press, New York, p.11.

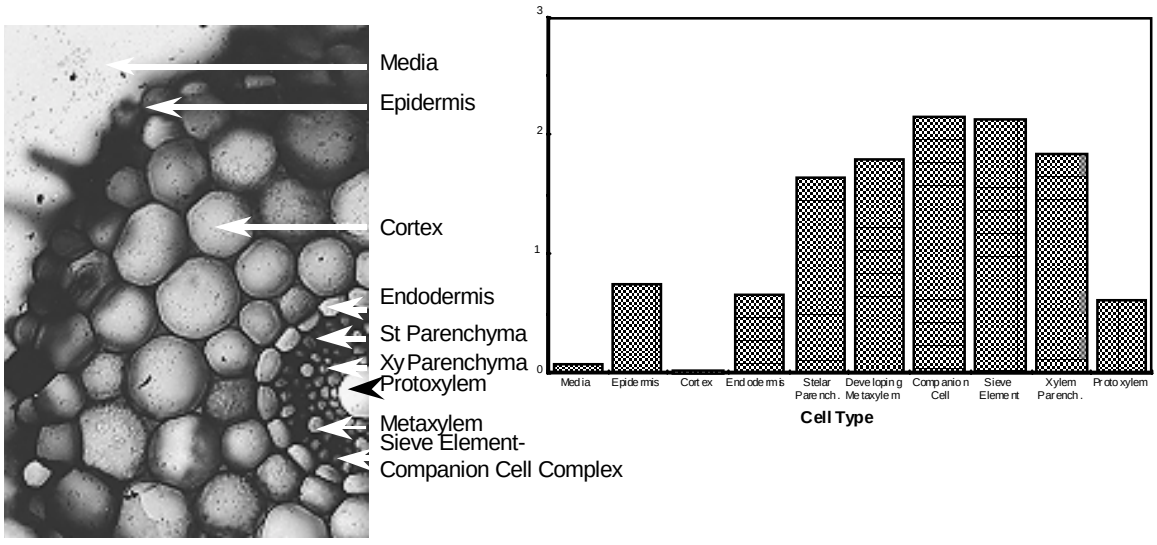

Figure 4. Micrograph of oat root cross section identifying cell types within root and graph giving the relative fluorence at 394 nm

NMR-Based Structural Genomics

Michael A. Kennedy, John R. Cort, Paul A. Bash, Eugene J. Koonin, Aled D. Edwards, Cheryl H. Arrowsmith

Study Control Number: PN99052/1380

The scientific study of structural genomics will lead to new discoveries on the purpose and function of proteins. The structures of proteins and protein folding relationships are keys to protein function. Experimental methods for determining protein structure are slow and tedius. With as many as 100,000 proteins to study in the human genome, our scientists have been working to develop faster methods, using nuclear magnetic resonance, for characterizing the three-dimensional structures of genomic proteins. This new approach has potential to make high-throughput protein studies more productive and will establish a significant role for NMR in structural genomics.

Project Description

Structural genomics presents an enormous challenge with up to 100,000 protein targets in the human genome alone. Two facets of structural genomics were addressed in the project. First, estimates of the required number of structures needed to either experimentally represent all desired structures or to provide a basis for reliable homology modeling range on the order of 10,000 structures. Target selection remains a central focus of structural genomics projects to ensure that the novel sequence-fold information is gained with each new experimentally determined protein structure. In this project, a phylogenetic approach to target selection was examined using the National Center for Biotechnology Information database of Clusters of Orthologous Groups (COGS). The strategy is designed so that each new protein structure is likely to provide novel sequence-fold information. Second, the role that NMR will play in structural genomics has remained an open question. This project was in part aimed at demonstrating the utility and potential role that NMR can play in structural genomics.

Results and Accomplishments

Structure Determination and Fold Classification of E. coli *YciH*

The solution-state structure of YciH was determined using NMR methods (Figure 1). The structural classification databases CATH (class, architecture, topology, and homologons super family, the hierarchical classification of protein domain structures) Dali/FSSP, and SCOP (structural classification of c/a proteins) were used for comparative analysis of the YciH structure. The fold of YciH clearly resembles many others with the open-faced (or 2-layer) β-sandwich form, a fold in the

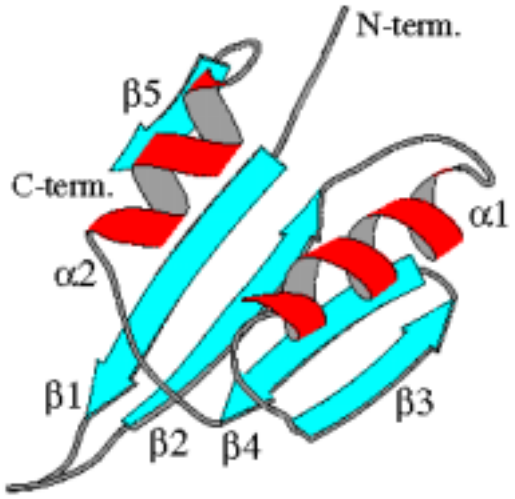

Figure 1. Molscript rendition of the secondary structure of E. coli YciH. The structure contains the ββαββαβ topology which folds into a two-layer α+β open sandwich. The YciH sequence-fold defines a new homologous superfamily within this common fold family.

α+β class. A Dali search returned 10 unique domains (including eIF-1) with z-scores greater than 3.0, indicating significant structural similarity. Thirty-two additional structures had scores between 2.0 and 3.0; in a Dali search scores above 2.0 are considered evidence of structural similarity. Most have the same or a quite similar topology, or ordering of secondary structure elements within the sequence, as YciH.

In the SCOP classification of protein structures, the structures found in the Dali search are members of one of twofold categories (similar to topology in CATH): the ferredoxin-like fold (23 superfamilies) and the DCoH-like fold (2 superfamilies). In the CATH classification, all the similar structures fall into the α–β plait topology

classification (32 homologous superfamilies), which encompasses both of the SCOP folds. The two proteins in SCOP with DCoH-like topology, the arginine binding domain of the arginine repressor, and dimerization cofactor of hepatocyte nuclear factor-1 (DCoH), have the identical core topology as YciH: ββαββα. A domain of DNA gyrase that was located by Dali also has this topology but does not appear in CATH or SCOP. Structures with ferredoxin-like topology are slightly permuted: βαββαβ. Both contain the same placement of secondary structure elements—two helices running antiparallel to each other packed on the same side of a four-stranded antiparallel β-sheet. Furthermore, they have the same organization of the strands in the core of the sheet: β2, β3, and β4 in the DCoH topology correspond to β1, β2, and β3 in the ferredoxin topology. In other words, removal of the N-terminal and C-terminal β-strands, respectively, from the DCoH and ferredoxin topologies yields exactly the same structure. YciH has a fifth beta strand as well, which is parallel to β1 and thus its topology is ββαββα(β). In YciH, if β1 were removed and β5 moved sideways slightly to adjoin (antiparallel to) β2, the resulting topology would be βαββαβ, the ferredoxin-like fold.

Solution-State Structure and Structure-Based Functional Classification of a Hypothetical Protein, MTH538, from Methanobacterium thermoautotrophicum

The structure of a hypothetical protein, MTH538, from *M. thermoautotrophicum*, has been determined by NMR spectroscopy (Figure 2). MTH538 is one of numerous structural genomics targets selected in a genome-wide survey of uncharacterized sequences from this organism. MTH538 is not unequivocally similar to any other (known) sequences. The structure of MTH538 closely resembles those of the receiver domains from two component response regulator systems, such as CheY, and is also similar to structures of flavodoxins and GTP-binding proteins. Tests for characteristic activities of CheY and flavodoxin (phosphorylation in the presence of acetyl phosphate and flavin mononucleotide binding, respectively) were negative. However, a role in a two-component response regulator system may still be plausible.

A PSI-BLAST (position-specific iterated-basic local alignment search tool) search with the MTH538 sequence reveals weak (18 to 23%) similarity between a 95 residue segment of MTH538 and a common segment from members of a family of proteins annotated as putative ATPases or kinases (Figure 3). This family (COG1618 in the clusters of orthologous groups) contains another *M. thermoautotrophicum* ΔH protein, MTH1068 along with representatives from other archaebacterial species, including *Methanococcus jaanaschi*, and the primitive eubacterium *Thermotoga maritimium*. Two nucleotide-triphosphate binding motifs, GXXXXGK(S/T) and DXXG, are conserved in COG1618 but are not present in MTH538. No structural information is available for any proteins in this family.

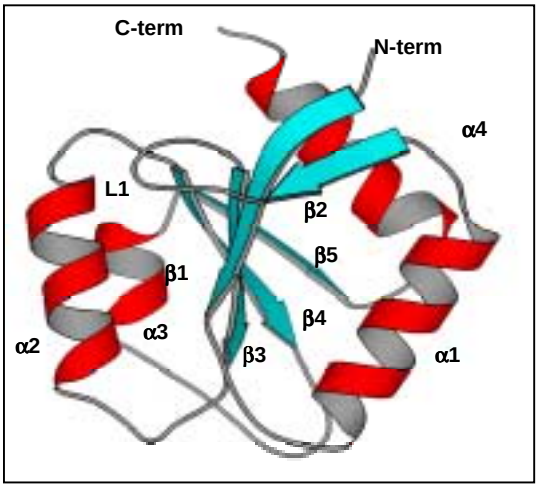

Figure 2. Molscript rendition of the secondary structure of M. therm MTH538. The structure contains the ββαββαβ topology which folds into a two-layer α+β open sandwich. MTH538 is a singleton in sequence space. Structure-based functional classification indicates a possible role as a phosphorylation-independent response-regulator signaling protein in a two-component signal transduction system.

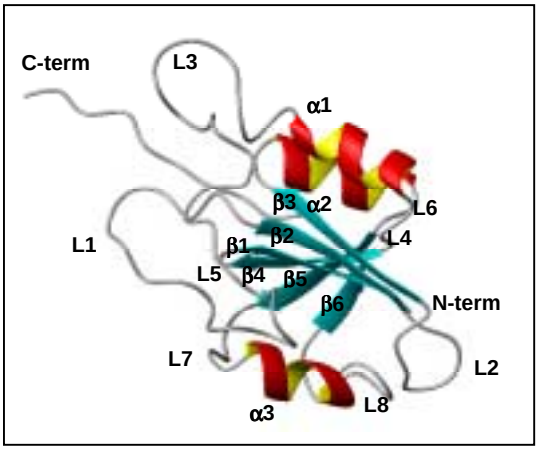

Figure 3. Molscript rendition of the secondary structure of M. therm MTH1175. The structure contains the ββαββαβ topology which folds into a two-layer α+β open sandwich. MTH1175 is a member of a conserved family of mainly archaeal proteins whose function remains unknown.

Solution-State Structure and Fold-Classification of a Hypothetical Protein, MTH1175, from Methanobacterium thermoautotrophicum

The solution structure of MTH1175, a 124-residue protein from the archaeon *Methanobacterium thermoautotrophicum* has been determined by NMR spectroscopy. MTH1175 is part of a family of conserved hypothetical proteins (COG1433) with unknown functions that contains multiple paralogs from all complete archaeal genomes and the archaeal gene-rich bacterium *Thermotoga maritima*. Sequence similarity indicates this protein family may be related to the nitrogen fixation proteins NifB and NifX. MTH1175 adopts an α/β topology with a single mixed β-sheet, and contains two flexible loops and an unstructured C-terminal tail. The fold resembles that of Ribonuclease H and similar proteins, but differs from these in several respects, and is not likely to have a nuclease activity. A PSI-BLAST search with the amino acid sequence of MT1175 indicated similarity to the COG1433 proteins and some additional archaeal orthologs, as well as the bacterial nitrogen fixation proteins NifX and a C-terminal segment of NifB. The sequence similarity between MTH1175 and NifX or NifB is approximately 20 to 25% over a span of ~80 residues. Similarity to two Archaeal NifX proteins, from *M. thermoautotrophicum* and *Methanococcus maripaludis* was also revealed by the PSI-BLAST search. However, archaeal NifB proteins from *M. thermoautotrophicum* and *Methanococcus jannaschii* lack the C-terminal segment which is similar to COG1433 proteins and NifX. In a cluster dendrogram (not shown) of the aligned sequences, the expanded COG1433, NifX, and NifB families appear to constitute three distinct, but related, families. The limited sequence similarity between proteins from different families is probably not sufficient to unequivocally call them homologues, without knowing whether they are structurally similar. The cluster dendrogram also indicates that archaeal NifX proteins from *M. thermoautotrophicum* and *M. maripaludis* do not clearly fall into any one of these families, in terms of sequence similarity, although the branch point in the dendrogram lies closest to the cluster of NifB sequences.

Summary and Conclusions

The aim of this project was to 1) demonstrate the effectiveness of a phylogenetic approach to target selection for structural genomics, and 2) to demonstrate the utility and potential role for NMR in structural genomics.

The YciH sequence was targeted using the phylogenetic target selection approach with the goal in mind of identifying a new sequence-fold relationship. In this example, it was found that the YciH structure corresponded to a well-known and highly represented fold class in protein fold space, albeit this relationship between sequence and fold could not be identified in the absence of the structure using the sequence information alone. This method was successful at identifying a new homologous superfamily in a known fold class, (a new sequence-fold relationship was discovered). This one example indicates that a phylogenetic approach to target selection for structural genomics would be effective.

The two remaining protein structures determined in this project were part of a pilot demonstration to illustrate the effectiveness of using NMR methods for protein structure determination for structural genomics. Each protein structure determined in the project required about 4 to 6 weeks of NMR data collection. With new technological advances occurring in NMR science, it is possible that that data collection times can be reduced by another order of magnitude and the molecular weight of proteins for which structures can be determined using NMR methods is likely to be significantly increased compared to the existing limit of ~40 kD today. Furthermore, in this project it was shown that NMR methods likely provide a complementary approach to x-ray crystallographic methods allowing rapid functional testing for substrate or ligand binding and a means of characterizing dynamic and unstructured regions in proteins that have a potentially important function and that are difficult or impossible to characterize by other methods.

Publications

Christendat D, A Yee, A Dharamsi, Y Kluger, A Savchenko, JR Cort, V Booth, CD Mackereth, V Saridakis, I Ekiel, G Kozlov, KL Maxwell, N Wu, LP McIntosh, K Gehring, MA Kennedy, A R Davidson, EF Pai, M Gerstein, AM Edwards, and CH Arrowsmith. 2000. "Structural Proteomics of M. thermoautotrophicum: A global survey of non-membrane protein expression, solubility and structure." *Nature Structural Biology*, 7:903-909.

Cort JR, EJ Koonin, PA Bash, and MA Kennedy. 1999. "A phylogenetic approach to target selection for structural genomics." *Nucleic Acids Research* 27(20):4018-4027.

Cort JR, A Yee, AM Edwards, CH Arrowsmith, and MA Kennedy. 2000. "Structure-based functional classification of hypothetical protein MTH538 from Mehtanobacterium thermoautotrophicum." *J. Mol. Biol*., 302:189-203.

Cort JR, A Yee, AM Edwards, CH Arrowsmith, and MA Kennedy. 2000. "NMR structure determination and structure-based functional characterization of a conserved, hypothetical protein MTH1175 from *Methanobacterium thermoautotrophicum." J. Structural & Functional Genomics* (submitted).

Acknowledgments

We are grateful to L. Aravind for his help in the analysis of the COGs for target selection. John R. Cort is a 1999 recipient of an American Cancer Society postdoctoral fellowship.

Plant Root Exudates and Microbial Gene Expression in the Rhizosphere

Mark T. Kingsley

Study Control Number: PN99056/1384

Nucleic acid arrays are widely used in the pharmaceutical industry to provide information on differentially expressed genes when screening drugs and drug candidate compounds. Nucleic acid, DNA array analyses provide an automatable, compact, discrete, reproducible format for analyzing genomic information of microbes and higher organisms. Gene chips are also being developed for the specific identification of organisms by both government and industry. This project explored the use of an array based on short oligonucleotide targets, for identifying agricultural pathogens by differential pattern development and recognition.

Project Description

This research involved 1) developing DNA microarray analytical methods for 16S rRNA from environmental samples to rapidly identify members of microbial communities, and 2) genotyping arrays for environmental organisms and potential food pathogens, and "fingerprinting" arrays for discriminating closely related organisms. We are developing fluorescent polymerase chain reaction analytical methods for agricultural crop pathogens (Kingsley 2000; Kingsley and Fritz 2000) that could have the potential to be employed in agricultural bioterrorism. DNA microarrays offer a unique ability to provide inexpensive, rapid, and specific identification of microbes. Since productivity of renewable energy biomass sources (crop, forest) can be drastically limited by bacterial, fungal, or viral pathogen attack, rapid methods for the specific identification of the causitive agent(s) is desirable. The high density of diagnostic probes achievable on microarrays provides for a highly robust analytical tool. The array technology can be integrated into online analytical devices currently under development. A goal of this project was to develop appropriate DNA diagnostic suites of oligonucleotides for agricultural and forest pathogens. As part of this initial proof-of-concept demonstration, we tested microarrays for analysis of bacterial pathogens in the genus *Xanthomonas* and fungal pathogens in the genus *Fusarium*. Some members of the genus *Fusarium,* in addition to leading to crop productivity losses, produce mycotoxins which are toxic and/or carcinogenic to humans or animals.

Introduction

The development and use of nucleic acid arrays in detection, genotyping, and analysis of gene expression, is increasing rapidly (Behr et al. 1999; Cockerill 1999; Tao et al. 1999; Westin et al. 2000). Currently, many groups are developing DNA arrays for microbial detection and identification. Genetic arrays, once prototyped and developed, offer extremely robust, yet relatively inexpensive means (the array itself is cheap) for identifying organisms. Arrays offer the ability to create multiplexed (combined) assays providing for the analysis of multiple targets simultaneously. Exploiting this powerful analytical tool for analysis of phytopathogens has not been reported. This project aims to explore the use of DNA microarrays for differentiating and identifying various *Xanthomonas* (bacterial) and *Fusarium* (fungal) phytopathogens.

Since agricultural and forest productivity can be compromised by rhizosphere inhabiting pathogens such as the *Fusarium* species, and foliar pathogens such as *Xanthomonas*, rapid and sensitive methods for analysis of seeds, plant tissues, and soils by DNA microarrays offers the benefit of a highly accurate method of detection and pathogen identification. Often these pathogens remain undetected until the plants are symptomatic, which often is too late. Preventing crop losses due to early pathogen detection could become an important issue for DOE's Bioenergy initiative where the goal is to triple the use of renewable crops for fuels and feedstock by the year 2010. Phytopathogen analysis, especially of orgranisms in the bacterial genus *Xanthomonas* and the fungal genus *Fusarium* would benefit greatly from the power of nucleic acid array analysis. Numerous clonally derived species and subspecies are known within both *Fusarium* and *Xanthomonas*. Historically, these organisms were classed according to their pathogenicity to particular hosts. Issues of genetic relatedness to other members of the genus that attacked different hosts were ignored. Only with the advent and power of nucleic acid analysis have a number of issues of taxonomic position and relatedness been

resolved (Gabriel et al. 1988, 1989; O'Donnell and Gray 1995; O'Donnell et al. 2000; Vauterin et al. 1995).

More than 100,000 fungal species are known. Most are saprophytic living off dead/decaying organic matter. While approximately 50 fungal species can cause disease in humans and animals, more than 10,000 fungal species can cause disease in plants (Kingsley 2000). Therefore problems of identification of specific organisms are often large.

This work is an outgrowth of a prior project that isolated, characterized, and cloned rhizosphere inducible bacterial promoter elements for use in bioremediation (phytoremediation) applications and biocontrol.

Approach

Our approach involved attaching a series of 47 9-mer (9 bases long) oligonucleotides (probes) to a glass slide to which biotinylated polymerase chain reaction products (targets) are hybridized. Probes are spotted in a high pH buffer to facilitate covalent attachment. Spotting is accomplished with a Genetic Microsystems 417 arrayer, and we used 12-well Teflon-masked slides (Eri Scientific Co., Portsmouth, New Hampshire). This permitted printing 12 full arrays on a single slide, useful for running replicate reactions and multiple samples. The microbial polymerase chain reaction products were labeled using biotinylated primers (REP, ERIC, BOX bacterial repeat primers).

Denatured, biotin-labeled polymerase chain reaction products were applied to individual wells (40 µL maximum volume), hybridized, and washed. Streptavidin-alkaline phosphatase is then added (AMDEX, Amersham Piscataway, New Jersey) to each well and incubated, washed, and reacted with fluorescence visualization reagents. The fluorescent emissions were captured using a BioRad Fluor-S imager. Fluorescent array images were quantified using Phoretix software (Ver. 1.00, Phoretix International, Newcastle, United Kingdom). The polymerase chain reaction fingerprint products were also visualized by traditional gel electrophoresis, and the gel image was captured and analyzed using GelComparII (Version 2, Applied Maths, Kortrijk, Belgium) to produce a cluster analysis of the similarity of the samples. This approach provided a means for comparing the resolving power of the array versus the traditional gel-based approach.

Results and Accomplishments

Polymerase Chain Reaction Amplifications, Labeling of Microbial DNA, Analysis of REP-PCR Gels

Xanthomonas (bacteria, Figures 1 through 4) and *Fusarium* (fungus, Figure 5) genomic DNA was labeled with a biotin-tagged forward REP primer by standard REP-PCR amplification. Prior to array analysis, and to provide a reference between traditional gel-based analyses of the reactions and the analysis performed on the 47-target 9-mer array(s), all reactions were analyzed by gel-electrophoresis. To visualize the reactions run in the gel, the gels were stained with the fluorescent dye ethidium bromide, illuminated with ultraviolet light, which visualizes the DNA bands, and photographed. Figure 1 shows an example of 17 *Xanthomonas* REP-PCR DNA

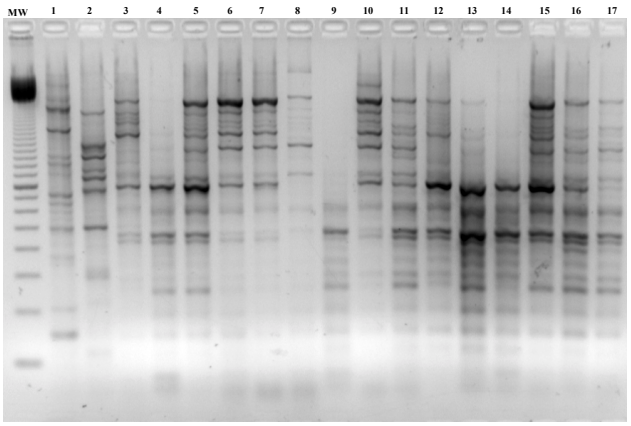

Figure 1. Agarose gel electrophoresis analysis of 17 *Xanthomonas* isolates. The banding patterns were generated using REP-PCR primers that recognize a conserved DNA repeat sequence. The forward primer included a biotin tag that labeled the products for DNA array analysis (see Figure 3). Lanes 1-3 contain reactions from control strains and lanes 4-17 from various *X. axonopodis* pv. *citri* isolates from diverse geographical locations worldwide.

fingerprints analyzed by gel electrophoresis. The digital image of the gel was loaded into the analysis program (GelComparII) for homology analysis of the REP-PCR DNA fingerprints. This analysis is based on the similarity/differences of the banding patterns between and among the various samples included in the analysis. The results of the analysis can be displayed as a cluster dendrogram that indicates the relatedness of the analyzed patterns. The strains of *Xanthomonas* are highly related and this is reflected in the level of clustering and the linkage points (Figure 2).

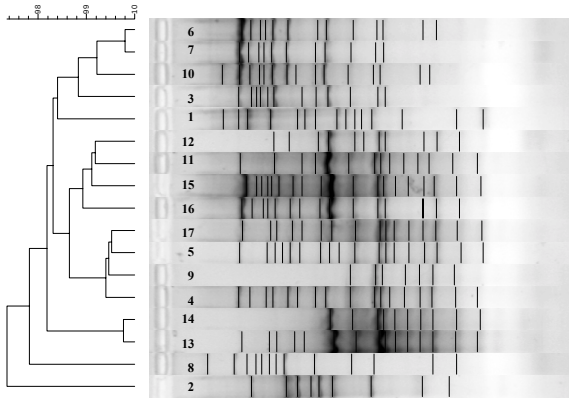

Figure 2. Results of homology studies (cluster analysis) of the gel (Figure 1) using GelComparII. The most unrelated sample (Lane 2) based upon band sharing was the Type strain of the species *Xanthomonas axonopodis* (ATCC 19312).

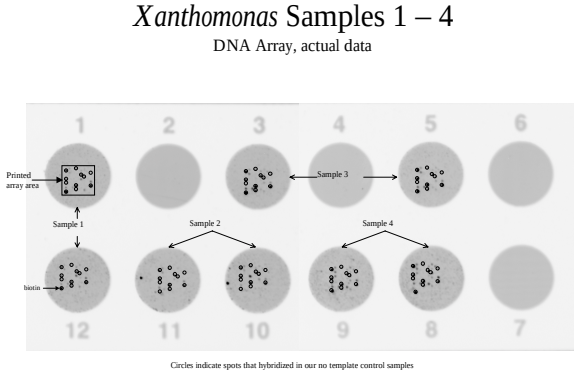

Figure 3. An example of the visualize results of the DNA array analysis with *Xanthomonas* DNA samples 1-4 (correspond to lanes 1-4 in Figure 1)

Once the REP-PCR reactions were verified by gel electrophoresis, they were subjected to DNA array hybridization and detection. Figure 4 shows an example of such an array analysis. In this case samples 1 through 4 correspond with samples 1 through 4 in Figure 1. Employing statistical algorithms previously developed for MALDI mass spectrometry and other peak detection methods, the array analysis data for samples 1 through 17 were clustered (Figure 4). The one major difference that appeared in this analysis was sample 17, which appeared to be completely unrelated to the other xanthomonads (a result not seen by the gel electrophoresis analysis). This result was, in fact an artifact due to poor hydridization and lack of corresponding data (not shown).

Figure 5 shows a sample gel of two *Fusarium graminearum* strains and two *Gibberella zeae* strains (*Gibberella zeae* is the teleomorph [sexual form] of *F. graminearum* [asexual form]).

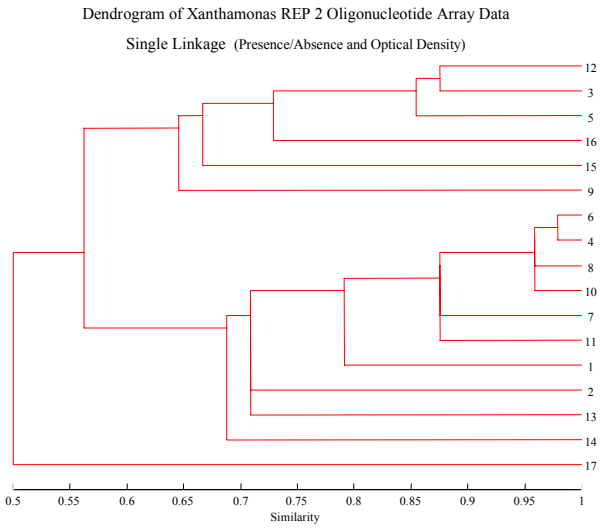

Figure 4. Cluster analysis of the relatedness of *Xanthomonas* samples 1-17 based upon results of DNA array analysis. While the broad associations between the different isolates are somewhat similar (i.e., more or less the same strains in major clusters, compare with Figure 2), there are several differences. Isolate 17 is shown by the array analysis to be completely unrelated to the other strains, however this apparent difference stems from a problem with the hybridization reaction and is therefore an artifact.

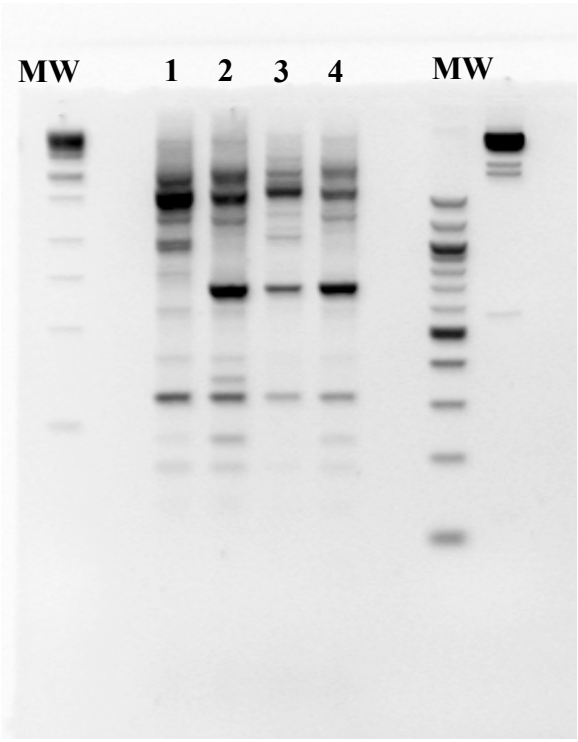

Figure 5. REP-PCR fingerprints of four fungal DNA samples (2 strains of *Fusarium graminearum* and two strains of *Gibberella zeae*)

Summary and Conclusions

The simple 47-target 9-mer array provided a resolving power that appeared equivalent to a traditional REP-PCR gel-based analysis.

The total analysis was both simpler and faster than the traditional gel-based fingerprinting approach. This method holds great promise for resolving agricultural pathogens. Some issues with optimization of the probes (i.e., the specific DNA sequences employed, increased number of targets) on the array and some background reactions remain to be resolved.

The data shown is a worst-case scenario; the *X. citri* (*X axonopodis* pv. *citri*) strains were chosen due to their high degree of relatedness and the difficulty in distinguishing individual strains despite the fact they are from diverse geographic origins (clonal organism).

References

Behr MA, MA Wilson, WP Gill, H Salamon, GK Schoolnik, S Rane, and PM Small. 1999. "Comparative genomics of BCG vaccines by whole-genome DNA microarray." *Science* 284:1520-1523.

Cockerill III FR. 1999. "Genetic methods for assessing antimicrobial resistance." *Antimicrob. Agents Chemother.* 43(2):199-212.

Gabriel DW, JE Hunter, MT Kingsley, JW Miller, and GR Lazo. 1988. "Clonal population structure of Xanthomonas campestris and genetic diversity among citrus canker strains." *Mol. Plant-Microbe Interact.* 1:59-65.

Gabriel DW, MT Kingsley, JE Hunter, and T Gottwald. 1989. "Reinstatement of Xanthomonas citri (ex Hasse) and X. phaseoli (ex Smith) to species and reclassification of all X. campestris pv. citri strains." *Int. J. Syst. Bacteriol*. 39:14-22.

Kingsley MT. 2000. *Technical Requirements Document: Nucleic acid-based detection and identification of bacterial and fungal plant pathogens*. PNNL-13124, Pacific Northwest National Laboratory, Richland, Washington.

Kingsley MT and LK Fritz. 2000. "Identification of the citrus canker pathogen Xanthomonas axonopodis pv. citri A by fluorescent PCR assays." *Phytopathology* 60 (6 suppl.):S42.

O'Donnell K and LE Gray. 1995. "Phylogenetic relationships of the soybean sudden death syndrome pathogen Fusarium solani f.sp. phaseoli inferred from rDNA sequence data and PCR primers for its identification." *MPMI* 8(5):709-716.

O'Donnell K, HC Kistler, BK Tacke, and HH Casper. 2000. "Gene genealogies reveal global phylogeographic structure and reproductive isolation among lineages of Fusarium graminearum, the fungus causing wheat scab." *Proc. Natl. Acad. Sci. USA*. 97:7905-7910.

Tao H, C Bausch, C Richmond, FR Blattner, and T Conway. 1999. "Functional genomics: expression analysis of Escherichia coli growing on minimal and rich media." *J Bacteriol*. 181(20):6425-40.

Vauterin L, B Hoste, K. Kersters, and J Swings. 1995. "Reclassification of Xanthomonas." *Int. J. Syst. Bacteriol*. 45:472-489.

Westin L, X Xu, C Miller, L Wang, CF Edman, and M Nerenberg. 2000. "Anchored multiplex amplification on a microelectronic chip array." *Nat. Biotechnol*. 18:199-204.

Acknowledgements

The contributions of the following PNNL staff members are gratefully acknowledged: Lucie Fritz (PCR Assays), Darrell Chandler, Doug Call, Tim Straub (DNA array analyses), Sharon Cebula, Don Daly, and Kris Jarman (DNA array statistical analysis and dendrograms).

Rapid NMR Determination of Large Protein Structures

Paul D. Ellis, Michael A. Kennedy, Robert Wind

Study Control Number: PN00077/1484

Functional and structural genomics is the science that correlates protein structure with function in living cells, and proteomics is the study of the entire complement of proteins expressed by a cell. This project seeks to develop new methods of nuclear magnetic resonance (NMR) analysis of large protein structures so that data collection times for analyses are significantly reduced, allowing more proteins to be studied.

Project Description

Dielectric losses associated with biological NMR samples at high magnetic fields (>17 T) ultimately determine the potential NMR signal to noise (S/N) ratio. These losses have a direct effect of lengthening (quadratically) the time needed to acquire NMR data sets required to deduce the three-dimensional structure of a protein in solution. The goal of this research is to develop technical means for minimizing dielectric losses in biological NMR experiments. If successful, this could lead to a significant reduction in NMR data collection times leading to more rapid structure determinations. One of the most innovative new ideas for reducing the dielectric losses in biological NMR samples is to encapsulate proteins in reverse micelles dissolved in low dielectric bulk solvents. Preparing and characterizing such systems by small angle x-ray scattering and NMR spectroscopy will be the primary focus of this project.

Introduction

In the post-genomic era, the scientific focus is changing from determining the complete DNA sequence of the human genome to characterizing the gene products. The expected number of proteins from the human genome is ~100,000. Proteomics, defined as the study of the entire complement of proteins expressed by a particular cell, organism, or tissue type at a given time for a given disease state or a specific set of environmental conditions, promises to bridge the gap between genome sequence and cellular behavior. An integral challenge involves the characterization of the biological functions of these proteins and analysis of the corresponding three-dimensional structure. This is referred to as functional and structural genomics, respectively. Ultimately, the goal of structural genomics is to determine the structure of a sufficiently large subset of the approximately 100,000 proteins such that a "basis" structure could be formulated. This basis would, in turn, be used as a predictor of the remaining structures while simultaneously providing a rationale for the observed function of all of the gene products.

Currently, x-ray crystallography requires diffraction-quality crystals, selenium-labeled proteins, and access to high-intensity light sources available at the DOE national laboratory synchrotrons. Given these conditions, x-ray data sets can be collected in a matter of 2 to 4 hours and virtually have no limitation with respect to protein size. However, dynamic or statically disordered regions of proteins are invisible to x-ray crystallography. NMR spectroscopy has several unique capabilities that are complementary to x-ray crystallography: 1) proteins can be examined under physiological solution-state conditions; 2) dynamic regions of the proteins can be well characterized; 3) intermolecular complexes can be easily studied as a function of pH, ionic strength, etc. However, NMR currently has two significant limitations when compared to x-ray crystallography: 1) data sets currently take about 60 days to collect, and 2) the size of proteins amenable to NMR structure determination is currently limited to ~50 kDa.

If the structures of a large subset among approximately 100,000 proteins must be determined, then x-ray crystallography data collection would require maximally between 24 and 45 years of synchrotron time (assuming proteins protein crystals are obtainable at high enough quality in all cases). On the other hand, for this same subset, given the current technology, NMR spectroscopy would require approximately 16,438 years of NMR time. Estimates of the cost per structure with current technologies are running around $50,000 to $100,000 each. The cost of such an effort would be between $5 billion and $10 billion. Ideally, one could imagine dividing the task of structural genomics equally between x-ray crystallography and NMR, but, at the current state

of technology, it is anticipated that NMR has a limited role. If NMR spectroscopy is to contribute significantly to this effort, then the data collection time for the NMR experiment must be dramatically reduced, and the applicable molecular weight range must be expanded to >100 kDa.

Given the existence of high field (>17 T magnets) NMR spectrometers, why does it take so long to collect the critical data sets? A significant recent advance is the introduction of cryoprobe technology in which the NMR coil and preamplifier are cooled to near liquid helium temperatures. This advance, that can theoretically increase NMR sensitivity by a factor of 3 to 4, holds the prospect of reducing NMR data collections times by as much a factor of 10. However, cryoprobe performance will reach a practical limit at high fields because of the consequences of the dielectric losses of the sample on NMR sensitivity. If the sample losses could be significantly reduced, the sensitivity would increase and optimal cryoprobe performance could be obtained. Virtually all proteins require water as a solvent in the presence of varying concentrations of salts (typically <200 mM). This solvent/salt/buffer combination produces a conductive sample that, in turn, generates inductive losses that arise from the formation of eddy currents in the sample. Under normal circumstances, these sample losses and not losses associated with the coil itself dominate the Q of the receiver coil of the probe. The consequences of these losses increase strongly with the frequency of the spectrometer and the sample diameter. Hence, the higher the field or the larger the sample at a fixed field, the worse the problem becomes. If these losses could be eliminated, then the length of time required for data collection could be significantly reduced. In this project, research will be carried out to determine if a general approach for encapsulating proteins in reverse micelles dissolved in low dielectric bulk solvents as a way of minimizing dielectric losses during NMR data collection can be realized.

Results and Accomplishments

The primary technical task for the project was to assemble and characterize reverse micelle systems containing encapsulated proteins. A systematic approach was taken to explore the range of solution conditions under which stable and well-behaved, spherical, nonaggregated, or noncomplex lipid structures are formed. The primary characterization method was small-angle x-ray scattering. Preliminary experiments were carried out and were successful in demonstrating that small-angle x-ray scattering was an effective technique for characterizing the dimensions of reverse micelles that contained either solvent or were in the presence of encapsulated proteins. A single anionic micelle system was explored, the surfactant dioctyl sulpsuccinate sodium salt and pentane. Small-scale x-ray scattering proved to be a sensitive means of characterizing reverse micelle structure in terms of dimensions and geometrical organization.

Summary and Conclusions

The work carried out in this project demonstrated that the combination of small-angle x-ray scattering as a screening method for the preparation of encapsulated protein samples in reverse micelles for NMR data collection is an effective strategy and if systematically pursued, and can provide an efficient means of developing a broad range of possible reverse micelles systems for use in protein structure determination by NMR.

References

Fulton JL and RD Smith. 1988. "Reverse micelle and microemulsion phases in supercritical fluids." *J. Phys. Chem.* 92:2903-2907.

Fulton JL, JP Blitz, JM Tingey, and RD Smith. 1989. "Reverse micelle and microemulsion phases in supercritical xenon and ethane: Light scattering and spectroscopic probe studies." *J. Phys. Chem* 93:4198-4204.

Wand AJ, MR Ehrhardt, and PF Flynn. 1998. "High resolution NMR of encapsulated proteins dissolved in low-viscosity fluids." *Proc. Natl. Acad. Sci.* 95:15299-15302.

Role of Unculturable Bacteria in the Wheat Rhizosphere

Fred J. Brockman, Harvy Bolton

Study Control Number: PN99064/1392

An improved understanding of plant-microbe interactions in the rhizosphere is important to DOE programs aimed at understanding how plant-soil systems may be manipulated to increase productivity of crops (improved nutrient supply, increased control of pathogens) and potentially increase carbon sequestration in soils.

Project Description

The objective of this project was to develop and employ nucleic acid approaches for rapid detailed analysis of microbial community structure and function in the rhizosphere. Because only a very small percentage of microorganisms are successfully cultured, improved approaches are needed to answer these critical research questions: What rhizosphere microorganisms are dominant in the community but uncultured? How does rhizosphere community structure vary with soil management practices (e.g., high versus low fertilization rate, no-till versus conventional tillage)? This project extracted DNA and RNA from the microbial communities in rhizosphere soil and soil without plants under four soil management regimes, amplified the corresponding 16S targets, analyzed the community nucleic acids by terminal restriction fragment analysis, and statistically analyzed the resulting profiles by heirarchical cluster analysis. The results indicate that plant effects were greater than tillage effects and that nitrogen level had little to no effect. Terminal restriction fragment analysis is a rapid and robust means of fingerprinting the set of dominant and largely uncultured microorganisms in the microbial community.

Introduction

The rhizosphere is the region in and around roots that is influenced by the plant. Approximately 10 to 25% of the total carbon fixed by the plant is released into the rhizosphere, and sloughing root cells also provide high levels of other microbial nutrients. The rhizosphere microbial community is important in plant health and productivity, including nitrogen fixation, mycorrhizae, biocontrol of plant pathogens, and plant-growth promoting bacteria. However, the composition of these microbial communities and the factors that determine community structure and metabolism (plant and microbial signaling, physical and geochemical heterogeneity) are largely unknown. As with other microbial ecosystems, fewer than 1 to 5% of resident microorganisms can be cultured in the laboratory. Hence, only a small fraction of the total rhizosphere microbial community has been adequately described. This leaves a considerable gap in our knowledge of rhizosphere structure and function.

Approach

A growth chamber study was conducted with soil (homogenized from 0 to 10 cm) from no-till and conventionally tilled fields. Each soil was supplemented with a low (8 kg nitrogen/hectare) and a high (80 kg nitrogen/hectare) fertilization rate. Winter wheat (12 seeds) was planted to 5 replicate pots of each of the 4 treatments and grown with spring photoperiod and temperature regimes. Pots without wheat plants were maintained under identical moisture, photoperiod, and temperature regimes to provide a bulk soil microbial community for comparison to the rhizosphere soil microbial community. Six weeks after germination, rhizosphere soil was isolated from each pot containing wheat plants and soil was sampled from pots without wheat. Soil from each pot was plated to isolate all morphotypes of culturable aerobic heterotrophic bacteria, and DNA and RNA was extracted and purified from soil in each pot.

Extracted DNA was amplified using the polymerase chain reaction (PCR) and eubacterial 16S ribosomal DNA (rDNA) primers with one primer labeled with a fluor (Figure 1). The amplified rDNA was subjected to a restriction enzyme and the labeled 16S rDNA terminal fragments separated on a DNA sequencing gel. This approach was used to characterize each cultured isolate and the community as a whole. For the community, the resulting electropherogram shows the size of each fragment in base pairs for the dominant bacterial ribotypes in the sample. This approach, terminal restriction fragment analysis, was selected over construction, analysis, and sequencing of clone libraries because it is much faster and because fingerprints of

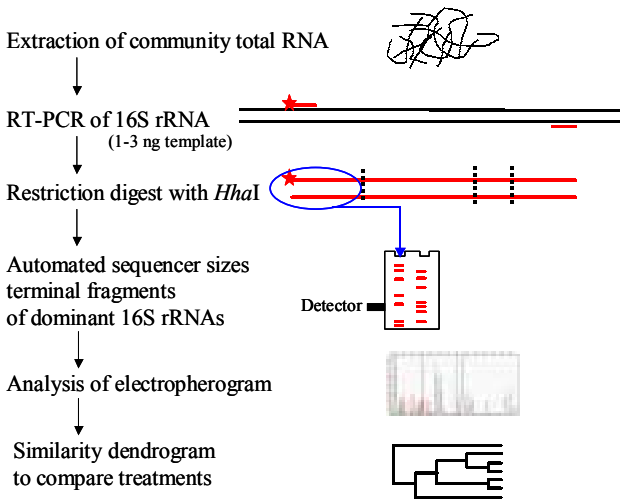

Figure 1. Analysis of microbial communities using terminal restriction fragment analysis

microbial community structure were deemed more important than specific phylogenetic identifications for this project. Terminal restriction fragment analysis typically identifies approximately 30 to 60 of the dominant ribotypes in the microbial community of a particular sample.

In fiscal year 2000, we focused our analysis on ribosomal RNA (rRNA) to determine if greater differences could be observed between the experimental treatments. rRNA levels in bacteria vary depending on how metabolically active the cells are, whereas rDNA levels per cell are invariant. Reverse transcriptase polymerase chain reaction (RT-PCR) is more sensitive to inhibition by soil humic acids, so effort was devoted to maximizing rRNA purity in order to obtain robust rRNA terminal restriction fragment analysis profiles. In addition, terminal restriction fragment analysis was performed on each end of the rRNA molecule (versus one end of the rDNA molecule in fiscal year 1999) to improve assay robustness. Software was used to simultaneously compare the edited electropherograms and construct similarity dendrograms using heirarchical cluster analysis.

Results and Accomplishments

The following major results were found when analyzing rDNA. Approximately 80% of the rhizosphere soil ribotypes were not detected in isolates from the rhizosphere soil, demonstrating that most of the microorganisms that most heavily colonize the rhizosphere were not cultured and were only detected by molecular analysis. rDNA terminal restriction fragment analysis profiles in rhizosphere soil were nearly identical regardles of tillage or N level (Figure 2, panel A). Terminal restriction fragment analysis profiles in soil without wheat plants were more variable, with a greater effect from tillage than from nitrogen level. The highest order difference was between rhizosphere and no-plant soils.

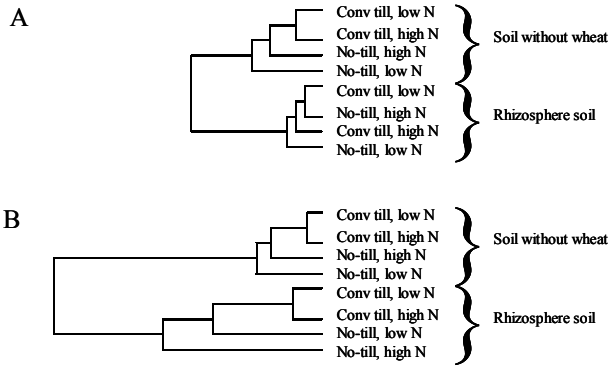

Figure 2. Representative dendrograms derived from statistical analysis of terminal restriction fragment analysis profiles showing the relationship of microbial communities in rhizosphere soil and soil without wheat plants under four soil management practices. Two soils that are horizontally connected by shorter lines are more similar than two soils horizontally connected by longer lines. Panel A, using rDNA; panel B, using rRNA. Conv, conventional; N, nitrogen.

These results suggested that the wheat root influences the structure of the microbial population and does so to a greater degree than soil management practices (that were examined).

In rhizosphere soil, profiles showed more variability between the four treatments than profiles generated from rDNA. In contrast, in soil without wheat, the rRNA terminal restriction fragment analysis profiles differed little from those seen using rDNA terminal restriction fragment analysis and there was less variability than in the rhizosphere soils. In both types of soil, tillage showed a greater effect than nitrogen level. rRNA also yielded a greater difference between rhizosphere and no-plant soils, as evidenced by the more horizontal profile in Figure 2. As in the rDNA terminal restriction fragment analysis analysis, the highest order difference was between rhizosphere and no-plant soils. Overall, the rRNA terminal restriction fragment analysis results confirm the general conclusions from the rDNA analysis: the wheat root strongly influences the microbial population structure and overrides the soil management practices that were examined.

Summary and Conclusions

- The great majority of the ribotypes present in the rDNA from the microbial community were not found in the isolates that were cultured, highlighting the importance of molecular-based analyses for understanding the integrated soil-plant system.

- Terminal restriction fragment analysis using rRNA molecules from the microbial community showed greater differences between management strategies than use of rDNA molecules.

- Tillage practices affected microbial community structure while nitrogen level appeared to have little to no effect.

- The highest order difference in the study was between rhizosphere and no-plant soils, indicating that the influence of the wheat root overrides the soil management practices that were examined.

- Terminal restriction fragment analysis is a rapid and robust means of fingerprinting the set of dominant and largely uncultured microorganisms in the microbial community. Proper editing and computer analysis of the electropherogram profiles was by far the most time-consuming portion of the project. This was in part due to a learning curve associated with the software. However, even in the future, editing and computer analysis of the profiles will remain more time-consuming than RNA extraction/ purification or obtaining the terminal restriction fragment profile.

Computational Science and Engineering

Code Development for NWGrid/NWPhys

Harold E. Trease

Study Control Number: PN00021/1428

The NWGrid/NWPhys system represents enabling technology for solving dynamic, multiscale, coupled computational physics problems on hybrid grids using massively parallel computers in the following areas: computational biology and bioengineering, atmospheric dynamics and transport, subsurface environmental remediation modeling, engineering, computational and molecular chemistry, and semiconductor design. The NWGrid/NWPhys system provides one of the components for building a new Problem Solving Environment modeled after EECE/NWChem. NWGrid/NWPhys brings advanced grid and computational simulation technologies to the Laboratory and to the DOE research community.

Project Description

The purpose of this project is to develop NWGrid/ NWPhys into production codes that integrate automated grid generation, time-dependent adaptivity, applied mathematics, and numerical analysis for hybrid grids on distributed parallel computing systems. This system transforms complex geometries into computable hybrid grids upon which computational physics problems can then be solved. To run the necessary, large memory problems, NWGrid has been ported to other platforms including those in the EMSL Molecular Science Computing Facility (MSCF) and at the National Energy Research Scientific Computing Center (NERSC), with more memory and central processing unit power. Additional Global Array sparse matrix operations that are needed to parallelize NWPhys have been defined and tested. A first draft of the NWGrid Users Manual is being reviewed and a Graphical User Interface is being designed.

Introduction

In the past, NWGrid was run in parallel on the ASCI Silicon Graphics, Inc., System cluster (a predominantly global memory, 64-bit machine) at Los Alamos National Laboratory with ASCI parallelization software. To be able to run the necessary, large memory problems, NWGrid needed to be ported to other platforms, with more memory and central processing unit power.

In the past, NWPhys was run in parallel on CRAYs and Connection Machines at Los Alamos National Laboratory. It is not currently running in a full-assembled configuration in parallel anywhere. Pieces are running in serial on a Silicon Graphics, Inc., system at our Laboratory. Portions of the code are being rewritten on an as-needed-basis for ongoing work. To be able to parallelize it, functions for sparse matrix operations were needed.

The NWGrid/NWPhys command suite was not well documented and there were few examples. Most experienced users knew only small portions that applied to their specific applications. The code currently runs with a command line driven interface. A users manual and graphical user interface are needed.

Results and Accomplishments

NWGrid Code Development. To run the necessary, large memory problems, the scalar version of NWGrid has been ported to other platforms including those in the EMSL/MSCF and at NERSC, with more memory and central processing unit power. This involved converting it from a 64-bit Silicon Graphics, Inc., code to 32-bit architectures, such as IBM (MPP1), LINUX INTEL PC, LINUX ALPHA PC, and SUNs and porting it to each machine's parallel libraries. NWGrid is evolving from FORTRAN 77 and C to FORTRAN 90.

NWPhys Code Development. To be able to parallelize NWPhys, a number of sparse matrix operations are being added to the EMSL internal software package, Global Arrays, to support unstructured meshes. These new functions are compatible with the directives provided by the Connection Machine, which are already used by NWPhys. They have been defined and tested and are in an initial parallel implementation of NWPhys. NWPhys is being rewritten to FORTRAN 90 during this conversion process.

Documentation. The first draft of the NWGrid Users Manual has a full description with format, parameters, examples, and special notes of the over 120 NWGrid

commands. There are instructions on how to install the dictionary and execute the code. To try to make the code easier for the new user, a core set of commands and the command sequence for specific kinds of problems have been defined. There are also examples from simple geometry, such as creating a box or sphere and cutting out a portion of the grid, to smoothing, partitioning the grid, adaptive mesh refinement and converting between file formats. There is a reference section on mesh objects and on code development. The NWGrid Users Manual has been established on an internal web site at this Laboratory. Several new users are accessing it and it is being reviewed by experienced users.

Graphical User Interface. A requirements list for the NWGrid graphical user interface has been completed and the design document is being developed. The graphical user interface will be written in Python using Tkinter. It will directly access the web-based users manual. To try to make it easier for the new user, command sequences for different technical disciplines will be developed and the examples will be expanded. To make it useful to the experienced user, it will be compatible with the current command line version, have access to the full NWGrid command suite, provide a command syntax checker, and provide direct access to the web-based users manual.

Summary and Conclusions

Porting the codes to EMSL machines has allowed us to run a number of applications, including:

Building several gridded variations of the virtual lung (Figure 1).

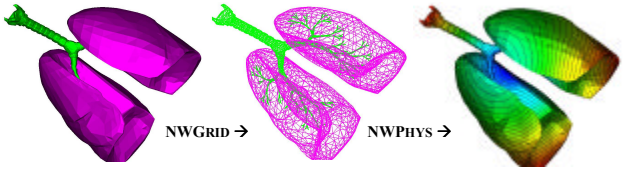

Figure 1. Lung modeling

Remapping the shell element mesh data for structural mechanics.

Deriving adaptive average Laplaeian surface grids for different molecular configurations (Figure 2).

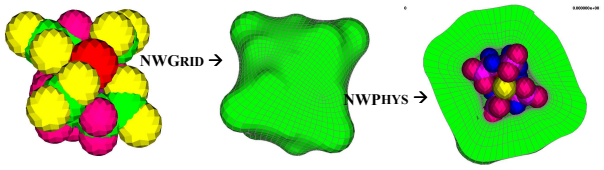

Figure 2. Shrink wrapping molecules

Modeling fluid flow within a virtual lung configuration. Partitioning the virtual lung for parallel processing (Figure 3).

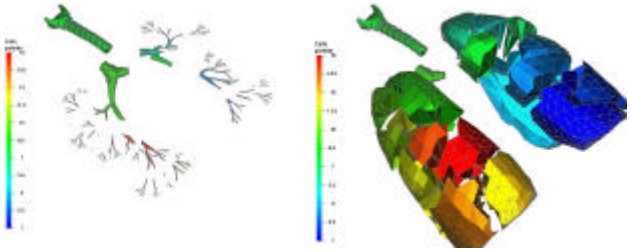

Figure 3. Parallel processing—virtual lung is partitioned and mapped to 16 processors

Time-dependent mesh adaptivity (Figure 4).

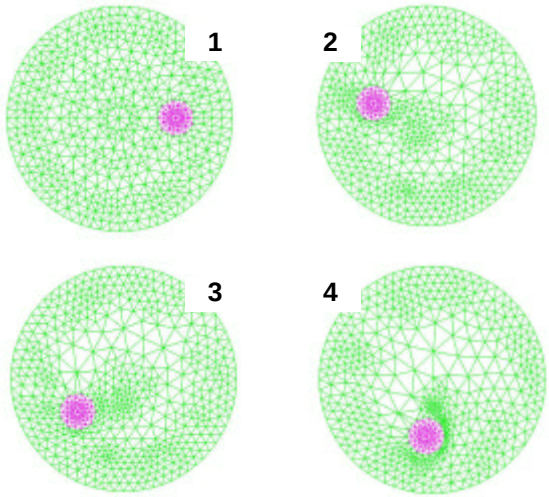

Figure 4. Time-dependent Delaunay mesh

As the problems get larger, the need to parallel the codes becomes more important. As more applications are using NWGrid/NWPhys, the need for the code to be easier to use becomes more important. Further applications will be explored in the next fiscal year.

Publications and Presentations

Jones-Oliveira JB, JS Oliveira, GK Schenter, and HE Trease. "Mathematical Modeling of Molecular Surfaces Using Unstructured Mesh Techniques." (to be submitted).

Jones-Oliveira JB, JS Oliveira, HE Trease, and LL Trease. September 2000. "Hybrid grid generation using NWGrid." Presented at the 7th International Conference on Numerical Grid Generation in Computational Field Simulations.

Jones-Oliveira JB, JS Oliveira, HE Trease, and P Eiseman (Program Development Corp.). September 2000. "Automated geometry blocking using an adaptive mesh refinement algorithm." Presented at the 7th International Conference on Numerical Grid Generation in Computational Field Simulations.

Oliveira JS, HE Trease, and JD Fowler (LANL). September 2000. "A symmetry invariant first-order remapping methodology." Presented at the 7th International Conference on Numerical Grid Generation in Computational Field Simulations.

Collaborative Problem-Solving Environments

Deborah K. Gracio, Karen L. Schuchardt, Brett T. Didier

Study Control Number: PN99008/1336

Advanced computational techniques are critical to improving our understanding of scientific processes in a multidisciplinary research environment. The development of collaborative problem-solving environments, which apply current research and state-of-the-art technology to create a powerful and convenient computing environment, is one key to transcending current methods of solving complex problems. General-purpose components that enable the construction of domain-specific collaborative problem-solving environments are being developed on this project.

Project Description

The purpose of this project is to develop general-purpose infrastructure components that are required to develop and deploy collaborative problem-solving environments. Our requirements were derived from work in the areas of climate change, chemistry, manufacturing engineering, and subsurface reactive transport. We developed prototypes of several components this year: resource information management and discovery, portal services, and distributed data and meta-data management. In addition, we developed a conceptual prototype of a climate change problem-solving environment with an emphasis on flexible workflow. This project produced technology that is now being applied to programmatic work and advanced our ability to develop domain-specific collaborative problem-solving environments.

Introduction

A collaborative problem-solving environment is a computational system that provides a complete and convenient environment for solving problems in a specific domain. The target problems are increasingly distributed in nature. Collaborators, often physically remote and working for different organizations with different infrastructures, require access to distributed resources such as supercomputers, instruments, and research data. A collaborative problem-solving environment must support this complex work environment in addition to supplying the domain-specific tools and capabilities. Constructing such a system is cost prohibitive unless components that address the basic infrastructure issues are readily available. The specific aim of this project is to apply state-of-the-art technologies to create new solutions for selected infrastructure components, thus enhancing our ability to develop and deploy collaborative problem-solving environments.

Another important characteristic of problem-solving environments is that they must be readily adaptable to new problems and new solution strategies. The users require the capability to define and redefine their process or workflow. We continued our research in this area by developing a conceptual prototype of a flexible workflow environment for atmospheric research.

Results and Accomplishments

Two years ago, a collaborative problem-solving environment was only an idea. Today, it has been embraced as one of the key capabilities of the Laboratory in Information Sciences. The research and technologies being developed by the collaborative problem-solving environments team are sought out by many of the research entities in the Laboratory to provide solutions to aid scientists, decision makers, and policy planners in their work.

Portal Services

We designed and developed a web-based component for submission and monitoring of computational jobs. The design was implemented as a portal service that can be accessed by applications written in Java, C++, or any browser supported language. We tested this service by successfully running computational jobs under a variety of computing environments including UNIX and Linux workstations, Linux clusters running the Portable Batch System, an IBM SP running Maui Scheduler and Load Leveler, and an Silicon Graphics, Inc. Origin 2000 running the Network Queuing System. The service has the following features:

- accepts XML job requests over a secure web-based connection (https)

- securely moves files to a target resource and submits job
- provides reporting on progress of job and allows jobs to be terminated
- monitors the running job, parsing text output files and returns data to the client
- makes use of existing infrastructure thus providing for low-cost deployment.

Distributed Data Management

We developed a set of written requirements for distributed data management through our interactions with scientists and engineers in chemistry, atmospheric sciences, manufacturing, materials, and electronic notebooks. Alternative technologies for addressing these requirements were investigated. We focused our efforts on prototyping solutions with the distributed authoring and versioning protocol, a proposed internet engineering task force standard. We installed an Apache web server with a plug-in module for providing back end data and meta-data storage and performed load and stress testing.

Our research included the development of a three-layer client application programmer interface. This layering technique provides clean separation of the protocol implementation, a data storage abstraction, and an object abstraction. We also developed the concept of the virtual document as a key abstraction for dealing with complex concepts such as calculations or workflows.

Resource Information Services

The primary function of a resource information service is to provide yellow- and white-page access to information about system- and user-defined resources. The incorporation of a resource information service into the computing infrastructure provides for the use of common data representations and a shared data source across projects and organizations.

We researched the use of meta-languages to support the definition and manipulation of objects in an resource information service. We settled on the use of the developing XML Schema standard as the meta-language and adopted and extended the Directory Services Markup Language, another developing standard, as a dialect. Using this dialect, we defined resource information objects based on previous investigations and our continuing work with the Gridforum Grid Information Services working group. We developed software to generate Netscape Directory Server schema and a Java binding for accessing and manipulating the objects from the XML-based object definitions. The use of a meta-language and automatic code generation provides an easy-to-use application programmer interface for collaborative problem-solving environments developers, an easy way to modify and extend the object definitions, and an abstraction that allows for the replacement of the underlying service without affecting the applications that rely on the service. Significant effort was invested to develop a layered application programmer interface that hides the implementation details of the underlying service and communications protocol.

Atmospheric Sciences Prototype

We worked closely with Laboratory atmospheric science researchers in many analysis and design sessions. The purpose of the collaboration was to gather user requirements for a collaborative problem-solving environment for regional climate change modeling and to develop a conceptual prototype. The resulting prototype provides an overall experimental process representation or workflow for doing atmospheric research and coupling impact assessment models for researchers and policy planners. The prototype is being used to drive an understanding of the requirements for developing a new software suite for atmospheric sciences.

Summary and Conclusions

The application of web-based technologies to problem-solving environments allows the scientific community to benefit from the robust growth of low-cost commercial and open-source technologies. We successfully applied these technologies in the development of multiple components. We found the performance of http to be viable for expected use patterns and the prospects for sufficient scalability to be within reach for many applications.

We concluded that discovering key abstractions is very important to component-based architectures for two reasons:

1. it insulates the client program from changes to the underlying technology
2. it enables the insertion of a middle layer that can provide service mappings or translations thus enabling interoperability.

Additional research is required in this area.

Publications and Presentations

Chin G, K Schuchardt, J Myers, and D Gracio. "Participatory workflow analysis: Unveiling scientific research processes with scientists." *Sixth Biennial Participatory Design Conference Proceedings*. (accepted).

"Resource information services on the grid." May 2000. Grid Forum 3, San Diego, California.

"Collaborative problem solving environments." December 1999. Briefing to DOE–Office of Science, Germantown.

"Collaborative problem solving environments for the Engineering Simulation Initiative." January 2000. Briefing to DOE – Office of Transportation Technology.
"Collaborative problem solving environments." January 2000. Computer Graphics and Applications Editorial Board.

"Collaborative problem solving environments." February 2000. Briefing to Rich Carlson & Thomas Ndousse-Fetter, DOE – MICS.

"Collaborative technologies and problem solving environments." March 2000. Briefing to Joint Virtual Analysis Center.

"Collaborative problem solving environments for SciDAC." May 2000. Congressional Demonstrations.

"Collaborative problem solving environments. June 2000. Maui High Performance Computing Center.

"Collaborative technologies." June 2000. Briefing to NASA Ames Numerical Analysis Center.

"Representation of people for information services." July 2000. Grid Forum 4, Seattle, Washington.

"Research: The rise of scientific virtual facilities." 1999. *In proceedings of the 1999 International Chemical Information Conference*, October 28-30, ISBN: 1-873699-63-8, Annecy, France.

Combustion Simulation and Modeling

Jeffrey A. Nichols, Robert J. Harrison

Study Control Number: PN98013/1259

High-performance calculations require efficient computer algorithms to achieve efficient modeling of the thermodynamics and kinetics of gasoline and diesel fuel combustion. Combustion simulation and modeling have important practical applications for predicting reaction rates and products.

Project Description

The purpose of this project is to develop high-performance computational chemistry software for massively parallel processor systems in the area of coupled cluster (CCSD(T)) methods for treating the electron correlation problem. Coupled cluster methods are needed to achieve the accuracies required to replace experimental measurements for many areas of chemistry, but especially for the combustion simulation and modeling community. Unfortunately, the coupled cluster method scales as N^7, where N is the number of atoms in the system. This greatly limits the range of applicability of this method to combustion and other problems. The project focuses on developing methodological and computational approaches to bring about a dramatic reduction in the computational cost of coupled cluster calculations. This entails algorithm redesign with the use of new methods in order to achieve the reduced scaling and increased massively parallel processor efficiencies needed to accurately model the thermodynamics and kinetics of large molecular systems such as those found in gasoline (C_8) and diesel fuel (C_{16}) combustion.

This work is accomplished within the framework of NWChem (Kendall et al. 2000), a computational chemistry suite that is part of the Molecular Sciences Computing Facility in the Environmental Molecular Sciences Laboratory. In addition, POLYRATE (a chemical dynamics package developed at the University of Minnesota, in collaboration with PNNL staff, and used to predict rate constants) (Steckler et al. 1995; Corchado et al. 1998) will be integrated with NWChem in order to provide improved means for the calculation of chemical reaction rate constants.

Results and Accomplishments

The integration of POLYRATE with NWChem to perform direct dynamics has been completed and will be widely distributed in NWChem version 4.0, which is due for release in fall 2000. It is already available for Laboratory internal use and is being used by the atmospheric oxidation study.

Alternative representations of the Møller-Plesset perturbation theory and coupled cluster wave functions have been explored with some limited success. Our goals were to develop a framework to improve the scaling of high-accuracy calculations in large atomic orbital basis sets by using a low-rank representation of both the wave function (coupled-cluster amplitudes) and integrals.

Our investigation into the Laplace-factorized algorithm for the 4^{th}-order linear triples contribution is continuing in collaboration with Professor J.H. van Lenthe, from U. Utrecht, who visited this summer.

Most of the effort this fiscal year has been devoted to the new production code for CCSD(T). Several prototypes were finished earlier this year, with the objectives of validating the equations and exploring various methods. Significant highlights of the new CCSD(T) code include the following:

- Hartree-Focks RHF/ROHF and UHF reference functions.
- Full use of Abelian point-group symmetry.
- Design goals set by considering calculations on molecules using cc-pVnZ (n=2-6) basis sets (also with augmentation) that could be executed in one week on a 1 TFLOP/s computer with 1 gigabyte of

week on a 1 TFLOP/s computer with 1 gigabyte of memory per processor. This leads to about 1,500 basis functions without symmetry and 3,000 with full symmetry. Larger calculations are possible.

- Direct algorithm based upon the sequential semi-direct algorithm of Koch et al. (1994, 1996). Only the amplitudes and iterative solution vectors are stored on disk. The AO/SO integrals are recomputed as necessary each CCSD iteration or for each pass of the triples code. If sufficient memory/disk space is available, the atomic orbital integrals can be cached.

- Many new capabilities were developed that can be reused by other applications within NWChem (integrals over symmetry adapted orbitals).

- The framework of the code is extensible to support eventual integration of the Laplace triples and local correlation methods.

- Detailed performance models support scaling of the most expensive triples component to 10,000 processors with an expected efficiency of 99%. Much effort has gone into achieving this since the code does a large volume of communication. Some of the techniques used are pre-sorting and blocking to improve memory-locality and to bundle communications, full dynamic load balancing, and randomization to avoid communication hot spots. The CCSD calculation will scale to a similar number of processors, but not with such high efficiency (perhaps 80% to 90%); however the CCSD portion typically costs a factor of 5 to 10 less.

- Efficient execution on both massively parallel computers and workstation clusters by avoiding excess network traffic and reducing sensitivity to latency.

- A new accelerated inexact Newton algorithm has been formulated for solving the CCSD equations.

References

Corchado JC, Y-Y Chuang, PL Fast, J Villà, EL Coitiño, W-P Hu, Y-P Liu, GC Lynch, KA Nguyen, CF Jackels, MZ Gu, I Rossi, S Clayton, VS Melissas, R Steckler, BC Garrett, AD Isaacson, and DG Truhlar. 1998. POLYRATE-version 7.9.1. University of Minnesota, Minneapolis.

Kendall RA, E Aprà, DE Bernholdt, EJ Bylaska, M Dupuis, GI Fann, RJ Harrison, J Ju, JA Nichols, J Nieplocha, TP Straatsma, TL Windus, and AT Wong. 2000. "High performance computational chemistry; an overview of NWChem a distributed parallel application." *Computer Physics Communications* 128, 260.

Koch H, O Christiansen, R Kobayashi, P Jorgensen, and T Helgaker. 1994. "A direct atomic orbital driven implementation of the coupled cluster singles and doubles (CCSD) model." *CPL* 228 233.

Koch H, A Sanchez de Meras, T Helgaker, and O Christiansen. 1996. "The integral-direct coupled cluster singles and doubles model." *JCP* 104 4157.

Steckler R, W-P Hu, Y-P Liu, GC Lynch, BC Garrett, AK Isaacson, D-h Lu, VS Melissas, TN Truong, SN Rai, GC Hancock, JG Lauderdale, T Joseph, and DG Truhlar. 1995. POLYRATE-version 6.5. *Computer Physics Communications* 88, 341-343.

Presentations

Nichols JA, DK Gracio, and J Nieplocha. 1999. "The challenge of developing, supporting and maintaining scientific simulation software for massively parallel computers." Germantown.

Seminar, "The Challenge of Developing, Supporting and Maintaining Scientific Simulation Software for Massively Parallel Computers." San Diego Supercomputer Center, San Diego, California, January 2000.

Plenary lecture, "NWChem: A MPP Computational Chemistry Software Developed for Specific Application Targets." Spring 2000 Meeting of the Western States Section of the Combustion Institute, Colorado School of Mines, Golden, Colorado, March 2000.

FLC Awards Presentation, Charleston, South Carolina, May 2000.

Invited lecture, "New Molecular Orbital Methods within NWChem," at the conference "Molecular Orbital Theory for the New Millennium - Exploring New Dimensions and Directions of the Molecular Orbital Theory." Institute of Molecular Science, Okazaki, Japan, January 2000.

"High Performance Computing in the Environmental Molecular Science Laboratory." Real World Computing Institute, Tsukuba, Japan, January 2000.

Plenary invited lecture, “The Electronic Structure of Molecules – Theory, Algorithm and Application” first SIAM conference on computational science and engineering (CSE00), Washington, D.C., September 2000.

Acknowledgments

Dr. Benny Johnson worked on the NT port of NWChem. Dr. David Bernholdt worked on the reduced rank representations for the CCSD(T). Prof. Joop van Lenthe worked on the Laplace factorization.

Conservation Laws in Support of Reactive Transport

Janet B. Jones-Oliveira, Joseph S. Oliveira, Harold E. Trease

Study Control Number: PN98017/1263

This project focused on the development of an applied mathematics capability to provide new and more accurate scalable, parallel, computational methods, and grid technologies for solving the reaction-diffusion type equations that are required for higher resolution of the concentration fronts in reactive transport modeling. Tracking and resolving moving fronts and their multiscale characteristics are important for such multi-material problems as predicting the migration pattern of contaminated groundwater (as it interacts with solid and/or porous material walls in the flow path), particle transport in a human lung, transport of molecules through the cell wall, and modeling the propagation of transient local climate effects that are closely coupled to topographic surface boundary effects imposed by complex terrain within a regional and/or global climate context.

Project Description

This project provided computational and mathematical physics support for the development of new analytical methods, hybrid grid technologies, algorithms, and numerical techniques for the solution of partial differential equations (PDEs) that are relevant to all scales of physical transport, fluid-solid interactions, moving shock fronts, and molecular chemistry interactions. This work will affect a variety of modeling areas including the Hanford vadose zone, design of new combustion systems, bioengineering, and atmospheric chemistry and global change.

Approach

The focus of this project was to improve the level of applied mathematics and computational mathematical physics in the areas of temporal and spatial multiscale analysis, fluid-solid interaction, conservation-law mathematics, and invariant numerical discretization methods using multidimensional, hybrid grid generation/refinement. Improved capability is required to form the basis of more accurate simulations, as well as more scalable high-performance computer codes, particularly in the area of reactive transport.

The transport of material from one location to another is a central tenent of most environmental issues. These flows can be of an unreacting material or, as is more common, the flow can contain reacting species that change their chemical identity, thus potentially changing the characteristics of the flow. In reactive transport, there is the added difficulty of multiphase flow, with chemical pumping. A key issue in the reactive transport area that requires high resolution is the fluid-solid interaction across media and modeling scales. However, underlying all of these physical modeling issues is the absolute need to model the geometry correctly. If the geometric modeling of the physical space where the physics and chemistry occurs is not accurate, the propagation of the species will be wrong. Hence our emphasis on precise gridding technology.

We determined that either a Free-Lagrange (FL) or an Arbitrary L`agrangian-Eulerian (ALE) formulation on hybrid structured/unstructured/stochastic grids with adaptive mesh refinement is required to resolve problems observed in numerical implementations, which have been attributed to the geometry/mesh resolution and interaction of the front with that of the nonlinear model components. An additional complexity that front-tracking methods must resolve correctly is to capture the oscillatory behavior of some of the variables behind the advecting front. Therefore, we worked to develop the capability to model problems using full-physics/full-chemistry FL/ALE technology with adaptive mesh refinement on hybrid grids. Development of this technology and approach is directly applicable to problems in combustion, atmospheric, subsurface, and particulate-in-lung modeling.

Results and Accomplishments

A clearer understanding of the transition from the micro-scale (chemistry), to the meso-scale (pore-scale), and to the macro-scale (field response) is necessary to ultimately obtain an accurate long time-scale, large spatial-scale model. In order to tackle this cross-scale problem, we initially approached it via pursuit of numerical/analytical

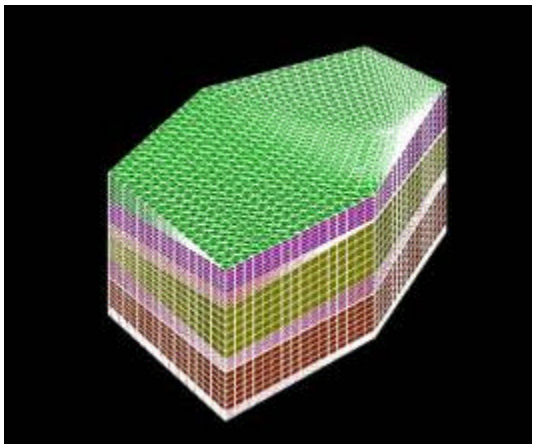

Figure 1. X3DGEN tetrahedral mesh of SST S-SX stratigraphic data (provided by Bruce Williams) for Handford Site wells W22-39, W22-44, W22-45, W22-46, W23-13, W23-14, and W23-15. Note the numerous geologically induced geometric pinch points in the three-dimensional volume.

methods for solving the fundamental physical conservation laws. Such a hybrid approach was highly successful in linearized, but fully coupled, fluid-solid interaction modeling using special functions and power series expansion arguments. In FY 1998, we experimented with numerical homogenization of nonlinear ordinary differential equations (ODEs). The idea was to use wavelet homogenization methods for a given system of nonlinear ODEs so that, for a given tolerance, the algorithm would derive a numerical solution that captures a coarse-scale solution with just enough resolution such that the averaged contribution from the fine-scale would be within acceptable tolerance. This work was continued in FY 1999; however, the wavelet method did not turn out to be as promising as we had hoped.

We decided to apply the unstructured mesh technology to model the pore-scale physics, with the aim of capturing the geometry as precisely as possible, thereby hoping to capture the subgrid scale physics more exactly, in order to gain insight into what information can and must cross scales. We initiated work with Dr. George Zyvoloski at Los Alamos National Laboratory, and Dr. Tom Russell at University of Colorado in this regard. Further, we began working with Dr. Harold Trease, then at LANL to incorporate into the computer code X3D[(a)] the fluid-solid interaction capability, i.e., to build in a mechanism to define the compatability conditions across the fluid-solid interface and optimize the dynamics modeling in two acoustic impedance mismatched materials.

In FY 1999, our modeling efforts were directed primarily in two areas: 1) bringing to PNNL new computational capabilities, to address similar physical problems using alternative methods that may be more suitable for compressible flow and reactive transport, including subgrid modeling, Free-Lagrangian and ALE methods with adaptive mesh refinement; and 2) determining example problems to test the strengths and weakness of the structured versus the unstructured mesh approaches.

We obtained serial versions of Lawrence Livermore National Laboratory's DYNA3D[(b)], NIKE3D[(c)], and ALE3D[(d)] with the understanding that parallel versions of some subroutines could be made available on an

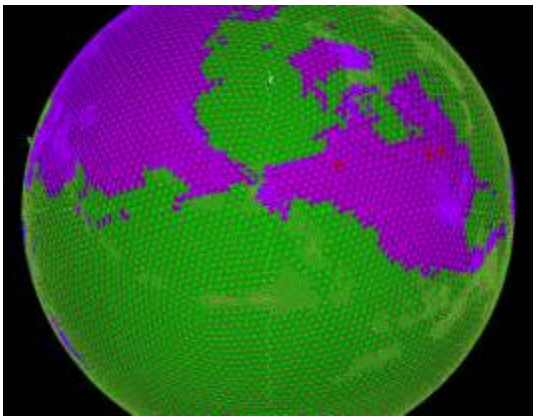

Figure 2. X3D unstructured global grid with adaptive mesh refinement, which is driven by steep gradients in the vorticity, $\mathbf{S}$. When the ratio of the vorticity to its gradient is > 1, the mesh is refined. When this ratio is < 1, the mesh density is coarsened.

(a) X3D is a full-physics, first principles, time-domain code that was designed at LANL for parallel processing on unstructured grids. Its principal author is Dr. Harold E. Trease, who developed the code based upon his dissertation in Free-Lagrange methods.

(b) DYNA3D is a nonlinear, explicit, 3-D finite element code for solid and structural mechanics, which was originated by Dr. John O. Hallquist while at LLNL.

(c) NIKE3D is a nonlinear, implicit, 3-D finite element code for solid and structural mechanics, which also was originated by Dr. John O. Hallquist while at LLNL.

(d) ALE3D is an arbitrary Lagrange/Eulerian, 3-D hydrodynamics code with material strength, which was developed to model the behavior of objects undergoing gross deformation due to the application of shocks in the kilobar regime. ALE3D employs arbitrarily connected hexahedral calculational elements and has slide surfaces. The ALE algorithm is implemented by carrying out a complete Lagrangian calculation followed by an advection step.

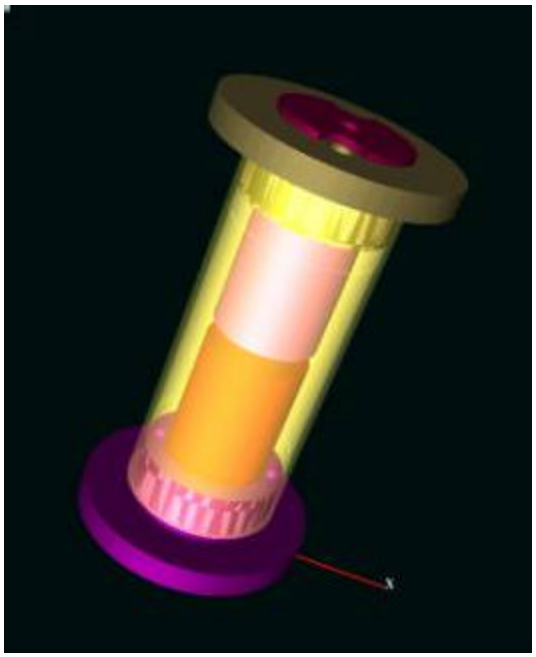

Figure 3a. Transparent Oso rendering of a particle trap flow field experiment with thermal coupling being developed in the EMSL. Two thick hollow cylinders are aligned end-to-end along the long axis of an enclosing cylinder. A laminar flow field is induced within the enclosing cylinder such that there will be a constant inflow (or outflow) into the gap space between the two opposing cylinders. The purpose of the computational experiment is to determine how to control the flow field within the gap as a function of gas material, geometric gap separation distance, and the flow parameters.

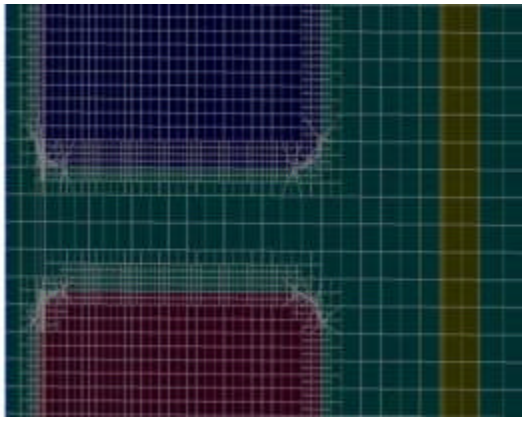

Figure 3b. Slice of a NWGrid quarter mesh through the flow cell in Figure 3a. The left-most edge is the vertical centerline, and the right-most edge is in the air field external to the apparatus. The horizontal centerline passes through the middle of the gap space between the two opposing annuli. Note the variation of the mesh resolution as a function of geometric complexity. Faithful modeling of the curved surfaces leading into and out of the central core gap region is extremely important to the accuracy of the hydrodynamic flow model.

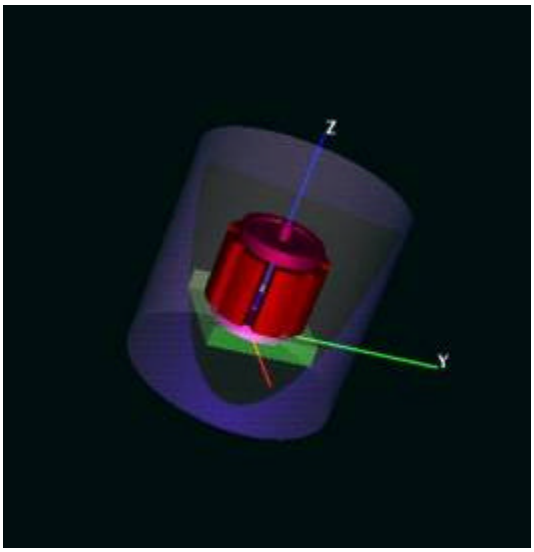

Figure 4a. Oso rendering of a stable, 3D ion trap, which is designed to investigate the behavior and properties of ions in coupled electric and magnetic fields. The apparatus has been designed such that there are two ceramic insulation supports, into which fit two symmetrically opposing gold-plated end disks. There is a pinhole in each end cap, through which an ion stream will run for alignment purposes. The eight gold-plated aluminum ring electrodes sit on the ceramic insulation supports such that each electrode is isolated, including from the top and bottom end caps.

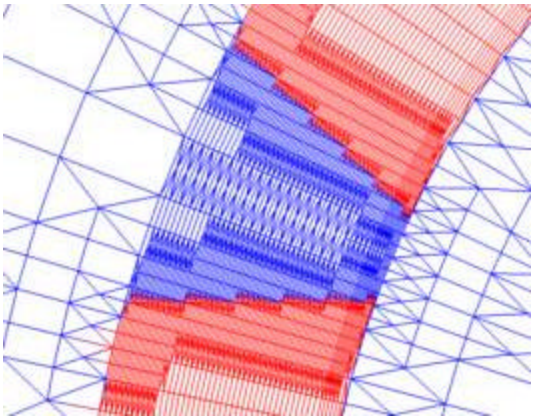

Figure 4b. Slice of a NWGrid mesh through the gap between the gold-plated aluminum ring electrodes of the ion trap experiment in Figure 4a. Refinement of the mesh through the gap has been designed to allow the physics package to resolve the boundary conditions of the field with the geometric constraints of the electrodes.

as-needed basis. We also obtained LANL's fully parallelized X3D (for the generation of unstructured grids), OSO (their volume rendering code to which may be input CAD output), FEHM (their subsurface modeling code), and CHAD (their combustion code). We developed test problems. We also purchased

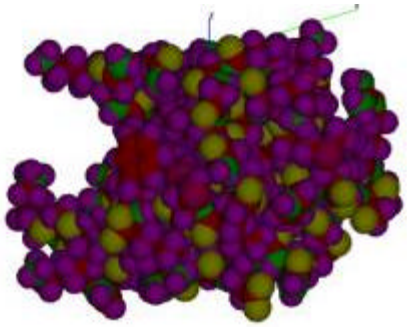

Figure 5a. OSO volume rendering of a 1240 atom portion of the protein with empirical formula C382H632N115O106S5. This macromolecule will be used for charge density distribution modeling by Tjerk Straatsma. This work requires extremely fast Poisson solves on minimal surfaces.

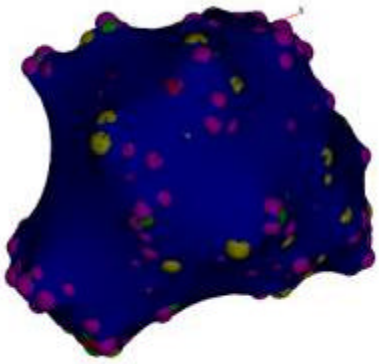

Figure 5b. The adaptive average Laplacian surface enclosing the 1240 atom macromolecule built using NWGrid and NWPhys. This is a minimal surface with the property that the local average curvature of any point on the surface grid is nearly flat relative to its nearest neighbor points. The surface has the minimal surface area to enclosed volume ratio.

The TRUEGRID package (XYZ Scientific Applications, Inc., Livermore, California) for generating structured grids. Each of these codes contains full-physics capability and is quite complex, so that we continue to invest extensive efforts toward learning to run these codes.

We have models in development of SST S-SX embedded with single-shell tanks, a 1240 atom biomolecule, two ion trap experiments designed by Dr. Steven Barlow (EMSL), and a local atmospheric flow through a mountain ravine in New Mexico. We also have demonstrated that these grid technologies may be used in molecular modeling studies, for example, protein folding, and in systematic extension of hydrodynamics to the molecular scale.

The computational applied mathematics that underlies the areas of reactive transport and computational chemistry includes PDEs, stochastic analysis, and numerical methods. These applications require the fast and accurate solution of quasi-linear and nonlinear PDEs derived from equilibrium and nonequilibrium phenomena that are formulated as coupled dynamical systems composed of reaction-diffusion equations. In terms of mathematical techniques, the difficulties lie in the development of methods to manipulate discontinuous functions and derivatives, as well as multidimensional singularities and couplings. Many of the mathematical challenges in solving these problems have a common origin in the inherent geometry of the physics, and include highly oscillatory coefficients, steep gradients, or extreme curvatures at the moving and mixing shock fronts at interfaces that are singular analytically.

To simulate the physical process more accurately, new mathematical formulations of the physical problem, its inherent geometry, its boundary conditions and solution techniques, such as that developed previously by us, were developed in conjunction with applications, grids, and algorithmic and computational implementations. We continued this work in FY 2000, with increasing emphasis on geometrically faithful gridding, and plan to initiate an investigation of stochastic grids. In FY 2000, we hired Dr. Harold E. Trease and established NWGrid and NWPhys as the flagship codes for the Applied Mathematics Group within Theory, Modeling and Simulation at EMSL.

Summary and Conclusions

It is our intention to identify and analyze the inherent assumptions in each model and analyze the ramifications of those assumptions on the appropriateness of the presently used solution techniques, as well as the constraints that they impose on the integration process of the information generated/shared by the multiscale physical chemistry models. It is our belief that when the invariant geometry of a problem is captured and maintained throughout an analysis, the greatest fidelity of the results will be achieved and the physical mechanisms of information transport across temporal and spatial scales will be revealed. Our focus is on capturing the relevant physics/chemistry—selection of the particular numerical solution scheme is to be based in the inherent geometric constraints of the problem to ensure preservation of invariants. Subsequently, we will begin to unify the models via a mid-scale model that will capture the fundamental physics and chemistry of the problem of interest.

The resulting software that will be developed will run on modern, high-performance, massively parallel computer systems such as those available in the Molecular Science Computing Facility in EMSL.

Publications and Presentations

Jones-Oliveira JB, JS Oliveira, GK Schenter, and HE Trease. "Mathematical modeling of molecular surfaces using unstructured mesh techniques." (to be submitted).

Jones-Oliveira JB, JS Oliveira, HE Trease, and LL Trease. September 2000. "Hybrid grid generation using NWGRID." 7th International Conference on Numerical Grid Generation in Computational Field Simulations.

Jones-Oliveira JB, JS Oliveira, HE Trease, and P Eiseman. September 2000. "Automated geometry blocking using an adaptive mesh refinement algorithm." 7th International Conference on Numerical Grid Generation in Computational Field Simulations.

Oliveira JS, HE Trease, JD Fowler. September 2000. "A symmetry invariant first-order remapping methodology." 7th International Conference on Numerical Grid Generation in Computational Field Simulations.

Development of Models of Cell-Signaling Pathways and Networks

Joseph S. Oliveira, John H. Miller, William R. Cannon, David A. Dixon

Study Control Number: PN99020/1348

This work focuses on development of the fundamental mathematics and model-building capabilities for a problem-solving environment called the Virtual Cell. This research environment will culminate in the ability to model multiscale, complex, whole-cellular processes with predictive capability for environmental signal recognition and response. The cell-signaling model of the virtual cell provides us with a computational test bed that will enable an experimentalist to test cellular processes computationally. This methodology will greatly enhance our capability to effectively understand and control fundamental biological processes from a bioengineering systems point of view.

Project Description

Coupling theory and experiment to understand complex cell-signaling networks requires a sophisticated applied-mathematical/computational-modeling capability to integrate back into the context of a functioning cell. In addition, acquired knowledge is needed on signaling kinetics, pathway cross-talk, protein structure/function and interactions, and metabolism coupled to other peripheral controlling and self-modifying phenomena. The goal of this work is to develop the fundamental mathematics and model-building capabilities for a problem-solving environment called the Virtual Cell. Three critical cell-signaling research issues have been identified and validated by a variety of means. These include 1) the need to analyze and understand the subcellular components involved in cell signaling, 2) the need to study cell signaling in vivo, and 3) the need to synthesize the experimental knowledge and acquired understanding into an integrated cellular context by the development of models and computation. These three research issues will also be used to further the development of a suite of computational biophysics problem-solving tools that links the multiscale biophysics of cytoplasmic diffusive reactive molecular hydro-transport to the emergence of both perturbative and nonperturbative cell-signaling pathways. The future goal is the construction of a computational biophysical systems engineering test bed that will enable us to explore the dynamic structure and function of cell complexes that specialize into tissue assemblies and finally organ transport systems.

Approach

Databases

A goal of this work is to continue to collect the available experimental and model data on cell signaling, in order to develop models. These data will be used to develop models for some critical cell-signaling pathways, based on an operations systems approach.

Petri Nets

The complex operational processes associated with cell signaling—communications—lend themselves to being faithfully modeled by Petri nets. A Petri net is a directed, simply connected graph, composed of nodes (vertices) and edges. Every Petri net has two types of nodes: state nodes (S) and transition nodes (T). State nodes hold information called tokens. Transition nodes define a set of conditions that regulate the flow of information from one state node to another; e.g., information from state S1 is transferred to state S2 when a set of transition conditions T1 are satisfied.

Petri nets represent a rich mathematical framework for modeling dynamically complex operational process control systems. Every network ensemble provides us with a number of discrete data abstractions for representing an object and its attributes, together with a set of constraints that determines the regulation of complex operational processes. An incidence (connectivity) matrix defines a framework for

determining the combinatorial state and transition network invariants that characterize both the flow and conditional regulation of information flow in the signaling reaction network.

In addition, we will investigate the algebraic symmetries of these nets in terms of a path algebra representation. These algebraic representations will be used to identify the existence of operational signal processing symmetry group invariants in terms of process semiorder relations. These symmetry invariants are shown to correspond to the state and transition invariants and will be used to obtain sets of optimal paths that indicate observably reachable states with optimal molecular signaling bandwith. We will also explore the use of incidence matrix representations of circuits, and both path and relational algebraic representations of network path configurations to computationally establish the existence of hypergraph isomorphisms between different signaling paths. Additionally, we will explore the use of reverse Bayesian inference (abductive inference) methods to identify and define the characteristics of hidden states. We conjecture that the multi-dimensionality of molecular communications in a pathway can be modeled by using a dimension-matched hierarchy of scale-invariant Petri nets.

Petri nets are stochastically extensible as an application for modeling the microscopic reactive diffusive transport kinetics of signal pathways within and between cells. We will use the discrete (hidden) Markov nature of timed stochastic Petri networks to discretely represent the continuous Markov state transition models of diffusive molecular transport systems. In turn, the associated sets of state transition probability measures will be used to define the molecular analogs of classical information theory (as developed by Shannon and Weaver) that underly the emerging theory of molecular communications.

Coupled Rate Equations

Cell signaling is a complex phenomena, yet it is such a fundamentally important part of cellular behavior that the basic principles of cell signaling are the same in essentially all organisms. The response of a cell to its environment is governed by cell-signaling mechanisms. Figure 1 illustrates a network of signaling pathways that activate the mitogen-activated-protein kinase (MAPK) in response to ligand binding to the epidermal-growth-factor receptor (EGFR). Co-activation of phospholipase C-γ1 (PLCγ) modifies MAPK signal characteristics by interaction between modules K and H mediated by protein kinase C (PKC). A feedback loop connects H and K through module E (cf. Figure 1). Figure 2 shows a Petri net representation of component A of the MAPK-activating network.

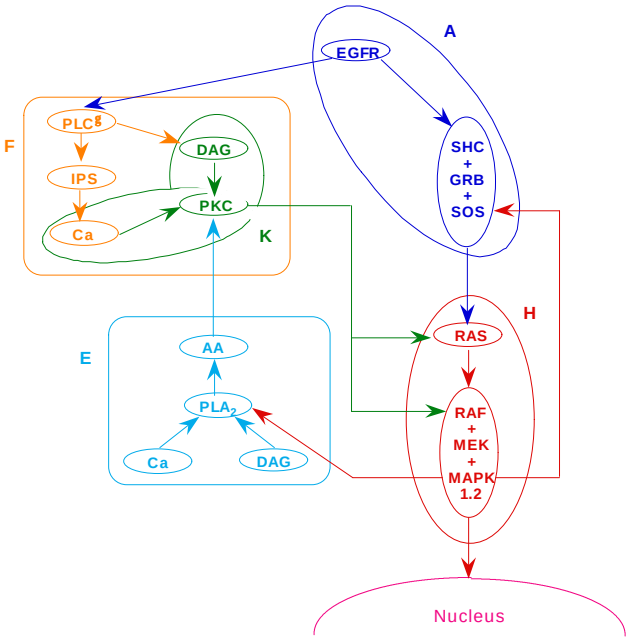

Figure 1. A network of signaling pathways associated with MAPK activation

Even though kinetic data are sparse, Iyengar and coworkers at the Mount Sinai School of Medicine maintain a database of kinetic parameters for modules found in well-studied pathways. Signaling networks, like that shown in Figure 1, assembled from these modules have emergent properties, like bistatic activation profiles, that may be biologically significant. We will use Petri net representations to evaluate the bistability of the network shown in Figure 1.

Nonhomogeneous Kinetic Models

Localization of reactants is an important mechanism by which cells regulate signaling processes. In collaboration with Professor Leslie Loew at the University of Connecticut Health Center (UCHC), we are including spatial inhomogeneity in kinetic models of signaling pathways. We will expand the capabilities of the problem-solving environment being developed in Dr. Loew's laboratory through links to NWGrid and NWPhys, the Laboratory's grid generation and physics solver codes, respectively. More efficient computational methods and extended functionality are required for the applications of virtual cell technology that we envision. For example, changes in cell morphology are often a part of signaling dynamics. We are also applying spatial inhomogeneous kinetic models in our collaboration with

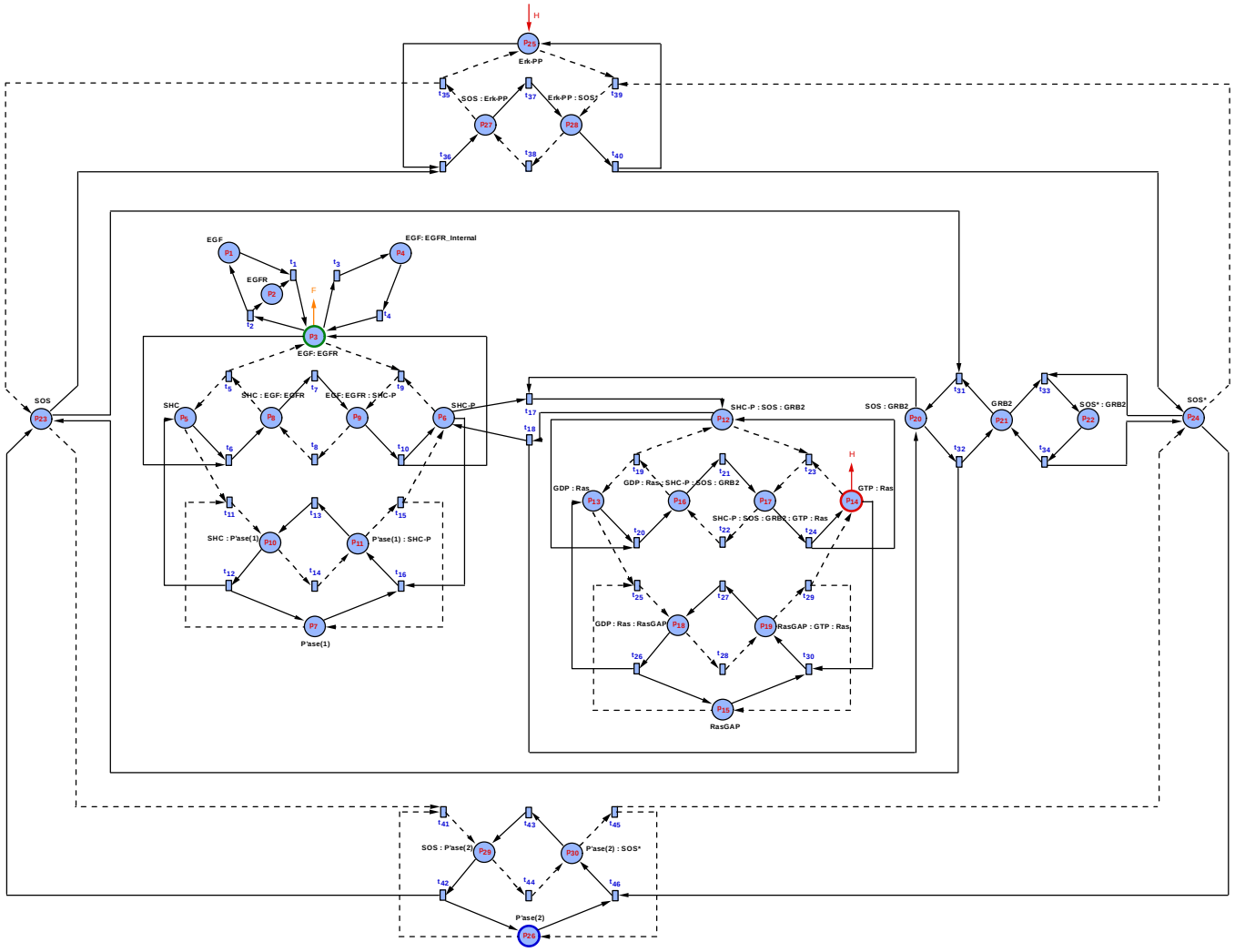

Figure 2. This is a Petri net of the EGFR pathway, SOS. Linkage to other components in the network shown in Figure 1 are indicated by arrows labeled F and H.

Professor Rodland at Oregon Health Science University to investigate the signaling pathways that connect the extra-cellular calcium-sensing receptor (CaR) to cell proliferation. Like skin fibroblast, normal cells of the ovarian surface layer respond to elevated calcium by proliferation and return to a quiescent state when the extra-cellular calcium concentration is reduced. Nonhomogenous chemical kinetics is required to model this system because signaling involves the release of calcium from the endoplasmic reticulum that is not homogeneously distributed in the cell.

Results and Accomplishments

We have initiated the development of a Petri network model of cell signaling. The Petri net model transforms the molecular signal into a linear algebra representation of a systems process model. The linear algebra representation defines the stoichiometric system of energy-mass balanced chemical equations. The Petri network model provides us with a representation of the molecular signal that enables us to mathematically predict the behavior of a molecular communications pathway when it is no longer in an equilibrium state. This model will direct us to the eventual construction of the molecular information analog of Shannon's laws of information and communication theory. We will also have an opportunity to examine the orders of both physical and computational complexity associated with reliable molecular communications within and between cells. Accomplishments include the following.

1. We have shown that cell-signaling pathways are represented by sets of chemical kinetic rate-reaction graphs, where the reacting species themselves are generated from the products of multiple subreaction cascades of subspecies. In particular, we examined several subnetworks of the EGFR signaling network

and showed that a Petri net faithfully represents each subnetwork. Any family of chemical kinetic rate-reaction graphs that is defined by the same order structure as the EGFR signaling network is also faithfully represented by a Petri net. We observe that this family of networks is both simply connected and directed, there are no self-loops, and as such, defines a set of directed graphs (digraphs), where each digraph is a multi-graph. Every such multi-graph (hyper-graph) is characterized by a path algebra representation. This algebraic representation defines an oriented matroid (an n-dimensional hyper-cube combinatorial geometry). We next proved that effective combinatorial optimizations of the oriented matroid geometry of any chemical kinetic rate-reaction graph is optimally searched by the "greedy algorithm" in O (n) time and space complexity for circuit sub-paths that satisfy an objective function (i.e., are defined by the state and transition invariants).

2. We have proven a graph isomorphism representation theorem that asserts that the directed graph network representation of the now linearized kinetic reaction model of an inter-cellular signal transduction pathway is faithfully represented by a discrete digraph that will be referred to as a Petri net. The proof of the graph isomorphism representation theorem follows from equating the linear matrix representation of graph network representation of the now linearized kinetic reaction model to the linear incidence matrix representation of a Petri net. We can also define a decision procedure that determines if two or more networks of reaction paths are isomorphic.

3. The combinatorial representation theory further allows us to define a linearized kinetic reaction model of an inter-cellular signal transduction pathway as a "birth and death" stochastic process, which in turn defines a continuous Markov process. This continuous Markov process can be discretized. We next obtain discrete Markov systems representation. This representation defines a stochastic Petri net. With this Petri net representation, we can now develop an application of hidden Markov models to find missing reaction parameter data.

4. The stochastic formulation of chemical kinetics is being employed for two reasons. First, stochastic simulations provide statistical data regarding product distributions that are not obtained from the usual deterministic kinetic formulation. Second, use of the stochastic kinetic simulation allows for an easy extension of the simulation to include diffusion through a Brownian dynamics simulator, and hence to also include structural information of the cell and its components. In principle, the simulation could extend downward to include organelle structure, protein structure, protein charges, etc. The extension downward to include more detail is only limited by the availability of data and computational resources. Petri nets are being developed that provide the same information as stochastic simulations.

Summary and Conclusions

During the last 2 years, we described some of the mathematical and systems engineering foundations that are key to understanding the complex nature of emerging cell-signaling communications networks. We also outlined some of the requirements for building a set of computational tools for the construction of a complete adaptive computational model of a living cell. The following is a list of objectives set for the current year:

- paper defining equation-based graph isomorphisms, based upon a process control network model of cell-signaling pathways
- develop computational simulation code for both generating Petri nets and their optimized process control model
- model transport of activated kinase from cytoplasm to nucleus by diffusion kinetics and prove that there is a correspondence between the Markov state model representation of a timed stochasatic cell-signaling Petri net model and the underlying Markov transport in the cytoplasmic hydrodynamic medium
- extend UCHC virtual cell PSE by application of NWGrid and NWPhys
- test model for signaling from the CaR by experimental data from OHSU.

Publications and Presentations

Oliveira JS and CG Bailey. "Computational complexity of emerging cell signaling networks." (in progress).

Oliveira JS and CG Bailey. "Combinatorial symmetries of emerging cell signaling networks." (in progress).

Oliveira JS, JB Jones-Oliveira, and CG Bailey. "A combinatorial representation theory of inter-cellular signal transduction pathways." (in internal peer review).

Oliveira JS, JB Jones-Oliveira, and CG Bailey. "Matroidal optimizations of emerging cell signaling networks." (in progress).

Dixon DA. May 2000. Co-organized the *Computational Challenges In The Post-Genomic Age Symposium*, San Francisco.

Dixon DA. May 2000. "An overview of the virtual cell." Presented at the *Computational Challenges In The Post-Genomic Age Symposium,* San Francisco (invited).

Oliveira JS. August 2000. "Computational Grand Challenges Associated with Combinatorial Models of Intra-Cellular Signaling Transduction Networks." Presented at the *Mathematical Challenges of the 21st Century,* American Mathematical Society, UCLA.

Oliveira JS. August 2000. Chaired the Session on Mathematical Applications to the Natural Sciences (Mathematical Biology) at the *Mathematical Challenges of the 21st Century,* American Mathematical Society, UCLA.

Distributed, Real-Time Decision Support Environments

Ryan Hohimer, Dennis McQuerry

Study Control Number: PN00036/1443

Teams of dispersed people need collaborative tools to support decision making. Technologies developed under this project maximize natural interactions with data and collaborators and create a prototype geospatial data visualization and selection application.

Project Description

The purpose of this research effort was to meet the need for an environment that supports decision making by geographically dispersed people. This type of environment is needed to support the intelligence community, emergency response command and control, or resource and land management teams.

This research concentrated on enabling users to manipulate virtual objects (abstract and geospatial data sets) as if they were tangible objects.

Introduction

Two technologies were brought together to create a new, natural way to interact with data (virtual models). These two technologies are "HI-space" and "ARToolkit." The ARToolkit is an augmented reality toolkit used to render graphics of virtual models onto views of the actual world in real time. Both the HI-space video camera and cameras attached to head-mounted displays were used to detect markers in their field of view. The location and orientation of the markers are tracked from the head-mounted displays camera video stream, and the virtual model associated with the marker is overlaid on the video stream with the same location and orientation.

The end result of this technique is that a virtual object behaves like a tangible object. By moving the tangible marker, the virtual object is moved accordingly. The visual cues make it seem as if you are handling the virtual object, not the real marker.

Results and Accomplishments

This effort resulted in a prototype application that uses the HI-space technologies and augmented reality technology. The application allows users to view geospatial data in in multiple forms. The first form of view is as a physical map located on the HI-space tabletop (Figure 1). The second form of view is by association of a marker with a location on the physical map (Figure 2). In other words, by placing a marker on the physical map and associating the marker with the data set that has the geometry of that location, an augmented view of the region is made.

Summary and Conclusions

The ability to select virtual objects to visualize by physically interacting with tangible objects in a tangible environment is a powerful ability. It is a very natural way to work with data. This ability to treat abstract data as tangible objects helps reduce the complexity of the abstraction.

That we can reorient our perspective of the data by physically reorienting our eyes to the physical marker removes an abstraction layer barrier.

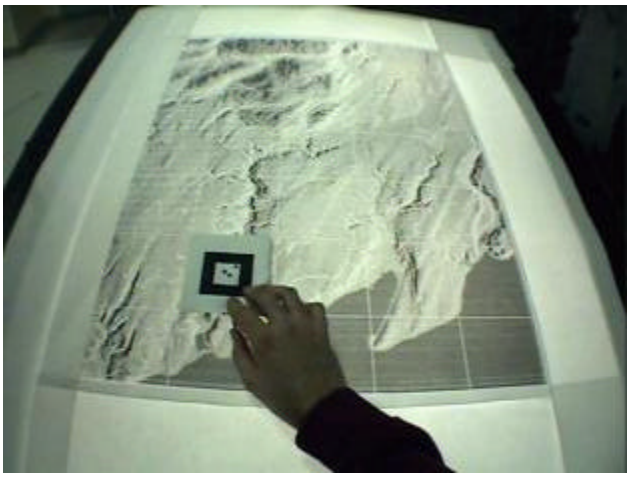

Figure 1. Selecting a geographical region on a physical map on the HI-space tabletop

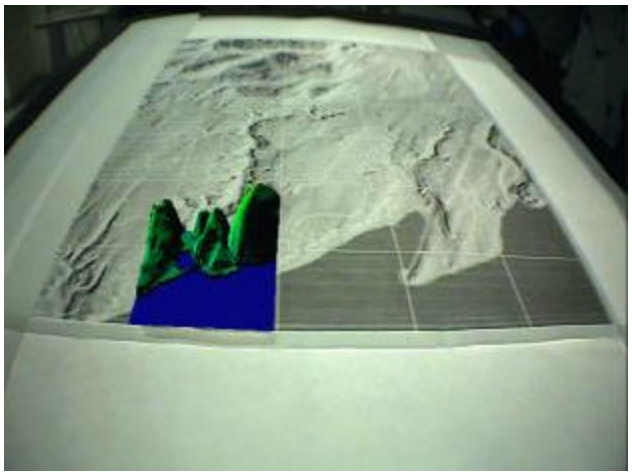

Figure 2. Associating a dataset marker with a physical region provides an augmented view of that region

Framework for Integrating Multiple Platform Computational Models

Randal Taira, Mitch Pelton

Study Control Number: PN00046/1453

The Department of Energy has invested significant funds to develop computer models for predicting contaminant transport associated with waste sites across the DOE complex. These computer models are typically media specific (vadose zone, saturated zone, etc.), dimension-specific (one-, two-, or three-dimensional), and platform-specific (PC or UNIX), which makes integrating them as part of a multimedia assessment very difficult. The software system developed through this project provides a platform for the integration of these computer models.

Project Description

The objective of this project was to develop an integrated, user-friendly software system that can use multiple environmental computer models regardless of media, dimensionality, platform, or operating system. We developed this system based on the multimedia software system known as FRAMES (Framework for Risk Analysis in Multimedia Environmental Systems). We linked the UNIX-based models CFEST (a finite-element groundwater model) and STOMP (a finite-difference vadose and saturated zone model) with the PC-based FRAMES source term model. We demonstrated the functionality of the linked software using hypothetical contaminantion transport events. By linking these models, the project advances our ability to perform detailed multimedia assessments with efficiency and reproducibility.

Introduction

Assessing the fate and transport of contaminants in the environment has been and will continue to be a major concern for DOE. These assessments typically include some type of computer modeling to try to recreate the conditions of past releases or to predict the results of current or future contaminant releases. The recent trend in environmental assessments has been toward a holistic approach to modeling. This approach requires models of different type (source, fate and transport, exposure, health impact, and sensitivity/uncertainty), resolution (analytical, semi-analytical, and numerical), and operating platforms to be combined as part of the overall assessment of contaminant fate and transport in the environment.

Our Laboratory developed FRAMES in 1997. The objective of FRAMES was to provide a user-friendly platform for integrating medium specific computer models associated with environmental assessments. FRAMES is a fully functional software system and has been used on assessments across the country. FRAMES has several limitations, however; two of which were addressed by this project. The first limitation was that the FRAMES data file specifications addressed only one-dimensional model input and output. The second limitation was that FRAMES was limited to PC-based computer codes. Therefore, codes designed for UNIX or other operating systems were inaccessible to FRAMES. The development of the two-dimensional and three-dimensional data file specifications and the multiple platform capabilities greatly expand the usability and applicability of FRAMES as well as the models that are incorporated into it. The ability to seamlessly connect models together expedites the modeling process and facilitates sensitivity and uncertainty analyses.

Approach

This project consisted of five distinct tasks:

1. expand the file specifications for FRAMES to incorporate two- and three-dimensional numerical models
2. develop the network data exchange between models on a PC and models on a UNIX machine
3. integrate CFEST into the system via preprocessors and post-processors in order to get the model to match the FRAMES specifications
4. integrate STOMP into the system using the same process used for the integration of CFEST
5. demonstrate the functionality of the system by linking three-dimensional UNIX-based models with one-dimensional PC-based models within FRAMES. This scenario would demonstrate the system's ability

to 1) incorporate three-dimensional models, 2) mix and match one- and three-dimensional models, and 3) mix and match UNIX and PC models.

Results and Accomplishments

Expansion of the FRAMES Specifications

We successfully developed a new FRAMES file specification that will allow us to incorporate two- and three-dimensional models into the system. The file specification standardizes the format for passing results from one model to the next; in this case, from the vadose zone model (STOMP) to the saturated zone model (CFEST). The temporal and spatial integrity of the data were two of the main issues that had to be resolved. We worked with the CFEST and STOMP developers and model users to determine what data needed to be passed between the models and to determine the best format of that data. The file specification we developed maintains spatial integrity by use of polygons and fractions to transfer data between disparate grid systems (Figure 1), maintains mass balance and temporal integrity (time stepping issues) by use of cumulative curves (Figure 2), and is a generic format such that any media can be passed between models using the same specification (water, contaminants, energy, salinity). It was necessary to develop a processor to address the temporal and spatial integrity issues. The processor reads in the two disparate grid systems, creates polygons based on the grid points if necessary, determines the fractions for data transfer, and develops the cumulative curves needed to meet the file specification.

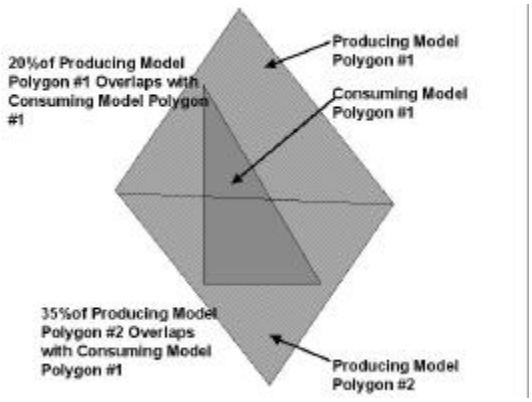

Figure 1. Description of polygon fractions used to address spatial integrity issue

Network Data Exchange

We successfully developed a system that allows FRAMES to access computer models on different computers via the Internet. The system consists primarily of a model client, a model server (both coded in Java), and a TCP/IP network connection. The obvious advantage to using Java is that our protocol is platform independent (i.e., can be used on both PCs and UNIX platforms). The system contains protocols for dealing with long model run times and error handling. Also the model client provides the user with the status of model runs via a text window. Figure 3 provides the schematic for our network data exchange protocol.

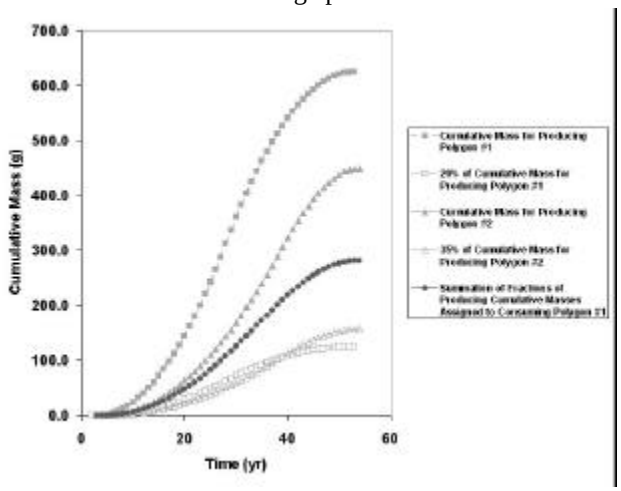

Figure 2. Description of cumulative curve development based on polygons described in Figure 1

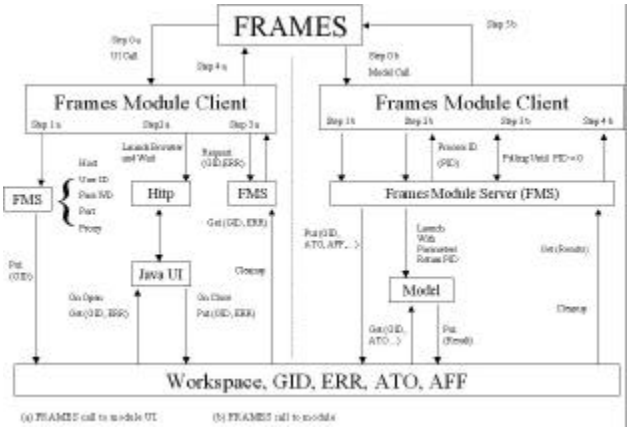

Figure 3. Schematic of FRAMES system developed to access models on different platforms (PCs and UNIX) over networked machines

Integration of STOMP and CFEST

Both STOMP and CFEST were integrated into the system successfully. The complete functionality of all of the STOMP and CFEST options was not an objective of this project. Our objective for the project was to incorporate the options with enough functionality to run a specific base case. The integration of both models required us to develop pre- and post-processors in C++.

Software Demonstration

We successfully demonstrated a base case using the completed software system. Our case started with a one-dimensional PC-based FRAMES source term model. We then connected to a UNIX machine via the Internet to run STOMP for the vadose zone. Next we connected to a different UNIX machine via the Internet to run CFEST for the saturated zone. Our endpoints were time-varying water concentrations at two different well locations. These results were ported back from the UNIX machine to the PC. The CFEST post-processor converted the results to a format that could be read by our FRAMES data viewers. The system worked without error and as expected. All of the data processing that is typically required to connect a vadose zone model with a separate groundwater model was seamless to the user. Figure 4 is a screen capture of the system and shows the scenario that was modeled.

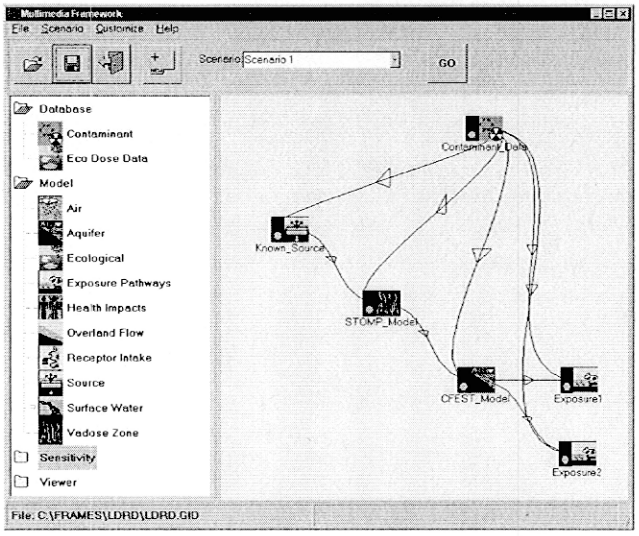

Figure 4. Screen capture of FRAMES user interface showing the conceptual site model of base case scenario

Summary and Conclusions

The framework for integrating multiple platform computational models was successfully designed, developed, and demonstrated. We concluded that the advantages of the system include the following:

- automated connections between media being modeled
- models being used can be located on different networked computers and on different platforms
- reproducibility of modeling assessment
- graphical user interface provides a view of the basic conceptual site model
- automated system allows the modeler to run a sensitivity/uncertainty analysis of the entire system.

Bibliography

Buck JW, G Whelan, JG Droppo, DL Strenge, KJ Castleton, JP McDonald, C Sato, GP Streile. 1995. *Multimedia Environmental Pollutant Assessment System (MEPAS) application guidance.* PNL-1039, Pacific Northwest Laboratory, Richland, Washington.

Wurstner SK, PD Thorne, MA Chamness, MD Freshley, MD Williams. 1995. *Development of a three-dimensional ground-water model of the Hanford Site unconfined aquifer system: FY 1995 status report.* PNL-10886, Pacific Northwest Laboratory, Richland, Washington.

Free-Surface Hydrodynamics and Fish Behavior Simulation

Chris B. Cook, Marshall C. Richmond, John A. Serkowski

Study Control Number: PN99026/1354

The effect of hydroelectric projects on the migration of anadromous fish is of considerable interest, especially in the Pacific Northwest. The Laboratory is developing and applying methods to numerically model the environment around hydroelectric structures so that various future management strategies can be tested without harm to endangered aquatic species.

Project Description

This report summarizes the development and application of free-surface hydrodynamic and fish-behavior models. These models were developed to enable engineers and biologists to assist government agencies and private utilities with ongoing modifications to hydroelectric power projects. Environmental conditions in areas upstream, downstream, and through these projects are among the most violent experienced by migrating anadromous fish. These areas are also the most difficult to study in both the field and laboratory. Scenarios investigated during this research include comparisons to laboratory experiments, simulation of several historical project operation periods with comparison to field observed data, and near-field modeling near the plunging jet of a high flow sluice chute. By combining physically based, three-dimensional hydrodynamic models and simplistic fish movement models, this project has advanced our ability to conduct cost-effective evaluations of various hydroelectric management scenarios.

Introduction

As a specific application of this developing technology, we sought to understand the potential relationship between endangered Chinook salmon migration and Bonneville Project operations. The Bonneville Project splits the upstream Columbia River flow into three parts: Powerhouse 1 on the south, the spillway in the middle, and Powerhouse 2 on the north. Opening and closing of the 18 individual turbine units in Powerhouse 1 and 2 and the 18 spillway bays control project operations. Once a unit or bay is opened, various upstream gates control the quantity of water released. Decisions regarding which units/bays operate and how far each gate opening is set depend upon such competing interests as fish-specific needs, hydroelectric power demands, hydrologic events, and downstream water needs.

The U.S. Army Corps of Engineers is evaluating the positive and negative impacts of using ice and trash sluice chutes as an alternative route to allow juvenile migrating salmon to pass through the dam. These suspended cantilever chutes, usually operated at relatively large flows (> 2000 cfs), can be suspended tens of feet above the tailwater pool. The ability of a juvenile salmon to survive passage through a high flow outfall depends on a number of factors, including quantity of flow released, height of the drop, velocity difference between the jet impact velocity and the tailwater pool velocity, and the location of the salmonids within the jet (edge or center). As the salmon enters the tailwater pool via the outfall jet, they are subjected to high deceleration forces, resulting in shear forces that have the potential to harm internal and external organs. Accurate prediction of shear forces under a variety of operating conditions allows managers to maximize juvenile salmon survival.

Approach

Modeling of high flow outfalls (i.e., free-surface jets and plunge pools) is still a developing technology. A commercially available three-dimensional free-surface hydrodynamic model, FLOW3D, was tested against peer-reviewed and published laboratory experiments.

A widely used hydraulic structure for controlling sudden vertical changes in river elevation is a “drop structure.” These simple devices are usually constructed by fortifying a pool of a specific river reach. The riverbed upstream of the pool is then leveled out, so as to increase the vertical drop just upstream of the pool. In this manner, the river is then forced to dissipate potential energy contained in the flow over a controlled vertical drop into the fortified pool.

Rajaratnam and Chamani (1995) monitored a simplified two-dimensional drop structure in the laboratory. A time sequence of the numerically simulated drop structure is

shown in Figure 1. Simulated results matched observed data well: observed drop angle = 57-deg, simulated = 55-deg; observed downstream/drop depth = 0.094, simulated downstream/drop depth = 0.088, observed brink/drop depth=0.18, simulated brink/drop depth = 0.15.

Figure 1. Evolution through time of the numerical model's solution for a drop structure. Contours relate to velocity magnitude.

A second, commercially available three-dimensional hydrodynamic model, STAR-CD, was used to simulate the larger scale flow field upstream and downstream of the Bonneville Project. These flows were simulated in a steady-state mode using a rigid lid approximation (non-free surface). These two assumptions simplify the numerical complexity, allowing for greater grid mesh detail. STAR-CD was applied to the forebay, intakes, and tailwater of the Bonneville Dam Project.

The model was verified by simulating February 7, 2000, field conditions. Inflow boundary conditions for the First and Second Powerhouses and Spillway were set using recorded Project operations. Bottom roughness was estimated using a Manning's n value of 0.020. Results showing simulated water velocities downstream of the Bonneville Project are shown in Figure 2.

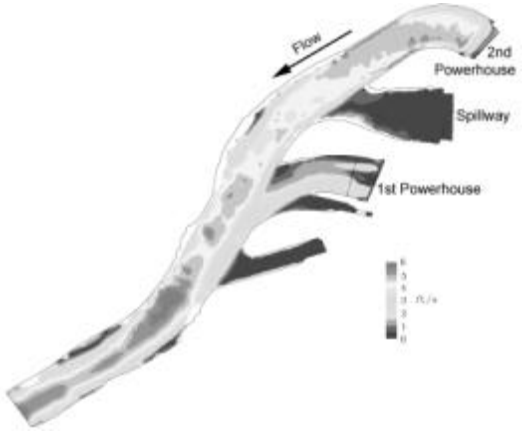

Figure 2. Numerically generated contours of velocity magnitude downstream of the Bonneville Project

Model data was then compared to water velocity data collected using an acoustic Doppler current profiler. Water velocities were compared at three depths through the water column. A graphical comparison of observed versus modeled data is shown in Figure 3.

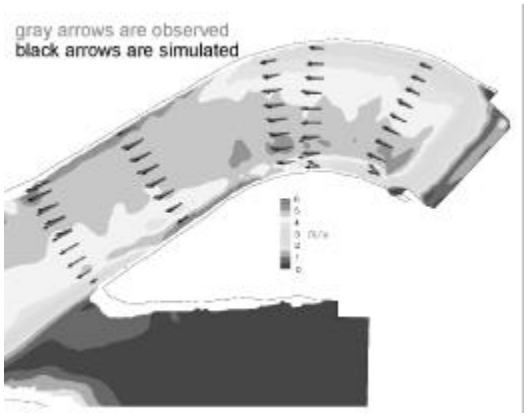

Figure 3. Close-up of velocity magnitude contours near the second powerhouse. Arrows compare numerical and observed data at various locations.

Simulating Fish Behavior

Steady-state hydrodynamic results from the STAR-CD application to the Bonneville tailrace were used as input to NWGrid, developed by Harold Trease of PNNL. NWGrid is capable of simulating the evolution of particles introduced into the flow field. In addition, these particles can be assigned various statistical properties representing fish behavior. This ongoing area of research is only beginning hence behavioral properties were appropriately simplistic for this project. For the purposes of this project, the "fish" particles were given a simple uniform normal random distribution (Figure 4).

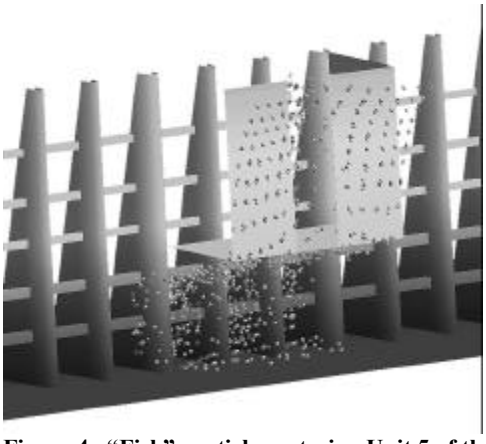

Figure 4. "Fish" particles entering Unit 5 of the first powerhouse. Foreground structure is a prototype surface collector which isolates flow from two of the turbine bays.

Results and Accomplishments

We developed and applied mathematical models capable of simulating the hydrodynamic flow field and fish behavior near large hydroelectric projects by applying two hydrodynamic models. One model, Flow3D, is capable of simulating free-surface flows, which are of critical importance near high flow outfalls. The other model, STAR-CD, is capable of easily simulating the complex hydroelectric dam structure as well as complicated bathymetry. By applying both of the models, a complete hydrodynamic description of the entire hydroelectric project was achieved.

Results from STAR-CD were then used as the driving flow field in NWGrid. NWGrid then simulated the paths of particles introduced into the flow. Particle paths were modified using statistical processes to coarsely simulate fish behavior. Simulation of actual fish behavior, driven by external (non-hydrodynamic) forces, is an ongoing research effort, and a complete description in NWGrid is beyond the scope of this project. It is anticipated, however, that by continuing research in this area, a continued blend of modeling hydrodynamic forces and fish behavior will produce management tools capable of predicting the most beneficial solution to these types of problems.

Summary and Conclusions

Two, three-dimensional hydrodynamic models were applied to simulate the turbulent hydrodynamic regime downstream of a hydroelectric project. Results indicate that these models are capable of simulating these environments with a reasonable degree of confidence, as compared to laboratory and field data.

A third model was applied to simulate fish movement. Although behavioral methods used to simulate the fish movement were simplistic, linkage of these three models provides the first step toward the complete simulation of fish response to hydrodynamic forces.

References

Gharangik AM and MH Chaudhry. 1991. "Numerical simulation of hydraulic jump." *Journal of Hydraulic Engineering,* American Society of Civil Engineers, 117(9), September.

Rajaratnam N and MR Chamani. 1995. "Energy loss at drops." *Journal of Hydraulic Research 33(3):373-384.*

HostBuilder: A Tool for the Combinatorial Generation of Host Molecules

Benjamin P. Hay

Study Control Number: PN00051/1458

Host molecules that selectively complex targeted guests have potential broad application to problems currently challenging DOE including detection of species in groundwater and chemical process streams; the separation and concentration of radionuclides and other ionic species from nuclear waste, contaminated soils, and groundwater; and the encapsulation of radionuclides in medical applications. Motivated by the expense of host development in the laboratory, we are creating software to evaluate large numbers of possible host architectures and rapidly identify the best candidates prior to synthesis and testing.

Project Description

The purpose of this project is to create software for rapid discovery of new host architectures. The approach involves a combinatorial method in which we examine every possible architecture for a set of donor groups. In the first year of the project, we developed and coded an algorithm for connecting two host fragments to form candidate structures and to rank-order the results with respect to the best fit to a guest. In addition, we constructed a comprehensive link library derived from small alkane and alkene fragments. Tests demonstrate that the algorithm is computationally very efficient and with recent hardware we estimate that speeds in excess of one million host molecules per second will be attainable. Code development remains in progress and a final version of the software will be completed in 2001.

Introduction

Many fundamental studies of host-guest interactions have been performed. Effective computational methods are available for ranking proposed host structures in terms of their binding affinities for specific guests on a case-by-case basis. However, no effective method exists for computer-aided design of new and improved host molecules. What is missing is an efficient and systematic means of generating trial structures. To fill this gap, we are working to develop a code, HostBuilder, that will be capable of generating and rank-ordering millions of possible host architectures from a given set of donor groups. This new capability will provide DOE with an alternative to expensive Edisonian experimentation that currently dominates host-development research.

The objective is to develop a computational approach for discovering new host molecule structures with the potential to tightly bind to a specified guest. To achieve this goal, we are combining fundamental knowledge of guest-donor group interactions with a combinatorial geometric structure generator to produce and rank a large library of possible host structures. The project has two distinct tasks: 1) developing and encoding the algorithms for the combinatorial geometric structure generator, HostBuilder; and 2) constructing a large database of linking groups. Our efforts focused on the first task with the development of a prototype version of the HostBuilder program. Our future objective will be the improvement of the HostBuilder program, completion of a larger linker database, and validation of the final version of the software. The successful completion of this project will yield a powerful software package to guide the development of molecular and ion recognition agents. To our knowledge, this capability currently does not exist elsewhere.

Results and Accomplishments

We successfully completed a prototype version of the HostBuilder code. This code, which consists of 8,500 lines of standard FORTRAN, takes two host fragments and builds every possible architecture that can be made by connecting the fragments to linkage structures taken from a database. By examining all rotamers and enantiomers, all possible configurations of each molecular connectivity were considered during the building process. After construction, each candidate host architecture was rank-ordered with respect to guest complementarity based upon knowledge of the optimal coordination geometry of each donor group. After all candidates were evaluated, the best structures were written to a graphics file for viewing. The current linker database contains molecular fragments representing all possible connectivities that can be formed from alkanes and alkenes containing four carbon atoms or less.

Developing and testing the prototype code was done on an IBM Risc/6000 processor (67 MHz). In the largest test to date, HostBuilder generated and evaluated 104,172 possible architectures for connecting two chelate rings to form a tetradentate host for a metal ion guest. The time spent building and ranking these structures was 55 CPU seconds, (a rate of 1,894 molecules per second). Given recent advancements in processor speed, use of newer hardware should increase this rate to better than 20,000 molecules per second, allowing us to evaluate more than a million molecules per minute. We have demonstrated that HostBuilder executes with sufficient speed to allow the development of multi-generation building algorithms. In a multi-generation building mode, the user will specify the number of host fragments that would form the final structure and the code would build the host by sequentially connecting these fragments. For example, the best hits from the initial generation (linking two unidentate fragments to form a bidentate host) would be used as input for the next generation (adding a unidentate fragment to a bidentate host to form a tridentate host).

Summary and Conclusions

Prototypes of the HostBuilder program and link library have been completed. Tests demonstrate that the building and evaluation algorithms are computationally very efficient and with recent hardware, we estimate that speeds in excess of one million molecules per second are attainable. Completion of this project in FY 2001 will entail

- switching from disk-based data storage to RAM-based data storage
- developing improved methods for building macrocyclic structures
- developing logic and control algorithms for the multi-generation building mode
- increasing the number of structures in the link library.

Invariant Discretization Methods for n-Dimensional Nonlinear Computational Reactive Transport Models

Joseph S. Oliveira

Study Control Number: PN99034/1362

The objective of this research has been to investigate, develop, and apply a new set of scale invariant, discrete algebraic and geometric symmetry preserving algorithms to the problem of effectively defining and remapping multiscale, multidimensional hybrid computational meshes. This effort provides a critical part of the applied mathematical infrastructure needed to solve complex computational problems. The primary goal is to develop new combinatorial methods for generating and preserving computationally, symmetry-invariant, coordinate-free, three-dimensional and n-dimensional spatial discretizations, on mixed (structured and/or unstructured), hybrid, moving, and stochastic grids.

Project Description

We are building the mathematical tools to create invariant grid discretizations of adaptive moving hybrid grids that are coordinate free. We are using algebraic combinatorial, combinatorial geometric, and combinatorial topological invariants to remap, reconnect, and renormalize multiscale, multidimensional, adaptive, moving hybrid grids. In each of these cases, scalars, vectors, and tensors are remapped by sets of coordinate-free transformations between logical and real physical n-space. This emerging computational technology implies that the boundaries (external and internal) of the computational domain must be canonically based on the invariance of the solution(s) to the partial differential equations that model the physical problem domain. These may include, but are not limited to: material interfaces, liquid-gas interfaces, contact discontinuities, and shock fronts. Furthermore, the grid covering the computational domain (subdomains) has to be constructed using information about the position of the free moving boundary and the information about the invariance of the solution to the system as a whole. Lastly, finite difference schemes have to be reformulated in such a way that they do not depend on the components of vectors and tensors, but rather, the discrete analogs of coordinate-free differential forms. The coefficients of the finite difference equations should depend only on the coordinate-free characteristics of the grid, lengths of the edges, nearest neighbor point distributions, areas of faces, volumes of mesh cells, and angles between edges, and not specific vector coordinate representations.

Approach

The violation of physical symmetry in the discrete geometric representation of the partial differential equations is a principal cause of the numerical instabilities that lead to large numerical errors. If this type of problem is to be eliminated, we must generate computationally invariant hybrid discretization methods (three-dimensionally, mixed [structured and unstructured] grids, and stable three-dimensional numerical schemes built on these grids) for obtaining stable, high-accuracy numerical solutions to the partial differential equations that preserve the inherent symmetry of the physical domain space. The overall goal is to generalize these methods to n-dimensions, multiscale, hydro-transport physics models. The extension to n-dimensions will allow us to more accurately model physical parameter space by representing each algebraic parameter by a corresponding geometric dimension.

The geometric invariance that is preserved by the grid discretization of the physical continuum is spatial symmetry, which is realized as algebraic invariant symmetry. For example, the preservation of physically based fluid flow symmetries—associated with multiscale, multiphase advective and reactive diffusive fluid flows in subsurface transport, magnetohydrodynamic flow, combustion systems, reactive atmospheric transport chemistry, and intra-inter cellular communications—must remain scale invariant. The divergence from spherical and rotational symmetries due to discretization errors can lead to large errors in the discretized systems of ordinary differential equations with large convergence ratios. The

loss of local and global curvature data will introduce large scaling errors. Also, the uncertainty as to whether a nonsymmetric result is due to numerical errors or to the physical continuum model severely limits our predictive capabilities and our basic understanding of the dynamics of coupled transport phenomena.

For the linearized equations of mathematical physics, there exists a well-developed theory of finite difference schemes. These schemes are based on three fundamental concepts: 1) truncation error analysis, 2) numerical stability analysis, and 3) convergence, which follows from an estimate of the truncation error and the stability of the numerical scheme. It is possible to extend truncation error measures to nonlinear equations, but investigating the numerical stability of methods for solving such equations is much more complex. A general mathematical theory of numerical stability for three-dimensional advection-diffusion equations does not currently exist. The hope of obtaining an n-dimensional characterization requires that we first determine the "observability" and identification of the symmetry invariants of the partial differential equations state variable representation, given as an n-dimensional manifold. By carefully examining the parameter space data of both the time and phase space domains of quasi-linear and nonlinear equations in terms of their linear equation analogs, we can begin to develop identifying measures of stability and instability. We will begin to develop n-dimensional grids to discretize the multiscale, multidimensional energy surfaces of phase space representations of these equations. Given that there is currently no mathematical theory for obtaining quantitative a priori estimates for the accuracy of finite difference approximations to full three-dimensional (and generalized to n-dimensional) nonlinear hydro-transport equations, we will initially use qualitative multidimensional grid methods to derive approximate measures of the time and phase space domains of multiscale hydro-transport physics domains. Therefore, it is natural to require that the invariant grid discretized models should preserve the physical symmetry of the physical continuum model by maintaining both accurate measures of local and global curvature, together with the local algebraic symmetry groups that provide us with a Lie Group symmetry invariant based definition of "adequate numerical approximations," where "adequate" still needs to be defined.

Preservation of spatial symmetry is one of the manifestations of the more general notion of invariance of finite difference methods, related to the preservation of group properties (up to isometric-isomorphisms) of the continuum equations and both local and global curvature symmetry. The theory of Lie Groups, which has been a classical tool for the analysis of the fundamental symmetries of continuum ordinary differential equations for over 100 years, has been used recently to construct finite difference schemes with symmetry preserving group invariance in one-dimensional (Vorodnitsyn 1994). A number of results also are available for three-dimensional advection-diffusion equations in Eulerian form (Leutoff et al. 1992). Extending these approaches to two- and three-dimensional Lagrangian advection-diffusion-transport equations will lead to significant improvements in our simulation capabilities.

Results and Accomplishments

The principal investigators have continued to investigate and apply the Fowler, Oliveira, and Trease (Millennium) remapping algorithm to three-dimensional particle transport in a fluid that interacts with a visco-elastic membrane. (See examples in figures below.) We have demonstrated that the Millennium algorithm has a near-optimal space and time complexity, that is O (n log (n)) and preserves the underlying invariant SO(3) symmetry of this hybrid grid by faithfully remapping coordinate-free representations of sets of scalars, vectors, and tensors. We can show that each of the measure-preserving maps are symmetry invariant with respect to the SO(3) and the O(3) groups and that the computational efficiency of the intersection algorithm depends on the SO(n) invariance of the spherically bounded search space of polyhedral face intersections.

The Malard-Oliveira remapping algorithm has a conjectured computational amortized complexity of O (n). Significant improvements over the original algorithm design have been made, which is described as follows: During the first year of this project, we developed a novel remapping algorithm, whose expected run-time was potentially linear in the number of pairs of overlapping elements. Our second year goal for refining and implementing the algorithm was to initially develop and implement an abstract data type for dynamic list representations that would be more computationally effective on nonuniform memory access multiprocess architectures. Figure 1 shows the remapping time for all three variants. The remapping time excludes both the input time and the time needed to compute adjacency relations between elements of the same grid. The run-time of the bridge variant appears more uniform for large problems than the other two variants.

A novel remapping algorithm has been simplified, implemented using abstract data types built on top of freely available software, and benchmarked on a Silicon

Graphics, Inc., workstation. The complexity of this algorithm is conjectured to be linear in the number of pairs of overlapping elements.

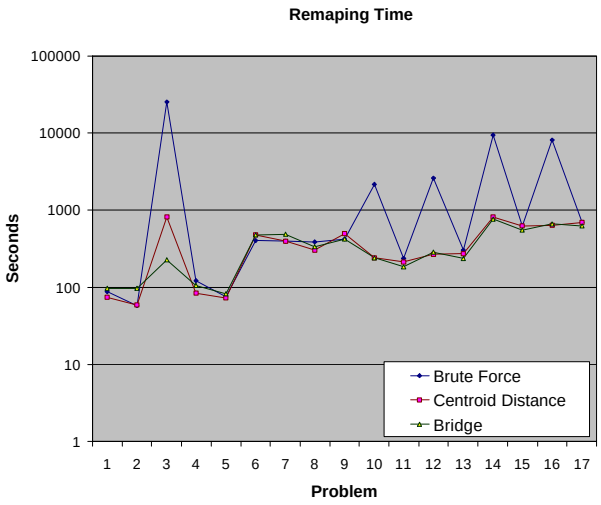

Figure 1. Tre-remapping 3-D hydro-transport calculation

Summary and Conclusions

During the last 3 years, we have researched and applied the mathematical theory of combinatorial algebraic-geometric and topological invariants to remap, reconnect, and renormalize multiscale, multidimensional, adaptive, moving hybrid grids. In each of these cases, scalars, vectors, and tensors are remapped by sets of coordinate-free transformations between logical and real physical n-space. This emerging computational technology, based upon multiscale, multidimensional Free-Lagrangian numerical methods, implies that the boundaries (external and internal) of the computational domain must be canonically based on the invariance of the solution(s) to the partial differential equations that model the physical problem domain. These may include, but are not limited to material interfaces, liquid-gas interfaces, contact discontinuities, and shock fronts.

References

Leutoff D, KG Roesner, et al. 1992. "Numerical investigation of 3-dimensional shock focusing effects by an invariant difference scheme." *Fluid Dynamics Research* 10(4-6):469.

Vorodnitsyn V. 1994. "Finite difference models entirely inheriting continuous symmetry of ordinary differential equations." *Int. J. of Modern Phys*., C 5(4):723.

Publications and Presentations

Oliveira and Trease. September 2000. "A symmetry invariant first-order remapping methodology." *7th International Conference on Numerical Grid Generation in Computational Field Simulations.*

Oliveira JS and Bailey. "Another universal axiomatization of cubes." *Algebra Universalis* (submitted).

Oliveira JS and Bailey. "The theory of cubic lattices." *Mathematical Association of America* (submitted).

Oliveira and Bailey. "Automorphisms of cubic algebras-I." *Journal of Algebraic Combinatorics* (submitted).

Oliveira and Bailey. "Free cubic algebras." *Advances in Mathematics* (submitted).

Oliveira and Bailey. "Automorphisms of cubic algebras-II." (in internal peer review).

Oliveira and Bailey. "Automorphisms of cubic algebras-IV." (in internal peer review).

Oliveira and Bailey. "Some remarks on the algebra of filters of a cubic algebra." (in internal peer review).

Oliveira and Bailey. "Cube-like structures generated by filters." (in internal peer review).

Oliveira and Bailey. "MV-Algebras and cubic algebras." (in internal peer review).

Oliveira and Bailey "The face lattice of a multicube." (in internal peer review).

Oliveira and Bailey. "Congruencies and homomorphisms of cubic algebras." (in internal peer review).

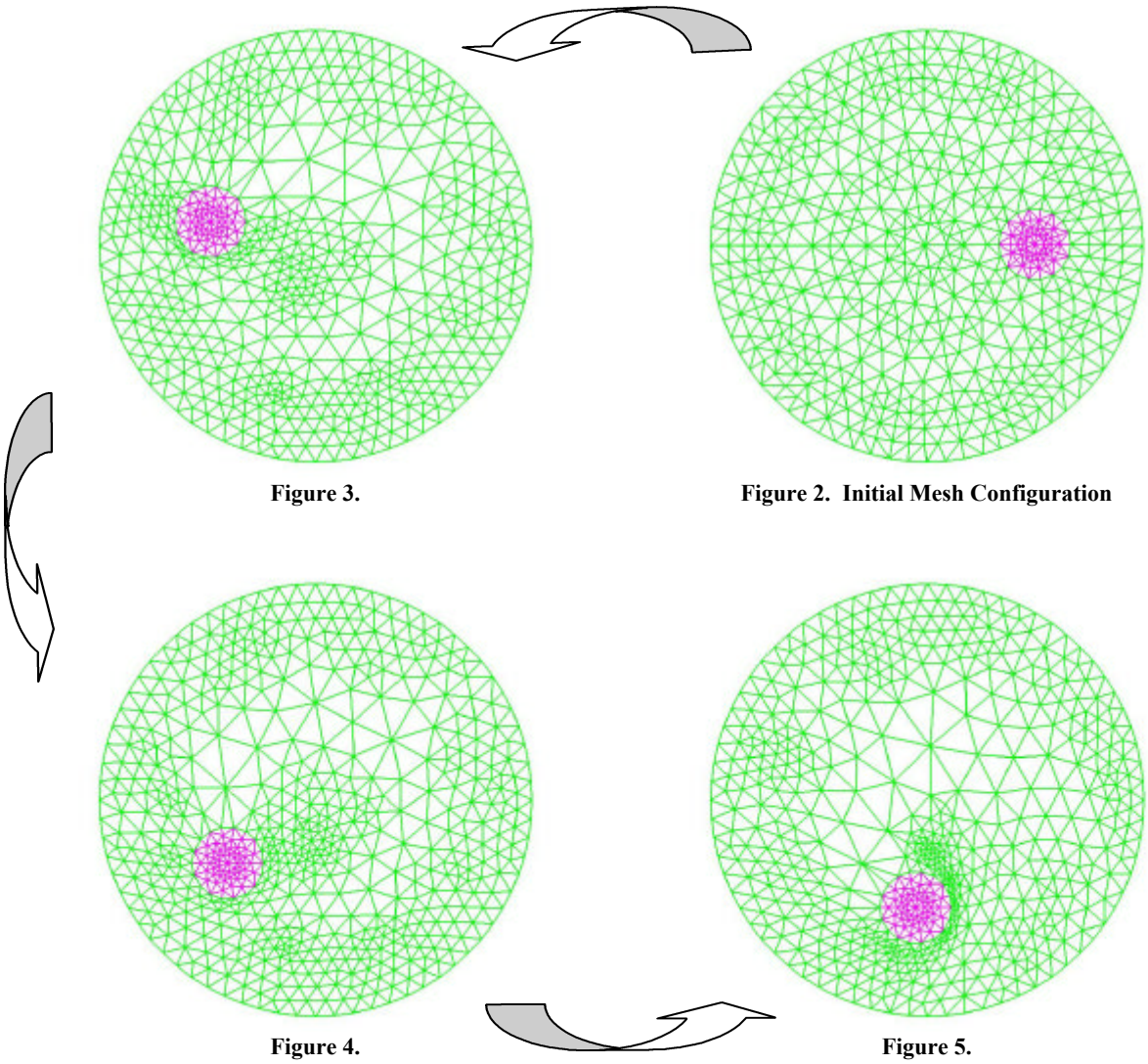

Figure 3. Figure 2. Initial Mesh Configuration

Figure 4. Figure 5.

Figures 2-5. Two-dimensional projections of a continuously remapped three-dimensional Delauney grid that preserves the rotational symmetry of a particle moving counterclockwise in a three-dimensional vortical transport flow field

Lattice Boltzmann Methods

David R. Rector, Bruce J. Palmer, Brian Wood

Study Control Number: PN00063/1470

Computational fluid dynamics simulations employ lattice Boltzmann equations for modeling multiphase flows in many practical areas of environmental, energy, and chemical processing research. This project develops new lattice Boltzmann equations for thermal and multiphase flow simulations.

Project Description

Lattice Boltzmann simulations have emerged as a promising method for simulating fluid flow in several regimes where traditional computational fluid dynamics simulations are inadequate or fail altogether. These include flows in topologically complex geometries such as those encountered in porous media and multiphase flows. Flows of these types are important in environmental, energy, and processing applications. Over the last several years, the Laboratory has made extensive progress in extending and refining the capabilities of the lattice Boltzmann technique for calculating flow and transport behavior.

Although the original lattice Boltzmann (scalar) code was suitable for simulating small systems and for demonstrating the capabilities of the algorithms, simulations of more complicated systems required code and algorithm enhancements. The target application of these capabilities is the simulation of microbial transport through porous media. These enhancements include implementing the algorithm on a parallel computer, beginning work on an adaptive mesh refinement capability, developing surface boundary conditions to reflect microbe-wall interactions, and demonstrating these capabilities by simulating transport through complex porous media.

Results and Accomplishments

A major strength of the lattice Boltzmann simulation method is that it is inherently parallelizable. We parallelized the lattice Boltzmann program by performing a block domain decomposition using the Global Array tools developed at the Laboratory. The program shows near linear speedup on both the Silicon Graphics, Inc., Power Challenge and the EMSL IBM SP computers for typical porous media simulations.

Another method of increasing the accuracy of the lattice Boltzmann method is to embed a more detailed lattice grid in those regions where more resolution is required. For example, multiphase systems typically only require greater resolution in the regions surrounding the interface. A significant portion of this work is the passing of information between the lattice subgrid and the primary lattice through interpolation.

In FY 2000, we evaluated methods for incorporating lattice subgrids into the lattice Boltzmann program. An initial implementation of an adaptive mesh algorithm was achieved using an adaptive mesh toolkit developed at NASA, in Gaithersburg. In FY 2001, we plan to investigate if adaptive mesh refinement routines in NWGrid (grid generation software) can be used to get improved results.

We have evaluated methods for generating porous media geometries using experimental data and simulation. A simulation method was established for generating model porous geometries using randomly places spheres. A three-dimensional image of a soil sample was obtained using nuclear magnetic resonance imaging capabilities in the EMSL, which were converted into a lattice Boltzmann grid. Lattice Boltzmann simulations were performed on both types of geometries to determine flow as a function of applied pressure drop to determine permeability. Figure 1 shows the x-direction velocity through a y-z plane for a computer-generated model geometry.

For the upscaling portion of this research, the primary accomplishment has been the development of an effective reaction rate model for the process of microbial attachment/detachment on mineral surfaces. The effective model was developed by integrating a general (Smoluchowski) transport equation that includes the effects of cell-surface interaction forces. The new model illustrates how fundamental physical properties (such as the local diffusivity and the interaction force) can be used

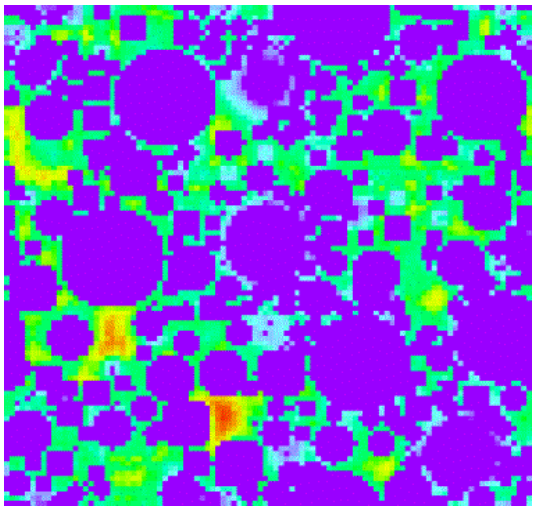

Figure 1. Computer-generated model geometry

to predict a priori the kinetic attachment and detachment rate coefficients, and represents the first steps in relating molecular-scale phenomena to the macroscopic scales that are typically considered in the laboratory and field. One publication is currently in preparation for these results.

Two journal articles were published documenting the lattice Boltzmann algorithms developed at PNNL for thermal and multiphase flow simulation.

Summary and Conclusions

The parallelization and initial implementation of the adaptive mesh refinement capability has expanded the range of application of the lattice Boltzmann simulation method to systems with complex geometries. The development of porous media geometry generation capabilities and an effective reaction rate model for use as a boundary condition makes it possible to simulate microbial transport through porous media.

Publications and Presentations

Palmer BJ and DR Rector. 2000. "Lattice Boltzman algorithm for simulating thermal two-phase flow." *Phys. Rev. E* 61:5295.

Palmer BJ and DR Rector. 2000. "Lattice Boltzmann algorithm for simulating thermal flow in compressible fluids." *J. Comput. Phys*. 161:1.

Wood BD and S Whitaker. "Use of Smoluchowski equation to derive and interfacial flux constitutive equation for particle adsorption and desorption." *Chemical Engineering Science* (submitted).

Palmer BJ. August 2000. Invited presentation to 9th International Conference on Discrete Simulation of Fluid Dynamics, Sante Fe, New Mexico.

Wood BD, EM Murphy, and S Whitaker. July 2000. "An effective model for colloid-surface interactions." Presented at the 2nd Computer Methods for Engineering in Porous Media Flow and Transport, Besancon, France.

Wood BD, DR Rector, EM Murphy, and S Whitaker. September 2000. "Prediction of Darcy-scale colloid and microbe transport in porous media." Presented at the SEPM/IAS Research Conference Environmental Sedimentology: Hydrogeology of Sedimentary Aquifers.

Mixed Hamiltonian Methods for Geochemical Electronic Structure Studies

Eric J. Bylaska, James R. Rustad, Michel Dupuis

Study Control Number: PN00066/1473

Oxidation/reduction (redox) processes at mineral surfaces are some of the most important and least understood processes affecting the fate and transport of contaminants in the subsurface. Redox processes are difficult to understand because electron exchange between oxidants and reductants can involve multiple pathways and numerous intermediate species and structures, all of which can vary with geochemical conditions. Computational methods are being developed in this project that will allow us to study important redox processes at solvated mineral surfaces.

Project Description

The purpose of this project is to develop a combined plane-wave quantum mechanics/molecular mechanics methods to study important geochemical processes (structures and reactivity) at solvated redox-active natural mineral surfaces and interfaces. When developed, this capability will allow us to simulate geochemically important interfacial processes that are not easily amenable to classical models. These include changes in oxidation states, changes in coordination and oxidation states (bond breaking and bond formation), and redox reactions of pollutants such as chlorinated hydrocarbons on iron-oxides and other environmentally important surfaces. To do this, we are combining Blöchl's projector-augmented-wave formalism with the popular mixed Hamiltonian techniques of quantum chemistry to create a unique capability for a quantum treatment of increasingly complex and realistic models of interfacial processes. During the first phase of the project, we have developed a massively parallel code employing Blöchl's projector-augmented-wave method, and have begun incorporating a classical treatment of solvating molecules into it. In addition, the project has developed a method for implementing free-space boundary conditions into plane-wave methods, performed calculations of iron-oxides using traditional pseudopotential plane-wave methods (not projector-augmented-wave).

Introduction

Modeling redox-active mineral/water interfaces is difficult for several reasons. First, redox active mineral surfaces are difficult to treat at a first-principles level, and the addition of solvent and bulk mineral makes it even more arduous. Accurate simulations of the reduction of a pollutant, such as carbon tetrachloride, at the mineral/water interface will require an accurate quantum mechanical description of the water-pollutant-surface-complex. Moreover, the simulation region must be exceedingly large so that the reaction involves the chemical participation of solid and water.

In recent years, there have been a number of significant advances that facilitate quantum mechanical modeling of reduction processes at these interfaces. One recently emerged technique, Blöchl's projector-augmented-wave method, is an all-electron approach that has many of the advantages of typical pseudopotential plane-wave approaches with the added ability to handle first-row elements with d electrons (Blöchl 1994). Another emerging technique, the quantum mechanics/molecular mechanics approach, combines first-principles simulations with classical modeling, to include long-range effects of solvent and bulk (Gao and Furlani 1995). The computational cost of such simulations is thus greatly reduced by representing the solvent molecules classically. In the quantum mechanics/molecular mechanics approach, the system is broken up into two parts: a localized quantum mechanical region surrounded by a molecular mechanical region (Figure 1). This will allow for a water-pollutant-surface-complex to be modeled quantum mechanically, while at the same time the long-range effects of solvent and bulk mineral can be included with classical modeling.

Results and Accomplishments

Progress was made in several tasks on this project. A parallel projector-augmented-wave code was developed, a method for implementing free-space boundary conditions into a plane-wave method was developed, a calculation of iron-oxides using traditional pseudopotential plane-wave methods was performed, and water pseudopotentials were tested.

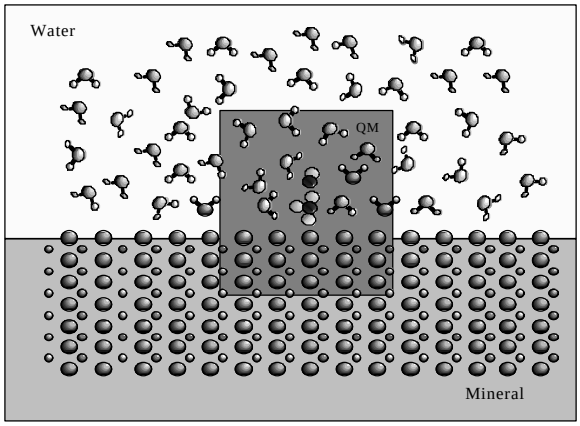

Figure 1. Schematic representation of the partition of a mineral/water/pollutant interface region

Massively Parallel Projector-Augmented-Wave Program

Over the past year, with the help of M. Valiev at the University of California, San Diego, we developed and coded a parallel projecter-augmented-wave method. This code was based on a serial FORTRAN 90 code written by M. Valiev. The code was parallelized using the Message Passing Interface standard library and uses a slab-decomposed Fast-Fourier Transform module written by E. J. Bylaska. The code gives good parallel performance, and compares well to other plane-wave methods.

We performed simulations on a variety of molecular systems using the parallel projector-augmented-wave code. Our results showed that

- The accuracy of the code is similar to the density functional calculations based on local basis sets.
- The convergence with respect to the plane-wave basis set leads to practical calculations, even for very difficult systems (F, O, Fe, Cr).
- The method is robust with respect to the choice of the local basis set.
- For a given plane-wave basis set size, the execution times of projector-augmented-wave calculations are similar to those of pseudopotential plane-wave methods.
- The size of the plane-wave basis is smaller compared to the norm-conserving pseudopotential plane-wave method.

Free-Space Boundary Conditions

Our proposed quantum mechanics/molecular mechanics development requires that the quantum mechanics system is solved using free-space boundary conditions. During the last year, we developed a technique to implement free-space boundary conditions into plane-wave methods. Equations providing a highly accurate implementation were developed (see Figure 2). We showed that the energies calculated using a modified free-space plane-wave code could be directly compared to a conventional periodic plane-wave code for problems in which the choice of boundary conditions was not important. Furthermore, implementing free-space boundary conditions into an existing parallel periodic plane-wave code would not significantly degrade its parallel efficiency.

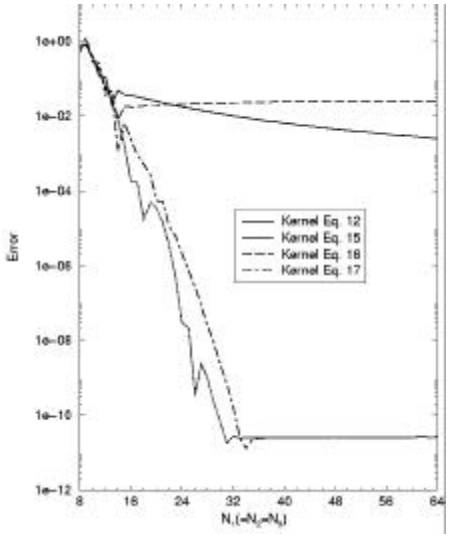

Figure 2. Error in calculating the electron-electron Coulomb energy for a test density composed of three normalized Gaussian functions located at (8.0,8.0,10.0), (12.0,12.0,12.0), and (8.0,13.0,10.0) on the W=[0.0,20.0)^3 domain. The normalized Gaussians have decay rates of 0.4, 0.4, and 0.5 respectively. A dramatic increase in accuracy is seen with our developed formula (legend: Eq. 15 and 17) compared with other published formula (legend: Eq. 12 and 16).

Studies of Iron-Oxides

Studies of iron-oxides were performed using traditional pseudopotential plane-wave methods. Pseudopotential plane-wave methods were used to investigate the structures and total energies of AlOOH and FeOOH in the five canonical oxyhydroxide structures: diaspore (goethite), boehmite (lepidocrocite), akaganeite,

guyanaite, and grimaldiite (see Figure 3). The local density approximation was used in conjunction with ultra-soft pseudopotentials in full optimizations of both AlOOH and FeOOH in each of these structures. Structures are in reasonably good agreement with experiment, with lattice parameters and bond lengths within 3% of the experimental ones. However, the relative energetics between the isomorphic structures only converged for the AlOOH structures and not the FeOOH structures, regardless of the type of pseudopotential or exchange-correlation functional used. This indicates the need for highly accurate methods like projector-augmented-wave, to assess relative energetics between FeOOH isomorphic structures.

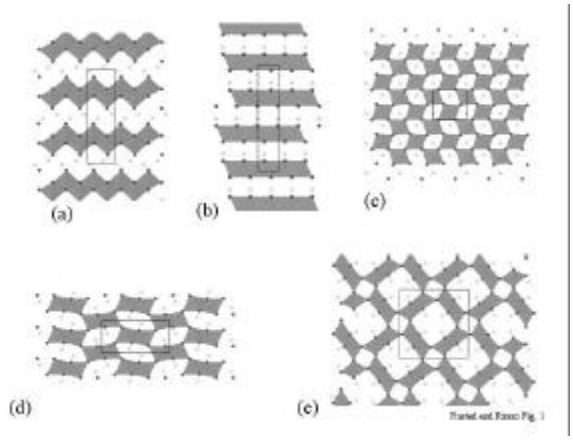

Figure 3. Iron-oxide and aluminum-oxide polymorphs studies using pseudopotential plane-wave methods

Water Pseudopotentials

With the completion of our parallel projector-augmented-wave code, we recently began to incorporate a water pseudpotential. Our current results suggest that our water pseudopotential is numerically stable and induces the correct polarization (see Figure 4). We have already incorporated most of the quantum mechanics/molecular mechanics interactions needed to describe a quantum mechanics water and molecular mechanics water. We are currently parameterizing the van der Waal's interaction between the quantum mechanics and molecular mechanics part using the water dimer.

Summary and Conclusions

A massively parallel projector-augmented-wave program was developed and tested. It has proven effective for systems containing first-row transition-metals, which are difficult to treat with traditional plane-wave methods. In addition, important new capabilities were added to the program. Our program can handle free-space boundary conditions and periodic boundary conditions on equal footing. Finally, the addition of water pseudopotentials to the projector-augmented-wave program will allow ab initio solvation studies to be performed at a lower cost.

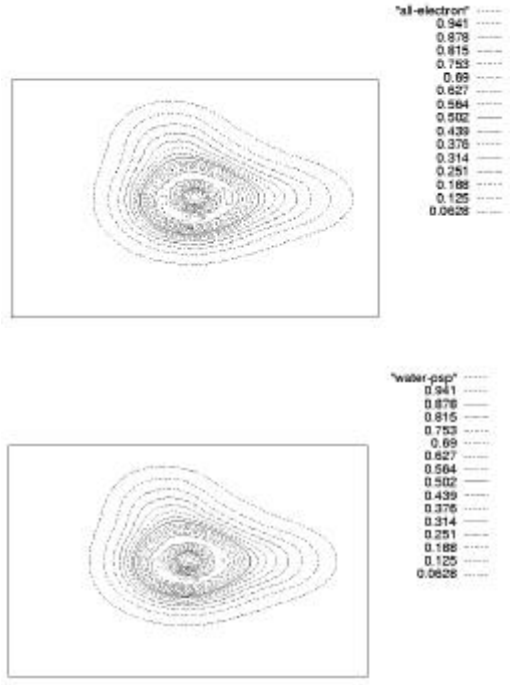

Figure 4. Comparison of the density polarization from a water molecule described by quantum mechanics (top figure) and by a pseudopotential (bottom figure). Each contour plot shows the electron density of a water molecule polarized by another water molecule (quantum mechanics and pseudopotential, R_{OO}=2.7Å.).

In FY 2001, this project will develop an embedding procedure to incorporate a classical treatment of long-range solid-state effects; for example, the surrounding lattice framework can then be excluded from the plane-wave treatment for additonal computational benefit.

References

Blöchl PE. 1994. "Projector augmented-wave method." *Phys. Rev. B* 50:17953-17979.

Gao J and TR Furlani. 1995. "Simulating solvent effects in organic chemistry: Combining quantum and molecular mechanics." *In IEEE Comp. Sci. Technol.*, 24-33.

Presentation

Rustad JR and KM Rosso. April 2000. "Total energy calculations of iron and aluminum oxyhydroxide bulk phases and surfaces." MRS 2000 Spring Meeting, San Francisco, California.

Modeling Ras:Ras-Effector Complexes: Key Components of Stress-Signal Transmission

John H. Miller, Tjerk P. Straatsma

Study Control Number: PN00067/1474

Stress responses play a central role in the potential health effects of low-level exposure to radiation and toxic chemicals. This project addresses a fundamental aspect of cellular stress response, the transmission of signals through low-molecular-weight guanosine triphosphate (GTP)-binding proteins and will demonstrate the capability to model molecular processes that are important for understanding health effects from environmental stress.

Project Description

Environmental health issues involve the transmission of and response to stress signals at the cellular level. Low-molecular-weight GTP-binding proteins play a key intermediate role in transferring the signals to a complicated phosphorylation cascade involving the protein kinase family. The transduction of the signal involves the interaction of GTP-binding proteins, of which p21Ras is the most extensively studied, with their effectors such as the signal generators Raf-1 and PI3K or the negative regulator GTPase activating protein (GAP). This project focuses on the computational study of Ras:Ras-Effector complexes using all atom molecular dynamics simulations. During the past year, various molecular dynamics simulations were performed for the p21Ras and p21Ras:p120GAP complex bound by GTP. These simulations have shown for the first time that the GTP binding site of Ras:RasGAP complex may actually have a configuration different than what is observed in the x-ray diffraction experiments. Conclusions drawn from this newly observed configuration agree with and can explain several key experimental results. The similarity between p21Ras and the Gα components of heterotrimeric guanine nucleotide binding proteins extends the relevance of our project to the much broader area of signaling through G-protein coupled receptors.

Introduction

A multitude of chemical and physical stimuli regulate the functions of cells by controlling the activities of a relatively small number of core signaling units that have been duplicated and adapted to achieve the necessary diversity. The G-protein coupled receptor (GPCR) is the most common of these units discovered so far. The prevalence of GPCRs makes the heterotrimeric guanine nucleotide binding proteins (G-proteins) the largest class of signaling proteins. The signaling mechanism of low molecular weight GTP binding proteins (p21Ras) is similar to that of G-proteins in that guanine nucleotide exchange activates the signal and GTPase activity turns it off. Like Ras, the Gα subunit exhibits affinity for downstream signaling proteins only when it binds GTP. The Gα subunit has a weak GTPase activity that determines duration of the active state when bound to downstream effectors. The GTPase activity of Gα is controlled by the regulators of G-protein signaling (RGS) that are analogous to RasGAP in their function. Interaction with RGS proteins greatly enhances the GTPase activity. The catalytic mechanisms responsible for the GTPase activities of p21Ras and Gα in the absence and presence of GAP and RGS, and the GTPase activity difference between p21Ras and Gα are poorly understood. In the so-called arginine finger hypothesis, it has been proposed that the arginine residue (Arg178 in $G\alpha_{i1}$ and Arg789 in RasGAP) that resides in the catalytic site and points to GTP is the main contributor to the increase in the GTPase activity. This project investigates the structural properties of p21Ras and p21Ras:RasGAP complex using molecular dynamics simulations aiming to determine the structural factors effecting the GTPase activity. Such studies allow us to make comparisons with the Gα system and help to understand the reasons behind the observed GTPase activity differences.

Approach

Classical molecular dynamics simulations and the protonation state (pKa shift) calculations were the main computational approaches used during the past year. The molecular dynamics simulations used all atom molecular models. Large unit box sizes were used to better represent the solvation effects. The necessary software to pursue the project is available in the NWChem computational chemistry package developed at the Laboratory. The relatively large size of the system requires that the supercomputer facility resources to be used. NWChem is a massively parallelized code well suited for using the supercomputation resources at the Molecular Sciences Computing Facility (MSCF) located

in the Environmental Molecular Sciences Laboratory. In addition to the resources at MSCF, the DOE super-computers at the National Energy Research Scientific Computing Center, Lawrence Berkeley National Laboratory were also used to perform parts of the computations.

Results and Accomplishments

Molecular dynamics simulations for p21Ras alone and in complex with p120GAP were successfully completed during the last year. In the p21Ras complexed with p120GAP, only the Ras binding domain of GAP was included in the simulations because only that part of the protein is resolved in the x-ray experiments. The molecular dynamics simulation systems were carefully set up by first studying the protonation states (pKa) of the protein residues and of the bound GTP. Our pKa calculations showed that the protonation state of GTP bound to p21Ras alone and bound to p21Ras:p120GAP complex may be different. It was computed that the terminal γ-phosphate group of GTP would be protonated when p21Ras is alone, and it is unprotonated when p21Ras forms a complex with p120GAP. Since it would change the initial proton transfer to the GTP step of the reaction, this difference in the protonation states implies that the reaction mechanism of GTP to GDP hydrolysis may be different for the p21Ras alone and p21Ras:p120GAP systems.

Gln61 is believed to play an important role in the structural stabilization of the catalytic site. In the molecular dynamics simulation of p21Ras alone, Gln61 stays fully solvent exposed as in the experimental x-ray structures. Gln61 is far from GTP, and therefore, most likely does not get involved in the hydrolysis reaction directly. It, however, contributes to the structural stability of the local structure around the GTP binding pocket. In contrast to the p21Ras alone system, Gln61 is close to the GTP in the p21Ras:p120GAP complex and interacts with GTP through a bridging water. It was observed in the molecular dynamics simulations that Gln61 might be occupying a position different than what was reported in the x-ray structure. In its observed configuration, it interacts with the GTP less specifically and contributes to the hydrolysis reaction by helping to align the bridging water in the proper orientation for the nucleophilic attack.

The x-ray crystal structure of the p21Ras:p120GAP complex contains a water between Gln61 and GTP. This water (we named it nucleophilic water) is believed to be the precursor of the nucleophilic hydroxyl that attacks the γ-phosphate of GTP during the hydrolysis. In the crystal structure, the nucleophilic water interacts with the sidechain carbonyl group of Gln61. During our simulation, there was a structural rearrangement of the GTP binding pocket of the protein complex. During the rearrangement, the nucleophilic water lost its interaction with the carbonyl group of Gln61 and started to interact with the NH_2 sidechain group of the same residue. The structure after the rearrangement supports the earlier studies that Gln61 is probably not the general base in the hydrolysis reaction.

The arginine residue (arginine finger) of p120GAP pointing toward GTP may increase the GTPase activity of Ras by stabilizing the transition state through favorable electrostatic interactions. This hypothesis successfully predicts that the GTPase activity of p21Ras increases when it binds p120GAP and that the activity of Gα (with its existing arginine finger) is higher than that of p21Ras. It, however, cannot explain why the GTPase activity of p21Ras:p120GAP is several orders of magnitude higher than that of Gα even though both members of the systems contain the arginine finger. In our p21Ras:p120GAP molecular dynamics simulations, we have observed a dominant structure of the GTP binding pocket. This dominant configuration is quite different from the x-ray crystal structure of the same complex. In this configuration, the nucleophilic water moves into a position such that its motion, orientation, and structural stability is controlled by its interactions with the backbone carbonyl of the arginine finger (Arg789 of p120GAP) and with the NH_2 sidechain group of Gln61. In the corresponding structure of Gα, the water molecule does not interact with the backbone of the arginine finger residue. Based on our observations, we have postulated that, in addition to its transition state stabilization role as in the Gα system, the arginine finger of p120GAP also controls the orientation of the nucleophilic water while initiating the hydrolysis reaction. It is the single-handed operation of orienting the attacking water and the transition state stabilization by the same residue that makes the GTPase activity of p21Ras:p120GAP complex higher than that of the Gα system.

Summary and Conclusions

Protonation state and molecular simulation computations of the p21Ras and the p21Ras:p120GAP complex were successfully completed. We found that the protonation state of the bound GTP may be different in these two

systems. The dominant structure of the GTP binding site in the Ras:RasGAP complex was different from the corresponding x-ray structure. The dominant structure, which has not been reported before in the literature, is consistent with several key experimental results.

These studies provide understanding the function of several key residues of the involved proteins. Next, we will determine the energetics and the pathways of the hydrolysis reaction. These studies will be performed by using quantum mechanical or hybrid quantum mechanical-classical mechanical approaches.

Publication

Resat H, TP Straatsma, DA Dixon, and JH Miller. "The arginine finger of RasGAP helps Gln61 align the nucleophilic water in GAP-stimulated hydrolysis of GTP." *Science* (in preparation).

Simulation and Modeling of Electrochemistry and Performance Assessment of Solid Oxide Fuel Stacks

Mohammad A. Khaleel, Kurt P. Recknagle, Z. Lin, John E. Deibler, John E. Jaffe, Rick E. Williford, Byung K. Ahn

Study Control Number: PN00081/1488

Development of methods for calculating current density, cell voltage, and heat production in planar solid oxide fuel cells (SOFC) stacks with various fuels is critical for coupling an electrochemical model and thermo-fluids and stress analysis.

Project Description

The objective of this project was to develop computational methods and simulation tools for predicting electrochemical behavior in SOFC stacks, and to gain a fundamental understanding of the effect of various operation conditions on the V-*i* relation. This project also was performed to provide analytical insight into the correlation between cell efficiency and fuel use. The technical work involved developing numerical procedures to simulate the heat generation from Joule heating and chemical reaction, and species production and destruction via mass balance to analyze the dependence of the Nernst potential on temperature and pressure. Also, the effect of having CO oxidation at the anode as an added contribution to the total current was investigated.

Introduction

Solid oxide fuel cells (SOFCs) produce direct current power from fuel and oxidant via an electrochemical process. The efficiency of such power generating methods compares favorably with conventional thermal power generation that is limited by Carnot-type constraints. Current SOFCs represent a highly developed, but immature technology. One advance necessary is to increase efficiency. Although the design and operation of a SOFC appears simple, many of the phenomena dominating the performance of a SOFC are complex, competing, and poorly understood; this is especially true of the electrochemistry. Mathematical models are required to incorporate the known physics and behavior of SOFC materials to predict and improve performance. It is well established that the cell direct current voltage and current depend on conditions that include fuel flow, oxidant flow, pressure, temperature, and the demands of the load circuit. These parameters affect the electrochemical processes that ultimately determine the generated power and cell voltage. By taking into account 1) ohmic losses, 2) concentration polarization based on the assumption of binary diffusion of gaseous species through porous electrodes, and 3) Tafel-type activation polarization in composite electrodes, it is shown that the V versus *i* traces can be adequately described by:

$$V(i) = E_{open} - iR_i - b\ \sinh^{-1}(i/2i_0) + (RT/4F)\ln(1-i/i_{O2}) + (RT/2F)\ln(1-i/i_{H2}) - (RT/2F)\ln[1+p^0_{H2}i/(p^0_{H2O}i_{H2})]$$

In the above equation, E_{open} is the open circuit voltage, usually referred as Nernst potential. R_i is the area specific resistance of the cell, b is the Tafel parameter. i_{O2} and i_{H2} are respectively the cathode- and anode-limiting current density, p^0_{H2} and p^0_{H2O} are respectively the partial pressure of hydrogen and water vapor in the fuel channel, R is the gas constant, F is the Faraday constant, and T is the temperature.

It should be noted, however, that the above equation is valid only for a SOFC using H_2 as the input fuel. To accommodate multifuel capacity, which is one of the main advantages of SOFCs, modification is required. Fuels other than pure hydrogen generally contain CO, reacting with H_2O to produce CO_2, and this reaction needs to be included in the mathematical modeling for a more accurate electrochemistry analysis. At present, PNNL is in the process of including the CO effect in an already-established electrochemistry code programmed by current authors for pure hydrogen-fed SOFCs. This effort will soon be linked to FEA modeling using Marc to complete interfacing the electrochemistry analysis with the thermo-fluids and stress analysis.

Results and Accomplishments

Electrochemistry Modeling

An electrochemistry code was written in Fortran based on Kim et al. (1999). Prior to the main analysis, dependence of Nernst potential on temperature and pressure has been examined, and the summary is listed below.

1. E_{open} is weakly dependent on temperature. E_{open} changes less than 1% when T changes by 50 K.

2. The change of E_{open} versus T is approximately linear.

3. The temperature difference in air and fuel does not affect E_{open} significantly. With 20°C difference across a PEN structure, computations using the average T may cause about 1% error.

4. E_{open} is strongly dependent on fuel composition. E_{open} drops by 20% from 1.11V at the fuel inlet to 0.89V at the gas outlet for an 80% utilization.

5. Higher fuel utilization does not always mean higher efficiency, although this is usually true. There exists an optimal fuel utilization for the best cell efficiency.

The main goal of the electrochemistry code is to generate the V-*i* curves, current-power curves, and heat-current curves with various temperatures because practical SOFC performance is usually described in terms of these parameters. The analyses of the results are summarized with figures below. The thickness of electrolyte, cathode, and anode are 10, 50, and 750 μm, respectively.

1. Voltage- and power-current curves for different temperatures are very different from each other. The maximum output powers differ by a factor of 5 for 600°C and 900°C (Figure 1).

2. The cell operating voltages corresponding to the maximum output powers are almost identical. They are 0.47V at 600°C and 0.49V at 900°C (Figure 1).

3. The electrical heat (generated in the PEN structure due to the current passage) is large and increases rapidly with increasing current passage (Figure 2).

4. The heat may increase the PEN temperature and induce temperature gradient field and thermal stress.

5. The heat generation severely limits the cell performance.

CO Oxidation at Anode

This task studied the effect of CO on the total current. A one-dimensional steady-state model of an SOFC stack was developed. The spreadsheet-based stack model accounts for overpotentials due to ohmic resistance of the cell components, to contact resistance at electrode-current

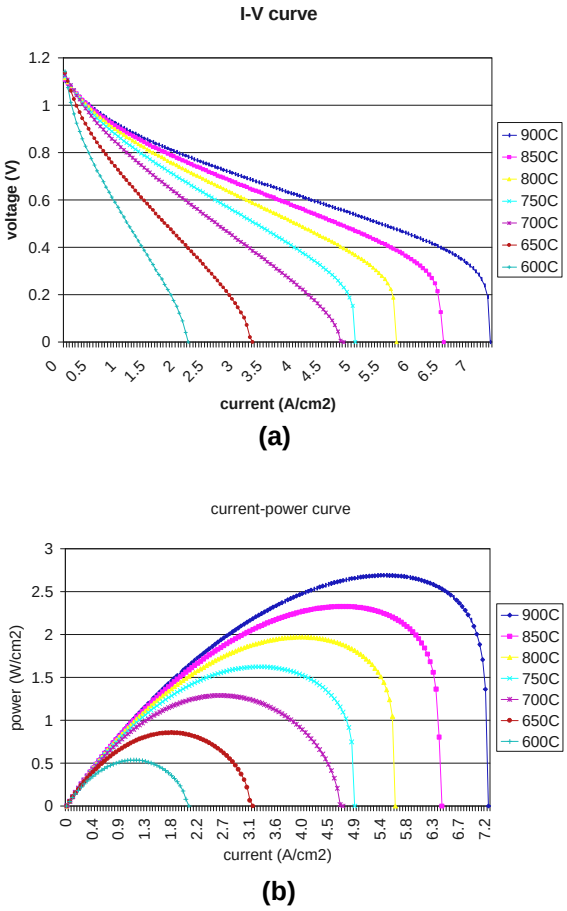

Figure 1. (a) Voltage vs. current density and (b) Power density vs. current density at seven temperatures

collector interfaces, to charge transfer at the electrodes, to diffusion of reactants into and products out of the porous electrodes, and to leakage of gaseous oxygen into the anode side of the cell. The model is capable of simulating anode gases derived from hydrogen fuels. It is assumed that anode gas compositions are determined by attainment of equilibrium for the water-gas shift reaction.

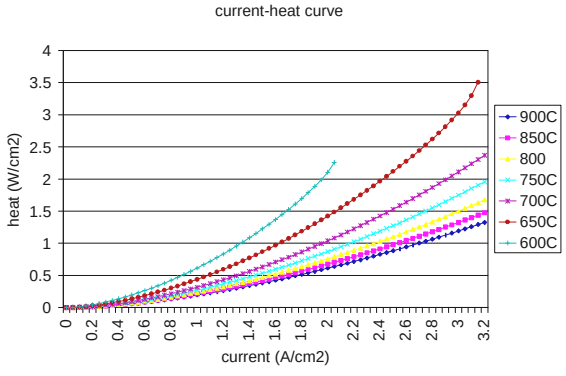

Figure 2. Heat generated by current passage. $P(H_2)$=0.97 atm, $P(O_s)$=0.21 atm, $P(H_2O)$=0.03 atm.

Summary and Conclusions

We implemented an electrochemical model for planar SOFC operations. Theoretical analysis and modeling calculations on the cell voltage, output power and heat generation versus current density at various operating conditions are given. Numerical results and discussions provided insight into the overall system operation and its optimization.

Future plans include adding CO to the electrochemistry code mentioned in the previous sections, developing an interface code between electrochemistry code and FEA so that more realistic stress analysis can be performed, and studying fracture and fatigue to predict the life of planar SOFC.

Reference

Kim JW, A Virkar, KZ Fung, K Mehta, and S Singhal. 1999. Polarization effects in intermediate temperature, anode-supported solid oxide fuel cells." *J. Electrochem. Soc*., 146:69-78.

Publications

Chick LA, JW Stevenson, KD Meinhardt, SP Simner, JE Jaffe, and RE Williford. "Modeling and performance of anode-supported SOFC." (in preparation).

Jaffe JE and LA Chick. "Fuel cell elment model with reforming, shift and CO electrochemistry." (in preparation).

Khaleel MA, KP Recknagle, Z Lin, JE Deibler, LA Chick, and JW Stevenson. "Thermo-mechanical and electrochemistry modeling of planar SOFC stacks." (in preparation).

Khaleel MA and Z Lin. "Electrochemistry modeling of solid oxide fuel cells." (in preparation).

Computer Science and Information Technology

Advanced Anomaly Detection

Brad Woodworth

Study Control Number: PN00003/1410

The Department of Energy needs technology to protect its computer networks and information systems. Neither current technology nor other options available from the computer security industry offers adequate protection levels for the security requirements of DOE.

Project Description

Most threats to a data center are from internal sources. Many commercial and public domain security products focus on the external threat and detect internal abuse only as it occurs. These products may indicate that a loss has occurred thus creating a gap between the internal threat detection and protection from the threat. This project explored new, more sensitive methods of anomaly detection that can decrease or eliminate the gap between the detection of the internal threat and protection from the threat. The particularly difficult problem of theft of sensitive data by "non-network" or "sneaker-net" means by those with legitimate access to the information has been viewed as the ultimate application of this work. This problem may not be solved, but it has been considered throughout the research process for any unexpected approaches that may be suited to this problem. Anomaly detection is a sub-field (CMAD IV 1996; Dean) of intrusion detection. Although anomaly detection may detect malicious behavior, it may also detect valid anomalous behavior. This feature of false positives that has beleaguered prior research will actually be used as a feature in the design of the advanced anomaly detection engine described.

Introduction

The current state of commercial products still has a long way to go before they can adequately address the security concerns of DOE. The latest systems are now combining network and host-based intrusion detection techniques (Shipley 1999). No single system passed all the tests (Shipley 1999) that were given at the network computing laboratories. Some government and academic tools are available but these tools lack the broad coverage of detection capabilities desired. Insider threats are difficult to detect (Figure 1).

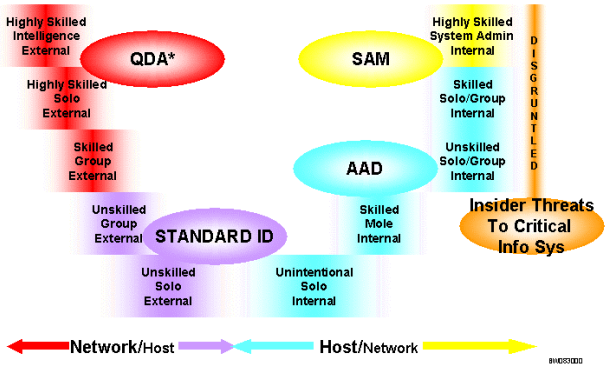

Figure 1. Malicious activity detection solution spectrum

Approach

The solution proposed for advanced anomaly detection involves a three-step process.

1. A general anomaly detection engine monitors system activities and detects when this activity deviates outside the normal range.

2. Upon detection of anomalous behavior, the general anomaly detection engine signals an algorithm decision engine, which selects one or more enhanced anomaly detection engines for final analysis.

3. The enhanced anomaly detection engine(s) monitor data harvested from memory and attempts to identify the type of activity that caused the alarm. The activities are then characterized as malevolent, benevolent, or inconclusive.

If the activities are inconclusive, a human analyst will make the final decision. Once the decision has been made, this information can be fed back into the general algorithm and enhanced engines for accurate response in

the future. The process that the analyst used to make the final decision is recorded so that these processes can be used in an automated manner in future systems. Researchers have recently concluded that no single method or algorithm is able to detect all types of intrusions. Thus, research has shifted from single to multiple solution methods. This proposed design is modular and anticipates the required empirical testing for fine-tuning and expansion.

Most researchers today are trying to directly reach the "malicious behavior" conclusion with limited success. Our proposed approach included a three-step process. The first step included a general-purpose anomaly detection engine that detects a wide variety of anomalous behaviors. Upon detection of these anomalous behaviors, this engine will signal an algorithm engine that will select one or more enhanced anomaly detection engines to interrogate new data being supplied based on the type and source of the first anomaly to discern the type and nature of the behavior and report the results. The following block diagram (Figure 2) illustrates this structure.

Another new approach being used is the data metric selection and collection criteria. Typical anomaly and intrusion detection systems use audit and system logs. It is the intent of this design to go directly to the source of the data—the system memory. In the system memory, one will have access to all activity on that host, including all network traffic. Both host and network information is readily available for analysis.

General Anomaly Detection Engine

The general anomaly detection engine can use algorithms that have been developed for anomaly detection and/or intrusion detection. These algorithms tend to produce a higher incidence of false positive signals, which is a desired feature in this application. Some of the algorithms considered are

- artificial neural networks
- SRI International Menlo Park, California, covariance algorithm
- Carnegie Mellon University, Pittsburgh, Pennsylvania, algorithms.

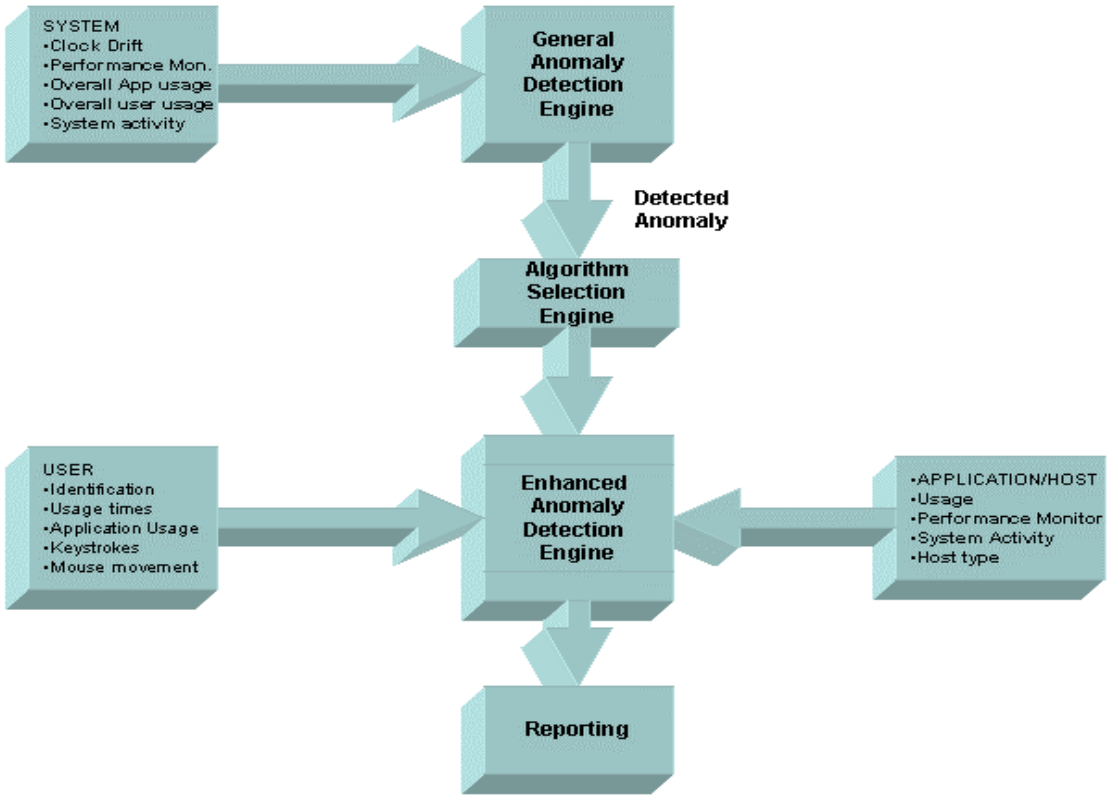

Figure 2. Block diagram

Since the implementation of the general anomaly detection engine can be accomplished in an algorithm-independent fashion, multiple algorithms could be empirically tested for preliminary suitability to the task. The added cost will be minimal while the benefit could be great.

Initially, standard systems metrics supplied by the operating system on Windows NT will be used as input into the general anomaly detection engine. If these metrics do not provide the required information to detect anomalies, we can switch to the memory harvester agents to access any information required. However, we do not expect this will be the case.

Algorithm Selection Engine

The algorithm selection engine likewise can use an algorithm that has been studied. The algorithms that have been considered for this block are commonly used in decision theory.

Fuzzy Logic

Although not all decisions in this application are fuzzy, fuzzy logic will not fulfill all decisions required of the system. Fuzzy logic would be an ideal technology (Hammell) where approximate reasoning based on those situations where fuzzy input is available. This technology might be applicable where a new exploit based on an old one might be recognized.

Case Based Reasoning

Case based reasoning has limitations in a multi-agent environment and is unable to capture deep knowledge. The ability to capture deep knowledge is a requirement when input data diverges from the norm. This is best for analogical reasoning. New problems are solved by analogy with old ones and explanations are stated in terms of prior experience.

The main disadvantage is the high cost of computation in obtaining a solution. This method may be appropriate when an unknown situation is happening. In this application, this disadvantage is better than doing nothing or waiting for a human response. Case based reasoning is most often used in the context of intelligent agents that address several issues including anticipation, experimental learning, failure avoidance, goal attainment, and adaptive behavior.

Case Based Planning

This approach centers on the generation of scenarios (a collection of examples of future events). The focus is placed on the cases that are the most relevant to the success or failure of the given plan. We will not pursue this path until proactive planning in the cyber security arena becomes a real need.

Reactive, Planning, Deliberative Components

Under the reactive, planning, deliberative architecture, information from the environment is perceived and either a reactive action or a planning action occurs. If the information is not perceived as an action or a goal, identification and recognition are needed. If the information is ambiguous or a goal needs elaboration due to an unfamiliar environment, then deliberative decision making takes place in order to commit to achieving a goal that spawns the planning. The identification and recognition and planning modules for the reactive, planning, deliberative components.

Neural Networks and Bounded Neural Networks

The following functions are well suited to artificial neural networks:

1. pattern classification
2. clustering or categorization
3. function approximation
4. optimization
5. predictions or forecasting
6. content based data retrieval
7. control.

Of particular interest, artificial neural networks have been used to successfully model the human decision-making process.

Artificial neural networks provide a cost-effective alternative to knowledge engineering. In general, artificial neural networks are a good choice for efficiently processing large amounts of data in a near real-time environment.

Disadvantages include

1. cannot transfer their knowledge
2. work on numeric data only
3. cannot use legacy information from other systems.

Unknowns include

1. What is a representative set of data?

2. How do you know when training is complete?

3. How do you know that the artificial neural networks is fully trained?

4. How do you know that the artificial neural networks has not found local minima?

5. How do you know that the artificial neural networks will generalize properly?

Genetic Algorithms and Evolution Programming

Genetic algorithms and evolution programming are unlikely to be useful in this complex near real-time reactive environment. However, genetic algorithms have been used successfully in optimizing neural networks. They may also be used to support new procedures required in a dynamic environment.

Lattice Automata

Lattice automata is a relatively new field being developed for the British defense community. Preliminary results show that a particular strength of this method is the ability of several autonomous agents to plan a simultaneous meeting time and location even in the event that the domain topology changes in a dramatic way. These agents will then be able to renegotiate a new plan. This strength could be used to coordinate several other decision-making engines, but not as part of the anomaly detection engine core.

Artificial Intelligence Planning Systems

Generative planning systems are computing intensive and are usually not considered in near real-time scenarios.

Petri Nets and Colored Petri Nets

Petri nets were developed to overcome the limitations of finite state machines, which could handle only a single event at any given time. Coordinated actions are difficult to model. Petri nets are good at describing actions, but are not good at describing the reasons behind the actions.

Petri nets have been used to model network protocols and information flow. Other applications include

1. Naval Command and Control System
2. Intelligent network simulation
3. Work flow model in a nuclear waste plant
4. Model for document storage system
5. Purdue IDIOT intrusion detection system.

At the level of this research, petri nets are not applicable. Petri nets are not suitable for detection of novel and new threats (Bace 2000).

Enhanced Anomaly Detection Engines

With the multiple algorithm solution in mind, the enhanced engines will take advantage of any algorithm specially suited to a particular scenario that is presented. The decision engine allows from one to all available engines to be engaged upon the general engine detecting anomalous behavior. This allows us to implement methodologies that span the whole solution spectrum with minimum impact to the system. The following algorithms are considered top candidates for these engines.

Operational model (Bace 2000) – event counters

- Quantitative analysis (Bace 2000)
- Threshold detection
- Heuristic Threshold detection
- Signature Analysis
- Target Based Integrity Checks
- Quantitative Analysis and Data Reduction

Statistical Methods

- Mean and Standard Deviation (Bace 2000)
- Multivariate (Bace 2000)
- Markov process (Bace 2000)
- Parametric statistical methods
- Non-parametric statistical methods

Neural Networks

- Neural networks will be used for one or more of the enhanced engines

Rule Base Approaches

- Time Based Induction Machine
- Markov.

Obviously, not all of these methods will be implemented. A subset of the above methods will be selected on the

basis of previous performance, perceived performance under the new paradigm, and the perceived ability of the algorithm to positively impact the accuracy of the final decision based on its interplay with other algorithms being used at the same time.

Results

The results of the research are as follows:

1. The current state of commercial intrusion detection is not meeting customer needs.

2. Commercial products have recognized the need for centralized management.

3. The latest thrust in commercial products is security frameworks that tie multiple security functions—including firewalls, virtual private networks, intrusion-detection systems, virus/content scanning and URL- and mobile-code-filtering—into a unified whole, thus not much progress is expected in the anomaly detection arena.

4. We see a problem with balancing a high incidence of false positives with detection of new and novel attacks.

5. Network-based intrusion detection systems have difficulty keeping up with expanding network bandwidth.

6. Host-based intrusion detection systems use inadequate information supplied by audit and log files to properly function, while network-based systems have little information on the activities inside the host.

7. Algorithms already exist that can be used for the first stage or the general anomaly detection engine.

8. Research by SRI International, Los Alamos National Laboratory, Purdue University, and others over a 17-year period have produced methodologies that are used in current commercial products. These products have nearly universally taken a one-step approach from detection to reporting. This approach has not produced results required of the market.

9. Carnegie Mellon University conducted research that produced the following results.

    a. Several non-parametric statistical algorithms were tested (Maxion 2000) against artificially produced data sets of varying structure, and the top candidate algorithms announced.

    b. Maxion (2000) announces that the intrusion detection problem cannot be properly solved on dynamically changing networks.

Summary and Conclusions

The design proposed for the advanced anomaly detection engine attempts to address the issues listed in the research results. To date, intrusion detection has focused on signature matching technologies to detect intrusions. What little research into anomaly detection that has been done so far has produced few results. Because of this, researchers have recommended that anomaly detection become a sub-field of intrusion detection so that the novel and new exploits can be detected as they happen.

With the new design in place, and a brief description of the options considered, the following conclusions are made regarding anomaly detection as a whole, then anomaly detection as it applies to this research.

Anomaly detection will be required as long as the demand for shrinking the gap between known and unknown exploits continues to exist. Proper anomaly detection is a difficult problem, but technologies exist today that can move the performance of anomaly detection devices forward. We account for the dearth of available data, using both host and network data in a very integrated manner, and bring several technologies together in an attempt to overcome the difficulties encountered.

References

Bace R. 2000. “Intrusion Detection.” MacMillan Technical Publishing.

CMAD IV - Computer Misuse & Anomaly Detection Conference, Monterey, California, November 12-14, 1996.

Dean C. Command Decision Modeling Technology Assessment, Rule Based Systems. SAIC.

Hammell II RJ, Command Decision Modeling Technology Assessment, Fuzzy Logic, Army Research Laboratory.

Maxion R. 2000. “Attacking the Insider Threat,” Carnegie Mellon University.

Maxion R. 2000. Non-parametric.

Shipley G. 1999. Intrusion Detection, Take Two. http://www.networkcomputing.com/1023/ 1023f1.html

Bibliography

Rand Report, Robert J. Hammell II, Army Research Laboratory.

Psychology Dictionary.

Command Decision Modeling Technology Assessment, Genetic Algorithms, Rick McKenzie, SAIC.

Command Decision Modeling Technology Assessment, Neural Networks and Bounded Neural Networks, Howard Mall, Dirk Ourston, SAIC.

Command Decision Modeling Technology Assessment, Lattice Automata, Andrew Webster, Defense Research Agency.

Command Decision Modeling Technology Assessment, AI Planning Systems, Christopher Elsaesser, Mitre Corporation.

Command Decision Modeling Technology Assessment, Petri Nets and Colored Petri Nets, Dirk Ourston and Noemi Paz, SAIC.

Final Report "Insider Threats To Critical Information Systems," Eric D. Shaw, Kevin G. Ruby, Jerrold M. Post, Political Psychology Associates, LTD, September 25, 1998.

GE Liepins and HS Vaccaro. Anomaly detection: Purpose and framework. In Proceedings of the 12th National Computer Security Conference, pages 495-504, October 1989.

Nina Stewart, Deputy Assistant Secretary of Defense, Counterintelligence & Security in 4 InfoSecurity News 32 (May/June 1994).

Eric Shaw, Kevin Ruby, Jerrold Post. "Insider Threats to Critical Information Systems," Political Psychology Associates, LTD, September 1998.

Bioinformatics for High-Throughput Proteomic and Genomic Analysis

William Cannon, Heidi Sophia, Kristin Jarmin

Study Control Number: PN00015/1422

Our goal is to develop the underlying science and technology for analyzing high-throughput genomic and proteomic data, and for identifying proteins and elucidating the underlying cellular networks. Biology as a system has a logical and mathematical foundation. Proteomics and DNA microarrays will provide the prerequisite data necessary for such a systematic understanding of the cell.

Project Description

The long-term objective for this project is to provide the tools for analyzing proteomic data from high-throughput mass spectrometry experiments and for elucidating cellular networks. Initial work focused on 1) developing optimal clustering tools for examining either proteomic data or DNA microarray data, 2) creating a library of graph algorithms for use in the network analysis, and 3) for conceptual development of probability networks for analyzing proteomic data.

Introduction

The goal of this project is to develop the underlying science and technology for analyzing high-throughput genomic and proteomic data, especially elucidating the underlying cellular networks. We are taking a two-pronged approach. First, statistical and/or mathematical modeling of the biological data in the form of protein/gene expression levels will inferentially determine networks of interactions. Second, previous biological knowledge in the form of known regulatory motifs at the DNA and protein levels will be incorporated to complement the mathematical modeling. These tools will be usable in isolation or in combination. It is anticipated that the combinatorial use of these tools will provide the synergy to bootstrap our way to biological networks much more powerfully than the use of either set of tools in isolation. The tools developed in the initial stage of the project will be expanded in subsequent stages to 1) incorporate the ability to statistically infer cellular networks from high-throughput data and 2) to sort the high-throughput data by cellular regulatory function as determined by, for example, cis-regulatory elements of DNA and signal peptides.

Results and Accomplishments

New Clustering Techniques

The development of new clustering techniques for proteomic data has focused on the use of NWGrid to generate clusters. The distance metric is based on Delauney triangulation and Voronoi polyhedra routines within NWGrid. Initial results using a fixed number of clusters have been encouraging. We are now proceeding to develop methods by which the program can determine the optimal number of clusters from the data itself.

Development of Software Library of Graph Algorithms for Network Analysis

Work to date has been in optimizing existing algorithms for use with expression data, and in making robust versions of the algorithms.

Conceptual Development of Probability Networks for Analyzing Proteomic Data and Strategic Planning

Much of the time during this period was spent developing the concepts needed for long-term success. This includes expanding the proposal with clear near- and long-term goals. Also, a considerable amount of time is being spent early in this project to develop a probability network model that will serve as the foundation of our cellular networks. Issues regarding connectivity of the network, nature of the data, conditional independence of data are being addressed.

Summary and Conclusion

In establishing a project foundation, we initiated new clustering algorithms and a software library for analyzing graph structures.

Collaborative Environments for Large Information Spaces

Ryan Hohimer, Richard May

Study Control Number: PN98012/1258

A true collaboration happens when multiple people interact in such a way as to understand each other, advance each other's knowledge, and make progress toward sound decisions. This research project developed an "information space" where a spatial understanding of the collaborators and the electronic and physical information that they work with was formed.

Project Description

The purpose of this project was to develop a next-generation environment for information exploration. Integration of both electronic and physical information was used to build a collaborative interaction space of people and data. Applications with dynamic electronic data, and users providing dynamic physical interaction data brought together prior research in human interaction spaces. Through experimental efforts with Jini technologies (JavaSpaces), new understandings of HI-space network communications were attained. Prototype software for network communication between a HI-space service and client was written.

Introduction

The objective of this effort was to prototype a collaborative environment by merging HI-space technology and a shared application by implementing a communications protocol between them. Previously serial mouse events were emulated by the HI-space and sent to an application computer. This mouse emulation method did not lend itself to networked or distributed or shared applications.

Although network latency issues discovered by experimenting with Jini's JavaSpaces deterred further development of JavaSpaces as an architecture for this effort, using Jini distributed computing environment technologies to discover and establish direct TCP/IP connections between HI-spaces is an architecture with promise.

Results and Accomplishments

A direct client/server shared application was prototyped to display the spatial orientation of people interacting in a remote HI-space. The client graphical user interface (Figure 1) demonstrates that remote users in a HI-space (Figure 2) can be depicted locally and the physical and electronic data they work with can be shown as well.

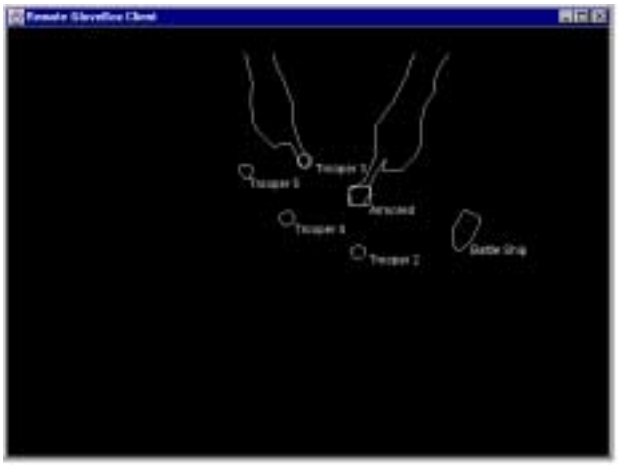

Figure 1. Projection of a client graphical user interface

Figure 2. Remote users in a HI-space environment

Summary and Conclusions

In previous versions of HI-space, the communication between the gesture recognition and the applied application computers was through simulated mouse signals. The HI-space computer generated the mouse signals and the serial mouse port of the application computer received them. The effort of this project extended the communications capabilities of the HI-space by allowing communications through socket connections to a prototype geospatial visualization application.

Distributing objects from the HI-space server to remote clients is very effective at passing a spatial context of individuals working in the HI-space environment to an observing client. At this stage in the implementation, two types of objects are shared between server and client: 1) objects encapsulating information about pointers that enter the space, and 2) objects that encapsulate the information about physical objects placed in the space.

The strong sense of the remote collaborator's spatial context in relationship to the shared information space has great promise for advancing the productivity of people working together.

Critical Infrastructure and Protection Simulator (CIPS)

Steve Ouderkirk

Study Control Number: PN99010/1338

The Department of Energy has an urgent requirement for technology to protect its computer networks and information systems. Neither current technology nor the computer security industry offers adequate capabilities for the level of cyber protection expected of DOE.

Project Description

The Critical Infrastructure and Protection Simulator (CIPS) project investigates a framework for an integral offensive and defensive cyber environment to serve as a model for simulating cyber events. This CIPS research addresses a problem of national stature. It builds additional computer security expertise at the Laboratory to address the urgent DOE computer security concerns and a specific new technology that could become key to a future DOE computer security solution. The expected research results are a cyber simulation concept that can serve as a foundation for cyber security products, a CIPS user facility, and certified infrastructure services to DOE. A simulator that includes both offensive and defensive cyber tools does not exist today. The CIPS project will investigate this possibility and will create a proof-of-concept prototype to demonstrate the essential components.

Introduction

The scope of this project was to perform research and develop a proof-of-concept prototype tool that allows simulation of computer and network cyber attacks concurrently with intrusion detection tools and other countermeasures. The objective was to create a computational environment that allows for extensive experiments with offensive and defensive cyber tools to determine their effectiveness, to determine the limitations, and to proactively explore new vulnerabilities before they occur in the real world.

Approach

The technical approach for CIPS was to develop the concept of a simulator for computer security and information assurance. More specifically, CIPS provided a framework and connectivity to leverage the many offensive and defensive cyber tools existing today into a single environment. Through software agents and encapsulation, it provided an environment for the simlution of offensive and defensive cyber security functions. The approach provided for the unfolding of capabilities as the research progresses.

Results and Accomplishments

The intent of this project was to create the tools necessary for creating a cyber security analysis laboratory. These tools would comprise the roles of cyber threat source and cyber threat mitigation. These tools would be applied to problems with testing of security policy effectiveness, security tool analysis, threat signature analysis, and security training.

The coordinated attack tool is the component of CIPS that serves as the source of cyber threats. The second-generation prototype is completed. It is planned to now be incorporated into the System Administrator Simulation Trainer program (DoD). The coordinated attack tool consists of two elements, a client (supervisor) that controls the operation and servers (agents) that execute the attacks. The client application is hosted on NT 4.0 and the server applications can be hosted on NT and UNIX systems. Figure 1 illustrates the coordinated attack tool process.

Current supervisor functionality includes

- an exploit library and database that includes over 900 applications and scripts
- manual initiation attacks against specific targets utilizing one or more agents
- attacks can include combinations of exploits from the exploit library, other exploits, and normal command line interface system commands

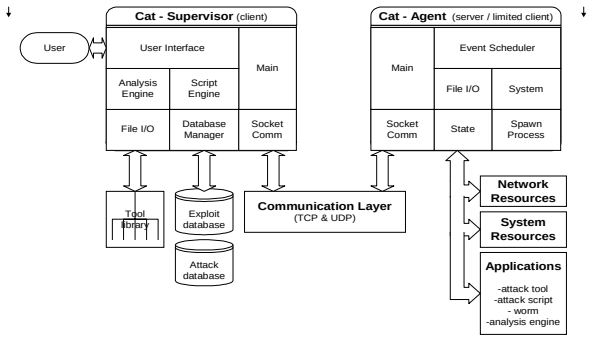

Figure 1. Coordinated attach tool process

- attacks can be recorded, edited, and played back
- recorded attacks may be archived in a library of attacks
- an attack scenario may be created, edited, and executed
- the system provides a graphical display of active agents and agent relationships
- perl scripts analyze data collected from the agents to create a characterization of the target systems.

Current agent applications provide the following functionality:

- communication by TCP/IP or UDP on any port
- ability to spawn or execute processes on the host system
- ability to execute command line interface functions on the host system
- agent scheduling for temporal coordination
- agent relay capability.

The Hacker Oriented Unified Network Defense System (HOUNDS) was intended to complement the coordinated attack tool in the simulator, serving as a locus for the integration and analysis of system defenses. Analysis of the major players performing research in the area of coordinated network intrusion detection was conducted and it was found the Intrusion Detection Working Group was actively developing a protocol for the integration of the various network-and host-based intrusion detection tools that were deployed. Since this protocol would significantly enhance the HOUNDS concept, it was decided to defer implementation until the protocol was finished.

In addition to the need to simulate computer security offense and defense, we needed to provide realistic network traffic to simulate a user base. Several venders of network traffic analyzers were evaluated to provide this functionality but none provided the degree of control necessary for a viable simulation. The hardware solutions were more appropriate for load testing and the software solutions tended to provide only unidirectional traffic that poorly modeled a real network. A proof-of-concept application (TrafficBot) was developed that allows the creation of avatars on remote systems that will mimic uni-directional and bi-directional TCP/IP network traffic. This traffic can consist of combinations of web browsing, e-mail, and replay of recorded network traffic. Further development of this will continue under the System Administrators Simulation Trainer program.

Summary and Conclusions

The CIPS project has yielded significant results in the creation of tools necessary for performing research in cyber security. This capability directly resulted in the imitation of the system administrators simulation trainer and has allowed development of infrastructure and personnel for future growth in the cyber security arena.

Interactive Network Traffic Modeling

Newton Brown

Study Control Number: PN00060/1467

The Department of Energy has an urgent requirement for technology to protect its computer networks and information systems. Neither current technology nor the computer security industry offers adequate capabilities for the level of cyber protection expected of DOE.

Project Description

The computer and network intrusion detection research field is in its infancy. This field is driven by the emerging electronic commerce, the Internet, and highly publicized and ever increasing computer hacker attacks. A total intrusion protection capability does not exist and is unlikely in the near future. Most, if not all, commercial and shareware intrusion detection solutions provide data on a small percentage of the total network transactions for external sources. These systems require highly skilled computer system administrators to configure, operate, and analyze the massive logs that they can generate. They are labor-intensive, expensive, rigid, and slow. Network traffic is dynamic and the rate of increase in volume is accelerating. Today's intrusion detection technology in the current architecture of static, signature-based configuration cannot adapt to change in an automated way. To adequately respond to these conditions, the system administrator needs to study massive logs, then reconfigure the tools for change.

The interactive network traffic modeling hypothesis seeks to enhance the infrastructure for the next generation of intrusion detection capabilities that will include the real-time display of sniffer data in the form of interactive visual and textual models. These models will have the capability to dynamically adjust sniffer collection parameters based on network conditions and the decisions made by analysis tools running on top of the models. The capability to dynamically alter collection parameters based on model changes will allow for greater detection granularity, number of incidences, and efficient use of skilled system administrators, who are costly and in short supply.

The most important aspect of intrusion detection is the ability to capture compromising threats at the time of occurrence. In today's environment, organizations assume significant risk by letting any single intrusion event go undetected. Security breaches can have a profound effect on a company's bottom line and reputation. In the case of DOE, the event could be a compromise of national security information associated with nuclear weapons.

Introduction

Within the domain of intrusion detection sensors, this research focuses on new technologies to improve the collection of data, both in quality and in quantity. First, automated control of dynamic sensors provides the capability to alter collection parameters on the fly in reaction to events. Second, for the information display component, the research focus is on displaying more data rapidly in a means readily comprehensible by the analyst. Third, for real-time capture component, the research investigates detection methods conducive to real-time processing. Integration of these three components will form a tightly coupled system that operates during the data collection process. Thus, this project is creating interactive intelligent models that will control the collection and dissemination of data for intrusion detection sensors systems and other analysis tools.

For intrusion detection sensors, the goal was to encapsulate standard network sniffers with intelligent agent technology created in the Internet Technology Library for the Internet characterization tool, presentation server, and the flash ROM projects. Advances in software agent technology specific to intrusion detection sensors were used to interface with network sniffers, to create those that can be modified, moved, and controlled at run time. This will allow for a small window of the data that we can see and process to be moved around dynamically and adjusted directly in response to certain events and thresholds. The agent event engine can allow for automated focusing on specific events based on actions or stimuli that it detects or that are defined by the analyst. Agent technology will also allow for more complex filters that can weed out noise and allow for more targeted data collections.

The second goal was to research ways to reduce the massive data logs that need to be reviewed by experts for detecting unusual events or compromises for which there is currently no signature. New concepts for log presentations will be created using multidimensional representations. Network packet data will be vectorized by mapping the packet meta data into three dimensions with source, destination intellectual property, and port numbers and time constituting the major axis. A unique clustering algorithm, which had already been developed, will dynamically convert and map Internet protocol addresses to "x" and "y" coordinate pairs while preserving network topological relationships. This approach will allow the display of current and historical network traffic data. Most intrusion detection sensors systems today work only on single packets or a small window of packets. The interactive network traffic modeling model will collect and preserve session data (collections of packets) that will allow the opportunity to detect the "low and slow" attacks which confound most intrusion detection sensors systems that are available today.

Last, the analysis techniques used for providing visual representation will also serve as a provider of updated threshold data for the sniffer sensors described above. Analysts will be able to make changes manually and programatically through the interactive network traffic modeling API in the continually updated visual model that subsequently will alter data collection agents (sniffers) allowing real-time detection and adaptation to changing events.

Results and Accomplishments

The original scope of this project was redefined as a proof-of-concept functional prototype. (See Figure 1.)

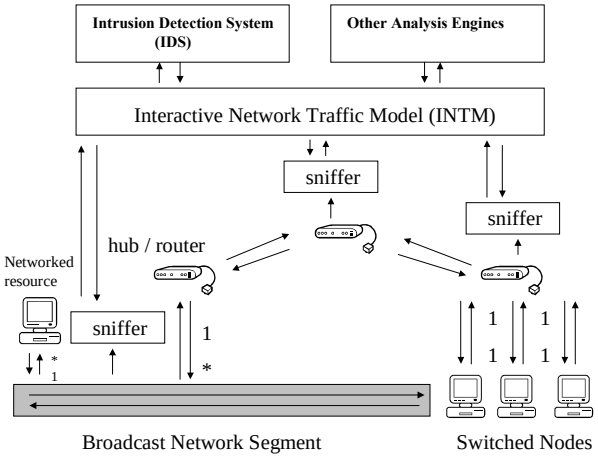

Figure 1. Interactive network traffic model architecture

Summary and Conclusions

Existing and potential DOE clients have expressed strong interest in interactive network traffic model technology. Our strategy for pursuing this technology in the Intrusion Detection field is to develop a proof-of-concept prototype to demonstrate capability and implementation feasibility. Demonstration of true, real-time intrusion detection at high bandwidth is a necessary prerequisite in this research domain.

Mathematical Learning of Patterns and Exceptions from Text

Pak Chung Wong

Study Control Number: PN99040/1368

The U.S. Department of Energy (DOE) is faced with a rapidly expanding collection of text-based information in the areas of national security and environmental cleanup and monitoring, making it nearly impossible to sort through all the information, and to determine its value. In an attempt to alleviate this problem, we developed new text mining and visualization techniques to discover hidden association rules, anomalous exceptions, and sequential patterns among major topics of large corpora. This harvested knowledge allows us to manage and understand the expanding collections of text-based information more effectively and efficiently.

Project Description

The purpose of this project is to develop new techniques and algorithms to discover hidden patterns and exceptions among major topics of large bodies of written material (corpora.) We invented multiple data mining and visualization techniques to determine association rules and anomalous exceptions of large corpora. These text-mining capabilities were further improved by introducing sequential patterns detection of large corpora. These newly developed techniques were tested and evaluated using multiple corpora.

Introduction

We introduce multiple novel techniques to discover association rules, anomalous exceptions, and sequential patterns among major topics of large corpora. As our computers become more powerful, we are able to mine larger datasets and to obtain hundreds of thousands of rules and patterns in full detail. With this vast amount of data, we argue that neither data mining nor visualization by itself can manage the information and reflect the knowledge effectively. We therefore apply visualization to augment data mining in a study of mathematical learning of patterns and exceptions in large text corpora. The results show that we can learn more, and more quickly, in an integrated, visual data-mining environment.

Approach

An association rule in our investigation is an implication of the form $\mathbf{X} \rightarrow Y$ where **X** is a set of antecedent items and Y is the consequent item. A sequential pattern is a finite series of elements such as $A \rightarrow B \rightarrow C \rightarrow D$ where A, B, C, and D are elements of the same domain. An anomalous exception is an article within a corpus that contains very different topics from the other articles.

While the definition of an anomalous article is obvious, the definitions of the other two techniques—association rules and sequential patterns can be confusing. An association rule is the study of "togetherness" of elements. An example association rule is 80% of the people who buy diapers and baby powder also buy baby oil. A sequential pattern is the study of "ordering" or "arrangement" of elements. An arbitrary example of a sequential pattern is 90% of the die-hard fans who saw the movie Titanic went on to buy the movie sound track CD, followed by the videotape when it was released.

Results and Accomplishments

This project produced multiple major techniques in text mining and visualization as documented in eight invention disclosures. In this report we highlight three visualization techniques that were designed to analyze the results of the corresponding mining engines. The details of these engines and their results can be found in our publications listed at the end of this report.

Figure 1 depicts a snapshot of a sequential pattern visualization system prototype. Each vertical axis represents the topics of one time step. Each connecting line represents a sequential pattern. Colors are used to show the support of the patterns. The beginning of a pattern is marked by a black dot. The four white dashed circles highlight the four appearances of the same two pattern sequences "plutonium → red" and "plutonium → mercury." These patterns came from the articles recorded right after the collapse of the former Soviet Union in 1992.

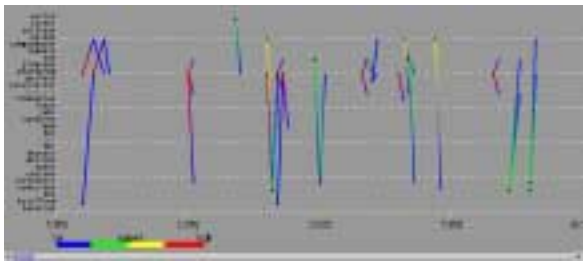

Figure 1. A visualization technique to explore sequential patterns

Figure 2 presents a novel technique to visualize many-to-one association rules. The rows of the matrix floor represent the topics, and the columns represent the item associations. The blue and red blocks of each column (rule) represent the antecedent and the consequent of the rule. The identities of the items are shown along the right side of the matrix. The confidence and support levels of the rules are given by the corresponding bar charts in different scales at the far end of the matrix. The system supports basic query commands through the use of pop-up menus to restrict key items to be included in the visualization.

In Figure 3, each data record of a multivariate data set is represented as a series of line segments that together create what we refer to as a line plot. Each line segment reflects two measures of a characteristic of that data record. Line plots are placed next to each other in the visualization such that when no variation occurs in their line segments, they are parallel with one another. When used to represent a multivariate data set, the line plots visually represent the degree to which the derived measures for each parameter vary.

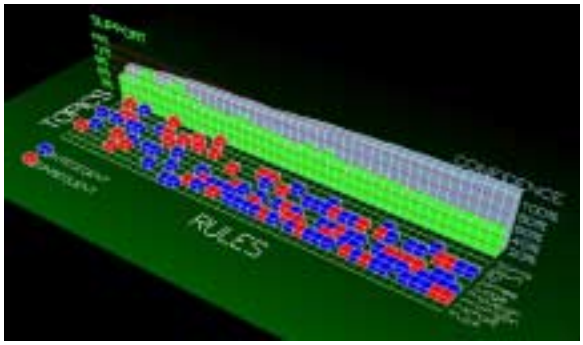

Figure 2. A visualization technique to explore association rules

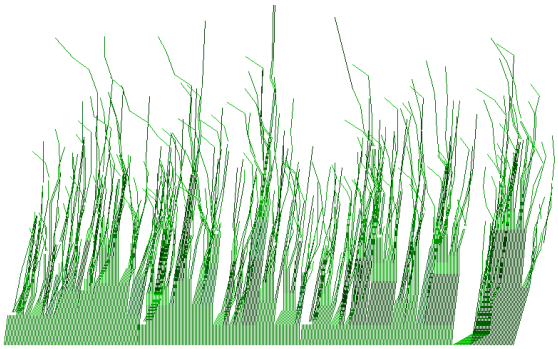

Figure 3. A visualization technique to explore anomalous exceptions of a large multivariate dataset

Summary and Conclusions

This project presents data mining and visualization techniques for discovery of patterns and exceptions from large corpora. The strengths of the two approaches (data mining and visualization) can compensate for each other's weakness. We subsequently introduced a powerful visual data-mining environment that contains multiple data-mining engines to discover different patterns and exceptions, and multiple visualization front-ends to show the distribution and locality of the mining results. Our experimental results show that we can quickly learn more in such an integrated visual data-mining environment.

Publications and Presentations

Wong PC, W Cowley, H Foote, E Jurrus, and J Thomas. 2000. "Visualizing sequential patterns for text mining." Presented and *In Proceedings IEEE Information Visualization 2000*, October 2000, IEEE Computer Society Press, Los Alamitos, California.

Rose S and PC Wong. 2000. "DriftWeed - A visual metaphor for interactive analysis of multivariate data." *Proceedings IS&T/SPIE Conference on Visual Data Exploration and Analysis*, January 24 - 26, 2000, San Jose, California.

Wong PC, P Whitney, and J Thomas. 1999. "Visualizing association rules for text mining." Presented and *In Proceedings IEEE Information Visualization 99*, October 1999, IEEE Computer Society Press, Los Alamitos, California.

Wong PC. 1999. "Visual data mining." *IEEE Computer Graphics and Applications*, 19(5).

Non-Verbal Communication in Virtual Collaborative Environments

Irene Schwarting, Scott Decker

Study Control Number: PN99053/1387

Collaborations are becoming increasingly prominent as a part of daily working life. Increasingly, work is being done between individuals in spatially separated locations who work together with data in an electronic environment. This change in working habits has pointed up an urgent need for tools that support distributed individuals in working together in real time. The tools need to enable users to represent themselves in trustworthy, reliable ways, as well as to manipulate their own representations and the data with which they are working in the collaborative environment.

Project Description

Although collaborative tools are offered for teamwork and learning, electronic communication still tends to be strictly sequential and static. This research describes a Java three-dimensional-based prototype electronic collaboration tool that supports dynamic creation of gestures and behaviors among users interacting in a data-centric virtual environment. This report also describes comparisons and evaluations of a range of interaction technologies used to control position and motion in a three-dimensional environment. In addition to enabling users to work directly with data, this technology will greatly enhance the ability of users in disparate spatial locations to effectively communicate by providing a mechanism for dynamically and in real-time manipulating the objects and user-representatives in the environment. It also has the potential to support long-term and widespread enhancements in virtual collaboration technologies.

Introduction

Three significant reasons that tools for interaction and collaboration in three-dimensional "virtual" electronic environments fail to achieve the efficiency of real, face-to-face collaboration are as follows. First, virtual tools poorly support nonverbal and social interactions. Second, traditional, two-dimensional interaction devices, such as the ubiquitous mouse and keyboard, are fundamentally unsuited for six-degree-of-freedom motion and manipulation in three-dimensional virtual worlds. Third, few virtual environments support dynamic, real-time updates to objects and the environment itself, making them unwieldy and inconvenient as interaction environments.

The research described in this report approached this issue through the use of a dynamic virtual environment in which users are represented by human-form "avatars." The user can dynamically manipulate the posture of the avatar, as well as other information objects, to move and interact with the virtual environment. This technology in a virtual collaborative workspace has the potential to increase the efficacy of distance collaboration because users can interact in real time with each other as well as collaboratively interact with data. Avatar technology is well established and a number of agencies are working with avatars in attempts to create collaborative virtual environments. This research developed a uniquely dynamic type of avatar that gets around the traditional problems of avatars and virtual environments as a collaborative tool. Through additional research in alternative interaction and control devices, we have addressed the problem of controlling movement and position in three-dimensional spaces.

Approach

The dynamic avatars software was developed based on an architecture jointly developed by the Laboratory and by the Human Interface Technology Laboratory at the University of Washington. This virtual world uses a client-server architecture based on Java and Java3D. The architecture allows for actions, such as geometry manipulation, data passing, and interactions, to happen in real time across all client machines connected to the environment. Any connected user can enter data into the environment, making it visible and accessible to all users of the environment. All types of data can be represented as dynamic objects within the environment. Visual object formats, such as Virtual Reality Modeling Language, can easily be represented, but the architecture equally supports representation of nonvisual data. Any object can be assigned any behaviors, interactions, information, and accessibility options that the user wishes to assign it. Dynamic objects interact with each other, providing each other with the ability to view their information, behaviors,

and interactions. The flexibility of the environment enables any user to add, delete, or modify objects in real time, within the environment.

This dynamic architecture naturally supports the creation of dynamic avatars. Each avatar consists of a number of independent dynamic objects (limbs) that are connected at user-defined points (joints). The objects communicate their relative positions, configurations, etc., to each other, so that, for instance, rotating the torso of the object automatically rotates the legs and arms, but the legs can be raised independently of each other. In this way, the user can posture the avatar in real time to create unique and distinctive mannerisms. As people are very good at learning and identifying people by their behavioral mannerisms, this will enable others to trust that the user is who it appears to be.

Usability evaluations conducted midway through this project indicated that the dynamic avatars had significant potential as collaborative tools by facilitating nonverbal communication. However, these studies also indicated the serious deficits of the mouse-and-keyboard control mechanism. The second year of this project, therefore, was focused primarily on developing alternative mechanisms for controlling position and motion in six dimensions. Three approaches were studied: the traditional mouse/keyboard combination, a six-degree-of-freedom controller referred to as the Spaceball™, and the PNNL-developed gesture-based controller known as the Human-Information Workspace (HI-space). Pros and cons of each of these interaction tools were identified, and a potential solution described with a prototype developed.

Results and Accomplishments

Human-form avatars were created; each with 14 independently flexible joints, including the neck, shoulders, elbows, wrists, waist, hips, knees, and ankles. The joints can be constrained to meet natural human limitations (the head cannot rotate down through the chest, for instance) or left unconstrained, at the user's choice. Figure 1 illustrates the avatars' posture and motion flexibility.

The second phase of this project explored the utility of various interaction mechanisms beyond the mouse and keyboard, which were deemed inadequate in usability testing. Initial exploration was done using a Spaceball. The Spaceball consists of a sensor ball and an array of buttons. Sensors inside the ball detect pressure: push, pull, or twist, and use that information to move the appropriate object in the virtual space. The buttons can

Figure 1. Multi-jointed avatars "dancing"

be mapped to task appropriate commands. For this effort, the buttons were mapped to the various limbs of the avatar: arms and legs. For example, to use the Spaceball controller, the user pressed a button to select for the upper arm and then pushed on the ball to contort the arm as appropriate.

The Spaceball controller provides one valid mechanism for controlling the avatars in the virtual world. However, like the mouse, it is still inherently limited to moving a single limb or object at a time. Further, the mapping of limbs to buttons must be hard-coded and cannot be dynamically adjusted. This lack of flexibility suggested that continued research needed to be done to explore alternative control mechanisms. Accordingly, the final phase of this project explored incorporating into this effort other ongoing research into next-generation interfaces. This effort uses the HI-space to posture and move the avatars. The prototype controller, shown in Figure 2, uses a video camera mounted over a table-sized surface to track the user's gestures. Selection of a body part to move is done by extending the forefinger and

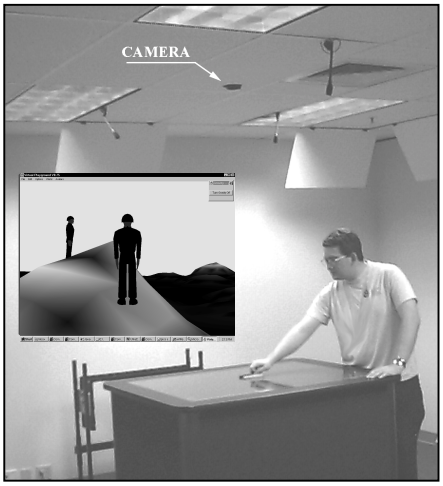

Figure 2. The HI-space being used to control an avatar

thumb in a "gun" type configuration, and snapping the thumb against the finger to cycle through limbs, stopping when the appropriate body part is highlighted on the screen. Once the body part is selected, the user simply moves his or her hand in the camera's view to move the limb. This control mechanism has the advantage of being natural and intuitive once a few basic gestures (such as the selection gesture) are learned. It is also very flexible, because the gestures that are used to control the avatar can be easily and intuitively mapped to controlling other objects in any virtual environment.

A significant disadvantage to this controller is that the HI-space is the size of a table and has a ceiling-mounted camera, an extremely inconvenient configuration. Therefore, the final effort of this project will be to develop a prototype Human-Information Workpad (HI-PAD) as illustrated in Figure 3. This desktop device incorporates a small camera mounted about 18 inches above a nonreflective black pad. The user places his or her hand on the pad and gesticulates with the fingers to manipulate the avatar or other objects in the virtual environment. This simple device, which incorporates the gesture-tracking software already developed for the HI-space, combines the natural gesture-based controls of the HI-space environment with the convenience of being mountable on a desktop and used in conjunction with a traditional keyboard and/or mouse.

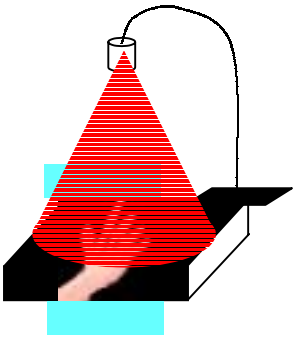

Figure 3. Illustration of the HI-PAD concept. The cone indicates the field of view of the infrared camera mounted above the hand pad.

This research has applicability in a wide variety of applications. Some of the most obvious arenas where dynamic virtual environments and dynamic avatars would be of value are the following.

Simulations and training

The ability to dynamically interact with a simulated environment will enormously increase the flexibility and versatility of a wide variety of simulation applications. Although this effort used human-form avatars to illustrate the flexibility and adaptability of the dynamic virtual environment, the same properties could be applied to any sort of virtual object. For instance, the avatar might be a plane, in a flight simulation, or a tornado, in a disaster-recovery scenario.

Modeling

To reiterate the discussion of simulations and modeling, there is no reason to constrain the dynamic avatars to human form. The collaborative, dynamic nature of the avatars, combined with the infinite flexibility of scale inherent to virtual worlds, will support a variety of collaborative modeling applications.

Telemedicine

The ability to represent both physicians and patients in a virtual environment could be superior to a real surgical environment because medical images can be overlaid or integrated with a representation of the entire patient. Micro- and macro-level views can be simultaneously available. Finally, physicians can use realistic physical interaction and dynamic behavior in the virtual environment to explore range-of-movement exercises without risk.

Virtual command posts

This tool will enable commanders in distributed physical locations to coordinate as efficiently as if they were physically collocated.

The DNA Approach to Organic Data Memory

Pak Chung Wong, Kwong Kwok Wong, Harlan Foote

Study Control Number: PN00085/1492

We can create and alter existing DNA sequences. With a careful coding scheme, we have shown that we not only are able to put important information in a tiny DNA sequence safely and permanently but also are able to retrieve it later. This technology has many potential applications, including storing and protecting information.

Project Description

The purpose of this project is to prove that we can plant and recover meaningful information in DNA sequences. Our results show that we can store a sizable amount of information in the DNA strands of certain micro-organisms, such as bacteria. The treated bacteria in our experiments were able to grow and multiply with the embedded information. More importantly, we were able to retrieve all the information from the bacteria.

Introduction

A data preservation problem looms large behind today's information superhighway. During the prehistoric age, people preserved their knowledge by engraving bones and rocks. About two millennia ago, people invented paper and started writing and publishing. In today's electronic age, we use magnetic media and silicon chips to store our data. But bones and rocks erode, paper disintegrates, and electronic memory simply loses its contents. Each of these storage media require constant attention to maintain their information content. Each can easily be destroyed intentionally or accidentally by people or natural disasters. Because of the vast amount of information generated by society, we undertook new efforts to explore a new generation of data memory.

Results and Accomplishments

The creation of our DNA memory prototype consisted of four major steps:

1. encoding meaningful information as artificial DNA sequences
2. transforming the sequences to living organisms
3. allowing the organisms to grow and multiply
4. extracting the information back from the organisms.

We were successful in all four steps. Figure 1 shows a part of the DNA analysis after the last step of our experiment. The English interpretation is a part of the Disney theme song, "It's a Small World" (Sherman and Sherman 1963).

Summary and Conclusions

With the current technology, we can generate artificial DNA molecules or alter the DNA sequences of existing DNA molecules. With a careful coding scheme and arrangement, we have shown that we can encode important information as an artificial DNA strand and store it safely and permanently in a living host. This technology can be used to identify origins and to protect research investments such as agricultural products and endangered species. It can also be used in environmental research to track generations of organisms and observe the ecological impact of pollutants. Today, there are microorganisms that can survive heavy radiation exposure, high temperatures, and many other extreme conditions. They are among the perfect protectors for the otherwise fragile DNA strands that preserve our encoded information. Finally, we have living organisms such as weeds and cockroaches that have existed on earth for hundreds of millions of years. These organisms may be candidates for preserving critical information for future generations.

Reference

Sherman RM and RB Sherman. 1963. "It's a small world." The Disneyland and Walt Disney World Attraction, California.

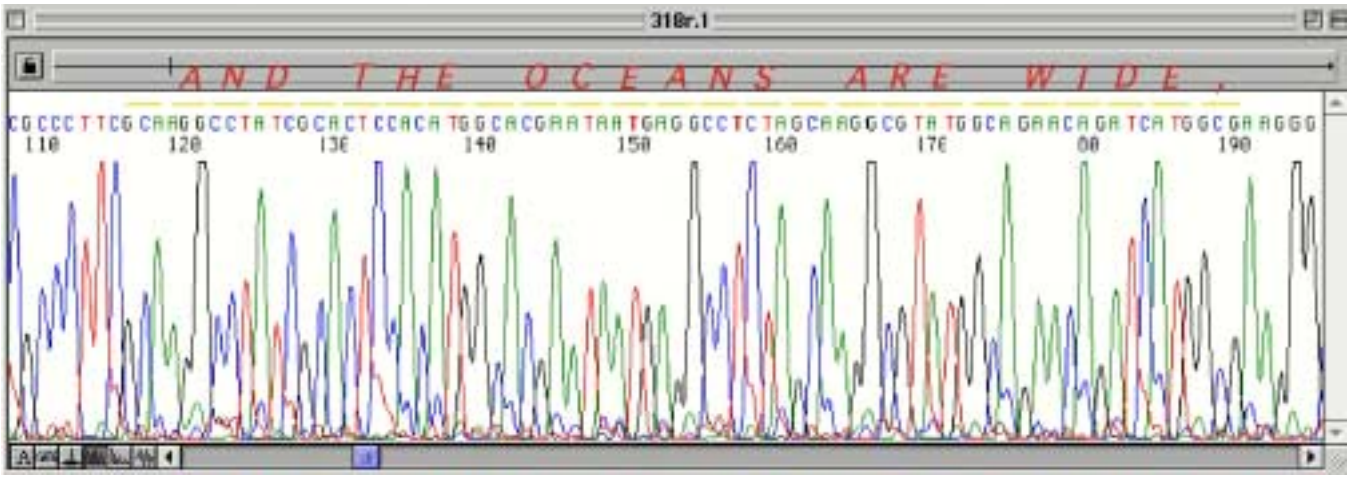

Figure 1. DNA analysis result and its interpretation. The English text is a part of the Disney theme song, "It's a Small World."©

Visualization and Active Guidance of Scientific Computations

Pak Chung Wong

Study Control Number: PN99078/1406

We developed the concept of a data signature, which captures the essence of a large, multidimensional scientific data set in a compact format, and used it to conduct analysis as if using the original. Our results have shown that the technology can be applied to a wide variety of computational sciences and engineering studies—such as climate, combustion, imaging, and computational fluid dynamics.

Project Description

The purpose of this project is to develop the concept of a data signature that captures the essence of a multi-dimensional scientific data set in a compact format, and use it to conduct analysis as if using the original. A data signature, because of its compact design, always requires fewer computational resources than its original. We developed two novel approaches based on feature extraction and wavelet transforms for creating data signatures of very large time-dependent data sets. We successfully developed our first signature design (feature-based) on multiple parallel and desktop computer platforms. This system was applied to different simulation studies, including global climate and combustion. The experimental results were documented in two peer-reviewed journal and conference papers.

Introduction

Today, as data sets used in computations grow in size and complexity, the technologies developed over the years to manage scientific data sets have become less efficient and effective. Many frequently used operations, such as Eigenvector computation, could quickly exhaust our desktop workstations once the data size reached certain limits. While building new machines with more resources might conquer the data size problems, the complexity of today's computations requires a new breed of projection techniques to support analysis of the data and verification of the results. Our solution is the data signature, that captures the essence of a scientific data set in a compact format and is then used to conduct analysis as if using the original.

A data signature can be described as a mathematical data vector that captures the essence of a large data set in a fraction of its original size. It is designed to characterize a portion of a data set, such as an individual time frame of a scientific simulation. These signatures enable us to conduct analysis at a higher level of abstraction and yet still reflect the intended results as if using the original data.

Approach

To date, we have investigated designing signatures for scalar fields, tensor fields, and a combination of them with multiple parameters. The construction of a data signature is based on one or more of the following features and approaches:

- velocity gradient tensors
- critical points and their eigenvalues
- orthogonal and non-orthogonal edges
- covariance matrices
- intensity histograms
- content segmentation
- conditional probability.

The selected features often depend on data type. Information such as velocity gradient and critical points is suitable for vector and tensor field data. Edge detection, covariance, and histogram can be applied to scalar data. For large scientific simulations, we sometimes rely on a multi-resolution approach to determine the desirable size of the signatures.

Results and Accomplishments

In theory, a data signature can never be as descriptive as its full-size original. In practice, however, a well-defined data signature can be as good or better from many perspectives because it brings out specific details and eliminates less important information from consideration. The concept is useful when we study the characteristics of scientific simulations, such as global climate modeling.

We demonstrate our design using a climate modeling data set provided by the Laboratory's Global Change Program. The basic multivariate time-dependent data set has all the characteristics and features for experiments. The data set has five data variables (pressure, temperature, water vapor mixing ratio, and two wind-velocity components) of different types (scalars and vectors) and dimensions (two- and three-dimensional) recorded daily.

Figure 1 shows a cluster analysis of 92 scalar fields (water vapor flux) encoded into grayscale images with the highest moisture value mapped to the white end. Each of the individual three-dimensional scalar fields, shown in Figure 1 as two-dimensional images for simplicity, has over 120,000 real numbers. Each of the data signatures that represent individual scalar fields in the cluster analysis has only 200 real numbers. The analysis process clearly separates individual images into clusters according to their patterns and characteristics.

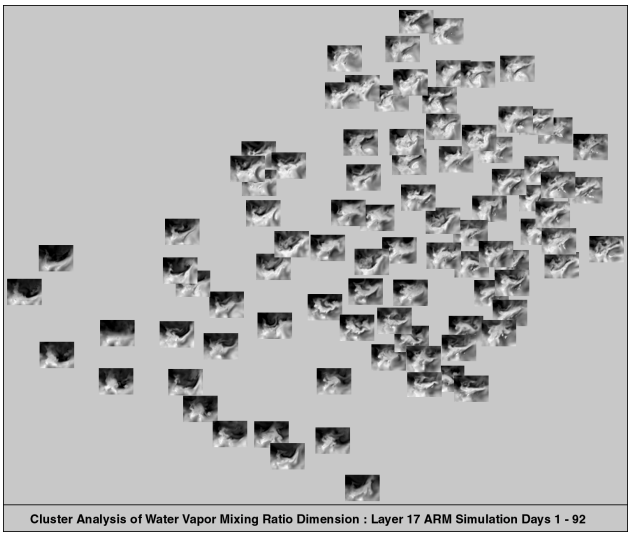

Figure 1. A cluster analysis of 92 scalar fields of a time varying climate simulation

Our data signature approach is powerful and flexible enough to merge multiple data dimensions of different data types into a signature vector for computation. In this example, we merge a scalar field (water vapor flux) and a vector field (wind velocity) for each of the 92 simulation steps into a single signature for cluster analysis. Figure 2 shows 92 icons (one for each signature) that are color-coded according to the sequential order of the simulation. The simulation starts from the left (red and orange), across the middle (yellow, green, and cyan), and stops at the right (blue and purple). The three-dimensional scatterplot based on the combined signatures correctly separates the seven periods that are characterized by three heavy rainfall episodes (orange, green, and blue) in the simulation.

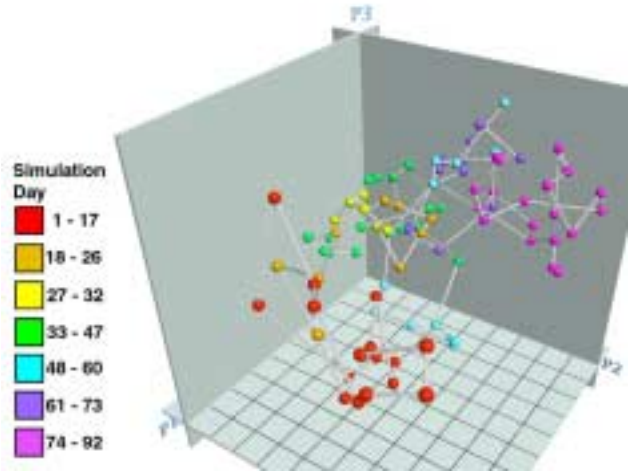

Figure 2. A cluster analysis of 92 scalar and 92 vector fields of a time varying climate simulation

We also explored the idea of using data signature in scientific data mining and developed a feature decimation technique to simplify a vector flow field in visualization. Figure 3 shows a three-dimensional atmospheric space crowded with flow field information such as critical points, flow field lines, and boundary regions. Figure 4 shows a filtered version of Figure 3 with threshold relative vorticity magnitudes of 6. In both Figures 3 and 4, critical points are grouped together into saddle (cross) and non-saddle (cube) classes to simplify the visualization.

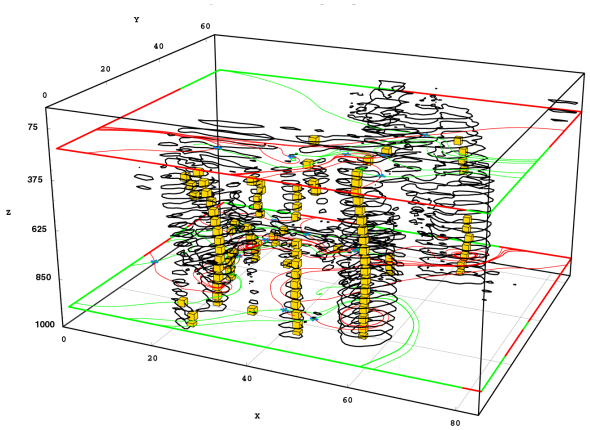

Figure 3. An atmospheric data volume with all critical points and field flow lines

Summary and Conclusions

Data signatures allow scientists with limited resources to conduct analysis on very large data sets at a higher level of abstraction. Its novel design is flexible enough to merge different data types into a quantitative data vector

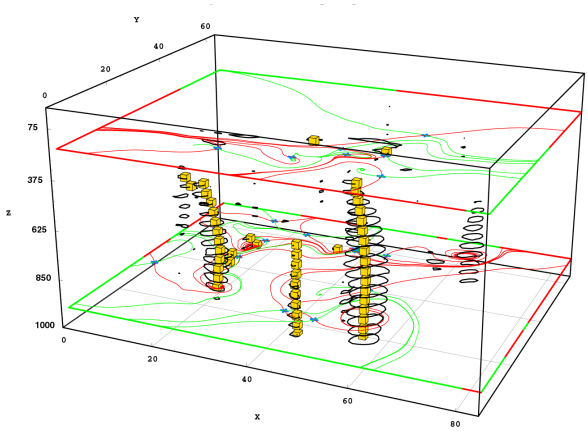

Figure 4. A filtered version of Figure 3 with threshold relative vorticity magnitudes of 6

for scientific computation and analysis. Our examples show that we can apply the data signature concept to cluster analysis of different kinds of scientific data sets. The results also suggest that the data signature approach shows promise in simplifying the analysis and understanding of large data sets. Our approach is still under active development. Among the ongoing tasks is to develop a new wavelet-based data signature design.

Publications and Presentations

Wong PC, H Foote, R Leung, D Adams, and J Thomas. 2000. "Data signatures and visualization of scientific data sets." *IEEE Computer Graphics and Applications* 20(2):12-15.

Wong PC, H Foote, R Leung, E Jurrus, D Adams, and J Thomas. 2000. "Vector fields simplification – A case study of visualizing climate modeling and simulation data sets." Presented and *In Proceedings IEEE Visualization 2000*, IEEE Computer Society Press, Los Alamitos, California.

Design and Manufacturing Engineering

Development of Modeling Tools for Joining of Multicomponent Lightweight Structures

Mohammad A. Khaleel, Ken I. Johnson, John E. Deibler, Richard W. Davies

Study Control Number: PN00034/1441

Welded assemblies of hydroformed aluminum structures are critical to developing fuel-efficient vehicles. This project is developing methods to facilitate the implementation of these lightweight structures.

Project Description

The objective of this project is to develop computational methods and simulation tools for predicting weld durability of hydroformed thin-walled aluminum alloy extrusions and tube assemblies, and to gain a fundamental understanding of the effects of severe deformations associated with hydroforming on the weld microstructure, residual stress state, and distortions in welded assemblies. The technical work involves developing numerical procedures to simulate the hydroforming process in a parallel computing environment and predicting formability to optimize the process conditions for a given part geometry and tube or extrusion material. Computational methods and simulation tools for modeling welding operations of individual multi-weld joints also are being developed.

Introduction

The goal of developing more efficient vehicles has prompted the increased use of lightweight materials. Hydroforming of aluminum components is a developing technology for the production of automotive structures. Complex lightweight assemblies then can be fabricated by welding or other joining techniques. To date, the experience of manufacturers with hydroforming is primarily trial-and-error with little understanding of the process parameters (pressure, end feed, material behavior) necessary to achieve geometrically stable parts. Similarly, the development of welding procedures for aluminum structures to minimize weld distortions has been empirical and is complicated by the residual stresses caused by the severe deformations associated with hydroforming. In addition, concerns have been raised concerning weld durability and the effects of material thinning in long-term fatigue and impact situations. The goal of this project is to develop modeling tools that can be used to optimize the process conditions for a given part geometry and tube or extrusion material and predicting the distortions of large assemblies composed of hydroformed components.

Results and Accomplishments

Computational Methods for Optimization of Hydroforming Process Parameters

The MARC finite element code was used to simulate expansion of a tube into a conical die. MARC was chosen for this work because of the ability to develop user-defined control routines (MSC Software Corporation 2000). During the forming process, several limiting conditions must be considered in determining the proper combination of pressure and end-feed. These include the

- axial load required to seal the mandrels in the ends of the tube
- column buckling of long tubes (high length-to-diameter ratio) during initial sealing and end-feed
- local, axisymmetric wrinkling of shorter tubes (lower length-to-diameter ratio) during end-feed
- bursting due to eventual unstable, local wall thinning.

Our basic strategy was to apply maximum end-feed throughout the forming process, which introduces more material into the die to minimize thinning. Axial compression also causes yielding and plastic deformation to occur at lower pressures, which are beneficial from a forming limit consideration.

A user-subroutine was written to track several parameters in the finite element solution that indicate the development of an unsupported wrinkle in the tube. These include

- localized bending strains that indicate formation of a wrinkle around the circumference of the tube

- localized motion of the elements in the direction normal to the plane of the shells

- significant softening in the axial stiffness (change in axial force/end-feed displacement) indicating instability of the cross section under axial load.

The combination of both high bending strain and high normal velocity is a strong indicator that unstable deformation is occurring. Elevated bending strain is allowed to occur alone when the tube wall bends to conform to the die surface. In that case, the bending strain would be high, but the element normal velocity low. Softening of the axial stiffness will also result when a full circumferential wrinkle forms. However, this may be suppressed if the tube is being formed into a nonsymmetric die such as a T-section. Therefore, an additional parameter is calculated to estimate the circumferential extent of the wrinkle. Rings of elements along the length of the forming tube are checked and the ratio of wrinkling elements (both high bending strain and normal velocity) divided by the total number of elements in the ring is calculated. A value of one indicates the full circumference is wrinkling.

The test problem geometry (Figure 1a) involves forming a tube into a conical die shape. Because this tube is relatively short, wrinkling is the primary mode of axial instability (rather than buckling). Both the shell model and a finer axisymmetric two-dimensional model (Figure 1b) were used to test the control routine.

Material Data and Constitutive Equations for Modeling Implementation

The material data and associated constitutive equations required to develop accurate finite element models of the hydroforming process were investigated. Most aluminum alloys for hydroforming are produced by extrusion. The extrusion process normally results in tubular materials with crystallographic textures that have the primary slip planes oriented in particular directions. Therefore, extrusion produces a tube with the flow stress heavily dependent upon the direction of material loading. An experimental investigation of this material anisotropy was conducted with a typical extrusion material to develop an anisotropic yield criterion for use in the finite element model. A tube was instrumented with strain gauges to measure the circumferential and axial strain and was subjected to different stress ratios of axial load and internal pressure. These experiments were conducted on

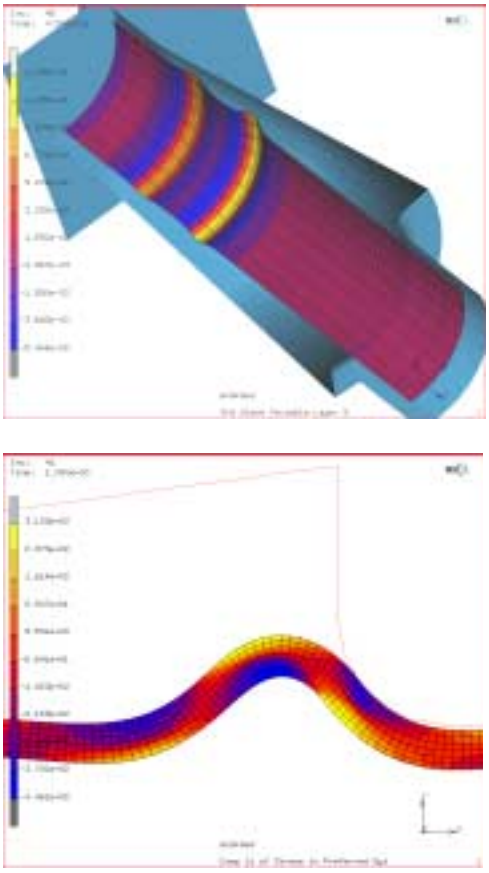

Figure 1. Tube formed into a conical die shape (top); Axisymmetry two-dimensional model (bottom)

a new tube and the same tube after 15% plastic strain was applied. Comparison of the experimental data to an isotropic von Mises yield criteria showed that the flow stress is significantly anisotropic.

Hydroforming may be performed using many different operating conditions. Therefore, a complete description of the formability of the material under different directions of loading is required. Biaxial stretching experiments were conducted on AA6061-T4 material to determine the forming limit diagram for the material. A sample population was subjected to a series of experiments to determine the level of plastic strain that developed under various ratios of internal pressure and axial load. A schematic of the experimental apparatus is shown in Figure 2, which also illustrates typical results for a single population of samples tested under free hydroforming conditions. The specimens are arranged in this figure such that the bottom specimen received the highest axial compression during testing, and the top specimen was a uniaxial tensile specimen (with no internal pressure). If axial compression was imposed on a tube specimen in excess of the specimens in Figure 2, buckling and wrinkling began to occur. Regions

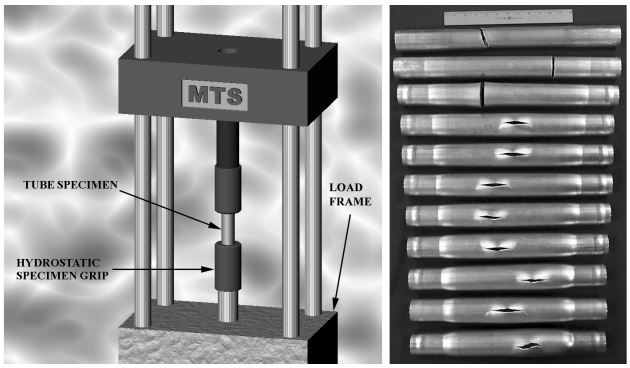

Figure 2. Schematic of experimental apparatus and photo of sample tested

surrounding the fractures were characterized using a strain grid analysis system. This system determined the magnitude of strains that developed in the specimen in the region around the failure. Each of the originally 2.54 mm square grids characterized in the area surrounding fracture were identified as necked if the nodes near the failure showed elevated levels of local strain (necking) in the grid, or the fracture had penetrated under (undercut) the grid surface. These types of forming limit definitions must be defined and applied in the finite element analysis in order to accurately capture the material limits of formability.

Welding Experiments and Modeling

The experimental fixture shown in Figure 3 was constructed for use in validating the weld modeling. An automated TIG welding system was used to provide accurate control of the welding parameters (electrode speed, welding current, and voltage). Their parameters were recorded at selected intervals and used as inputs to the finite element weld models.

Figure 3. Experimental fixture for use in validating the weld modeling

Welds were performed in the circumferential direction on 6-inch outside diameter by 0.125-inch wall thickness 6061-T6 aluminum tubing. Thermocouples were located at various distances from the weld. The weld was also monitored with strain gauges located opposite the weld. Data were recorded to characterize the temperature profile and development of distortions in the tube. Data were also recorded periodically during cool down after the weld was completed. The gross distortion in the tube was measured at the end of the test for comparison with the modeling results.

Finite element analyses of the experimental welds on the aluminum tubes were performed using MARC analysis. A three-dimensional shell model representing the tube was constructed. The weld was modeled in two steps, a thermal analysis followed by a structural analysis with the loading provided by the temperatures from the thermal analysis. The heat input to the thermal model was based on the voltage, current, and electrode speed used during the experiment. Figure 4 shows the comparison of the analytically determined temperatures with the thermocouple data. Strains from the structural model were compared to the strain gauge data taken during the test. The final distortion was then compared with the experimentally determined deformation.

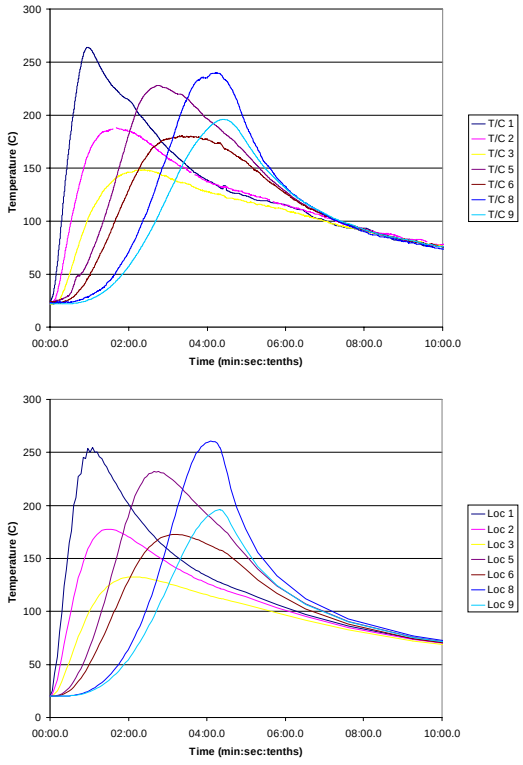

Figure 4. Comparison of the analytically determined temperatures with the thermocouple data

Summary and Conclusions

We developed computational methods and simulation tools for predicting weld durability of hydroformed thin-walled aluminum alloy extrusions and tube assemblies

and gained an understanding of the effects of severe deformations associated with hydroforming on the distortions in welded assemblies. Our accomplishements included the development of numerical procedures to simulate the hydroforming process and to predict formability to optimize the process conditions for a given part geometry and tube/extrusion material.

Reference

MSC Software Corporation. 2000. "MSC MARC, Volume D: User Subroutines, Version 2000." Los Angeles, California.

Publications and Presentations

Davies RW, GJ Grant, MA Khaleel, and MT Smith. 2000. "M-K method analysis of formability during biaxial stretching of weld joined dissimilar sheet metals." *In Proceedings of Plasticity' 2000.*

Davies RW, GJ Grant, MA Khaleel, and MT Smith. 2000. "Forming Limit diagrams of Tailor Welded Blanks" *Metallurgical and Materials Transactions A* (accepted).

Davies RW, MT Smith, and MA Khaleel. 2000. "Formability of aluminum extrusions during hydroforming applications." *In proceedings of Automotive Alloys 2000, TMS Annual Meeting,* March 15, 2000.

Integrated engineering modeling and simulation environments – presented as an invited talk at the first AMER-PAM User conference, November 1, 1999.

Hydroforming of Steel Structures – presented to the American Iron and Steel Institute on March 15, 2000.

Formability of Aluminum Extrusions during hydroforming Applications – presented at TMS Annual meeting, Nashville, Tennessee, March 16, 2000.

Integrated Modeling and Simulation for Fabrication of Lightweight Structures

David A. Thurman, Kenneth I. Johnson, Kristine M. Terrones, Deborah K. Gracio

Study Control Number: PN99031/1359

The next generation of vehicles (cars and trucks) will be made of lighter weight materials than todays vehicle. This project provides DOE with an opportunity to develop an integrated modeling and simulation environment for manufacturing of lightweight structures with minimum trial and error in process development and expand the ability to manufacture larger components with increasing complexities.

Project Description

This project developed modeling and simulation technologies for lightweight material manufacturing and performance assessment to provide the means for an integrated simulation capability. This effort provides software tools to ensure that data is passed accurately from one finite element simulation to the next so that the effects of the deformation history and material microstructural evolution of one process to another can be predicted. By employing a common data format for representing finite element results, developing data transformation tools to translate between commercial finite element codes and the common data format, and data pedigree representations to ensure that an accurate simulation history is kept, such a capability will have dramatic impact on the overall design and manufacturing process and enable the "all-digital mock-up" of manufacturing of lightweight materials.

Introduction

The automotive industry is interested in using larger components to build future cars. To cost-effectively utilize the performance attributes of aluminum products, designers are altering traditional design practices that historically have been used for steel components. Material producers and automotive companies have limited experience with making parts from lightweight materials that in turn will increase the trial and error in tool and process development.

This research is focused on a problem experienced by engineers who use multiple commercial finite element analysis packages. The basic problem is that commercial finite element analysis products use proprietary file formats, and few are compatible with the others. As a result, engineers spend vast amounts of time massaging the output of one finite element analysis package to prepare the input deck for another. The primary goal of this project is to create the ability to perform sequential analyses so that information is passed between analyses while preserving the material history effects.

Approach

The activities on the project can be roughly grouped in the following four areas.

***Engineering Data Representation*—**Focused on the development of data translation tools, together with a common data format, to support the transfer of data among existing finite element codes at PNNL.

***Remeshing and Remapping Capability*—**Provided the capability to modify the mesh and map the results data onto the modified mesh between steps in multistep simulations is critical to the success of these efforts. To accomplish this, the NWGrid-based remeshing and remapping capability was integrated into the integrated modeling and simulation suite of tools by providing data transformation capabilities between the common data format and the NWGrid format.

***Data Pedigree Representation*—**Focused on defining what information should be stored in a data pedigree and how to collect and store such information when engineers are using commercial codes in distributed environments. In multistep simulation efforts, the accurate recording and retrieval of such information will enable scientists to facilitate the reuse of research results where relevant.

***High-Performance Computing*—**Explored issues associated with the use of high-performance computing environments to run larger and more complicated models more efficiently which is of great interest to scientists in this area.

In addition, three test problems were defined to demonstrate the combined capabilities of these efforts.

The three problems were built on one another and demonstrate the ability to simulate a sequential metal forming/joining process using simple finite element models that include the features of larger industrial manufacturing problems. The three test problems used to demonstrate research outcomes are described below.

Results and Accomplishments

In keeping with the four focus areas, the results and accomplishments of this effort are presented below, followed by a description of the results obtained from the three test problems that demonstrate the capabilities of the integrated suite of tools.

Engineering Data Representation

We extended the use of Exodus as a common data format and provided the capability to store stress/strain data in addition to deformed geometry and thickness.

We also developed data transformation tools to convert between the Exodus-based common data format and the following commercial finite element codes:

- MARC Analysis (output format)
- MARC Analysis (input format)
- PAM-CRASH (input format)

Last, we developed and extended of a number of MARC "user routines" to ensure that the appropriate data was accessible to enable the appropriate transformations.

Remeshing/Remapping Capability

We explored the use of commercial remeshing tools (e.g., Hypermesh) to provide required remeshing capability with the idea of adding a remapping capability through some other means. This effort was abandoned when a NWGrid-based remeshing and remapping capability appeared feasible.

We also developed data transformation tools to support translation between common data format and formats used by NWGrid.

Last, we integrated NWGrid-based remesh/remap capability into an IMS tool suite to provide the capability required for the demonstration of test problems 2 and 3 (see below).

Data Pedigree Representation

We defined data representations (object representations) for information that must be captured as part of a data pedigree during multistep finite element simulation efforts.

We also explored similar data pedigree efforts on other projects, including ARM, the regional climate modeling, Ecce, and the DOE 2000 projects and collaborated with CPSE projects on the use of WebDAV technologies for storage of result sets and data pedigree information.

We designed and completed a "model transformation tool" to invoke data transformation tools and gather pedigree information from users.

High Performance Computing

We demonstrated that the CDF-to-PAM-CRASH data transformation tool works for simulations run on the Zodiac. Currently, we are building on the accomplishments in these four areas, three test problems were undertaken to demonstrate the integrated modeling and simulation capabilities provided.

Test Problem 1—Analysis Restart

The first test problem simulated a two-step stretch-forming of sheet metal between a spherical punch and a cylindrical die (see Figure 1). At the completion of this step, the common data format had the capability to store stress/ strain data, data transformation tools were completed to convert between the common data format and Marc input and output formats and, subroutines were written to transform the model data from the local shell element system to the global coordinate system for storage in the Exodus common data format.

Since the element results are based on the shape and orientation of each element, the element coordinates and their shape functions were used to perform the data transformations for each individual element. Figure 2 shows the detailed multiple data transformation steps associated with this process and the data translators that were developed to execute this example problem. This example problem performs a restart analysis without saving the standard MARC restart file. It provides, a demonstration of the capability to save results from MARC into the common data format and

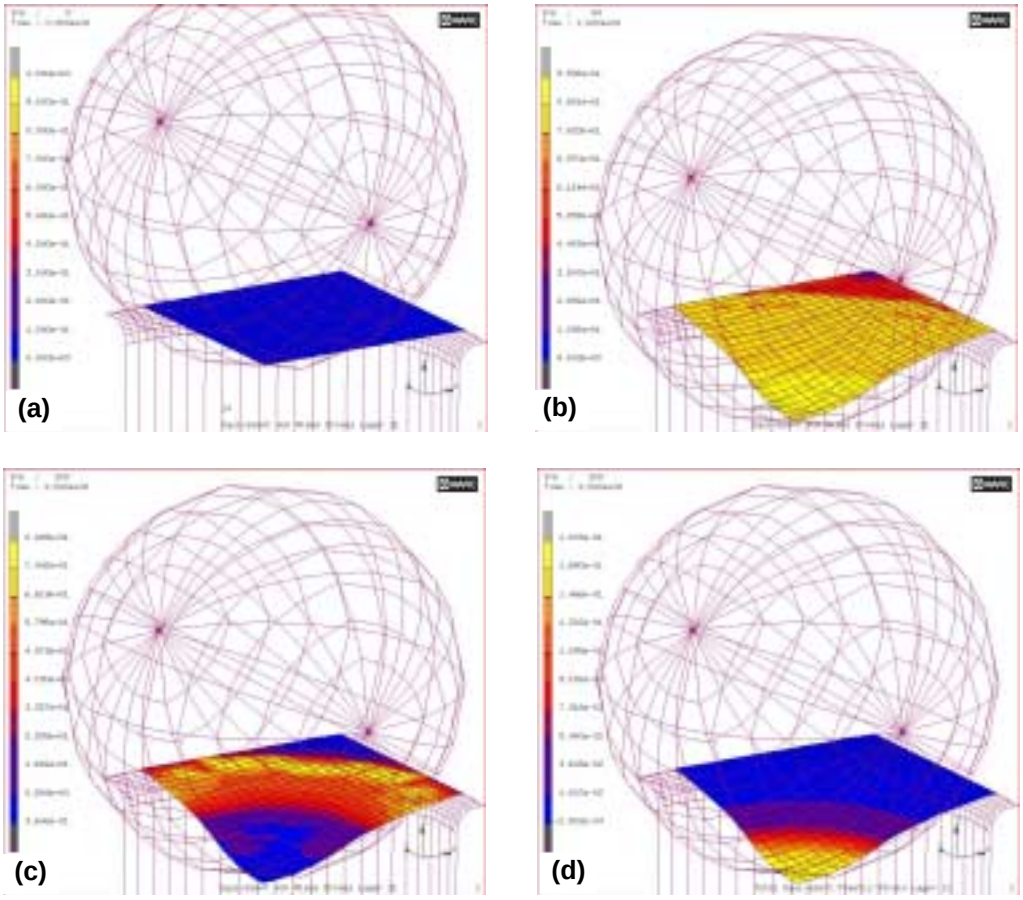

Figure 1. Results of Test Problem 1. First Stage of two-stage stretch-forming using an spherical punch and cylindrical die. (a) Initial flat sheet, (b) Equivalent stress, punch displaced 15 mm, (c) Equivalent stress, punch retracted to 13 mm, and (d) Equivalent plastic strain after punch is retracted.

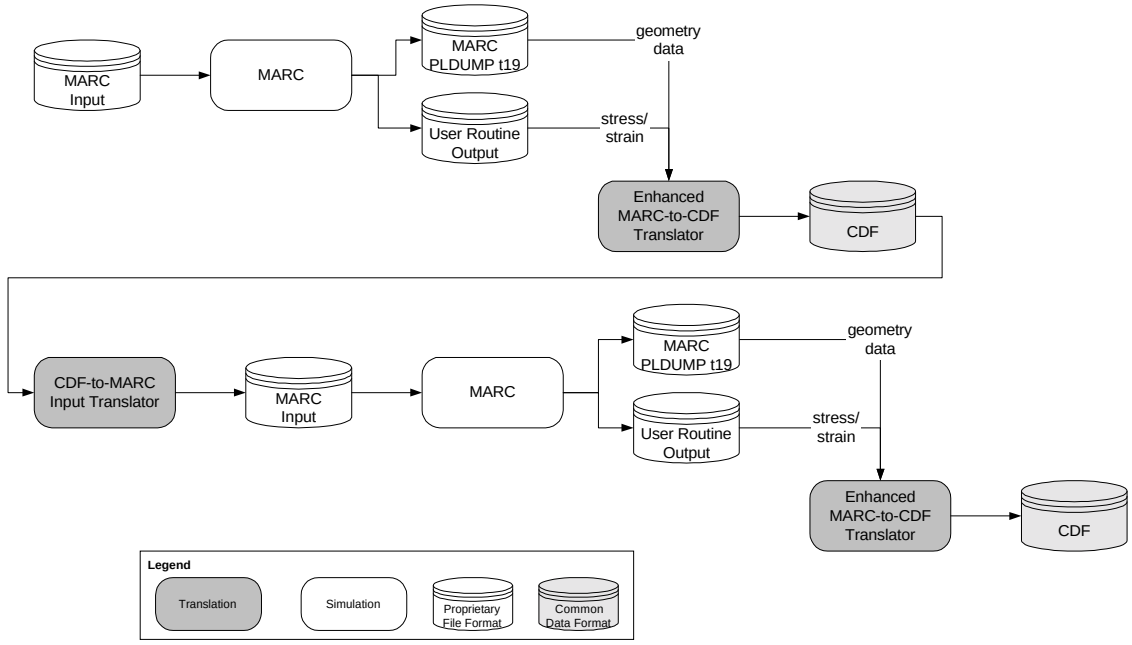

Figure 2. Processing and translation steps and intermediate files produced in Test Problem 1

subsequently transform them back into the MARC input format. This capability was crucial to the subsequent example problems that incorporated remeshing and multiple analysis steps. Figure 3 shows the second stage for the stretch forming process. A continuous 2-step analysis was also performed in MARC to confirm that the results were for all purposes identical.

Test Problem 2

The second problem added mesh refinement to Test Problem 1. The goal was to stop the forming analysis, refine a region of the mesh, remap the intermediate results to the new mesh, and restart the analysis. Using internally developed gridding software, NWGrid, we developed data transformation tools to convert between the common data format and NWGrid. Modifications to NWGrid were required to support shell elements with multiple layers and support the reflection of results. Figure 4 illustrates the additional data transformation routines that are required to support the remapping of model results between different meshes. Figure 5 compares the equivalent plastic strain distributions at the intermediate forming stage for the original analysis in Test Problem 1 with the refined mesh in Test Problem 2. Figure 5 also shows the significant capability in NWGrid to reflect the results to construct a full 360-degree model from the previous ¼-symmetry model. This is an important capability when the forming process is symmetric, but subsequent operations; such as welding, introduce non-symmetric thermal or mechanical loads.

Test Problem 3

The intent of the third problem was to combine and extend the capabilities developed for test problems 1 and 2 to prepare the meshes for a welding analysis shown in Figure 6. The schematic of the complete process is shown in Figure 7. The goal was to map the results of a forming simulation to a new mesh that included the necessary mesh detail to simulate joining of a beam to the hydro-formed part. Mesh refinement is also necessary in this case to capture the thermal gradients of the welding analysis. Remeshing the formed part to have coincident node spacing with the attached beam proved to be an ambitious goal, and this problem was only partially completed with the allotted funding. Figure 6 shows a final thickness plot of the hydroforming analysis and the combined meshes of the hydroforming analysis and the beam introduced for welding. However, additional work is required to generate a mesh at the intersection of these two geometries that was well defined enough to provide accurate analysis results. This work was still in progress.

Summary and Conclusions

The software components developed under this effort now provide scientists and engineers with the ability to perform integrated multistep finite element analysis using a small collection of commercial finite element software applications. The present work to support the use of NWGrid further promises to extend this capability to provide robust remeshing/remapping capabilities.

Critical technical issues have been identified and addressed, providing a robust solution to integrated modeling and simulation needs of automotive manufacturing scientists and engineers. Future development efforts should expand the collection of data transformation tools to support additional finite element application formats. Future research efforts should focus on increasing the ease with which NWGrid can be used by scientists and engineers, the incorporation of material properties into the common data format and data pedigree representations, and the development of a Web-based architecture for supporting data transformation tools (i.e., Web-based translation services).

Presentations

Johnson KI. September 2000. "Integrated Modeling and Simulation, Joining of Hydroformed Structures, Glass Process Modeling." Presented to Reza Sadeghi and John Long, MSC Software Corporation.

Thurman DA. February 2000. Collaborative Problem Solving Environments: What Use Are They? Policy and Management Science Technical Network, Battelle Seattle Research Center.

Thurman DA and T Peterson. March 2000. Information Technology to Support Public Involvement Processes. Puget Sound Chapter of the American Urban Planning Association.

Thurman DA. April 2000. Collaborative Problem Solving Environments for Wastewater Management. Modeling and Assessment Unit, Water Treatment Group, Department of Natural Resources, King County, Washington.

Thurman DA. June 2000. Collaborative Environments and Virtual Facilities. Members of the Battelle/PNNL Mexican Alliance.

Thurman DA. August 2000. Collaboratories, Virtual Facilities, and Collaborative Problem Solving Environments. Ed Sheffner, Applications, Commercialization, and Education Division, NASA Office of Earth Science and Participants in Pacific Northwest Regional Collaboratory for Remote Sensing and Natural Resource Management.

Thurman DA. September 2000. Collaborative Problem Solving Environments: Application in Environmental Policy. J. Daniel Ballbach, CEO, Marten Brown, Inc.

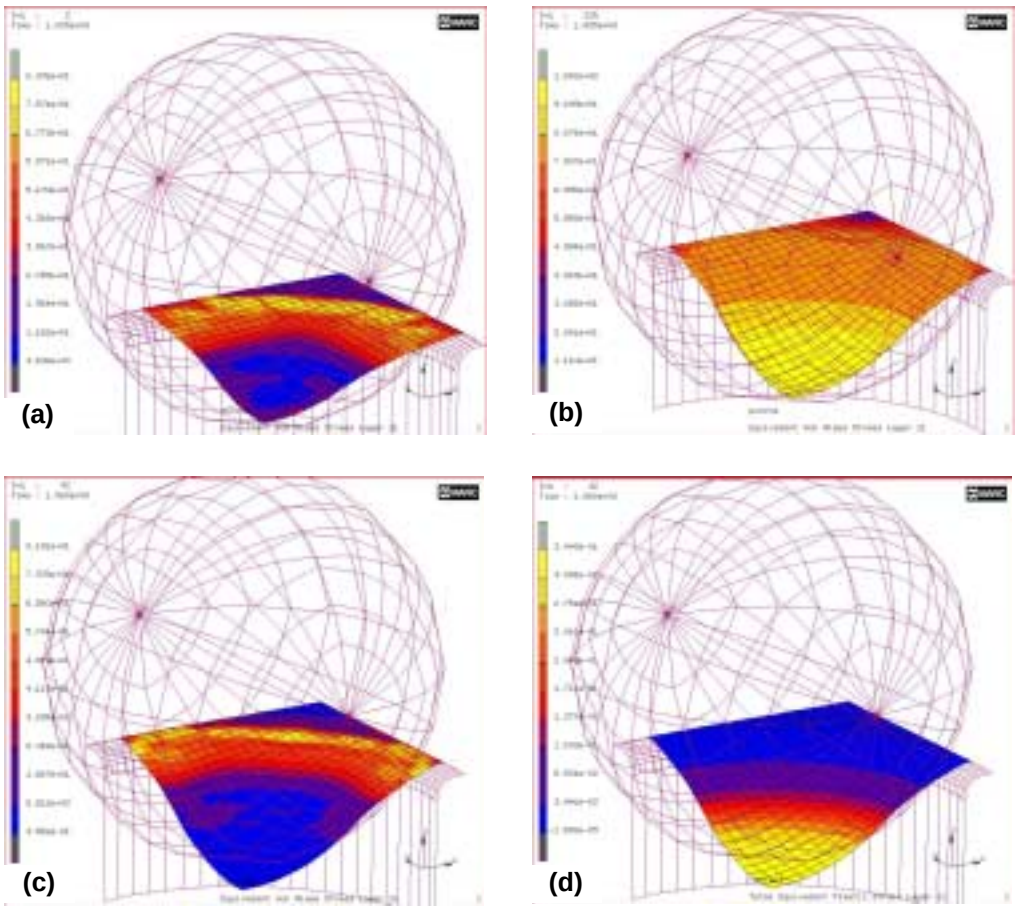

Figure 3. Results of Test Problem 1. Second stage of two-stage stretch-forming using a spherical punch and cylindrical die. a) Equivalent stress at beginning of second stage, b) Equivalent stress, punch displaced 25 mm, c) Equivalent stress after punch retracted to 15 mm, and d) Equivalent plastic strain after punch is retracted.

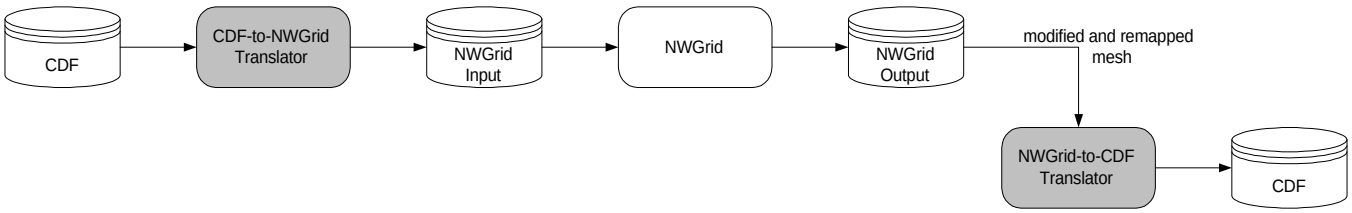

Figure 4. Additional processing and translation steps and intermediate files used in Test Problem 2

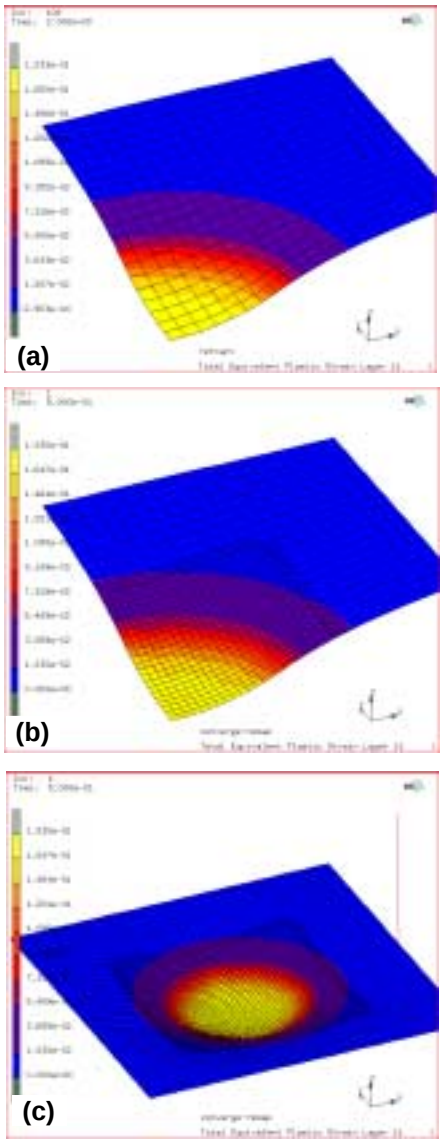

Figure 5. Test Problem 2 showing remeshing and data remapping applied to intermediate stage of Test Problem 1. (a) Equivalent plastic strain on intermediate deformed shape, (b) Refined mesh at center of 1/4-symmetry model showing remapped equivalent plastic strain, and (c) Reflected mesh with equivalent plastic strain mapped onto new mesh.

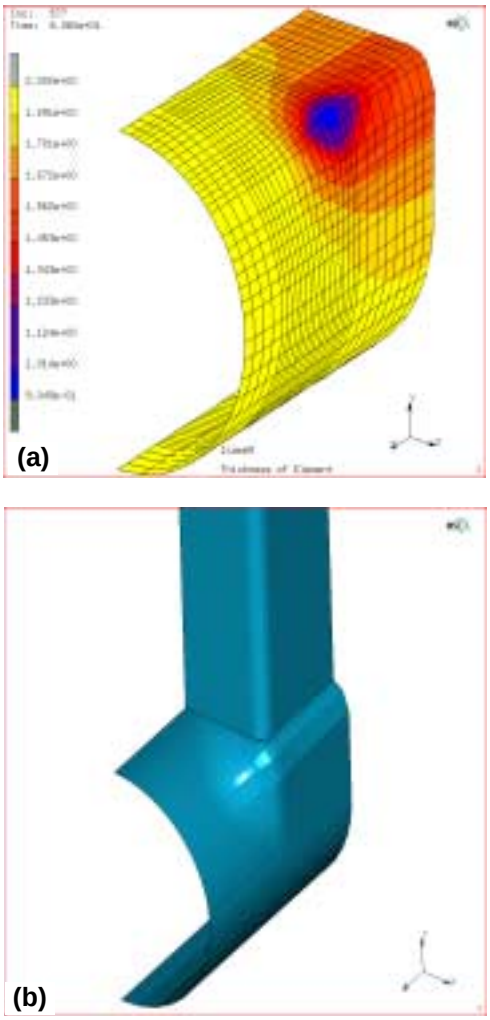

Figure 6. Progress on Test Problem 3. (a) Thickness contour plot from hydroforming analysis, and (b) shaded plot of hydro-formed geometry with beam section introduced for welding.

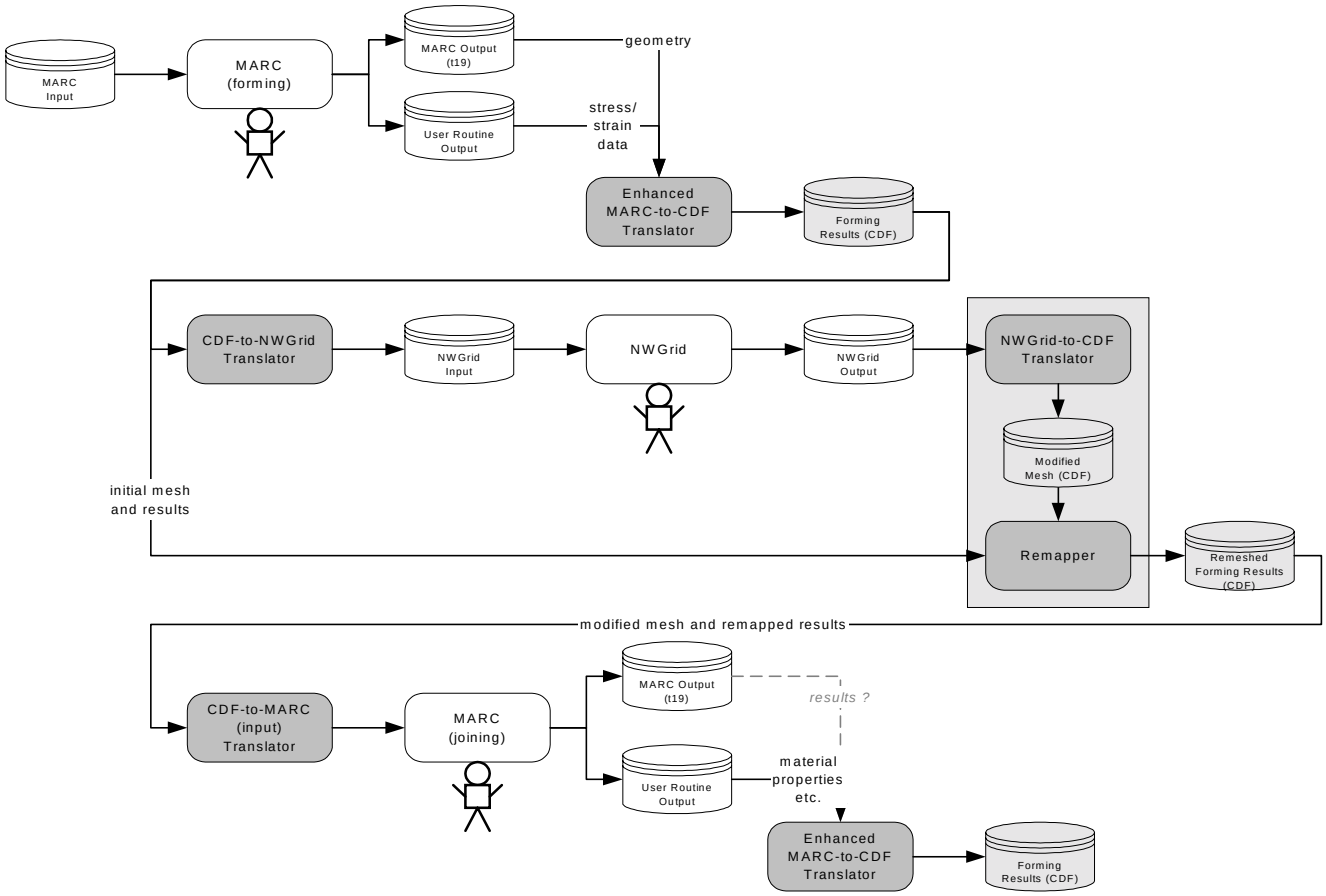

Figure 7. Complete schematic of finite element analysis, data transformation, remeshing/remapping, and data storage steps involved in Test Problem 3

Joining of Dissimilar Materials for Lightweight Automotive

Richard Davies, Mohammad Khaleel, Darrell Herling, Danny Edwards

Study Control Number: PN00062/1469

The automotive industry is working continually to develop and apply technology that reduces the weight of its product, thus minimizing the fuel consumption and environmental impact of future vehicles. We are developing materials and associated technologies for potential use in future automotive applications. The results of this research indicate that the optimum next generation automobile will likely be a hybrid material structure. A critical enabling technology for the production of hybrid material vehicles is the joining of dissimilar materials. This project focused specifically on developing technical capabilites in the area of joining of dissimilar materials for automotive structures.

Project Description

The automotive industry is focused on the overall reduction of vehicle weight to ultimately reduce fuel consumption and vehicle emissions. We are developing materials and associated technologies for potential use in future automotive applications. The results of this research indicate that the optimum next generation automobile will likely be a hybrid material structure. A critical enabling technology for the production of hybrid material vehicles is the joining of dissimilar materials. This work specifically focused on developing technical capabilites in the area of joining of dissimilar materials for automotive structures. This project will focus on friction stir welding to address relevent future material joint combinations. The work focused on dissimilar cast and wrought aluminum alloys, aluminum-magnesium, and metal matrix composites joints. The associated solutions to these emerging automotive and heavy vehicle needs will help meet the requirements of the next generation hybrid material automotive structures.

Introduction

The automotive industry, aerospace industry, and the United States military have expended a tremendous amount of effort to investigate and develop new materials for applications that improve the quality and reduce the weight and costs of their respective products. Current and past efforts have developed many substantially different materials, and have dramatically increased the need for the joining of unique and dissimilar materials. Many of these new and dissimilar materials may not be practically or reliably joined via classical welding and mechanical fastening methods. Therefore, the ultimate assembly of future hydrid material transportation and military products must rely on advanced and substantially more complex joining methods. This work focused on developing technical expertise with experimental and modeling capabilities for joining of dissimilar materials.

The friction stir welding technique developed and patented by The Welding Institute uses a rotating and translating mechanical probe that advances through a joint to create a bond. A schematic of the friction stir welding process is shown in Figure 1. The friction stir welding process is a simple process that relies only on the energy of the rotating welding head to produce the weld. No additional external power is input into the system and the heating, stirring, and friction welding of the two materials creates the bond. Friction stir can be used for joining many types of materials and material combinations, if tool materials and designs can be found that operate at the forging temperature of the work pieces. Most efforts developing this process have focused on the joining of aluminum and its alloys. The process has been proven to weld 2000, 5000, 6000, and 7000 series aluminum alloys

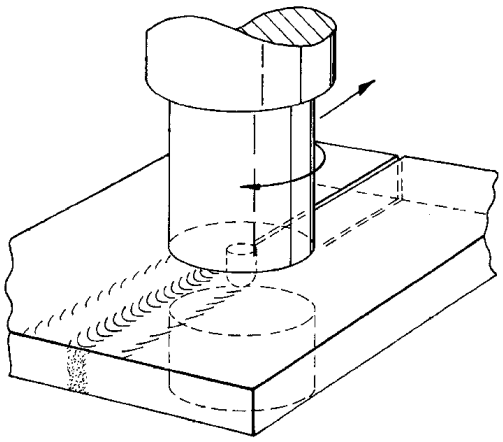

Figure 1. Schematic illustration of the friction stir welding process

(Johnson 1999; Colligan 1999; Gould et al. 1998; Kallee and Nicholas 1998; Thomas and Nicholas 1997; Liu et al. 1997; Rhodes et al. 1997). Most of the efforts have focused on welding wrought and extruded materials. Single-pass butt-weld joints with aluminum alloys have been made in thickness ranging from 1.2 mm to 50 mm without the need for a weld preparation. Parameters for butt-welding of most similar aluminum alloys have been developed in a thickness range from 1.6 mm to 10 mm. The process has been shown to produce welds of the highest quality, and has led to the development of a number of new product designs previously not possible. The fine microstructure created via friction stir welding also has shown the ability to create weld materials with higher strength and resistance to failure during uniaxial tensile tests. Friction stir is revolutionizing the welding of aluminum in industry. Friction stir already produces cost-effective welds in aluminum alloy plates with higher quality and lower distortion than is possible using fusion welding techniques. Friction stir also can weld aluminum alloys that are virtually unweldable by conventional techniques.

Results and Accomplishments

We investigated existing dissimilar joining technologies, and identified potential research areas at PNNL. After identifying technologies of interest, research and development was conducted to investigate the joining of dissimilar materials using friction stir welding methods.

Friction stir welding was conducted on three main materials: wrought aluminum sheet materials, wrought and cast magnesium alloys, and aluminum metal matrix composites. An illustration of a friction stir welding tool, dissimilar aluminum sheet butt-welds, and magnesium sheet butt-welds is shown in Figure 2. These welds were produced on conventional milling machines. The aluminum sheet weld consists of several welds produced between dissimilar aluminum alloys of potential automotive interest, as well as Sky 5083 alloy conventionally used for superplastic forming applications. The weld on the right side of the aluminum coupon is between a 5754 alloy 2 mm thick and two 6111 alloy sheets stacked to create a total 2 mm thickness.

We also investigated the ability to friction stir weld aluminum metal matrix composites. A micrograph of a typical aluminum-SiC metal matrix composites joint is shown in Figure 3. Fusion welding of aluminum metal matrix composites is typically very difficult and/or undesirable due to particle pushing and subsequent

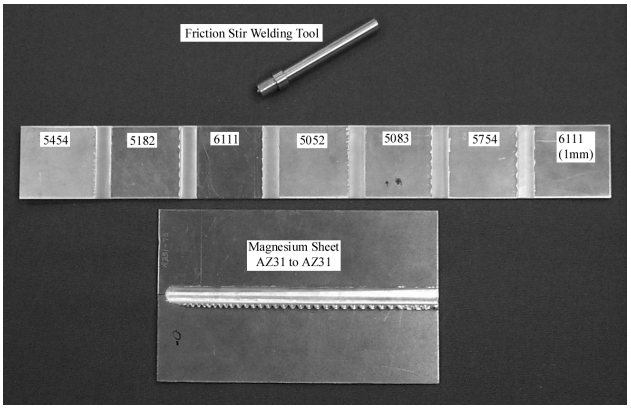

Figure 2. A friction stir welding tool together with dissimilar aluminum and magnesium welds

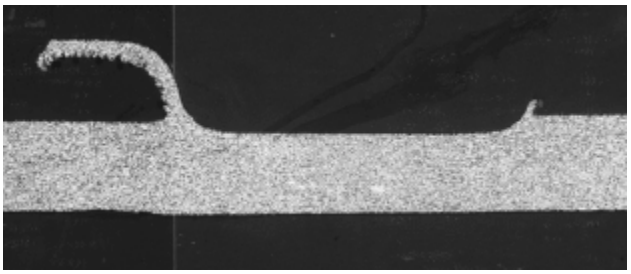

Figure 3. Cross section through an aluminum-SiC metal matrix composite weld joint processed through friction stir welding

particle segregation, and formation of undesirable aluminum carbide and aluminum oxycarbides. The friction stir welds exhibited no particle segregation and resulted in continuous welds. However, the tool steel used to construct the welding tool deteriorated at a relatively high rate, resulting in tool debris in the weldment microstructure.

Summary and Conclusions

Solid-state friction stir welding methods were investigated for potential application to lightweight and hybrid material automotive structures. The weld methods produce joints between dissimilar materials not normally possible using fusion welding techniques. The weld methods also show promise for potential metal matrix composite joints not normally possible using fusion welding methods.

References

Colligan K. 1999. "Material flow behavior during friction stir welding of aluminum." *Supplement to the Welding Journal* pp.229-s-237-s.

Gould JE, Z Feng, and T Lienert. 1998. "Recent developments in friction stir welding." SAE paper no. 981875, Aerospace Manufacturing Technology Conference & Exposition, Long Beach, California.

Johnson MR. 1999. "Friction stir welding takes off at Boeing." *Welding Journal* pp. 35-39.

Kallee S and D Nicholas. 1998. "Application of friction stir welding to lightweight vehicles." SAE paper no. 982362, International Body Engineering Conference & Exposition, Detroit.

Liu G, LE Murr, C-S Niou, JC McClure, and FR Vega. 1997. "Microstructural aspects of the friction-stir welding of 6061-T6 aluminum." *Scripta Materialia*, Issue: 3, 37:245-384.

Rhodes CG, MW Mahoney, WH Bingel, RA Spurling, and CC Bampton. 1997. "Effects of friction stir welding on microstructure of 7075 aluminum." *Scripta Materialia*, Issue 1, 36:1-144.

Thomas WM and ED Nicholas. 1997. "Friction stir welding for the transportation industries." *Materials And Design*, Issue: 4-6, 18:203-414.

Modeling of High-Velocity Forming for Lightweight Materials Applications

Mark R. Garnich, Anter A. El-Azab

Study Control Number: PN99047/1375

Electromagnetic forming has the potential to overcome formability barriers that prevent more widespread use of aluminum for lightweight energy-efficient vehicles. This project develops numerical modeling technology essential for designing electromagnetic forming systems for general sheet metal applications.

Project Description

This project aims to develop theoretical and computational models to simulate electromagnetic forming electromagnetic forming of lightweight metal sheets. Electromagnetic forming is a high velocity metal working process that uses electromagnetic driving forces. The work is multidisciplinary in nature, as it involves simultaneous development and numerical treatment of Maxwell's equations, finite deformation elastoplasticity and elasto-viscoplasticity, as well as heat generation. As Maxwell's equations are significantly affected by the deformation field in the work piece, an incremental formulation of the boundary-value problem of electromagnetics is first developed. This, along with the conventional metal plasticity models for finite deformation, render the work computationally intensive. The work is intended for use in simulation of high-speed metal forming related to auto and aerospace industries and in design and performance analyses of high-speed, electromagnetic metal forming systems. The main benefit of such advanced forming techniques lies in the improved formability limits of materials at high speeds, as well as in providing solutions for other issues related to spring-back and material damage exhibited during conventional forming processes.

Introduction

The basic electromagnetic forming process involves a low inductance electrical circuit with large capacitance and high speed switches to deliver a high frequency (~20 kHz) current pulse to a working coil. Conducting work pieces, such as the aluminum sheet, close to the coil are exposed to an intense transient magnetic field that generates eddy currents in the work piece. The currents interact with the magnetic field to create force (Lorentz forces) that pushes the work piece away from the coil. The forces can be large and the work piece can achieve velocities on the order of 100 m/s in less than 0.1 millisecond. The high speed and associated impact with die surfaces result in dynamics-related benefits to metal forming not seen with quasi-static forming processes. The most important benefits are increased ductility and reduced springback.

Electromagnetic forming is an old technology that has had limited use due to the complexity in applications that go beyond simple cylindrical geometry. The main issues are the difficulty in designing a system that results in a desired part shape and the durability of working coils for high volume production. Both of these issues could be effectively dealt with using advanced modeling technology. Models could predict the time and space distributions of forces and temperatures that affect material behavior in both the coil and work piece. The challenges in modeling are to accurately and efficiently capture the physics of the interaction between the electromagnetic, mechanical, and thermal fields.

Results and Accomplishments

We previously reviewed the state of technology for modeling electromagnetic forming. We identified the need for a general robust numerical capability for simulating electromagnetics in deforming media. We then developed a new form of the electromagnetic constitutive laws based on a Lagrangian form of Maxwell's equations. In addition, we developed a numerical algorithm, based on least-squares finite element method (Bochev and Gunzburger 1998) to deal directly with the first-order set of Maxwell's equations. This formulation avoids some of the numerical difficulties associated with the "potential formulations" that have seen widespread use (Jiang et al. 1996).

This year, we focused on developing software. A code was written in FORTRAN 77 that solves the first-order set of Maxwell's equations in a least-squares finite element method numerical framework. A preconditioned conjugate gradient solver was applied for efficient solution of the sparse system of equations stored in optimized skyline form. A limited implementation that

requires fixed electromagnetic boundary conditions and prescribed deformation on rectangular domains has been achieved. The element formulation is a standard tri-linear, 8-node hexahedron.

A series of test problems was simulated to aid in debugging the code and to verify satisfaction of boundary conditions and fundamental divergence conditions required by the theory. A three-dimensional rectangular mesh is shown in Figure 1 that represents an aluminum plate. This aluminum plate is assumed initially motionless and bathed in a uniform magnetic field of unit strength. Since the ability to capture the effects of deformation on electromagnetic fields is a key feature, a series of simple deformation fields was prescribed in this model so that the effects on electromagnetic fields could be observed. One of those deformation modes is indicated in Figure 1 as biaxial stretching of the plate with the initial magnetic field oriented normal to the plate.

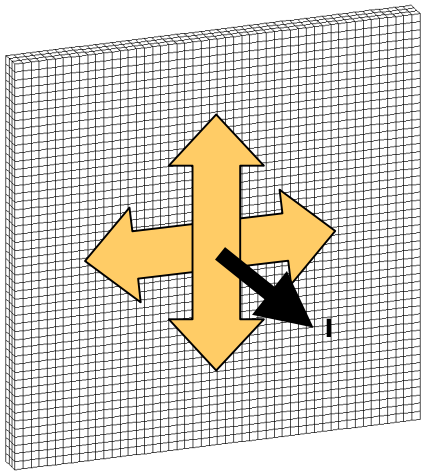

Figure 1. Finite element mesh of an aluminum plate with biaxial stretching and initially uniform magnetic field

The symmetry of the problem allows the mesh to represent only one-quarter of an actual plate so that two edges are fixed while the other two edges stretch and displace in accordance with the prescribed uniform strain field. An example of the spatial distribution of disturbance to the magnetic field (B) within the plane of the quarter plate is shown in Figure 2. This result indicates the correct symmetry of the solution and shows that the main disturbance occurs at the fast moving edges of the plate and propagates inward toward the center of the plate. In Figure 3, a predicted distribution of Lorentz

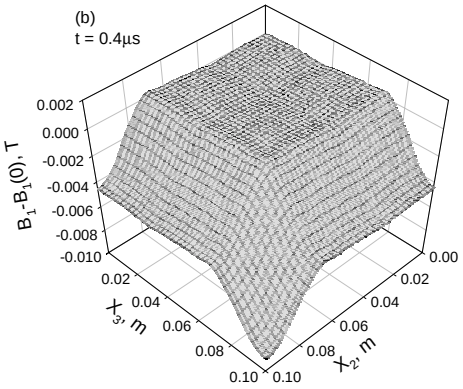

Figure 2. Snapshot of the magnetic field (B) distribution in the plate

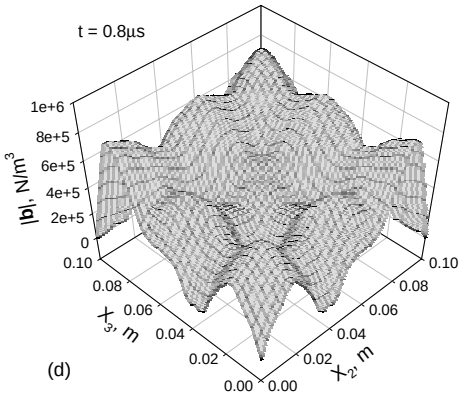

Figure 3. Snapshot of the Lorentz (body) force field distribution in the plate

force (interaction of electric current and magnetic field, JxB) is shown. Again the required symmetry is preserved in the simulation and strong coupling is indicated by the significant forces generated by the deformation. Finally, results of divergence error calculations are shown in Figure 4. In each of the three curves found in Figure 4; for the electric displacement, magnetic induction, and conduction current, the divergence of the field is very small compared to the field strength within the plate. These divergence conditions are required to satisfy Maxwell's equations and are a strong indicator of the correct numerical implementation of those equations.

Summary and Conclusions

Building on the theory developments, this year's project produced a numerical analysis code capable of solving

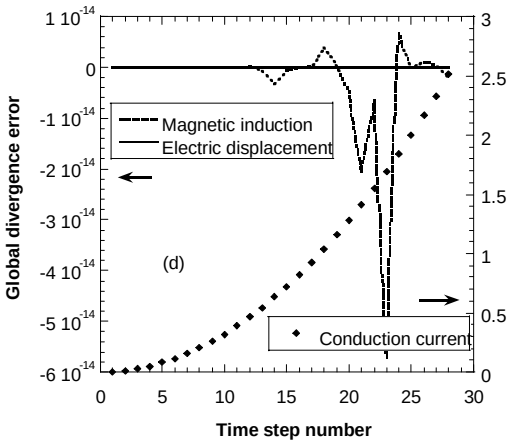

Figure 4. Global divergence errors

Maxwell's equations in a Material (Lagrangian) frame. Our work was motivated by the need for a simulation tool to study advanced (three-dimensional) applications of the electromagnetic forming process. The code was based on the finite element method and employs the least squares variational principle to solve the first order system of equations directly. The code is presently limited to 8-node hexahedral elements.

For numerical efficiency, a preconditioned conjugate gradient solver was employed along with optimized skyline matrix storage. The code was tested on a series of simple problems to verify the numerical implementation of the theory. This software has proven to be robust and will serve as a basis for further development into a very general numerical capability for solving Maxwell's equations in deforming media. This is a first of its kind numerical capability that will have very broad application.

Future work under programmatic funding will involve developing the code to efficiently implement general boundary conditions and systems with multiple electromagnetically interacting bodies. The code must also be coupled to a mechanics code that solves systems involving three-dimensional elasto-viscoplasticity and general three-dimensional contact.

References

Bochev PB and MD Gunzburger. 1998. "Finite-element methods of least-squares type." *SIAM Reviews* 40:789-837.

Jiang B-N, J Wu, and LA Povinelli. 1996. "The origin of spurious solutions in computational electromagnetics." *Journal of Computational Physics* 125:104-123.

Publications and Presentations

El-Azab A and MR Garnich. "Lagrangian treatment of the initial-boundary-value problem of electromagnetics in deforming media." *Journal of Computational Physics* (submitted).

El-Azab A and MR Garnich. 2000. "On the numerical treatment of Maxwell's equations in deforming electromagnetic media" Presented at the Int. Conf. Computational Engineering Sciences, August 2000, Anaheim California. *In Advances in Computational Engineering & Sciences*, Vol. II, 1687-1692, Eds. SN Atluri and FW Brust, Tech Science Press, Palmdale, California.

Virtual Modeling and Simulation Environment

David A. Thurman, Kristine M. Terrones, Alan R. Chappel

Study Control Number: PN00093/1500

The shift in the automotive industry toward lightweight materials, such as aluminum and magnesium, requires the development of new metal forming, joining, and assembly methods. Accurate and efficient analysis of these process histories, using the finite element method, is necessary to ensure that forming processes are within material forming process limits, and that the vehicle satisfies crashworthiness standards. Successful development of a virtual modeling and simulation capability will lead to the increased use of lightweight materials in transportation systems—resulting in significant energy savings.

Project Description

This research project developed a prototype virtual environment to support collaborative manufacturing design. This research developed the Virtual Modeling and Simulation Environment (VMSE), in which multistage processing history can be reviewed, annotated, and modified by manufacturing designers. We took advantage of the finite element common data format, data transformation, and model remeshing and remapping tools produced earlier under the Integrated Modeling and Simulation project.

Using a combination of open source software, publicly available Web-browser plug-ins, and locally developed software applications, we developed a virtual environment in which automotive engineers can collaboratively review the results of multistage finite element modeling and simulation. The virtual environment enables design engineers to view results produced by traditional finite element codes (MARC, Abaqus, PAM-STAMP), even when they do not have access to the codes themselves, to collaborate with other engineers, and to see how steps in a multistage modeling and simulation process contribute to differences in the end result. The virtual environment gathers critical processing history, or "data pedigree" information, and attaches it to modeling results, ensuring that an accurate lineage of the modeling and simulation effort is kept throughout the entire multistage process.

Introduction

The Virtual Modeling and Simulation Environment project is focused on a problem experienced by research engineers who use finite element analysis software in their daily work, particularly those engaged in multistep modeling and simulation that involves the use of multiple commercial finite element analysis packages. As shown in Figure 1, an example of this approach is the application of multiple analysis codes to the automotive manufacturing problem of forming a structural assembly, welding two or more assemblies together, and then assessing their performance in a crash simulation. The basic problem is that the commercial finite element analysis products each use proprietary file formats, and few are compatible with the others. Thus, engineers who do not have access to the application in which a simulation was carried out cannot review the results, greatly hampering efforts at collaboration. The Virtual Modeling and Simulation Environment project is focused on producing an environment that will not only facilitate the viewing of modeling results regardless of the commercial tool in which they were produced, but also support the collection, viewing, and annotation of processing history or data pedigree information in multistep simulation efforts.

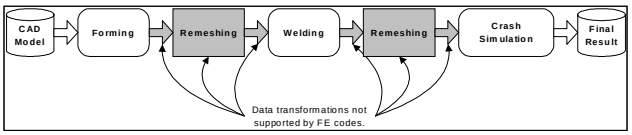

Figure 1. Illustration of multistep modeling and simulation process and critical data transformation steps that are not supported by commercial finite element software applications

Approach

The initial approach focused on using the Virtual Playground, a collaborative environment test bed developed at this Laboratory in cooperation with the University of Washington, as the baseline environment. The plan was to develop "plug-ins" that enabled commercial finite element software applications to be used within the Virtual Playground environment. This approach was abandoned, however, after analysis showed

that users were unlikely to appreciate the value of the Virtual Playground environment. User input to the design process suggested that a simpler, yet more robust approach was needed.

Analysis of the underlying problem showed that while scientists and engineers engaged in multistep finite element analysis efforts are comfortable with the commercial finite element applications available to them, these applications tend not to inter-operate with one another. Each uses a different, proprietary data format and transforming the results of one modeling exercise conducted in application A (such as the Forming simulation in Figure 1) into an appropriate input format for application B (the Welding simulation in Figure 1) consumes vastly larger amounts of the users' time than the actual modeling does. Results gathered from discussions with users indicated that what was needed was a collection of data transformation tools that would support the transformation to results between the different commercial codes and provide the ability to review results from modeling efforts by users without access to the commercial applications that produced them. One of the critical features lacking in multistep finite element analysis efforts is the ability to keep an accurate processing history or data pedigree that describes all of the analyses carried out in the effort. Thus, as part of the data transformation process, we sought to capture such information and store it with the results for later review and annotation.

The project scope was modified at midyear to remove the development of an environment based in the Virtual Playground. Project efforts then focused on developing Web-based and multi-platform tools for results visualization, data pedigree capture and visualization, and asynchronous collaboration among users. Web-based technologies were explored to provide the ability for results to be shared by geographically distributed users without access to the same set of underlying finite element analysis tools.

Results and Accomplishments

Based on the user analysis described above, four architectural components were design and developed.

***Model Transformation Capability*—**Though the integrated modeling and simulation project focused on the development of a common data format and data transformation tools, it provided no simple mechanism for users to invoke such transformation tools. As part of the overall environment, a model transformation capability was created that enabled users to invoke the transformation tools and supply the necessary information to complete the data transformation process.

***Data Pedigree Capture and Visualization*—**At the same time the user is supplying information for the data transformation process, he or she also is prompted for data pedigree information describing the finite element analysis steps completed. As shown in Figure 2, this step-specific information is gathered and incorporated into the data pedigree that accompanies the results. Figure 3 shows the visualization of a few steps of the pedigree, showing the forming and remeshing steps near the beginning of a finite element analysis process modeled after the example discussed above and in Figure 1.

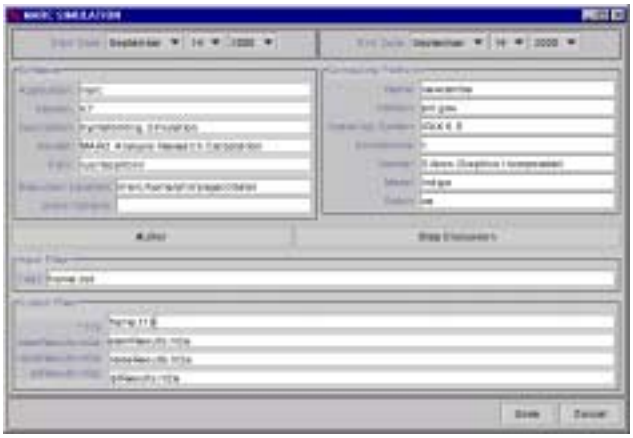

Figure 2. Graphical user interface 'wrapper' for data transformation tool that captures data pedigree information about the previous finite element analysis step

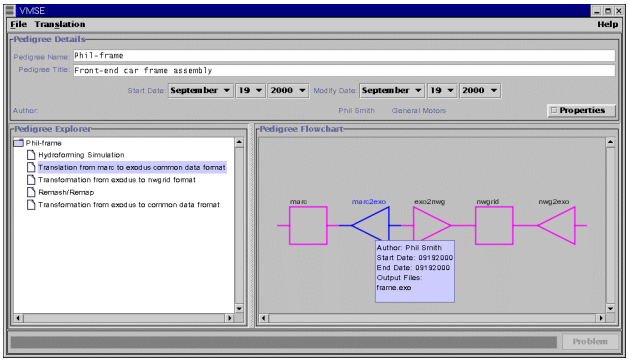

Figure 3. Pedigree viewer showing collection of results from hydroforming and remeshing steps in multistep finite element analysis effort

***Three-Dimensional Model Visualization*—**Building on the common data format adopted in the integrated modeling and simulation project, a data translation tool was developed that translates finite element analysis results into the Virtual Reality Modeling Language. Then, using freely available Web browser plug-ins that

support Virtual Reality Modeling Language, model results can be viewed by anyone, without requiring access to the commercial application that produced them. Because Virtual Reality Modeling Language is a three-dimensional modeling language, both the model and information about the finite element analysis can be reviewed. Figure 4 shows a snapshot of the three-dimensional model visualization tool in use.

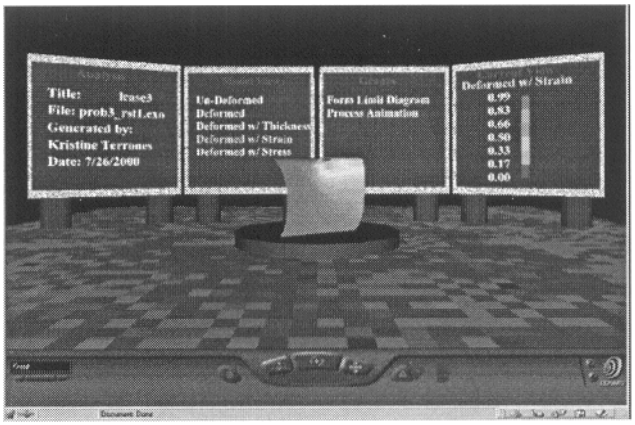

Figure 4. Three-dimensional model visualization tool, showing deformed model with plotted strain values

Web-Based Data Management—A Web-based data management architecture was developed to provide simple access to modeling results as shown in Figure 5. As results become available at the end of each step in the analysis process, the results, their translation into a common data format, and the meta-data describing the evolving data pedigree are copied to a Web-based data storage device. This enables other team members to review the results to date, using the three-dimensional Model Visualization and Data Pedigree Visualization tools.

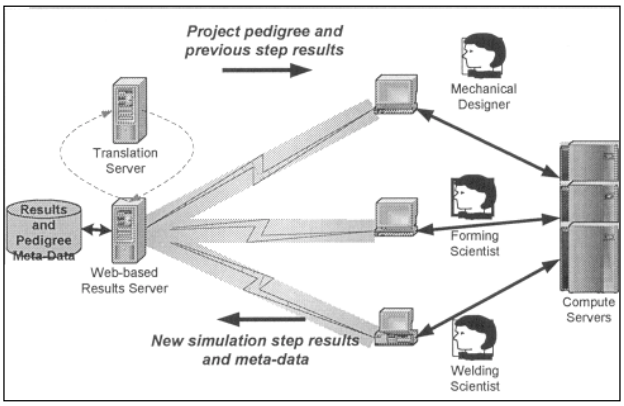

Figure 5. Web-based data management architecture

Summary and Conclusions

The software components developed this year provide a proof-of-concept demonstration that a virtual environment could be developed to support multistep finite element analysis as described above. Through the combined efforts of the integrated modeling and simulation and Virtual Reality Modeling Language projects, the critical technical issues have been identified and addressed. Future efforts in this area, supported through programmatic funding, should concentrate on the development of a more robust Web-based architecture, including Web-based data transformation services and expanded capabilities to support results remeshing and remapping between simulation steps.

Presentation

Johnson KI. September 2000. "Integrated Modeling and Simulation, Joining of Hydroformed Structures, Glass Process Modeling." Presented to Reza Sadeghi and John Long, MSC Software Corporation.

Earth System Science

An Engineering Design Tool for Redox Barriers

Ashok Chilakapati, Mark Williams, Charlie Cole

Study Control Number: PN0008/1415

In Situ Redox Manipulation (ISRM) technology is an innovative technology that, for the first time, is being implemented at a large scale at the Hanford Site to remediate groundwater contaminated with chromate. Technical and design uncertainties can significantly affect performance and cost-effectiveness. This project seeks to reduce this uncertainty by creating a tool to evaluate critical design parameters and the resulting effect on life cycle remediation costs.

Project Description

Harmful contaminants such as Cr(VI) and trichloroethylene can be removed from groundwater by reactions with chemically reduced subsurface sediments. This project examined the optimal selection of the number of wells, the injection rate, and the number of regenerations of a large-scale Fe(II) barrier for Cr(VI) remediation at Hanford. The process model developed consists of two parts: 1) the creation of the Fe(II) barrier by the injection of a dithionite reagent, and 2) the reoxidation of the barrier by Cr(VI) and oxygen in the invading groundwater.

The solution to the process model is used to develop the total cost as a function of the design variables. This cost model is applied to the Cr(VI) contamination at Hanford to obtain the optimal design configuration and its sensitivity to cost and process uncertainties.

Introduction

In Situ Redox Manipulation technology alters the reduction-oxidation potential of an aquifer to create a permeable treatment zone capable of reducing many highly mobile oxidized metal contaminants (e.g., Cr(VI)) into their more immobile forms and dehalogenating several halogenated-hydrocarbon compounds which are common groundwater contaminants (such as, trichloroethylene, trichloroethane, and carbon tetrachloride). The application of permeable treatment zones for groundwater remediation will result in substantial cost savings over the life cycle of the project compared to a pump-and-treat system because these passive systems require no long-term operational costs after emplacement. Currently, emplacement costs of a permeable treatment zone should be comparable to start-up costs for a pump-and-treat system. Even when savings can be demonstrated on life cycle costs, the ability to demonstrate a savings in start-up costs could make the application of innovative technologies for remediation even more attractive. A number of techniques, at various stages of development, are currently being studied to alter the redox potential of an aquifer. This project involves developing a methodology and design that refines the emplacement of an In Situ Redox Manipulation permeable treatment zone using dithionite to make it more cost-effective and to minimize waste generated in the deployment of this innovative technology for the remediation of groundwater contaminant plumes.

The objective of this project was to build an engineering design tool for use in optimizing the In Situ Redox Manipulation technology for cost-effectiveness. This required development and coupling of a reoxidation submodel to a reduction submodel. The solution to the reoxidation submodel supplies the design criteria such as the width of the barrier to be established and the number of regenerations; the solution to the reduction submodel determines the amount of the chemical reagent and the duration of the operation to establish a barrier of a desired width. The combined reduction/reoxidation model forms the core of the cost model which yields the optimal number of wells, flow rate, and the number of reinjections. The process model captures the bulk of the important chemistry and hydrology, but a number of simplifying assumptions were required in each submodel to facilitate an analytic treatment of the problem. Important among them is the assumption of physical and chemical homogeneity of the aquifer, without which numerical models would have had to be employed, which was beyond the scope of this proposal.

Results and Accomplishments

Figure 1 (A, B, C) illustrates key components of the barrier design, process model concepts, and some of the optimization parameters. A rectangular geometry for the barrier (Figure 1A) extending through the vertical extent, H, of the aquifer with a porosity, θ, was considered. The length, L, of the barrier perpendicular to the average ambient groundwater flow is chosen to match or exceed

the lateral extent of the plume so that all of the plume may pass through the barrier. The dimensions of the required barrier are achieved by a series of single well injections (Figure 1B). Other complex emplacement strategies such as dipoles are feasible but less attractive because they are operationally complex and can lead to the undesirable extraction of the injected dithionite. The reoxidation submodel which accounts for the advancement of the reoxidation front is illustrated in Figure 1C.

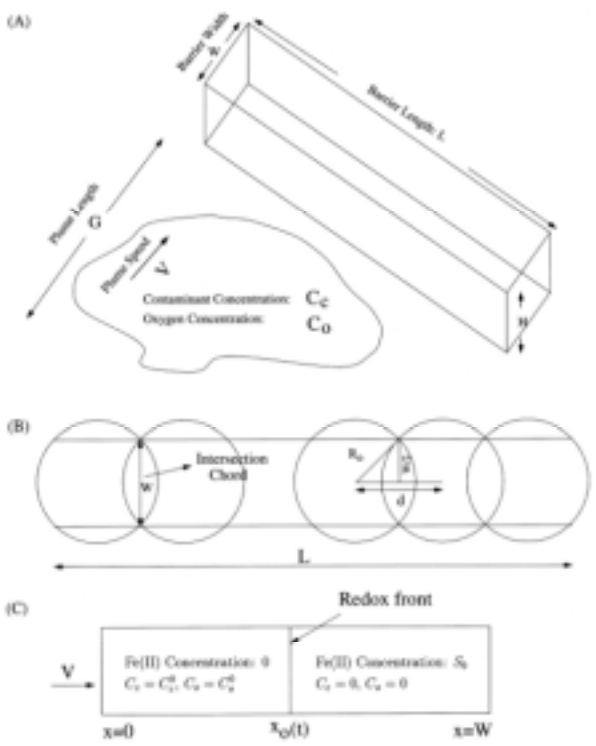

Figure 1. (A) Geometry of the barrier. (B) Barrier is created by overlapping the reduction zones from adjacent injections. (C) Transport limited reoxidation of the barrier. All Fe(II) is consumed to the left of the redox front, and no contaminant/oxygen is present to its right.

The width of the barrier is determined by requiring that the total treatment capacity (the accessible, reducible Fe(III) content) of the barrier be sufficient to consume the oxidizing capacity of the plume migrating through the zone. The oxidizing capacity of the plume results from both the Cr(VI) contaminant and the dissolved oxygen. Long and highly concentrated plumes require wider barriers for complete treatment. Because the creation of wide barriers from central injection wells is often inefficient, it is advantageous to create a barrier of smaller width but regenerate it periodically. The number of regenerations controls the required barrier width, the injection rate plays a key role in creating the barrier with that width, and the number of wells is the key variable in building a barrier that spans the entire lateral extent of the plume. Given the generally large costs of field-scale remediation systems, the goal of the engineering design tool developed is to present an approach to pick these three design variables (the injection rate, the number of wells, the number of regenerations) to minimize the total cost of operation. The main components of the total cost are the costs of chemicals, waste disposal, drilling, and labor. Each of these costs are directly affected by the requirements for the barrier and the strategy for design. The functional relationship between the total cost and the design variables is provided by the process model for the barrier creation and the model for reoxidation of the barrier.

An analytical engineering design tool was developed and applied to the Cr(VI) at Hanford to obtain an optimal design and determine its sensitivity to key assumptions and to cost and process uncertainties. Results are illustrated in Figure 2.

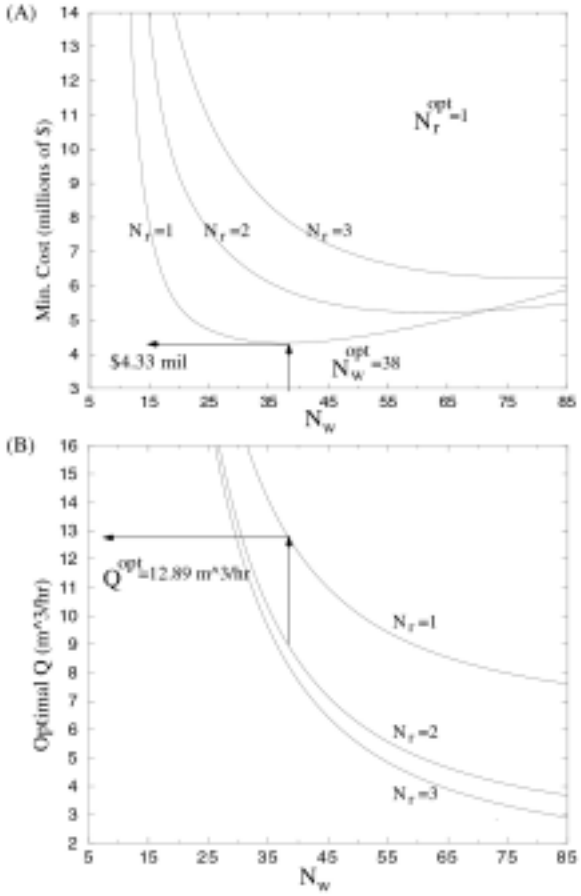

Figure 2. The optimal design variables are obtained by obtaining the optimum Q for a range of values for the number of regenerations (N_r) and the number of wells (N_w) and picking the (N_r, N_w, Q) combination with the least minimum cost.

Summary and Conclusions

Over the past few years the Laboratory has made great strides in advancing the use of In Situ Redox Manipulation technology for the transformation/ degradation of redox-sensitive contaminants such as chromate and trichloroethylene. The technology involves the injection of a dithionite solution that transforms (structural) Fe(III) to Fe(II), thus establishing a reductive Fe(II) barrier in the flow path of the plume. Large-scale field implementation of the In Situ Redox Manipulation technology is now under way at Hanford for chromate remediation. Given the large magnitude of the operation, it is critical to evaluate the performance and cost-effectiveness of any proposed design for the barrier. The main components of the cost model are the drilling costs, the cost of reagents, the cost of waste disposal, and the labor costs. The key design variables are the number of wells, their flow rate, and the number of regenerations of the barrier. The design variables affect the total cost in different ways. Increasing the number of wells will decrease the total amount of dithionite required and will generate less waste. A smaller barrier width will decrease the loss and wastage of reductive capacity, but will increase the costs related to more frequent regeneration.

We developed a code for optimal selection of key design parameters that would yield a robust design and also minimize the total cost of the remediation effort. The cost model is driven by the process model consisting of two parts: 1) the creation of the barrier by injecting the reducing agent, and 2) the reoxidation of the barrier by the contaminant (and also oxygen if aerobic) in the invading groundwater. We also considered the loss of reducing capacity that can occur due to rainfall events and due to the diffusion of oxygen from the atmosphere. The solution to the reoxidation submodel was combined with the known solution to the reduction submodel to develop an analytic objective function (cost of the operation) in terms of the key decision variables (assuming a homogeneous system). We developed an engineering design tool to obtain optimal design parameters and also their sensitivity to uncertainties in the physiochemical description of the problem.

Publication

Chilakapati A, MD Williams, SB Yabusaki, CR Cole, and JE Szecsody. 2000. "Optimal design of an in situ Fe(II) barrier: Transport limited reoxidation." *Environmental Science and Technology* (submitted).

Biogeochemical Processes and Microbial Characteristics Across Groundwater Surfaces

Jim Fredrickson, David Geist

Study Control Number: PN00014/1421

The hyporheic zone is defined as the region where groundwater mixes with surface waters resulting in distinct geochemical gradients that can influence the composition and activity of the associated microbiota. In spite of the potential importance of this zone on the transport of groundwater contaminants into surface waters and exposure to sensitive biota, very little scientific information is available regarding the microbiology and geochemistry of this environment.

Project Description

We evaluated a freeze-core method for collecting samples suitable for microbiological and geochemical analyses from the groundwater/surface water mixing zones of large, cobble-bed rivers. The development of effective methods for collecting samples from the groundwater/ surface water interaction zone will allow researchers to investigate 1) how microbial communities within the mixing zones are affected by hydrologic and geochemical processes occurring at groundwater/surface water boundaries, and 2) how microbial communities may affect contaminant transport, and ultimately fate and effects, across groundwater/surface water boundaries. As a consequence of developing this unique capability, future programs can be undertaken to study microbiological and geochemical processes within these mixing zones that can provide additional information about how the geochemistry, hydrogeology, and microbial communities interact to affect contaminant transport through this dynamic interface. This will result in an improved conceptual model of the structure and function of groundwater/surface water mixing zones and will reduce the uncertainties inherent in current numerical models of contaminant transport from groundwater to surface water. Resulting scientific information will allow for a more accurate prediction of contaminant fate and transport and effects on surface water biota.

Introduction

Chemical, physical, and microbiologic processes within the groundwater and vadose zones beneath the Hanford Site are being studied by Laboratory scientists to better understand the fate and transport of contaminants as they migrate with groundwater in the unconfined aquifer toward the Columbia River. Previous and current research has focused on processes in the saturated zone and more recently, the vadose zone. Although the fundamental processes that control contaminant fate and transport in these regions of the subsurface are still poorly understood, the microbiological, geochemical, and physical properties of these regions have been reasonably well characterized. In contrast, there is little or no information regarding the microbiological and geochemical characteristics within groundwater/surface water interaction zones, especially in large rivers such as the Columbia. This is largely because of the difficulty in sampling the subterranean environment beneath large, cobble-bed rivers.

The main objective of this project is to develop and evaluate methods for collecting samples from the groundwater/surface water mixing zones suitable for microbiological and geochemical characterization and to obtain preliminary scientific information on this zone in the Columbia River. Presently, techniques do not exist that can provide relatively undisturbed samples from the mixing zones beneath large, cobble-bed rivers such as the Columbia. The results of this effort will be primarily proof of principle in nature but are also expected to provide some of the first scientific insights into the structure and function of microbial communities that reside in these zones. The development of these approaches provide a unique research capability within the DOE system and will enable the development of future projects and programs investigating processes in and the characteristics of this zone.

Approach

A modified freeze-core technique was used to collect sediment blocks within the hyporheic zone. Freeze-core techniques are frequently used in lotic environments (streams and rivers) to obtain in situ samples of benthic fauna within stream-bed sediments and to characterize sediment size distribution. In the modified freeze-core technique, three tubes are driven into the sediments in a

triangular configuration. Once the tubes and shield are in place, liquid nitrogen is injected into the tubes for approximately 20 to 30 minutes (Figure 1, top). Immediately after the liquid is injected, a chain hoist is used to lift the frozen tear-drop-shaped core (Figure 1, bottom) from the bed of the river. This method is capable of extracting 70 cm cores that weigh, on average, about 24 kg. Once the core is extracted, it is photographed, bagged, and placed on dry ice in a sample transport box for further processing and analysis at the laboratory.

Figure 1. Filling hollow tubes with liquid N_2 to freeze river sediments in situ (top). Intact frozen core obtained from the Columbia River using the freeze core technique (bottom).

Although the focus of this project is on the development and evaluation of approaches for collecting samples from the hyporheic zone, select microbiological and geochemical analyses were applied to the collected samples to assess the effectiveness of the methods described above and to gain preliminary insights into the characteristics of this environment. Frozen and unfrozen samples were analyzed using microbiological cultivation techniques and direct extraction and characterization of nucleic acids using methods that have been developed and employed by our Laboratory for analyses of microbial communities in subsurface sediments and soil. Pore waters were extracted from sediments by centrifugation and analyzed for total cations and anions, dissolved organic and inorganic carbon, and trace metals.

Results and Accomplishments

Freeze-Core Sampling

Intact frozen cores of Columbia River sediment were successfully collected from near the 100 H area of the Hanford Site in March and again in May 2000. Three intact frozen blocks of sediment were removed on each occasion and treated as replicates. Unfrozen sediment was collected adjacent to the freeze core location and used as controls to assess the impact of freezing on viable microbial populations, metabolic activity, and on pore water geochemistry. Collected samples were returned to laboratories in the 331 Building. Freeze-cores remained frozen during transport and subsequent sampling.

Microbiological Analyses

Microbial characterization of Columbia River sediments revealed an unexpectedly large and diverse microbial community, whereas, previous experience with saturated subsurface sediments from the Hanford confined aquifer suggested the opposite. Direct community diversity analysis based on terminal restriction fragment polymorphism analyses of 16S ribosomal RNA genes showed between 10 and 15 major ribotypes, indicative of significant microbial diversity. Populations of viable aerobic heterotrophic bacteria in unfrozen sediment ranged from 10^6 to 10^7 colony-forming units per gram; in the frozen sediments, the populations were lower, between 10^5 to 10^6 colony-forming units g^{-1} (Figure 2). These results suggest that freezing does have an impact on bacterial cell viability, reducing populations by approximately 10-fold or less. Although the results shown in Figure 2 are from the May sampling, identical trends were also observed in the March samples.

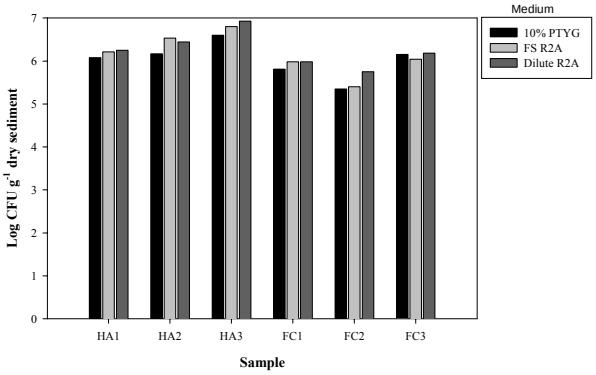

Figure 2. Populations of viable aerobic heterotrophic bacteria in hyporheic ambient (HA) and freeze-core (FC) Columbia River sediments

Analyses of populations of viable anaerobic bacteria showed significant populations of anaerobic bacteria during both sampling periods. These populations included nitrate-respiring, sulfate-reducing (Table 1), and ferric iron-reducing bacteria.

Table 1. Population estimates of viable anaerobic bacteria in Columbia River hyporheic sediments sampled by freeze-core (FC) and ambient hand auger (AC)

Sample ID	Sampling Date	Denitrifying Bacteria	Fe(III)-reducing Bacteria	Sulfate-reducing Bacteria
		cells g^{-1} sediment		
FC1	3/23/2000	10^3	10^2	$>10^4$
FC2		$>10^4$	10^2	$>10^4$
FC3		$>10^4$	10^2	$>10^4$
AC1	3/23/2000	$>10^4$	10^2	10^3
AC2		$>10^4$	10^2	$>10^4$
AC3		$>10^4$	$>10^3$	$>10^4$
FC4	5/2/2000	10^4	10^1	10^4
FC5		$>10^6$	$>10^3$	10^4
FC6		10^5	10^2	10^3
AC4	5/2/2000	$>10^6$	10^2	10^5
AC5		$>10^6$	$>10^3$	10^4
AC6		$>10^6$	$>10^3$	10^4
River water (cells mL^{-1})	5/2/2000	$<10^0$	$<10^1$	$<10^1$

Pore Water Geochemistry

Pore waters were extracted from sediments by centrifugation and filtered through a 0.22 μm membrane filter before analysis. In addition to those species listed in Table 2, a complete suite of cations was determined on pore waters collected from the individual sediment samples. The parameters listed in Table 2 are those that are most relevant to microorganisms and sediment biogeochemical processes. The results indicated sufficient dissolved organic carbon was available to support heterotrophic activity. In the absence of oxygen, sufficient nitrate and sulfate were available to support anaerobic respiration. Spatial and temporal differences were greater than differences due to sediment freezing.

Summary and Conclusions

Intact sediment cores from the Columbia River were successfully collected using an in situ freeze-core technique. In situ freezing is an ideal approach for collecting high quality sediment samples for DNA- and phospholipid-based analyses of microbial populations and for pore water geochemical analyses. Although populations of heterotrophic bacteria were slightly less in the frozen cores, a wide range of bacterial physiotypes include aerobic, denitrifying, sulfate-reducing, and Fe(III)-reducing bacteria were enriched from both frozen and ambient sediment samples. The finding of high populations of strictly anaerobic bacteria was unexpected and has important implications for the fate and transport of contaminants from contaminated Hanford groundwaters into Columbia River waters. For example, Fe(III)- and sulfate-reducing bacteria are effective at reducing toxic Cr(VI) (chromate) to relatively benign Cr(III).

This project will continue and will focus on collecting frozen and ambient sediment cores for processing under strictly anaerobic conditions to examine the redox status of pore waters (Fe(II), sulfide) and to obtain an accurate measure of viable anaerobic bacterial populations. Also, a passive multi-level sampler method will be evaluated for spatial delineation of geochemical gradients across the surface and ground water boundary in the Columbia River.

Table 2. Select geochemical parameters from 3/00 and 5/00 Columbia River sediment sampling

Ion	D.L.[a]	CRH 3/00 mg L^{-1}			CRH 5/00 mg L^{-1}					
		Freeze 1	Freeze 2	Freeze 3	Ambient 4	Freeze 4	Ambient 5	Freeze 5	Ambient 6	Freeze 6
Chloride	0.05	2.27	3.54	3.09	3.41	4.20	2.65	1.78	1.55	2.41
Nitrate	0.30	6.50	14.27	13.76	1.90	2.86	1.68	11.99	3.27	6.00
Sulfate	0.50	12.75	13.99	13.15	13.03	15.88	12.68	13.80	9.76	12.04
IC[b]	0.1	6.12	3.38	9.29	18.96	12.40	14.67	26.60	16.59	21.53
DOC[c]	0.1	4.52	4.55	5.89	18.32	24.23	24.76	14.73	4.59	5.85

(a) D.L. = detection limit
(b) IC = inorganic carbon
(c) DOC = dissolved organic carbon

Development and Validation of Mesocosms for Experimentally Investigating Carbon Dioxide Sequestration in Wetlands

Ron Thom, Michael Huesemann, Dana Woodruff

Study Control Number: PN00027/1434

Carbon dioxide, the principal greenhouse gas emitted by fossil fuel combustion and deforestation, adds annually about 3.5 billion metric tonnes of carbon to the atmosphere. Soil carbon sequestration is needed to reduce accumulation of carbon in the atmosphere to reduce risks of climatic change. Restoration of wetlands, fertilization, hydrological manipulation, and other methods might allow wetlands to sequester an additional 0.1 to 0.7 billion metric tonness per year.

Project Description

Restoration of wetlands is a potental method for sequestering large amounts of carbon in the soil, thereby reducing accumulation of atmospheric carbon. Recently, the National Panel on Carbon Sequestration (Reichle et al. 1999) estimated that wetland carbon sequestration could be substantially increased. Restoration may be the least costly and least uncertain alternative for sequestering carbon in wetlands. However, no comprehensive program has studied how such restorative actions affect carbon sequestration rates. This project examined the use of mesocosms to measure carbon sequestration in natural and restored wetlands. This study also demonstrated the use of mesocosms for evaluating enhanced carbon sequestration in wetlands, developed new methods for assessing soil organic carbon, and established the groundwork for verifying enhanced carbon sequestration via remote sensing on regional and larger scales. We conducted greenhouse experiments where hydrology and salinity were manipulated in small mesocosms, collected and analyzed soil samples from several restored and natural tidal marshes as well as eelgrass meadows of varying post-restoration age marshes, investigated the use of spectral radiance in monitoring differences in the amounts of carbon stored in wetland systems, and constructed a prototype automated gas flux mesocosm. Greenhouse mesocosms did not show increased total organic carbon content after a 5-month study period, but did show total organic carbon content similar to that of field-sampled plots. Total organic carbon measured from natural and restored marsh systems indicated that restoration of tidal flooding resulted in a recovery of soil total organic carbon to natural levels after about 10 years following restoration. Several indices used to measure crop stress and photosynthetic function were applied to our spectral reflectance data, including the normalized difference vegetation index, the red-edge vegetation stress index, and the photosynthetic reflectance index. The photosynthetic reflectance index appeared most promising and may be an indicator of photosynthetic radiation use and net CO_2 uptake. Construction of the automated gas flux mesocosm was completed.

Introduction

No comprehensive studies have determined whether wetland restoration affects carbon sequestration rates. This project examined the use of mesocosms to measure carbon sequestration in natural and restored wetlands. We wanted to know how well mesocosms compare to field conditions and resolve differences in carbon sequestration. To this end, we tested the following hypotheses:

Ho_1: Organic carbon storage is the same in mesocosms as compared with natural wetland systems.

Ho_2: Restoration of hydrologically altered wetlands does not enhance carbon sequestration.

Ho_3: Spectral radiance does not differ between systems differing in carbon sequestration rate.

We expected that the mesocosms would provide a good match to natural systems and that restoration would result in enhanced carbon sequestration.

Approach

The technical approach focused on five tasks that addressed our three hypotheses.

The first task was to establish five mesocosms (~0.1 m^2) with the natural-vegetated community of a natural salt marsh. These mesocosms were maintained in ambient (atmospheric) conditions under a natural hydrologic regime. Plant growth rate, species abundance, aboveground biomass, soil moisture, and salinity and soil temperature were monitored and compared to measurements of plants and soil at a reference site.

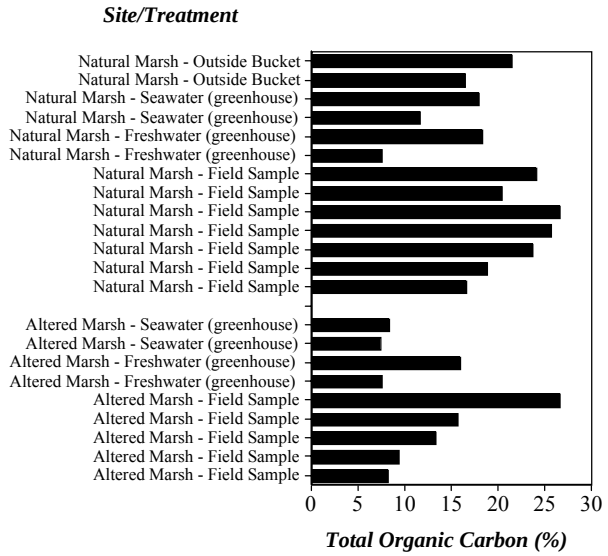

Figure 1. Total organic carbon measurements for natural and altered marsh treatments during the test period

The second task established 20 mesocosms (~0.1 m^2) with natural-vegetated communities of natural and restored wetland soil/vegetation cores (Figure 2). These mesocosms were maintained in a greenhouse under natural and altered hydrologic regimes. Plant growth rate, species abundance, aboveground biomass, soil moisture, and salinity and soil temperature were monitored.

Figure 2. Greenhouse mesocosms

The third task involved collection and total organic carbon analysis of soil samples from several restored and natural tidal marshes, as well as eelgrass meadows of varying post-restoration age marshes in Sequim Bay and Grays Harbor estuary, Washington, and Coos Bay, Oregon.

The fourth task explored the use of spectral radiance to detect changes in carbon sequestration by detecting differences in spectral signatures from the various treatments established in the second task. A spectral radiometer was used to determine spring and summer spectral signatures from all treatments, including the natural and hydrologically altered marshes.

The fifth and last task initiated construction of an automated gas flux mesocosm. This 1.0-m^3 chamber with four partitioned compartments will be able to continuously monitor CO_2 flux rates for mesocosms constructed in each section.

Results and Accomplishments

The following sections highlight the findings of our studies.

Reference Sites and Greenhouse Mesocosms

Total organic carbon measurements were constant for the natural salt marsh reference site and for the altered salt marsh (pasture) reference site based on winter and summer sampling.

Aboveground biomass was similar for greenhouse mesocosms started with natural marsh plants and the natural salt marsh reference site. Less aboveground biomass was available in altered marsh mesocosms.

Within the greenhouse mesocosms, the natural salt marsh mesocosms (mean total organic carbon = 22.3%) contained about 35% more total organic carbon on average than did the altered marsh mesocosms (mean total organic carbon = 14.6%). Total organic carbon did not increase in altered marsh mesocosm soils. In fact, all treatments in the mesocosms showed either a decrease or no change in total organic carbon over the 8-month period of the experiment, leading us to believe that maintaining the plants in pots confounded results for artificial manipulation of hydrology and resultant total organic carbon measurement.

Total Organic Carbon and Marsh Age

Samples from restored marshes in Grays Harbor estuary, Washington, and Coos Bay, Oregon, showed that restoration of tidal flooding resulted in a recovery of soil total organic carbon to natural levels after about 10 years following restoration (Figure 3).

Total organic carbon was higher in the two natural salt marshes (12.4%) as compared to the tidal freshwater marsh (mean = 3.9%).

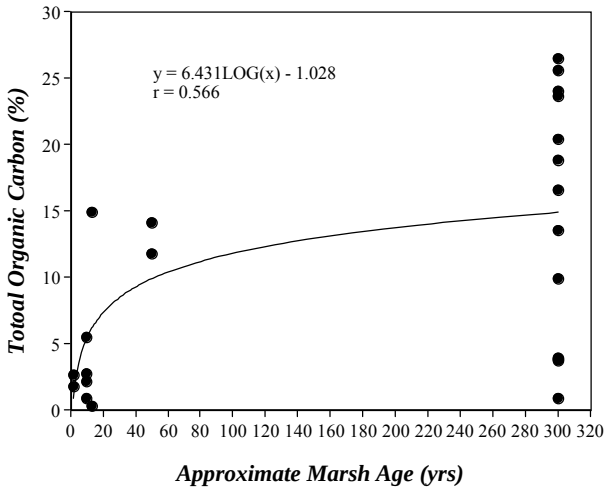

Figure 3. Total organic carbon versus marsh age

A 3-year-old eelgrass meadow established initially in low-organic-content sand in a large (9.5-m diameter) tank at the Marine Sciences Laboratory in Sequim, Washington, showed total organic carbon levels 74% greater than a sand-only control. The sand in the eelgrass tank was within the range of total organic carbon (mean =1.04%) found in natural meadows.

Spectral Measurements

An Analytical Spectral Devices FieldSpec® spectroradiometer was used to measure spectral reflectance of plants in the mesocosm treatments between 350 and 2500 nm. The reflectance signatures of various treatments, as well as clipped live biomass and dead, senescent material were collected.

We applied several indices routinely used to measure crop stress and photosynthetic function, including normalized difference vegetation index) (Rouse et al. 1973), the red-edge vegetation stress index (Merton 1998), and the photosynthetic reflectance index (Gamon and Serrano 1997). The most promising index for future work appears to be the photosynthetic reflectance index which has been explored as an indicator of photosynthetic radiation use efficiency. Gamon and Serrano (1997) tested the index across functional types (annual, deciduous perennial, and evergreen perennial) and found a significant correlation between photosynthetic reflectance index and net CO_2 uptake and radiation use efficiency measured by gas exchange, as well as by a fluorescence-based index of photosystem II photochemical efficiency.

Our data are representative in some cases of water-stressed plants. Our relatively high photosynthetic reflectance index values are also indicative of plants in a shaded environment, rather than representative of full sun environment.

Automated Gas Flux Mesocosm

The mesocosm test chamber was constructed in the Marine Sciences Laboratory greenhouse (Figure 4). The apparatus consisted of a Plexiglas tank divided into four 0.25-m^3 chambers. Each chamber was provided a 2-inch diameter opening at the top of the chamber, a 0.3-inch drain hole in the floor of the chamber, and a 0.25-inch gas flow line out of each chamber 6 inches above the bottom (floor).

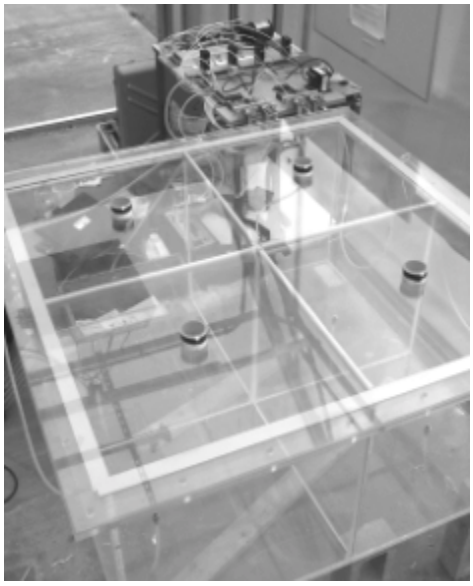

Figure 4. Prototype automated gas flux chamber

The test chamber is connected by four gas lines to a CO_2 analysis system. The configuration of the system is as follows:

- The configuration of the pumping consists of a vacuum pump to draw the sample through the system. The flow rate is regulated by four needle valves. The volume of gas through the system is measured by four Cole Palmer flow meters. The gas flow from the chambers is directed to the test equipment via four three-position solenoid valves.

- The solenoid valves are controlled by a programmable micro controller that is programmed to sample each chamber for 2 minutes every 1 hour. The duration and delay between samples is program-selectable. The microcontroller is also programmed to activate a Fluke data logger after each chamber is

purged for 2 minutes. The gas sample is measured and logged for each chamber every hour.

- Data from the data logger will be collected in a time-stamped tabular form. These data will be post-processed to convert voltages to engineering units. The analysis will be done in Excel spread sheets for evaluation.

Summary and Conclusions

Our field sampling in marshes of varying ages validated our initial assumption that restoration of natural hydrology resulted in a gain in soil total organic carbon after only a few years. The experimental eelgrass meadow total organic carbon levels were also much greater than background after 3 years, indicating that restoration of eelgrass meadows may provide additional carbon storage. Although the initial experiments on manipulated hydrology did not provide demonstrable change in soil total organic carbon, we suspect that both the short duration of the experiments and the small size of the pots that were used may partially explain the results. The effect of the manipulations on gas fluxes into and out of the soil is not known. Initial runs with the system prototype automated mesocosm indicate that it will be very useful in resolving short- and long-term gas flux rates and processes.

Spectral research indicated that some plants in the greenhouse might have been stressed for water. After making modifications to the mesocosm setup to reduce this effect, we plan to conduct further studies in a controlled greenhouse environment under full sun and under shaded conditions that include species-specific measurements of CO_2 flux and photosynthetic reflectance index through diurnal cycles. Effects of nutrient depletion or enhancement will also be examined. Other indices related to canopy or water stress also may be examined.

References

Gamon JA and L Serrano. 1997. "The photochemical reflectance index: An optical indicator of photosynthetic radiation use efficiency across species, functional types, and nutrient levels." *Oecologica*, Vol. 112, pp. 492-501.

Merton R. 1998. "Monitoring community hysteresis using spectral shift analysis and the red-edge vegetation stress index." *Proceedings of the Seventh Annual JPL Airborne Earth Science Workshop*.

Reichle D et al. 1999. Working paper on carbon sequestration science and technology. Office of Science, Office of Fossil Energy, U.S. Department of Energy.

Rouse JW, RH Haas, JA Schell, and DW Deering. 1973. "Monitoring vegetation systems in the Great Plains with ERTS." *Proceedings, Third ERTS Symposium,* Vol. 1, pp. 48-62.

Presentation

"Carbon Sinks in Nearshore Marine Vegetated Systems." October 2000. Advances in Terrestrial Ecosystem Carbon Inventory, Measurements, and Monitoring, North Carolina State University.

Development of a Tool for Investigating Multiphase and Multiscale Atmospheric Chemical and Physical Processes

Carl M. Berkowitz, Xindi Bian, Rahul Zaveri, Jerome D. Fast

Study Control Number: PN99015/1343

A high performance reactive transport code was designed to simulate atmospheric processes that control tropospheric oxidants and aerosols. Simulations can be produced at high spatial and temporal resolutions while also incorporating detailed numerical representations of chemical and physical processes. State-of-the-art process modules, numerical methods, and computational techniques are being incorporated in the model. This research will help us address key issues on the formation and distribution of fine aerosols and tropospheric oxidants.

Project Description

The Department of Energy has a strong interest in air quality and climate change. New national ambient air quality standards for tropospheric ozone and particles less than 2.5 micron diameter (PM2.5) are of special concern to DOE. DOE is interested in developing a clearer understanding of how emissions from energy production lead to oxidant and aerosols, and under what conditions emission controls will be effective. Complicating this task is a lack of understanding of the basic mechanisms by which fine particles are formed, how they interact with atmospheric oxidants and ozone, and the mechanisms by which they affect human health. As a result, the scientific community recognizes that improved modeling capabilities are needed to address the key issues facing policymakers regarding ozone and particulate matter smaller than 2.5 microns in diameter.

Introduction

Our objective has been to develop a computational tool for analysis of multiphase atmospheric processes, which occur over multi-decadal scales in space and time. The modules have been built into a highly flexible and portable framework and are capable of simulating chemical reactions in the gas phase, in the aqueous phase, and in and upon solid and mixed-phase particles. Additional modules will treat the dispersion, transport, scavenging, and deposition of trace materials in the gaseous phase and in aerosols, cloud drops, and precipitation. We have also begun using this model to investigate the interaction of processes acting on different scales. This tool now appears to be capable of performing research in atmospheric chemistry linking results obtained in laboratory studies with large-scale air quality and climate change models.

Approach

The code we have developed is called PEGASUS, taken from the winged horse of Greek mythology. The acronym also identifies our Laboratory for developing the code (PNNL), the mathematical framework (Eulerian), the multiple chemical phase capability (gas and aerosols), its scalability on high-performance computers, and that it brings together, or creates a unified system, to describe both chemical and meteorological processes. Modules are being added to this basic gas-phase-only code that allow the code to simulate the following processes:

- heterogeneous reactions on the surface and in the interior of aerosols and cloud drops
- formation of new particles through multi-species gas-to-particle nucleation
- detailed treatment of the microphysical dynamics of aerosol and droplet growth
- scavenging of gases and aerosols by clouds and precipitation.

Whereas the formulations for simulating many of these processes are available in the open literature, a substantial effort has gone into integrating the various algorithms into a computational architecture that enables them to easily interact with existing and future modules. Along with the addition of advanced process modules, we have maintained the computational efficiency and accuracy by

developing code architecture to minimize numerical diffusion in the transport algorithms

- ensure mass conservation among the governing equations for reactive trace gas species
- maintain the efficiency of numerical solvers for systems of coupled sets of nonlinear differential equations
- maintain scalability.

Results and Accomplishments

A central component of any air chemistry model is the mathematical description of the chemical processes themselves. The results from these algorithms provide input for subsequent mathematical descriptions of transport and removal. Many chemical mechanisms have been put forward in the open literature. The diversity of mechanisms represent efforts to balance the thousands of known reactions against finite computer resources. In principle, each mechanism is tailored to the scientific problem of concern to the investigator. The chemical mechanisms vary widely in the detail with which they treat the dominant long-lived chemical species (such as ozone or various nitrogen oxides), and key short-lived species (such as HO_2 or OH) that affect these longer-lived trace gases.

Recent work on the development of PEGASUS has included the insertion of a new mechanism designed to balance details against finite computational resources. This newly developed photochemical mechanism, called the Carbon-Bond Mechanism – Zaveri or CBM-Z (Zaveri and Peters 1999) extends the framework of an earlier lumped-structure mechanism to function properly at larger spatial and longer timescales, of interest for a variety of problems of concern. As a preliminary quality control check, the performance of CBM-Z has been compared with an older mechanism based on Lurmann et al. (1986). As illustrated in Figure 1, CBM-Z produces lower peak ozone concentrations than the old mechanism. We attribute these differences to the refined treatment of isoprene, one of the most reactive biogenic hydrocarbon species in the U.S., in CBM-Z.

Keeping in mind the need for computational efficiency to offset the added detail in CBM-Z, we have also added a novel numerical solver that is regime-dependent. With this new algorithm, the CBM-Z mechanism is optimized at each grid point and at every transport time step. The optimization works by solving only the necessary

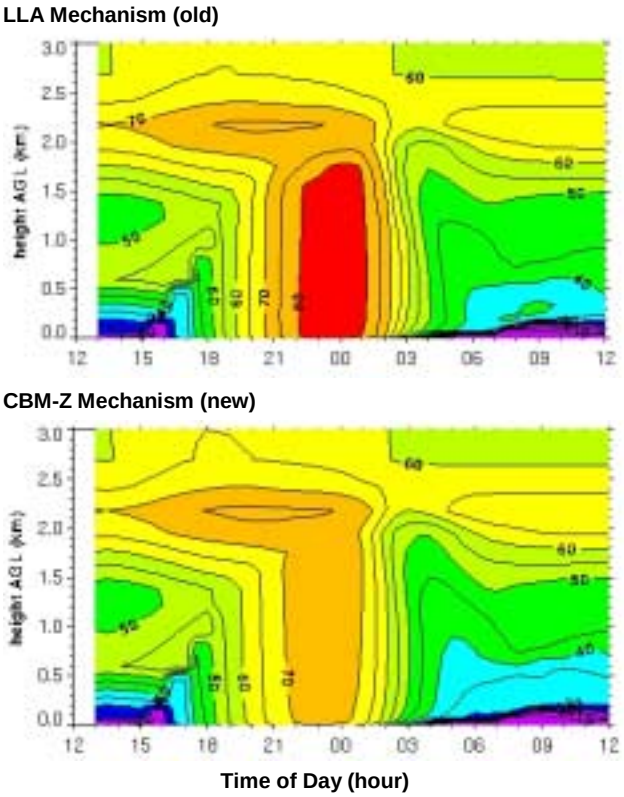

Figure 1. Comparison of O3 production by the method of Lurmann et al. (1986) (top) and CBM-Z chemical mechanisms in PEGASUS (bottom). Differences are primarily due to the refined treatment of hydrocarbons, especially isoprene, in CBM-Z.

chemical reactions. For example, dimethylsulfide chemistry is turned on only when the dimethylsufide concentrations are appreciable. Similarly, isoprene chemistry is turned on only when the dimenthylsulfide are appreciable. This approach will reduce the overall computer time by about 30% in a large-scale simulation.

The "A" in PEGASUS stands for "aerosol." One of the most challenging tasks for a large model like PEGASUS is the prediction of the equilibrium phase of the aerosol (solid, liquid, or mixed) and the associated water content as a function of ambient relative humidity. While methods based on the direct minimization of Gibbs free energy of the aerosol system are available (Ansari and Pandis 1999), they are computationally extremely expensive and therefore not amenable for use in large three-dimensional Eulerian air-quality models. We have developed an alternative solution algorithm, which appears to be much faster than the existing methods. Instead of searching for the minimum Gibbs free energy of the system to calculate the equilibrium phase state, we recast the problem in terms of set of hypothetical, dynamic ordinary differential equations, and allow its solution to reach equilibrium.

This new aerosol module is called MOSAIC (Model for Simulating Aerosol Interactions and Chemistry) (Zaveri 1997), and has recently been included in the PEGASUS framework. MOSAIC is capable of simulating the multi-stage (mixed-phase) growth features in multicomponent aerosols consisting of various salts of sulfate, nitrate, chloride, ammonium, and sodium. An example of two-stage deliquescence curve (increasing relative humidity) is illustrated in Figure 2 for a sea-salt aerosol consisting of equimolar mixture of Na_2SO_4 and NaCl. On the efflorescence curve (decreasing relative humidity), the particle is shown to remain supersaturated (liquid-phase) all the way down to 50% relative humidity.

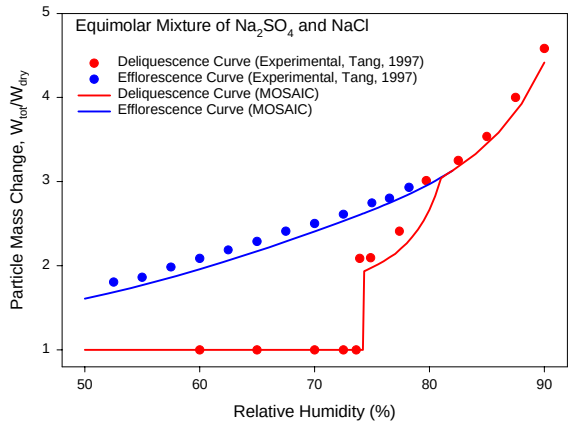

Figure 2. Particle mass change at 298 K of a mixed Na_2SO_4-NaCl particle (equimolar mixture): model predictions and experimental results

Summary and Conclusions

This project broadens the range of environmental media being investigated at the Laboratory. It also greatly increases the range of spatial and temporal scales and processes that are being addressed. As part of the testing of PEGASUS, we have evaluated the downward transport of fine filaments of reactive gases from the stratosphere that span geographical scales of thousands of kilometers. We have also tested the new chemical mechanism against observations made within air masses that started their journey on the west coast of North America and have been transported inland to Phoenix, Arizona. Molecular-scale homogeneous and heterogeneous reactions and mass transfer processes occur within both processes. Because of its performance, as measured by the proportionality between speedup and the number of processors, PEGASUS can include detailed information for processes that would otherwise be too computationally expensive for a standard air chemistry model. Access to this tool will position scientists to perform research in atmospheric chemistry that links the results obtained in laboratory studies with large-scale air quality and climate change models.

References

Ansari AS and SN Pandis. 1999. "Prediction of multicomponent inorganic atmospheric aerosol behavior." *Atmos. Environ.* 33:745-757.

Berkowitz CM, X Bian, and RA Zaveri. 2000. *Development of a tool for investigating multiphase and multiscale atmospheric chemical and physical processes.* PNNL-13203, Pacific Northwest National Laboratory, Richland, Washington.

Lurmann FW, AC Lloyd, and R Atkinson. 1986. "A chemical mechanism for use in long-range transport/acid deposition computer modeling." *Journal of Geophysical Research* 90:10,905-10,936.

Tang IN. 1997. "Thermodynamic and optical properties of mixed-salt aerosols of atmospheric importance." *Journal of Geophysical Research* 102:1883-1893.

Zaveri RA. 1997. *Development and evaluation of a comprehensive tropospheric chemistry model for regional and global applications.* Ph.D. dissertation, Virginia Polytechnic Institute and State University, Blacksburg, Virginia.

Zaveri RA and LK Peters. 1999. "A new lumped structure photochemical mechanism for large-scale applications." *Journal of Geophysical Research* 104:30,387-30,415.

Publications and Presentations

Fast JD, X Bian, and CM Berkowitz. 1999. "Regional-scale simulations of stratospheric intrusions of ozone over Eastern North America during the summer of 1991." Preprints, Symposium on Interdisciplinary Issues in Atmospheric Chemistry, January 10-15, 1999, Dallas, Texas, pp. 16-23. American Meteorological Society, Boston, Massachusetts.

Zaveri RA and LK Peters. 1999. "A new lumped structure photochemical mechanism for large-scale applications." *Journal of Geophysical Research* 104:30,387-30,415.

Berkowitz, CM. June 2000. "Atmospheric chemistry modeling at PNNL: what it is and where we're going." Computer Sciences and Engineering Seminar Series, Richland, Washington.

Bian X, CM Berkowitz, RC Easter, JD Fast, SJ Ghan, and R Zaveri. 1999. "Development and application of an atmospheric modeling system for use on a massively parallel computer." 1999 Annual Conference on Super-Computer, Portland, Oregon.

Development of an Aquatic Bio-Optical Monitoring Buoy

Dana Woodruff, Paul Farley, Karen Steinmaus

Study Control Number: PN99018/1346

Satellite algorithm development is needed in coastal and nearshore waters to take advantage of a new generation of higher resolution, recently launched satellites. This project evaluated the use of a bio-optical monitoring buoy with a complement of environmental and optical sensors to provide near real-time, remotely accessible data for algorithm development and natural resource/damage assessment of coastal and inland waters.

Project Description

This project developed an approach to collect bio-optical data in coastal nearshore, and inland waters using a near real-time remotely accessible bio-optical monitoring buoy designed to validate ocean color algorithms for satellites collecting data in coastal environments. The recent successful launch of the NASA Sea-Viewing Wide Field-of-View Sensor ocean color satellite and scheduled launch of future ocean color sensors requires validation, modification, and development of ocean color algorithms for specific use in optically complex nearshore waters. In situ calibration data has traditionally been collected from shipboard platforms, requiring labor-intensive field efforts. This project will provide a streamlined, flexible approach to collect bio-optical data in geographic regions (coastal, nearshore, or inland waters) that require further algorithm development. A portable buoy with a unique complement of environmental and optical sensors will allow for a quick response monitoring capability for natural resource and/or damage assessment in inland and coastal waters.

Introduction

Global climate change issues have necessitated multidisciplinary assessment approaches, including the use of satellites to understand the role of oceanic phytoplankton and primary production in global ocean carbon cycling. Although coastal waters account for approximately 10% of the surface area of the global oceans, they contribute almost 40% of the total global primary production. One of the differences between coastal and oceanic primary production is thought to be partly a consequence of human-induced activity and associated impact to nearshore systems. To this end, the role of satellite monitoring in coastal waters has become increasingly important, including the ability to convert satellite-acquired data into reliable estimates of environmentally significant parameters.

The use of satellite ocean color imagery in biologically productive coastal regions requires modification of standard oceanic algorithms and development of new algorithms for optical properties unique to coastal waters. Nearshore waters contain higher concentrations and greater varieties of optical constituents (chlorophyll, suspended sediments, colored dissolved organic matter) than oceanic waters. The first ocean color satellite, the Coastal Zone Color Scanner was operational between 1976 and 1986 and provided extensive data on ocean chlorophyll estimates; however, the algorithms and sensor could not adequately address coastal waters due to a limitation in gain and response of the sensor near land. The second generation of ocean color satellites recently became operational with the launch of the Sea-Viewing Wide Field-of-View Sensor satellite which has improved radiometric response and additional wavebands making it more useful in coastal waters than Coastal Zone Color Scanner was. NASA developed a well-calibrated and validated suite of algorithms for chlorophyll estimation in the open ocean. However, these algorithms are proving to be inadequate for viewing coastal regions, which are optically more complex. Rapid and accurate methods of collecting in situ absorption (chlorophyll and DOM) and backscattering (suspended particulates) data are needed to develop these new algorithms and to define regional algorithm boundaries for imagery application. Optical and environmental data that can be collected from a remote platform such as a buoy will reduce the cost significantly and will provide temporal coverage that is not available using traditional collection methods.

Results and Accomplishments

We evaluated the use of an aquatic bio-optical monitoring surface buoy to collect ground-truth data for satellite algorithm development in semiprotected coastal areas (Figure 1 and the schematic in Figure 2). Incorporated into the buoy platform were the following capabilities: 1) multipurpose combined satellite validation and

environmental monitoring, 2) portability for quick response in varied coastal waters, 3) data accessibility in near real-time, 4) varied data acquisition scenarios programmable for up to a 4-month collection, and 5) a multisensor platform capable of adding and changing sensors quickly to accommodate client needs and changing environmental scenarios. The buoy was powered by four recombinant gel cells augmented with solar charging. Data acquired from the buoy was accessed remotely using cell phone technology.

Figure 1. Costal bio-optical monitoring buoy

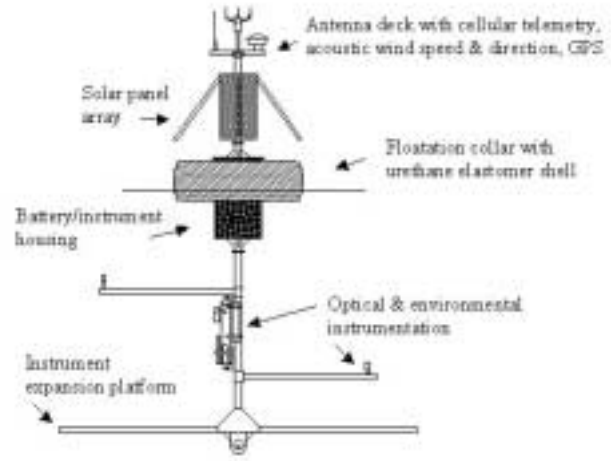

Figure 2. Schematic of current configuration of monitoring buoy

The current suite of sensors incorporated into the buoy collects the following data:

In-water (~ 1 m depth)

- chlorophyll concentration
- turbidity
- dissolved oxygen
- salinity
- solar irradiance at 1 m and 2 m depth
- light attenuation.

Atmospheric (~ 2 m above water surface)

- wind speed and direction
- global positioning.

Summary and Conclusions

All buoy components were successfully tested including all software and sensor hardware, environmental sensors, data logger and processing software, and telecommunications package. We will next collect buoy data in local coastal waters, including acquisition and analysis of corresponding satellite imagery.

The advantages of this platform for satellite algorithm development and environmental monitoring include

- reduced cost in data collection relative to ship-board data acquisition
- near real-time acquisition of data
- multisensor platform capability with use-programmable data collection scenarios.

Electrochemical Enhancement of Permeable Treatment Barriers

Johanes H. Sukamto, Wesley E. Lawrence, Vilayanur V. Viswanathan, Jonathan S. Fruchter

Study Control Number: PN00038/1445

In Situ Redox Manipulation (ISRM) is an innovative technology for treating chromate-contaminated groundwater plumes at the Hanford Site. Currently, the technology requires injection of expensive reducing agents. This project evaluated the feasibility of using ex situ electrochemical synthesis of dithionite to reduce both the chemical cost and waste volume associated with the current process. The successful demonstration of this technology may lead to further development of a process for in situ generation of dithionite.

Project Description

A procedure for the electrochemical synthesis of dithionite ($S_2O_4^{-2}$) was developed through modification of a single-pass process developed by Oloman et al. (1999). The effects of reactant concentration, reactant flow rate, and current density on product concentration were investigated. This process was used to generate dithionite from a simulant of spent in situ redox manipulation solution. The stability of the generated dithionite in air and under nitrogen was investigated. In addition, a cost analysis was performed to estimate large-scale production cost using this method. This project advanced our ability to electrochemically synthesize dithionite from low-cost feedstock such as spent in situ redox manipulation solution.

Introduction

In situ redox manipulation creates a permeable treatment zone in the subsurface by reducing ferric iron in the aquifier to ferrous iron. Conventional groundwater wells are placed at the treatment site. Sodium dithionite solution is injected into the wells for 10 to 20 hours. The goal of the in situ redox manipulation method is to create a permeable treatment zone in the subsurface to remediate redox-sensitive contaminants. Redox-sensitive contaminants in the plume are immobilized or destroyed as they migrate through the manipulated zone.

The chemical solution of sodium dithionite is injected into the wells and when the solution reaches the groundwater it reacts with iron in the soil to form a large barrier. When the groundwater flows through the barrier, the targeted contaminants are destroyed or immobilized. Activation of a permeable treatment barrier requires the use of reducing agents. Currently, the reducing agents are purchased and shipped to the treatment site and the spent reducing agent solutions disposed of as waste. Using electrochemical synthesis of dithionite, it is possible to generate reducing agents on-site and possibly recycle (reuse) the spent solution. This approach could reduce chemical costs and minimize waste generation. In this study, electrochemical preparation of dithionite was studied. The effect of residence time; feed concentration; and residence time on dithionite concentration, conversion, and coulombic efficiency was determined. A cost estimate was completed to determine production cost for dithionite using this method.

Results and Accomplishments

Dithionite Generation

Dithionite was generated electrochemically using a microflow cell (Electrocell AB). Sodium hydroxide of varying concentration was used as the anolyte. The catholyte consisted of a 0.2 M solution of sodium sulfite in either deionized water or in a mixture of sulfurous acid and sodium hydroxide. The anode was platinized titanium, while the cathode consisted of a nickel foam electrode with 80 pores per inch and a surface area of 32 cm^2/geometric cm^2. The flow pattern within each chamber consisted of flow past the electrode at varying rates, such that the residence time inside the cell ranged from 1 to 10 seconds. The cathode and anode compartments were separated by Nafion 450 membrane. The membrane was pretreated by immersion in boiling deionized water for 40 minutes, followed by overnight immersion in deionized water. The exit solution pH was controlled at 6.0 by addition of 0.5 M and 1.5 M sulfuric acid or 1 M sulfurous acid. The catholyte was continuously purged with nitrogen during the process. Catholyte samples were taken downstream of the cathode compartment exit and analyzed for dithionite concentration by titrating against 0.5 M $K_3Fe(CN)_6$ using methylene blue as an indicator. Calibration was done by titrating a known volume of 0.2 M sodium dithionite against 0.5 M $K_3Fe(CN)_6$ under a nitrogen atmosphere. The current ranged from 0.13 to 0.51 A, which

corresponded to a current density of 0.4 to 1.6 mA/cm^2. The coulombic efficiency was lowest for runs with 0.5 M sulfuric acid addition, while, as expected, it was highest for 1 M sulfurous acid addition due to higher reactant concentration.

Figure 1 shows the dithionite concentration profile for low sulfite concentration (pH control by sulfuric acid addition) as a function of total charge input at various currents and residence times. For a fixed residence time, the dithionite concentration increased with a decrease in current, while for a fixed current, the concentration increased with a faster catholyte flow rate. This indicated that the rate of sulfite generation was limited by diffusion under the test conditions. The subsequent drop in dithionite concentration was shown to result from dithionite decomposition.

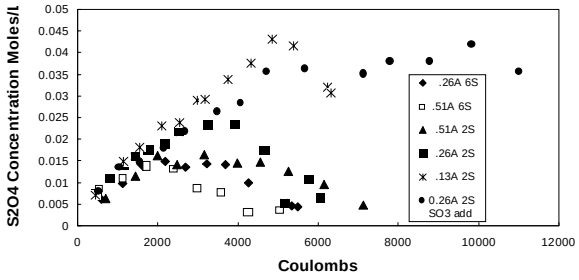

Figure 1. Effect of current and residence time on dithionite concentration—pH controlled at 6 by 1.5 M sulfuric acid addition. ♦ corresponds to 0.5 M H_2SO_4 addition; ● corresponds to sulfurous acid addition.

Figure 2 shows the dithionite profile for high sulfite concentration in the feed (pH control by sulfurous acid addition) at a current of 0.5 A and a residence time of 10 seconds. The feed consisted of 0.2 M Na_2SO_3 prepared in water, or 1 M sulfurous acid or in a Fort Lewis simulant solution, with the indicated addition of 5 M NaOH and 1 M sulfurous acid to keep the feed pH at 6. Under these conditions, dithionite generation was not diffusion limited, thus allowing use of high current at low flow rates. The poor results up to 5000 coulombs for the 100 mL deionized water sample was attributed to the use of low current (0.13 A) and low residence time (1.5 seconds). The use of low current corresponds to long reaction time for a fixed charge input, thus leading to decomposition of the dithionite product, while the high flow rate prevented full access to the bulk of the electrode. At 5380 coulombs, the residence time was increased to 10 seconds, which resulted in a significant increase in dithionite concentration. At 11,000 coulombs, the current was increased to 0.4 A, which led to a further increase in the slope of the curve. At 14,000 coulombs,

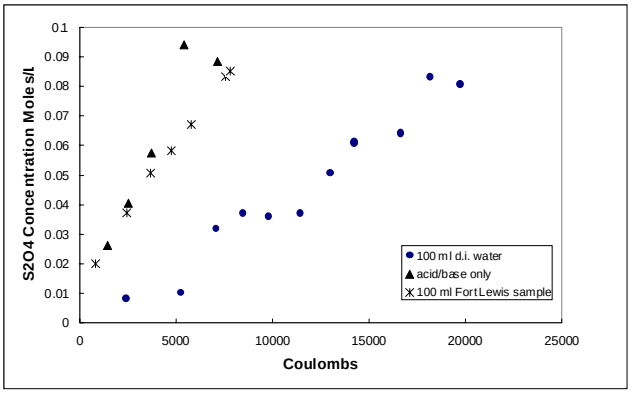

Figure 2: Comparison of result for 1 M H_2SO_3 addition; feed is 0.2 M Na_2SO_3 prepared in ● 100 mL water+168 mL 1 M H_2SO_3+29 mL 5 M NaOH; ▲250 mL 1 M H_2SO_3+50 mL 5 M NaOH; ✱100 mL Fort Lewis sample, 250 mL 1 M H_2SO_3, 50 mL 5 M NaOH

the residence time was decreased to 1.6 seconds, leading to a flatter profile.

The residence time was increased to 10 seconds at 16,300 coulombs, which resulted in a greater slope. This result confirmed that a very high flow rate is detrimental for a high sulfite concentration.

To determine the stability of dithionite concentration over time, the current was increased at the end of one of the runs until the catholyte pH reached 11. The power was then turned off, and the initial dithionite concentration was determined. A portion of the catholyte was then left open to atmosphere, while nitrogen was bubbled through the remaining catholyte. After 57 hours, the dithionite concentration was about 50% of initial concentration for nitrogen bubbling, while the corresponding time was 9 hours without nitrogen. Similar results were obtained when the pH was raised by addition of sodium hydroxide.

Cost Analysis

The efficiency was highest at low current/low residence time for sulfuric acid addition, while for sulfurous acid addition, best results were obtained at high current and high residence time. Calculations were completed for both high and low currents at various residence times accounting for the detrimental effect of sulfite conversion to sulfate.

The cost of electrochemical synthesis of dithionite ranging from $0.51/mole to $0.75/mole compares favorably with an estimated cost of $1.5 to $2/mole using current regeneration processes. However, this estimate does not include facilities and labor costs.

Summary and Conclusions

A process for the ex situ electrochemical synthesis of dithionite was developed and its applicability evaluated. A cost estimate was completed for large-scale dithionite generation. We concluded that

- The process was diffusion-limited at low catholyte concentrations, requiring low current and high flow rate.
- At high sulfite concentrations, the use of higher currents gave better conversions due to minimization of dithionite decomposition.
- At high sulfite concentrations, a low residence time was detrimental, due to incomplete access to the entire electrode surface area. Improvement in the flow pattern through the electrode is expected to allow use of shorter residence time and higher coulombic efficiency.
- These results allowed determination of optimum conditions for various dithionite regeneration rates and catholyte compositions.
- Dithionite was more stable under nitrogen than in air by a factor of 5.
- A cost estimate showed this process can be competitive with other generation methods.
- The next step will be investigation of in situ dithionite generation.

Reference

Oloman C, B Lee, and W Leyten. 1999. "Electrosynthesis of sodium dithionite in a trickle-bed reactor." *Can. J. Chem. Eng*. 68:1005-1009.

Bibliography

Chemical Market Reporter, 257 (16), April 17, 2000.

Enhancing Emissions Pre-Processing Capabilities for Atmospheric Chemistry

Elaine G. Chapman, Jerome D. Fast, W. Richard Barchet

Study Control Number: PN00040/1447

Atmospheric chemical transport models are used in research ranging from global climate change to pollution abatement strategies for meeting urban air quality standards. Emissions are an essential input to these models. This project enhanced the efficiency, effectiveness, and accuracy with which model-ready emissions may be generated.

Project Description

The purpose of this project was to enhance our capability for modeling atmospheric pollutants. Observed pollutant concentrations result from local emissions reacting with chemical species transported into an area from long distances. To accurately model and understand such situations, we need to capture the local, regional, and synoptic meteorological and chemical factors, as well as to provide accurate local-, regional- and continental-scale emissions inputs. We designed algorithms and developed computer codes to combine different pollutant emissions inventories with differing spatial and temporal scales. The resulting nested emissions provide substantially improved model input relative to the standard procedure of using only one inventory. We also expanded the chemical detail and number of emissions inventories available for routine use with our models, and generalized our in-house emissions preprocessing programs. This project advanced our ability to readily and efficiently assemble the most appropriate emissions input for a given model application.

Results and Accomplishments

We successfully realized substantial increases in efficiency by generalizing, standardizing, and automating selected in-house emissions processing programs. Staff prepared emissions inputs for two separate modeling efforts, one of which involved emissions inputs from a new global inventory that we had not previously worked with. Using programs enhanced under this project, one person was able to generate the necessary model-ready emissions inputs, with selected graphics and summary information, in less than 8 hours. We estimate it would have required 3 days for each modeling effort (6 days total) prior to the improvements realized under this project.

The more efficient processing programs were used to generate a prototype nested emissions data set for modeling applications. We successfully wrote and tested computer codes for reading, regridding, speciating, and nesting emissions inventories with different temporal and spatial scales. The codes were developed in a generic format, to permit ready use in future modeling efforts. We used these programs to generate a prototype double-nested, model-ready emissions input data set for modeling air quality in the vicinity of Phoenix, Arizona. The final, model-ready emissions data set included California Air Resources Board emissions for southern California and Arizona Department of Environmental Quality emissions for Phoenix nested within the continental-scale National Emissions Trends Inventory of the U.S. EPA, all nested within global emissions data from the Global Emissions Inventory Activity. Model predictions capture the major features, and many minor features, of chemical measurements taken in Phoenix, and unequivocally show that ozone concentrations in the Phoenix area are governed mainly by hydrocarbons, rather than by locally emitted nitrogen oxide (NOx) compounds. Interpretation of regional influences on Phoenix urban chemistry was significantly enhanced through use of the detailed nested emissions input, emphasizing the importance of emissions on overall model results.

Summary and Conclusions

Although significant improvements in processing capabilities were realized and a novel, nested emissions set successfully generated and used, the major conclusion of this work is that such advances represent only a stopgap measure relative to the direction of atmospheric chemistry modeling. Publicly available, gridded emissions inventories represent static levels. These inventories generated assuming average conditions over a given time period. Such inventories are processed off-line to produce model-ready emission fluxes. We foresee modeling efforts, particularly regional-scale modeling programs, moving toward needing dynamically derived emissions that reflect specific meteorological conditions in a specific time period in a specific geographic region. We also foresee a need to eventually couple emissions-generating modules directly with the chemical,

meteorological, and numerical integration modules within all chemical transport models, rather than continuing with off-line processing. Additional efforts to establish such a modeling capability will advance future atmospheric research.

Publication and Presentation

Fast JD and EG Chapman. 2000. "Regional-scale transport in the vicinity of Phoenix during a spring field campaign." In *Preprints, Symposium on Atmospheric Chemistry Issues in the 21st Century*, Long Beach, California, pp. 108-113. American Meteorological Society, Boston, Massachusetts. (AMS Annual Meeting, Long Beach, California, January 10-13, 2000).

Environmental Fate and Effects of Deep Ocean Carbon Sequestration

Ann Drum Skillman, Michael Huesemann, Eric Crecelius

Study Control Number: PN00041/1448

The emission of man-made sources of CO_2 into the atmosphere is considered a major factor in the greenhouse effect leading to global warming. Several options for capturing and sequestering this CO_2 have been proposed. These options include deep-ocean injection. This study examined the effects of CO_2 ocean sequestration on marine nitrification processes and associated environmental impacts.

Project Description

In an attempt to slow down global warming, it has been proposed to reduce the rise of atmospheric carbon dioxide concentrations by disposing CO_2 (from the flue gases of fossil fuel fired power plants) into the ocean. The release of large amounts of CO_2 into mid or deep ocean waters will result in large plumes of acidified seawater with pH values ranging from 6 to 8. To determine whether these CO_2-induced pH changes have any negative effect on marine nitrification processes, surficial (euphotic zone) and deep (aphotic zone) seawater samples were sparged with CO_2 for varying time durations to achieve a specified pH reduction and the rate of microbial ammonia oxidation was measured spectrophotometrically as a function of pH. For both seawater samples taken from either the euphotic or aphotic zone, the nitrification rates dropped drastically with decreasing pH. Relative to nitrification rates in the original seawater at pH 8, nitrification rates are reduced by about 50% at pH 7 and by more than 90% at pH 6.5. Nitrification is essentially completely inhibited at pH 6.

Introduction

The combustion of fossil fuels during the last two centuries has significantly increased the concentration of carbon dioxide in the atmosphere and this is predicted to result in global warming and a wide range of concomitant negative environmental and social impacts (Houghton 1997; Rayner and Malone 1998). To reduce the future potential impacts of global warming, carbon dioxide could potentially be removed from either the atmosphere or from the flue gases of power plants by sequestering it in terrestrial ecosystems, geological formations, or oceans. A number of different ocean disposal strategies have been proposed including the release of CO_2 enriched seawater at 500 to 1000 m depth, or the injection of liquid CO_2 at 1000 to 1500 m depth. The CO_2 injections will result in large pH plumes around the injection points (Figure 1) (DOE 1999; Caulfield et al. 1997; Herzog et al. 1996). Modeling results indicate that the pH around the injection point could be less than 5.8 and the steady-state plume of seawater with a pH less than 6.6 could be at least 25 km long and 1000 m wide and after a 20-year continuous CO_2 injection could be more than 1000 miles long (DOE 1999; Caulfield et al. 1997; Herzog et al. 1996).

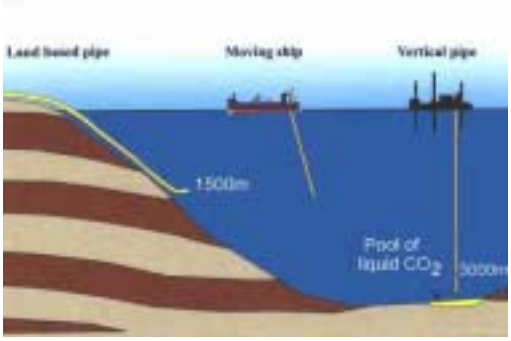

Figure 1. Conceptual diagram of several methods of ocean sequestration of CO_2

Little is known about the potential environmental effects of CO_2 disposal in oceans including impacts to the marine nitrogen cycle. Figure 2 shows a conceptual model of the oceanic nitrogen cycle (Libes 1992). Most of the nitrogen from phytoplankton growing in the euphotic zone is recycled by bacteria and zooplankton while the remaining nitrogen sinks as particulate organic material into the aphotic zone. While slowly sinking toward the ocean floor, aerobic bacteria first convert the particulate organic nitrogen into dissolved organic nitrogen and subsequently cause the release of free ammonium into the seawater. Ammonium is readily oxidized to nitrite and then to nitrate in a stepwise process called nitrification. The resulting nitrate accumulates in the deep ocean but is eventually up-welled back into the euphotic zone where it serves as new nitrogen for the growth of phytoplankton. The import of new nitrogen from the aphotic zone is very substantial and serves as an important nutrient source for oceanic primary productivity and world fisheries (Libes 1992; Capone 2000; Falkowski et al. 1998).

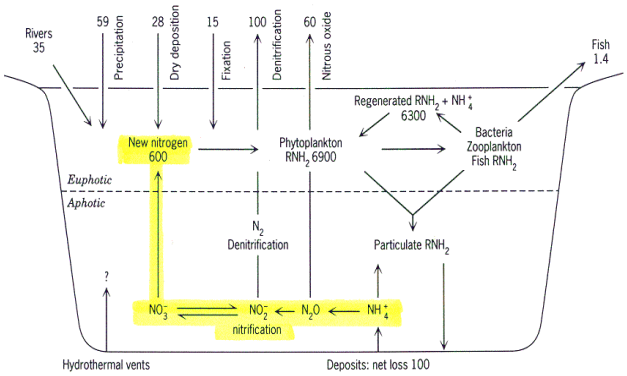

Figure 2. The marine nitrogen cycle including estimates of nitrogen transport rates in 10^{12} g N/y

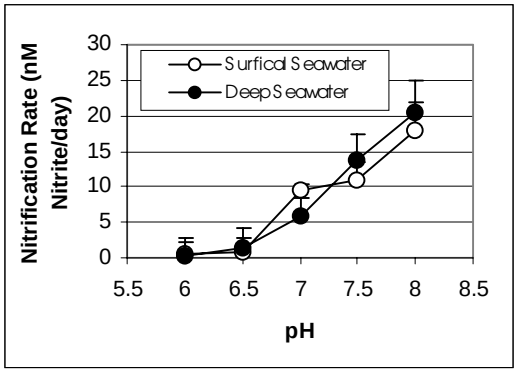

Figure 3. Nitrification rates as a function of pH in seawater samples taken from the euphotic (at 1 m) and aphotic (at 160 m) zone

The objective of this study was to determine whether pH changes induced by CO_2 sparging have any effect on the rate of nitrification, particularly ammonia oxidation in seawater samples taken from both the euphotic and aphotic zone.

Results and Accomplishments

Figure 3 shows nitrification rates as the function of pH for seawater samples taken from both the euphotic and aphotic zone. In both cases, the nitrification rates drop drastically with decreasing pH. Relative to nitrification rates in the original seawater at pH 8, nitrification rates are reduced by about 50% at pH 7 and more than 90% at pH 6.5. Nitrification is essentially completely inhibited at pH 6. Although the seawater samples were taken at different depths, the effects of pH on nitrification rates appear to be comparatively similar.

The finding that nitrification is inhibited at low pH values is generally supported by earlier results reported in the literature. The deep-sea environment is generally considered stable, and temporal or spatial changes in physicochemical factors are small. Based on this assumption, it has been suggested by others that deep-sea organisms must be exceptionally sensitive to environmental disturbances because any species with the ability to adapt to changes have long been eliminated in the process of evolutionary selection in this stable eco-system. A major change in proton concentrations (by a factor 100 or 2 pH units) would result in the inhibition of ammonia oxidation. Since nitrifying bacteria are chemolithoautotrophs that obtain all of their energy requirements from the oxidation of ammonium or nitrite, we conclude that a pH-induced inhibition of ammonia oxidation will also lead to a drastic reduction in the growth rate of nitrifying bacteria such as *Nitrosonomas* and *Nitrobacter*.

As shown in Figure 3, the ammonia oxidation rate in undisturbed seawater at pH 8 was around 20 nM/d for both surface and deep-water samples. The magnitude of observed nitrification rates in this study are comparable to those reported in the literature. The low pH within the plume will most likely result in the reduction of ammonia oxidation rates and the concomitant accumulation of ammonia (instead of nitrate). The concentration of un-ionized ammonia inside a plume of pH ≤6 would be only 0.1 µg/L and would most likely not cause unacceptable toxicity effects to aquatic organism (according to EPA's ambient water quality criteria for ammonia in saltwater). The fate of up-welled ammonium into overlying seawater with a higher pH is twofold. In the absence of light, nitrification will resume and nitrate will be formed. In the presence of light, phytoplankton will assimilate ammonium as an important source of nitrogen for growth. Since nitrite and nitrate both serve as substrates for denitrifying bacteria, it is possible that the inhibition of nitrification and the subsequent reduction of nitrite and nitrate concentrations could result in a decrease of denitrification rates.

Summary and Conclusions

The disposal of CO_2 into mid- or deep oceans will likely result in a reduction of ammonia oxidation rates within the pH plume and accumulation of ammonia instead of nitrate. It is unlikely that ammonia will reach concentration levels at which marine aquatic organisms are known to be negatively affected. However, phytoplankton ecology would be impacted if the ammonia-rich seawater from inside the pH plume reaches the euphotic zone. Large-scale inhibition of nitrification and the subsequent reduction of nitrite and nitrate concentrations could also result in a decrease of denitrification rates that could lead to the buildup of

nitrogen and unpredictable eutrophication phenomena. Additional research on the environmental effects of ocean disposal of CO_2 is needed to determine whether the potential costs related to marine eco-system disturbance and disruption can be justified in terms of the perceived benefits that may be achieved by delaying global warming for a few hundred years.

References

Capone DB. 2000. "The marine microbical nitrogen cycle." *Microbial Ecology of the Oceans*, David Kirchman, ed., John Wiley and Sons, Inc., New York.

Caulfield JA, DI Auerbach, EE Adams, and HJ Herzog. 1997. "Near field impacts of reduced pH from ocean CO_2 disposal." *Energy Convers. Mgmt. (Suppl.)*, 38:S343-S348.

Falkowski PG, RT Barber, and V Smetacek. 1998. "Biogeochemical controls and feedbacks on ocean primary production." *Science* 281:200-206.

Herzog HJ, EE Adams, D Auerbach, and J Caulfield. 1996. "Environmental impacts of ocean disposal of CO_2." *Energy Convers. Mgmt.* 37(6-8):999-1005.

Houghton J. 1997. *Global warming: The complete briefing.* Cambridge University Press, 2nd edition.

Libes SM. 1992. *An introduction to marine biogeochemistry.* John Wiley and Sons, Inc., New York.

Rayner S and EL Malone, editors. 1998. *Human choice and climate change.* Volumes 1-4, Battelle Press, Columbus, Ohio.

U.S. Department of Energy, Office of Science and Office of Fossil Energy. 1999. *Carbon Sequestration Research and Development.* DOE/SC/FE/1, Washington, D.C.

Extension of Site Soil/Plant Physical Properties to Landscape and Regional Scales Using Remote Sensing

Chris J. Murray, Eileen M. Perry

Study Control Number: PN00044/1451

Terrestrial carbon sequestration research requires estimates of plant and soil characteristics across a landscape. Field measurements, however, are generally limited in number and represent individual sites. Remote sensing imagery may provide continuous data that can be used to interpolate the limited site data across landscapes. A successful approach to interpolation would have applications in many areas of environmental sciences.

Project Description

The purpose of this project was to develop new capabilities in scaling site measurements or modeled point data over an entire landscape. Remote sensing datasets were used to derive both 2 m and 15 m estimates of plant biomass over farm and range test sites. The 2 m resolution datasets were used to evaluate three approaches to interpolation of the 2 m data over a landscape: linear regression, ordinary kriging, and Gaussian simulation with locally varying means. For a 46-ha farm test site, ordinary kriging yielded the best results, in terms of both root mean square error and the simulated green biomass images produced. The kriging results did improve with the number of 2 m samples used; 100 was the minimum number of samples required, and significant improvement was seen with 200 and 400 samples. The investigators feel that boundary effects may be the reason that the Gaussian simulation with locally varying means did not perform as well as ordinary kriging for this test case.

Introduction

Our Laboratory is frequently involved in natural resource research that requires datasets for spatial models, and measured and modeled physical soil/plant characteristics at landscape to regional scales. Murray et al. (1999) developed geostatistical methods to interpolate shrub-steppe transect data to landscape scale based on continuous plant cover data. Our project objective was to develop new capabilities for scaling site measurements or modeled data to the landscape or regional scales. This research was directed to 1) define the current state of knowledge, and 2) refine or develop new methods to extend measured or modeled results from sites (plant or soil carbon) to landscape or regional scales.

Approach

Our approach was to 1) review relevant research; 2) select a suitable data set; 3) perform an initial evaluation of data; and 4) perform interpolation based on linear regression, ordinary kriging, and Gaussian simulation with locally varying means.

Results and Accomplishments

The literature survey revealed a keen interest in multi-scale issues within the ecology, geosciences, and remote sensing communities. However, no prior research (other than performed by the investigators) was directly applicable to this project. A dataset was selected that had relevance to a current rangeland health program. Airborne imagery at 2 m spatial resolution and satellite imagery at 25 m resolution were acquired during 1999 near Grand Junction, Colorado. These image sets were used to derive green biomass based on the normalized difference vegetation index. The purpose of the research was to evaluate the ability of different methods to interpolate biomass site data (represented by randomly selected pixels from the 2 m imagery) to landscape scale. The first method was linear regression based on fitting the 2 m pixels to 15 m normalized difference vegetation index values derived from the satellite imagery. The second method was ordinary kriging (Goovaerts 1997), where only the 2 m imagery was used; randomly selected pixels were used to fit a variogram, and then kriging was used to interpolate to the landscape scale. Ordinary kriging was performed using datasets with 100, 200, and 400 randomly selected 2 m pixels; the results are shown in Figure 1. The third method was Gaussian simulation with locally varying means (Goovaerts 1997), which used the satellite imagery to partition the landscape into three

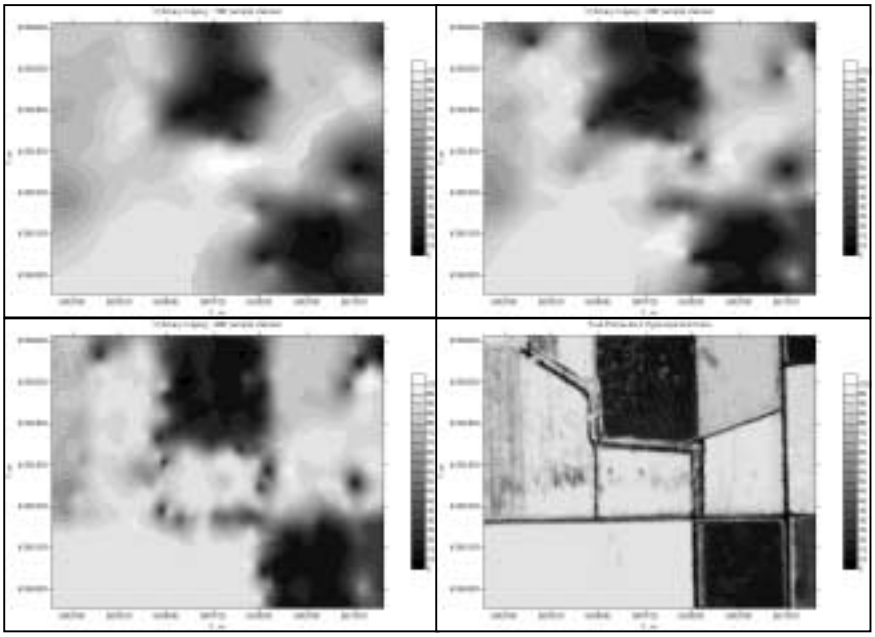

Figure 1. Ordinary kriging of 2 m data using 100 samples (upper left), 200 samples (upper right), and 400 samples (lower left). The original 2 m imagery is shown in the lower right for comparison.

classes. The local mean used for each 2 m airborne pixel was then determined by the corresponding landscape class each pixel was situated in. The results of the Gaussian simulation with locally varying means are shown in Figure 2, as with the ordinary kriging, the simulations were performed using 100, 200, and 400 samples.

Summary and Conclusions

The most significant result was our evaluation of three methods for interpolating biomass data, and an estimation of the number of samples required. This result is summarized in Figure 3, which shows the root mean square error for linear regression (top), Gaussian simulation with locally varying means (middle), and ordinary kriging (bottom) plotted as a function of the number of 2 m samples used. For the 46-ha farmland site that was evaluated, increasing the number of samples did little to improve the regression error, but greatly improved the simulation and kriging errors. Another result was that the Gaussian simulation with locally varying means did not provide an improved interpolation over the ordinary kriging for this test site. We believe that this is a result of what is referred to as the mixed pixel problem; that is, a 15 m satellite pixel is viewing several 2 m pixels of possibly differing targets or compositions. The mixed pixel problem is inherent to almost any application with spatial analysis applied to imagery at different scales. We see this as edge effects in the test site. Figure 4 shows the highest absolute errors for the simulated map occur near field edges and roads. Boundary conditions such as roads and field edges may cause different pixel classification in the 15 m satellite imagery relative to the 2 m airborne data. Thus, a 2 m pixel representing a road might actually be categorized as field and assigned the local mean based on that misclassification. These boundary conditions are a challenge that could be explored in other datasets.

References

Goovaerts P. 1997. *Geostatistics for natural resources evaluation*. Oxford University Press, New York.

Murray CJ, LL Cadwell, JL Downs, and MA Simmons. 1999. "Fusing vegetation data sets to provide a spatial analysis of Sage Grouse habitat on the Army's Yakima Training Center." In: ED McArthur, WK Ostler, and CL Wambolt (eds.) *Shrubland Ecotones*; Proc. RMRS-P-00. Ogden, Utah: U.S. Department of Agriculture, Forest Service, Rocky Mountain Research Station.

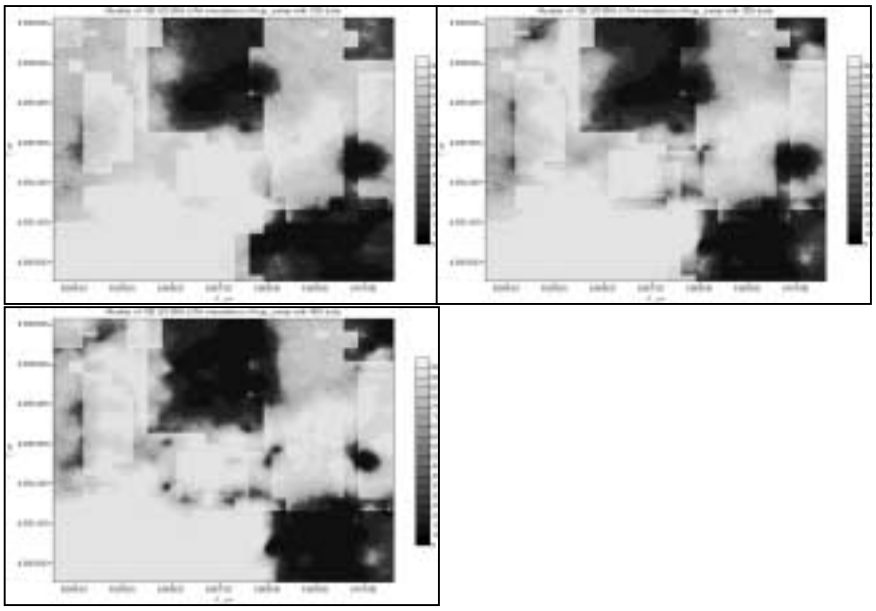

Figure 2. Gaussian simulation with locally varying means based on 2 m data using 100 samples (upper left), 200 samples (upper right), and 400 samples (lower left)

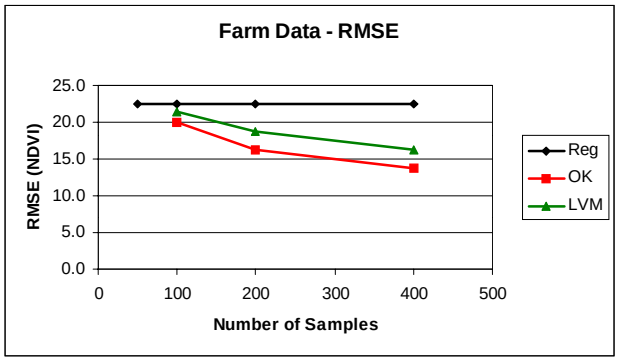

Figure 3. Root mean square errors for linear regression (top line), Gaussian simulation with locally varying means (center) and ordinary kriging (bottom line) plotted against number of samples used

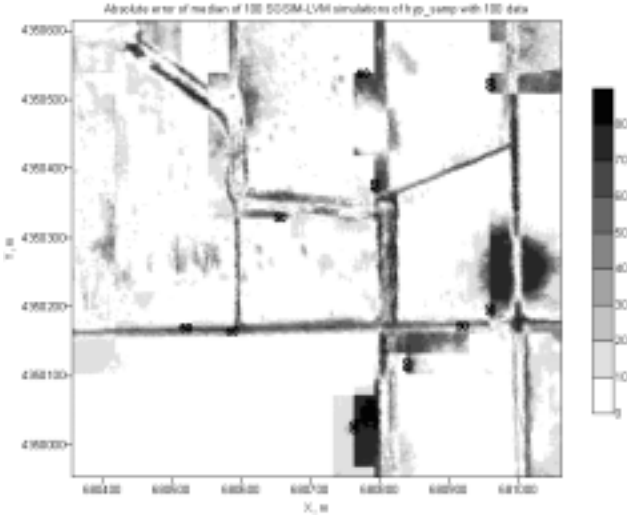

Figure 4. Absolute error of interpolated imagery based on Gaussian simulation with locally varying means. Note that the errors are greatest near boundaries (field edges, roads).

Impacts of CO_2 Injection on Deep Geologic Formations

B. Peter McGrail, Paul F. Martin, K. Prasad Saripalli, Toni Owen

Study Control Number: PN00053/1460

Sequestration in deep geologic formations is one option being considered by the Department of Energy to reduce the global atmospheric concentration of the greenhouse gas CO_2. This project addresses fundamental issues regarding the effects of CO_2 injection on the chemical and physical properties of these geologic formations.

Project Description

Injection of CO_2 in deep geologic formations is one option being considered by DOE (Office of Fossil Energy) for managing man-made CO_2 emissions. Cost-effective CO_2 sequestration is being considered in depleted oil or gas wells, coal seams, and deep underground saline formations. However, the long-term impacts of CO_2 injection on the physical and chemical properties of the host formation are not well understood. The purpose of this project is to develop a better understanding of the effects of carbonate mineral precipitation during CO_2 injection on the hydrogeologic properties of porous rocks. A pressurized unsaturated flow apparatus was developed and used to conduct alkali-flooding experiments. Injection of CO_2(g) caused pore plugging near the injector and poor use of the available sediment porosity for carbonate mineral trapping. Therefore, a counter-flow, pulsed injection method was developed that takes advantage of the properties of precipitation waves to achieve much higher efficiency in use of the sediment capacity for sequestering CO_2.

Introduction

The three mechanisms of CO_2 sequestration applicable to deep geologic formations are hydrodynamic, dissolved, and mineral phase trapping (DOE 1993; Hitchon 1996). Reporting on the injection of supercritical CO_2 into deep geological formations, Gupta (1999) emphasized that understanding the geochemical behavior of disposed CO_2, including the kinetics and equilibria of precipitation-dissolution reactions, is critical to the success of CO_2 injection and storage. Lackner et al. (1997) recommend the chemical binding of CO_2 by chemical reactions with oxides and hydroxides of calcium and magnesium to form stable carbonates as an attractive and significant sequestration mechanism. Based on batch experimental studies, Lackner et al. (1997) found $Mg(OH)_2$ to be particularly suitable, because of faster reaction kinetics. A significant finding from their work was that several geochemical processes may be suitable for mineral trapping of CO_2, but only a few may have sufficiently fast kinetics to be of practical use. Similar observations were made by Bachu et al. (1994). However, none of these studies has been conducted in partially saturated sediments. Because of the high solid-liquid ratio under unsaturated conditions, significant increases in precipitation kinetics may occur such that use of simpler and cheaper $Ca(OH)_2$ solutions is practicable.

Approach

Two sets of experiments were conducted to assess the influence of injection of CO_2 in porous media. The first set of experiments was conducted with a modified pressurized unsaturated flow apparatus (McGrail et al. 1999a), as shown in Figure 1. The sensor/effluent collection package was pressurized with helium to prevent modification of the effluent pore water pH.

Figure 1. Picture of modified pressurized unsaturated flow apparatus for CO_2 injection experiments. The pressurized unsaturated flow system is patented.

Effluent pH and electrical conductivity were monitored continuously with a computer data acquisition and control system. Total mass of the column was also monitored and used to calculate the pore water saturation level during the tests. After test termination, samples were removed from the column and analyzed for major mineral phases with powder x-ray diffraction and optical microscopy.

The second set of experiments involved sequential flooding of a 500 millidarcy Berea sandstone core with a saturated $Ca(OH)_2$ solution and pressurization with CO_2. The radial area of the sandstone was sealed with an ultraviolet resin prior to emplacement in a pressurized unsaturated flow column. The amount of pore water injected and extracted during each cycle was recorded to estimate the change in porosity from calcite precipitation. Unsaturated hydraulic conductivity and water retention as a function of capillary pressure were measured before and after the CO_2 injections with an ultracentrifugation method (McGrail et al. 1999b). X-ray microtomography was used to image pore structure changes as well.

Results and Accomplishments

Pressurized Unsaturated Flow Experiments

Figure 2 shows the results from the computer-monitored test metrics. Initially, deionized water was injected into the column at 0.25 mL/h to establish baseline conditions. After 34 hours, a 1.5 M $Ca(NO_3)_2 \cdot 4H_2O$ solution was injected. However, calcite did not form in this solution due to the formation of a $Ca(NO_3)^+$ complex. After 55.5 hours, a saturated $Ca(OH)_2$ solution was then injected. Breakthrough was observed after 8 hours and the electrical conductivity dropped dramatically, indicative of $CaCO_3$ precipitation. The calculated equilibrium pH of a fluid saturated with respect to calcite and quartz at a pCO_2 of 1.8 bar is 5.8, which is close to the observed effluent pH.

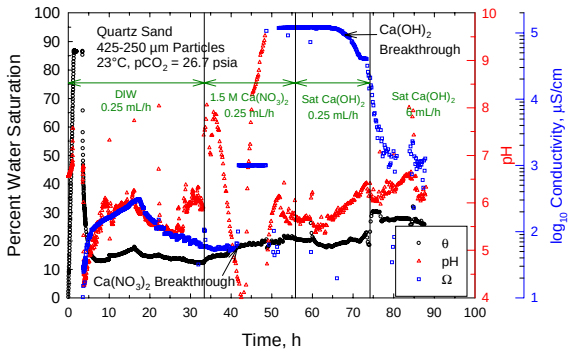

Figure 2. Computer-monitored test metrics from pressurized unsaturated flow test

After 74 hours, the $Ca(OH)_2$ influent solution was doped with a cresol red plus thymol blue pH indicator, and the flow rate increased to 6 mL/h. Water content in the column increased to about 30% saturation but the effluent pH remained near pH 6. Visual observations showed that the blue color (indicating alkaline pH) remained within a few millimeters of the CO_2 injection port. Essentially all of the calcite was formed within 10% or less of available pore space in the column. Consequently, simple injection of CO_2 into a host rock would cause pore plugging immediately around the injector and poor use of the reservoir capacity for sequestering CO_2.

To solve this problem, we developed a modified injection strategy. The column was flooded with the saturated $Ca(OH)_2$ solution and then pressurized with CO_2. The gas supply was then turned off and the residual pore water allowed to drain. A time-lapse series of photographs shown in Figure 3 illustrates the procedure. The change in pore water pH after CO_2 injection was visible, indicating more extensive use of the available pore volume for $CaCO_3$ precipitation. The column was then reflooded with the $Ca(OH)_2$ solution and the procedure repeated a total of 15 times. As seen in Figure 3, rapid neutralization of the pore water and concomitant

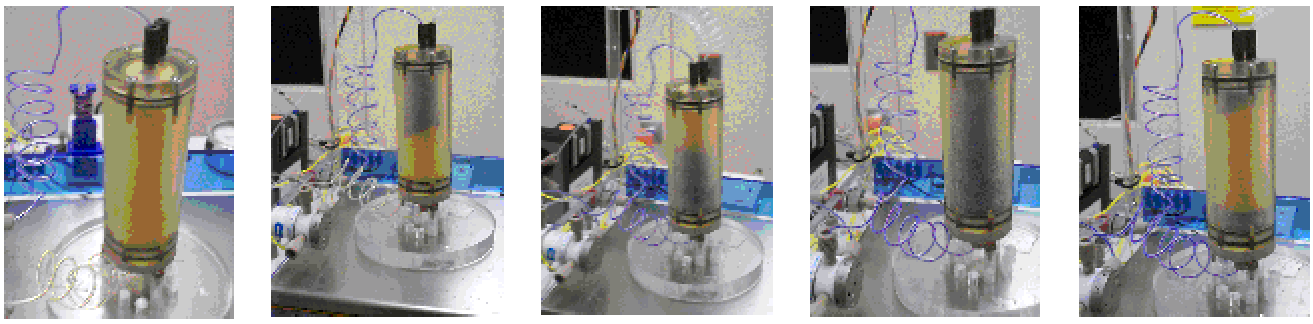

0 **13 min** **28 min** **38 min** **50 min**

Figure 3. Time lapse photos of pulsed CO_2 injection experiment. Blue color is a cresol red plus thymol blue pH indicator dye, with a critical pH for color transition of 8.3.

precipitation of calcite occurred in these experiments. Consequently, pore water conditioning appeared to be a viable mechanism for rapid in situ sequestration of CO_2.

After test termination, the quartz sand was extruded from the column, and the reacted grains were examined with an optical microscope. Figure 4 shows grains obtained from the bottom and top of the column near the injection ports. The quartz grains near the top of the column were coated with a precipitate, which was confirmed as calcite from x-ray diffraction and scanning electron microscopy analyses. However, grains from near the bottom of the column appeared essentially pristine, with only a few calcite nodules observed.

Sandstone Experiments

Figure 5 shows x-ray microtomography images of the Berea sandstone before and after the CO_2 injections. The reduction in available porosity was clearly visible. Digital image analysis showed that the available porosity decreased by 60% and that the pore size distribution shifted to a smaller median pore size. This affected the water retention and hydraulic conductivity of the core sample. Approximately 50% less water was extracted from the core at a given rotational speed in the unsaturated flow apparatus indicating that the available water is more tightly held after the CO_2 injection. This finding was consistent with expectations from the observed pore size reduction as higher capillary pressures are required to remove water from small pores as compared with large pores.

Conclusions

Modifications to the Laboratory-developed pressurized unsaturated flow apparatus were accomplished so that CO_2 injection experiments can be conducted at pressures up to 200 psi. Alkali flooding experiments with the gas and pore water injectors located adjacent to one another caused pore plugging near the injector and pore utilization of the available pore volume for carbonate mineral trapping. Although a pulsed injection method significantly improved use of the available pore space for carbonate mineral trapping, models of dissolution/ precipitation waves in porous media suggested that a counterflow injection method would allow better control of the precipitation process. In this case, CO_2 was injected near the bottom of the column, allowing buoyancy effects to cause the gas to rise counter to the direction of fluid flow. By controlling the injection rate of CO_2 and the pore water conditioner, the location of the calcite precipitation front can be controlled. This sliding in situ precipitation concept will be tested as this project continues. Precipitation of $CaCO_3$ in quartz sand and sandstone was observed to occur rapidly in contrast to the geologic timescales that are suggested in the literature (Bacher et al. 1994). Mineral trapping was also observed to cause significant changes in the hydraulic properties of Berea sandstone, an important process that must be considered when modeling the impacts of CO_2 injection in deep geologic reservoirs.

References

Bachu S, WD Gunter, and EH Perkins. 1994. "Aquifer Disposal of CO_2: Hydrodynamic and mineral trapping." *Energy Conversion and Manag.* 35.

Gupta N. 1999. *Experimental evaluation of chemical sequestration of CO_2 in deep saline formations*. DOE Office of Fossil Energy Project Fact Sheet, DE-AC26-98FT40418, Washington, D.C.

Hitchon B. 1996. *Aquifer disposal of carbon dioxide, hydrodynamic and mineral trapping - proof of concept*. Geoscience Publishing Ltd., Sherwood Park, Alberta, Canada.

Lackner KS, DP Butt, and CH Wendt. 1997. "Progress on binding CO_2 in mineral substrates." In *Proc. Third Int. Conf. on Carbon Dioxide Removal*, HJ Herzog ed., Cambridge, Massachusetts.

McGrail BP, CW Lindenmeier, and PF Martin. 1999b. "Characterization of pore structure and hydraulic property alteration in pressurized unsaturated flow tests." *Mat. Res. Soc. Symp. Proc.* 556:421-428.

McGrail BP, PF Martin, CW Lindenmeier, and HT Schaef. 1999a. **"**Application of the pressurized unsaturated flow (PUF) test for accelerated aging of waste forms." *In Proceedings of Aging Studies and Lifetime Extension of Materials,* July 12-14, Oxford, UK.

U.S. Department of Energy. 1993. *A research needs assessment for the capture, utilization and disposal of carbon dioxide from fossil fuel fired power plants*. DOE/ER-30194, Washington, D.C.

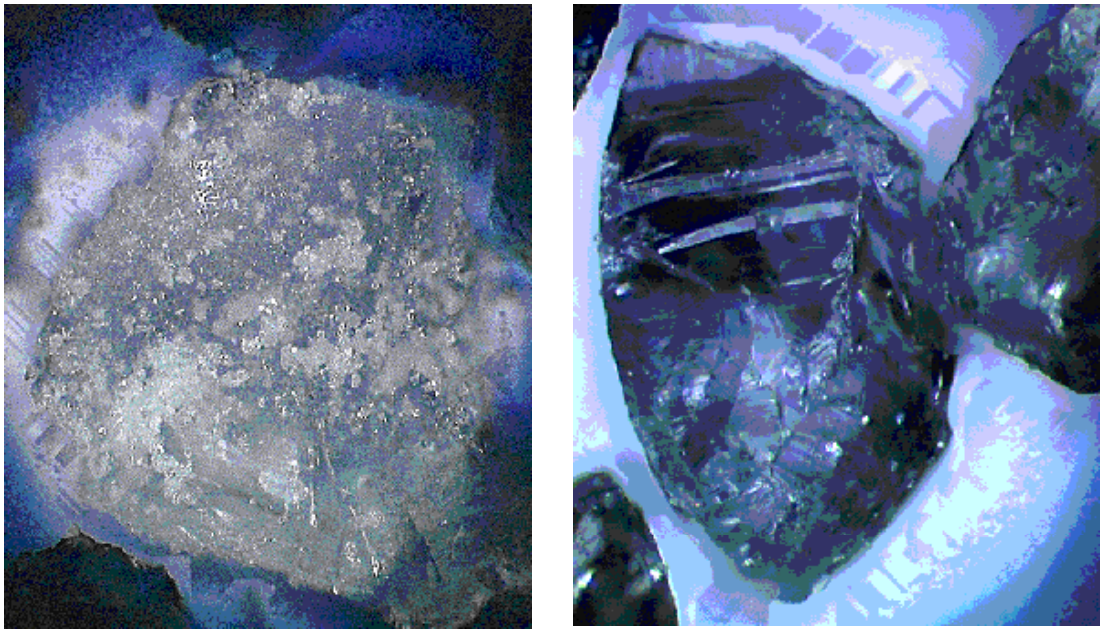

(a) (b)

Figure 4. Optical photos of quartz grains removed from top (a) and bottom (b) of column after pressurized unsaturated flow test. Note extensive calcite precipitation on quartz grain near top of the column.

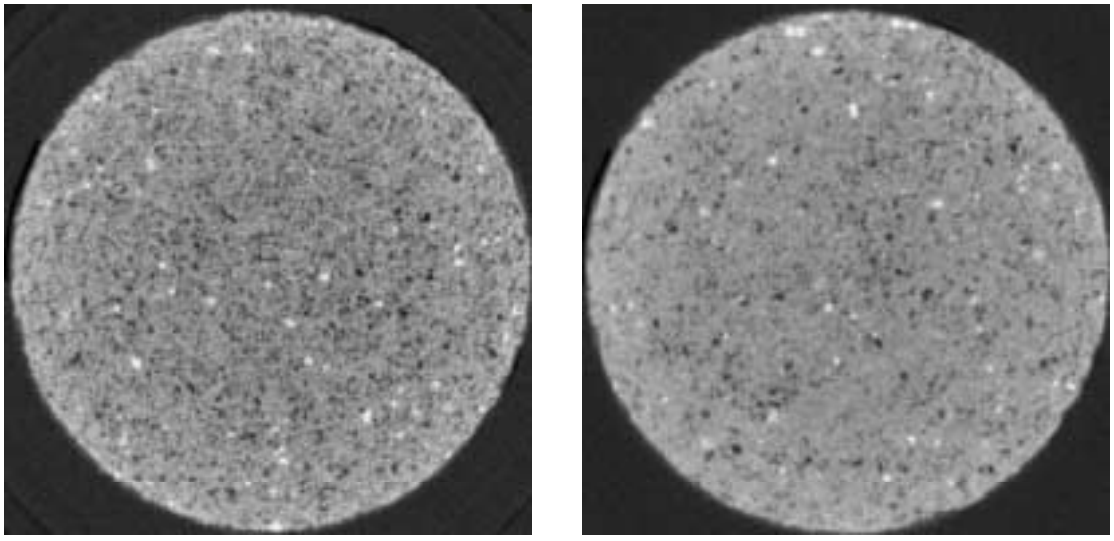

Before After

Figure 5. X-ray microtomography images of Berea sandstone core before and after five sequential injections of a saturated $Ca(OH)_2$ solution followed by CO_2(g). Digital image analysis gives a total porosity of 16.9% for the before picture and 6.9% for the after picture.

In Situ Destruction of Contaminants Using Ozone

Tyler Gilmore, Kirk Cantrell

Study Control Number: PN00054/1461

This project addresses remediation of organic contamination in the soil. The project was specifically focused on the treatment of TNT explosive, which has the potential for contaminating aquifers.

Project Description

Ozone was used to degrade the organic contaminant, TNT (trinitrotoluene), on unsaturated soil. Several soil columns were run where the degradation of TNT over time was measured. The results indicated that 50% of the TNT was degraded in 2 hours with 80% degraded in 16 hours. A nitrate balance indicated the TNT was essentially completely oxidized. The major degradation products of TNT oxidation are carbon dioxide and nitrate. This study provided proof-of-principle testing in support of a new environmental remediation technology for treating contaminated soil in the vadose zone.

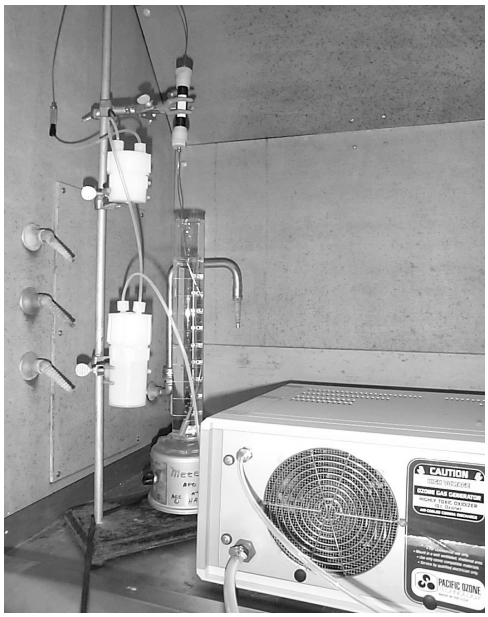

Figure 1. Experimental setup with ozonator

Introduction

This research provides the technical basis for in situ destruction (or treatment) of contaminants in the vadose zone by oxidation using ozone. Ozone has been shown to be very effective at oxidizing a range of contaminants from chlorinated solvents (perchloroethylene, trichloroethylene) to energetic compounds (TNT) in groundwater. This research will extend the application of ozone to unsaturated soil in the vadose zone. We focused on the contaminant TNT because of the heightened concerns of explosive contamination in regional aquifers.

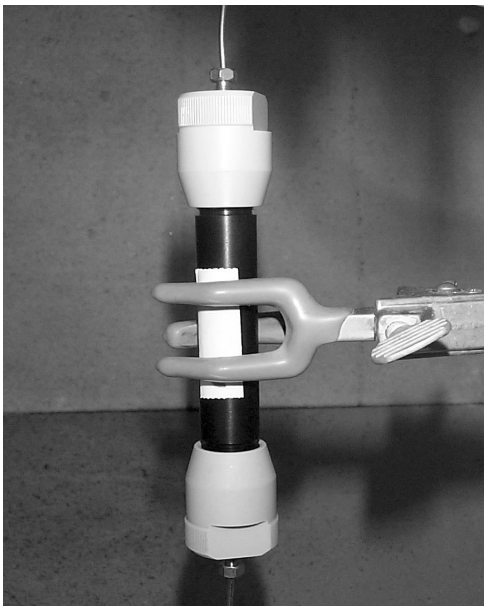

Figure 2. Soil column

Approach

A series of soil column experiments were conducted in which ozone at a concentration of approximately 10% oxygen was passed through soil contaminated with TNT (Figures 1 and 2). Two types of soils were used in the columns: Pasco sands from Washington State, and alluvium from the White Sands Missile Range, New Mexico. The silty, sandy alluvium from White Sands was spiked with approximately 50 μg/Kg TNT and the Pasco sands were spiked with approximately 10 μg/Kg. The soils were spiked by soaking them in water solutions of TNT. The water was mixed into the soil and then allowed to air dry to a moisture content of approximately 5 to 10 % by weight, or the typical moisture content

encountered in the field. The contaminanted soil was then packed in columns. Ozone was passed through the columns at discrete time increments of 1, 2, 4, 8, and 16 hours. Each time increment represents one experiment after which the column was dismantled and the concentrations of TNT in the soil were measured. A control column was also conducted by passing oxygen through the column for 16 hours. Figure 3 shows the results of these time series experiments.

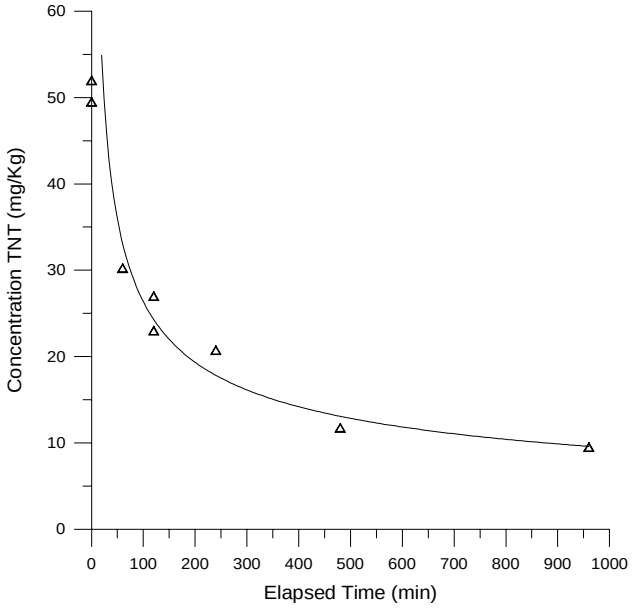

Figure 3. Degradation of TNT in ozone

Results and Accomplishments

Initial proof-of-principle data were obtained for treatment of TNT-contaminated sediment with ozone. In these tests, a silty sandy alluvium from White Sands was spiked to a concentration level of about 50 ppm TNT and then exposed to concentrated ozone gas (several percent in oxygen). After 2 hours of exposure, 50% of the TNT was decomposed, and after 16 hours the concentrations were reduced by 80%. This was not an exponential decline in concentrations and therefore not a first-order reaction. In a shorter, 4-hour test, a Hanford sandy loam sediment spiked to a concentration level of 10 ppm was tested for two time increments. After 1 hour of exposure, 30% of the TNT decomposed, and after 4 hours, 70% decomposed. In this 4-hour experiment, we determined that essentially all the TNT that was degraded was converted completely to nitrate and carbon dioxide, though trace levels of trinitrobenzene were observed.

Summary and Conclusion

Interaction of ozone with the sediment matrix was determined to be insignificant based on ozone breakthrough characteristics for a control column test conducted with uncontaminated sediment. Based on this limited testing, ozone appears to be capable of degrading TNT in unsaturated sediment. Additional testing will be required to determine the factors controlling the degradation rates in the soil.

Bibliography

Thornton EC, JT Giblin, TJ Gilmore, KB Olsen, JM Phelan, and RD Miller. 1999. *In situ gaseous reduction pilot demonstration—Final Report.* PNNL-12121. Pacific Northwest National Laboratory, Richland, Washington.

Interrelationships Between Processes Controlling Loading Level, Release Rate, and Biological Activity of Contaminated Porous Media

Robert G. Riley, Christopher J. Thompson

Study Control Number: PN00061/1468

Hydrophobic organic contaminants are common sources of subsurface contamination at DOE and other federal sites. A better understanding of the magnitude and behavior of hydrophobic organic contaminants resistant fractions could 1) enhance the rationale for using more cost-effective, passive cleanup options (e.g., natural attenuation) at DOE sites, and 2) lead to improved approaches for evaluating soil/sediment organic contaminant analysis methods. In this project, circulating supercritical carbon dioxide is evaluated as a laboratory method for rapidly aging soils/sediments and investigating the behavior of hydrophobic organic contaminants resistant fractions.

Project Description

The objective of this project was to evaluate the potential for supercritical fluid technology to simulate on a laboratory time scale (hours to days) the natural aging process (the interaction of contaminants with soils and sediments over several years). Phenanthrene (a hydrophobic organic contaminant) was loaded onto Hanford formation soil using supercritical carbon dioxide. Aqueous desorption of phenanthrene from the loaded soil in laboratory columns showed release behavior consistent with what would be expected for hydrophobic organic contaminants releasing from a naturally aged soil or sediment. Of particular interest was the demonstration of the presence of a phenanthrene resistant fraction controlled by adsorption and diffusion processes in the organic carbon fraction of the soil. The results of this project suggest that application of the supercritical fluid technology to a broader range of soils and sediment types (such as those found across the DOE complex) would be possible with improved system robustness and parameter modification.

Introduction

A hydrophobic organic contaminant resistant fraction is defined as that fraction of hydrophobic organic contaminants that is slowly released to an aqueous phase (groundwater). Hydrophobic organic contaminant resistant fractions are generated over years (decades) of interaction of contaminants with soils and sediments under unsaturated and saturated conditions. Hydrophobic organic contaminants that have been in contact with soils, sediments, and aquifer solids for many years typically exhibit very slow releases to the environment (such as vadose zone unsaturated moisture or groundwater) as a result of the presence of resistant fractions within these materials. Current scientific thinking suggests that organic matter diffusion is a major mechanism responsible for the presence of resistant fractions resulting in slow release of contaminants from geosorbents that contain organic carbon. This raises questions about the influence of resistant fractions on the availability of hydrophobic organic contaminants to the environment and how this relates to soil and sediment quality criteria for hydrophobic organic contaminants and remediation cleanup goals. As a consequence of sorption to soils or sediments and subsequent slow release, the resistant fractions of hydrophobic organic contaminants may be significantly less leachable by water and less toxic as measured by simple tests. Fate, transport, and risk assessment models all contain terms for desorption; therefore, an understanding of the dynamics of hydrophobic organic contaminant resistant fractions is crucial to their success. Ignoring the magnitude of a hydrophobic organic contaminant resistant fraction and its influence on slow kinetics can lead to an underestimation of the true extent of adsorption, false predictions about the mobility and bioavailability of contaminants, and perhaps the wrong choice of cleanup technology (Pignatello and Xing 1996; Luthy et al. 1997).

Classes of hydrophobic organic contaminants most commonly found in DOE site soils and sediments subject to cleanup include fuel hydrocarbons, chlorinated hydrocarbons, and polychlorinated biphenyls (Riley and Zachara 1992). Understanding the magnitude and behavior of resistant fractions could lead to the development of more realistic release criteria that reduce the costs of remediation of sites contaminated with these chemicals. Higher concentrations of contamination may be allowed to remain in soils and sediments in meeting site closure requirements. Of particular interest is the application of natural attenuation as a remediation

strategy option at DOE sites (Brady et al. 1999). The first comprehensive assessment of natural attenuation for groundwater cleanup was recently reported (Macdonald 2000). A key assumption made in measuring the potential success of natural attenuation is the likelihood that release of hydrophobic organic contaminants from resistant fractions in the subsurface environment occur on time scales commensurate with natural attenuation process rates (such as microbial degradation). Growing acceptance of the natural attenuation option by regulators and the public as a viable cleanup option will depend on being able to demonstrate such assumptions are correct suggesting that there would be acceptable risk in its application.

One method for providing support for acceptable risk would be to quantify the magnitude of the resistant fractions for different hydrophobic organic contaminant classes for a range of soil and sediment types found across the DOE complex. Unfortunately, laboratory study of hydrophobic organic contaminant resistant fractions has been confounded by the inability to accurately evaluate the performance of traditional analytical methodologies to quantify resistant fractions in naturally aged soils and sediments. Traditional methods for artificially aging soils and sediments have proven inadequate because contact times require years for adsorption and diffusion processes to achieve the extent of contaminant penetration found in naturally aged soils and sediments. These problems might be overcome by use of supercritical carbon dioxide for loading soils and sediments with hydrophobic organic contaminants. The solubility of hydrophobic organic contaminants in supercritical carbon dioxide is controllable through the adjustment of temperature and pressure. The favorable properties of supercritical carbon dioxide (i.e., high diffusivity and low viscosity) have the potential for allowing rapid incorporation of hydrophobic organic contaminants into the natural organic component of soils and sediments.

Results and Accomplishments

Phenanthrene was loaded onto nonporous glass beads and a Hanford formation soil using the closed loop supercritical carbon dioxide system. Both materials had similar surface areas (2 versus 9 m^2/g), and the Hanford soil had an organic carbon content of 0.03%. Phenanthrene rapidly established equilibrium with the nonporous beads with no organic carbon content. In contrast, the Hanford formation soil showed a continuous slow uptake of phenanthrene likely attributable to adsorption/diffusion into the soil organic matter (Figure 1b versus 1a). Phenanthrene continued to adsorb (diffuse) into the Hanford soil after 24 hours of exposure (Figure 1b versus 1c). Adsorption and diffusion into the organic matter was expected to be more extensive in the 24-hour loaded Hanford soil than the 5-hour loaded Hanford soil. Differences in resistance of phenanthrene to aqueous soil column leaching was expected to be observed between 5-hour and 24-hour aqueous desorption experiments. After approximately 7 hours, desorption occurred slower for the 24-hour loaded soil than for the 5-hour loaded soil (Figure 2). Differences in the extent of adsorption/diffusion into Hanford soil organic matter (5-hour versus 24-hour loading) are likely responsible for differences in the observed leachate behavior. Evidence of a greater resistant fraction was demonstrated for the 24-hour loaded soil.

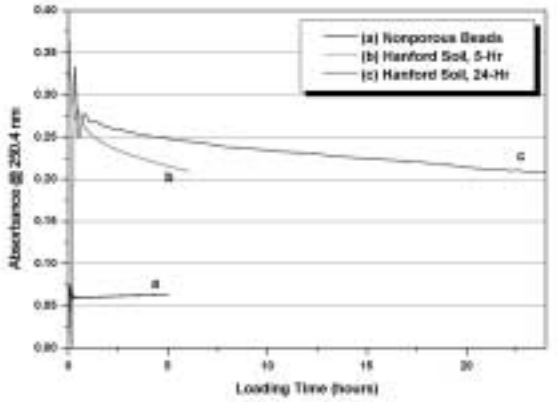

Figure 1. Supercritical fluid loading profiles for nonporous glass beads and Hanford soil

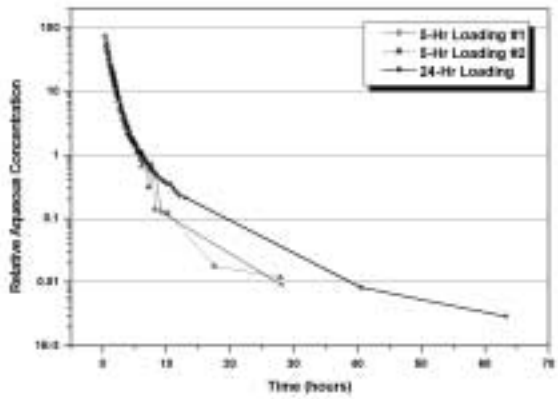

Figure 2. Aqueous desorption of phenanthrene from 5-hour and 24-hour loaded Hanford soil

Summary and Conclusions

Phenanthrene artificially loaded onto Hanford Site soil samples showed release behavior consistent with what would be expected for hydrophobic organic contaminants releasing from a naturally aged soil or sediment. The artificially aged soils demonstrated the presence of a

phenanthrene resistant fraction controlled by adsorption and diffusion processes in the organic carbon fraction of the soil (Pignatello and Xing 1996; Luthy et al. 1997). The results of this project suggest that application of the supercritical fluid technology to a broader range of soils and sediment types (such as those found across the DOE complex) would be possible through improved system robustness and parameter modification.

Potential applications of the technology are

- generation of well-characterized artificially aged soils/sediments for laboratory study of subsurface process (natural attenuation) involving organic contaminants
- development of soil and sediment standards for evaluating characterization methods performance and establishment of improved remediation release criteria
- improvements in parameterization of models that predict fate and effects.

References

Brady PV, BP Spalding, KM Krupka, RD Waters, P Zhang, DJ Borns, and D Brady. 1999. "Site screening and technical guidance for monitored natural attenuation at DOE sites." SAND99-0464, Sandia National Laboratories, Albuquerque, New Mexico, and Livermore, California.

Luthy RG, GA Aiken, ML Brusseau, SD Cunningham, PM Gschwend, JJ Pignatello, M Reinhard, SJ Traina, WJ Weber Jr., and JC Westall. 1997. "Sequestration of hydrophobic organic contaminants by geosorbents." *Environ. Sci. Technol.* 31:3341-3347.

Macdonald JA. 2000. "Evaluating natural attenuation for groundwater cleanup." *Environ. Sci. Technol.* 34:346A-353A.

Pignatello JJ and B Xing. 1996. "Mechanisms of slow desorption of organic chemicals to natural particles." *Environ. Sci. Technol.* 30:1-11.

Riley RG, and JM Zachara. 1992. "Chemical contaminants on DOE lands and selection of contaminant mixtures for subsurface science research." DOE/ER-0547T, U.S. Department of Energy, Office of Energy Research, Washington, D.C.

Modeling the Sequestration of CO_2 in Deep Geological Formations

K. Prasad Saripalli, Ashok Chilakapati, Pete McGrail

Study Control Number: PN00068/1475

The Department of Energy has identified carbon management as a critical component of its mission. This project is developing the analytical and numerical tools needed by DOE to evaluate management alternatives involving carbon sequestration in deep geologic formations.

Project Description

The purpose of this project is to develop analytical and numerical models to evaluate carbon sequestration in deep geologic formations. Specifically, these tools are needed to evaluate issues such as the capacity of the geologic formation around a carbon injector, the relative apportioning of carbon mass among the three states (hydrodynamic, dissolved, and mineral phase), the long-term fate of sequestered CO_2, the potential for CO_2 release, and the effect of formation plugging on CO_2 injection. Equations governing the radial injection of CO_2 into deep saline aquifers, axisymmetric flow of CO_2 around the injector, and eventual buoyancy-driven floating with simultaneous dissolution were formulated. Two models were prepared: the semi-analytical model PNLCARB and the numerical model STOMP-CO_2. The models effectively simulate deep-well injection of water-immiscible, gaseous, or supercritical CO_2. The models were used to investigate the effect of pertinent fluid and reservoir and operational characteristics on the deep-well injection of CO_2. The results indicated that the injected CO_2 phase initially grows as a bubble radically outward, dissolves partially in the formation waters, eventually floats toward the top due to buoyancy, and settles near the top confining layer. Formation permeability, porosity, the rate and pressure of injection, and the rate of CO_2 dissolution influenced the growth and ultimate distribution of the CO_2 phase. The first-generation tools developed by this project will help to evaluate and optimize methods for sequestering carbon in deep geologic repositories.

Introduction

Geological sequestration of CO_2 has been recognized as an important strategy for reducing the CO_2 concentration in the atmosphere. However, economically viable technologies for geological sequestration and models describing the same are in their infancy. This project focused on modeling the injection, sequestration, fate, and escape of CO_2 in geological formations. The three mechanisms of CO_2 sequestration are hydrodynamic, dissolved, and mineral phase trapping. These mechanisms can influence one another; for example, in addition to providing a carbon sink, mineral trapping can significantly alter hydrogeologic properties (such as secondary porosity and permeability) and hence, the efficiency and capacity for hydrodynamic and dissolved trapping. Dissolved-phase trapping, a strong function of pressure, salinity, and temperature, can similarly influence the other two processes. As such, modeling geological sequestration requires an accurate representation of the individual processes and their interaction. Following are the primary processes that need to be considered in modeling geological sequestration: 1) multiphase, radial injection of CO_2 and the growth of its area of review around the injector, 2) buoyancy-driven migration of CO_2 toward the top aquifer confining layer, 3) dissolution of CO_2 during injection and vertical migration, and the resulting aqueous speciation of carbon, 4) carbon mass exchange via precipitation and dissolution of minerals through the interaction of dissolved and gaseous phase CO_2 with the formation, and 5) changes in hydrogeological properties due to mineral trapping and the resulting formation damage and injectivity decline. The reservoir-scale numerical codes typically do not model the above processes around an injection well with adequate mechanistic detail. Over the past several years, our team developed significant expertise in many of these multiphase and reactive transport processes, and their modeling for deep-well waste injection applications. This experience can be combined to develop effective modeling tools for geological sequestration of CO_2.

Approach

Two mathematical models were developed for the injection, sequestration, distribution, and long-term fate, including release to the atmosphere, of CO_2. One of them is PNLCARB1.0, a semi-analytical model for modeling the injection and sequestration around a single injection well. Governing equations were derived for the radial

injection of an immiscible gas phase into confined formations (representing deep saline aquifers and reservoirs), its axisymmetric flow around the injector, and eventual buoyancy-driven transport with simultaneous dissolution and mineral trapping. In addition, a numerical model (STOMP-CO_2) has been developed by adding additional phase behavior algorithms to our STOMP simulator.

Results and Accomplishments

Simple and easy-to-use modeling tools would be valuable for assessing the performance of a deep-well operation during and after injection. We have completed a semi-analytical model (PNLCARB) and a numerical model (STOMP-CO_2) by adding additional phase behavior algorithms to the STOMP simulator, to model 1) multiphase, radial injection of CO_2 and the growth of its area of review around the injector, 2) buoyancy-driven migration of CO_2 toward the top confining layer, and 3) dissolution of CO_2 during injection and vertical migration, and the resulting aqueous speciation of carbon. The models effectively simulate deep-well injection of water-immiscible, gaseous or supercritical CO_2. Equations governing the radial injection of CO_2 into deep saline aquifers, its axisymmetric flow around the injector and eventual buoyancy-driven floating with simultaneous dissolution were formulated. The effect of pertinent fluid, reservoir and operational characteristics on the deep-well injection of CO_2 was investigated. Shown in Figures 1 through 4 are some key findings from simulations using PNLCARB1.0 and STOMP-CO_2. Results indicate that the injected CO_2 phase initially grows as a bubble radially outward, dissolves partially in the formation waters, eventually floats toward the top due to buoyancy, and settles near the top confining layer. Formation permeability, porosity, the rate and pressure of injection, and the rate of dissolution of CO_2 influence the growth and ultimate distribution of the CO_2 phase.

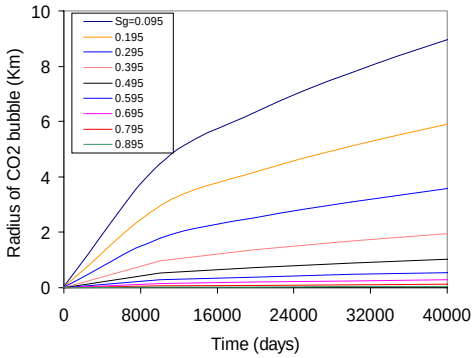

Figure 1. CO_2 saturation profiles at thousands of days after injection

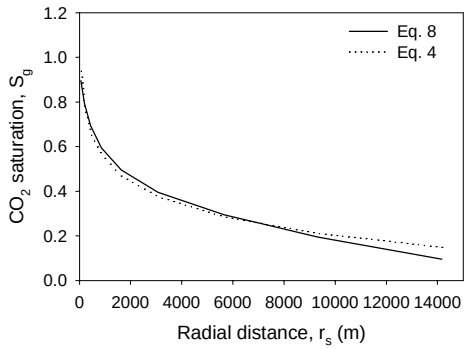

Figure 2. As a function of radial distance away from well

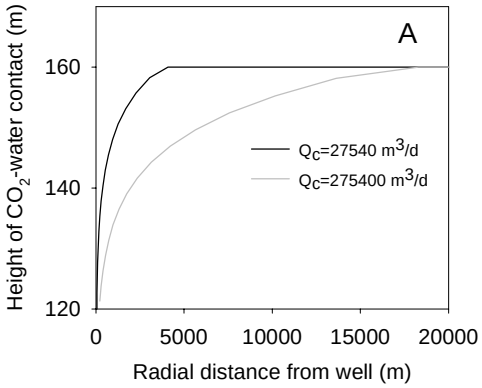

Figure 3. Effect of injection rate on ultimate CO_2-water contact

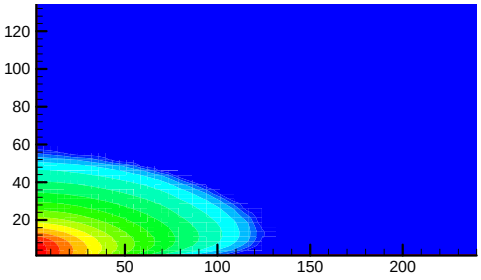

Figure 4. CO_2 bubble growth prediction by STOMP-CO_2 at a low flow rate

Publication

Saripalli P. 2000. *Simulations using PNLCARB1.0 to model deep-well injection of CO_2 for geological sequestration at Mt. Simon Site.* Prepared for BCO Columbus, as a part of model validation effort for DOE-FE funded research project.

Oxidation of Volatile Organics Leading to Tropospheric Aerosol Formation

Michel Dupuis, Shawn Kathmann, Robert Disselkamp

Study Control Number: PN00072/1479

Because atmospheric aerosols have been shown to have important effects on human health, climate, and visibility they are currently the focus of intense research activity. Among the atmospheric aerosols, organic aerosols are the least well understood. An important mechanism leading to the formation of organic aerosols is the oxidation of volatile organic compounds. The reaction pathways are not well understood and the oxidation products can serve as condensation nuclei leading to organic droplets.

Project Description

Much of the uncertainty in volatile organic compounds/NO_x atmospheric chemistry lies in knowledge about the mechanisms of degradation of the organic species. The oxidation degradation products act as condensation seeds to organic aerosol droplets. Improved atmospheric models are in need of more detailed elucidation of gas-phase photo-oxidation pathways and rates of organics degradation. This project is targeted at providing mechanistic and kinetic information about a key class of volatile organic compounds, the alkenes, and to illustrate the possible impact of computational chemical studies on atmospheric models. Data to be calculated include enthalpies of formation, vibrational spectra, electronic excitation spectra, and rate constants from the electronic structure calculations of transition state structures together with transition state and unimolecular rate theories. An important aspect of this project is identifying the atmospheric modeling group that will make use of molecular kinetics data.

Introduction

Volatile organic compounds play central roles in tropospheric oxidation chemistry that lead to ozone and secondary aerosol formation. Ozone is a critical pollutant for which the U.S. Environmental Protection Agency (EPA) has set regulatory thresholds for violating national tropospheric air quality standards. Urban ozone is of concern primarily because of its impact on health (breathing and eye irritation). Rural ozone is of concern because of damage to crops and forests. Ozone levels are controlled by NO_x and by volatile organic compounds in the lower troposphere. The volatile organic compounds can be from either natural emissions from such sources as vegetation and phytoplankton or from anthropogenic sources such as automobiles and oil-fueled power production plants. It is of critical importance to DOE in developing national energy use policies to understand the role of volatile organic compounds in determining ozone levels and how volatile organic compounds emission or NO_x emission control strategies should be designed.

The initial means of classifying hydrocarbons and their impact on air quality focused on the initial OH rate constants just as had been done for the CFC alternatives. However, just as found for the CFC alternatives such as HFC-134a, it has become critical to know what products are formed and what is the ultimate fate of all of the various products resulting from the oxidation. Indeed a number of reviews have summarized the uncertainties that limit our ability to understand the impact of volatile organic compounds on air quality. As noted by Paulson in JR Baker, Ed. (1994, Chap 4, 111-144), *"the ability of a compound to contribute to oxidant formation can only be derived from the detailed oxidation mechanism for each hydrocarbon."* Thus, one must examine the complete oxidation mechanism including the primary step and subsequent radical and oxidation reactions of the products in order to develop more accurate measures of how a compound contributes to oxidant formation. The farther one moves from the emission source, the more important the mixture of partially oxidized hydrocarbons becomes as many of these compounds can be transported for long distances. Thus, the rates of the initial reactions of the hydrocarbons with OH, O_3, and NO_3 and the type of partially oxidized products as well as the numbers of free radicals that the reactions produce along the way, all combine to determine how much an individual hydrocarbon contributes to oxidant formation. Furthermore, Paulson notes that major uncertainties still exist in the 1990s even after three decades of research. For the homogeneous gas phase processes, these uncertainties fall into the area of degradation mechanisms as opposed to kinetic measurements, although there are

still some key kinetic issues that have yet to be resolved. Major areas of mechanistic uncertainty include 1) aromatics, 2) OH chemistry of hydrocarbons C_n, with n>4, 3) O_3 chemistry of hydrocarbons Cn with n>2, and 4) NO_3 chemistry of alkenes. Paulson's statements are supported by Seinfeld's view, also in JR Baker, Ed. (1994, Chap. 2, 34-57), that the principal uncertainty in volatile organic compounds/NO_x chemistry lies in the knowledge about the mechanisms of degradation of the organic species (Figure 1).

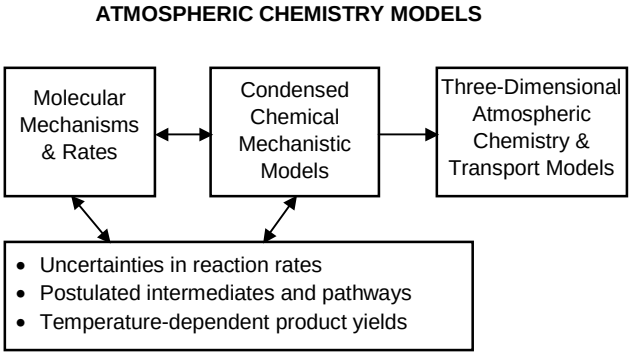

Figure 1. Interplay between molecular reactions and atmospheric chemistry and transport models

A revolution in science has taken place over the last 2 decades. This revolution is based on the utilization of high performance computers to solve the complex equations that describe natural phenomena. Both software and hardware developments have contributed to this revolution. The impact on chemistry and atmospheric chemistry has already been seen. For example, modeling has played a significant role in determining the effects of ozone on the stratosphere and in the formulation of the Montreal Protocol and its subsequent amendments. In the area of electronic structure modeling, the methods of computational quantum chemistry have developed to the point that both novel insights and chemically accurate data can be provided for many chemical species and reactions, including those relevant to atmospheric processes and combustion processes. Such computational studies have contributed to the definitive assignment of reaction pathways and mechanisms through direct calculations of reaction enthalpies and rate constants. Accurate computational studies have been important in helping to experimentally identify novel species based on calculated infrared and Raman vibrational spectra and electronic absorption spectra. If one is striving to replace experimental measurements by calculations, the mark is for direct calculations of chemical accuracy, generally defined as less than 1 kcal/mol in bond energies. Ab initio determination of reaction rates are even more demanding owing to the exponential dependence of the rate on the activation energy and the fact that a factor of two in a rate constant has a very significant effect on the overall reaction mechanism.

The objective of this work is to demonstrate the impact that computational chemistry can have on atmospheric modeling by providing mechanistic chemistry and reaction rate information about the oxidation of volatile organic compounds and their degradation byproducts. As an initial step, we will identify and establish a collaboration with a leading atmospheric modeling group that will use the molecular mechanistic and kinetics data in their atmospheric models. These contacts will put us in a position to select a small number of model volatile organic compounds reactions for which we will carry out structure and kinetic calculations.

Results and Accomplishments

We used modern methods of computational chemistry to characterize the elementary reaction pathways for OH reacting with ethene, butadiene, isoprene, and alpha- and beta-pinene. All of these systems play an important role in volatile organic compounds oxidation. Selected adducts and transition states for these systems have been determined using medium level of theory (UHF with 6-31G*). Higher levels of theory have been used for the OH + ethene and OH + butadiene systems (MP2 with aug-cc-pVDZ and aug-cc-pVTZ basis sets) (Figure 2).

For the simpler system OH + ethene, extensive calculations have been carried out to map the important regions of the potential energy surface that play a key role in the first-principles calculation of reaction rates. Addition of OH to C=C bonds have a very small activation energy or no activation energy. Rate calculations are very sensitive to the minimum energy pathway minimum energy pathway and the shape of the energy surface in the vicinity of the minimum energy pathway. The computed VTST rates shown in Figure 3 correspond to scaled UCCSD(T) computed reaction energies. While the agreement with experimental rate is excellent at 400 K, the temperature dependence of the rates is not well reproduced from the computations. The discrepancy is attributed to inaccuracies in the calculation of the partition functions that enter the rate expressions. The inaccuracies arise from the low frequency reactions modes as well as the level of electronic structure theory. The overall methodology (level of accuracy required, characterization of pathway) is being refined on the smallest systems OH + ethene and OH + butadiene. The computational protocol will be applicable to the more complex systems with activation energies less than 2 cal/mol.

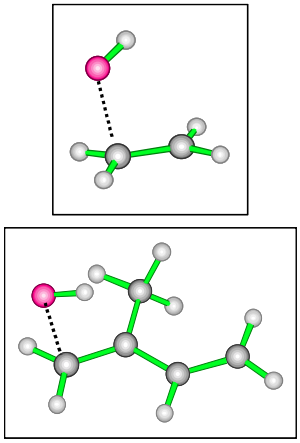

Reaction	Exothermicity (kcal/Mol)		
	MP2/vdz	UCCSD(T)/vdz/MP2/vdz	expt
OH• + C_2H_4			
Channel 1	-31.1	-26.5	29-36
OH• + C_4H_6			
Channel 1	-35.5	-20.9	
Channel 2	-26.9	-7.7	
OH• + C_5H_8 (trans)			
Channel 1	-34.0	-19.9	
Channel 2	-27.9	-8.9	
Channel 3	-26.6	-7.9	
Channel 4	-31.8	-17.9	

Figure 2. Transition state structures and computed reaction enthalpies for OH+ ethene, OH+ butadiene, and OH+ isoprene

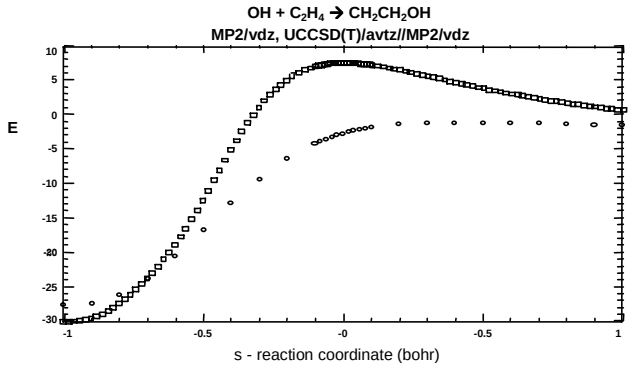

RATE

T	K(exp) [10^{-12} cm^3/molecule-s]	K(VTST)
300	6.2	3.3
400	5.1	5.4
500	4.2	7.0

Figure 3. Experimental and computed reaction rates for the OH+ethene reaction. The computed rates are for scaled UCCSD(T) energies. The computed rate at 400 K is in agreement with the experimental value, but the temperature dependence is not well reproduced.

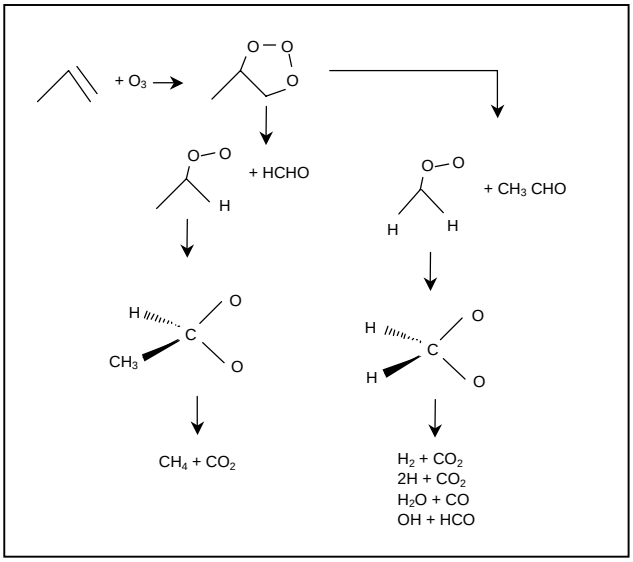

Figure 4. Reaction diagram for the ozonolysis of propene. For the first time CH_4 was identified as a product of the O_3 + propene reaction in a temperature-controlled reaction chamber. Formation of CH_4 was calculated to be highly exothermic. The activation energy for the elementary step leading from the dioxirane species to CH_4 was shown to be small.

Ozonolysis of propene: temperature-controlled reaction chamber measurements of the ozonolysis of propene yielded for the first time a direct observation of methane CH_4 product. Electronic structure calculations using the G2 protocol established by Pople and coworkers (Curtiss et al. 1991) were carried out to establish the reaction energies and pathways for the products of the O_3 + propene (Figure 4). The computations showed that formation of CH_4 is highly exothermic and that the elementary step leading from a dioxirane species to CH_4 has a small activation energy.

References

Baker JR, Ed. 1994. "Progress and problems in atmospheric chemistry." *World Scientific*.

Curtiss LA, K Raghavachari, GW Trucks, and JA Pople. 1991 *J Chem. Phys.* 94:7221.

Publication

Disselkamp RS and M Dupuis. "A temperature dependence study of the ozonolysis of propene." *J. Phys. Chem. A* (in preparation).

Prototype Regional Climate Collaboration Center

L. Ruby Leung

Study Control Number: PN99059/1387

Understanding climate change and its regional consequences is important for supporting national and international energy and environmental policies. A prototype Regional Climate Collaboration Center is being assembled for the generation of regional climate change scenarios and assessment of climate change impacts in water resources and agriculture. A problem-solving environment is being developed to support the advanced modeling framework.

Project Description

A prototype Regional Climate Collaboration Center is being assembled that makes use of a regional climate model, a watershed hydrology model, a hydrosystem management model, and a crop model for the purpose of assessing regional impacts of global climate change. A parallel version of the regional climate model has been developed, and selected physics parameterizations have been modularized for contribution toward the development of a community regional climate model. A problem-solving environment is being developed for regional climate modeling. Several proofs of principle have been demonstrated.

Introduction

This project was proposed to support the missions of the DOE Accelerated Climate Prediction Initiative. One component of Accelerated Climate Prediction Initiative is the establishment of Regional Climate Collaboration Centers, which would provide the link between advanced climate prediction models and those who will use output of these models for scientific research and assessment of possible impacts of climate change. Products to be developed and maintained to support climate change impact assessment activities include downscaling tools that bridge the spatial scales typically resolved by global climate models and that needed to resolve hydrological and ecological processes for assessing the impacts of climate change and variability. This project is aimed at developing and maintaining a suite of physically based process models and product delivery tools for the impact assessment community.

We have developed a regional climate-hydrology modeling capability that has proven to be very useful for assessing climate change impacts. An outstanding feature of our regional modeling system is its capability to provide high spatial resolution (1 to 10 km) simulations of climate and hydrologic conditions in regions with complex topography through a subgrid parameterization of orographic precipitation. High spatial resolution is critical for water resources and ecosystem managers for reliable and defensible estimates of water and fisheries management impacts. Our ability to couple the regional climate model, PNNL-RCM (Leung and Ghan 1995, 1998), and the watershed model (DHSVM) (Wigmosta et al. 1994; Leung et al. 1996) has been enthusiastically received as the state-of-the-science tool for assessing water, fishery, and ecosystem management options.

Results and Accomplishments

Parallelization of a Regional Climate Model

One of the most computationally demanding components of the Collaboration Center is regional climate modeling. We have adapted the regional climate model to massively parallel architectures. Two parallel versions of the regional climate model have been developed. In collaboration with Professor Suresh Kothari of Iowa State University, the automatic parallelization tool (ParAgent) has been applied to develop a one-dimensional decomposition parallel version of PNNL RCM. The code has been tested on Beowulf clusters. Load balancing associated with the subgrid parameterization of orographic precipitation is tackled by assigning different numbers of longitude bands with approximately equal numbers of subgrid elevation bands to each processor. This parallel regional climate model is, however, not ideal for massively parallel computation.

In collaboration with John Michalakes of Argonne National Laboratory, we have developed a parallel regional climate model by implementing the subgrid orographic precipitation scheme to the parallel Penn State/NCAR Mesoscale Model (MM5) that runs on a

wide variety of parallel computing platforms using two-dimensional decomposition with shared or distributed memory. This effort also contributes toward the development of a community regional climate model based on MM5.

Figure 1 shows the speedup attained with the two-dimensional decomposition parallel version of MM5 with and without subgrid orographic precipitation. Results are based on benchmarks on the EMSL IBM-SP computer. A number of 1-day simulations have been performed using different configurations of the model domain. Higher speedup is achieved with larger domain sizes. When the subgrid orographic precipitation scheme is applied, a simple load-balancing algorithm is needed to improve the performance. Figure 2 shows the two-dimensional domain decomposition when the load-balancing algorithm is applied. Because computational burden increases with an increasing number of subgrid elevation bands, smaller domains are assigned to processors that are required to handle a larger number of subgrid elevation bands.

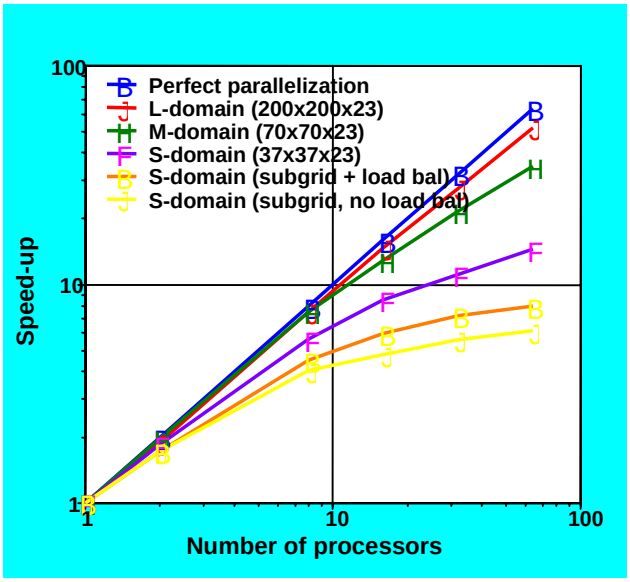

Figure 1. Speedup of the two-dimensional decomposition parallel RCM on the PNNL EMSL IBM-SP machine. Results are based on 1-day simulations with the RCM applied to different geographical domains.

Hydrologic Modeling

Assessments of fisheries management conducted by various federal, state, and tribal agencies (including Bonneville Power Administration) are driven to the spatial scale of the 6th-level Hydrologic Unit Code (HUC6). The channel system in each hydrologic unit code is subdivided into a number of geo-referenced river

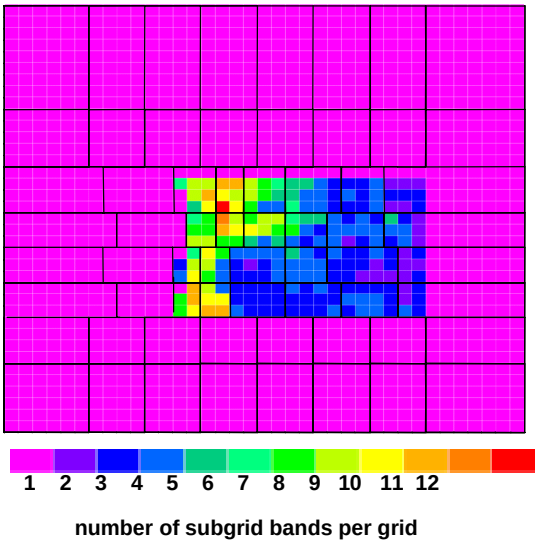

Figure 2. Two-dimensional domain decomposition when the PNNL subgrid orographic precipitation is applied. Smaller domains are assigned to processors that cover regions with a large number of subgrid elevation bands.

reaches. More than 7500, 6th-level hydrologic unit codes exist in the Columbia Basin, of which less than 1% has gauged streamflows. The Distributed Hydrology-Soil-Vegetation Model has been enhanced to operate either on the original square-grid domain or a more generic watershed/channel representation that allows direct application at the HUC6 level. Linkage with the Laboratory's regional climate model has been maintained. Support utilities have been developed to subdivide each HUC6 into elevation bands with a simplified representation of subband topography. Each band is mapped to the appropriate River Reach(s). The model is currently being run for the entire Columbia River basin at the HUC6 level using five elevation bands per hydrologic unit code.

Development of a Hydrosystem Management Tool

The developments under the hydrology task enable us to provide estimates of natural streamflows. However, dams and diversions significantly alter these natural streamflow patterns. Any adaptation to changes in the future climate will involve changes to the operating policies of dams and diversions. A numerical procedure to express the multiple-objective tradeoffs for a single reservoir system had been developed. The procedure linked a niched Pareto genetic algorithm with a simple reservoir model. This method has been modified to consider a system of multiple reservoirs. The system has been implemented on massively parallel computer platforms.

Application of a Crop Model

The resolution of global climate models is far too coarse to drive crop models, particularly in regions with topography as complex as in the Pacific Northwest. The high spatial resolution meteorology simulated by the PNNL RCM provides the opportunity to drive crop models directly at the farm levels. The Erosion Productivity Impact Calculator was driven by meteorology simulated by the regional climate model to assess the impact of a $2xCO_2$ "greenhouse" scenario of climate change on winter wheat production in the Palouse region in eastern Washington and portions of Oregon and Idaho. The climate scenarios were extracted from the regional climate model baseline and $2xCO_2$ simulations for each 90 km grid cell of the regional climate model, with differentiation by elevation. Winter wheat crop yields for the baseline climate averaged 4.52 Mg ha^{-1} across the study region. The lowest yields (0 Mg ha^{-1}) occurred at the higher elevations where temperatures were not sufficient to allow for crop maturity. The highest yields (7.32 Mg ha^{-1}) occurred at intermediate elevations with sufficient precipitation and mild temperatures. Winter wheat mean yield increased to 5.45 Mg ha^{-1} for the $2xCO_2$ climate, which was markedly warmer and wetter than baseline. Yield increases were principally explained by decreases in both cold temperature and water stress.

Development of a Problem-Solving Environment

The collaboration center modeling system must be intuitive and convenient if it is to be useful to the climate impact assessment community. This will require integration and coordination of each of the steps involved in using the modeling system. A user interface for the modeling system has been designed to guide the user through the process of defining the regional domain and resolution, selecting and interpolating the boundary conditions, compiling and running the regional climate model, mapping the regional climate simulation to the selected resolution, and displaying the data. As a proof of concept, a graphical user interface is being developed to facilitate the preprocessing of information that provides all data necessary for performing regional climate simulations. The model preprocessing is a very straightforward procedure masked by repetitive steps of script editing, source code editing, and data file renaming. By wrapping this process with Java codes to do the nonintuitive and repetitive parts, the user will be given a friendly, simple interface to the model.

Summary and Conclusions

Major accomplishments have been achieved toward the development of a prototype Collaboration Center. A two-dimensional decomposition parallel version of the Laboratory's regional climate model has been developed and tested on various supercomputing platforms. The hydrologic model has been enhanced to represent river basins of different spatial scales. A reservoir model and an optimization routine can be used to evaluate the impacts of climate change using realistic water management strategies for the altered climate conditions. The procedures of using regional climate model outputs to assess climate change impacts on crop yields have been demonstrated using regional climate model simulations of the control and $2xCO_2$ conditions to drive a crop model over the Pacific Northwest Palouse region. A prototype graphical user interface is being developed to facilitate the preprocessing of information for performing regional climate simulations. With the completion of these tasks, we will be ready to operate an Collaboration Center to deliver information of relevance to the climate change impact assessment community.

References

Leung LR and SJ Ghan. 1995. "A subgrid parameterization of orographic precipitation." *Theoretical and Applied Climatology* 52:95-118.

Leung LR and SJ Ghan. 1998. "Parameterizing subgrid orographic precipitation and surface cover in climate models." *Mon Wea Rev.* 3271-3291.

Leung LR, MS Wigmosta, SJ Ghan, DJ Epstein, and LW Vail. 1996. "Application of a subgrid orographic precipitation/surface hydrology scheme to a mountain watershed." *J. Geophys. Res.* 101:12,803-12,817.

Wigmosta MS, LW Vail, and DP Lettenmaier. 1994. "A distributed hydrology-vegetation model for complex terrain." *Water Resour. Res.* 30:1665-1679.

Publications

Contributor 1999. "Impacts of climate variability and change in the Pacific Northwest." *A Regional Report for the USGCRP National Assessment*. Pacific Northwest Regional Assessment Group, pp 109.

Contributor 2000. "Chapter 10. Regional Climate Information – Evaluation and Projections." *IPCC Third Scientific Assessment of Climate Change*, Cambridge University Press (in review).

Kothari SC, Y Deng, J Cho, S Mitra, X Bian, LR Leung, SJ Ghan, and AJ Bourgeois. 2000. "Mesoscale climate modeling on PC clusters." *In Proceedings of the Second International Conference on High Performance Computing*, New Delhi, India.

Kothari SC, Y Deng, J Cho, S Mitra, X Bian, LR Leung, SJ Ghan, and AJ Bourgeois. 2000. "Software toolkit for PC clusters with application to climate modeling." *Journal of Computational Science* (in review).

Mote P, A Hamlet, and LR Leung. 2000. "Chapter 4: Possible future climate." *In Rhythms of Change: An Integrated Assessment of Climate Impacts on the Pacific Northwest*, MIT Press (in press).

Thomson AM, RA Brown, SJ Ghan, RC Izaurralde, NJ Rosenberg, and LR Leung. 2000. "Potential impacts of climate change on winter wheat production in eastern Washington state: A simulation study linking the PNNL Regional Climate Model with EPIC." *Climatic Change* (submitted).

Wigmosta MS and LR Leung. 2000. "Potential climate change impacts on flooding and streamflow in forested basins." *In The Influence of Environmental Change on Geomorphological Hazards in Forested Areas*, RC Sidle and M Chigira (eds.), Centre for Agriculture and Biosciences International (in review).

The Nature, Occurrence, and Origin of Atmospheric Aerosols and Their Role in Gas-Particle Chemistry

Leonard A. Barrie, Herman Cho, Greg Patton, Michael Alexander, Chris Aardahl, V. Shuttahanandan, Don Baer, Dan Gaspar, Robert Disselkamp, James Cowin, Alex Laskin

Study Control Number: PN00086/1493

This research enhances the Department of Energy's ability to understand and manage problems involving atmospheric aerosol pollution related to energy production through application of sophisticated measurement capabilities. It contributes to a national effort to reduce the impacts of aerosols on human health, urban smog, visibility, and climate.

Project Description

Pacific Northwest National Laboratory staff are involved in the application of aerosol and related gas measurement methodologies to research on aerosol-related environmental problems associated with energy production. Measurement capabilities and methods are developed based on particle-induced x-ray emission spectrometry, mass spectrometry, nuclear magnetic resonance, laser spectroscopy, and micro-particle devices. These will be applied to yield new insight into the nature, occurrence, and origin of atmospheric aerosols and their role in gas-particle chemistry through measurements at the Laboratory and as part of Department of Energy research programs. Measurements are adapted for use in field campaigns using the Department of Energy research aircraft facility.

Introduction

The objective of this research is to apply the analytical capability of the Pacific Northwest National Laboratory to better understand, through laboratory and field measurement research, the important role of atmospheric particulate matter (aerosols) in environmental issues such as human health, urban smog, visibility, and climate change.

Approach

Specific hypotheses driving this project are that

1. Significant insights into the elemental composition and organic fraction of ambient aerosols—are gained using a combination of nuclear magnetic resonance spectroscopy, particle-induced x-ray emission spectroscopy, membrane ion trap mass spectrometry, micro-particle analysis, and conventional aerosol measurement techniques.

2. Proton transfer mass spectrometry and ion trap mass spectrometry—can be used to measure the transformation of gaseous precursors of aerosols and improve understanding of aerosol production mechanisms.

Specific activities incorporated in the project to test these hypotheses include

1. Nuclear magnetic resonance spectroscopy of aerosol extracts to investigate speciation of water soluble organics yielding insight into the origin of aerosols.

2. Volatile organic gas measurements using proton transfer mass spectrometry and membrane separation-ion trap mass spectrometry to study the mechanism of gas to particle conversion.

3. Proton-induced x-ray emission and proton elastic scattering analysis of atmospheric aerosols using the Environmental Molecular Sciences Laboratory tandem ion accelerator to make high time resolution multi-elemental aerosol analyses.

4. High resolution individual particle analyses to determine the origin and nature of atmospheric particles that enter the lung and potentially cause respiratory problems.

5. Nucleation detection of atmospheric mercury vapor to study the exchange of atmospheric mercury between Earth and atmosphere.

Results and Accomplishments

This project effectively began in May 2000. After 5 months the following progress has been made on the following five activities:

1. *Nuclear Magnetic Resonance Spectroscopy*. A research plan was prepared. Concentrated fogwater samples collected by the research group of Professor S. Fuzzi who had attempted similar measurements (Descari et al. in press) were analyzed for soluble carbonaceous aerosol constituents (Figure 1). An aerosol high volume sampler for sample collection and a continuous PM2.5 aerosol mass sampler for high time resolution event characterization were acquired.

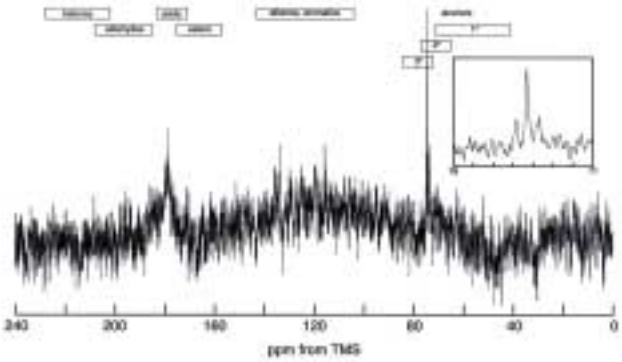

Figure 1. A proton decoupled ^{13}C nuclear magnetic resonance (NMR) spectroscopy spectrum of fogwater measured at 75 MHz. The sample was collected in the polluted Po River valley of Italy. The frequency scale is expressed as a parts per million (ppm) shift from the reference ^{13}C signal of tetramethylsilane (TMS). *Inset spectrum: Expansion of the alcohol region showing the power of this technique for even higher resolution than displayed.* Identification of compounds by the frequency and their carbon content by the peaks makes this nondestructive analysis technique a powerful analytical tool for characterizing complex organic aerosol mixtures.

2. *Volatile Organic Gas Measurements Using Proton Transfer Mass Spectrometry and Membrane Separation-Ion Trap Mass Spectrometry.* Collaboration with the world's leading authority on proton transfer mass spectrometry was initiated through a visit by Professor Werner Lindinger (U. of Innsbruck) to the Laboratory in June 2000. A plan was developed whereby M. Alexander will make a technical visit to Prof. Lindinger's laboratory, we will acquire a proton transfer mass spectrometer, and a graduate student of Prof. Lindinger will spend 1 to 2 months at Pacific Northwest National Laboratory in a collaborative effort to apply the instrument to aircraft measurements. In late September, an experienced atmospheric instrumental chemist was interviewed for a research position that will expedite the application of this instrumentation.

3. *Proton-Induced X-Ray Emission and Proton Elastic Scattering Analysis of Atmospheric Aerosols*. The tandem ion linear accelerator facility was developed for high time resolution chemical analysis of atmospheric aerosols. An exchange of visits with Professor T. Cahill of the University of California at Davis and the DELTA group was followed by joint participation in aerosol collection and comparative multi-elemental analyses during the Texas 2000 Air Quality study (August and September 2000). An x-y-z manipulator was installed on the accelerator's beam end and tests with artificial aerosol samples were performed in preparation for analysis of ambient aerosols. Duplicate analysis of the same samples from Houston by Pacific Northwest National Laboratory and the DELTA group will mark the beginning of our multi-elemental capabilities.

4. *High Resolution Individual Particle Analysis System.* This activity involves the analysis of individual aerosol particles after collection on carbon films using automated scanning electron microscopy and on cascade impactor stages by time-of-flight secondary ion mass spectrometry. Samples from the Texas 2000 Air Quality study (August and September 2000) were collected. This proposal supported the time-of-flight secondary ion mass spectrometry analysis and resulted in a presentation by D. Gaspar at the American Vacuum Society Annual Meeting.

5. *Nucleation Detector for Atmospheric Mercury Vapor.* Proof-of-concept experiments were conducted to demonstrate the feasibility of two-photon laser excitation and nucleation detection of elemental mercury (Figure 2). The methodology shows sensitivity at better than 0.1 ng Hg /m^3. Atmospheric Hg^0 is 1 to 5 ng Hg /m^3.

Summary and Conclusions

In 5 months, a program of aerosol measurement research has been initiated within the Fundamental Science Division of Pacific Northwest National Laboratory. In this short period, collaborations with two internationally recognized measurement research groups have been established and the powerful analytical tools of the Environmental Molecular Sciences Laboratory mobilized

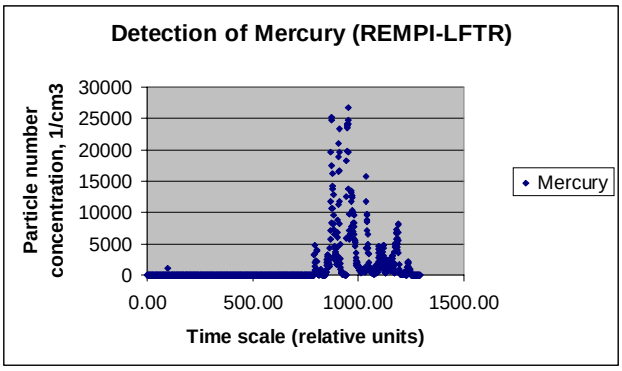

Figure 2. Particle production as laser irradiated elemental mercury is suddenly added to a carrier gas passing through a laminar flow tube reactor. The peak particle production indicates sensitivity of detection at 0.1 ng/m^3 which is more than enough for atmospheric applications. Decrease in signal is due to fogging of quartz windows by particles. This can be prevented by heating.

to study aerosol composition and formation processes. Participation in the Texas 2000 Air Quality study has demonstrated a field measurement capability and will contribute to the goals of this project.

Reference

Decesari S, MC Facchini, S Fuzzi, and E Tagliavini. *J. Geophys. Res.* (in press).

Publication

Gaspar DJ, MA Carpenter, JP Cowin, DR Baer. 2000. "Structure and composition of size- and time- resolved outdoor aerosols determined using TOF-SIMS." In *Proc. 47th International Symposium on Vacuum, thin films, surfaces/interfaces and processing.* October, American Vacuum Society, Boston.

Thermodynamics and Kinetics of Cation Exchange at Defects in Micas

Kevin M. Rosso, Eric J. Bylaska

Study Control Number: PN99071/1399

Understanding the fate and transport of radionuclides like cesium-137 in the subsurface is a key element of characterizing the environmental status and risks associated with contaminated DOE sites. This project uses molecular level modeling to analyze a key element for understanding the interactions and binding of these elements by layered silicate minerals.

Project Description

This project involves development of a molecular modeling capability for radionuclide-layered silicate mineral interactions. The focus of this work is calculation of thermochemical cycles for important cation exchange reactions, such as cesium (Cs) → potassium (K), in interlayer sites in the mineral muscovite. Such reactions limit the transport of the otherwise highly mobile contaminant ^{137}Cs in natural sediments. Density functional theory methods were used to calculate optimized structural parameters and energies for muscovite with cesium or potassium in the interlayer site. The independent effects of layer charge and structure have been separated out and their influence on the exchange energetics has been evaluated. The project has greatly improved our understanding of the factors affecting the uptake and fixation of cesium in the layered silicate family of minerals.

Results and Accomplishments

Accomplishments include the successful implementation and benchmarking of planewave density functional theory codes on model mineral systems, calculation of optimized structural parameters for muscovite and cesium-exchanged muscovite, and calculation of Cs/K cation exchange thermodynamics. The results are discussed in more detail below.

Benchmarking Density Functional Theory Methods

A variety of planewave density functional theory methods and calculation parameters are potentially applicable to the problem of cation exchange. The relative accuracies of the particular methods can be difficult to gauge against experiment on complicated systems. Therefore, the various methods were applied to simpler but related model mineral systems to benchmark their performance. Using the mineral diaspore, we evaluated the ability of local-density and generalized gradient approximation density functional theory methods to mimic the compressibility of an anisotropic mineral structure as a function of pressure up to 25 GPa (Figure 1). Calculated structures, bulk moduli, and anisotropic compressibilities for diaspore using the generalized gradient approximation density functional theory method demonstrated the best agreement with experiment. The test implies that generalized gradient approximation density functional theory is sufficiently accurate to describe changes in the total energy of a mineral phase as a function of subtle structural changes.

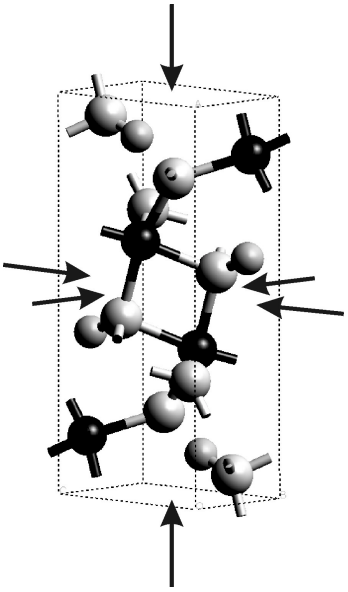

Figure 1. The structure of the mineral diaspore. The structure is known to compress unequally along the three unit cell axes. Generalized gradient approximation density functional theory methods accurately reproduce this anisotrophy in the compressibility.

Density functional theory methods were also benchmarked to evaluate their ability to calculate relative energies for different structures of equivalent chemical composition, or polymorphs. Phase relationships for

geometry optimized AlOOH and FeOOH polymorphs were calculated. Local density functional theory methods outperformed generalized gradient approximation in properly depicting the relative stabilities of these phases, as compared with experiment.

The Structure of Muscovite

The structure of muscovite is complicated because it contains both strongly covalent and ionic interactions. So-called 2:1 layers are composed of two tetrahedral Si_2O_5 sheets sandwiching an octahedral AlO_6 sheet, each composed of relatively rigid covalent bonds (Figure 2). Interlayer potassium cations bind the layers together with ionic bonds. The strength of the ionic bonding depends on Al → Si substitutions in the 2:1 layers, which lead to permanent layer charge. Using a variety of density functional theory methods to predict the minimum energy structure, we found that the generalized gradient approximation approach resulted in the best agreement with the experimental structure. The unit cell parameters were predicted to an accuracy of 1%.

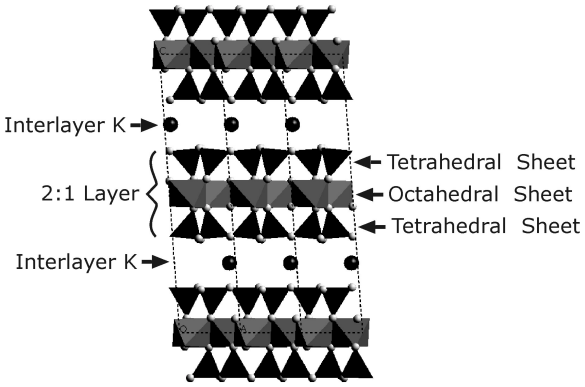

Figure 2. The structure of muscovite. Interlayer cations bind the layers together. Cesium from solution slowly exchanges with interlayer potassium at this site over time. Density functional theory modeling approaches are being used to estimate the thermodynamics of this process to understand how tightly bound cesium becomes and why.

We were able to go beyond experimental methods by designing a variety of closely related muscovite models that vary in both layer charge and degree of distortion of structure at the interlayer cation site. For the condition of zero layer charge and no interlayer site distortion, the difference in the optimal interlayer spacing for cesium relative to potassium is very small, indicating a baseline indifference of the muscovite structure to cation size. The presence of 2:1 layer charge or interlayer site distortions clearly change this outcome. Analysis of the dependence of the interlayer spacing on layer charge shows that while the spacing collapses with increasing layer charge for potassium as the interlayer cation, the reverse is true for cesium. We attribute the contrasting behavior to inherent differences in the ability of these cations to screen 2:1 layer-layer repulsions. Such effects are likely to be at play during cesium/potassium exchange at interlayer sites available at the interface with solution.

Thermodynamics of Cation Exchange

The overall cesium/potassium exchange reaction at interlayer sites is envisioned to require several general component steps: 1) opening of the interlayer spacing (delamination), 2) hydration and release of interlayer potassium, 3) sorption and dehydration of cesium, and 4) closing of interlayer spacing. In this project, we developed an exchange model that concerns the initial and final states. The initial state consists of interlayer potassium in muscovite structure and cesium in aqueous solution at infinite separation. The final state consists of interlayer cesium in muscovite and potassium in aqueous solution at infinite separation. This approach reduces the contributions to the exchange reaction into the relative energy differences for potassium and cesium to be solvated by aqueous solution and to be incorporated into the muscovite structure. The necessary calculations are shown in Figure 3.

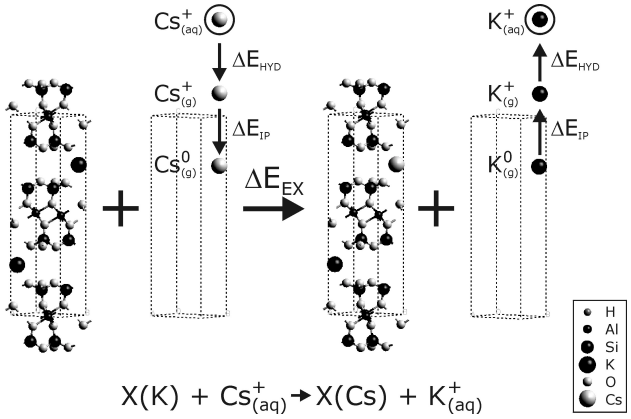

Figure 3. The energy terms required to estimate the Cs/K exchange energy (ΔE_{EX}). Terms were included to correct the free atom calculations to conditions for aqueous solution.

Density functional theory optimizations of the various model types were performed to collect the energy values needed to estimate driving force for the exchange reaction. The unit cell parameters for the structures were allowed to vary to mimic conditions where the structures are free to expand or contract. The results suggest that, under these conditions, the exchange energies are surprisingly small, with the energies for each of the models varying only by a few kJ/mol. This result would

undoubtedly not be the case for fixed unit cell conditions where the forward exchange reaction would be large and unfavorable. The small exchange energy overall suggests that the muscovite structure is essentially indifferent with respect to interlayer cation when the interlayer spacing is free to change. Between the various models, the results indicate that the exchange energy systematically follows changes in this parameter, which in turn depends on the layer charge. Where the interlayer site distortion is small, the forward exchange reaction was found to be favorable, and more so with increasing layer charge. But a large deleterious effect on the exchange energy arises from slight distortion of the interlayer site structure.

Overall, the calculations suggest that the incorporation of cesium into muscovite interlayers is energetically feasible and nearly isoenergetic when the expansion of the interlayers is not inhibited. The driving force for the overall exchange reaction is very small and therefore the forward exchange behavior is likely to be dominated by diffusion kinetics. Likewise, any long-lived fixation of cesium in the interlayers of muscovite is likely due to kinetic barriers, rather than thermodynamics.

Future work in this area should incorporate more exchangeable cations and a larger variety of substitutions in the 2:1 layers. Kinetic aspects of the exchange process must also be addressed if the models are ever to be used to simulate experimentally observed behavior.

Publications and Presentations

Rosso KM and JR Rustad. "The structures and energies of AlOOH and FeOOH polymorphs from plane wave pseudopotential calculations." *American Mineralogist* (in press).

Rosso KM, JR Rustad, and EJ Bylaska. "The Cs/K exchange in muscovite interlayers: An ab initio treatment." *Clays and Clay Minerals* (submitted).

Rustad JR and KM Rosso. "Equation of state of diaspore (α-AlOOH) calculated from plane wave pseudopotential methods." *Geophysical Review Letters* (submitted).

Rosso KM, EJ Bylaska, and JR Rustad. December 1999. "The energetics of cation exchange in muscovite mica." Presented at the National Meeting of the American Geophysical Union, San Francisco, California.

Tracer Development for Tank Leak Detection

Richard J. Cameron

Study Control Number: PN00088/1495

Tanks containing chemical and radioactive waste are the focus of stabilization and remediation efforts at DOE sites. These efforts require a reliable method of tank leak detection and quantification. Partitioning interwell tracer test technology provides reliable leak detection and quantification capabilities, immune to electrical and electromagnetic interference that can affect the accuracy of leak detection.

Project Description

Partitioning interwell tracer tests (PITTs) have been developed and field-proven as a new technology for detecting and quantifying nonaqueous-phase liquids at hazardous waste sites. Laboratory studies and field tests have proven that soil moisture content also can be quantified using partitioning interwell tracer tests. Repeated partitioning tracer tests beneath Hanford Site waste tanks provide soil moisture measurements that indicate a tank leak, and can quantify the size of the leak. Additionally, the constituents of tank wastes include volatile vapors (Agnew 1997) such as ammonia or radioactive gases (^{135}Xe) that may be detected in the partitioning interwell tracer tests advection flowfield, thus providing an additional (and perhaps faster) method of leak detection. We formulated mathematical models of tracer behavior under the fast-flow conditions required for timely leak detection. We also conducted laboratory experiments to confirm the theoretical predictions of tracer partitioning behavior under nonequilibrium transport conditions. A full-scale field test of soil moisture measurement in Hanford soils may be performed during in the next year of study on this project.

Introduction

The partitioning interwell tracer tests technology is carried out by establishing a flowfield in the subsurface using a system of wells that inject and extract air (for vadose zone tests or water (for saturated zone tests). A suite of conservative (non-partitioning) and partitioning tracers are injected and their elution curves analyzed by temporal-moment methods to determine the quantity of the component of interest in the subsurface. Gaseous tracers that partition into water can be used with a conservative tracer to quantify soil moisture. In the past, these tests have been carried out under equilibrium conditions, with the flow between wells slow enough for mass-transfer processes to achieve equilibrium. Timely detection of tank leaks requires fast-flow conditions between injection and extraction wells that produce nonequilibrium mass-transfer conditions. This project focuses on the investigation and development of gas-phase tracer suites for soil moisture quantification under nonequilibrium transport conditions, and the investigation of nonequilibrium partitioning properties of gaseous and vapor-phase tank-waste components for their use in tank leak detection.

Previous partitioning interwell tracer tests have demonstrated the capability to accurately quantify even small amounts of nonaqueous-phase liquids in the subsurface. With the use of a water-partitioning tracer whose behavior under nonequilibrium transport conditions has been accurately characterized, partitioning interwell tracer tests should be able to detect and quantify a tank leak of well under 1500 gallons. In the presence of a leak, small amounts of radioactive gases and volatile waste components such as ammonia and butanol may be advected along the partitioning interwell tracer tests flowpath. Characterization of the nonequilibrium partitioning properties of these waste components will provide an estimate of retardation times and elution concentrations. A complete partitioning interwell tracer tests underneath a tank requires 4 to 12 hours to provide leak information. Since waste-tank components may be detected at any time during the partitioning interwell tracer tests such measurements provide early indication of a tank leak.

The partitioning interwell tracer tests technology is not affected by heavy machinery, piping systems, or other metal artifacts in the vicinity of the tank. This is in sharp contrast to most electric and electromagnetic methods of leak detection that are adversely affected by these artifacts and suffer a loss of sensitivity, resolution, and an increase in the possibility of false positive leak-detection results.

Approach

The adaptation of partitioning interwell tracer tests technology to tank leak detection requires the characterization of tracer and tank-waste partitioning behavior under nonequilibrium mass-transfer conditions and an analysis of flow-field design requirements. The partitioning interwell tracer tests concept is illustrated in Figure 1. A sample data analysis is shown in Figure 2. The proposed flow velocity for the partitioning interwell tracer tests would sweep one pore volume (the area under the tanks) every 4 to 12 hours. While tracer behavior can give real-time indications of a leak after only a short time, accurate quantification of the leak might require two or three swept pore volumes. One method of implementing the leak-detection technology is to use tank-waste components as leak detectors, and use the partitioning interwell tracer tests as a quantification method after a leak has been detected through the presence of volatile waste components or radioactive gases in the advection exhaust stream.

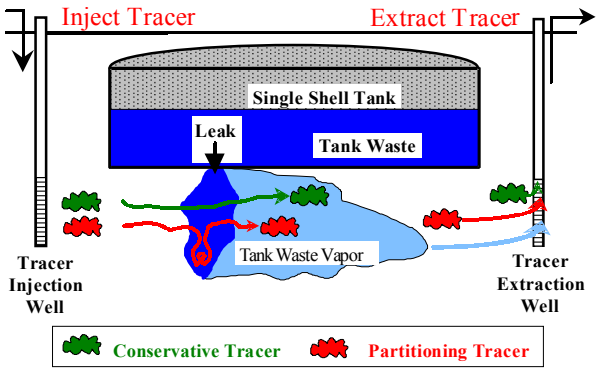

Figure 1. Partitioning interwell tracer test for tank leak detection

Experimental Results of Partitioning Tracer Test in a Soil Column at 3.83 cc/min

	Methane	Difluoromethane
Mean Residence Volume (cc)	37.6	61.7
% Tracer Recovered	93%	95%
Retardation Factor	1.00	1.64
Water Saturation	-	0.274
Mean Residence Time (hrs)	0.16	0.27

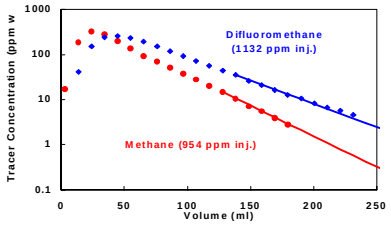

Figure 2. Data from a fast-flow soil-column experiment, using methane as the conservative tracer and difluoromethane as the partitioning tracer. Temporal moment analysis measures the difference between the centroids under the elution curves to provide water saturation and mean residence volume (or pore volume). Note the higher concentration peak of the conservative tracer, and the lower peak concentration and higher tail concentration of the partitioning tracer; this is characteristic of partitioning tracer behavior.

Since tracer behavior governs the shape of the elution curve required for soil moisture quantification, the partitioning behavior of the tracer and its elution under conditions of exposure to actual tank-waste saline solutions must be fully understood before tank leaks may be accurately quantified. As this project continues, tracer behavior will be investigated both by theoretical studies that predict tracer behavior using mathematical modeling and thermodynamic approximations of partitioning behavior. Soil-column experiments using representative soil samples with varying moisture contents will be flushed at high flow rates with tracers (see Figure 3) and the elution curves will be studied for their adherence to theoretical models. The alterations of water-partitioning behavior in the presence of the concentrated metallic salts, ammonia, and organics present in the tank wastes are being investigated by thermodynamic modeling methods, and may soon be the subject of soil-column experiments using simulated tank wastes to experimentally quantify the non-ideal partitioning behavior of potential tracers.

Non-Equilibrium Partitioning Experiments

Chromatographic Column Apparatus

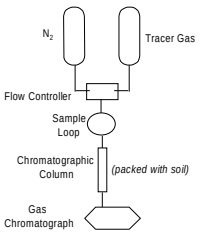

- Measure partitioning and elution in fast-flow regime
- Values measured in experiments:
  - –Gas flow rate
  - –Water saturation of soil in chromatographic column
  - –Swept pore volume
  - –Tracer elution
  - –Tracer recovery percentage

Figure 3. Apparatus for nonequilibrium tracer characterization experiments using soil-column chromatography

The soil moisture in the area under the tanks swept by the partitioning interwell tracer tests will affect the elution behavior and peak concentration of gaseous tank-waste components used as adjunct leak detection gases. Potential leak-detection gases will be screened for

allowable parameters using thermodynamic modeling, and candidate gases will undergo soil-column experiments using simulated tank wastes to verify predicted behavior.

Results and Accomplishments

Our research team derived a mathematical model of tracer behavior under nonequilibrium transport conditions. Soil-column experiments using the proposed tracer suite (methane and difluoromethane) have verified the theoretical conclusions. The tracer residence time was found to be independent of the Damkholer number (mass-transfer rate/advection flow rate), and the mass-transfer rate was found to be independent of the water saturation of the soil. Experimental results from soil-column tests show that residence time (flow rate through the pore volume) has little effect on the accuracy of water saturation measurements under transport conditions with Damkholer numbers greater than unity (see Figure 4).

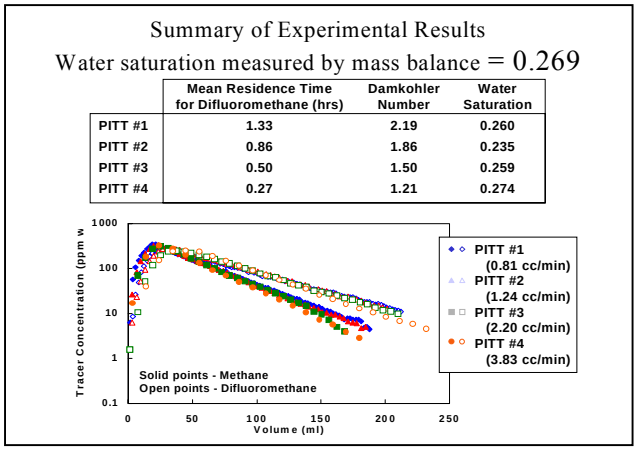

Figure 4. Experimental results for the methane-difluoromethane tracer system show accurate water saturation measurements are possible at fast flow rates (low mean residence times)

Thermodynamic approximations of ammonia partitioning show that it would be severely retarded in its transport in the subsurface, but it is thought that preferential flow-patterns will saturate with continued passage of ammonia and reduce the apparent retardation. Butanol and other organics with lower aqueous partitioning coefficients are under consideration as waste-component leak indicators.

^{135}Xe is present in tank wastes (Agnew 1997) at very low molar concentrations, but its gamma signature is easily detectable at 1 Bq/m^3. Its relatively high solubility in water gives it a correspondingly high retardation factor, but soil-column experiments may reveal preferential flow-pattern saturation (as with ammonia). We are studying other noble-gas, waste-component radioisotopes of lower atomic number (less polarizable, and so less soluble) and tritium as leak detection agents.

Summary and Conclusions

A mathematical model of tracer behavior under nonequilibrium mass-transfer conditions was formulated. Soil-column experiments verified the theoretical predictions of the independence of the Damkholer number and tracer residence time and the independence of mass-transfer rate and soil water saturation. Our research team concluded that

- The accuracy of water saturation measurements are substantially unaffected by advection flow rates or tracer residence times for transport conditions with Damkholer numbers greater than unity.
- The methane/difluoromethane tracer suite is well suited for soil moisture characterization.
- Volatile organic, inorganic, or radioactive tank-waste components may function effectively as leak indicators if partitioning and preferential-flow behavior is adequately characterized.

This project will continue as we perform preferential-flow experiments and characterize tracer behavior in simulated Hanford tank waste. We also will seek to conduct a field demonstration where a soil-moisture partitioning interwell tracer tests will be used to quantify a simulated tank leak in Hanford soils.

Reference

Agnew SF. 1997. *Hanford Tank Chemical and Radionuclide Inventories: HDW Model Rev. 4* LA-UR-96-3860, Los Alamos National Laboratory, Los Alamos, New Mexico.

Use of Reduced Metal Ions in Reductive Reagents

John S. Fruchter, Jim E. Szecsody

Study Control Number: PN00090/1497

In the past 15 years, groundwater cleanup of chlorinated solvents has involved installation of reactive subsurface iron barriers in over 25 sites in the U.S. One method used, which relies upon the reduction of iron in natural sediments, is applicable to deep aquifers (more than 100 feet). In this laboratory study, we modified geochemically the sediment reduction method to make the process more efficient and, ideally, less expensive.

Project Description

The purpose of this study was to determine a more efficient method for introducing chemical reducing capacity into the subsurface. After an initial reduction of aquifer sediments with sodium dithionite, reduced cations, such as ferrous iron (Fe(II)) or titanous ion (Ti(III)) would be injected into the aquifer. The expected results are an understanding of the proportions of Fe(II) and Ti(III) metal ions to use and the chemical conditions needed for achieving a successful reduced zone. In this way, a reactive barrier can be developed that is more effective for destroying dissolved contaminants such as chlorinated solvents and explosives.

Over the past several years, a major effort at Pacific Northwest National Laboratory was the development of reductive barrier remediation techniques for use on shallow and deep (>50 feet below ground surface) contaminant plumes. The most promising method is in situ redox manipulation. The basis of the method is the use of a strong reducing agent (dithionite) to reduce normally trivalent structural iron in the soil matrix to the more reactive divalent form. The presence of the immobile divalent iron in the treated zone creates a chemically active barrier to the transport of reducible species, which can last for decades before renewal.

Despite these successes, dithionite addition alone is an inefficient and expensive way to add reducing capacity to the aquifer. Because the reduction of some contaminants (trichloroethylene for example), the surface has a catalytic or surface coordination role in reduction, the presence of specific metals on the iron oxide surface can increase the electron transfer (reduction) rate. This concept has been applied to zero-valent iron walls, with the incorporation of trace amounts of Cr and Ni. A more efficient method would be to inject dithionite to produce reducing conditions in the aquifer, then add one or more reduced metal ions directly. We propose to amend the in situ redox manipulation technique through addition of additional reduced metal ions (e.g., Fe(ii), Ti(III)) to the redox injection. Cationic adsorption of reduced metal ions on the soil matrix should the produce a more reactive barrier.

Introduction

In this study, we investigated electron donors or reaction catalysts potential chemical additions.

Fe(II) and Mn(II) additions (electron donors) resulted in a significant increase in trichloroethylene dechlorination. Trichloroethylene dechlorination with the Fe(II) addition was predictable and more efficient than the Mn(II). The additions of Ti(III), Ni(II), Pd catalyst, and EDTA did not enhance the trichloroethylene dechlorination rate in sediments, even though these compounds are used in engineered systems. Because the addition of an electron shuttle had only a slight positive effect, the rate of trichloroethylene degradation is not limited by electron transfer, so an additional electron donor rather than catalyst is likely more efficient. While an Fe(II) addition is expected to be more cost efficient than the use of reduced sediment alone, amending the redox treatment at the field scale involves additional hydraulic and geochemical considerations. Upscaling these results of using small to large experimental systems is needed to design viable field-scale injection schemes.

Trichloroethylene dechlorination with reduced sediment relies on the oxidation of ferrous iron [adsorbed Fe(II), $Fe(II)CO_3$, reduced smectite clays; Szecsody et al. 2000a, b]. In addition, adsorbed or structural Fe^{II} on an Fe^{III}-oxide or clay surface is necessary for dechlorination, either as a catalyst, a semiconductor, or to provide surface Eh conditions (Scherer et al. 1999; Wehrli 1992). The trichloroethylene degradation pathway using zero-valent iron (Roberts et al. 1996) and reduced sediments (Szecsody et al. 2000b) is reductive elimination producing chloroacetylene, then acetylene:

$TCE + 3H^{+} + 3Fe^{2+} <=(>Fe)=> acetylene + 3Fe^{3+} + 3Cl-$

Laboratory experiments with partially and fully reduced sediment showed a highly nonlinear relationship between the fraction of reduced iron and trichloroethylene reactivity (Szecsody et al. 2000a), where more than 40% of the iron needs to be reduced for trichloroethylene dechlorination to proceed. Field sites that contain a large fraction of iron may not be able to be economically reduced, so an alternative approach may be to add an electron donor or catalyst.

Approach

In this study, electron donors or reaction catalysts were added to partially reduced sediment in order to determine the efficiency of the amendments to dechlorinate trichloroethylene. Naturally occurring electron donors added included Fe(II), Mn(II), 2:1 iron-bearing clays, and humic acid. Engineered electron donors added included Ti(III) and Ni(II). The addition of Ti(III)EDTA should result in the slow ligand-promoted dissolution of iron oxides (Heron et al. 1994), removing Fe(III). Ni(0) is currently being used with Fe(0) at the field scale (Su and Puls 1999). Anthroquinone-2-6-disulfonic acid and humic acid are biotic and abiotic electron shuttles (Curtis and Reinhard 1994). Palladium catalyst is currently being used for trichloroethylene dechlorination at the field scale with Fe(0) (Li and Farrell 2000).

Results and Accomplishments

The addition of Fe(II) to partially reduced sediment could result in the increase in the trichloroethylene degradation rate, but only under specific geochemical conditions. Trichloroethylene degradation rate for the partially reduced sediment [no addition of Fe(II)] of 17.5 hours indicated that the sediment was about 40% reduced, relative to 100% reduced sediment which would result in a 1.2-hour half-life. The addition of a mass of Fe(II) (Figure 1) showed that the trichloroethylene reduction rate with the Fe(II) addition had a 6.5-hour half-life, or about the 8- to 10-hour rate predicted based on the mass of Fe(II) added. However, the Fe(II) addition was successful at high pH (10.5) when added with dithionite, but was not successful at lower pH (6.8 to 9.9) or if added after the dithionite reduced the sediment. This result may have been caused by the formation of $Fe(OH)_2$, which precipitated and blocked the reduced sediment. The addition of Mn(II) to partially reduced sediment (Figure 2) also resulted in an increase in the trichloroethylene degradation rate. Because Mn(II)

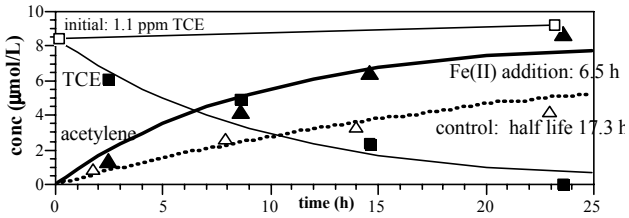

Figure 1. Trichloroethylene dechlorination to acetylene in the presence of reduced natural sediment and with the addition of Fe(II)

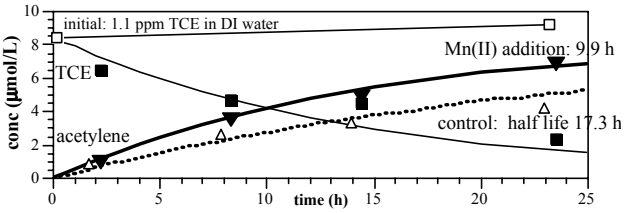

Figure 2. Trichloroethylene dechlorination to acetylene in the presence of reduced natural sediment and with the addition of Mn(II)

oxidizes to Mn(IV) (donates two electrons), the Mn(II) addition experiment should have resulted in a 3- to 4-hour trichloroethylene degradation half-life and not the10-hour half-life observed.

Three smectite clays were added that had differing amounts of iron in the structure: hectorite (0% Fe), montmorillonite (2.3% Fe), and nontronite (22% Fe). The addition of oxic clays, as predicted, had a large negative impact on dechlorination (Figure 3), correlated with the fraction of iron in the clay. When reduced smectite clays (Stucki et al. 1984) were added, trichloroethylene dechlorination decreased (17- to 22-hour versus 10-hour for the control), even though the separate sediment and clay could dechlorinate trichloroethylene faster. This may have been caused by the clay coating reactive sediment surfaces.

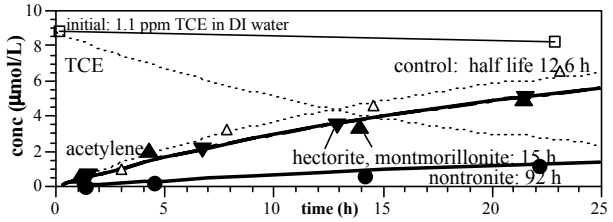

Figure 3. Trichloroethylene dechlorination to acetylene in the presence of reduced natural sediment and with the addition of oxic smectite clays showing that the iron content in the clay correlated with the impact on the trichloroethylene dechlorination rate

The additions of Ti(III), Ni(II), palladium catalyst, and EDTA resulted in small to large decreases in the rate of trichloroethylene dechlorination, possibly indicating adsorption of these metals or complexes blocked access by trichloroethylene. The addition of AQDS (electron shuttle) resulted in a small but insignificant increase in the trichloroethylene dechlorination rate (Figure 4).

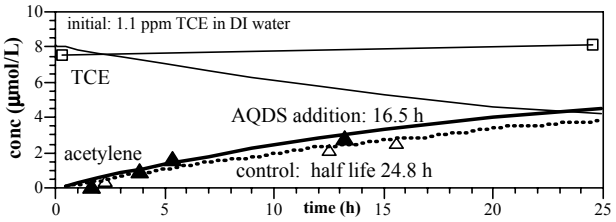

Figure 4. Trichloroethylene dechlorination to acetylene in the presence of reduced natural sediment with the addition of an aqueous electron shuttle (AQDS), which resulted in a small increase in the dechlorination rate

Summary and Conclusions

Fe(II) and Mn(II) additions to partially reduced sediment resulted in a significant increase in trichloroethylene dechlorination. Trichloroethylene dechlorination with the Fe(II) addition was more efficient than Mn(II). The additions of Ti(III), Ni(II), Palladium catalyst, and EDTA did not enhance the rate of trichloroethylene dechlorination by the partially reduced sediment. Because the addition of an electron shuttle (AQDS) had only a slight positive effect, the rate of trichloroethylene degradation is not limited by electron transfer, so the addition of an additional electron donor rather than a catalyst is likely more efficient. While an Fe(II) addition is thought to be more cost-efficient than the use of reduced sediment alone, amending the redox treatment at the field scale involves additional coupled hydraulic and geochemical considerations. Because both Mn(II) and Fe(II) adsorb strongly to natural sediments, engineered small pulse injections with a high ionic strength or low pH would be needed at the field scale to result in a dispersed addition of adsorbed Fe(II) or Mn(II), as indicated by reactive transport modeling, and could be tested in experimental systems.

References

Curtis G and M Reinhard. 1994. "Reductive dehalogenation of hexachloroethane, carbon tetrachloride, and bromoform by anthrahydroquinone disulfonate and humic acid." *Env. Sci. Tech.* 28:2393-2401.

Heron G, TH Christensen, and J Tjell. 1994. "Oxidation capacity of aquifer sediments." *Environ. Sci. Technol.* 28:153-158.

Li T and J Farrell. 2000. "Reductive dechlorination of trichloroethene and carbon tetrachloride using iron and palladized-iron cathodes." *Environmental Science and Technology* 34(1):173-179.

Roberts A, L Totten, W Arnold, D Burris, and T Campbell. 1996. "Reductive elimination of chlorinated ethylenes by zero-valent metals." *Environ. Sci. Technol.* 30(8):2654-2659.

Scherer M, B Balko, and P Tratnyek. 1999. "The role of oxides in reduction reactions at the metal-water interface." *In kinetics and mechanisms of reactions at the mineral/water interface,* eds. D Sparks and T Grundl, ACS Symposium Series #715, American Chemical Society, Atlanta, Georgia, p 301-322.

Stucki JW, DC Golden, and CB Roth. 1984. "Preparation and handling of dithionite-reduced smectite suspensions." *Clays and Clay Minerals* 32(3):191-197.

Su C and RW Puls. 1999. "Kinetics of trichloroethene reduction by zerovalent iron and tin: Pretreatment effect, apparent activation energy, and intermediate products." *Environmental Science and Technology*, 33(1):163-168.

Szecsody JE, JS Fruchter, DS Sklarew, and JC Evans. 2000a. *In situ redox manipulation of subsurface sediments from Fort Lewis, Washington: Iron reduction and TCE dechlorination mechanisms*. PNNL-13178, Pacific Northwest National Laboratory, Richland, Washington.

Szecsody J, M Williams, J Fruchter, V Vermeul, and J Evans. 2000b. "Influence of sediment reduction on TCE degradation, remediation of chlorinated and recalcitrant compounds." book chapter, ed. G Wickramanayake, *Chemical Oxidation and Reactive Barriers,* p. 369-376.

Wehrli B. 1992. "Redox reactions of metal ions at mineral surfaces." *In aquatic chemical kinetics*, ed. W Stumm, Wiley Interscience, New York.

Publication

Szecsody J, M Williams, J Fruchter, and V Vermeul. 2000. "In Situ Reduction of Aquifer Sediments for Remediation: 1. Iron Reduction Mechanism." *Environmental Science and Technology* (submitted).

Use of Shear-Thinning Fluids for Injection of Colloidal Size Reactive Particles

Kirk J. Cantrell, Tyler J. Gilmore

Study Control Number: PN00091/1498

In situ remediation is an important technique for creating an in situ permeable reactive barrier against halogenated hydrocarbons. This project has identified a shear-thinning polymer that is effective in porous materials for reducing most halogenated hydrocarbons to harmless and less-mobile forms.

Project Description

Shear-thinning polymers have been used in slurry formulations for the injection of colloidal size zero-valent iron particles into porous media for the purpose of forming a permeable reactive barrier for in situ remediation of contaminated groundwater (Cantrell et al. 1997a,b). Successful proof-of-principle of the concept has been conducted at the bench scale using pure quartz sand as the porous media. When the same formulations that were successful in quartz sand media were applied to natural Hanford sediments or aquifer materials plugging at the inlet occurred almost immediately upon injection. This plugging was attributed to adsorption of the shear-thinning polymers onto mineral surfaces in the Hanford sediments and solubility reduction due to interaction with dissolved calcium. Identification of a suitable shear-thinning polymer that will not strongly adsorb to natural minerals or become insoluble in the presence of calcium is critical for the development of an effective slurry formulation for injecting zero-valent iron particles into porous media. One particularly promising compound has been identified. This compound will be referred to as AMX.

Batch and column adsorption experiments indicated that this compound does not adsorb to Hanford sediments to any significant extent. A series of experiments were conducted to determine the effectiveness of slurry formulations developed with this polymer for injection of micron size iron particles. The results of these experiments indicate that slurry formulations using AMX will be effective for creation of an in situ permeable reactive barrier composed of zero-valent iron particles by slurry injection through wells. This approach has many advantages over current approaches for constructing a permeable reactive barrier. The most important advantages are that the treatment zone can be injected to any depth or location that can be reached by drilling, and zero-valent iron is a very strong reductant. Zero-valent iron is capable of reducing most chlorinated hydrocarbon contaminants (trichloroethylene, trichloroethane, carbon tetrachloride), explosive compounds (TNT, HMX, RDX, and Tetryl), and inorganic contaminants such as Cr, Tc, and U at rates that are practical.

To assess the impact of the injection process on the permeability of the porous media, pressure measurements were taken before, during, and after slurry injection. These results indicate that the slurry injection process used does not adversely impact the permeability of the porous media.

Introduction

Significant effort has been directed to laboratory and field research studies on the use of zero-valent iron as a material to remediate certain groundwater contamination problems (Tratnyek 1996; Fairweather 1996; Wilson 1995). Zero-valent iron is a strong chemical reductant and has the capability to render most halogenated-hydrocarbon compounds harmless (Gillham and O'Hannesin 1994; Matheson and Tratnyek 1994; Orth and Gillham 1996; Roberts et al. 1996). Recently published data have shown that zero-valent iron can effectively destroy RDX (Singh et al. 1999) and can reduce TNT to its corresponding aromatic polyamine (Hofstetter et al. 1999). Zero-vlaent iron can also chemically reduce many highly mobile oxidized metal contaminants (e.g., CrO42-, UO22+, and TcO4-) to their less mobile forms (Gould 1982; Cantrell et al. 1995).

Zero-valent iron shows great promise as an permeable reactive barrier material because of its applicability to a broad range of contaminants, rapid reaction kinetics, and the low cost and wide availability of the material (Wilson 1995). Permeable reactive barriers are permeable zones emplaced within the aquifer that react with contaminants as contaminated groundwater flows through the zone. Between 1994 and 1998, 24 pilot-scale and full-scale zero-vlaent iron permeable reactive barriers have been installed (EPA 1999).

Most of the permeable reactive barriers have been constructed using trench-and-fill techniques, such as digging a trench in the flow path of a contaminant plume and backfilling the trench with reactant material (Gillham et al. 1994; Yamane et al. 1995) or auger techniques (Puls et al. 1995). Although the trench-and-fill approach is effective, it is limited to sites where the aquifer material is porous, as opposed to fractured, depths that are shallower than about 20 m, and aquifers which are relatively thin (because excavations must be dewatered during construction). Although many sites have these characteristics, many important sites do not. Because of these factors and the fact that trench construction tends to be the single greatest expense for this remediation technique, innovative methods for installation of reactive barriers in the subsurface are needed, especially in geologic settings where current barrier installation technologies are of limited practical value (fractured media and/or at depths of greater than 20 m).

Previous work at our Laboratory demonstrated an innovative approach for emplacement of an in situ treatment zone composed of zero-valent iron (Kaplan et al. 1994; Kaplan et al. 1996; Cantrell and Kaplan 1997). In this approach, colloidal size (1 to 3 micron diameter) zero-valent iron particles are injected as a suspension into the subsurface. As the suspension of particles moves through the aquifer material, the particles are filtered out on the surfaces of the aquifer matrix. As a result of the high density of the zero-valent iron particles (7.6 g/cm^3), it appears that the primary removal mechanism of zero-valent iron colloids in aqueous solution passing through sand columns is gravitational settling (Kaplan et al. 1996; Cantrell and Kaplan 1997).

Later work at the Laboratory using shear-thinning or pseudoplastic viscosity amendments media was shown to greatly improve the emplacement of the colloidal zero-valent iron suspensions in porous media (Cantrell et al. 1997a,b). In contrast to a Newtonian fluid, whose viscosity is independent of shear rate, certain non-Newtonian fluids are shear-thinning, a phenomena in which the viscosity of the fluid decreases with increasing shear rate (Chhabra 1993). By increasing the viscosity of the colloidal zero-valent iron suspension through the addition of a shear-thinning polymer, the rate of gravitational settling of the zero-valent iron particles will decrease, however, an increase in viscosity of the injection suspension will also have the adverse effect of decreasing the effective hydraulic conductivity of the porous media. The use of shear-thinning fluids in the formulation of a zero-valent iron colloid suspension will result in a high viscosity near the suspended zero-valent iron particles (due to low shear stress of the fluid near the particles) and a lower viscosity near the porous media surface, where the fluid is experiencing a high shear stress. These properties allow the development of a zero-valent iron colloid suspension solution which is viscous enough to keep the zero-valent iron particles in suspension for extended time periods, but will not cause an adverse decrease in hydraulic conductivity.

The results of this work have demonstrated that shear-thinning fluids greatly improves the emplacement profile of suspensions of micron-size zero-valent iron particles in porous media relative to suspensions without shear-thinning fluids. These fluids will also permit the use of much lower flow rates than would be possible without them. Lower flow rates are desirable because they will increase the distance from the well that the slurry can be effectively injected, decreasing the number of injection wells required to emplace the barrier, thereby decreasing the installation cost of the barrier. This will greatly increase the range of subsurface environments where this emplacement technology can be used.

Following the experiments conducted with pure quartz sand, further column injection experiments were conducted with natural Hanford sediments. Problems were encountered during the experiments using natural material. It was found that the shear-thinning polymer was adsorbing to the sediments and/or precipitating within the sediment creating large back pressures during the injection. The subject of this work is to identify and test a suitable polymeric shear-thinning material that does not interact significantly with aquifer materials and major ions in solution.

Results and Accomplishments

A literature search of commercially available shear-thinning polymers, resulted in the identification of several potential candidate materials that could be used for further testing. One particlularly promising compound (referred to here as AMX) was subjected to batch and column adsorption tests. The results indicated that this compound does not adsorb to the natural minerals in Hanford sediments to any significant extent. Essentially no adsorption in the batch experiments was observed. A slight loss of the compound may have occurred in the column adsorption experiment, but this was attributed to loss in dead-end pores as opposed to true chemical adsorption.

Viscosity measurements were conducted with various concentrations of the compound to determine the best concentration to make up slurries for injection of the micron-sized iron particles. We determined that an AMX

concentration of 0.5% AMX was the most effective. In Figure 1, results are shown for an injection experiment conducted in a 1.0-meter long column of Hanford sediment. This experiment was conducted by first pretreating the column with approximately two pore volumes of a solution containing only 0.5% AMX at a pH of 8.0. The injection slurry contained 0.5% AMX and 1.0% Fe^0 at pH 8.0. Three pore volumes of this slurry were injected at 7.2 cm/min. The results indicate a fairly even distribution of iron throughout the column, ranging from 0.5% Fe^0 at 10 cm to about Fe^0 0.3% at the effluent end of the column.

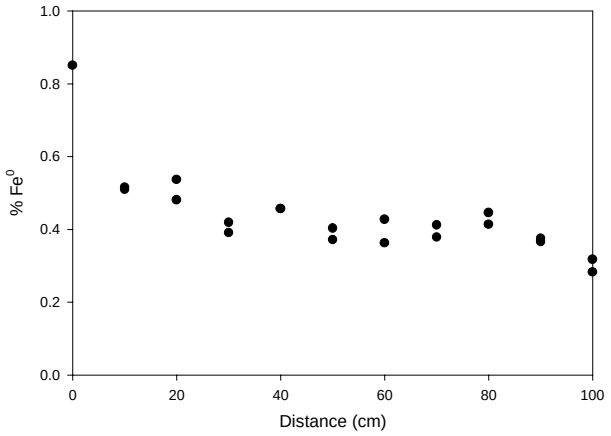

Figure 1. Distribution of Fe^0 in a 100-cm column of Hanford sediment resulting from injection of 3 pore volumes of slurry containing 1.0 % Fe^0, and 0.5 % AMX, using a flow rate of 7.2 cm/min, and a 2-pore volume pretreatment with 0.5 % AMX

The results for an experiment in which the pretreatment step was skipped are shown in Figure 2. In this case, the Fe^0 distribution is much less even, with lower concentrations observed in the first part of the column. Another experiment in which the injection rate was reduced to 1.6 cm/min is shown in Figure 3. In this case we can see that the iron concentrations were significantly higher than for the higher flow rate experiment illustrated in Figure 1. In addition, the Fe^0 concentrations were observed to drop off rapidly as a function of distance from the inlet.

To determine if the injection of Fe^0 into the columns caused any permanent reduction in permeability, a column injection experiment was conducted in an identical fashion to that of the experiment illustrated in Figure 1. However, in this case the inlet pressure was monitored prior to, during, and after the injection phase of the experiment. Prior to and after the pretreatment and Fe^0 slurry injection phase of the experiment, water was pumped through at a much slower flow rate. As can be

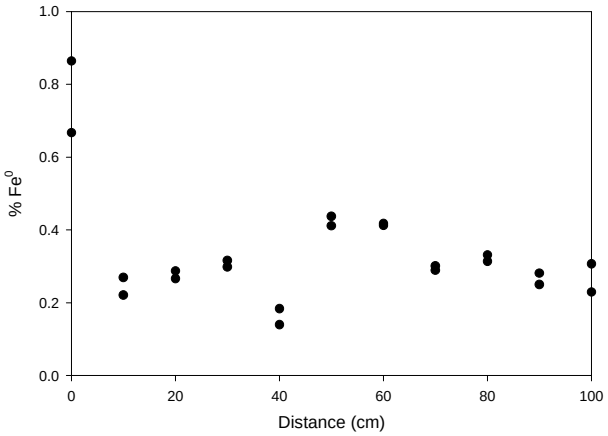

Figure 2. Distribution of Fe^0 in a 100-cm column of Hanford sediment resulting from injection of 3 pore volumes of slurry containing 1.0 % Fe^0, and 0.5 % AMX, using a flow rate of 7.4 cm/min, and no pretreatment with 0.5 % AMX

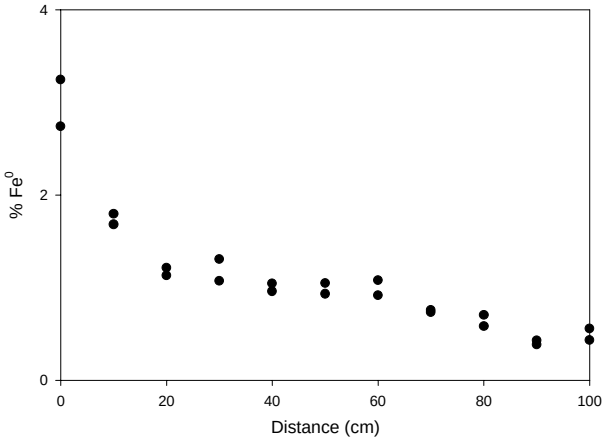

Figure 3. Distribution of Fe^0 in a 100-cm column of Hanford sediment resulting from injection of 3 pore volumes of slurry containing 1.0 % Fe^0, and 0.5 % AMX, using a flow rate of 1.6 cm/min, and a 2-pore volume pretreatment with 0.5 % AMX

seen from Figure 4, injection of water at 0.76 cm/min resulted in a very low back pressure at the column inlet (0.7 psig). As the 0.5% AMX pretreatment solution was injected into the column at a flow rate of 7.0 cm/min, the back pressure began to increase. During the slurry injection, the back pressure continues to increase. After the injection phase of the experiment, water at a flow rate of 0.85 cm/min was pumped through the column. When this was done, the back pressure decreased significantly from about 70 psig to 11 psig. This is a significant decrease in back pressure; however, it is significantly higher than the initial back pressure measured prior to the injection phase. After 3.4 pore volumes of water were pumped through the column, the back pressure returned to

0.9 psig, indicated the injection process does not cause a significant decrease in permeability to the system.

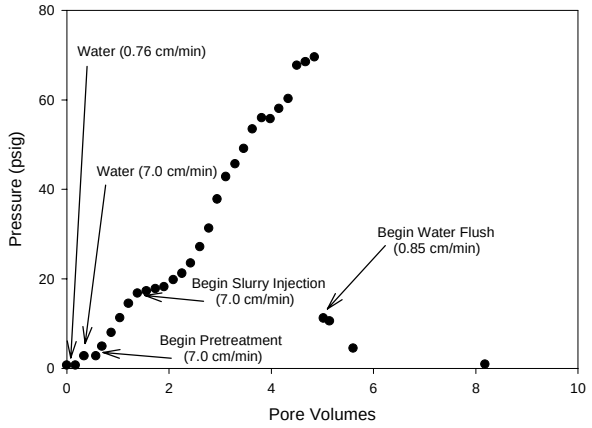

Figure 4. Inlet back pressure before, during, and after slurry injection

References

Cantrell KC and DI Kaplan. 1999. In-Situ Chemical Barrier and Method of Making. Patent Number 5,857,810.

Cantrell KJ and DI Kaplan. 1998. "Sorptive barriers for groundwater remediation." In *The Encyclopedia of Environmental Analysis and Remediation*. RA Meyers ed. John Wiley & Sons, Inc., New York.

Cantrell KJ, DI Kaplan and TJ Gilmore. 1997a. "Injection of colloidal Fe^0 particles in sand columns with shearthining fluids." *J. Environ. Eng.* 123:786-791.

Cantrell KJ, DI Kaplan and TJ Gilmore. 1997b. "Injection of colloidal size particles of Fe^0 in porous media with shearthining fluids as a method to emplace a permeable reactive zone." *Land Contamination & Reclamation* 5(3):253-257.

Cantrell KJ, and DI Kaplan. 1997. "Zero-valent iron colloid emplacement in sand columns." *J. Environ. Eng.* 123:499-505.

Cantrell KJ, DI Cantrell and TW Wietsma. 1995. "Zero-valent iron as a material for the remediation of selected metals from contaminated groundwater." *J. Haz. Mat.* 42:201-212.

Chhabra RP. 1993. Bubbles, drops and particles in non-newtonian fluids. CRC Press, Boca Raton, Florida.

EPA. 1999. *Field Application of In Situ Remediation Technologies: Permeable Reactive Barriers*, EPA 542-R-99-002, U.S. Environmental Protection Agency, Washington, D.C.

Fairweather V. 1996. "When toxics meet metal." *Civil Eng*, May, 44-48.

Gillham RW and SF O'Hannesin. 1994. "Enhanced degradation of halogenated aliphatics by zero-valent iron." *Ground Water*, 32, 958-967.

Gillham RW, DW Blowes, CJ Ptacek and SF O'Hannesin. 1994. "Use of zero-valent metals in in-situ remediation of contaminated ground water." *In In-situ remediation: Scientific Basis for Current and Future Technologies* (eds. GW Gee and NR Wing), pp. 913-930. Battelle Press, Columbus, Ohio.

Gould JP. 1982. "The kinetics of hexavalent chromium reduction by metallic iron." *Water Resour* 16, 871-877.

Hofstetter TB, CG Heijman, SB Haderlein, C Holliger, and RP Schwarzenbach. 1999. "Complete reduction of TNT and other (poly)nitroaromatic compounds under iron-reducing subsurface conditions." *Environ. Sci. Technol*. 33, 1479-1487.

Kaplan DI, KJ Cantrell, TW Wietsma, and MA Potter. 1996. "Formation of a chemical barrier with zero-valent iron colloids for groundwater remediation." *J. Environ Qual* 25, 1086-1094.

Kaplan DI, KJ Cantrell, and TW Wietsma. 1994. "Formation of a barrier to groundwater contaminants by the injection of zero-valent iron colloids: Suspension properties." *In In-situ remediation: Scientific basis for current and future technologies* (eds. GW Gee and NR Wing), pp. 820-838. Battelle Press, Columbus, Ohio.

Matheson LJ, and PG Tratnyek. 1994. "Reductive dehalgenation of chlorinated methanes by iron metal." *Environ Sci Technol* 28, 2045-2053.

Orth WC and RW Gillham. 1996. "Dechlorination of trichloroethene in aqueous solution using Fe0." *Environ Sci Technol*, 30, 66-71.

Puls RW, RM Powell, and CJ Paul. 1995. "In situ remediation of ground water contaminated with chromate and chlorinated solvents using zero-valent iron: A field study." Preprint of Extended Abstracts from the 209th ACS National Meeting, Anaheim, California 35, 788-791. Div of Environ Chem, Am. Chem Soc, Washington, D.C.

Roberts AL, LA Totten, WA Arnold, DR Burris, and TJ Campbell. 1996. "Reductive elimination of chlorinated ethylenes by zero-valent metals." *Environ. Sci Technol.* 30, 2654-2659.

Singh J, SD Comfort and PJ Shea. 1999. "Iron-mediated remediation of RDX-contaminated water and soil under controlled Eh/pH." *Environ. Sci. Technol.* 33, 1488-1494.

Tratnyek PG. 1996. "Putting corrosion to use: remediating contaminated groundwater with zero-valent metals." *Chem & Ind*, July 1, 499-503.

Wilson EK. 1995. "Zero-valent metals provide possible solution to groundwater problems." *Chem Eng News*, 73, 19-22.

Yamane CL, SD Warner, JD Gallinatti, FS Szerdy, TA Delfino, DA Hankins, and JL Vogan. 1995. "Installation of a subsurface groundwater treatment wall composed of granular zero-valent iron." Preprint of Extended Abstracts from the 209th ACS National Meeting, Anaheim, California, 35, 792-795. Div of Environ Chem, Am Chem Soc, Washington, D.C.

Vadose Zone and Pore-Scale Process Modeling

Mark D. White, Jim A. Fort, Matt Rosing

Study Control Number: PN99076/1404

Numerical simulation on massively parallel computers provides scientists and engineers with the analytical tools necessary to assess risks and devise effective remediation schemes for subsurface contamination. Computational tools are being developed on this project that allow researchers to accurately represent geologic and engineered subsurface features, while maintaining the efficiencies of parallel computing.

Project Description

The objective of this project is to develop computational capabilities for massively parallel computers for modeling multifluid flow and transport in the subsurface on physical domains that contain complex geologic features and engineered structures. Of particular interest are preferential pathways, such as clastic dikes in the deep vadose zone at the Hanford Site, which potentially provide conduits for fluid and contaminate migration to the groundwater. Conventional methods for modeling complex geometries in the subsurface involve computing on unstructured grids using finite-element discretization of the mathematical equations that describe multifluid flow and transport through geologic media. In an attempt to maintain scalability and parallel computing efficiency, this project is directed at solving subsurface flow and transport problems using multiple grid blocks, where each grid block (sub-grid) is a curvilinear orthogonal structured grid. The critical issues are to develop parallel computing schemes that balance the computational load and minimize communications across the processors on a massively parallel computer. We have implemented capabilities for computing on curvilinear coordinate systems into a suite of subsurface flow and transport simulators and developed FORTRAN preprocessor (Rosing 1999) directives and interpreters for multi-block grids of structured blocks. When applied to environmental restoration and stewardship, the resulting software will provide a stronger scientific rationale for management decisions concerning the vadose zone, particularly at the Hanford Site, where preferential pathways and subsurface structures are critical issues.

Introduction

The vadose zone is defined as the hydrologic region that extends from the soil surface to the water table. Preferential pathways within the vadose zone include natural geologic structures (clastic dikes), engineered structures (monitoring wells and boreholes), and unstable multifluid systems (high density brines migrating through freshwater aquifers). Heterogeneous subsurface environments of particular concern to this project include geologic discontinuities (faults and embedded structures) and engineered structures (underground storage tanks). Accurate representations of the geologic structure, stratigraphy, and buried engineered structures are critical to numerically modeling subsurface flow and transport behavior. Scientists and engineers interested in assessing risks and devising remediation strategies for contaminants migrating through the vadose zone toward the groundwater need high performance analytical tools with capabilities for modeling subsurface complexities.

Numerical models of subsurface flow and transport operate on tellesations of the physical domain, where hydrologic and thermodynamic properties are computed at discrete points (grid cells), as an approximation to the continuum of physical space. Analyses of contaminant migration through three-dimensional, field-scale domains requires the computational capacity of massively parallel computers. For example, to numerically model a cluster of six underground storage tanks, (typical of those on the Hanford Site, which are known to have leaked radioactive contaminants into the vadose zone) at 1-m resolution in three-dimensions, requires approximately 1 million grid cells. Depending on the assumptions taken to develop the conceptual model for the simulation, each grid cell can have between one and five unknowns which must be solved implicitly to resolve the system nonlinearities. Memory and execution-speed limitations make executing this scale of problem prohibitive on sequential computers. However, these types of problems have been successfully solved on a distributed-memory 512-processor IBM-SP parallel computer using 64 processors. Incorporating subsurface complexities into the computational domain by increasing the grid resolution within the region of the complexity (clastic dike, underground storage tank) can increase computational requirements beyond the range of

tetra-scale computing, envisioned as being in the near future for parallel computing. Multi-block grids comprising orthogonal sub-grids will allow incorporation of subsurface complexities into the computational domain without significantly increasing the total number of required grid cells.

Approach

This project has focused on implementing capabilities for orthogonal curvilinear coordinate grids and multi-block grids into a series of sequential and parallel multifluid subsurface flow and transport simulators. Curvilinear coordinate grid capabilities were implemented into the software using the conventional approach of transforming the governing differential equations that describe subsurface flow and transport, using grid metrics (i.e., geometric transformations between the physical domain and computational domain). For static grids the grid metrics are computed once, resulting in minimal additional computational effort. For dynamic grids, such as adaptive grids used to simulate the migration of dense brines from leaking storage tanks into the vadose zone, grid metrics are computed for each grid level. The parallel implementation of the subsurface flow and transport simulator uses a FORTRAN preprocessor, which interprets directives imbedded in the source coding, to convert the source coding from sequential Fortran to parallel FORTRAN with message passing protocols. Multi-block grids require different data structures and distributions than the conventional single-block structured grid. The principal focus for implementing multi-block capabilities in parallel has been in the development of directives and preprocessor translators to handle multi-block data forms.

Results and Accomplishments

The principal outcomes of the project have been the development of capabilities for solving multifluid subsurface flow and transport problems on curvilinear coordinates and the development of a FORTRAN preprocessor directive, data structure, and interpreter for multi-block grids. To demonstrate these computational capabilities, an experiment involving multifluid flow in a bedded porous media with a sloped interface is being simulated using a structured Cartesian grid, tilted Cartesian grid, and boundary-fitted orthogonal grid. Simulation results for the different grids will be compared against laboratory data, where the key issues are the behavior of a light-nonaqueous-phase-liquid near a sloped textural interface. The ability of the simulator to predict the observed behavior of the light-nonaqueous-phase-liquid migration strongly depends on the soil-moisture characteristic function and the geometric representation of the computational grid. For this study, a boundary-fitted curvilinear grid has a significant advantage over Cartesian and tilted Cartesian grids in that it accurately honors both the geometry of the sloped interface and the container boundaries.

Curvilinear coordinate system capabilities have been incorporated into eleven operational modes of the multifluid subsurface flow and transport simulators (sequential and parallel implementations): 1) water (aqueous system with passive gas), 2) water-air (aqueous-gas system), 3) water-salt (aqueous-brine system with passive gas), 4) water-salt-air (aqueous-brine-gas system), 5) water-air-energy (nonisothermal aqueous-gas system), 6) water-salt-air-energy (nonisothermal aqueous-brine-gas system), 7) water-oil (aqueous-nonaqueous liquid system with passive gas), 8) water-oil-air (aqueous-nonaqueous liquid-gas system), 9) water-oil-dissolved oil (aqueous-nonaqueous liquid system with passive gas and kinetic dissolution), 10) water-oil-surfactant (aqueous-nonaqueous liquid-surfactant system with passive gas), and 11) water-oil-alcohol (aqueous-nonaqueous liquid-ternary mixture with passive gas).

Writing long-lasting computer codes that distribute data and computations across an array of parallel processors is difficult in the advancing technology of computer hardware and system software. The concept chosen to develop enduring scientific software for this project was that of using a programmable parallel FORTRAN preprocessor, which translates sequential FORTRAN coding with embedded directives into parallel coding. The embedded parallel coding distributes arrays, supports task and data parallelism, implements parallel input/output and other processes required to use distributed memory, shared memory symmetric multiprocessor, and clustered parallel computer systems. This approach allows the code developer to focus on the science and applied mathematics of multifluid subsurface flow and transport without having to deal with the details and protocols of parallel processing. Implementing this approach for multi-block grids required the development of preprocessor directives and programming the preprocessor to interpret these directives. The preprocessor has been programmed to handle block structures using the derived types and structures capabilities of FORTRAN 90. Preprocessor routines were written to handle defining blocks, allocating variables, creating variables, and distributing blocks across the processors.

Summary and Conclusions

Boundary-fitted curvilinear grid capabilities were incorporated into a suite of multifluid subsurface flow and transport simulators (sequential and parallel implementations), being used to provide scientific rationale to the restoration and management of the vadose zone and groundwater at contaminated government sites (e.g., Hanford Site). Directives and coding were developed for a FORTRAN 90 programmable preprocessor for multi-block applications. We concluded that multi-block grids comprising structured curvilinear sub-grids are an effective approach for simulating complex geometries in the subsurface (such as geologic features and engineered structures), yielding accurate representations while maintaining the efficiencies of parallel computing.

Reference

Rosing M. 1999. A Programmable Preprocessor for Parallelizing Fortran-90. Peak Five, Fort Collins, Colorado.

Watershed Model and Land-Use Decision Support

Lance W. Vail, Mark S. Wigmosta, Duane Neitzel

Study Control Number: PN99079/1407

Innovative approaches are required to transcend the structural differences in physical and biological models, if such models are to be successfully linked to support natural resource management decision-making. Fuzzy computational methods were shown to be a valuable tool in linking physical and biological models.

Project Description

The purpose of this project was to support a science-based approach to natural resource management by assessing the effectiveness of fuzzy computational methods in linking advanced physical and biological models. We developed several prototype fuzzy tools that were able to incorporate "approximate reasoning" for representing processes and for developing categorical conclusions regarding the environment. We showed that fuzzy methods provide both an intuitive and technically defensible approach for linking physical and biological models.

Introduction

This study represents the second year of a 3-year effort to develop an integrated natural resource management framework. A significant obstacle to successfully linking physical and biological models was identified as the fundamental structural differences between such models. Physical models are more likely to involve a continuum representation, whereas biological models are more likely to rely on rules. Two significant issues, the pervasive vagueness of rules and the multivaluedness associated with temporal and spatial upscaling, suggested that fuzzy methods might be useful in overcoming some of the structural differences between physical and biological models.

Fuzzy methods allow computing based on linguistic variables (words) as opposed to numbers. Words are less precise but closer to intuition and accommodate the pervasive imprecision of biological process understanding. Fuzzy computational methods exploit the tolerance for imprecision, uncertainty, and partial truth to achieve tractability, robustness, and efficient solutions.

Fuzzy methods complement but do not reduce the need for probabilistic methods in either physical or biological process models. Whereas, randomness (probability) describes the uncertainty of an event occurring, fuzziness describes the degree to which an event occurs.

Approach

This project used a variety of fuzzy methods including: fuzzy arithmetic, fuzzy logic, fuzzy clustering, and adaptive neural fuzzy inference systems. Fuzzy arithmetic was employed using standard programming methods. The evaluations of fuzzy logic, fuzzy clustering, and inference systems employed a commercial software package. A series of rules and a database from the Multispecies Framework Process was employed to test the various fuzzy methods. These rules and data are used to define aquatic habitat diversity in the Pacific Northwest.

Results and Accomplishments

Fuzzy Arithmetic. To establish a clearer understanding of basic fuzzy computational methods, we developed a fuzzy rainfall runoff model. Fuzziness (expressed as a membership function) was defined for saturated soil hydraulic conductivity, effective soil porosity, soil depth, and rainfall intensity. Fuzzy characteristics of habitat capacity (river width and depth) were estimated using standard fuzzy methods as a function of time. The fuzzy results are reasonable based on comparison with other (non-fuzzy) methods, but convey the uncertainty associated with the fuzzy input parameters.

Fuzzy Logic. Fuzzy logic is an extension of multi-valued logic. It is based around the concept of fuzzy sets. Fuzzy sets relate to classes of objects with unsharp boundaries. Membership in a fuzzy set is a matter of degree. Fuzzy logic has been shown to be valuable for computing process interactions and is currently employed in many control applications (such as focusing camcorders, automatic transmissions) and decision support systems

(portfolio selection). We developed a tool called Fuzzy Hab. Fuzzy Hab is used to estimate habitat diversity from a set of categorical statements about the environment (embeddedness, icing, pool spacing, riparian function, and woody debris). Each of these categorical statements is vaguely defined. Estimates for each categorical statement are derived from physical process models. Fuzzy Hab supports a variety of canonical forms of membership functions and generates source code in C that can be transferred to any platform for integration into a natural resource modeling framework.

Fuzzy Clustering. The purpose of clustering is to identify groupings from a large data set to produce a concise representation of a system's behavior. Allowing membership in a group to be fuzzy (i.e., a matter of degree) results in a considerably more flexible and robust representation of the system. We reviewed recent literature where fuzzy clustering had been applied in natural resource management. We determined that fuzzy clustering characterizes data richness and complexity, easily adapts to new data, and is not particularly sensitive to type of membership function chosen.

Adaptive Neural Fuzzy Inference Systems. Adaptive inference systems provide a method to develop fuzzy rules from large but sparse environmental datasets. Data goes in and rules come out. In this project, fuzzy rules for making categorical conclusions of aquatic habitat diversity were derived from partially complete tables developed for the Pacific Northwest Multispecies Framework Process. Inference systems are able to generalize large datasets while developing rules that are less prone to reflect arbitrary and sometimes conflicting threshold effects.

Summary and Conclusions

Fuzzy computational methods are useful in overcoming the structural differences between physical and biological models. While initially fuzzy methods were expected to benefit mostly biological models through improved categorical representation of the physical environment, they are now expected to have significant benefit to physical process representation such as for geomorphological processes critical to habitat.

We conclude that fuzzy methods

- provide a compact and flexible process representation
- accommodates the pervasive imprecision of process understanding
- exploit the tolerance for imprecision, uncertainty, and partial truth to achieve tractability, robustness, and low-cost solutions
- exploit neural networks' ability to use large, sparse datasets in developing rules.

As this project continues during the next fiscal year, fuzzy methods will be incorporated into a web-based integrated natural resource management framework.

Energy Technology and Management

Conversion of Natural Gas/Methane to High Octane Liquid Fuel

Alex Mitroshkov, Khris B. Olsen, John C. Evans, Ed G. Baker, Don J. Stevens

Study Control Number: PN00024/1431

Alternate sources of liquid fuel will be needed for the United States to obtain energy independence or be cushioned from a potential impending oil crisis. We may have located a breakthrough process that converts natural gas/methane into a liquid fuel in a single-step process.

Project Description

The purpose of this project was to perform proof-of-concept testing of a unique process to convert natural gas, using methanol as a reaction initiator, to a high-octane liquid fuel. To assess this process, we conducted several different kinds of experiments with a variety of flow rates and volumes of catalyst. We collected products of synthesis and found that for one catalyst, which was available, conversion of methane was 1 to 25% depending on the condition of the experiments.

Introduction

For the past 80 years, petroleum has been the primary energy source for the U.S. transportation system. In addition, many consumer products are based on petrochemical-based plastics. Petroleum reserves are projected to decrease below world demands, resulting in significantly higher energy costs, and inevitably, a worsening energy crisis. For the U.S. to obtain energy independence and be cushioned from this impending energy crisis, alternate sources of energy will be needed. Natural gas, which is readily available with large amounts of future reserves, has been considered as an alternative either in liquefied form or as a feedstock for production of liquid fuels. However, because of the high methane content of natural gas, high pressures and low temperatures are needed to liquefy natural gas. This makes it an unlikely candidate for a convenient replacement for motoring fuel in the 21st century. Numerous attempts have been made to produce liquid fuel from natural gas, but the high methane content of natural gas complicates this conversion. Methane is difficult to reform into a liquid product. Presently, no energy-efficient, cost-effective commercial scale process is available to convert methane to a high-octane liquid fuel. We may have identified a breakthrough process that converts natural gas/methane into a liquid fuel in a single step. This technology has direct applications toward conversion of natural gas at orphan gas sites (such as the North Slope of Alaska and offshore drilling platforms) or landfills where methane is normally flared or simply released. In addition, another application associated with the agricultural use may be available. If animal waste can be converted via bio-mass conversion into methane and the methane converted to a liquid fuel product, a major source of non-point pollution to our rivers and streams would be eliminated.

Approach

Proof-of-concept tests were conducted using two methods:

1. Prepared mixtures of methanol/methane were passed through a heated glass tube containing the catalyst heated to 350° to 400°C (see Figure 1).

2. Methanol was injected via syringe pump onto the front surface of the catalyst. The flow rate of the methanol was regulated independently from the flow rate of methane or helium (see Figure 2).

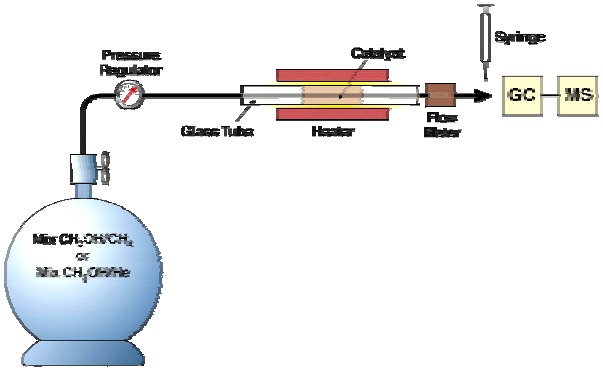

Figure 1. Setup for the first experiment

Results and Accomplishments

The yield of the hydrocarbons was slightly higher at 350°C than at 400°C. Synthesis of CH_3OH+CH_4 produced mixtures of hydrocarbons with total concentration of 3.0 to 3.8 µg/mL. Synthesis using only

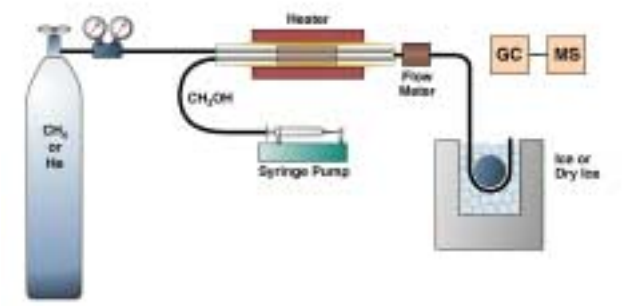

Figure 2. Setup for the second experiment

CH_3OH + He produced mixtures of hydrocarbons with total concentrations in the range of 2.5 to 2.8 µg/mL. A comparison of chromatograms for the two mixtures can be seen on Figure 3.

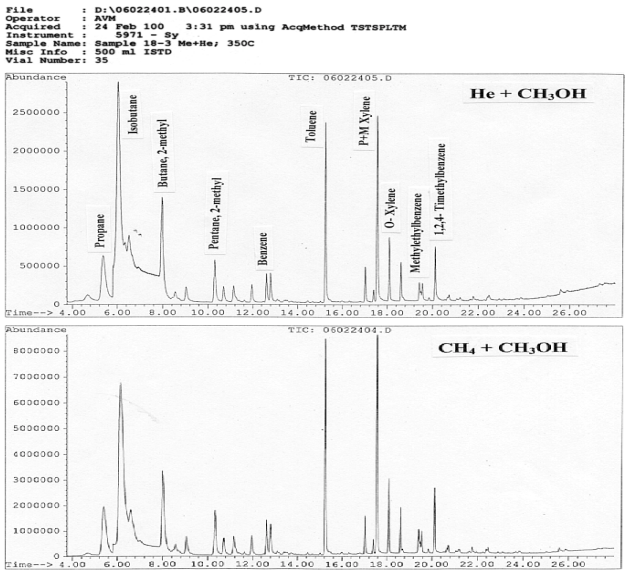

Figure 3. Comparison of chromatograms for two different prepared mixtures

The concentration of CH_3OH in both initial mixtures was 5.6 µg/mL. Therefore, if all methanol were converted to hydrocarbons, it should produce approximately 2.8 µg/mL, because only half of methanol molecules participated in synthesis of hydrocarbons. The conversion of methane in these experiments was estimated at only 1 to 2%.

The recovery of the water and hydrocarbons in the absence of methane was determined. The composition of products of synthesis differed from those of the first experiment, as seen in Figure 4.

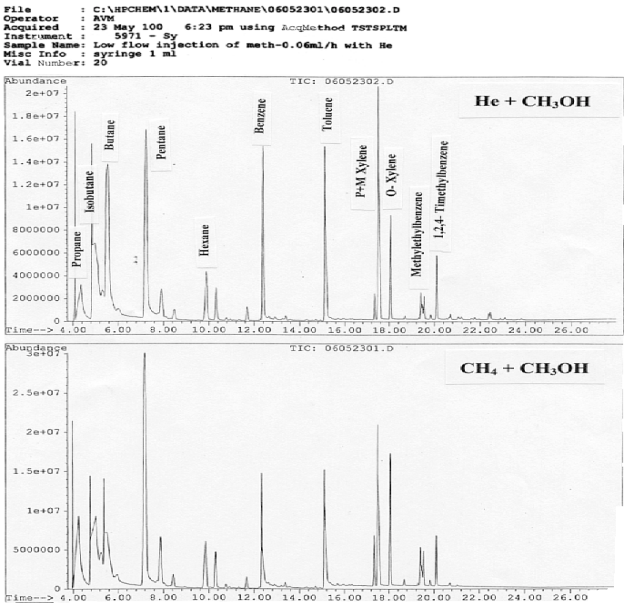

Figure 4. Comparison of chromatograms for He and methane with methanol injection

The conversion of methane to liquid product was much higher with this configuration, estimated at 20 to 25%.

Summary and Conclusion

The experiments performed demonstrated that conversion of methane into liquid fuel is feasible with this approach. However, the amount of methanol required to initiate reaction was very high. The efficiency of the conversion of natural gas (methane) was significantly lower than reported in similar work in the former Soviet Union (Polyakova et al. 1984). The difference may be attributable to differences between in the exact compositions of the catalyst used in this and the Soviet Polyakova work. Our experiments were limited to only one catalyst (obtained gratis from Mobil in proprietary form) since other variants were not available with the limited resources of this project. Although only partial success was achieved, the results are encouraging and further investigation may be warranted particularly in view of the extreme importance of the problem investigated.

Reference

Polyakova AA, GI Krilova, LO Kogan and GB Belan. 1984. Authors Certificate issued by State Committee of USSR for Invention and Discovery Affairs, 3795531/23-04.

Probabilistic Assessment of Power System Security

Chi-Hung Kelvin Chu

Study Control Number: PN00075/1482

Domestic utility systems are vulnerable to disruption from many types of threat including natural events and malicious action. Tools are needed to protect our nation's electric power generation and delivery systems. This project is developing new approaches to reduce the vulnerability of the electric power infrastructure to internal and external threats.

Project Description

The goal of this research was to integrate both power system adequacy and security evaluation into a single framework. The scope of work focused on the security aspect of the power system. Specific objectives included: 1) validate existing techniques for the fast detection of power system instability; 2) develop a reusable computer code to implement the selected technique, this segment of the project is used to screen, rank, and select system contingencies before conducting probabilistic system security assessment; and 3) develop a prototype digital computer program to implement and conduct probabilistic power system security evaluation.

This project will quantify the system stability performance by providing information such as the probability of instability, and other useful and available indices. Once the approach is successfully developed and implemented, the overall goal of integrating both power system adequacy and security evaluation under one single framework can then be achieved.

Introduction

Power system security evaluation involves the determination of the stability of a power system under different contingencies. The common system planning approach is the use of a deterministic criterion such as "N-1" criterion. The system is designed to withstand and continue to function within established guidelines for any single contingency such as the outage of a line or the loss of a generator. The use of the N-1 criterion reduces the amount of time necessary to evaluate and simulate the performance of the system. This criterion was adequate for the North American interconnected transmission system because of the significant amount of transmission reserve in the system. As the economy grows, energy consumption also increases. In addition, as the electric industry moves into a deregulating and competitive environment, more energy is transmitted across the national grid and at longer distances. The power system has become more susceptible to instability as the load grows and the transmission reserve diminishes.

The stability of a power system depends on a large number of factors and conditions at the time of the contingency. Factors such as the load level at the time of the contingency, location and the type of the contingency, the conditions of the network, and the components that are required to clear the problem at the time of contingency can all affect the stability of the system. The factors are stochastic in nature. The deterministic N-1 criterion does not take into account the probabilistic nature of these factors. These, together with the addition of new players into the energy market and the unpredictable energy transactions across the nation, all contribute more uncertainties to the planning and operation of the modern power system. The ability to incorporate these uncertainties into the planning and operating processess and the ability to quantify the various risks and their consequences are therefore greatly needed.

Approach

The proposed project is divided into three stages:

1. Validation of existing techniques. The traditional approach to determine system stability has been the use of step-by-step simulation using the system swing equation. Faster stability detection is often done using various energy functions. The traditional approach is computationally expensive and slow, and the use of energy functions requires the development of appropriate energy functions. Currently, the "Fast Second Kick" technique seems to be the most promising. The first phase is to select and validate the latest techniques for the determination and detection of power system stability. The selected technique will be used in the second phase.

2. Implementation of the selected techniques. The selected technique will be implemented in the second

phase. The algorithms will be tested using smaller test systems. The first step of Phase 2 is to prepare all the relevant information for the test system. The second step of Phase 2 is to develop computer codes for all the required support program modules and for the implementation of the selected detection technique.

3. Development of a prototype digital computer program to implement and conduct probabilistic power system security evaluation. The techniques will first be implemented on a personal computer platform. If the whole national grid is to be included, the program may need to be ported to a multiple-processor workstation. This is beyond the scope of this project. The selected screening technique will be used at the front end of this program to screen and rank various contingencies that do not contribute significantly to the instability of the system. The final program emcompassing the stochastic nature of various components will be developed in the second year.

Results and Accomplishments

Validation of ExistingTechniques

Phase I was successfully completed. We reviewed various techniques that can be used in the probabilistic power system security assessment. The Second Kick technique was deemed to be the best method for detecting instability of the system, because it eliminated a complicated procedure in using transient energy function and provides equally accurate results.

Implementation of the Selected Techniques

The second phase of the project is to obtain and prepare relevant test systems for comparison and testing. Relevant test data for the two test systems have been collected and developed and will later be prepared in a standard industry-acceptable format.

Summary and Conclusions

Fast stability detection techniques have been reviewed and the Second Kick technique was selected for use in this project. Second Kick eliminates a complicated procedure in using the traditional transient energy function and provides equally accurate results.

Bibliography

Mansour Y, E Vaahedi, et al. 1995. “B.C. Hydro’s On-Line Transient Stability Assessment (TSA): Model Development, Analysis, and Post-Processing,” *IEEE Trans. Power Systems*, v. 10, no. 1, pp. 241-253.

Human Health and Safety

^{212}Pb as a Tracer for Urban Aerosols

Paul Bredt, George Klinger, Larry Greenwood, John Smart

Study Control Number: PN00001/1408

Aerosol particles generated in urban areas influence human health, global warming, and regional haze. Methods involving naturally evolved lead-212 (^{212}Pb) and lead-214 (^{214}Pb) are being developed to track aerosol distribution as a function of time, location, and altitude. Distribution tracking is fundamental to understanding the life cycle of these particles.

Project Description

Aerosol samples were collected in the Portland, Oregon, area and were counted in real-time for ^{212}Pb and ^{214}Pb activity. The goal of this work was to examine the release of these naturally occurring radioisotopes across a major metropolitan area. Previous studies have used these isotopes as tracers to study the horizontal and vertical mixing of air masses (Gaggeler et al. 1995; Assof and Biscaye 1972). However, the source strengths for these isotopes, ^{212}Pb in particular, are poorly characterized (Sheets and Lawrence 1999). Both of these isotopes are released from soil and share radon in their decay chains. However, ^{212}Pb has a physical half-life ($t_{1/2}$) of 10.64 hours and is a daughter of ^{220}Rn with a $t_{1/2}$ =55.6 seconds, while ^{214}Pb has a $t_{1/2}$ =26.8 minutes and is a daughter of ^{222}Rn with a $t_{1/2}$ =3.8 days. Due to these half-lives, ^{212}Pb activity is dominated by local sources while ^{214}Pb activity, which generally has local sources, is dominated by regional and global sources. Data from the Portland sampling compared well with a simple one-dimensional model for the transport of marine air over a fixed ^{222}Rn/^{220}Rn source.

Approach

Aerosol samples were collected during three successive days in and around the Portland metropolitan area during the month of June 2000. The samples were collected by filtering air through a 3M Filtrete GS-100 filter media mounted on the front side of a high volume air sampler. Samples were collected at a nominal flow rate of 7.5 m^3/min over 20 minutes. After collection, the filters were pressed into a pellet and were counted on a gamma spectrometer located in a lead cave in the sampling van. To determine the filter collection efficiency, tests were run with two filters mounted on the air sampler, then both filters were counted individually. Approximately 80 to 85% of the ^{214}Pb and ^{212}Pb activity was found on the first filter. Similar efficiencies are expected for these isotopes given they are both associated with similar particle sizes (0.07 to 0.25 μm for ^{212}Pb, and 0.09 to 0.37 μm for ^{214}Pb) (Papastefanou and Bondietti 1987).

Different routes through Portland were followed on each of the sampling days. The routes started in an area of low to moderate population density, crossed near the urban center, then generally continuing across the city into a low density area opposite to the starting location. Samples were collected over a relatively short time window of approximately 5 hours to minimize effects of changing atmospheric boundary layer heights. Changes in the altitude of the boundary over the course of a day can significantly affect the effective mixing volume and therefore significantly affect the concentration of radon and radon daughters measured at ground level. The boundary layer is generally observed to drop at night and rise to higher altitudes by the middle of the afternoon. This results in higher concentrations at night relative to later in the day. This cyclic effect in has been referred to as the “universal radon wave” (Gargon et al. 1986).

Meteorological data including wind speed, wind direction, humidity, and barometric pressure were collected at each sampling site. In addition, hourly routine aviation weather reports from the National Weather Service were collected at five airports: Portland International, Astoria, Kelso, Troutdale, and Hillsboro. These airports were near and/or upwind of Portland during the collection period.

Results and Accomplishments

No correlations were found between ^{212}Pb/^{214}Pb activity and proximity to the urban center. This shows that the fluxes of ^{220}Rn and ^{222}Rn under the regional weather conditions during this work were dominated by local geologic sources and not by urban construction.

While the measured ^{212}Pb activity was constant over the three sampling days within the associated counting error, the activity of ^{214}Pb was dependent on wind velocities. Figure 1 shows the hourly wind speed and direction

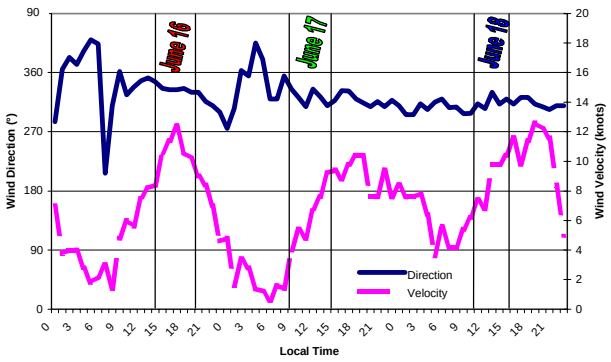

Figure 1. Measured activities of ^{212}Pb and ^{214}Pb versus transport time from the Pacific Coast

averaged every hour over the five METAR (National Weather Service) stations. The bracketed areas show the times samples were collected.

The winds during the collection period were blowing at an average angle of 330 degrees. At this angle, air coming into Portland was from the Pacific and traversed approximately 60 miles of land before entering the city. A transit time was calculated on a simple 1-hour average. For example, if the air speed was 5 knots over the first hour and 10 knots over the second hour, then the transit time for the first 15 nautical miles was 2 hours. Using this method, the time required to transit 60 nautical miles was calculated for each sample.

Figure 2 plots the measured ^{212}Pb and ^{214}Pb activities for each sample versus transit time for the associated air mass from the ocean to the sampling site. This plot shows the measured ^{212}Pb activity was independent of transit time (6 to 16 hours). The units in this figure are counts/m^3, not Bq/m^3. This correction will be made once detector efficiencies have been more rigorously calculated.

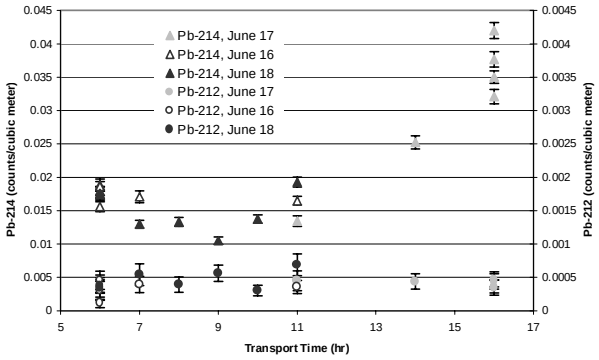

Figure 2. Average surface wind direction and velocity data

The measured ^{214}Pb activity shows an initial decrease followed by a steep rise. For comparison, a simple one-dimensional model was developed for both the ^{212}Pb and ^{214}Pb systems. Figure 3 plots the theoretical activity of ^{214}Pb as a function of several different land-based ^{222}Rn fluxes versus transit time. The ^{214}Pb model assumes that initially the ^{214}Pb is in equilibrium with the ^{222}Rn parent, therefore $[^{214}Pb]/[^{222}Rn]_o=1$. The model ignores the ^{218}Po intermediate due to its short half-life of 3 minutes. The following equation was used to calculate the theoretical activity of ^{214}Pb based on these assumptions

$$\left[{}^{214}Pb\right]=\left[{}^{214}Pb\right]_0 e^{-\lambda_2 t}+\left\{\lambda_1\left[{}^{222}Rn\right]_0\left(\frac{e^{-\lambda_2 t}-e^{-\lambda_1 t}}{\lambda_1-\lambda_2}\right)\right\}+\lambda_1 \frac{\left[{}^{222}Rn\right]_{flux}}{\left[{}^{222}Rn\right]_0}\left\{\frac{(\lambda_1-\lambda_2)+\lambda_2 e^{-\lambda_1 t}-\lambda_1 e^{-\lambda_2 t}}{\lambda_1\lambda_2(\lambda_1-\lambda_2)}\right\}$$

where t= transit time
λ_1=decay constant for ^{222}Rn
λ_2=decay constant for ^{214}Pb

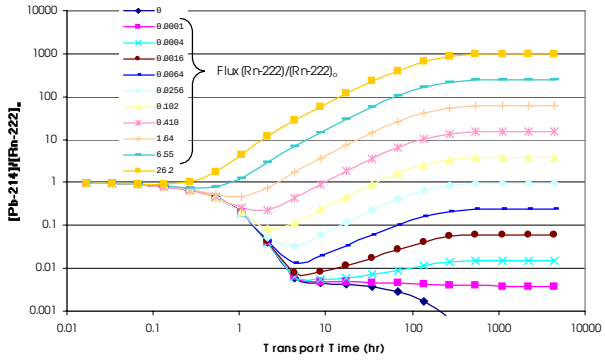

Figure 3. Theoretical concentration of ^{214}Pb versus transport time over land with several fixed ^{222}Rn source terms

similar model was developed for ^{212}Pb. The ^{212}Pb model assumes a final ^{212}Pb activity of 1 Bq/m^3 and ignores the ^{216}Po intermediate due to its short half-life of 0.15 seconds. Figure 4 plots the modeled ^{212}Pb activity as a function of several different geological flux rates over time.

From Figure 3, one sees that the model predicts the initial decrease observed in the measured ^{214}Pb activity. Based on the general shapes of the curves and the counting error associated with the ^{214}Pb measurement, this model is most sensitive for predictions between approximately 1 to 20 hours of transport time. The ^{222}Rn flux over the land

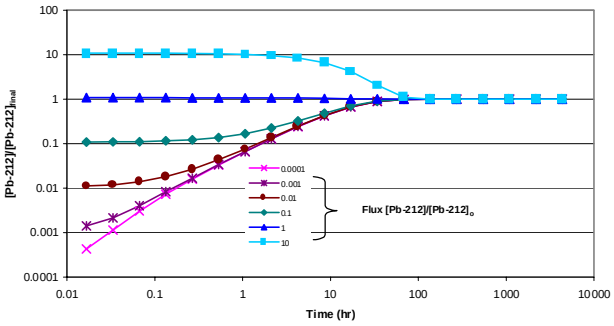

Figure 4. Theoretical concentration of ^{212}Pb versus transport time over land with several fixed ^{220}Rn source terms

should be greater than that over the ocean, therefore, flux ratios that result in a final $[^{214}Pb]/[^{222}Rn]_o$ ratio of less than one are not generally applicable unless they originate from a land mass with a significantly higher ^{222}Rn flux. Since this work did not examine air movement prior to the Pacific Coast, these curves have been included in the Figure 3. Once the data in Figure 2 has been corrected to Bq/m^3, this information along with vertical mixing can be used to calculate the average local ^{222}Rn flux rates. Conversely, if the local ^{222}Rn flux rates are known, then the measurements can be used to calculate mixing.

Assuming the initial $[^{212}Pb]/[^{212}Pb]_{final}<1$, the ^{212}Pb model in Figure 4 shows the greatest increase in ^{212}Pb activity occurs over the first 2 to 5 hours. After 5 hours, the predicted activities are not statistically different relative to our ~30% counting error. This resolution could be increased with longer sampling time and counting times, but this would be associated with a decrease in the total number of samples that could be collected and analyzed. Since the samples examined in this study had transport times between 6 to 16 hours, it is not surprising that an increasing ^{214}Pb trend was not observed. However, if samples were collected closer to the Pacific Coast, this technique would probably be effective in examining flux and missing rates on the order of 2 to 5 hours.

Summary and Conclusions

A system was successfully developed and deployed for real-time measurements of ^{212}Pb and ^{214}Pb with a potential resolution of 10 minutes. This resolution is suitable for detailed air modeling. The system can be easily adapted for aircraft studies and is based on an existing aircraft system called Real-Time Airborne Radiation Analysis and Collection. During the field study, ^{212}Pb and ^{214}Pb activities were relatively constant over the Portland urban area. Variability in the ^{214}Pb activity was well correlated with transport time from the Oregon coast and appears to be a good tracer for examining the mixing rates of marine air over land masses on the time scale of 1 to 20 hours. ^{212}Pb appears to be a good tracer for examining the mixing rates of marine air on the time scale of the first 2 to 5 hours.

References

Assaf G and PE Biscaye. 1972. *Science* 175 890.

Gaggeler HW, DT Jost, U Baltensperger, M Schwikowski, and P Seibert. 1995. *Atmospheric Env.*, 29 607.

Garzon L, JM Juanco, JM Perez, JM Fernandez, and B Arganza. 1986. *Health Phys*. 51 185.

Papastefanou C and EA Bondietti. 1987. *Health Phys*. 53 461.

Sheets RW and AE Lawrence. 1999. *J. of Radioanalytical and Nuc. Chem,* 242 761.

Publication and Presentation

This work will be presented at the 46th Annual Conference on Bioassay, Analytical, and Environmental Radiochemistry on November 14, 2000 in Seattle. A Report for submission to the Journal of Atmospheric Chemistry is being drafted.

Aerosol Control and Destruction

Chris Aardahl, Gary Josephson, Bill Heath

Study Control Number: PN00007/1414

Carbonaceous particulates are a major hurdle for increased use of diesel engines in U.S. vehicles. Dieselization is desired because of the enhanced gas mileage and engine life that can be obtained. However, exhaust emissions are notably higher for diesels. This project has shown that particulate emissions can be reduced significantly with a plasma discharge high-efficiency particulate air (HEPA) and that the cost of this method is within acceptable limits.

Project Description

An electrically based method was developed for separating and destroying organic particulate matter. The method was based upon impaction collection (filtering) enhanced with electrostatic forces and plasma degradation and regeneration. Plasma processing charges particulate matter, and image forces between collection media and the particulates result in attraction. Aerosols can be collected on much coarser filters than possible conventionally. Many of the particles (as organics) will undergo oxidation once trapped on the filter media, resulting in continual filter regeneration. Because filters are self-cleaning and made of coarser meshes, the pressure drop and loading rate are substantially reduced.

Novel reactor designs were employed to examine the collection and destruction of organic aerosols. Using instrumentation available through the Laboratory's Aerosol Wind Tunnel Research Facility, a particulate of known composition and concentration was used to examine the extent of collection and oxidation. A parametric study of reactor operational settings was performed to illucidate desirable operating conditions.

Introduction

The majority of fine particulate (PM2.5) is man-made. This particulate matter in air comes almost exclusively from combustion sources (power and transportation). Increasing concern is associated with particulate matter (PM2.5) because it is associated with lung diseases. During the last 10 years, research has shown that soot, originally considered carbon particles, can be covered with complex condensation products from combustion. Many of these compounds are potentially carcinogenic.

Aerosol control technologies have advanced significantly in recent years. Such progress will continue to take place because of new mandates from EPA regarding PM2.5 and potentially PM1.0 in coming years. Generally, particulate matter is controlled using fine, high-efficiency particulate air (HEPA) filters or electrostatic precipitators. Electrostatic precipators control particulate down to about 0.2 μm, and HEPA filters are used to remove smaller particles. Fine filters, however, have two major drawbacks: 1) to filter very small particles, the filter must be very tight, which causes high pressure drop, and 2) fine filters have low loading capacity that reduces life before higher pressure drop forces replacement.

As health concerns associated with fine particulate drive regulatory limits to finer particles, the standard approach to meet regulations with increasingly fine filters will not work. An approach involving nonthermal plasma treatment is a realistic solution, whereby the carbon core and the carcinogenic surface species are destroyed.

Approach

The initial phase of this program involved the assembly of an apparatus test stand for plasma oxidation of particulate matter. The setup is shown in Figure 1. The plasma reactor was filled with a relatively open bed of interwoven fiber optics (SiO_2). A loose fibrous packing allows for low pressure drop while maintaining electrically enhanced particle collection. As a charged particle moves close to a fiber, the fiber becomes polarized, resulting in an image charge. The image charge is opposite to that of the particle and attracts the particle to the surface where it becomes bound. It is these forces that allow for efficient particle collection with a low pressure drop architecture.

In order to probe the oxidation activity of the plasma reactor, graphite particles were passed through the device and collection and oxidation properties were measured. Graphite aerosol (1 μm) was generated using a fluidized bed generator. Particle size distributions were measured pre- and post-plasma using an Amherst Process Instruments Particle Sizer, and oxidation rates were obtained by measuring the carbon monoxide

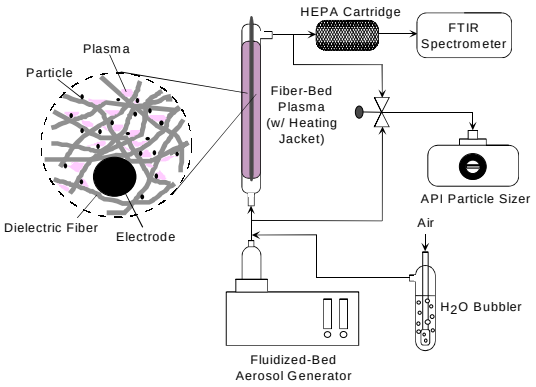

Figure 1. Test stand used for particulate collection/oxidation measurements

concentration at the outlet of the reactor with Fourier-transform infrared spectroscopy. Water could be added to the aerosol by introducing humid air, and the reactor could be heated up to 425 K using a heating jacket if desired.

Results and Accomplishments

Collection and oxidation of the graphite was measured as a function of temperature, humidity, and voltage applied to the plasma reactor. The collection results are shown in Figure 2. Here, data obtained from an unfilled reactor are compared to those from a fiber-filled reactor. In most cases the collection efficiency is above 70%, and the collection efficiency was above 90% at lower voltages. We observed that increased temperature resulted in about 5 to 10% reduction in collection and that increased humidity reduces collection at higher temperatures. We also observed that the collection efficiency dropped, particularly as the voltage was increased beyond 6 kV. We believe this is a function of the power supply used to drive the reactor.

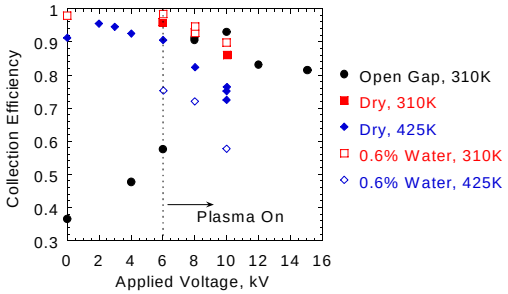

Figure 2. Collection efficiency as a function of voltage for a variety of conditions

The oxidation of carbonaceous particulate matter takes place via the following reactions:

$$C(s) + O\bullet \rightarrow CO$$
$$C(s) + O_3 \rightarrow CO + O_2$$
$$C(s) + \bullet O_2H \rightarrow CO + \bullet OH$$
$$C(s) + \bullet OH \rightarrow CO + H\bullet$$

In all cases, one atom of carbon is oxidized per atom of carbon monoxide evolved. Therefore, carbon monoxide production should be roughly equivalent to carbon oxidation. Figure 3 shows the measured levels of carbon monoxide as a function of energy consumed for a variety of stream conditions. At 310 K, the power consumption per oxidized carbon atom did not decrease if the fiber optic packing was added. This indicated that the silica fiber optics offered no catalytic enhancement to the oxidation. Other factors of interest included temperature and humidity. Results showed that temperature dramatically increased oxidation while the presence of water lowered the oxidation rate at a given temperature. At near room temperature (310 K), the plasma must overcome the entire heat of reaction to convert carbon to monoxide. At elevated temperature, the plasma must overcome only part of the heat of reaction, so the energy requirement is lower. When water is added to the gas mix, some of the water molecules will reside on the surface of the particulates and block oxidation sites, and this effect lowers the oxidation rate.

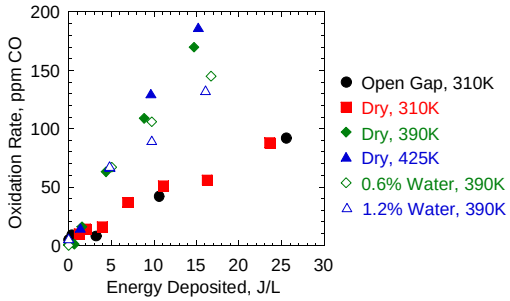

Figure 3. Oxidation rate as a function of energy deposited into the gas

Summary and Conclusions

We demonstrated that organic particulates can be collected and destroyed in alternating current-driven, nonthermal plasmas. Humidity and temperature have a slightly degratory effect on collection, but these effects are overwhelmed by particle losses at high voltages. We believe that this can be overcome by design of an appropriate power supply. Oxidation of particles was better at high temperature, but we observed that moisture inhibited oxidation. Crushed fiber optics (SiO_2) showed no catalytic activity for carbon oxidation.

Beyond Dose and Response: Relating Radiation and Detriment

Daniel J. Strom, Bruce A. Napier, Paul S. Stansbury, Sandra F. Snyder, Robert D. Stewart

Study Control Number: PN00013/1420

It is well known that the harmful effects of ionizing radiation cannot be predicted by dose alone. This project describes a comprehensive model relating radiation and detriment that includes not only dose, but also several other factors known to affect risk. The project developed software to compute radiation dose rates following intakes of radioactive materials and demonstrated that plutonium cleanup standards based on current simplistic models are too restrictive.

Project Description

The concept of "Beyond Dose and Response" with regard to radiation and detriment represents potentially a radical change in thinking from the traditional use of the linear nonthreshold dose-response model that currently forms the basis for radiation protection standards. We outlined a radiation-detriment model relating risk of stochastic health endpoints (cancer and heritable ill-health) to radiation exposure. Adoption by DOE of this fundamental paradigm shift would change the way environmental cleanup standards are set, and permit the full body of scientific knowledge to be brought to bear on radiation risk assessments and cleanup standards derived from such assessments.

We developed the capability to input radionuclide exposure to the GENII environmental pathway code to predict dose, dose rate, and its distribution in time (dose rate, dose fractionation, and dose timing) and then to predict detriment from these and other variables. Using this tool with human exposure data to radium, thorium, and plutonium, we demonstrated that cleanup standards are too restrictive by a factor of about ten.

Introduction

This project has

- enumerated what must be known for a comprehensive model relating radiation and detriment
- developed computational tools to permit calculation of needed input parameters to detriment modeling
- shown the impact of applying human threshold data directly to plutonium cleanup standards through this model, which become less restrictive when informed modeling is used.

Approach

The literature on parameters affecting radiation detriment (or expectation of harm; ICRP 1991) includes many factors in addition to dose. We developed a minimum parameter set needed to predict detriment. The project then focused on the computational tools needed to predict dose rate from alpha-emitters to all tissues and organs as a function of time, as well as to time-dependent tissue and organ activity content.

Results and Accomplishments

Elements of a Complete Radiation-Detriment Model

The ICRP's concept of detriment (ICRP 1991) is "expectation of harm," which is a comprehensive expression of risk. Currently, no single model predicts detriment and deterministic effects for populations and individuals, prospectively and retrospectively. The relationship of detriment to radiation is complicated, and a comprehensive model goes beyond new "Probability of Causation" software (National Cancer Institute, Bethesda, Maryland). The goal to this project is to outline a radiation-detriment model that incorporates all variables we know are important, that predicts all effects of interest, and that faithfully carries uncertainty throughout (especially when knowledge is absent). Such a model must include thresholds for bone and liver cancers, hormesis for some endpoints in some irradiation scenarios, adaptive response with its very complicated time dependence, sensitive or susceptible sub-populations, and use a probabilistic approach.

To develop a radiation-detriment model, one must first list all the organism-level outcomes of interest (various kinds of cancer, stochastic non-cancer somatic effects, heritable ill-health, deterministic effects), and for each outcome, one must then choose a risk measure (such as relative or absolute risk, severity, or frequency). For each outcome, one must list all variables known to affect it

(species, sub-species, and sex), space-and-time-course of irradiation, space-and-time-course of modifying factors, time-course of biological change, and damage. The species (human, animal, plant, cells in vitro), sub-species (racial makeup, ethnicity), genetic predisposition (DNA repair), susceptibility, and sex (e.g., in humans, thyroid cancer risk is proportional to the number of X-chromosomes, and breast cancer risk is proportional to [the number of X-chromosomes][10]) all affect radiation risk. The stage of development as a function of age (embryo, fetus, infant, child, adult, elderly adult), reproductive status, and hormonal status must be accounted for. The space-and-time-course of irradiation, the instantaneous spatial distributions of ionizations and excitations throughout existence of organism, the dose, the dose rate, the fractionation, the "quality" or (linear energy transfer, or lineal energy) all must be known as a function of time (age) and as a function of tissue or body part. The space-and-time-course of modifying factors include diet, temperature, infectious agents, combined injury (trauma, burns), the state of organ function, the state of adaptive response (DNA repair stimulation), the presence or absence of other initiators, promoters, tumor progressors (smoking), oxygen, dehydration, exogenous chemicals (antioxidants, free radical scavengers), drugs, and medical interventions such as surgery, and all must be know as a function of time (age) and location in an organism.

The dependent variable for such a radiation-detriment model is the time-course of biologic change and damage. The model must predict biomarkers, initiated cells, tumors, dermatitis, cataracts, etc., as a function of time (age) and location in organism. The same factors must be considered when calibrating the model from existing data.

Given this very ambitions project, what is knowable? What radiation measurements would be sufficiently predictive? For external irradiation, tissue-equivalent proportional counters to record lineal energy spectra as a function of time for the entire body for the entire life are externally used to infer that which is occurring inside the body. For internal irradiation, it is difficult to imagine precise enough measurements of emissions from radionuclides in the body to compare with external measurements, so one must model the dose-related quantities.

If thresholds exist, then only the irradiation that occurs above a certain dose rate matters (as shown below). Dose, especially committed dose, alone does not predict risk in this case. One must model the entire time course of irradiation in each tissue, and such models do not follow strictly linear dose-response relationships.

Enhancement of GENII Code

The GENII computer code for calculating 50-year committed effective dose equivalent (Napier et al. 1988a-c) has been modified to calculate instantaneous dose rates to each organ and tissue, as well as radioactivity contents as a function of time. This capability permits the examination of thresholds in dose rate as suggested by generalizing the Ames and Gold (1990) "mitogenesis increases mutagenesis" assertion (Figure 1).

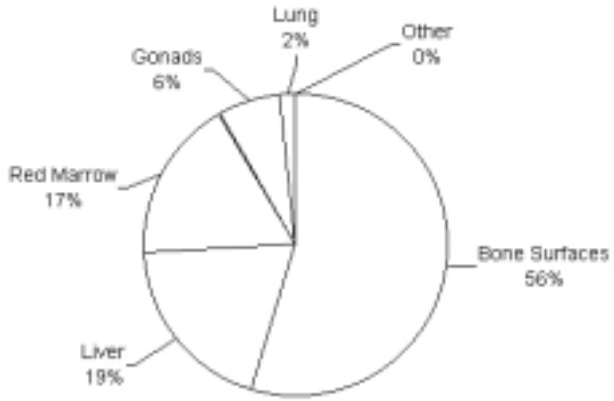

Figure 1. Fraction of 50-year committed effective dose equivalent due to Pu content of various organs and tissues calculated by enhanced GENII code. With threshold responses for osteosarcoma and liver cancer, only 25% of dose leads to any risk at low doses.

Thresholds

An unexpected discovery was that many simplistic and incorrect inferences of dose thresholds result from plotting incidence or mortality data on a logarithmic dose scale (Strom 2000). A number of representative examples are listed below.

Human Radium Exposure and Bone Cancer

Analysis of human data for exposure to radium (Rowland 1994) using new methods (Chomentowski et al. 1990) unequivocally indicates an alpha radiation dose threshold for osteosarcoma at about 8 Gy (Figure 2).

Human Thorium Exposure and Liver Cancer

The Advisory Committee on Radiological Protection (ACRP 1996) stated that there "appears to be a practical threshold of about 2 Gy to liver tissue for induction of liver cancer" by Thorotrast (p. E-9) based on epidemiology of Danish patients as reported in 1992 (Andersson and Storm 1992). Thorotrast-exposed patients are the fourth largest human population

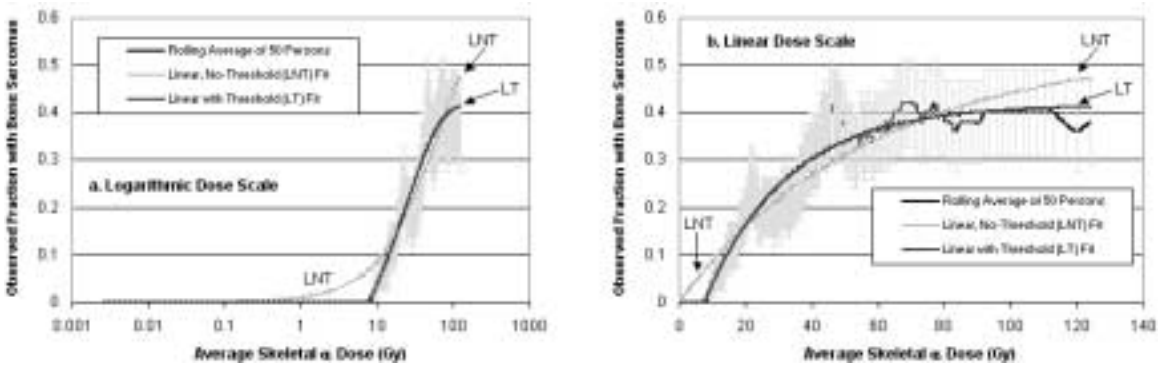

Figure 2. Argonne human radium data for bone cancer, rolling 50-person average, showing observed fractions of bone sarcomas plotted on both a. logarithmic and b. linear dose scales. Dose threshold is about 8 Gy as inferred from nonlinear least-squares fitting.

significantly exposed to an alpha-emitting heavy metal (Stannard 1988) and have been studied internationally. Research was conducted by others to verify the Advisory Committee statement using the latest available data from Danish (Andersson and Storm 1992; Andersson et al. 1994; Advisory Committee on Radiological Protection 1996), German (van Kaick et al. 1984; van Kaick et al. 1999), Japanese (Kido et al. 1999; Mori et al. 1999a; Mori et al. 1999b), Portuguese (dos Santos-Silva et al. 1999), and Swedish (Martling et al. 1999) studies. We conclude that the apparent threshold may be an artifact of the assumed 15-year latency period for Thorotrast-initiated liver cancer, and that the significant, possibly causal, dose accumulates over a latency period (even for minimal Thorotrast administrations). However, even at the lowest dosages of Thorotrast administered, the radiation dose to liver was great, admitting the possibility of a threshold.

Another trend we noticed in the Thorotrast data was that the latency period between the time of injection and death by liver cancer increased with decreasing amount injected. In the Danish studies (Andersson et al. 1994), the Kaplan-Meier curves are shifted to the right about 6 years between the high and medium dosage groups, and are shifted again about 6 years between the medium and low dosage groups. This trend implies that the dose rate is inversely related to the latency. Since the latency for liver cancer from Thorotrast is already significant (48 years to reach 50% cumulative frequency in this study), it is very possible that a dose rate exists at which the latency is so long that there is no risk of dying of liver cancer. There was inadequate data, at present, for us to estimate this "effective threshold" for Thorotrast dose rate.

Human Plutonium Exposure Related to Bone and Liver Cancer

Two papers (Gilbert et al. 2000, Koshurnikova et al. 2000) shed light directly on the human bone and liver cancer associated with very high exposures to plutonium. These authors analyzed dosimetry and medical records for 11,000 workers who began working at Mayak in 1948 to 1958, among whom were 23 cases that had bone cancer and 60 cases that had liver cancer at death. Of the 5,500 who were monitored for plutonium in urine (beginning in 1970), 10 had bone cancer and 36 had liver cancer. Stratifying by age and sex and accounting for external dose on a linear basis, the authors computed relative risk for the two upper ranges of body burdens compared with the lowest range (Figure 3). For both bone cancer and liver cancer the relative risk for cancer in the intermediate body burden range (1.48 to 7.4 kBq) was not statistically different from the lowest group. It was only in the highest group (of 251 individuals) that an increased relative risk can be seen. The authors did not give skeletal dose values for all cases, but sufficient information was available to infer that individuals in the middle group had skeletal doses on the order of 1 to 7 Gy. Thus, these data suggest a threshold for osteosarcoma above 7 Gy of alpha dose to the skeleton.

Impact on Cleanup Standards

If there are thresholds for bone and liver cancer in humans from relatively high doses of alpha irradiation, as our investigation shows, then DOE's cleanup standards and occupational dose limits for plutonium are too restrictive

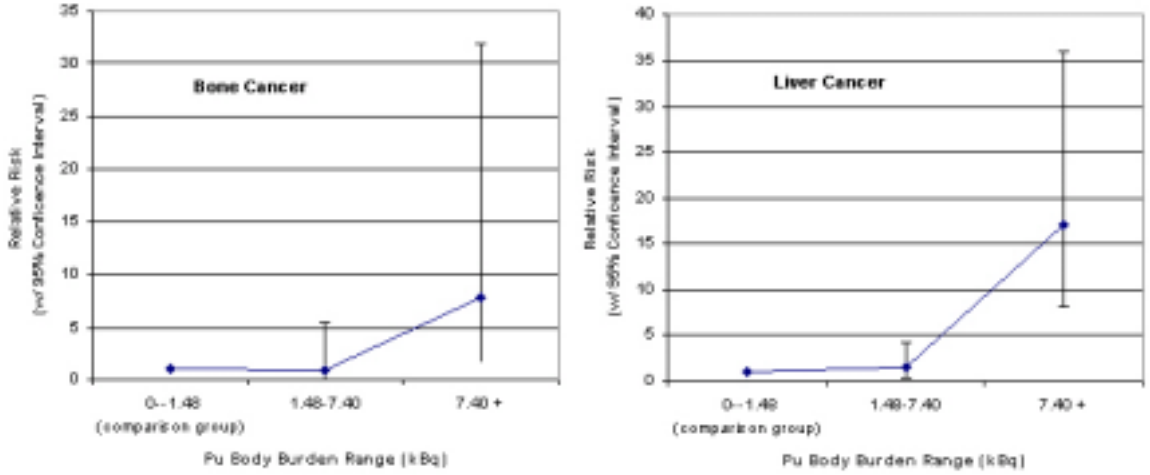

Figure 3. Relative risk of bone and liver cancer among a cohort of 5,500 Mayak workers as a function of plutonium body burden

by a factor of four. If it can be shown that cancer incidences for some of the other organs have a threshold, then it is possible that current standards are too restrictive by a factor of ten.

Summary and Conclusions

The notion of a "dose-response" relationship is simplistic. Knowing dose alone is not enough to predict detriment. Radiation measurements sufficient to predict detriment would be a challenge. For external sources, measurements can be imagined, but for internal sources, inference from models is necessary. Risks to populations may be inferred from studies of populations only to a very limited extent. Risks to individuals may be inferred only by exhaustive study of variables that we already understand. Our examination of human data for bone cancer and liver cancer from alpha-emitters shows the strong possibility of thresholds for liver cancer, and an almost certain threshold for bone cancer. Applying these thresholds to the case of plutonium shows that DOE's current cleanup standards are too restrictive by a factor of at least four.

The DOE could benefit if a comprehensive radiation-detriment model were to be developed and applied to DOE cleanup of legacy materials. Worker safety and peace of mind would represent other direct benefits.

References

Advisory Committee on Radiological Protection. 1996. *Biological effects of low doses of radiation at low dose rate.* ACRP-18. Ottawa, Canada: Atomic Energy Control Board of Canada.

Ames BN and LS Gold. 1990. "Too many rodent carcinogens: mitogenesis increases mutagenesis." [published erratum appears in Science 1990 Sep 28;249(4976):1487] [see comments] *Science* 249(4972):970-971.

Andersson M and HH Storm. 1992. "Cancer incidence among Danish Thorotrast patients." *Journal of the National Cancer Institute* 84(17):1318-1325.

Andersson M, M Vyberg, J Visfeldt, B Carstensen, and HH Storm. 1994. "Primary liver tumors among Danish patients exposed to Thorotrast." *Radiat. Res*. 137:262-273.

Chomentowski M, AM Kellerer, and DA Pierce. 2000. "Radiation dose dependences in the atomic bomb survivor cancer mortality data: a model-free visualization." *Radiat. Res.* 153(3):289-294.

dos Santos-Silva I, M Jones, F Malveiro, and A Swerdlow. 1999. "Mortality in the Portuguese thorotrast study." *Radiat. Res*. 152(6 Suppl):S88-S92.

Gilbert ES, NA Koshurnikova, M Sokolnikov, VF Khokhryakov, S Miller, DL Preston, SA Romanov, NS Shilnikova, KG Suslova, and VV Vostrotin. 2000. "Liver cancers in Mayak workers." *Radiat. Res*. 246-252.

International Commission on Radiological Protection (ICRP). 1990. *Recommendations of the International Commission on Radiological Protection.* ICRP Publication No. 60. Annals of the ICRP 21(1-3); 1991.

Kido C, F Sasaki, Y Hirota, K Kiyosawa, S Hayashi, T Mori, and T Sobue. 1999. "Cancer mortality of Thorotrast patients in Japan: the second series updated 1998." *Radiat. Res.* 152(6 Suppl):S81-S83.

Koshurnikova NA, ES Gilbert, M Sokolnikov, VF Khokhryakov, S Miller, DL Preston, SA Romanov, NS Shilnikova, KG Suslova, and VV Vostrotin. 2000. "Bone Cancers in Mayak Workers." *Radiat. Res*. 237-245.

Martling U, A Mattsson, LB Travis, L-E Holm, and P Hall. 1999. "Mortality after long-term exposure to radioactive Thorotrast: A forty-year follow-up survey in Sweden." *Radiat. Res.* 151:293-299.

Mori T, K Fukutomi, Y Kato, S Hatakeyama, R Machinami, H Tanooka, Y Ishikawa, and T Kumatori. 1996. "Results of the first series of follow-up studies on Japanese thorotrast patients and their relationships to an autopsy series." *Radiat. Res.* 152(6 Suppl):S72-S80.

Mori T, C Kido, K Fukutomi, Y Kato, S Hatakeyama, R Machinami, Y Ishikawa, T Kumatori, F Sasaki, Y Hirota, K Kiyosawa, S Hayashi, H Tanooka, and T Sobue. "Summary of entire Japanese Thorotrast follow-up study: updated 1998." *Radiat. Res.* 152(6 Suppl):S84-S87.

Napier BA, RA Peloquin, DL Strenge, and JV Ramsdell. 1988a-c. *GENII - The Hanford Environmental Radiation Dosimetry Software System. Volume 1: Conceptual Representation.* PNL-6584 Vol. 1. *Volume 2: Users' Manual.* PNL-6584 Vol. 2. *Volume 3: Code Maintenance Manual. PNL-6584 Vol. 3.* Pacific Northwest Laboratory, Richland, Washington.

Rowland RE. 1994. *Radium in Humans. A Review of U.S. Studies.* ANL/ER-3. National Technical Information Service, Springfield, Virginia.

Stannard JN. 1988. *Radioactivity and Health, A History, Volume 1: Laboratory Research.* U.S. Department of Energy, Richland, Washington.

van Kaick G, A Dalheimer, S Hornik, A Kaul, D Liebermann, H Luhrs, A Spiethoff, K Wegener, and H Wesch. 1999. "The German Thorotrast study: recent results and assessment of risks." *Radiat. Res.* 152 (6 Suppl):S64-S71.

van Kaick G, H Muth, and A Kaul. 1984. *The German Thorotrast Study.* Commission of the European Communities, FR of Germany.

Publications and Presentations

Strom DJ. "Beyond Dose and Response: What We Really Need to Know to Relate Radiation and Detriment." 1999. PNNL-SA-31526. Presented as 2-hour Professional Enrichment Program PEP 3-I, 1999 Health Physics Society Annual Meeting. Input from this course has helped focus and define the overall model.

Strom DJ. "A Logarithmic Dose Axis Produces an Apparent Threshold in a Linear Non-Threshold Dose Response Relationship." *Health Physics* (submitted).

Strom DJ. 2000. "Bridging Radiation Policy and Science." Health Physics Society Newsletter XXVIII(2):14-15. Dr. Strom was one of 75 invited international attendees at the "Bridging Radiation Policy and Science" conference December 1-5, 1999, partly sponsored by this project. Three other reports appear in that issue (on pages 3, 16, 29), and the final report of the meeting, to which Dr. Strom contributed substantially, appears at http://www1.misinc.net/burkinc/.

Strom DJ. 2000. "Beyond Dose and Response: Relating Radiation and Detriment. Abstract." *Health Phys.* 78(6 Supp.):S127. Presented at the Health Physics Society Annual Meeting, (June 24-29, 2000), Denver, Colorado.

Strom DJ. 2000. "Bridging Radiation Policy and Science." Health Physics Society Newsletter XXVIII(2):14-15.

Strom DJ. 2000. "Is a Linear Extrapolation of Cancer Risks to Very Low Doses Justified?" Invited Paper, Radiation Research Society, 3 May 2000, Albuquerque, New Mexico, Pacific Northwest National Laboratory; Richland, Washington.

Development of a Preliminary Physiologically Based Pharmacokinetic (PBPK) Model of Beryllium in the Rat and the Initial Acquisition of Pharmacokinetic Data

Charles Timchalk, James E. Morris, Lucie K. Fritz

Study Control Number: PN00029/1436

Beryllium exposure represents a significant occupational health concern that is of particular relevance to the Department of Energy based on the extensive use of beryllium within nuclear facilities. Beryllium is responsible for human disease, in particular chronic beryllium disease which results from a hypersensitivity (immune) response to beryllium in which an antigen-specific immune response plays a critical role in the pathogenesis of the disease.

Project Description

Initial research efforts on this project focused on development of a dosimetry model (PBPK) for beryllium (and other toxic materials) in rats and mice. This preliminary model forms the foundation for a modeling and research strategy for linking dosimetry and pharmacodynamic models capable of quantifying biological response. Our objectives were to develop an experimental strategy for obtaining data for a pharmacodynamic model capable of quantifying biological response. We conducted studies to investigate the early cellular dynamic responses associated with the immune hypersensitivity to beryllium that lead to a pulmonary granulomatous reaction.

Approach

In response to beryllium exposure, CD4+ lymphocytes (helper cells) are stimulated to divide, and in turn alveolar macrophages are activated (as are other immune cells which infiltrate lung tissue) and eventually result in the formation of granulomas. The experimental design is illustrated in Figure 1. Male C3H/HeJ mice were administered 2 mg $BeSO_4$/kg (soluble) or 14 mg beryllium oxide/kg (insoluble) as a single intratracheal adminstration directly into the lungs. Groups of mice (about 10 per treatment) where then humanely sacrificed at 2, 4, or 8 weeks post-treatment. The lungs were lavaged (0.9% saline) to isolate immune cells and cytokines in the bronchial alveolar lavage fluid. Immediately following the sacrifice, the lavage was performed and peripheral blood samples were obtained by cardiac puncture. The immune cells were then isolated, cultured for 24 hours in the presence of BeSO4, phytohaemaglutinin or culture medium only, and imaged by flow cytometry (Figure 2). In addition, peripheral blood was analyzed by differential cell counting.

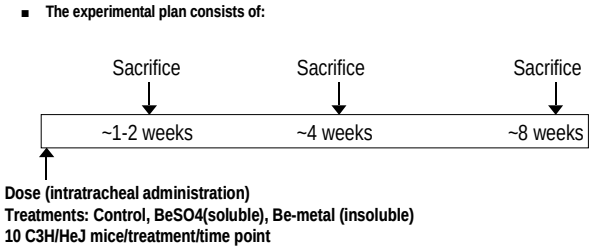

Figure 1. Experimental design

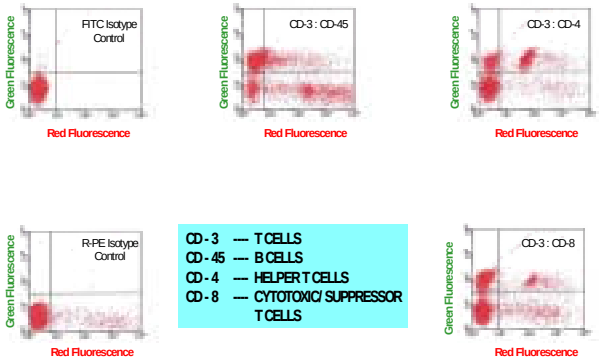

Figure 2. Distribution of lymphocytes and subtypes in peripheral blood of naïve mice

Results and Accomplishments

Initial work focused on identifying the distribution of lymphocytes and lymphocyte subtypes in nontreated mice. The lymphocyte subtype antibodies were titered against mouse peripheral blood lymphocytes, and 1 $\mu g/10^6$ cells was determined as optimal for flow imaging. The distribution of lymphocytes and subtypes in the peripheral blood is presented in Figure 3. These initial studies were conducted to establish the normal distribution of lymphocyte subtype populations in the C3H/HeJ mouse.

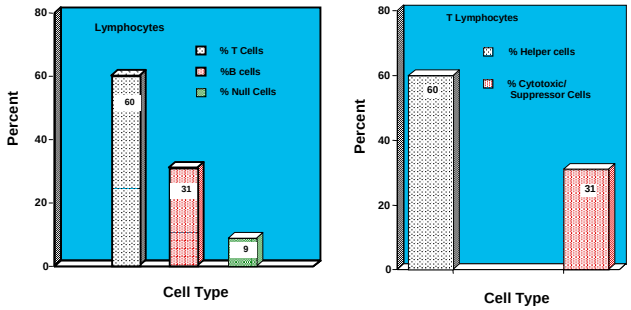

Figure 3. Example of flow cytometric analysis of peripheral blood cells obtained from naïve mice

Following $BeSO_4$ or beryllium-oxide treatments, no differences in the distribution of lymphocytes, neutrophils, or eosinophils in the peripheral blood of mice were observed, based on the differential blood counts (data not shown). However, analysis of immune cells isolated from the lavage fluid did suggest a temporal shift in cell populations following beryllium treatments (Figure 4). The percent of total cells expressing MAC-1 binding (alveolar macrophages) was about 20% at 2 weeks, decreased to about 5% at 4 weeks, but by 8 weeks post-dosing ranged from 40 to 50% of the total cells. Overall the MAC-1 response was similar for both the $BeSO_4$ and beryllium-oxide treatments, although beryllium-oxide was slightly higher by 8 weeks. A similar temporal profile was seen for CD-69 binding cells that represented activated T-cells, B-cells, natural killer cells, and alveolar macrophages. These CD-69 binding cells ranged from 5 to 20% of total cells from 2 to 4 weeks but were elevated from 40 to 60% by 8 weeks post-treatment. In contrast, the CD-4 binding cells (T-cells) did not show a similar profile of increasing with time post-treatment. Although the pathological status of the lungs were not evaluated in this project, the elevation in MAC-1 and CD-69 binding cells at 8 weeks post-dosing may represent early cellular responses associated with the inflammation process leading toward granuloma formation.

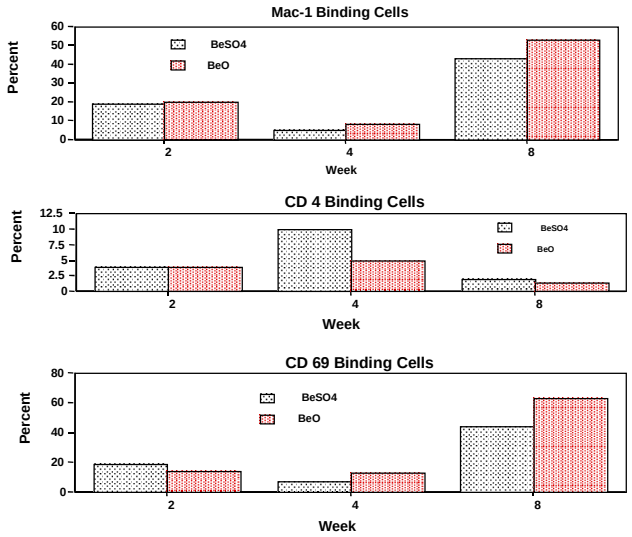

Figure 4. Flow cytometric analysis of BALF cellular distribution obtained from mice treated with $BeSO_4$ and beryllium-oxide and analyzed at 2, 4, and 8 weeks post-treatment

Summary and Conclusions

This project investigated the early cellular dynamic responses associated with the immune hypersensitivity to beryllium that lead to a pulmonary granulomatous reaction. The project established an in vivo mouse model that may be used to evaluate early responses to beryllium exposure. In addition, the project established the utility of flow cytometry for assessing changes in peripheral blood and broncial alveolar cell response to beryllium. Finally, the results of these experiments suggest that by about 8 weeks post-exposure, there is an elevation in MAC-1 alveolar macrophages and in CD-69 activated T-cells, B-cells, natural killer cells and alveolar macrophages in response to beryllium exposure. This represents a potential early indicator or biomarker of inflammatory response to beryllium exposure.

Development of a Virtual Respiratory System Model for Quantitation of Dosimetry, Clearance and Biological Response to Particulate Matter in the Mammalian Lung

Richard A. Corley, Charles Timchalk, Harold E. Trease, Joseph S. Oliveira, Kevin R. Minard, Donald N. Rommereim, Scott H. Elder

Study Control Number: PN00030/1437

Airborne particulate matter has been linked with a variety of adverse human health effects. Those most affected include the elderly, the young, smokers, and those with preexisting respiratory diseases such as asthma or chronic obstructive pulmonary disease. Several sources of airborne particulate matter are of concern, including the incomplete combustion of fossil fuels, and activities associated with the cleanup, demolition, and decommissioning of DOE sites. The development of accurate models of the dosimetry and clearance of particles from the respiratory tract will significantly improve our understanding of the health consequences associated with inhaled particulate matter.

Project Description

One of the research priorities recently identified by the National Academy of Sciences for improving our understanding of the potential human health impacts of airborne particulate matter is the need for improved mathematical models for predicting the regional dosimetry and clearance of inhaled particulate matter in the lungs (NRC 1998).

In this project, three-dimensional, biologically based models of normal and compromised respiratory tracts of laboratory animals and humans are being developed and experimentally validated. These models will provide a quantitative framework for integrating research from controlled animal studies with potential human variability and environmental exposure scenarios to facilitate more informed decisions regarding the potential for human health risks associated with airborne particulate matter.

A three-dimensional grid structure for the human lung was developed. This grid structure represents the first biologically based model to include equations of visco-elasticity to simulate the expansion and constriction of the lungs during respiration. The three-dimensional model was linked to a computational fluid dynamics model for inhalation, exhalation, and particle movement to complete the initial virtual lung model. The virtual lung model is linked to three-dimensional models of the upper respiratory tract in collaboration with Dr. J. S. Kimbell of the Chemical Industry Institute of Toxicology. Current, state-of-the-art particle deposition models were obtained to benchmark simulations of the regional deposition of particles predicted by the virtual respiratory tract model.

To experimentally validate the virtual respiratory tract model, several nuclear magnetic resonance imaging methods were developed. The NMR successfully quantitated particles phagocytized by pulmonary macrophages to determine the kinetics of a key component in the clearance of particles from the lung. NMR methods were also refined to improve the imaging of the pulmonary region in mice in an effort to quantitate the deposition of particles. If successful, the NMR may be used to determine the fate of inhaled particles in living animals over time and thus revolutionize experimental approaches for validation of the virtual respiratory tract model. Localized responses of the respiratory tract to inhaled particles are also known to influence the deposition and clearance of subsequently inhaled particles through a cascade of cell signaling pathways. The activation of several pathways was shown in this project to be responsive to various particles.

Introduction

Experimental research in particulate matter toxicity is based upon a variety of in vivo and in vitro animal and human model systems. Without validated models of lung dosimetry and biological response, however, controlled studies with particulate matter toxicity have only limited utility in predicting human responses. To adequately define the dose to the specific targets within the respiratory tract, particulate matter deposition models must have sufficient species-specific anatomic and physiologic detail to deliver the material to the appropriate sites within the respiratory tract. In addition, these models must include mechanisms of clearance and

other particulate defense systems to describe the overall fate of matter and further refine the definition of dose to the target cells.

Current, state-of-the-art dosimetry models, such as the ICRP lung model (ICRP 1994) and the multiple path particle deposition model (Anjilvel and Asgharian 1995; Asgharian and Anjilvel 1998), are either empirical, do not incorporate various clearance mechanisms, or are not amenable to inclusion of altered lung function in potentially sensitive human populations. These models are, therefore, limited in their ability to extrapolate beyond the experimental conditions from which the models were based. The only modeling approaches that can function reliably under a variety of exposure scenarios are those that are developed with a strong biological basis for the model structure. The goal for this project is to develop and experimentally validate a three-dimensional, biologically based model of the respiratory tract (virtual respiratory tract) capable of quantitating dosimetry, clearance, and biological response in both normal and compromised mammalian systems following exposure to complex particulate matter. To accomplish this goal, advancements were necessary in constructing three-dimensional grid structures of the respiratory tract and the development of new tools for imaging the structure of the lung and to quantitate particles in specific regions of the respiratory tract.

Approach

The project involved three, integrated thrust areas: 1) virtual lung model development and simulation, 2) NMR imaging of particulate matter and lung morphometrics, and 3) in vivo/in vitro model parameterization and validation studies.

Results and Accomplishments

Virtual Lung Model Development

An initial mathematical model was developed to establish the computational requirements for the three-dimensional models and to provide a backbone for overlaying a three-dimensional grid structure. Due to the high computational requirements, the NW Phys/NW Grid software was modified to operate on the massively parrallel computer in EMSL. A three-dimensional grid structure of the human lung (Figure 1), detailed to the level of the terminal bronchiolar region (about 2^{16} generations of airways), was developed using available data. The alveolar region was structured using a simple

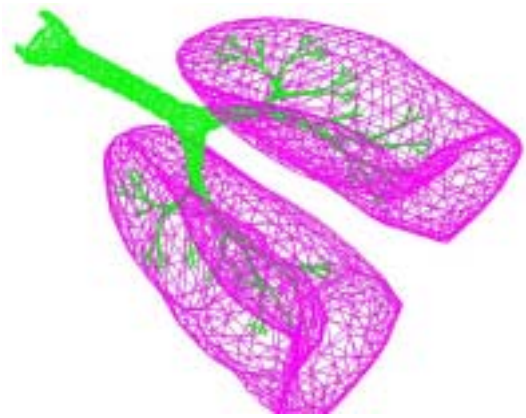

Figure 1. A three-dimensional grid structure for the human trachea and lung using NWGrid generation code

grid geometry to approximate the shapes of pulmonary acini. This model was subsequently modified to include visco-elasticity for expansion and contraction of airways and linked with a computational fluid model for airflows associated with inhalation and exhalation (Figure 2) and particle movement within the airways. The lung model was encased in a three-dimensional chest cavity with a diaphragm and chest expansion to drive inhalation and exhalation in the lungs (Figure 3). A particle deposition model (Anjilvel and Asgharian 1995) was obtained to compare simulations of the regional dosimetry (upper respiratory tract, bronchiolar and alveolar regions) in rats and humans with those predicted by the virtual lung model. Grid structures and original morphometric data for the upper respiratory tract were also obtained from Dr. Julie Kimbell (Chemical Industry Institute of Toxicology), a collaborator on the project to complete the description of the entire respiratory tract.

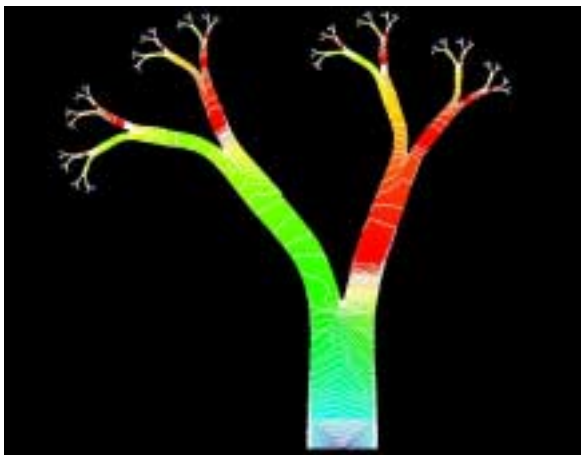

Figure 2. Contour plot of airflows determined by a computational fluid dynamics model through the terminal bronchiole region of the human lung using NWPhys code

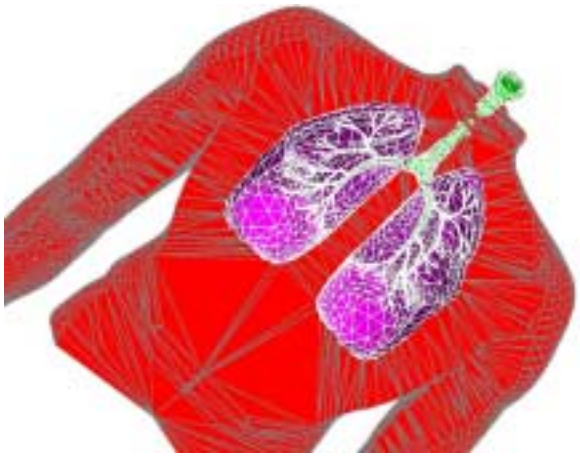

Figure 3. Use of the chest cavity and diaphragm to drive the expansion/contraction of the grid structure for the human lungs to simulate respiration

NMR Imaging Particle Deposition/Clearance and Lung Morphometry

To image particulate matter in the lungs by NMR, particles must have paramagnetic properties that alter the relaxation properties of surrounding water (T_1 relaxation time) in biological tissues. Therefore, initial efforts focused on assessing the properties of various particles and developing the imaging methods required for performing measurements of particle concentration. The paramagnetic properties of fusinite (carbon black) coupled with the extensive toxicity and dosimetry database and similarity to diesel exhaust made this particle an ideal candidate for further evaluation. Initial dose-response measurements for the uptake of carbon black by pulmonary macrophages indicated that this technique is useful for determining rate constants associated with this particle clearance mechanism.

A 2-tesla magnet, console, and high-resolution imaging software were configured to image mouse lungs. To quantify the concentration of particles in the lung, methods were developed for mapping the T_1 relaxation time for water throughout lung tissue (Figure 4). The results suggest that maps of particle concentration (T_1) with submillimeter resolution could be derived from magnetic resonance image data.

In Vivo/In Vitro Model Parameterization and Validation Studies

Preexisting disease conditions can dramatically alter the function of the lung and thus the dosimetry of inhaled particulate matter. Pulmonary macrophages may be activated by certain particulates and release reactive

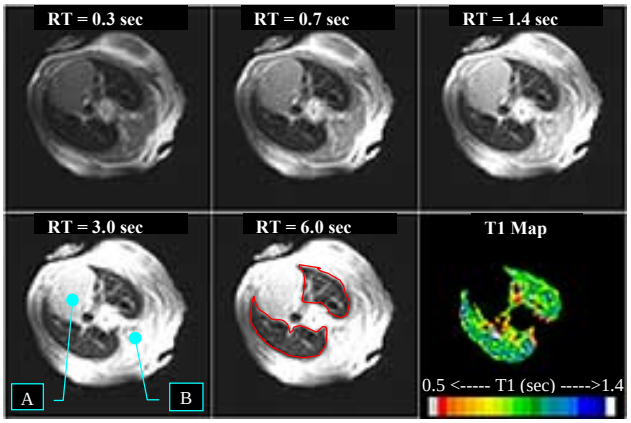

Figure 4. A spatial map of the T_1 relaxation time for water in lung tissue is created by first collecting a series of T_1-weighted magnetic resonance images. In the example shown above, five T_1-weighted magnetic resonance images of a mouse are shown. Each was acquired using a saturation-recovery sequence run with a different recovery time. All images show the same 2.0-millimeter-thick slice in which the heart (A), spinal column (B), and lung parenchyma (outlined in red) are clearly visible. By post-processing the raw image data, a synthetic T_1-map of the lung parenchyma is created where contrast only depends on the measured T_1 in each pixel of the image data. In the example shown, planar resolution is 0.5 x 0.5 squared millimeters and raw image data required 40 minutes to collect.

oxygen species, cytokines, or growth factors which may lead to further tissue damage and affect lung function. Various inhibitors of these pathways were used in preliminary studies to determine which cell signaling or inflammatory pathways were activated by particulates to evaluate their roles in tissue response.

Summary and Conclusions

An initial, three-dimensional lung model was developed that will serve as the basis for simulating the deposition of particles in the lung in the second year of the project. The three-dimensional grid structure and computational fluid dynamics model for the respiratory tract represents a significant improvement over existing models for defining detailed, regional-specific dosimetry of inhaled particles over a broad range of potential exposure scenarios. The model will ultimately have the flexibility to simulate the effects of preexisting disease conditions on particulate dosimetry. Preliminary studies with NMR imaging also demonstrated that this technique may be useful in developing the necessary data for further refinement of three-dimensional grid structures of the respiratory tract as well as particle quantitation. As further refinements are made to the imaging techniques, NMR may revolutionize experimental techniques for determining the deposition and clearance of inhaled particulate matter.

References

Anjilvel S, and B Asgharian. 1995. "A multi-path model of particle deposition in the rat lung." *Fund. Appl. Toxicol,* 28:41-50.

Asgharian B, and S Anjilvel. 1998. "A multi-path model of fiber deposition in the rat lung." *Tox. Sci.* 44:80–86.

ICRP. 1994. *Human respiratory tract model for radiological protection.* A report of a Task Group of the International Commission on Radiation Protection. ICRP Publication 66. *Ann. Of the ICRP* 24, Nos. 1-3.

National Research Council. 1998. *Research priorities for airborne particulate matter. I. Immediate priorities and a long range research portfolio.* National Academy Press, Washington, D.C.

Presentation

Timchalk C, RA Corley, HE Trease, K Minard, SH Elder, JS Oliveira, and DA Dixon. June 2000. "Development of a three-dimensional virtual respiratory tract model for studying the health implications of airborne particulate matter." Human Biology Models for Environmental Health. A Virtual Body Workshop sponsored by NIEHS/PNNL. RTP, North Carolina.

Examination of the Use of Diazoluminomelanin as a Component of a Three-Dimensional Imaging System for Localization of Ionizations Due to Boron Absorption of Neutrons

John A. Leonowich, Matthew H. Smith

Study Control Number: PN00042/1449

Diazoluminomelanin is a unique biopolymer that has found use in the field of radio frequency radiation dosimetry. Investigation of diazoluminomelanin's response to ionizing radiation will provide information on a material that could be used to perform dosimetry on more than one physical agent and that could contribute to improved ionizing radiation dosimetry for medical treatment and occupational safety.

Project Description

The purpose of this project was to determine whether diazoluminomelanin would respond to ionizing radiation, particularly neutrons. The response of diazoluminomelanin to radio frequency radiation has already been investigated and is the subject of continuing research by the Air Force Research Laboratory. Obtaining an output signal from diazoluminomelanin can be difficult due to self absorption of light emission. Evaluation of solids containing diazoluminomelanin did not yield an output signal significantly above background. However, measurement methods using diazoluminomelanin in liquid form are presently being evaluated for response to ionzing radiation. These methods are similar to processes currently used to perform radio frequency radiation measurements. Once a response to ionzing radiation is established, diazoluminomelanin will be incorporated into human phantoms for use in determining radiation dose for medical applications and verifying the performance of phantoms used to calibrate in vivo counting systems.

Introduction

Diazoluminomelanin is a unique biopolymer, because it exhibits the properties of luminescence, fluorescence, and slow fluorescence with a broad optical absorption spectrum. When it is properly activated, diazoluminomelanin can absorb and store electromagnetic radiation energy, and on subsequent activation, diazoluminomelanin can release that energy via rapid luminescence followed by slow fluorescence. Its ionic state can be manipulated after its synthesis, resulting in different extents of oxidation and reduction. Considerable work has been done on exploring the response of diazoluminomelanin to radio frequency radiation.

The work on this project is focused on investigating the response of diazoluminomelanin to ionizing radiation. While diazoluminomelanin has primarily been used in liquid form for radio frequency dosimetry, efforts were made on this project to use diazoluminomelanin in a solid form. One problem encountered using this method is the self-absorption of light emitted by diazoluminomelanin during fluorescence. Once this problem is overcome, the energy- and dose-dependent properties of diazoluminomelanin will be investigated. The long-term goal is to demonstrate the use of diazoluminomelanin in human phantoms using three-dimensional imaging equipment to capture light emission. This application will benefit ionizing radiation dosimetry for medical treatment and occupational safety.

Results and Accomplishments

Diazoluminomelanin in a solid form was investigated using three different preparations. First, undiluted diazoluminomelanin was allowed to dry on filter paper media. Second, diazoluminomelanin was diluted with sodium hydroxide prior to drying on the filter paper. Third, diazoluminomelanin was incorporated into a solid foam material.

After exposure to ionizing radiation, a readout of delayed-fluorescence was attempted by stimulating the samples with ultraviolet light (365 nm) and observing for fluorescence at 486 nm. A fluorescence signal above background was difficult to discern. This was most likely due to self-absorption of the light signal in the diazoluminomelanin. This phenomena has been noted during the radio frequency dosimetry studies of diazoluminomelanin. Further dilution of the diazoluminomelanin is proposed as a way to overcome this problem.

Summary and Conclusions

While observing the fluorescent signal from diazoluminomelanin exposed to ionzing radiation has proved problematic, it is believed that the signal can be viewed by diluting the diazoluminomelanin to overcome the self-absorption of light. Also, diazoluminomelanin is likely to perform well in a liquid form as it has in investigations for radio frequency dosimetry.

Indoor Air Pathways to Nuclear, Chemical, and Biological Agent Health Impact Modeling and Assessment System

Robert D. Stenner, Donald L. Hadley, Peter R. Armstrong, John W. Buck, Bonnie L. Hoopes, Michael C. Janus

Study Control Number: PN00055/1462

This project addresses the problem of detection, dispersion, and response associated with a terrorist attack on a major public or agency building, where nuclear, chemical, or biological agents are released. Thus, it relates directly to DOE-NN's safeguards and security responsibilities, as well as those of the other agencies with which DOE must interact to ensure adequate preparedness and response to these national terrorist threats.

Project Description

Indoor air quality effects on human health are of increasing concern to public health agencies and building owners. The prevention and treatment of "sick building" syndrome and the spread of airborne diseases in hospitals, for example, are well known priorities. However, increasing attention is being directed to the vulnerability of our public and agency buildings and places, public security, and national defense facilities to terrorist attack or the accidental release of airborne biological pathogens, harmful chemicals, or radioactive contaminants. This project reflects an effort to establish systems and capabilities at Pacific Northwest National Laboratory to address these concerns. The overall goal of this project is to develop a user-friendly, fully functional prototype indoor air nuclear, biological, and chemical agent health assessment system, which will operate under the FRAMES system for ease of use and to maximize the integration of the system with other modeling capabilities (ambient air fate and transport models, waterborne fate and transport models, and physiologically based pharmacokinetic models). The prototype system will serve both as a demonstration prototype and a basic modeling and assessment system that can be modified and tailored to meet client-specific building assessment needs.

Introduction

In a report to Congress, the Department of Defense states that, within the last 5 years, at least 11 states as well as other nations have experienced terrorist incidents (such as the World Trade Center bombing, the chemical attack on the Tokyo Subway, the Oklahoma City bombing, and the bombing in Centennial Park during the Olympics). With the increasing availability of raw materials and technology from worldwide sources, the potential use of weapons of mass destruction (which includes nuclear, chemical, and biological agents) by subversive groups has mounted dramatically (DoD 1997).

In their 1996 workshop, the National Governors' Association stated that they did not have adequate resources or training in the arena of chemical and biological terrorism. The Association also indicated the need for more resources to be made available to combat chemical or biological attacks and for federal assistance in the areas of monitoring and detection, technical assistance, manpower, and recovery efforts (DoD 1997). In their September 1996 meeting, the Federal Emergency Management Agency identified the need for subject matter experts that can provide advice and reference materials delineating the hazards, effects, and recommended protective response actions, for their response to chemical or biological agent attacks (DoD 1997). One of the significant needs identified by these various groups and by Congress (under Title XIV) is the need for adequate tools and training for the first responders.

In responding to a building under a chemical or biological agent attack by terrorists, two important questions need immediate answers: "what has been released," and "where has it spread?" The answers to these two questions tend to form the basis for determining the remaining actions of the first responders. Being prepared to answer these and the host of questions that follow them is essential for adequate management of the threat situation (reducing the threat through knowledge and planning). Thus, it is important to know ahead of time, if at all possible, the key vulnerability points of a building for such an attack and how the various forms of the different agents would be dispersed from each of these points. It is also important to understand the health effects associated with the potential agents that might be released under such an attack. The health effect

information coupled with the agent characterization and dispersion information provides the first responder with the necessary information to determine the critical areas for evacuation and immediate medical assistance response actions. "What if" scenarios also can be developed along these lines as part of the preparedness and training activities, so the first responders can be prepared for immediate action.

The critical information for estimating the dispersion of an agent throughout a building is primarily building-specific, which can be easily determined and developed as part of the up-front preparedness activities for a specific building. The health assessment system will serve as a key tool to understand the effects and dispersion of potential agents to help prepare potentially targeted buildings for such attacks.

Results and Accomplishments

The components and overall design of the health assessment system is shown graphically in Figure 1. The following research activities were completed:

- incorporation and setup of the CONTAM model for use in the prototype health assessment system
- incorporation of field data from a building dispersion study conducted on the Churchville Building located on the Aberdeen Proving Grounds to orient and calibrate the CONTAM model (Figure 2 shows the Churchville test facility with typical modeling versus measurement results for the Churchville Building)
- development of a Chemical Agent Health Effect Database (CAHED), focused around the test chemical agent sarin
- population of the CAHED with sarin health-effect data (incorporating only unclassified data, so the database can be used in the generic prototype to demonstrate capability to potential sponsors of all classification status)
- development of a Biological Agent Health Effect Database (BAHED), focused around the test biological agent anthrax
- population of the database with anthrax health-effect data (incorporating only unclassified data, so the database can be used in the generic prototype to demonstrate capability to potential sponsors of all classification status)
- integration of the CONTAM, CAHED, and BAHED into the FRAMES system (Figure 3 shows the layout of the system in FRAMES)
- development of global input and output routines so the models and databases can pass information back and forth within FRAMES
- development of a calculation routine to convert CONTAM output concentration data to dose and relate the calculated dose results to specific health effect data in CAHED and BAHED
- development of an output format for the building-specific concentration-dose-health effect results from the components of the nuclear, biological, and chemical health assessment system that can be easily used by first responders, hospital emergency staff, emergency coordinators and planners, and emergency preparedness staff (Figure 4 shows the FRAMES output format).

Summary and Conclusions

The individual system components have been developed and incorporated into an attractive and user-friendly prototype health assessment system that operates within the FRAMES package. The recent focus was on developing scientifically sound components for the system. Next year, the focus will be on critically examining the components, drawing from outside review and perspective where possible, and setting up an attractive prototype for use in active application of the system and its capabilities.

Reference

DoD. 1997. Department of Defense Report to Congress - Domestic Preparedness Program in the Defense Against Weapons of Mass Destruction. http://www.defenselink.mil/pubs/domestic/index.html. U.S. Department of Defense, Washington, D.C.

Bibliography

U.S. Army Handbook. 1996. *Handbook on the Medical Aspects of NBC Defensive Operations (Part II - Biological and Part III - Chemical.* ARMY FIELD MANUAL 8-9 (FM 8-9), NAVMED P-5059, AFJMAN 44-151V1V2V3, U.S. Department of the Army - Office of the Surgeon General, Washington, D.C.

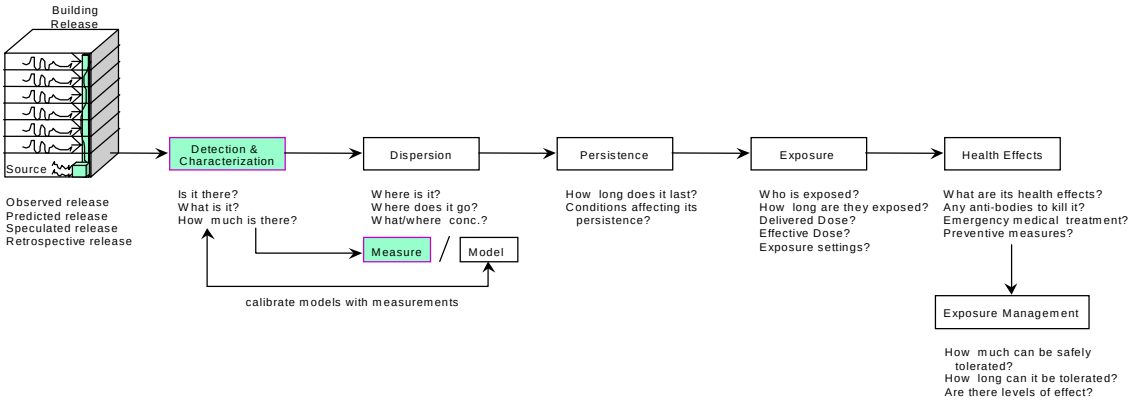

Figure 1. Components and overall design of the nuclear, biological, and chemical health assessment system for indoor air

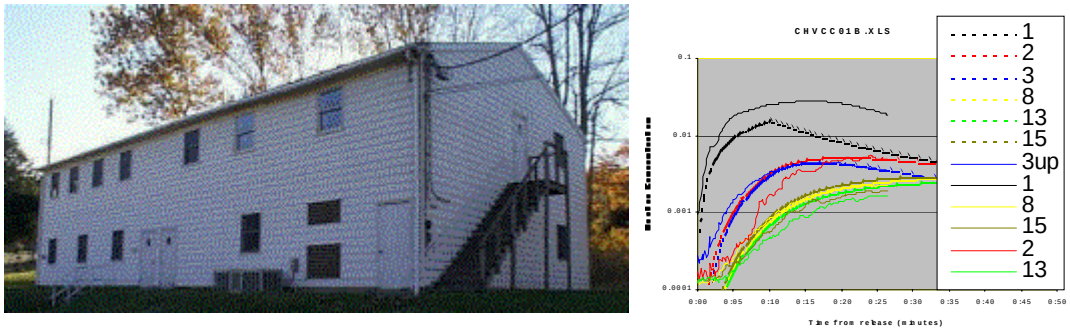

Figure 2. Churchville test facility – measured and simulated responses to 10-min release (solid=measured, dotted=simulated – concentration trajectory legend is keyed to room number) – Note outdoor air intakes near right end of long facing wall

Figure 3. FRAMES system layout for model and health effect database integration

Figure 4. FRAMES output format for system results

Walton GN. 1997. *CONTAM96--User Manual*, NISTIR 5385, National Institute of Standards and Technology.

Numerous open literature publications on building air flow design and measurement (a specific list is available upon request)

Numerous publications on properties and health effects of sarin and anthrax primarily from the Defense Technical Information Center (DTIC) Unclassified Information (a specific list is available upon request).

Publication

Armstrong PR, DL Hadley, RD Stenner, and MC Janus. *Whole-Building Airflow Network Characterization by Inverse Modeling*, TC4.10 Symposium: Nodal IAQ/Dispersion Model Validation, Paper submitted to ASHRAE for publication in the ASHRAE Transactions.

Mechanistic Modeling of Early Genotoxic Events for Chemicals and Radiation

Robert D. Stewart

Study Control Number: PN00064/1471

Mechanistic models are needed to improve our understanding of, and ability to predict and mitigate, the human health effects of exposure to hazardous agents found at many DOE facilities, such as tritium, beryllium, and organic solvents. Our project will advance the state of the art in mechanistic modeling of early biophysical events involved in the development of cancer.

Project Description

This project has two main goals: 1) develop a scalable and extensible modeling framework to bridge the gap between dosimetry and early events involved in the pathogenesis of cancer, and 2) perform the initial work needed to demonstrate the feasibility of using detailed molecular and cellular models to predict dose-response effects at the organ and tissue levels.

A calculational framework to integrate molecular and cellular dose-response models into three-dimensional tissue constructs has been developed. As a high-impact way to illustrate how such modeling tools might be used to study the effects of complicated workplace or environmental exposures, we used our modeling tools to examine ways that the temporal and spatial delivery of radiation to a tumor could be manipulated to improve treatment outcome.

Introduction

Genotoxic chemical agents and ionizing radiation create a multitude of different types of DNA damages. Regardless of the process or agent that initially creates the DNA damage, the same basic physiochemical and biochemical processes either correctly repair the damage or convert the damage into a lethal or nonlethal point mutation or chromosome aberration. Because of cellular adaptations in damage repair and effects associated with, for example, the mitotic cell cycle, the expected number of point mutations and chromosome aberrations created in a cell is a complicated and generally nonlinear function of a cell's exposure history.

Two fundamental questions that must be answered in order to quantitate the health risks associated with human exposure to man-made physical and chemical agents are: "How many and what kinds of abnormal genetic alterations are created in a cell per unit dose of the agent?" and "How many of these randomly created genetic alterations does it take to transform a normal cell into one capable of producing a cancer?" The central aim of this project is to help answer these questions by advancing the state of the art in mechanistic modeling of DNA damage formation, repair, and misrepair processes. Moreover, this project aims to better link these fundamental processes to cell transformation and killing effects in vitro and in vivo.

Results and Accomplishments

A major focus of the project this year has been to develop the scalable and extensible software tools needed to integrate molecular and cellular models into more realistic three-dimensional organ, tissue, and tumor models. We have also further refined our model calibration and testing strategy.

From Molecules to Man: Three-Dimensional Tissue Modeling

In our modeling approach, an organ, tissue, or tumor is first subdivided into a large number of smaller, rectangular tissue regions. Then, we use a molecular and cellular dose-response model to simulate the life history of a large number of cells (and their progeny) in each tissue region. Biophysical response quantities of interest such as the yield of lethal and nonlethal genetic alterations in critical subpopulations (stem cells) or in certain regions of the tissue can then be computed from the life histories of the individual cells. The main advantage of this ab initio approach is that the degree of realism in the tissue model is ultimately only limited by our computing capabilities, our understanding of intra- and intercellular biophysical processes, and the availability of appropriate experimental datasets for use as model inputs and in model testing.

To illustrate the potential impact of detailed, three-dimensional tumor response modeling, we used our modeling tools to examine ways that the temporal and spatial delivery of radiation to a tumor can be modulated to improve treatment outcome (Stewart and Traub in press). Figure 1 shows an illustration of a idealized cylindrical tumor that has been subdivided into 3,133 rectangular tissue regions. Figure 2 shows the results of two simulated radiation treatments. The first treatment design (Figure 2, left panel) shows tumor-cell survival after a conventional radiation treatment that delivers a uniform dose of radiation to all parts of the tumor. The right panel in Figure 2 shows the expected outcome of a radiation treatment that has been optimized to preferentially kill the radioresistant tumor cells located in region 4 (refer to Figure 1). Calculations (Stewart and Traub in press) suggest that biologically motivated treatment optimization could potentially improve some treatment designs by factors on the order of 5 to 20% (iso-effect dose).

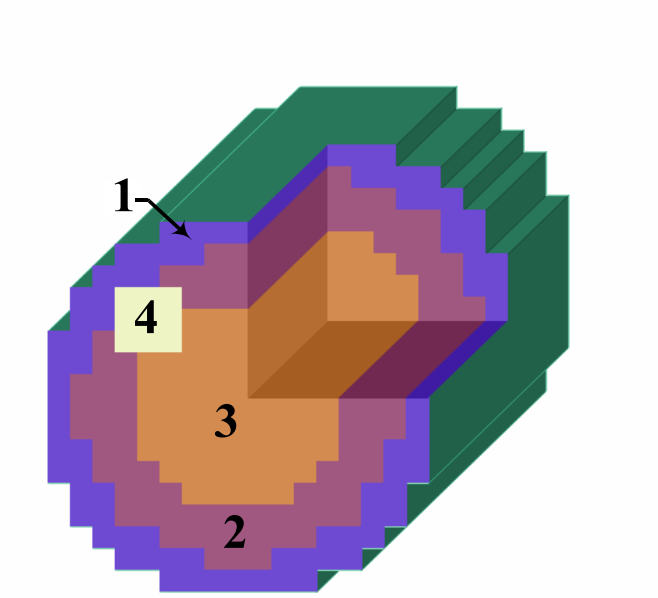

Figure 1. Cylindrical tumor model with heterogeneous biophysical properties (Stewart and Traub in press). The properties of the tumor cells in the four tumor regions give the same apparent "intrinsic radiosensitivity," as determined by a single acute dose of radiation. However, the cell density and damage repair characteristics used in the model are slightly different. For visualization purposes, the tumor is shown with a section cutout. Tissue region 4 is a particularly radioresistant portion of the tumor.

Summary and Conclusions

We have successfully demonstrated that detailed molecular and cellular dose-response models can be integrated into three-dimensional tissue simulations. Although calculations to date have focused on high-dose exposure conditions such as those found in radiation therapy, the basic framework of our model is equally applicable to low-dose exposure conditions. In fiscal year 2000, we plan to conduct several experiments to collect the data needed to further refine and test the damage repair model so that it is more useful for low-dose exposure studies and also for combined exposure to radiation and benzene, an organic solvent commonly found at many DOE sites.

References

Deschavanne PJ, B Fertil, N Chavaudra, and EP Malaise. 1990. The relationship between radiosensitivity and repair of potentially lethal damage in human tumor cell lines with implications for radioresponsiveness." *Radiat. Res.* 122(1): 29-37.

Stewart RD, and RJ Traub. "Radiobiological Modeling in Voxel Constructs." In *Proceedings of the MC2000*. An International Conference on Advanced Monte Carlo for Radiation Physics, Particle Transport Simulation and Applications. October 23-26, 2000 Lisbon, Portugal (in press).

Publications and Presentations

Marler RT and RD Stewart. "A Quasi-Newton code package to find the minimum value of a function." software package completed and benchmarked. User manual in progress.

Marler RT and RD Stewart. "GACM: A genetic algorithm code model to locate the global minimum of a multidimensional function." Initial version of software completed. Code testing and user manual in progress.

Stewart RD. 1999. "On the complexity of the DNA damages created by endogenous processes." *Radiat. Res.* 152(1), 101-105.

Stewart RD, JK Shultis, and BA Montelone. 2000. *A kinetic biological effects model for quiescent cells.* PNNL-13258, Pacific Northwest National Laboratory, Richland, Washington.

Stewart RD and RJ Traub R.J. "Temporal optimization of radiotherapy treatment fractions." In *Proceedings of the ANS* (RPS 2000). Radiation Protection for our National Priorities, Medicine, the Environment, and the Legacy, Spokane, Washington, September 17-21, 2000 (in press).

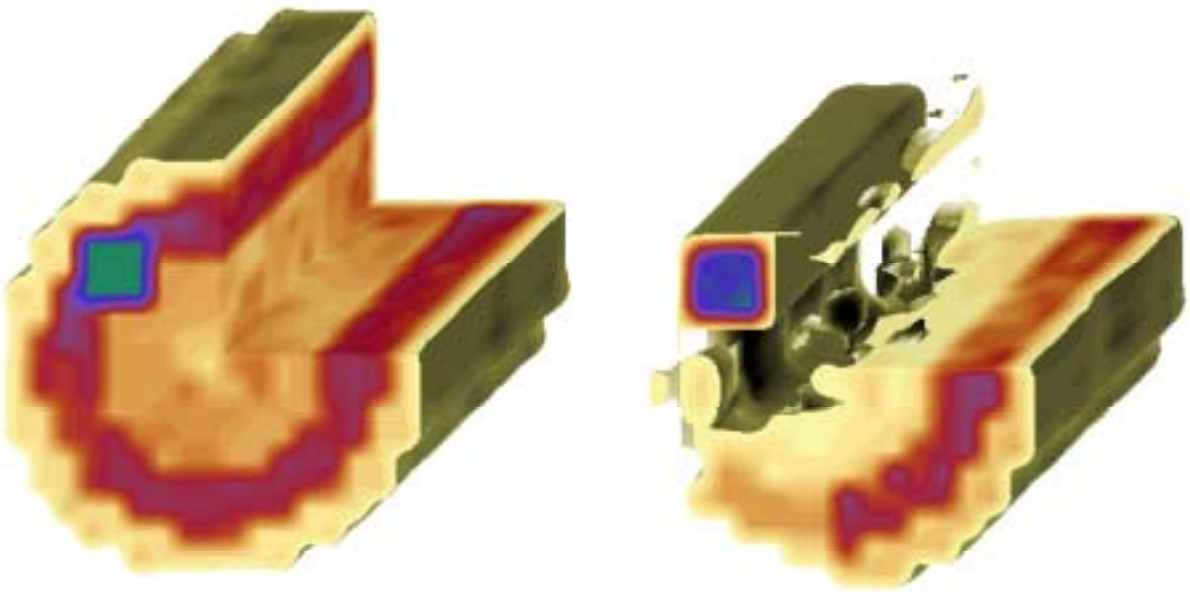

Figure 2. KBEM simulation of a 55 Gy radiation treatment delivered in 30 daily dose fractions (Stewart and Traub in press). Eight collimator beam configurations are used to deliver the dose fractions. Darker shades indicate regions where one or more tumor cells are likely to survive the treatment and lighter shades indicate tumor regions where no tumor cells are likely to survive. The cylindrical tumor, composed of about 10^{11} tumor cells, is subdivided into 3,133 voxels. Survival calculations are based on in vitro intrinsic radiosensitivity data for colon adenocarcinoma cells (Deschavanne et al. 1990). Left panel: uniform dose delivered to entire tumor. Right panel: the intensity and timing of the collimator beams have been optimized to preferentially eradicate the radioresistant tumor cells located in tissue region 4 (refer to Figure 1).

Stewart RD and RJ Traub. "Radiobiological modeling in voxel constructs." In *Proceedings of the MC2000*. An International Conference on Advanced Monte Carlo for Radiation Physics, Particle Transport Simulation and Applications. October 23-26, 2000 Lisbon, Portugal (in press).

Stewart RD. "Testing the LPL model." *Radiat. Res.* (submitted).

Stewart RD. November 2000. "Radiobiological modeling in voxel constructs." Abstract accepted for presentation. International Workshop on Monte Carlo Treatment Planning, Stanford, California.

Stewart RD and RJ Traub. October 2000. "Radiobiological modeling in voxel constructs." Abstract accepted for presentation at MC2000. An International Conference on Advanced Monte Carlo for Radiation Physics, Particle Transport Simulation and Applications. Lisbon, Portugal.

Stewart RD and RJ Traub. September 2000. "Temporal optimization of radiotherapy treatment fractions." Abstract accepted for presentation. ANS Topical RPS 2000. Radiation Protection for our National Priorities, Medicine, the Environment, and the Legacy, Spokane, Washington.

Stewart RD. May 2000. "Temporal optimization of radiotherapy treatment fractions." Invited talk. Lovelace Respiratory Research Institute, Albuquerque, NM.

Stewart RD. August 1999. "From dosimetry to biological effect—Implications for radiation therapy." *Third International Workshop on Electron and Photon Transport Theory Applied to Radiation Dose Calculation*, Indianapolis, Indiana.

Non-Invasive Biological Monitoring for Occupational Exposure to Metals

Karla D. Thrall, Yuehe Lin, Charles Timchalk

Study Control Number: PN98055/1301

The development of a noninvasive biological monitoring device for determining of occupational exposure to metals (such as lead) is directly relevant to the DOE mission of worker health and safety.

Project Description

Exposure data provide a basis for assessing compliance and adequacy of standards, and for developing improved risk estimates. This work involves the development of a portable monitoring device for on-site characterization of environmental contamination and for real-time noninvasive biological monitoring of occupational exposure to toxic metals using saliva as the biological medium.

Saliva is a body fluid that can be monitored to estimate exposure to an environmental contaminant, such as lead. The amount of metal in the saliva will depend on the concentration delivered to the gland from the circulating blood.

Results and Accomplishments

Development of a Portable Monitoring Device

The approach for development of the portable microfluidics/electrochemical sensor is based on the lab-on-a-chip concept. The electrochemical detector is sensitive, compact, and low cost and can easily be integrated into the small size of a portable monitoring device. Prototype construction of the microfluidic device was completed. All individual modules were integrated on the surface of the standard microfluidic platform based on a plug-and-play design. Recent efforts focused on investigating a permselective polymer coating on the electrode surface to prevent the surface fouling of the electrode. A coating will prevent proteins from reaching the electrode while allowing the Pb^{2+} ions to readily diffuse through. Lead-spiked saliva samples were used to evaluate the electrochemical sensor. Results indicated that the stability of the electrochemical sensor was greatly improved. An alternative design approach involves the use of a micro-membrane separator. The micro-membrane separator consists of two polycarbonate plates and one membrane, as shown in Figure 1.

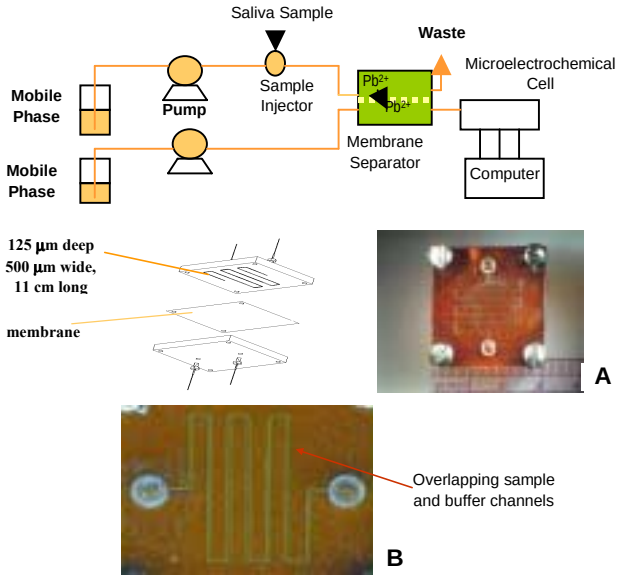

Figure 1. (A) Schematic diagram of micro-analytical system with a micro-membrane separator for on-line sample cleanup; (B) diagram and photo of micro-membrane separator

Serpentine flow channels were fabricated on two polycarbonate plates using laser micro-machining technology. When sample solutions flow into the separator, Pb^{2+} ions diffuse through a membrane, then into the micro-electrochemical cell for detection. Proteins and other components in saliva cannot diffuse through the membrane and will be removed to a waste outlet. Preliminary studies were conducted using Pb spiked saliva samples. Improvement of sensor reproducibility was observed with this approach (Figure 2).

A comparison of standard analysis of environmental water samples, using inductively coupled plasma mass spectrometry (ICP-MS), with results from the micro-analytical system, show excellent correlation (Table 1). Similar results were seen in saliva samples collected from rodents treated with Pb, although the micro-analytical system consistently under-predicted Pb concentrations

even after treating the saliva samples with acid prior to micro-analytical quantitation (Table 2).

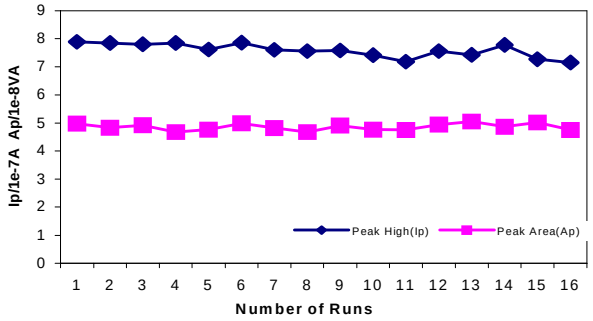

Figure 2. Measurement of the reproducibility of the microfluidics/electrochemical sensor at 6 ppb Pb in water over 16 independent runs. The relative standard deviation (RSD) = 4%.

Table 1. Comparison of the micro-analytical system to ICP-MS for the detection of Pb in water samples

Sample	Micro-Analytical System (ppb)	ICP-MS (ppb)
River Water 1	4.50	4.87
River Water 2	1.2	0.82
Lab Tap Water	20.5	21.8

Table 2. Comparison of micro-analytical system to ICP-MS for the detection of Pb in rodent saliva samples

Sample*	Micro-Analytical System (ppb)	ICP-MS (ppb)
Saliva 1	108	150
Saliva 2	110	116
Saliva 3	80	99

*Saliva samples were acidified to 0.5 M HCl to release the Pb.

Summary and Conclusions

In summary, a portable monitoring device capable of real-time analysis of environmental contaminants such as lead has been developed. Initial studies using experimental animals suggest that the device has good sensitivity (low ppb range), correlates with conventional approaches inductively coupled plasma mass spectrometry and is capable of measuring trace levels of Pb in saliva. It is anticipated that, after further development and validation, this technology will be used as an important tool for real-time analysis of nonvolatile environmental contaminants.

Publications and Presentations

Lin Y, R Zhao, KD Thrall, C Timchalk, WD Bennett, and DW Matson. 1999. "Integration of microfluidics/electrochemical system for trace metal analysis by stripping voltammetry." *Proceedings of SPIE*, Vol. 3877, Pp. 248-256.

Thrall KD, TS Poet, Y Lin, KK Weitz, and C Timchalk. 2000. "Saliva monitoring for exposure to lead utilizing real-time microfluidics/electro-chemical analysis." Presented at the 39th Annual Meeting of the Society of Toxicology, Philadelphia, Pennyslvania.

Timchalk C, TS Poet, Y Lin, KK Weitz, R Zhao, and KD Thrall. May 2000. "Development of microfluidics/electrochemical systems for real-time analysis of lead from saliva." Presented at the American Industrial Hygiene Conference and Exposition, Orlando, Florida.

Timchalk C, TS Poet, Y Lin, KK Weitz, R Zhao, and KD Thrall. 2000. "Saliva analysis for lead exposure using real-time microfluidics/electro-chemical system." Presented at the International Conference on Arctic Development, Pollution, and Biomarkers of Human Health, Anchorage, Alaska.

Timchalk C, TS Poet, Y Lin, KK Weitz, R Zhao, and KD Thrall. 2000. "Development of an integrated micro-analytical system for lead in saliva and linkage to a physiologically based pharmacokinetic model describing lead saliva secretion." *American Industrial Hygiene Association Journal* (in press).

Timchalk T, Y Lin, TS Poet, and KD Thrall. 1999. "Non-invasive biological monitoring for occupational exposure to metals." Presented at the National Institute of Dental and Craniofacial Research Conference, Virginia.

Real Time Biomarkers of Oxidative Stress

Thomas J. Weber

Study Control Number: PN00079/1486

Oxygen free radicals have been implicated in the pathophysiology of a number of human diseases, including cancer, atherosclerosis, neurodegenerative disorders, and aging. Oxidative stress is also central to the adverse effects of ionizing radiation. In the present study, we have investigated mass changes detected in exhaled breath of mice following hyperoxia, and in cell culture following exposure to hydrogen peroxide with the goal of identifying a preliminary set of candidate biomarkers of oxidative stress that can be measured in real time.

Project Description

A breath analyzer device for the real time measurement of chemicals in exhaled breath using mass spectrometry is a tool that is ideally suited for noninvasive population and worker monitoring under a variety of conditions. This breath analyzer may also be useful for investigating the effect of experimental parameters such as geography and diet on defined mass targets in exhaled breath. In the present study, we have investigated mass changes detected in exhaled breath of mice following hyperoxia, and in cell culture following exposure to hydrogen peroxide with the goal of identifying preliminary biomarkers of oxidative stress that can be measured in real time. Since most, if not all, human disease is dependent on the generation of an oxidative stress, a non-invasive biomarker of oxygen free radical exposure may have wide application in human health monitoring. A number of candidate mass targets increased in response to oxidative stress were identified. Additional studies are required to identify these targets and further characterize their application as biomarkers.

Introduction

Oxygen is a necessary requirement of aerobic organisms, however, its more reactive metabolites, termed reactive oxygen species, are implicated in a number of diseases, including cancer, atherosclerosis, neurodegenerative disorders, and aging (Janssen et al. 1993). The adverse effects of ionizing radiation are also attributed to reactive oxygen species generation (Dahm-Daphi et al. 2000). Mammalian cells have developed an elaborate defense system, which includes enzymatic and nonenzymatic antioxidants, to protect themselves against the damaging effects of reactive oxygen species. However, these defense systems are not always adequate and can be overcome, leading to reactive oxygen species-dependent damage to cellular macromolecules.

Current methods for analyzing reactive oxygen species-induced cellular damage are difficult and not easily extended to health monitoring on a broad scale. An accurate biomarker of oxidative stress that can be measured noninvasively in real time may eliminate this limitation. We have applied a noninvasive analytical tool (breath analyzer) to experimental model systems perturbed by an oxidative stress to determine if a preliminary set of candidate biomarkers could be identified. Volatile or exhaled masses from two experimental model systems were compared, namely, 1) cultured cells treated with hydrogen peroxide and 2) mice exposed to hyperoxia. Proper validation of these biomarkers may contribute to human health monitoring.

Results and Accomplishments

Mass Spectrometry Analysis of Cell Culture Head Space Following Treatment with Hydrogen Peroxide

Cells in culture (LLC-PK_1) were treated with hydrogen peroxide (0.27 mM) and volatile chemicals in the "head-space" monitored over time (1 to 75 minutes) by mass spectrometry. Mass differences between control and H_2O_2-treated cells were divided into two categories, termed persistent and transient changes. Specific masses categorized into these groups are summarized in Tables 1 through 3, and represent an increased appearance of the target mass, relative to control. As an additional control, we identified mass changes for volatile chemicals following treatment of cell culture media with hydrogen peroxide under identical conditions.

In a second model system, mice were exposed to 95% oxygen for 24 hours (hyperoxia) and mass changes in exhaled breath were determined. Mass changes are summarized in Table 4.

Table 1. Transient mass changes associated with media following H_2O_2 treatment

M/Z = 44, 59, 60, 63, 72, 87, **88**, 89

Table 2. Transient mass changes associated with cells following H_2O_2 treatment

M/Z = 24, 35, 37, 43, 44, 51, 56, 67, 75

Table 3. Persistent mass changes associated with cells following H_2O_2 treatment

M/Z = 41, 52, 65, **88**

Table 4. Mass changes in hyperoxic mice

M/Z = 28, 31, 32, 33, 47, 36, 37, 39, 41, 42, 48, 49, 50, 52, 53, 54, 55, 57, 58, 59, 60, 61, 62, 64, 68, 69, 70, 72, 76, 77, 78, 80, 81, 82, 83, 84, 86, **88**, 89, 92, 95, 96, 98, 99, 100, 101, 102, 103, 104, 105, 106, 108, 111, 112, 1113, 115, 116, 118, 119, 120, 122, 125, 127, 128, 129, 131, 133, 134, 135, 136, 137, 138, 140, 142, 145, 146, 151, 152, 154, 155, 156, 157, 158, 159, 160, 161, 1662, 163, 164, 165, 166, 180, 183, 200, 203, 205, 208, 209

Summary and Conclusions

A number of mass targets were identified in our study. Clearly, a more complex data set was identified in our preliminary studies in a hyperoxic whole animal model, relative to cultured cells treated with hydrogen peroxide. Of particular interest, a candidate biomarker (mass/change ratio; = 88) was observed both in vitro and in vivo in response to reactive oxygen species exposure, under conditions that are likely comparable to the steady-state response to reactive oxygen species. We have examined the literature for mass targets increased in pathologies associated with an oxidative stress to determine whether there is precedent for this M/Z = 88 target. A volatile M/Z = 88.2 was identified in burn patients with infection, a condition associated with the generation of an oxidative stress (Labows et al. 1980). The M/Z = 88.2 was identified as isopentanol. Therefore, future studies will be directed at determining whether the M/Z = 88 target identified in our studies is also isopentanol. The correlation between prooxidant states and an increased detection of M/Z = 88 raises the possibility that this mass may be a biomarker of oxidative stress that can be measured noninvasively in real time.

References

Dahm-Daphi J, C Sass, and W Alberti, W. 2000. "Comparison of biological effects of DNA damage induced by ionizing radiation and hydrogen peroxide in CHO cells." *Int. J. Radiat. Biol.* 76, 67-75.

Janssen YM, B Van Houten, PJ Borm, and BT Mossman. 1993. "Cell and tissue responses to oxidative damage." *Lab. Invest.* 69, 261-274.

Labows JN, KJ McGinley, GF Webster, and JJ Leyden. 1980. "Headspace analysis of volatile metabolites of Pseudomonas aeruginosa and related species by gas chromatography-mass spectrometry." *J Clin. Microbiol.* 12(4):521-526.

Materials Science and Technology

Advanced Thin Film Materials Based on Functionalized Carbon Nanotube Composites

Yufei Gao[(a)], Jay W. Grate, Johanes H. Sukamto, David A. Nelson, Theva Thevuthasan, Greg S. Herman

Study Control Number: PN00006/1413

Carbon nanotubes are emerging as a new, advanced material for the next century. Functionalization of these carbon nanotubes will further enhance their potential applications and usefulness. Applications envisioned include the next generation hydrogen storage material, durable and sensitive chemical sensors, and membranes for energy-efficient separation of ions.

Project Description

We investigated functionalized carbon nanotube composite materials with the aim of exploring their chemical and physical properties. The proposed research was based on our recently developed novel synthesis technique for producing carbon nanotube thin films with controlled properties, together with our expertise in metal decoration and polymer derivatization of various surfaces. The scope of the work encompasses fundamental studies on the growth and modification of carbon nanotube films, patterning, characterization of interactive properties, and exploratory experiments to demonstrate the functionality of these novel materials in applications such as hydrogen storage.

Introduction

Carbon nanotubes are emerging as a new advanced material for the next century. Because of the combination of their high mechanical strength, tailorable electronic properties, high surface area, light weight, and excellent chemical and thermal stability, carbon nanotubes exhibit a variety of potential applications ranging from hydrogen storage, electronic nano-devices, fuel cells, and batteries. To date, most of the fundamental research on carbon nanotubes has been focused on their growth mechanism and direct measurements of various physical properties. Modifying the surfaces of carbon nanotubes with functional materials exhibiting useful chemical and physical properties will add a new aspect of promise for the applications of this family of novel materials. However, the fundamental study of such advanced composite materials is absent in the literature, and their tremendous potential is yet to be realized.

Approach

Following an approach similar to one described by Li et al. (1996), support substrates for carbon nanotubes were initially coated with a thin film of porous silica impregnated with metal catalysts (such as, Fe, Ni, or Co). Carbon nanotubes were subsequently grown by chemical vapor deposition (CVD) techniques employing ethylene as the carbon source. The resulting carbon nanotube films were typically characterized by scanning electron microscopy and transmission electron microscopy.

We have investigated two types of surface modifications. First, nanoparticles of platinum were coated electrochemically using commercial solutions. Second, electroactive polymers (polyvinylferrocene) have been coated on carbon nanotubes by solvent casting methods.

For hydrogen storage studies, we used an element-specific ion-beam technique developed at this Laboratory based on nuclear reaction analysis for determining the concentration of absorbed hydrogen (H_2).

Results and Accomplishments

Aligned and crack-free carbon nanotube films are critical for many applications (field emission devices). We have successfully grown aligned carbon nanotube films on stainless steel foils as shown in Figures 1a to 1c. A stainless steel foil was first coated with a thin film of porous silica impregnated with iron. The carbon nanotubes were subsequently grown on the substrate at 750ºC using ethylene as the carbon source. The cracks seen in Figure 1a are possibly caused by cracks on the

(a) Yufei Gao and Johanes H. Sukamoto resigned from Pacific Northwest National Laboratory. Chris Aardahl assumed responsibility for this project.

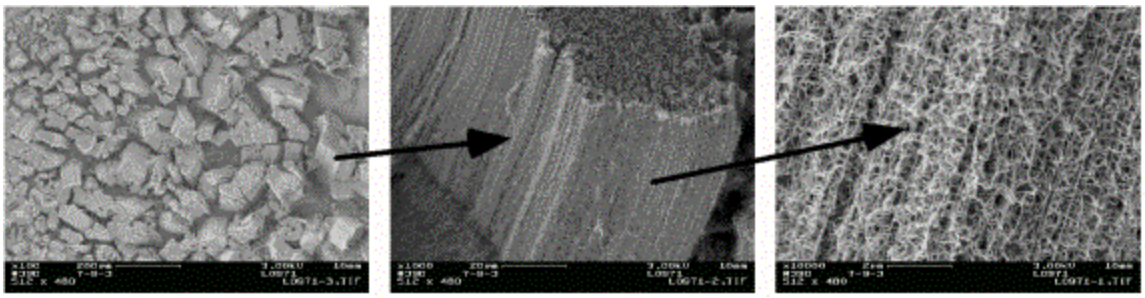

Figure 1. (a) – (c) Successive magnification of carbon nanotubes grown on a stainless steel substrate

porous silica film. Additional studies are under way to determine conditions required to grow crack-free carbon nanotube films.

Two types of surface modification activities were pursued: 1) decoration of carbon nanotubes with noble metals (such as platinum), and 2) derivatization of carbon nanotubes with polymers. Shown in Figure 2 is the secondary electron image from the in-lens detector of a carbon nanotube sample that has been decorated with platinum. The platinum was deposited electrochemically (5-second deposition period) using the electronically conductive carbon nanotubes as electrodes. Thus, we successfully demonstrated that carbon nanotube surfaces can be electrochemically modified with metal nanoparticles (approximately 10 nm platinum particles).

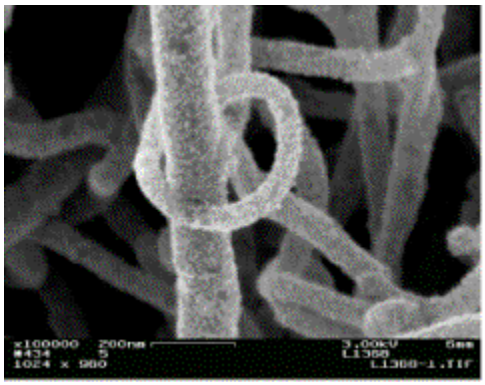

Figure 2. Secondary electron image from the in-lens detector for a 5-second deposition time of platinum

Platinum deposits on carbon nanotubes are of interest to a wide range of applications from catalysis in general to hydrogen storage. The use of carbon nanotubes for catalyst support is of interest because of the uniformity of carbon nanotube surfaces (defect-free carbon nanotubes are single crystals) and high thermal and electrical conductivities. The possibility of storing hydrogen in the hollow centers of carbon nanotubes has sparked interest worldwide. Because noble metals (such as platinum) are known to dissociate molecular hydrogen into atomic hydrogen, the kinetics of hydrogen uptake and release may be improved.

The high surface area of carbon nanotube films makes them viable support materials for electrodes. Commercial polyvinylferrocene from Polysciences Inc. was coated on carbon nanotube films using a solvent casting technique where the polyvinylferrocene was dissolved in dichloromethane. The cyclic voltammogram of the polyvinylferrocene-coated carbon nanotube film was obtained in a solution of 0.5 M $NaNO_3$. The result was then compared to the cyclic voltammogram of a polyvinylferrocene-coated carbon cloth electrode (GC-14 from the Electrosynthesis Co.). The integrated charge passed as a function of time for both electrodes is shown in Figure 3a. The polyvinylferrocene-coated carbon nanotube electrode exhibited a higher surface charge density. Furthermore, no difference in electrode accessibility (solution mass transport rates) was observed between the two electrodes. This was evident from Figure 3b, where required for passing the same relative amount of charge. Therefore, carbon nanotube films provide additional surface area with negligible mass transfer limitations.

We have verified the feasibility of using a nuclear reaction analysis to directly measure the amount of H_2 absorbed in carbon nanotubes. Briefly, a beam of ^{19}F with a specific energy is imparted on carbon nanotube samples. The nuclear reaction, $^{19}F + {}^{1}H \rightarrow {}^{16}O + {}^{4}He + \gamma$, occurs only when the ^{19}F has a specific energy (i.e., the resonant energy). Because the reaction is very specific to $^{19}F + {}^{1}H$, a measure of the γ yield provides a measure of the concentration of hydrogen. In addition, variation of the ^{19}F energy gives us the ability to obtain the concentration of hydrogen as a function of depth (the ^{19}F must expend sufficient energy before the resonant nuclear reaction will take place). Figure 4 shows the hydrogen content of a virgin carbon nanotube sample and the same sample after it has been dosed with hydrogen at 1 atmosphere for 1 hour. The amount of hydrogen is approximately 0.2 wt%. This is consistent with published

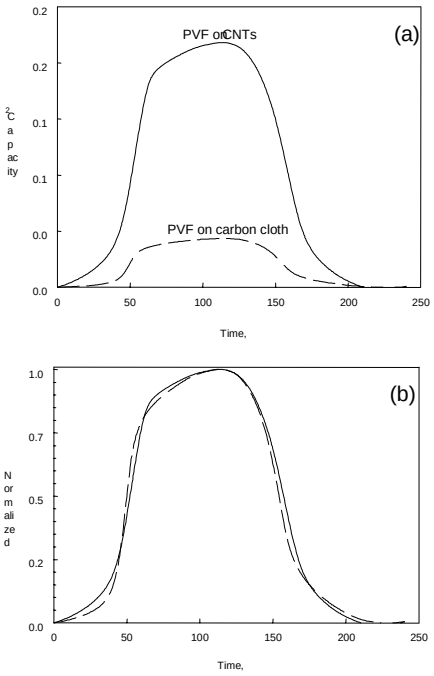

Figure 3. (a) Integrated charge passed from cyclic voltammogram of polyvinylferrocene-coated carbon nanotube thin film measured in 0.5 M $NaNO_3$ at 5 mV/sec. Time = 0 corresponds to beginning of the potential scan. (b) Same as (a) but normalized to the maximum charge passed.

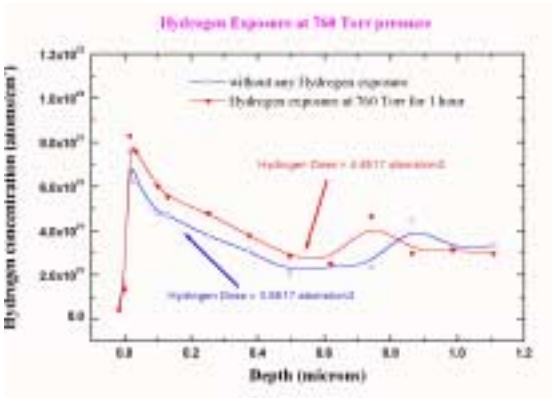

Figure 4. Hydrogen concentration determined using nuclear reaction analysis

reports on the hydrogen content of carbon nanotubes that have undergone similar treatments. Because this technique is a direct spectroscopic measure of hydrogen in carbon nanotubes, it provides an unambiguous measure of hydrogen content. The technique is especially useful for studying hydrogen uptake and release by means of pressure swings.

Summary and Conclusion

We have grown aligned carbon nanotubes over macroscopic domains (10s of μms). Current limitations in the size of crack-free domains are believed to be caused by cracks that developed on the precursor porous silica film. We have shown that surfaces of carbon nanotubes can be easily functionalized with metal nanoparticles and polymers. Platinum nanoparticles were electrochemically deposited on carbon nanotube thin films. Carbon nanotube films coated with electroactive polymers show an increase in the electrochemically active area with minimal mass transport limitations. An ion beam technique based on nuclear reaction analysis was successfully employed to measure the hydrogen content of thin carbon nanotube films.

Reference

Li WZ, SS Xie, LX Qian, BH Chang, BS Zou, WY Zhou, RA Zhao, and G Wang. 1996. "Large-scale synthesis of aligned carbon nanotubes." *Science* 274:1701.

Presentation

"Synthesis and Properties of Functionalized Carbon Nanotube Composites." Presented at Pacifichem 2000, December 14 - 19, 2000, Honolulu, Hawaii.

Component Fabrication and Assembly for High Power Density Solid Oxide Fuel Cells

Kerry Meinhardt, Jeff Stevenson, Steve Simner

Study Control Number: PN00023/1430

This project demonstrated our capability to design and fabricate an entire planar solid oxide fuel cell sub-stack using zirconia-based technology.

Project Description

The objective of this project was to develop the capabilities to fabricate key ceramic components for a high power density solid oxide fuel cell. The main goals were to fabricate thin, anode-supported electrolytes and both ceramic and metal interconnect plates and to assemble these into operable solid oxide fuel cell stacks. Components were designed to accommodate high-volume manufacturing techniques.

Introduction

Solid oxide fuel cells have been of interest for over 30 years due to their potential for high efficiencies and low environmental impact. Currently, solid oxide fuel cell technology is expensive, fragile, and from the perspective of manufacturing, impractical. There are numerous challenges with respect to making this technology cost-effective and attractive for wide application. Some of these challenges include lower temperature operation to incorporate metal interconnects (at the expense of power density), optimized designs that minimize the mechanical stress within the various ceramic components of the fuel cell stack, the development of simple and practical gasoline/diesel reformers, and the incorporation of ceramic processing methods, which could lower the cost and complexity of fabrication.

The conventional cell designs, with yttria-stabilized zirconia electrolyte thickness in the range 100 to 200 μm, require an operating temperature of near 1000°C to keep the electrolyte resistance in a practical range. Such high-temperature operation precludes use of metallic components, requiring fabrication of (heretofore) expensive ceramic interconnect plates. Acceptable power densities can be achieved at lower temperatures (< 800°C) by either replacing yttria-stabilized zirconia with a more conductive material, or by reducing the thickness of the yttria-stabilized zirconia electrolyte to below 50 μm. Conductivity of strontium-substituted lanthanum gallate is at least 3 times higher than yttria-stabilized zirconia at 800°C. This may allow use of thicker, self-supporting strontium-substituted lanthanum gallate structures at 800°C. However, mechanical strength is inferior to yttria-stabilized zirconia and cost is higher. On the other hand, as yttria-stabilized zirconia electrolyte thickness is decreased, the electrolyte ceases to be self-supporting and must be fabricated with a porous support layer, typically the anode electrode. This substrate is the mechanical support for the electrolyte allowing it to be handled and processed without breaking. However, fabrication of the anode-supported components is challenging; the electrolyte and anode must be co-sintered, requiring close matching of shrinkage curves. An additional complication is that the porous support layer will leak fuel gas if it extends to the edge of the stack. It must therefore be constrained to the active cell area, by surrounding it with a picture frame, which adds considerable fabrication and sealing complexity. Worldwide, the number of groups currently pursuing development of conventional, high-temperature, yttria-stabilized zirconia/ceramic interconnect technology is roughly equal to the number developing less conventional designs.

Results and Accomplishments

One of the primary goals of this project was to build capability in the area of solid oxide fuel cell fabrication. Our primary goal was to identify and characterize candidate cathode materials for lanthanum gallate-based cells. Electrolyte supported cells were fabricated by sintering screen printed electrodes onto sintered lanthanum gallate membranes which had been fabricated by tape casting. After sintering of the electrode materials, the cells were tested using air on the cathode side and 97% H_2 and 3% H_2O on the anode side. Representative results (at 700°C) are shown in Figure 1. Electrode studies (both cathode and anode) will continue in the future to determine the optimum compositions and morphologies for stable, high performance at temperatures in the 600 to 700°C range.

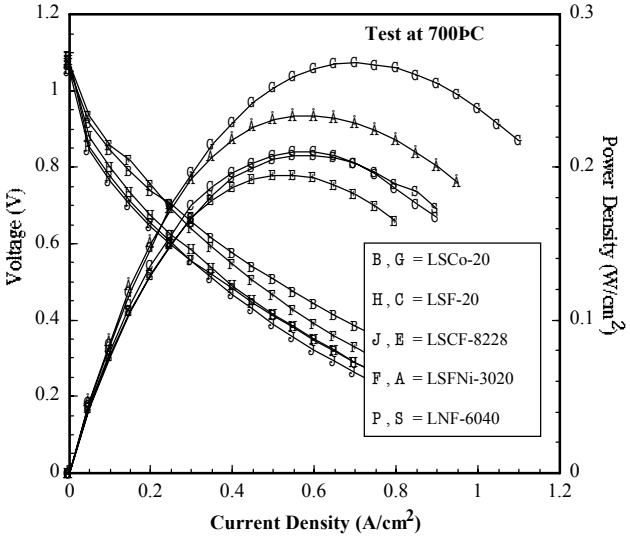

Figure 1. Effect of cathode material on performance of 400 µm strontium-substituted lanthanum gallat solid oxide fuel cells

Another goal is to build the capability to manufacture and test solid oxide fuel cell stacks. During the past year, a comprehensive cell test stand (consisting of custom-designed test furnace, electronic load bank, gas handling equipment, humidifier, and computer) was designed and built. A prototype planar solid oxide fuel cell stack was assembled using components fabricated. While the performance of the stack was disappointing, the test verified our stack testing capability, and provided several lessons learned, which will lead to improved stack testing in the future.

Summary and Conclusions

The development of fabrication techniques for anode supported electrolytes was successful. Several methods for the fabrication of ceramic interconnects were investigated. Both compression molding and injection molding could be viable processes, but due to the lower temperature of operation, ceramic interconnects are no longer being pursued. A number of potential electrode materials for the lanthanum gallate system were identified.

Development of a Low-Cost Photoelectrochemical Device for Hydrogen Production via Water Splitting by Sunlight

Maciej S. Gutowski, John E. Jaffe, Peter M. Martin, Larry C. Olsen

Study Control Number: PN00028/1435

The future vision for hydrogen is that it will be efficiently produced from renewable energy sources and made available for widespread use as an energy carrier and fuel. The objective of this project is to develop a low-cost photoelectrochemical device for hydrogen production via water splitting by sunlight.

Project Description

The purpose of this project is to develop an integrated low-cost photovoltaic/electrolysis system that produces hydrogen with a solar to hydrogen efficiency of greater than 20%. Copper indium diselenide solar cells were fabricated from substrates supplied by Siemens Solar Industries. A panel consisting of six of these cells wired in series was constructed for carrying out electrolysis studies. An electrochemical cell was constructed that consisted of two platinum electrodes immersed in an electrolyte. Hydrogen was produced with an efficiency of approximately 6%. Modeling calculations were performed to determine thickness of the cadmium telluride layer, which will be used in a two-cell tandem structure with copper indium diselenide, and a literature search was performed to identify low-cost electrode materials. Theoretical investigations relevant to high band gap materials were carried out. In particular, benchmark calculations were performed for bulk total energy, lattice constant, sublattice distortion for copper indium diselenide, equation of state (except copper indium diselenide), and band structure of ZnS, ZnSe, ZnTe, CdTe, and copper indium diselenide. Fully relaxed surface calculations were performed for the nonpolar (110) and polar (111) surfaces of ZnSe. Calculations on the copper indium diselenide nonpolar (110) surface with relaxation but without reconstruction have been completed. This project advanced our ability to produce hydrogen via water splitting by sunlight using low-cost materials.

Introduction

Progress in the production of hydrogen via water splitting by sunlight has been limited by three factors (Khaselev and Turner 1998): 1) corrosion of the semiconductors immersed in aqueous solutions (thermodynamically, the semiconductors with desired band gaps are photochemically unstable in water), 2) high voltage required to dissociate water is not compatible with the voltage produced by single cells, and 3) high cost of materials for tandem solar cells that might produce sufficiently high voltage. To overcome these obstacles, we suggest three paths. First, we proposed to separate the electrochemical part from the photovoltaic part to eliminate the problem of corrosion of semiconductors in aqueous solutions and to build a (modular but integrated) photovoltaic/electrolysis device (see Figure 1). Second, we proposed to develop a low-cost, thin-film solar cell structure to convert solar to electrical energy to achieve the required voltage for water splitting and high efficiency of the solar energy conversion. This tandem solar cell will be based on a $Cu(In,Ga)(Se,S)_2$ copper indium diselenide cell provided by Siemens Solar Industries, the world's leading thin-film solar cell manufacturer, and will require development of one additional high-band gap cell. We will consider cadmium telluride and copper- and silver-based chalcopyrites as candidate materials for the second cell. Third, in order to achieve a low-cost system, materials other than platinum will be investigated for electrodes of the electrochemical module. The benefit of our approach is development of a low-cost photovoltaic/electrolysis system that produces hydrogen with a solar to hydrogen efficiency of greater than 20%.

Approach

The approach involves experimental and theoretical studies being conducted in parallel. In order to eliminate the problem of corrosion of semiconductors in aqueous environments, we propose to separate the photovoltaic and electrochemical elements (Figure 1). The voltage from the photovoltaic module is passed to the electrochemical module but the interaction of semiconductors with water is eliminated. The experimental efforts were focused on constructing a prototype photovoltaic/electrolysis system. The theoretical efforts were focused on electronic structure studies of bulk, interface, and defect issues in the active materials used.

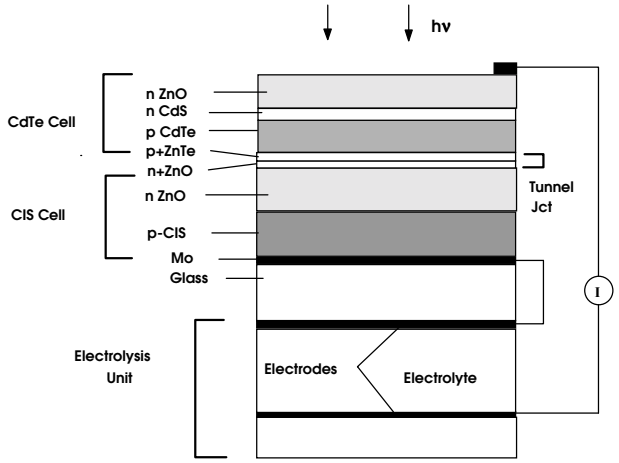

Figure 1. Schematic of integrated photovoltaic/electrolysis system

Results and Accomplishments

Experimental studies consisted of three key activities: 1) fabrication of thin-film solar cells based on copper indium diselenide, 2) electrolysis of water to produce hydrogen using copper indium diselenide solar cells coupled to simulated solar illumination, and 3) modeling studies to optimize the CdTe cell structure in a CdTe/ copper indium diselenide two-cell tandem configuration for a photovoltaic-electrolysis system.

Copper indium diselenide solar cells were fabricated from substrates supplied by Siemens Solar Industries. These substrates were based on n-CdS/p-copper indium diselenide junctions and were completed by depositing collector grids to yield cells with an area of 0.454 cm^2. A panel consisting of six of these cells wired in series was constructed for carrying out electrolysis studies. An electrochemical cell was constructed that consisted of two platinum electrodes immersed in a 2M KOH electrolyte. Experiments were carried out to generate hydrogen by supplying power from the copper indium diselenide panel to the electrochemical cell with the platinum electrode area set to be the same as the total copper indium diselenide cell area. Hydrogen was produced with an efficiency of approximately 6%. Two aspects of the experimental work can be identified as limiting performance, namely, the external contacts to the six-cell panel and the behavior of the platinum electrodes. Improved contacts would allow the efficiency to increase to 7 to 8%. Improvement in plutonium electrode preparation will lead to more efficient operation. Further improvement could be achieved by using electrodes with larger effective areas such as presented by a nanoporous film. Improvement in the platinum electrodes should allow the efficiency of hydrogen production to increase above 10%. Once these improvements are made, this efficiency would be significantly higher than the best reported result for a photovoltaic-electrolysis system that has the potential for being made at low cost, namely, 7%[(a)].

The ultimate objective of this work was to develop a two-cell tandem structure for an integrated photovoltaic/ electrolysis system. One candidate system was based on a CdTe cell combined with a copper indium diselenide cell. These two cells are connected in series in a monolithic tandem arrangement. In such a configuration, the short circuit current densities must be approximately equal in order for the efficiency to be maximized. This requires that the thickness of the CdTe layer be adjusted so that adequate photon flux passes through the CdTe cell structure to the copper indium diselenide cell. In particular, if the typical thickness for the CdTe cells (2 μm) were used, the copper indium diselenide cell would not produce adequate current. Modeling calculations indicate that equal short currents can be achieved if the CdTe thickness is reduced to approximately one micron. A literature search was conducted concerning sputtered CdTe solar cells. We determined that efficient CdTe cells have been grown by sputter deposition at substrate temperatures of 250°C, which should be low enough for growing a CdTe cell onto a copper indium diselenide structure without degrading the copper indium diselenide cell.

Benchmark calculations were performed for bulk total energy, lattice constant, sublattice distortion (copper indium diselenide), equation of state (except copper indium diselenide), and band structure of ZnS, ZnSe, ZnTe, CdTe, and copper indium diselenide. The performance of local density approximation and generalized gradient approximation was tested for ZnSe and CdTe. For selenides and tellurides (in contrast to oxides) the local density approximation was found preferable to the generalized gradient approximation (except for cohesive energy, and only there due to differences in how the isolated atom was treated). Thus, the local density approximation will be used for the rest of the study.

Fully relaxed surface calculations were performed for the nonpolar (110) and polar (111) surfaces of ZnSe. The (110) results for the surface relaxation agreed well with experiment and previous theoretical literature. The unreconstructed (111) surface was found to be metallic as expected due to the depolarizing charge transfer, and to exhibit only slight relaxation. Five- and six-layer slabs were found to have very close surface energies and

(a) O Khasalev, A Bansal, JA Turner, personal communication.

relaxations, indicating the adequacy of five layers (or pairs of layers in the polar case) for accurate results. At least three atomic layers will be relaxed at each surface. Calculations on the copper indium diselenide nonpolar (110) surface with relaxation but without reconstruction have been completed. Analogous calculations for the polar (112) surface are under way.

A literature search was performed to identify low-cost electrode materials. The hydrogen evolution reaction is one of the most studied electrochemical reactions, yet outside of the general agreement of electronic structure calculations. For the rate of the hydrogen evolution reaction on pure metals, there are no general theories covering all electrode materials. Even within alloys comprised from a series of transition metals there are sometimes anomalies in the trend of the observed kinetics. Metals with high exchange current densities for the hydrogen evolution reaction are plutonium, Rh, Ir, Re. These materials are not suitable for a high-surface area, low-cost device. However, as a baseline, the initial work will employ platinum electrodes for both anode and cathode. A complete evaluation of the performance characteristics of the known hydrogen evolution reaction cathode materials with the potential to be integrated into the photovoltaic/electrolysis system will be undertaken. Two promising candidates are the Ni-P(x) and the Fe(x)-Ni(y)-P(z) alloys, which when activated, show very good hydrogen evolution reaction kinetics and stability. Similarly a suitable anode will be determined. The kinetic performance of these systems will be investigated with geometries identical to the integrated cell under current densities where the photovoltaic system will operate and under a range of temperatures.

Summary and Conclusions

Our most important accomplishments are the following:

- copper indium diselenide cells based on Siemens Solar substrates were fabricated for electrolysis experiments. Individual cells displayed efficiency of 12 to 14%, the panel efficiency was 9%.

- Photovoltaic/electrolysis experiment was carried out with the copper indium diselenide cells illuminated by solar simulator and coupled to plutonium electrodes in 2M KOH electrolyte. Hydrogen was produced with an efficiency of 6%.

- Optimal thickness of the CdTe layer to be grown on the copper indium diselenide cell was determined to be 0.24 micron.

- Nonpolar (110) and polar (112) surfaces of $CuInSe_2$ were calculated for the first time. These results will guide us how to interface $CuInSe_2$ with other materials.

References

Rossmeissl NR. 1999. Presentation at the 218-th ACS national meeting, August 22-26, New Orleans.

Khaselev O and JA Turner. 1998. *Science* 280:425.

Development of Aqueous Based Sol-Gel Systems for Producing Durable Salt Waste Forms

Harry D. Smith, Liang Liang, Renee L. Russell, Gary L. Smith, Troy N. Terry, Brian J.J. Zelinski

Study Control Number: PN00031/1438

This project explores new materials for encapsulating and storing a wide range of wastes including salt wastes, soot, ashes, toxic metals, and other wastes containing low levels of radionuclides. One new material for this process is a sol-gel organic-inorganic hybrid, which has good mechanical integrity, chemical durability, low processing temperature, and is easy to fabricate.

Project Description

In the past, chemical approaches for the sol-gel synthesis of ceramics and polymer-ceramic (polyceram) hybrids have used organic solvents as the reaction medium with little consideration of their high volatility and flammability. However, alternative sol-gel processes in aqueous media may offer acceptable results without the need for hazardous solvents, precursors, or byproducts. To accomplish this, emulsions consisting of polymer and ceramic precursors suspended as micelles in water are substituted for the organic-based systems previously identified as being effective matrices for storing salt waste. Cross-linking and curing of the emulsions at low-temperatures produces mechanically robust waste forms able to accommodate high salt loadings. The leach resistance of these waste forms is strongly influenced by processing; where the use of faster acting cross-linking agents produce a more leach resistant material. Optimization of the cured emulsions should make them attractive alternatives to vitrification for low-level wastes, which would see broad use in many tank-related applications.

Background

Polycerams have been demonstrated to be viable candidates for use as waste forms for encapsulating salt wastes (Smith and Zelinski 1999). The major drawback to their use is the organic-based fabrication route with its associated flammability hazards. The development of water-based polymer-polyceram processing routes would facilitate the conversion of complex aqueous mixtures and low-level waste streams to stable waste forms using a simple, low temperature flowsheet. This capability represents a timely alternative to vitrification strategies which are currently experiencing unforeseen obstacles to their implementation. The process flowsheet for polyceram waste forms is projected to be much simpler and more cost-effective than vitrification and grouting approaches and so presents the DOE complex with a near-term, attractive alternative for quick retrieval and closure of the many sites containing large concentrations of salts, without generating secondary waste streams.

Polycerams based on the use of rubber (butadiene) as the organic component and silica as the ceramic component were first developed as candidate waste forms capable of stabilizing greater than 10 wt% salt waste through a joint collaboration between the Arizona Materials Laboratory of the University of Arizona and Pacific Northwest National Laboratory. These materials greatly exceeded the strength requirements set by the Mixed Waste Focus Area and exhibited leaching behavior sufficient to meet the Resource Conservation and Recovery Act Land Disposal Requirement standards. The current project builds on this experience by exploiting the chemical processing expertise at both participating institutions to develop waterborne emulsion systems for butadiene and other polymeric materials, in anticipation of eventual modifications to incorporate the ceramic component. The developed emulsions resemble latexes and consist of small, colloidal liquid droplets, or miscelles, suspended in water by surface charges introduced using a surfactant. With the addition of the appropriate cross-linking agent, the miscelles act like mini-reaction vessels in which the polymer precursors combine to form a tough, insoluble, chemically resistant material upon removal of water and cure.

Results and Accomplishments

Commercially available aqueous emulsion systems were screened for further development by assessing the strength, chemical durability, and leach resistance of samples cured as bulk pieces at various temperatures. The tested systems included: Styronal® ND 656, an emulsion of polystyrene/butadiene used as a general purpose offset binder; Dow Corning® 84 additive, a silicon emulsion used as an additive for inks and product finishes; Paranol® T-6300, a polyacrylic latex; and natural latex rubber emulsions from Hartex and Killian.

Promising chemical durability, as measured by weight gain during a 24-hour immersion in water, was shown by thestyrene/butadiene and acrylic latex samples when cured at 80°C. Natural latex samples have good resistance to water absorption but exhibit poor mechanical properties.

To test leach resistance, simulated waste (a mixture of 75% sodium nitrate [$NaNO_3$] and 25% sodium hydroxide [NaOH]) was mixed with the emulsion and the samples were dried and cured at 80°C. The dried waste form was placed in de-ionized water and the pH was monitored. As seen in Figure 1, both the styrene/butadiene and the acrylic latex samples effectively immobilize the salt waste. The pH of the waste form test solutions approach limiting values which are well below the baseline measured for an equivalent quantity of salt dissolved in water (the dashed line at pH = 12).

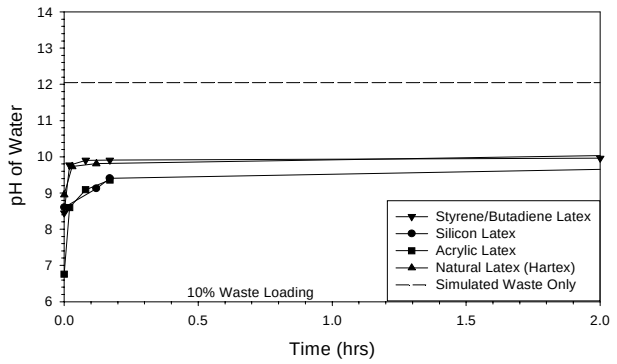

Figure 1. Leach resistance of cured samples of commercially available emulsions loaded with 10 wt% simulated salt waste

Multicomponent Stable Emulsions and Cured Materials

Multicomponent emulsions incorporating epoxy resin were developed to enhance the mechanical properties and chemical durability of the styrene/butadiene and the acrylic latex materials. Commercially available epoxy emulsions proved to be ineffective. In-house techniques for emulsifying epoxy resin, using a variety of surfactants, produced stable emulsions containing as much as 50% epoxy mixed with the polystyrene/butadiene and polyacrylic latex.

Addition of a suitable cross-linking agent caused the epoxy rings inside the emulsion particles to open up and react to form a tough plastic material. Materials cured at 80°C for 1 to 2 days are tough and hard and exhibit good chemical durability. To date, the best composites absorb only 6% water after immersion for several days.

Salt Loaded Waste Forms

The two-step flowsheet used to fabricate waste forms loaded with salt waste is shown in Figure 2. The epoxy resin is emulsified using sorbitan monopalmitate as a surfactant and mixed with either polystyrene/butadiene or polyacrylic emulsions. Sodium nitrate is added to the aqueous solution to simulate salt waste loading. Addition of the cross-linking agent and curing at 80°C produces a mechanically robust plastic matrix which surrounds the salt-rich regions of the material. The high degree of cross-linking makes the plastic matrix resistant to attack by organic solvents, as indicated by minimal material extraction during immersion in tetrahydrofuran. Mechanically sturdy waste forms loaded with as much as 60 wt% $NaNO_3$ can be made using the polyacrlic/epoxy resin emulsions. However, optical characterization suggests that the samples have phase separated at a coarse level into salt-rich and polymer-rich regions. Consequently, these materials do not display good leach resistance because of the inhomogeneous nature of the cured material.

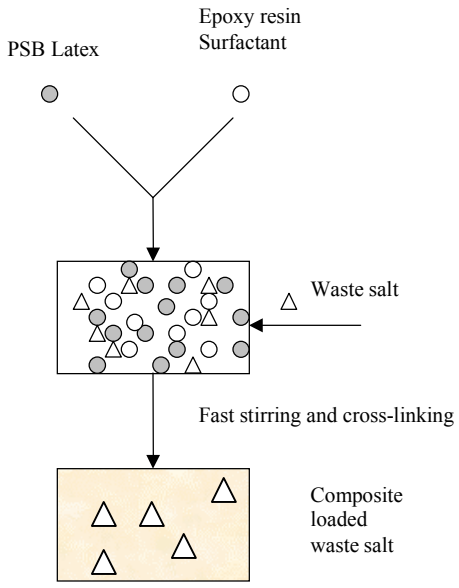

Figure 2. Process flowsheet for encapsulating salt waste in an aqueous-based polyceram waste form

An important result of this project was the discovery that use of a faster cross-linking agent results in improved homogeneity and a significant reduction in the leach rate. Figure 3 shows a waste form made from the polystyrene-butadiene/epoxy resin emulsion loaded with 20 wt% $NaNO_3$ using a fast acting cross-linking agent. This

monolith is mechanically robust and tough and is much more homogeneous than samples produced using a slower cross-linking agent.

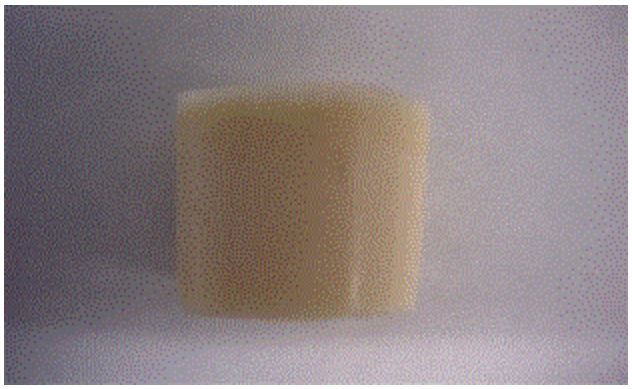

Figure 3. 50% polystyrene-butadiene/50% epoxy resin waste form loaded with 20 wt% $NaNO_3$ synthesized using a fast acting cross-linking agent

The impact of this improved homogeneity on leach resistance is shown in Figure 4, which shows the percentage of salt retained in samples loaded with 20 wt% $NaNO_3$ as a function of time immersed in water. Salt retention was calculated from the conductivity of the immersion solution. The data indicate that using a faster cross-linking agent (20 minutes versus several hours) reduces the leaching rate by a factor of about 50. Similar improvements in salt retention were measured for waste forms loaded with 30 and 40 wt% $NaNO_3$. It is speculated that speeding up the cross-linking rate counteracts a tendency for the emulsion to coarsen with time in the presence of the high salt concentration.

Summary and Conclusions

Commercially available styrene/butadiene and acrylic latex emulsions are good precursors for use in the aqueous fabrication of waste forms. When mixed with emulsified epoxy resins, they react to form monoliths with tough physical properties and good water resistance without generating significant volatile organic compound or flammability problems. The resulting waste forms can

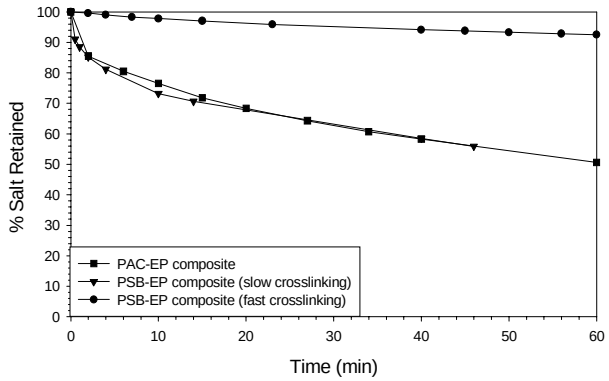

Figure 4. Leaching behavior of aqueous-based waste forms loaded with 20 wt% $NaNO_3$ measured as percentage of salt retained in the sample

physically incorporate large amounts of salt (up to 60% sodium nitrate) and their leach resistance is markedly improved by using fast acting cross-linking agents.

These results represent an important step in developing aqueous-based polyceram flowsheets. While preliminary in nature, they indicate that optimization of the current system and extension to systems which incorporate an inorganic or ceramic component should produce materials with very attractive characteristics for encapsulating and storing a wide variety of low-level wastes. Future work will establish the optimal performance of the current formulations through adjustment of solution pH, salt content and composition, surfactant, cross-linking initiator, curing time and temperature, and micelle concentration. Also, quantum improvements in performance will be sought by developing routes to incorporate an inorganic component to form polyceram waste forms.

Reference

Smith G and BJJ Zelinski. 1999. *Stabilize High Salt Content Waste Using Sol Gel Process.* OST Reference #2036, Mixed Waste Focus Area, Prepared for U.S. Department of Energy, Office of Environmental Management, Office of Science and Technology, Washington, D.C.

Development of In-Stack Reforming for Solid Oxide Fuel Cells

Olga A. Marina

Study Control Number: PN00033/1440

The goal of this project was to evaluate anode materials and designs for the solid oxide fuel cell operating on partially pre-reformed hydrocarbons and develop Pacific Northwest National Laboratory's capabilities to fabricate and test planar solid oxide fuel cells operating on partially pre-reformed hydrocarbon fuels.

Project Description

The primary objective of the project is to develop, fabricate, and test a thick porous anode that is compatible with other solid oxide fuel cell components, is coke resistant, exhibits excellent electrochemical properties, and has catalytic activity for internal reforming of methane. The development of such an electrode would allow solid oxide fuel cell stack operation on such inexpensive methane-containing fuels as natural gas or pre-reformed higher hydrocarbons, gasoline and diesel, provided they were desulfurized prior to use.

Introduction

For the solid oxide fuel cell with an yttria-stabilized zirconia electrolyte, a nickel-yttria-stabilized zirconia cermet is currently a favored anode material. State-of-the-art Ni-yttria-stabilized zirconia anodes exhibit polarization resistance as low as 30 and 60 $m\Omega cm^2$ at 1000 and 850°C, respectively, in moist hydrogen (Primdahl and Mogensen 1999) and are being used successfully by most developers for solid oxide fuel cells operating on the clean reformed fuel. However, solid oxide fuel cells require the anode be tolerant to fuels less expensive than hydrogen hydrocarbon fuels (natural gas, gasoline) without external reforming. The major disadvantage of the nickel cermet electrode arises from the promotion of competitive catalytic cracking of hydrocarbons leading to rapid carbon deposition. Steam reforming of methane at high steam-to-carbon ratio potentially prevents sooting of the anode, but causes intolerable temperature gradients throughout the anode due to the high reactivity of nickel toward this reaction. Moreover, nickel is unsusceptible to an oxidizing atmosphere and is readily poisoned by sulfur, which is always present in the feedstock. Also, sintering of nickel on prolonged operation is a potential problem for any type of fuel (van Berkel et al. 1993).

Application of internal reforming of methane in the solid oxide fuel cell offers several important advantages in comparison with external reforming: 1) no separate steam-reforming unit is needed; 2) smaller system size, lower equipment and operation costs, and lower capital investment are expected; 3) less cooling is required; 4) less steam is required; 5) more evenly distributed hydrogen load; and 6) higher methane conversion are achieved. However, internal reforming also poses some flaws: 1) intolerable temperature gradients, 2) sooting, 3) need to dilute fuel with steam in order to prevent carbon depositions, 4) recirculation and incomplete shift reaction adversely affect power generation, 5) gradual catalyst deactivation due to metal particle sintering, and 6) additional catalysts may be required.

Results and Accomplishments

A comprehensive literature review was conducted to search for a new anode material and improvements of the traditional nickel cermet anode capable of in-stack reforming. Two promising research directions have been identified: redox tolerant anode concept, and a new anode for internal reforming.

A multipurpose test rig was designed and built to enable anode materials testing in-house (see Figure 1). The test rig consisted of an electric furnace, a potentiostate, gas supplying/controlling system, and computer monitoring of anode and cathode temperatures. Electrolyte-supported cells can be tested both in hydrogen and methane by potentiometric and impedance spectroscopy techniques with the future possibility of simultaneous gas analyzing. PNNL's cell fabrication technique was adopted for manufacturing two- and three-electrode cells for the test in that rig.

Figure 1. Configuration of the testing setup

Summary and Conclusions

A comprehensive literature search was conducted. Promising research directions were identified, and testing equipment was designed and built.

References

Primdahl S and M Mogensen. 1999. *Proc. of the 6th Int. Solid Oxide Fuel Cell Symp.,* (S.C. Singhal, M. Dokiya, Eds.), PV 99-19. The Electrochemical Society, Inc., Pennington, New Jersey p. 530.

van Berkel FPF, FH van Heuveln, and JPP Huijsmans. 1993. *Solid State Ionics*, 72, 636.

Enzymatically Active Surfaces

Eric J. Ackerman

Study Control Number : PN98028/1274

Immobilized enzymes applied to microchannel applications represent a potential improvement in combining proteins with inorganic materials to create devices and materials with exciting new properties and capabilities. Our long-term objective is to use highly selective enzymes and protein ligands fused with micro- and nanotechnology to create microchannel reactors and sensors.

Project Description

Enzymes are known to catalyze more than 5000 diverse chemical reactions. Enzymatic reactions occur at ambient temperatures and pressures, thereby obviating the need for complex reaction vessels required by chemical catalysts. Our focus has been to develop the capability to build enzymatic microreactors and to demonstrate catalytic activity (as an example of enhanced microsystem performance through highly functional surfaces in microchannels). Building enzymatic microreactors requires 1) producing active enzymes, 2) linking the enzymes to suitable surfaces while retaining catalytic activity, and 3) integrating the immobilized enzymatic surface into a functional reactor. To develop our capability with enzymatic reactors, our initial choice in enzymes was microbial organophosphorous hydrolase, which inactivates nerve gas as well as some pesticides. No additional enzymes or cofactors are required for this reaction. The goal was to produce recombinant enzyme, immobilize it to a porous material without losing enzymatic activity, test for enhanced enzymatic stability as a consequence of immobilization, and assemble a prototype microchannel reactor. We succeeded in achieving all these goals, and production of a successful single-channel reactor represents a first step toward creating machines that mimic complex, multi-step chemical reaction pathways.

Introduction

The combination of enzymes with micro- and nanotechnology materials exploits the high specificity and reaction speed (thousands of reactions per second) of cellular nanomachines (enzymes) with the advantages of high mass transfer and reaction kinetics possible only through microchannel technology. Proteins outperform traditional inorganic catalysts because they lower the energy barrier for a specific reaction, thereby reducing the required conditions to ambient temperatures and pressures. Recombinant DNA technology enables the production of novel proteins with enhanced properties. Microchannel enzyme bioreactors provide an innovative, efficient technology to detect and/or destroy chemical and biological weapons. Enzymes combined with nanomaterials within microchannel devices are now possible because of recent advances in materials sciences, biotechnology, and microengineering. Thus, an extremely high density of fully functional protein becomes available to inactivate or bind substrate efficiently (e.g., chemical agents and biological pathogens) with high throughput.

The main drawback with enzymes and proteins is fragility. Enzyme stability can be enhanced by immobilization, but it is extremely difficult to immobilize high densities of enzyme while retaining catalytic activity. We have successfully developed methodologies to link an enzyme that is important in detecting and destroying chemical weapons to a nanomaterial. The enzyme, organophosphorous hydrolase, was immobilized at a density four times higher than previously known, and it retained full enzymatic activity. Our enzymatic material also exhibited markedly enhanced thermal and chemical stability over the free enzyme. Moreover, we successfully assembled the enzymatic material into a functioning microreactor prototype that exhibits high throughput and rapid reaction kinetics.

Approach

Our specific research objectives were to

- produce active recombinant organophosphorous hydrolase, and if necessary, introduce sequence changes to facilitate attachment to defined surfaces

- optimize attachment of organophosphorous hydrolase (without destroying its enzymatic activity) to defined surfaces containing high densities of enzyme-sized pores

- assemble immobilized organophosphorous hydrolase into improved microchannel reactors exhibiting high throughput and durability

- identify the practical limits of an organophosphorous hydrolase microchannel reactor in terms of efficiency, flow rate, pressure drop, and durability

- test immobilized organophosphorous hydrolase in traditional media and liquid foams to increase their utility for multiple applications.

Results and Accomplishments

This project consisted of the following four tasks:

1. identification of future suitable enzymes besides organophosphorous hydrolase

2. production of active enzyme via recombinant DNA technology

3. attach enzymes to porous, nano-surface without destroying enzymatic activity

4. assemble into a complete reactor and demonstrate functionality.

We subcloned the organophosphorous hydrolase gene into *E. coli* expression vectors and achieved ~2 to 4 g organophosphorous hydrolase per liter (Figure 1). (This is at least 100-fold higher expression than previously reported and approaches the highest levels obtainable.)

We attached organophosphorous hydrolase to derivatized silica containing enzyme-sized pores. Attachment stoichiometries of ~50 to 100 mg organophosphorous hydrolase per gram SAMMS retain 100% of enzyme activity. Furthermore, immobilized organophosphorous hydrolase better withstands treatment by acid, base, and lyophilization than organophosphorous hydrolase free in solution (Figure 2).

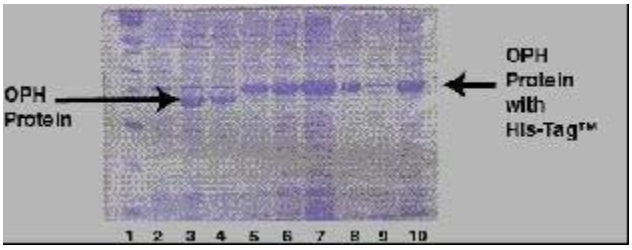

Figure 1. Sodium dodecylsulfate-polyacrylamide gel demonstrating high organophosphorous hydrolase expression (total *E. coli* lysates). Lane 1, molecular weight markers; 2, pET11a-organophosphorous hydrolase before induction; 3 and 4, pET11a- organophosphorous hydrolase clones after induction; 5 through 10, pET15b-organophosphorous hydrolase clones after induction.

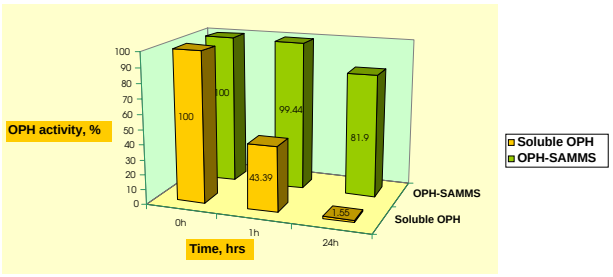

Figure 2. Enhanced stability of organophosphorous hydrolase immobilized to derivatized SAMMS. Organophosphorous hydrolase covalently linked to SAMMS and organophosphorous hydrolase at a comparable concentration in solution was tested at pH 5.0 for 1 and 24 hours. Similar experiments demonstrate enhanced stability to alkali treatment and lyophilization.

The organophosphorous hydrolase-SAMMS material has been fixed within a prototype microchannel reactor and shown to have excellent throughput, catalytic ability, and durability. Thus, our proof-of-principle experiments established that a useful enzyme can 1) be produced recombinantly at high yields, 2) be linked to suitable materials containing enzyme-sized pores, 3) retain its ability to inactivate a chemical weapon surrogate, 4) exhibit enhanced stability as a consequence of its immobilization, and 5) be used within a high throughput device that minimizes pressure drops but maximizes mass transfer to the catalytic surface.

Acknowledgment

We thank Jun Liu for making available his SAMMS material for testing.

High Power Density Solid Oxide Fuel Cell Stack Testing and Design

Larry A. Chick, Kerry D. Meinhardt, Gary D. Maupin

Study Control Number: PN00050/1457

The principal aim of this project was the development of concepts and processing methods for an advanced solid oxide fuel cell design. This project also enhanced our capabilities to test solid oxide fuel cell stacks.

Project Description

The main objective during the first year of this project was to set up a test stand and associated hardware and controls capable of running long-term, automated experiments on prototype solid oxide fuel cell stacks. The test stand is equipped to heat the solid oxide fuel cell stack in a furnace, to control air flow to the cathode and simulated reformat gas to the anode, and to control the current discharged from the stack, while measuring and recording the voltage. A series of stacks were tested during the year, including an all-ceramic design and a design that incorporates metal interconnects. Although the project goals were accomplished, this project was terminated mid-year because the scope was funded by two new DOE/FE projects, the Solid State Conversion Alliance (SECA) Core Technical Program and a CRADA project with Delphi as the industrial partner, Cooperative Development of Modular solid oxide fuel cell.

Introduction

Solid oxide fuel cells have been of interest for over 30 years because of their potential for high efficiencies and low environmental impact. Currently, solid oxide fuel cell technology is expensive, fragile, and from the perspective of manufacturing, impractical. There are numerous challenges with respect to making this technology cost-effective and attractive for wide application. Some of these challenges include lower temperature operation to incorporate metal interconnects (at the expense of power density), optimized designs that minimize the mechanical stress within the various ceramic components of the solid oxide fuel cell stack, the development of simple and practical gasoline/diesel reformers, and the incorporation of ceramic processing methods, which could lower the cost and complexity of fabrication.

Results and Accomplishments

A test stand was assembled (Figure 1) that will accommodate small stacks of one to several cells, with total active surface area up to a few hundred square centimeters. These are large enough to adequately test

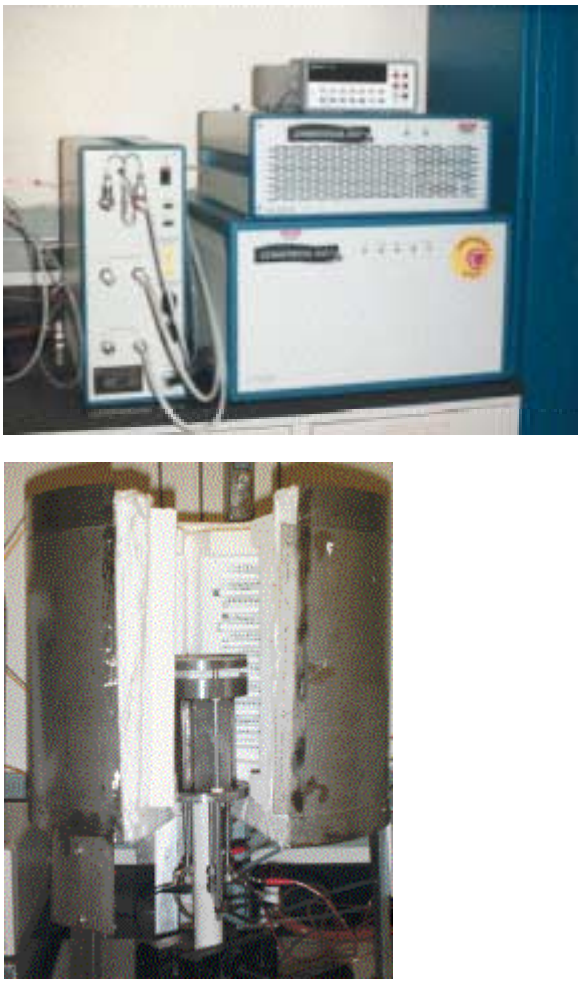

Figure 1. Top: Lynntech Fuel Cell Test System. Bottom: solid oxide fuel cell test stand, showing stainless steel hearthplate/gas header assembly in furnace.

cell performance, although not large enough to test thermal management issues. The test stand consists of a Lynntech Fuel Cell Test System (purchased with non-LDRD funding) and a stainless steel hearthplate/gas header assembly, which is situated in a furnace. The Lynntech apparatus controls gas mixing and flow as well as providing a controlled electrical load and data logger. The solid oxide fuel cell stack under test is placed between the top and bottom plates of the hearthplate.

One test was conducted by this project, on an all-ceramic solid oxide fuel cell design (Figure 2), which was operated at 1000°C. Several problems were encountered with this design, particularly with electrical contact through the stack and gas sealing. Designs have been improved since the work was transferred to follow-on DOE projects.

Summary and Conclusions

The project successfully completed purchase of equipment and setup of a solid oxide fuel cell test stand. One solid oxide fuel cell stack design was tested prior to terminating the LDRD project in favor of follow-on project funding.

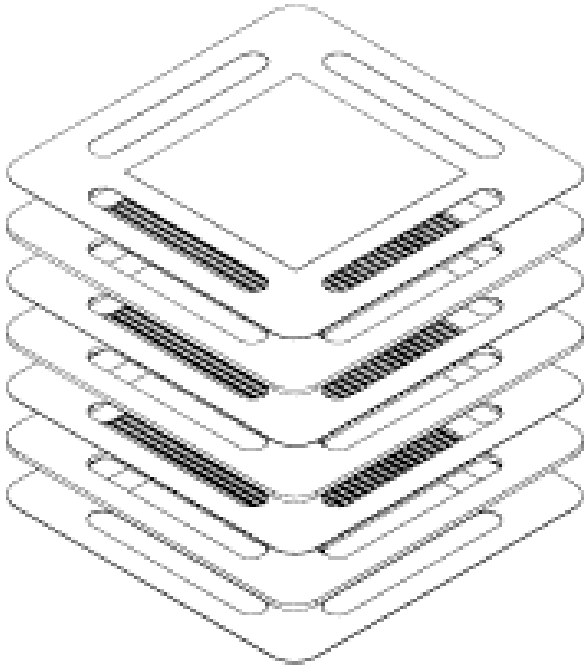

Figure 2. Exploded view drawing of all-ceramic, 1000°C solid oxide fuel cell stack that was tested in test stand.

Hybrid Plasma Process for Vacuum Deposition of Transparent Conductive Oxide Films

John D. Affinito

Study Control Number: PN00052/1459

Transparent conductive oxide films are needed for solar cell electrodes, flat panel display electrodes, solar-thermal control window films for buildings and greenhouses, and various military stealth applications. A new hybrid plasma process is being developed for vacuum deposition of transparent conductive oxide thin film coatins on low temperature substrates (below 70°C).

Project Description

A new plasma processing capability has been studied at Pacific Northwest National Laboratory. It involves a focused, two-phase project to develop and reduce to practice a hybrid plasma deposition process for the vacuum fabrication of high quality transparent conductive oxide coatings on low temperature substrates. Plasma diagnostic and process monitoring instrumentation may be integrated with the vacuum deposition chamber, process hardware, and a process monitoring and control strategy. For each phase, film quality may be assessed by a wide variety of ex situ optical, electrical, and surface science techniques. Hall and four-point probe measurements may be used to determine conductivity, carrier concentration, and mobility. Crystallinity may be determined by x-ray diffraction, scanning electron microscopy, atomic force microscopy, and step-height profilometry. The plasma frequency, free carrier collision time, and effective mass may be determined by optical transmission and reflectance measurements in the near ultraviolet, visible, near infrared, and infrared portions of the spectrum. Chemical composition of the coatings may be assessed by spectroscopy.

Introduction

Plasmas have a wide variety of materials processing and manufacturing applications. Some of the most attractive plasma processing technology applications include production of nano-particle powders, surface treatments, plasma-assisted vacuum thin film deposition, and plasma only reduced pressure-to-vacuum thin film deposition. Nano-particles have application in drug delivery, improved starting materials for sintering processes and high specific surface area materials for catalysis, wastewater treatment, and isotope separations. Plasma surface treatments may be used to improve wetting and adhesion of subsequent coatings or to provide controlled functionalization of surfaces for purposes of biocompatibility, sensing, and a variety of separation and treatment processes. Plasma, and plasma assisted, thin film deposition processes are increasingly being proven to provide higher density films with improved crystallinity at higher deposition rates than is attainable with conventional evaporation and sputtering techniques. One major advantage in the use of plasmas in surface treatments and coatings is the ability of the plasma to provide a great deal of surface energy with relatively modest bulk heating of the substrate being treated or coated. As well, in contrast to the use of ion beams, surface damage due to kinetic bombardment can be significantly reduced with plasmas since plasma sources do not rely on high voltage extraction of the ions to present the plasma to the substrate.

The hybrid plasma process for this study involves a close-couple output flux of a high density, forced flow, oxygen plasma source with the metal atom output flux from one or more radiatively heated precision thermal evaporation sources. The maximum deposition rate achievable, while maintaining high quality highly transparent and highly conductive transparent conductive oxide films, is dependent on both the degree and the intimacy of the flux mixing, as well as the degree of ionization of the mixed oxygen-metal atom flux. Metal atom source development is based on recent specialized, and proprietary sources for thermal vacuum evaporation deposition of lithium metal. The metal atom sources are designed and built as part of this work.

Several existing plasma sources must be tested using modified versions of hollow cathode, helical resonator, in-line hollow cathode plasma electron emitter sources, and a customized helical resonator with a pre-ignition stage. The plasma sources are evaluated with respect to film quality, deposition rate, and ease of integration with the metal atom sources.

In addition to design, fabrication, and integration of specialized plasma and metal atom sources, the achievement of the project goals requires development of

specialized process control sensors, methods, and algorithms. Process control sensors consist of a position-scannable Langmuir probe, multi-point optical plasma emission monitor, residual gas analysis mass spectrometer, and standard pressure, temperature, and quartz micro-balance sensors. These sensors measure, as a function of the position within the mixed oxygen-metal plasma, the relative concentrations of neutral and ionized atomic and molecular species, electron concentration and temperature substrate temperature, and absolute flux impingement rate per unit area onto the substrate. The in situ process monitoring and control strategy follows a method previously reduced to practice that permits calculation of film composition, from the plasma discharge characteristics alone, for reactively sputtered metal-oxides for compositions ranging all the way from pure metal to stoichiometric oxide (Affinito and Parsons 1984).

Eventually, the methods and results of this research should prove applicable to all transparent conductive oxide materials. Developing solar cell, solar-thermal control film and flat panel display applications are specific DOE program needs.

Results and Accomplishments

Since all of the transparent conductive oxide materials involve oxides of low melting point metals, this work focused on the most well-known transparent conductive oxide material, namely indium oxide and indium tin oxide. Preliminary studies were conducted on a generalized, hybrid, plasma processing method applicable to the deposition of In_2O_3 (indium oxide), SnO_2 (tin oxide), and ZnO (zinc oxide) transparent conductive oxide single-layer and multilayer thin films and films of these materials with various other dopant atoms added (like $In_2O_3[SnO_2]$ and $In_2O_3[ZnO]$). Particular emphasis was placed on films of $In_2O_3(SnO_2)$, known as indium tin oxide, since indium tin oxide is the most commonly used transparent conductive oxide material. Indium tin oxide is also the most thoroughly studied, and well understood, of the transparent conductive oxide materials. The process for ZnO was also studied, since it is the transparent conductive oxide of choice for application as a transparent electrode in solar cells. Since the conduction mechanisms, and related optical properties are similar for all of the transparent conductive oxide materials, the bulk of the experimental studies focused on In_2O_3 and indium tin oxide.

Vapor pressure-temperature calculations, which were proved accurate for thermal deposition of lithium films at the Laboratory, indicated that the to-be-developed thermal sources should produce 1000 Å thick transparent conductive oxide thin films at rates approximately 135 times as high as do the traditional transparent conductive oxide vacuum deposition techniques that employ conventional reactive sputtering.

This work was terminated early in the year when the principal investigator left the Laboratory to pursue other career opportunities.

Reference

Affinito JD and RR Parsons. 1984. "Mechanisms of voltage-controlled, reactive, planar magnetron sputtering of Al in Ar/N_2 and Ar/O_2 atmospheres." *J. Vac. Sci. Technol.,* A,2:1275-1284.

Microfabrication in Ceramic and Plastic Materials

Peter M. Martin, Dean W. Matson, Wendy D. Bennett

Study Control Number: PN98048/1294

Miniature devices have been engineered for a variety of special-purpose applications, such as hydrogen production, heating and cooling, and chemical separations. Microfabrication capabilities and methods are essential for developing devices used in microfluidic-based chemical processing and thermal control applications. This project was aimed at developing fabrication capabilities for polymer-based microfluidic applications.

Project Description

The purpose of this project is to build capabilities and methods for fabricating microfluidic devices for microchemical and thermal systems. Emphasis during the current fiscal year has been on laser micromachining and bonding processes, primarily for use in producing polymer-based microfluidic components. A major goal of the project was developing staff expertise on a through-mask excimer laser micromachining station procured with non-LDRD funding by the Laboratory during fiscal year 2000. We also investigated adhesives and methods for producing laminated microchannel plastic components. These capabilities were used extensively for other projects as well as a number of other programs within the Laboratory. We also designed and fabricated a plastic-based meso-scale electro-hydrodynamic fan intended to concentrate low-pressure gases.

Introduction

Development of microchemical and thermal systems requires the capability to produce laminated microchannel and other microfluidic components. Previous work in producing such laminated microfluidic devices has concentrated on using metals and ceramics because of the high-temperature capabilities of those materials. However, applications in which lower operating temperatures and/or reduced component weight are required make plastic materials attractive. Fabrication costs for microfluidic plastic components can also be considerably lower than for comparable metal or ceramic components where high temperature and vacuum bonding processes may be required. An additional attractive feature of plastic materials for microfabrication is that they are generally amenable to laser micromachining methods.

Approach

Laser micromachining is a powerful tool for producing micrometer to hundreds of micrometer-scale features in plastic components. A Resonetics Maestro Ultraviolet excimer laser micromachining station was purchased and evaluated for producing microchannels, micro-drilled hole arrays, and other microscale features in a variety of polymeric and other materials.

Bonding methods were evaluated for laminated plastic components to be used for a variety of applications and conditions. Adhesive application and bonding methods were evaluated, primarily for the production of multichannel laminates suitable for use in microfluidic heat exchangers and related components. Conditions necessary for heat bonding plastic components without distorting or destroying micromachined surface features were also evaluated.

Results and Accomplishments

Capabilities and limitations of the Resonetics Maestro laser micromachining station were established. The potential of the unit for machining individual holes and microhole arrays, microchannels, and other similar micromachined features were evaluated. The capability of the unit to machine a range of materials from thermoplastics and fluoropolymers to metals and ceramics was tested. Operators were able to spend the time to learn the programming software and develop the methods to import drawings and patterns to be machined from outside sources. Operators of the Resonetics system are now sufficiently familiar with the machine and its capabilities to use it effectively and efficiently as needed.

Plastic Laminate Bonding Processes Development

Methods were developed for bonding laminated plastic microchannel structures similar to those produced routinely using patterned metal shims. The laminated metal devices were formed using a high-temperature diffusion bonding process to fuse the assembled shims into a solid metal structure. Bonding of plastic shims must be accomplished at relatively low temperatures to 1) avoid thermal degradation or melting of the plastic material, and 2) avoid distortion of the completed device resulting from the high thermal expansion coefficients of many plastics (up to 10 times greater than the coefficients of typical metals). We developed a method for applying adhesives to patterned plastic shims. This method allowed the coated shims to be assembled into a stacked device, then the resin was thermally activated in a hot press to bond the assembly. An example of a series of microchannels produced in a plastic device using this method is shown in Figure 1. A procedure was also developed for bonding polycarbonate cover plates directly to polycarbonate chips containing laser machined microfluidic flow features without distorting the machined features and without the need for an adhesive layer. This allows the production of microchannels having uniform chemical properties on all surfaces of the enclosed channel.

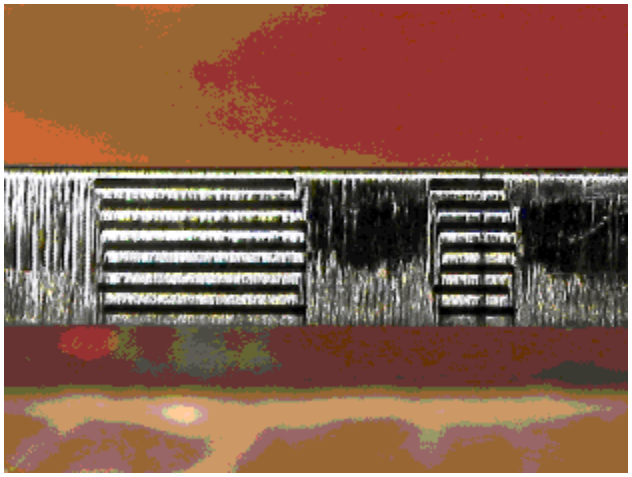

Figure 1. Cross section of microchannels in a bulk polyimide part produced by laminating 125 micron-thick laser-patterned polyimide shims. The channels are 125 µm high, 2.5 and 1.0 mm wide, and 28 mm long before being cross sectioned.

Design and Fabrication of Electro-Gas-Dynamic Fan

A meso-scale plastic-based device was designed that will allow slight pressurization of a gas feed (Figure 2). The device, using electro-hydrodynamic principles to produce and accelerate ionized gas species, moves nonionized gas by molecular collisions. The circular design of the device promotes an acceleration and pressurization of the gas, which is introduced at the center, as it moves toward the outer rim. We anticipate that such a device may have applications for space missions where low pressure background gases need to be collected and pressurized for chemical processing.

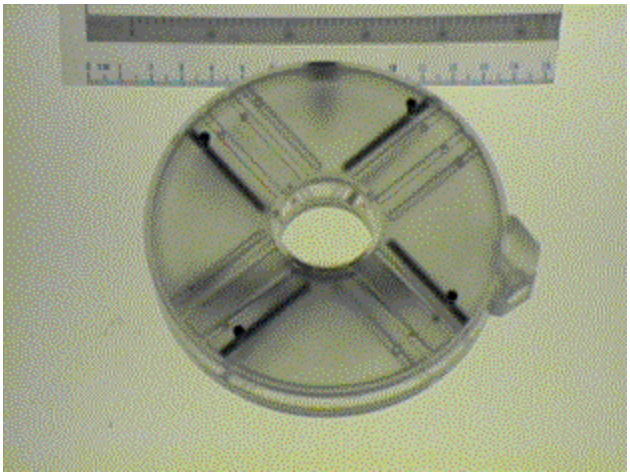

Figure 2. Meso-scale plastic electro-hydrodynamic fan

Summary and Conclusions

This project enhanced Pacific Northwest National Laboratory's in-house microfabrication capabilities by

- allowing development of laser micromachining expertise on the Resonetics Maestro micromachining station
- developing bonding technologies for laminated plastic devices
- developing a meso-scale electro-hydrodynamic fan.

Publications and Presentations

Martin PM, DW Matson, WD Bennett, and JW Johnston. 2000. "Thin film optical materials for use in micro-technology applications." Presented at the Society of Vacuum Coaters 43rd Annual Technical Conference, April 17-21, Denver. *In Proceedings of the Society of Vacuum Coaters 43rd Annual Technical Conference* (submitted).

Martin PM, DW Matson, WD Bennett, DC Stewart, and CC Bonham. 2000. "Laminated ceramic microfluidic components for microreactor applications." In *Topical Conference Proceedings of IMRET 4*, and presented at IMRET 4, 4th International Conference on Microreaction Technology, March 5-9, pp 410-415.

Matson DW, PM Martin, WD Bennett, JW Johnston, DC Stewart, and CC Bonham. 2000. "Sputtered coatings for microfluidic applications." Presented at the 46th International Symposium of the American Vacuum Society, October 25-29, Seattle. *Journal of Vacuum Science and Technology A--Vacuum, Surfaces and Films* 18(4):1677-1680.

Micropit Surface Technology Demonstration

John G. DeSteese, Zenen I. Antoniak

Study Control Number: PN98049/1295

Micropit surface technology has many applications. As a passive and durable means of increasing heat transfer, the concept is applicable generally to the thermal management design of many energy conversion and delivery systems.

Project Description

Surface modifications and associated miniature technology can modify thermal emissivity and provide other advantageous surface properties to essentially any device or product. The focus of this project was to demonstrate: 1) the potential emissivity enhancement of objects, and 2) the function of microstructures that can be activated to change surface emission and appearance characteristics. The basic elements of the concept were incorporated into test specimens giving them the ability to switch the thermal emissivity of their surfaces between high and low values, on command or under design conditions. These specimens were also used to show effects such as heat flow control, programmable thermal camouflage, and identification schemes at the proof-of-principle level.

Approach

We constructed test specimens to determine the effects of surface thermal emissivity enhancement. Test pieces were made from aluminum, 25-mm square and 5- to 7-mm thick. Simple test rigs were assembled to compare the emissivity of treated surfaces with otherwise identical, untreated surfaces. The test apparatus consisted of electrical heaters, thermocouples, and an infrared camera to permit evaluation of the test surfaces over a range of temperatures representing the potential application environment. Thermal emission observations recorded by the infrared camera and a computerized data logger were compared with thermocouple measurements and electrical power input to account for the energy balance during each test run. These measurements and the recorded infrared images allowed the net influence of the surface treatments to be distinguished from other heat flow components.

Results and Accomplishments

New aluminum test pieces were designed and fabricated to illustrate additional aspects of the concept. The first of the new samples was used to evaluate the optimal surface treatment producing the emissivity enhancement effect. The surface modification process was applied as a rectilinear matrix of treated areas with step-wise changes in the magnitude of the treatment. The test piece was heated in air through the temperature range 25ºC to 220ºC by a flat, insulated element attached to the unmodified rear surface of the aluminum block. As in previous work, an infrared camera was used to record radiant heat flux, temperatures, and surface images. Temperatures were confirmed and compared with indications provided by miniature thermocouples attached at various locations on the block. Surface emissivities were estimated and related to the degree of modification applied at each treatment site. This provided a measure of treatment effectiveness versus investment and the diminishing return point of the process.

A second test block was fabricated to investigate emissivity switching by microelements placed below the surface. This is in contrast with work reported previously that showed microstructures on and above the surface to be effective. Holes were drilled through the test block to provide access to the treated surface from the back of the block. Several devices were introduced through the holes and were energized in a manner that enabled them to interfere mechanically with the treated surface. The devices were activated by both mechanical linkages and air pressure to effectively turn the emissivity enhancement effect on and off. This was demonstrated for the array as a whole and for individual pixels.

Summary and Conclusions

We demonstrated emissivity enhancement, thermal camouflage, identification effects, and remote controlled emissivity switching. To meet cost objectives, work in this project was performed at a scale large enough to allow the use of conventional machine tools for the preparation of the test specimens.

We showed the proof-of-principle applicability of these concepts in the macro-scale world of everyday objects. In addition, several aspects and functions of smaller-scale mechanisms and devices were investigated and found effective, providing a basis of confidence that this concept can also be applied in the realm of microtechnology systems.

The Discovery of New Nanocrystalline Metal Oxide Materials

Yali Su, Scott H. Elder, Glenn Fryxell, John Fulton

Study Control Number: PN00084/1491

A new field of materials chemistry and physics is synthesis of nanocrystalline materials. Nanomaterials often exhibit novel properties that have potential applications in catalysis, electronics, optical-electronics, artificial photosynthesis, and nanoparticles (as biosensors). The synthetic route discovered as a result of this project is one of the first examples where stable nanocrystalline metal oxide powders have been synthesized and tailored to approximate size by controlling crystal growth.

Project Description

The focus of this project was to develop new molecule-by-molecule synthetic routes for preparing nanocrystalline metal oxide powders. The objective is to systematically control nanoparticle size and nanoarchitecture through a rational chemical approach, and determine how size quantization and unique nanostructural features influence photophysical and magnetic properties. We discovered a synthetic route to make stable nanocrystalline metal oxide powders with tailorable size and architecture. We studied and elucidated the reaction mechanism for the synthesis of nanoarchitectured transition metal oxides. We studied the thermochemical properties of nanoarchitectured transition metal oxides to fundamentally understand the key thermodynamic features that contribute to their stability. Our fundamental investigation enabled us to understand the critical nanoscopic issues that govern the photophysical and magnetic properties of nanoparticle metal oxides.

Introduction

Considering the technological importance of bulk metal oxides in catalysis, magnetic information storage, and electronics, it is surprising that very little synthetic work has been reported on nanocrystalline metal oxides (with the exception of titanium oxide [TiO_2]) with physical and chemical properties that can be tailored though size quantization and nanoarchitecturing. The primary difficulty faced in preparing nanocrytalline oxides of the early first, second, and third row transition metals is their propensity for crystal growth due to their large lattice energies. For example, these oxides have large heats of crystallization because of the electropositive nature of the early transition metals and the electronegative character of oxygen and their reactive hydroxylated surfaces.

Our approach was to prevent or retard crystal growth by chemically modifying the surface of nanocrytalline metal oxides as they are nucleated. Thus, we control crystallization using interfacial chemistry at the nanoscopic level. In addition, we expect the functionalization of nanoparticle surfaces to provide us with another viable route to tailor the physical and chemical properties of nanoparticle metal oxides since interfacial interactions tend to dominate such systems (i.e., a large fraction of the atoms are located at the surface/interface). To this end, we investigated a new class of solid-state metal oxide nanocomposite materials, whose crystallite size, chemical composition, surface structure, and electronic properties can be systematically modified through a molecular-chemistry synthetic approach.

Results and Accomplishments

We completed experiments to demonstrate our ability to synthesize core-shell TiO_2-(MoO_3) powders with tailorable nanoarchitecture and electronic properties. We elucidated the reaction mechanism of heterogeneous nucleation of nanocrystalline metal oxides from homogeneous micellar solutions. We also developed an understanding of the thermodynamic properties of nanoarchitectured metal oxides.

TiO_2-(MoO_3) Core-Shell Materials

We successfully synthesized a series of TiO_2-$(MoO_3)_x$ core-shell powders. This is the first example of a core-shell metal oxide system with tailorable nanoarchitecture and electronic properties. Figure 1 shows photoabsorption energy as a function of TiO_2-$(MoO_3)_x$ core-shell diameter and architecture.

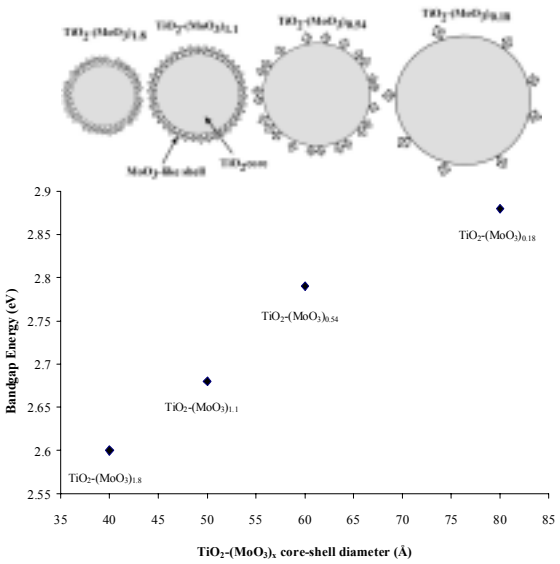

Figure 1. An idealized cross-section view of the TiO_2-$(MoO_3)_x$ core-shell particles and variation of band gap energy with core-shell diameter

Theoretical and experimental work on II-VI and III-V core-shell nanoparticle systems indicate that band gap Eg is a function of both size quantization effects and the relative composition of the core-shell particle (i.e., relative thickness of the core and shell) (Haus et al. 1993; Kortan et al. 1990). In the limiting case it is logical to expect the photoabsorption energy of a core-shell nanoparticle system to be greater than or equal to the smallest band gap material comprising the core-shell system.

In addition to this, a photoabsorption energy blue-shift, relative to the band gap energies of the bulk materials, is expected when the core-shell particle size is in the quantum regime (i.e., core diameter or shell thickness equal to or smaller than the Bohr radius of the valence/conduction band electron). For these reasons we expected the photoabsorption energy for the TiO_2-$(MoO_3)_x$ core-shell materials to be greater than 2.9 eV (E_g for MoO_3), and likely greater than 3.2 eV (Eg for TiO_2) due to the dominant size quantization effects, especially for TiO_2- $(MoO_3)_{1.8}$ where the core-shell size is approximately 40 Å. For example, a band gap energy blue-shift is observed for PNNL-1 (E_g 3.32 eV), which contains nanocrystalline TiO_2 with an average crystallite size of 25 to 30 Å (Elder et al. 1998). In contrast, the TiO_2- $(MoO_3)_x$ photoabsorption energies range from 2.88 to 2.60 eV, approximately equal to or lower in energy than bulk MoO_3, which places the photoabsorption energies of TiO_2- $(MoO_3)_{1.8}$ in the most intense region of the solar spectrum. The charge-transfer absorption properties exhibited by the TiO_2- $(MoO_3)_x$ compounds are due to charge-transfer processes at the semiconductor heterojunction that is established as a result of the chemical bonding between the TiO_2 core and the MoO_3 shell (Nozik and Memming 1996). This allows the core-shell wave functions to overlap at the interface giving rise to a heterojunction band structure. Figure 2 depicts the valence band/conduction band arrangement in TiO_2-$(MoO_3)_{1.8}$ after heterojunction formation. The lowest energy excitation is from the TiO_2 valence band to the MoO_3 conduction band, a core-shell charge transfer, and this energy closely matches what we measured for the photoabsorption energy of TiO_2 $(MoO_3)_{1.8}$ (Figure 1). This electronic transition is allowed due to the reduced symmetry at the core-shell interface. We attribute the regular decrease in band gap energy with increasing MoO_3 shell thickness to the reduced confinement of the electronic states in the shell as it evolves from isolated MoO_3 islands (TiO_2- $(MoO_3)_{0.18}$) to nearly two complete MoO_3 mono-layers (TiO_2- $(MoO_3)_{1.8}$).

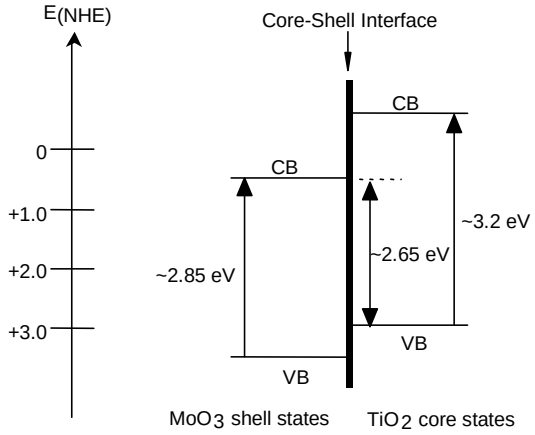

Figure 2. Arrangement of the TiO_2 core and MoO_3 shell valence bands (VB) and conduction bands (CB) for TiO_2-$(MoO_3)_{1.8}$ after heterojunction formation

Reaction Mechanism and Thermodynamic Properties

The TiO_2- $(MoO_3)_x$ core-shell powders are synthesized by co-nucleation of metal oxide clusters at the surface of surfactant micelles. Specifically, after $(NH_4)_2Ti(OH)_2(C_3H_4O_3)_2$ (Tyzor®, Dupont) was combined with cetyltrimethylammonium chloride (spherical micelles) and then diluted with water, nucleation of TiO_2 nanocrystallites occurred at the surface of flexible rod-like micelles—a heterogeneous nucleaton of nanocrystals from a homogeneous solution. The cross-section view shown in Figure 3 demonstrates the nucleation of TiO_2 nanocrystallites at the surface of cetyltrimethylammonium chloride micelles.

Removal of the organics (in Figure 3a) by heat treatment at 450°C will result in crystal growth. However, in the presence of metal oxide spacer, such as MoO_3 (Figure 3b), particle size and architectural features are stabilized due to interfacial diffusional barriers at the nanoscale. Figure 4 shows the entropies of nanoarchitectured materials and nanoparticle mechanical mixture relative to bulk rutile TiO_2 and bulk baddelyite ZrO_2. The two sets of entropy data are similar, and this indicates that the stability of the nanoarchitectured materials is due primarily to the presence of diffusion barriers (see Figure 3b).

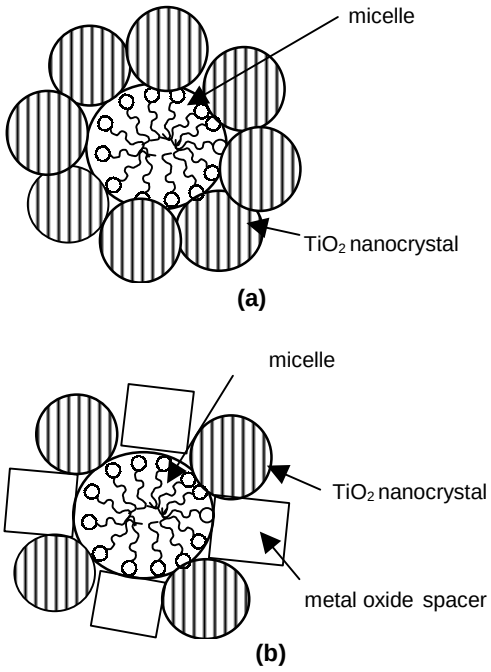

Figure 3. A cross-section view of nucleation of TiO_2 nanocrystallites at the surface of CTAC micelles: (a) TiO_2 only, (b) with metal oxide spacer

Summary and Conclusions

We have synthesized a series of solid-state nanocrystalline TiO_2- (MoO_3) core-shell materials from a novel surfactant micelle assisted reaction pathway. The structural and optical properties are governed by, and a direct result of, the intimate nanoarchitectured arrangement between the TiO_2 core and the MoO_3 shell. We also have a fundamental understanding of the reaction mechanism for the synthesis of nanoarchitectured materials and the underlying thermodynamics properties that gives rise to their stability. The TiO_2-(MoO_3) compounds are potentially a significant step in the right direction for understanding how to synthesize and design advanced metal oxides with fundamentally new physical and chemical properties.

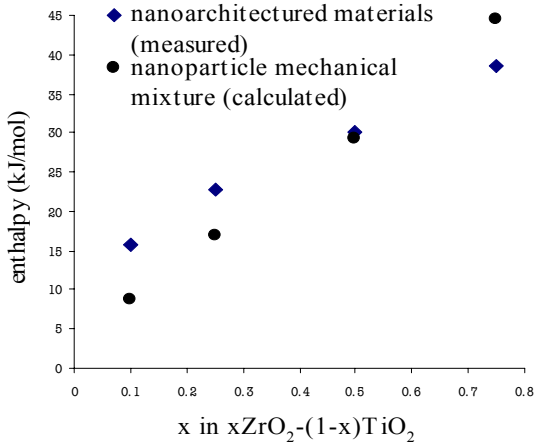

Figure 4. Comparison of entropies of nanoarchitectured materials and nanoparticle mechanical mixture relative to bulk rutile TiO_2 and bulk baddelyite ZrO_2

References

Haus JW, HS Shou, I Honma, and H Komiyama. 1993. "Quantum confinement in semiconductor heterostructure nanometer-size particles." *Phys. ReV.B 47*, 1359.

Kortan AR, et al. 1990. *J. Am. Chem. Soc. 112*, 1327.

Elder SH, Y Gao, X Li, J Liu, DE McCready, and CF Windisch, Jr. 1998. "Zirconia-stabilized 25-Å TiO_2 anatase crystallites in a mesoporous structure." *Chem. Mater.* 10, 3140.

Nozik AJ and R Memming. 1996. "Physical chemistry of semiconductor-liquid interfaces." *J. Phys. Chem.* 100, 13061.

Publication

Elder SH, FM Cot, Y Su, SM Heald, AM Tyryshkin, MK Bowman, Y Gao, AG Joly, ML Balmer, AC Kolwaite, KA Magrini, and DM Blake. 2000. "The discovery and study of nanocrystalline TiO_2-(MoO3) core-shell materials." *J. Am. Chem. Soc.* 122:5138-5146.

Ultrathin Solid Oxide Fuel Cell Fabrication

Peter M. Martin, Dean W. Matson, Kerry Meinhardt

Study Control Number: PN00089/1496

The development of ultrathin electrolyte layers for use in solid oxide fuel cells may allow both a significant reduction in operating temperature and improvement in power output compared with cells produced using conventional ceramic processing methods.

Project Description

The purpose of this project was to demonstrate the production and application of a vapor-deposited ultrathin electrolyte layer for solid oxide fuel cells. Ultrathin electrolyte layers are predicted to allow operation of solid oxide fuel cell units at lower temperatures than are possible using the thicker elecrolyte layers produced using conventional ceramic processed technology. Thin (1 to10 micrometer) yttria-stabilized zirconia (YSZ) coatings were deposited onto nickel-zirconia cermet electrodes using reactive sputtering from metal alloy targets. We have shown that, despite irregular surfaces on the underlying cermet substrates, dense, defect-free yttria-stabilized zirconia electrolyte layers can be produced. The microstructure and crystallographic phase of the yttria-stabilized zirconia electrolyte were related to the sputtering parameters used to produce the coatings.

Introduction

Solid oxide fuel cells provide a highly efficient means to convert fossil fuels to electricity. This is produced by migration of oxygen ions from a porous airside electrode through a solid gas impermeable electrolyte to a porous fuel-side electrode. The maximum power of these devices is limited by the resistance of the electrolyte to oxygen ion permeation and electrode/electrolyte interfacial reaction kinetics. In most solid oxide fuel cell designs, the electrolyte layer ranges in thickness from 40 to 200 microns. The maximum power is less than 400 milliwatts per square centimeter when operated at 1000°C. Recent work has shown that solid oxide fuel cells made with thin electrolyte layers (~10 microns) that were produced using colloidal processing methods may allow both a reduction in operating temperature and an increase in power to greater than 1 watt per square centimeter. Further reduction in the thickness of the electrolyte layers that were produced using colloidal processes is considered impractical without introducing pinholes and other defects detrimental to solid oxide fuel cells operation. Vapor deposition methods available at PNNL allow the production of very thin (micrometer scale) electrolyte layers that will permit solid oxide fuel cells operating temperatures to be lowered by hundreds of degrees while maintaining high power outputs.

Approach

This project focused on the production of thin yttria-stabilized zirconia electrolyte layers using reactive magnetron sputtering. The process involves removal of atomic species from an yttrium/zirconium metal alloy target by bombarding it with ionized argon atoms in the presence of a background oxygen concentration. The oxygen atoms combine with the atomized metal to produce oxide coatings on substrates placed in the path of the sputtered material. To produce yttria-stabilized zirconia that is stable at temperatures required to operate fuel cells, the yttria-stabilized zirconia deposit was made with an yttrium doping at an elevated temperature. The yttria-stabilized zirconia thin film electrodes formed in this study were produced from yttrium/zirconium targets containing either 7 or 12 atom percent yttrium and with the substrates heated to temperatures of up to 600°C during the deposits.

The substrates used for the yttria-stabilized zirconia electrolyte deposit were thin wafers of a porous nickel/zirconia cermet that was produced using conventional tape casting methods. The cermet layer acted both as a support for the yttria-stabilized zirconia electrolyte layer and as the fuel-side electrode for the fuel cell. The anodes were pre-sintered in air at 1350°C for 1 hour. The porous air-side electrode of strontium-doped lanthanum manganite was applied to the exposed face of the yttria-stabilized zirconia electrolyte using a conventional ceramic screen-printing process after the electrolyte deposition was completed. The cathode was sintered on at 1200°C. A platinum grid was screen printed and sintered on each electrode as a current collector. Platinum meshes with attached current and voltage leads were sintered to the platinum current collectors.

The testing setup consisted of a single alumina tube with the anode current and voltage leads down the center. The cathode electrical connections were made on the outside**.** The cell was cemented to the tube with Aremco cement to provide a gas seal. The fuel gas mixture of hydrogen with 3% water flowed inside the tube while the cathode was exposed to ambient air. The arrangement was placed inside a Kanthol tube furnace and heated to 800°C where measurements were taken with a test rig from Arbin Instruments.

Results and Accomplishments

Development of Yttria-Stabilized Zirconia Electrolyte Sputtering Conditions

The sputtering conditions required to produce dense, phase-stable yttria-stabilized zirconia electrolyte layers suitable for solid oxide fuel cell applications were established. Low temperature deposits in which the cermet substrate was not heated tended to produce an orthorhombic crystal structure in the yttria-stabilized zirconia deposit. This phase is unstable at temperatures required for subsequent processing of the electrodes and power output testing of the solid oxide fuel cell device (up to 1250°C). We found that at a 600°C deposit temperature, a tetragonal yttria-stabilized zirconia coating structure could be attained that was stable through electrode processing and cell operation. Both the 7 and 12 atom percent yttrium targets produced yttria-stabilized zirconia coatings with the tetragonal phase at 600°C.

Microstructure of the yttria-stabilized zirconia electrolyte layer was also deemed a potentially important variable for solid oxide fuel cell operation. The microstructures of sputtered coatings are known to be related to a number of factors, including the substrate surface characteristics, deposition temperature, and sputtering gas pressure. An example of yttria-stabilized zirconia microstructure differences resulting from variations in substrate surface smoothness is shown in Figure 1. While the deposition temperature variable was restricted due to the phase considerations noted, experimental efforts were made to optimize gas pressure and substrate properties to achieve dense electrolyte coatings. Low sputtering pressures ($\leq$ 2.5 m torr) were found to optimize production of dense coatings with minimal columnar structure. Similarly, during the course of this study, the processing parameters used to produce the cermet substrates were optimized to produce ceramic disks having a minimal surface texture. Optimization of these conditions allowed the production of highly dense yttria-stabilized zirconia microstructures. Figure 2 shows examples of high density ultrathin yttria-stabilized zirconia electrode layers produced under optimal sputtering conditions.

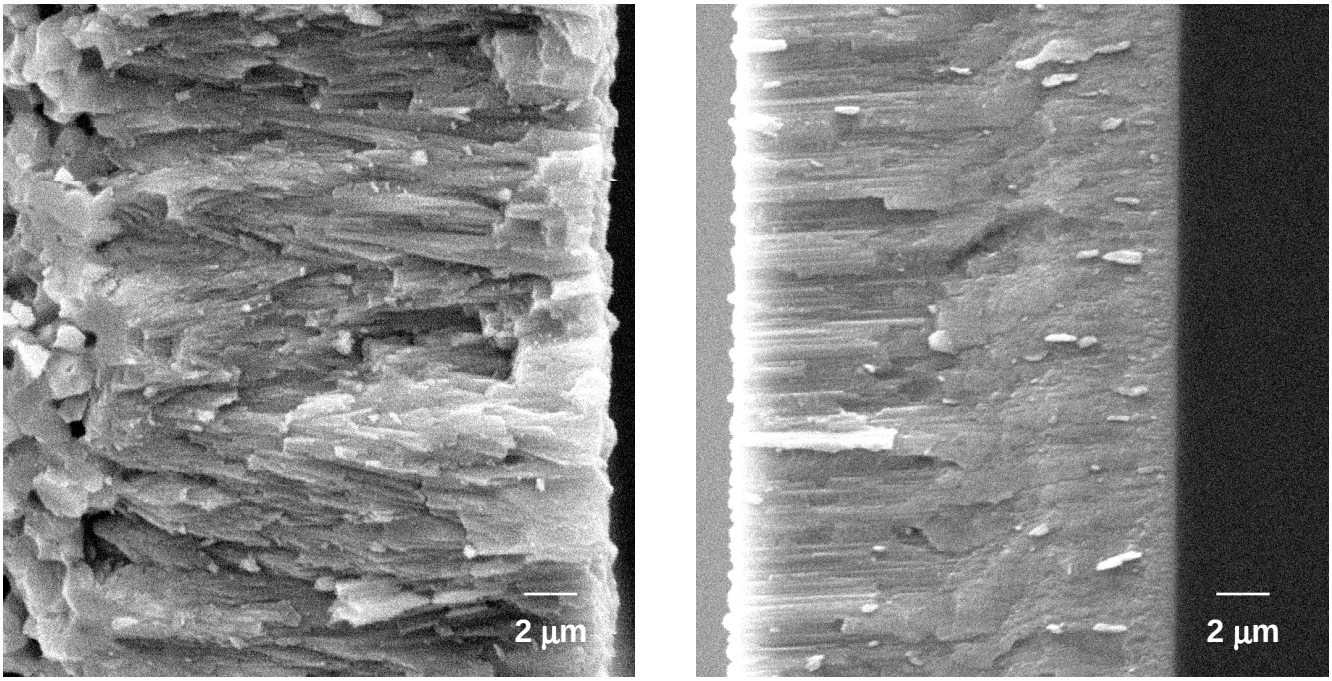

Figure 1. Effect of substrate surface texture on the microstructure of sputtered yttria-stabilized zirconia coating. The coating on the left was produced on a porous cerment substrate having an irregular surface. The coating on the right was produced in the same coating run, but on a smooth glass substrate.

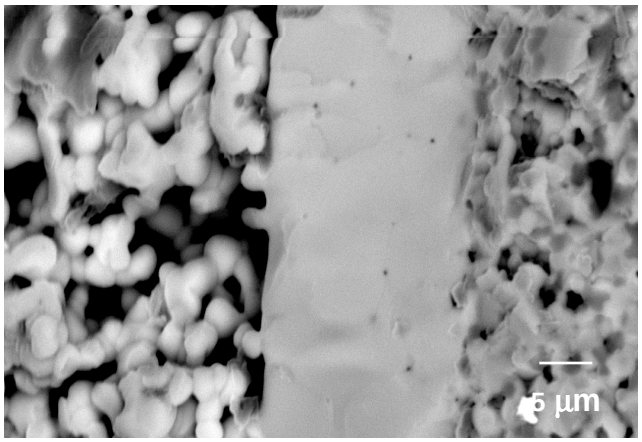

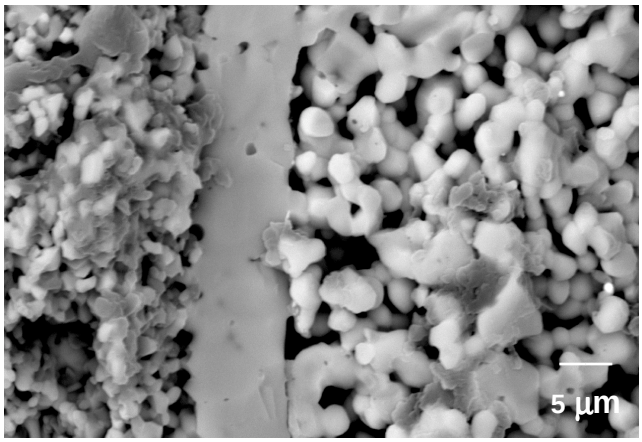

Figure 2. Scanning electron micrographs of representative dense sputtered yttria-stabilized zirconia electrolyte layers incorporated into fuel cell stacks. The less porous electrode layers are the nickel/zirconia cermet substrates on which the sputtered yttria-stabilized zirconia was deposited. The air-side (high porosity) electrodes were screen printed on the yttria-stabilized zirconia after its deposit.

Ultrathin Electrolyte Test Results

The initial cell test was conducted at 800°C with 200 sccm flow of hydrogen with 3% water. The plot of cell voltage and power as a function of current density is shown in Figure 3. The open circuit voltage was near 1 volt, which is near the theoretical value of 1.1 indicating a dense, pore-free electrolyte. The slightly lower than theoretical open circuit voltage is probably due to a leaky cement seal. The cell performance is lower than expected. At 800°C the losses of the 5 µm electrolyte would not be noticeable, and therefore the low performance is probably due to poor electrodes. An improved cathode of strontium-doped lanthanum ferrite showed an increase in performance over the initial manganite cathode. The performance of the improved cell is shown in Figure 4. Additional performance improvement may be gained through the modification of the anode electrode.

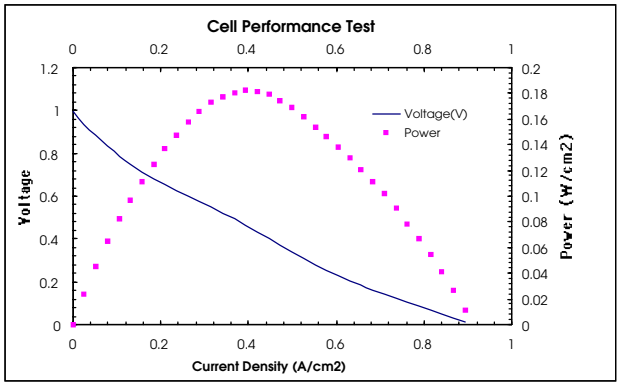

Figure 3. The plot of cell voltage and power as a function of current density

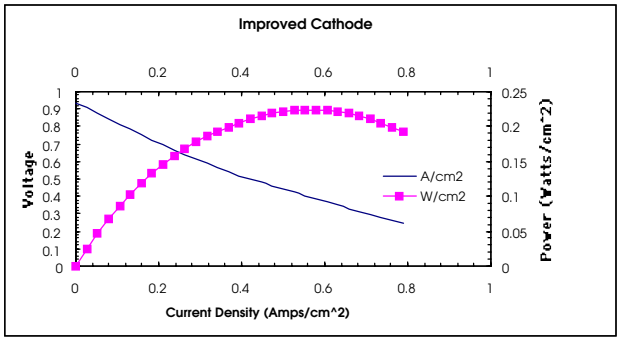

Figure 4. The plot of cell performance with improved cathode

Summary and Conclusions

Ultrathin (less than 10 µm) yttria-stabilized zirconia films were produced by reactive sputtering for testing as electrolyte layers in solid oxide fuel cells applications. By depositing the electrolyte films at elevated temperatures (600°C) and low pressures (≤ 2.5 m torr), high-density zirconia coatings having a tetragonal structure were produced. Preliminary tests of solid oxide fuel cells incorporating the sputtered electrolyte coatings indicated less than optimal performance, although this was probably related to electrode rather than electrolyte issues.

Micro/Nano Technology

Detailed Investigations on Hydrogen Formation by the Photocatalytic Splitting of Water

Gregory S. Herman, Michael A. Henderson, Charles H.F. Peden

Study Control Number: PN99012/1340

Titanium oxide (TiO_2) materials have shown substantial promise for applications is such areas as water treatment/purification and reduction of automotive emissions. However, in order to achieve this potential, a better fundamental understanding of these materials is required. In particular, studies of the anatase phase of TiO_2 are needed. The purpose of this project is to conduct such studies. The project is directly relevant to DOE's evolving efforts to encourage research in nanoscience and technology.

Project Description

Our program addresses some of the most poorly understood details of the photocatalytic splitting of water over TiO_2 (anatase) surfaces. These include the nature of the active catalyst surface site where the charge (electrons and holes) is trapped subsequent to electron transfer with water, and the origin of structure sensitivity in this catalytic reaction. In particular, we have focused our efforts toward investigating the anatase phase of TiO_2, which has been found to be the most photoreactive. The epitaxial growth of anatase thin films has allowed for a detailed comparison with commercially available rutile single-crystal surfaces. Although considerable work has previously been done on powders, a consistent methodology involving well-characterized single-crystal substrates has not yet been undertaken to determine the mechanism and structural specificity of photocatalytic hydrogen production from water. Furthermore, no experimental work to date addresses the detailed structure of anatase surfaces, and only theoretical methods have proposed the adsorption site of water on model anatase surfaces.

Results and Accomplishments

We have used anatase thin films grown at our Laboratory that have been bulk characterized with x-ray diffraction. These measurements indicate that the films grow as anatase on strontium titanate in a (001) orientation and on anatase mineral surfaces in a (101) orientation. The x-ray diffraction measurements are essentially a bulk structure probe. To address the available adsorption sites for water on the anatase, a more surface-sensitive probe is required. The effort to investigate the detailed geometric and electronic surface structure of these films has taken advantage of instrumentation and experimental techniques available in the William R. Wiley Environmental Molecular Sciences Laboratory (EMSL), and instrumentation in collaboration with the groups of Prof. Juerg Osterwalder at the University of Zurich, Prof. Charles Fadley at Lawrence Berkeley National Laboratory, and Prof. Ulrike Diebold at Tulane University, and theoretical calculations performed by Prof. Annabella Selloni at Princeton University.

Film Growth

After considerable effort, we have been able to grow pure epitaxial anatase films with both (001) and (101) surface orientations in the EMSL. We have found that the (001) surface is reconstructed, even during growth, with a (1x4) periodicity. The growth of the (101) surface was an important step forward since anatase powder samples are found to have primarily {101} surfaces exposed. Experiments on these (101) surfaces indicate that they are bulk-like terminated with a (1x1) periodicity. In Figure 1 we show reflection high-energy electron diffraction patterns obtained from anatase (001) and (101). The streaks indicate a smooth surface with a good epitaxial relationship with the substrate. Furthermore, both of these anatase surfaces appear to be resistant to surface reduction after heating to high temperatures in vacuum (up to 950 K) as indicated by x-ray photoelectron spectroscopy. Rutile surfaces will generally form Ti3+ states at the surface under similar annealing conditions, whereas anatase was only in the Ti4+ state.

X-Ray Photoelectron Diffraction

With the group at the University of Zurich we have used x-ray photoelectron diffraction to confirm that the top 5 to 100 Å in the surface region of the anatase (001) film is in fact anatase and does not convert to rutile (the more stable polymorph). There have been discrepancies in the literature whether rutile layers form on top of anatase particles, or whether anatase is stable under ultrahigh vacuum conditions (i.e., where most of our preliminary

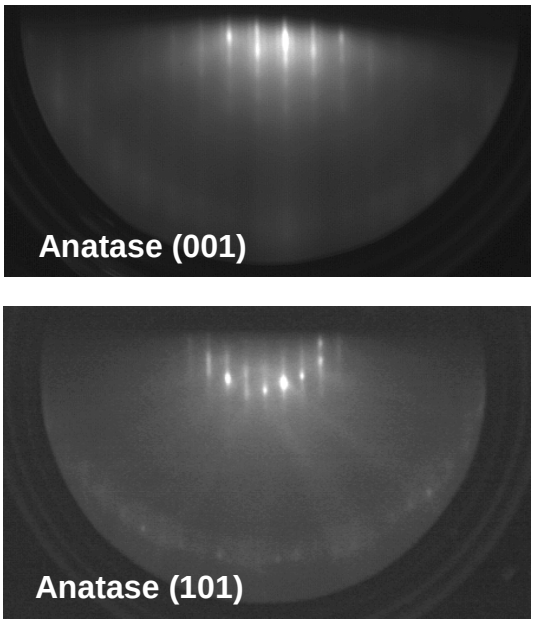

Figure 1. RHEED pattern obtained at 15 keV for an anatase (001) film (top) and for an anatase (101) film (bottom)

studies will be performed to better understand the interaction water). A comparison between experiment and single-scattering calculations gave good agreement for a model with a bulk-like anatase termination. These are the first measurements, with atomic specificity, that indicate anatase is stable under ultrahigh vacuum conditions. Furthermore, a direct comparison was made between rutile and anatase using x-ray photoelectron spectroscopy and it was found that the core-level binding energies were identical for the polymorphs for Ti 2p and O 1s emission.

Mass-Spectroscopy of Recoiled Ions

On further processing of the anatase (001) thin films, it was found that the surface undergoes a (1x4) reconstruction, as opposed to the expected (1x1) bulk termination. The low-energy electron diffraction pattern is shown in Figure 2 with the unit cells for a (1x1) termination and the two domain (1x4) termination indicated. This reconstruction was found to be very stable and has not previously been reported. We have used angle-resolved mass spectroscopy of recoiled ions (AR-MSRI), a technique that has recently been developed in the EMSL, to better understand the surface reconstruction, and the influence it may have on the photocatalytic hydrogen production from water. A comparison between our experimental data with theoretical simulations for over 30 reconstructions results in a best fit for a model which microfacets to expose lower energy {013} surface planes. It is clearly evident

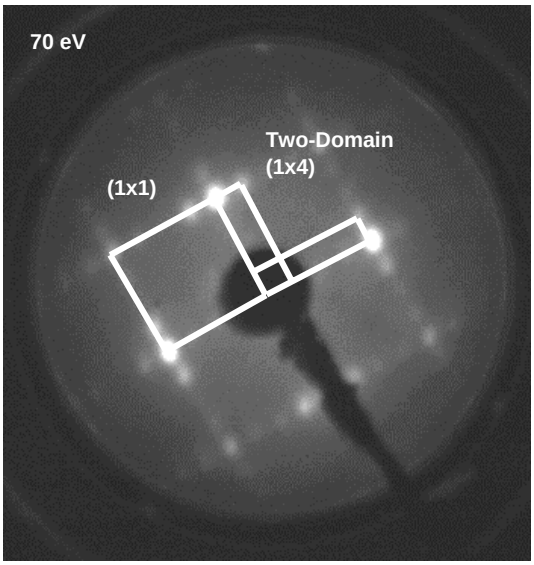

Figure 2. LEED pattern obtained for an anatase (001) film grown on $SrTiO_3$ (001). Note the presence of a two-domain (1x4) reconstruction.

that to fully understand the interaction of water with anatase surfaces it is essential to experimentally determine the detailed atomic coordinates of the surface. For example, prior theoretical studies on the interaction of water with anatase used a bulk terminated (1x1) anatase surface which apparently is not stable. We have also performed the AR-MSRI experiments on the anatase (101) surface. Preliminary results suggest that there are surface relaxations in the very top layers. Further analysis of the data is currently under way. Total energy minimization calculations are currently being performed by the group from PU to complement our studies.

Synchrotron Radiation Studies

With the group at Lawrence Berkeley National Laboratory, we have performed experiments to measure the electronic structure of anatase. We have measured the x-ray absorption spectra, x-ray photoelectron diffraction data, and high-energy resolution x-ray photoelectron spectra for both anatase and rutile surfaces. These experiments were performed at the Advanced Light Source in Berkeley, California, on beamline 9.3.2. The data confirm that the surface of anatase is fully oxidized, and the x-ray photoelectron diffraction data are currently being analyzed.

Scanning Tunneling Microscopy

Recently, we have performed scanning tunneling microscopy on the anatase (101) surface in collaboration with the group at Tulane University. The surface has several different types of defects. This work has also

identified low energy step structures that have not been investigated theoretically or experimentally. Much of the chemistry that occurs on surfaces may be tied to step edges due to the under-coordination of the ions.

Interaction with Water

Both the anatase (001) and (101) surfaces are under investigation to better understand their respective interaction with water. The (001) surface was found to dissociate water using high-resolution electron energy loss spectroscopy. Characteristic vibrational states for dissociated water are observed for the water desorption state at 305 K. Essentially, four desorption states are observed for water, and three of those states are indicated in Figure 3. They correspond to multilayer water (not shown at 160 K), water hydrogen bound to anion sites (185 K), water bound to cation sites (255 K), and dissociated water (305 K). Currently we are studying the interaction of water with the (101) surface as well. We find that there is no dissociation of water on this surface, and that the desorption state related to water bound to anions and cations at the surface is very similar to that observed for the (001) surface.

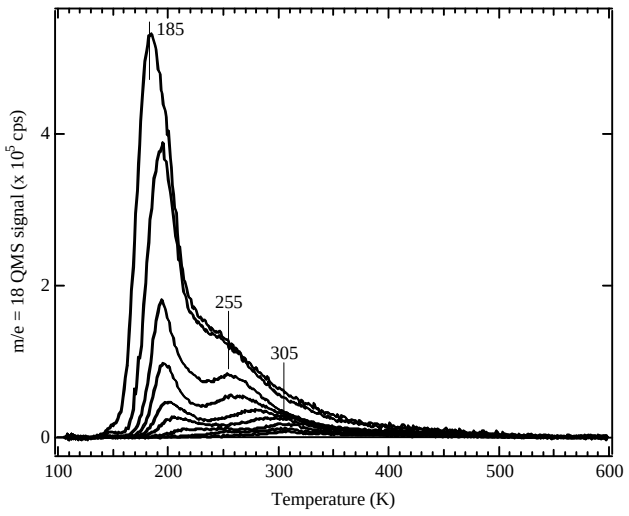

Figure 3. TPD spectra for water obtained from the anatase (001) – (1x4) surface. The desorption temperatures are indicated.

Summary and Conclusions

Our ability to grow epitaxial thin films of anatase has provided a unique opportunity to investigate the role of electronic and geometric structure effects in regards to TiO_2 photocatalysts. To date, these studies have provided new and unique information that will help clarify the structural sensitivity of the photocatalytic production of hydrogen from water. Both the geometric and electronic structure has been investigated in detail. Furthermore, we are initiating the first studies that investigate the interaction of water with well-characterized anatase single crystalline surfaces. We have found that the (001) and (101) surfaces behave differently with respect to water, where the (001) surface dissociates water and the (101) surfaces do not.

Publications and Presentations

Gan S, Y Liang, DR Baer, MR Sievers, GS Herman, and CHF Peden. "The effect of Pt nanocluster size and surface structure upon CO desorption chemistry on Pt supported TiO_2(110)." *Journal of Physical Chemistry B* (submitted).

Hebenstreit W, N Ruzycki, GS Herman, Y Gao, and U Diebold. "Scanning tunneling microscopy investigation of the TiO_2 anatase (101) surface." Physical Review Letters (submitted).

Herman GS and Y Gao. "Growth of epitaxial anatase (001) and (101) films." *Thin Solid Films* (submitted).

Herman GS, Y Gao, TT Tran, and J Osterwalder. 2000. "X-ray photoelectron diffraction study of an anatase thin film: TiO_2(001)." *Surface Science* 447:201-211.

Herman GS, MR Sievers, and Y Gao. 2000. "Structure determination of the two-domain (1x4) anatase TiO_2(001) surface." *Physical Review Letters* 84:3354-3357.

Perkins CL, MA Henderson, DE McCready, and GS Herman. "Comment to electron source in photoinduced hydrogen production on Pt-supported TiO_2 particles." *Journal of Physical Chemistry B* (submitted).

Henderson MA, GS Herman, and U Diebold. September 2000. "Measurement of the surface bandgaps of TiO_2 polymorphs using electron energy loss spectroscopy." Pacific Northwest American Vacuum Society Symposium, Forest Grove, Oregon.

Herman GS. January 2000. "Structural characterization of the anatase TiO_2(001) surface." Stanford University, Stanford, California (invited).

Herman GS. May 2000. "Structural characterization of the anatase TiO_2(001) surface." University of Washington, Seattle, Washington (invited).

Herman GS, M Hoesch, and J Osterwalder. September 2000. "Character of gap states associated with oxygen defects on TiO_2(110)." Pacific Northwest American Vacuum Society Symposium, Forest Grove, Oregon.

Herman GS, TT Tran, Y Gao, J Osterwalder, F Baumberger, and T Greber. July 1999. "Anatase-TiO_2(001)-a structural investigation by x-ray photoelectron diffraction." 6th International Conference on the Structure of Surfaces, Vancouver, Canada.

Osterwalder J, F Baumberger, T Greber, GS Herman, TT Tran, and Y Gao. July 1999. "Surface structure and crystallinity of CVD grown anatase-TiO_2(001) by x-ray photoelectron diffraction." 1st Annual EMSL User Meeting, Richland, Washington.

Sievers MR, Y Gao, and GS Herman. July 1999. "Surface structure of anatase TiO_2(001) determined by mass-spectroscopy of recoiled ions." 1st Annual EMSL User Meeting, Richland, Washington.

Sievers MR, Y Gao, and GS Herman. July 1999. "Surface characterization of anatase TiO_2(001) films." 6th International Conference on the Structure of Surfaces, Vancouver, Canada.

Sievers MR and GS Herman. October 1999. "Surface structure determinations by angle-resolved mass-spectroscopy of recoiled ions." Symposium of the American Vacuum Society, Seattle, Washington.

Acknowledgments

Dr. Mike Sievers was hired as a postdoctoral fellow for this program and has been involved with obtaining and analyzing the mass spectroscopy of recoiled ion and valence-band mapping results.

Development of Novel Photo-Catalysts Using Interfacial Engineering

Yong Liang, John L. Daschbach, Scott A. Chambers, Yali Su, Yong Wang, H. Luo

Study Control Number: PN98023/1269

This project focuses on developing novel photocatalysts with enhanced efficiency and using these photocatalysts to produce clean fuels with zero carbon emission.

Project Description

The focus of this project is to use a novel approach to enhance the performance of photocatalysts. The project is designed to address two issues critical to photocatalyst development: 1) increasing the efficiency of photocatalysts, and 2) enabling the use of visible light to facilitate reactions on catalysts. We are using interfacial engineering to tailor the catalysts to simultaneously achieve these properties. We conducted two main tasks including 1) fabrication and characterization of molecular beam epitaxial grown Cu_2O quantum-dot based heterostructures, and 2) synthesis and reaction tests of engineered nano-clusters fabricated through chemical routes.

Introduction

Photocatalysis has become increasingly important in chemical processes. It can be used to produce fuel with zero carbon emission, such as hydrogen production via photolysis of water. It can also be used to reduce CO_2 via activation and methanation processes. Although the potential of photocatalysis is tremendous, the use of photocatalysis in chemical processing has been limited, due largely to low efficiency and requirement of an ultraviolet light source. This project proposes to use interfacial engineering to address these two issues simultaneously.

Although interfacial engineering has been widely used in microelectronic applications, use of such a technology for chemical applications has been limited. Because interfacial engineering allows one to specifically tailor material properties, the potential of such technology in chemical processes is tremendous. One of the limiting factors that controls the efficiency of photocatalysis is the fast recombination between photoexcited electrons and holes. Another major limiting factor is the requirement for ultraviolet irradiation because most stable photocatalysts have band gaps in either ultraviolet or near ultraviolet regimes. For example, TiO_2, the most common photocatalyst, has an energy gap of 3.2 eV (390 mn). As a result, less than 7% of the light in the solar spectrum can excite electron-hole pairs in TiO_2. Efforts to overcome these limitations include organic dye-sensitization and mixed colloidal systems. With all of these approaches, the sensitizing moiety is not physically separated from the heterogeneous reaction interface and the major limitation in these schemes is the degradation of the sensitizer through parasitic reactions. By creating thin films with the desired properties, it is possible to separate the more reactive sensitizing layer from the surface, presumably resulting in a significant increase in the stability and efficiency of the system.

The essence of interfacial engineering is to tailor the electronic structure using thin film technology. The key factor that controls separation of photo-induced electron-hole pairs is the relative position of conduction and valance bands of films with respect to those of the substrates. Separation of electrons and holes between substrate and film can be accomplished upon photon excitation if both the conduction and the valance bands of the films are either lower (for reduction reactions) or higher (for oxidation reactions) than those of the substrates. In both cases, photoexcited electrons and holes will be separated at the interface via injection of either electrons or holes in the thin film. Such a scheme also enables the generation of photo-induced electrons and holes in smaller band-gap substrates and the injection of either electrons or holes into larger band-gap thin films, consequently realizing the use of the visible portion of sunlight to facilitate processes in catalysts with ultraviolet band-gaps.

Results and Accomplishments

We demonstrated that synthesis of engineered oxide materials can be accomplished. These materials have the appropriate band gaps and offsets for spatial charge separation and enhanced optical adsorption. We also

demonstrated that quantum dots with the desired electronic and optical properties can be formed via a self-assembled process.

Synthesis of Self-Assembled Cu_2O Quantum Dots

We successfully synthesized Cu_2O quantum dots on $SrTiO_3$ and TiO_2 (anatase) substrates using the molecular beam epitaxial (MBE) method. The structure and chemical states of these Cu_2O quantum dots were characterized using x-ray diffraction (XRD) and x-ray photoelectron spectroscopy (XPS). These data showed that by carefully controlling the partial pressure of oxygen and Cu flux during the growth we were able to selectively grow Cu_2O or CuO dots under different conditions.

Figure 1 is an atomic force microscopy (AFM) image that shows Cu_2O quantum dots grown on a $SrTiO_3$ substrate. By controlling the growth time and substrate temperature, we were able to control the dot size and density. For example Cu_2O dots with diameters ranging from less than 10 nm to over 100 nm were demonstrated by varying growth conditions.

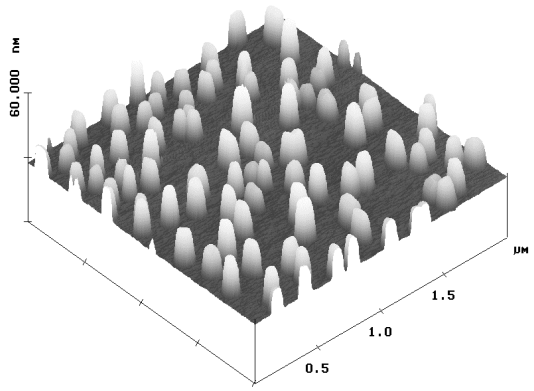

Figure 1. An atomic force microscopy image showing self-assembled Cu_2O quantum dots grown on a $SrTiO_3$ substrate

High-resolution scanning-Auger microscopy was used to determine the elemental distribution of the resulting surface after the growth to verify chemical identity of the dots observed by atomic force microscopy. These data confirmed that protrusions from the atomic force microscopy images were Cu_2O, as shown in Figure 2. The scanning-Auger microscopy also showed that the amount of copper in areas between the protrusions was only about 1.5%, less than a monolayer of Cu_2O. This suggests that $SrTiO_3$ substrates were exposed in the areas not covered by the Cu_2O dots—a prerequisite for surface charge separation and simultaneous photo-reduction and oxidation reactions upon above-gap-photon excitation. These results suggest that from the geometric-and-

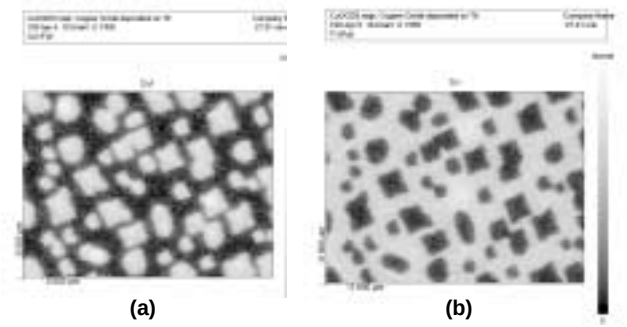

Figure 2. Scanning-Auger microscopy image showing distribution of copper (a) and titanium (b) on a $Cu_2O/SrTiO_3$ surface determined by scanning Auger microscopy

electronic-structure point of view, these Cu_2O/ $SrTiO_3$ systems can be used as electrodes for photoelectrochemical reactions.

Determination of Electronic Structures and Band Offsets Between Cu_2O and $SrTiO_3$

In addition to surface morphology and elemental distributions, x-ray photoelectron spectroscopy was used to examine the chemical state and electronic structure of $Cu_2O/SrTiO_3$. These data showed that the copper oxide grown under the appropriate conditions was indeed copper (I) in valance, consistent with the x-ray photoelectron spectroscopy finding. In addition, by conducting x-ray photoelectron spectroscopy measurements at different stages of growth, we determined that the conduction and valance band offsets between Cu_2O and $SrTiO_3$ were 0.6 and 1.8 eV, respectively. Combining this result with the known flat band potential of $SrTiO_3$, we found that energetics of $Cu_2O/SrTiO_3$ were favorable for splitting water via a photocatalysis reaction, as shown in Figure 3. We further examined the stability of Cu_2O quantum dots grown on $SrTiO_3$ substrates. We exposed a $Cu_2O/SrTiO_3$ sample to water (pH=9) and irradiated with white light (75W) for 45 minutes. Atomic force microscopy and x-ray photoelectron spectroscopy measurements of Cu_2O quantum dots before and after the water exposure showed no changes in Cu_2O morphology and chemical states.

Synthesis and Reaction Tests of Heterostructured $Cu_2O/SrTiO_3$ Powders

We synthesized heterostructure Cu_2O/TiO_2 powders through chemical routes to significantly increase the active surface area. By carefully controlling reaction routes, we were able to successfully synthesize single phase Cu_2O powders and coupled Cu_2O/TiO_2 powders. X-ray diffraction of these heterostructure powders showed

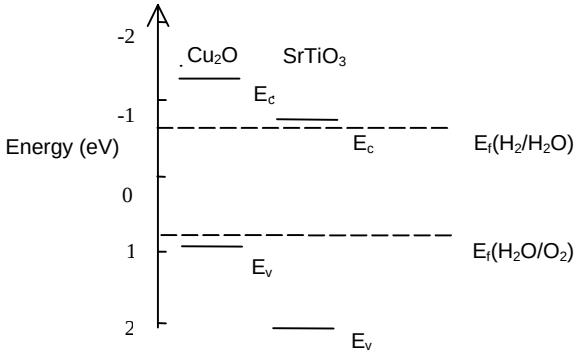

Figure 3. Relative band positions of Cu_2O and $SrTiO_3$ with respective to H_2 and O_2 levels in water

that the majority of them were Cu_2O and TiO_2 (anatase and rutile) phases, and these phases remained unchanged before and after the photocatalytic reactions. Figure 4 is an x-ray diffraction pattern of the coupled Cu_2O/TiO_2 powders before and after the photoreaction. No visible changes on those characteristic peaks were associated with Cu_2O and TiO_2 phases. However, x-ray diffraction measurement is insensitive to any charges that occur at the surface region.

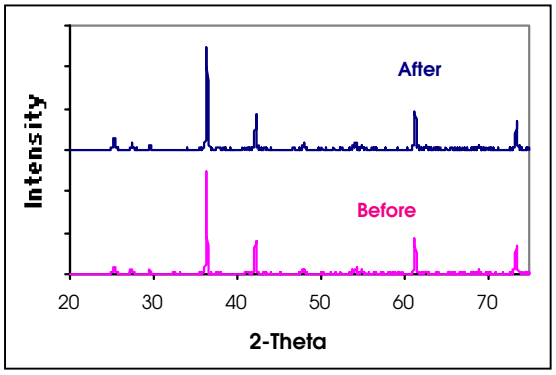

Figure 4. X-ray diffraction patterns of Cu_2O/TiO_2 before and after the photoreaction

In addition to powder synthesis, we also conducted photocatalytic reactions on these powdered systems. Both Cu_2O and Cu_2O/TiO_2 showed hydrogen evolution upon light irradiation. While the gas phase hydrogen to oxygen ratio was 2 to1 when Cu_2O was used as a catalyst, the amount of oxygen gas was significantly higher than hydrogen, indicating reductions occurred to some radical oxygen species likely bonded to the surface layer of Cu_2O/TiO_2 powders. Thus, for these heterostructure Cu_2O/TiO_2 to be used as robust photocatalysts, further synthetic refinement is needed.

Photoelectrochemistry of $Cu_2O/SrTiO_3$ in Water

$Cu_2O/SrTiO_3$ quantum dot electrodes, fabricated via gold ion implantation and vapor deposition on the reverse face, have exhibited, in all but one case, significantly enhanced photo-current when excited below the $SrTiO_3$ band gap energy. The wavelength dependent phase shift AC photo-current data at a single frequency, 20 Hz, is consistent with the charge separation mechanism indicated by the band structure in Figure 3.

Summary and Conclusions

We have demonstrated that synthesis of engineered oxide materials can be accomplished. These materials have the appropriate band gaps and offsets for spatial charge separation and enhanced optical adsorption. Using these materials as photocatalysts, we have demonstrated the production of hydrogen via splitting of water upon irradiation of white light.

Publications and Presentations

Chambers S, Y Liang, and Y Gao. 2000. "Noncommutative band offset at α-Cr_2O_3/α-Fe_2O_3(0001) heterojunctions." *Phys. Rev. B.,* 61, 13223.

Gan S, Y Liang, and Baer. 2000. "Atomic control of TiO_2(110) surface by oxygen plasma treatment." *Surf. Sci.* 459, L498.

Liang Y, S Gan, SA Chambers, and EI Altman. "Atomic structure of anatase TiO_2 (001)–an STM perspective." *Phys. Rev. B* (submitted).

Liang Y, S Gan, EI Altman. March 2000. "Reconstruction of MBE grown anatase TiO_2(001) surface–(1x4)/(4x1)." Am. Phys. Soc. Meeting, Minneapolis.

Liang Y, DE McCready, S Lea, SA Chambers, and S Gan. October 2000. "Synthesis and characterization of self-assembled Cu_2O quantum dots on $SrTiO_3$(001)." American Vacuum Society Meeting, Boston.

Liang Y, Y Su, J Daschbach, D McCready, S Thevuthasan, V Shutthanandan, and P Meethunkij. October 2000. "Interfaced controlled, self-assembled Cu_2O quantum dots as novel photocatalysts." 2000 National Lab. Catalysis Research Conference, Chicago.

Microscale Adsorption for Energy and Chemical Systems

Scot D. Rassat, Donald P. Mendoza, Dean W. Matson, Dustin D. Caldwell

Study Control Number: PN99044/1372

Microscale gas adsorption is useful for a wide array of energy and chemical processing applications. Applications include carbon dioxide and carbon monoxide scrubbing for fuel processing in fuel cells and for carbon management in combustion processes.

Project Description

With rapid cycling and continual regeneration of an adsorbent in a microscale adsorber, the mass of sorbent needed to treat a given volume of feed gas can be reduced significantly from conventional processing schemes. In this study, microscale adsorbers were successfully designed, fabricated, and tested in rapid thermal-swing adsorption experiments. The devices incorporated a single adsorbent channel and integrated heat exchangers. Several metal, plastic, and metal-plastic composite adsorbers were fabricated. Plastics (polyimides) were used to reduce adsorber mass and thermal capacity relative to all-metal units. Adsorption and desorption cycles of about 1-minute were readily attained with the various devices. Adsorber temperature and carbon dioxide desorption rate data suggest that the adsorption/desorption cycle frequency is heat-transfer limited, not mass-transfer limited. We also observed that the adsorbent in the metal-plastic adsorbers heated more quickly than in the all-metal and all-plastic devices and, as a result, released the stored volume of carbon dioxide more quickly during desorption (heating). Using conventional zeolite 13X adsorbent, the test devices were very effective at capturing carbon dioxide. Adsorbent working capacities as high as 93% of theoretical values were obtained for all-metal units and up to 62% of theoretical was measured for plastic-containing adsorbers. The variation in working capacity for the devices is thought to be due to differences in preconditioning and partial water poisoning of the adsorbent.

Introduction

Adsorption is one of many important industrial gas purification technologies applicable to the separation of a wide range of gas species (Kohl and Nielsen 1997). Carbon dioxide (CO_2) capture and sequestration is of concern, and novel adsorption processes are of interest for this application (Reichle et al. 1999). The reduction in adsorbent mass achievable in rapidly cycled microscale adsorbers is of potential benefit in all gas collection or purification applications where size and mass are a premium, such as man-portable systems, vehicle applications, or analytical applications. Commensurate with reduced adsorbent mass, the size and mass of other adsorber components shrink as well. A further reduction in overall device mass can be achieved by incorporating relatively lightweight materials, such as thin metals or plastics. Lightweight and low heat capacity materials can also reduce the excess thermal mass of an adsorber. In the preferred limit, only the adsorbent would be cooled and heated during thermal cycles. All other thermal mass that is heated or cooled during thermal cycling is energy-inefficient. We have developed and evaluated a series of metal, plastic, and metal-plastic composite microscale adsorbers seeking to minimize thermal mass.

Approach

In conventional adsorption-based gas purification processes, adsorbent bed loading and unloading cycles are typically on the order of hours (Kohl and Nielsen 1997). In microscale devices, the cycle times can be reduced to minutes or less, resulting in a time-scaled reduction in the mass of adsorbent needed to process an equivalent gas volume. The faster cycle times allow a small adsorbent mass to be regenerated more frequently and used more effectively. For example, a process requiring 25 kg adsorbent in an 8-hour cycle would use only 0.1 kg adsorbent in a 2-minute cycle.

We have developed microscale adsorbers for rapid thermal-swing adsorption processes, as depicted schematically in Figure 1. When the adsorbent bed is cooled, the capacity for the target gas species (such as CO_2) is relatively high, and when the bed is heated, some fraction of the sorbed species is evolved from the adsorbent. The difference in adsorbent capacity between the cooled and heated states represents the working capacity per cycle. The theoretical working capacity may be determined from adsorption isotherms (Trent 1995).

Here, we perform adsorption and desorption tests using a standard zeolite 13X adsorbent (PQ Corporation, 180 to 212-μm sieve fraction) and a pure CO_2 gas stream. To evaluate performance, we compare measured working capacities to those estimated from published CO_2 isotherms.[(a)]

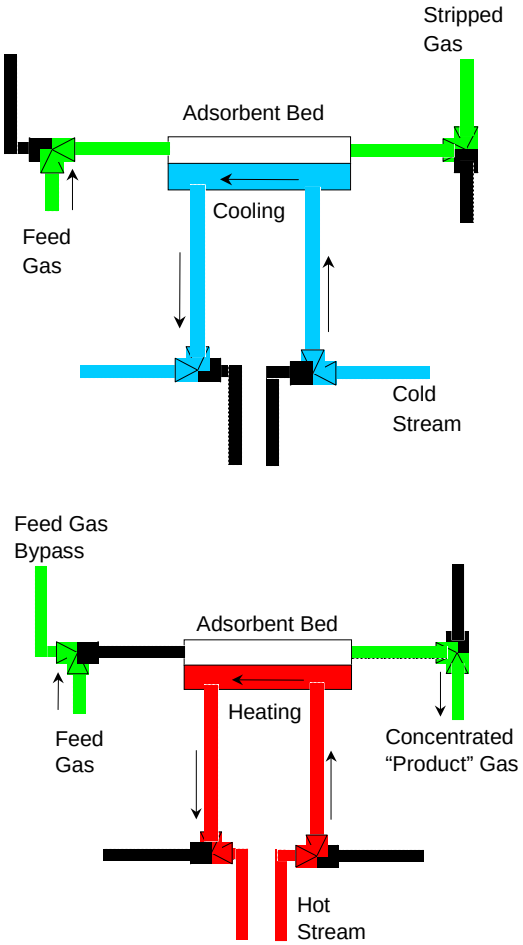

Figure 1. Schematic of the thermal swing adsorption process during adsorption (upper) and desorption (lower) cycles

Results and Accomplishments

We designed a rapid thermal-swing microchannel adsorber and successfully fabricated and tested a number of these devices. The test devices incorporated only a single adsorbent channel, although the design is suitable for a multichannel unit that would be expected to have comparable working capacity performance on a per mass basis. The single adsorbent bed was integrated with heat-exchange channels to affect adsorption and desorption. All-plastic (or all-metal) adsorbers incorporated plastic (or stainless steel) in both the heat exchanger and the adsorbent bed. The metal-plastic composite adsorber incorporated a metal shim as a component of the heat exchanger. The design of the all-metal heat exchangers was somewhat different from those incorporating plastic components, but the fluid channel thickness (0.010 inch) was comparable. The plastic and metal shims used in the adsorbers were fabricated using both conventional machining and laser micromachining processes. Channels in the relatively thick (0.05 to 0.06 inch) adsorbent bed shims were machined using a CNC milling machine. Except for the all-metal device, heat exchanger shims were patterned using a Resonetics Maestro Ultraviolet excimer laser machining station, which was operated with a laser wavelength of 248 nm. Various formulations of polyimide were used for all working plastic components. Layers of the all-plastic and metal-plastic adsorbers were bonded together using a high-temperature acrylic-laminating adhesive, and after assembly, the units were compressed in a laboratory press at ~5000 psi to seal all mating surfaces. Silicone (room-temperature vulcanizing rubber) was used to bond some components of the all-metal adsorbers, while other components were welded.

A test stand was assembled to control feed gas and heat-exchange fluid flow rates and to allow monitoring adsorber and heat exchange fluid temperatures, pressure drops, and evolved gas volumes. Type K surface mount and immersion probe thermocouples were deployed in all tests; in several tests, a type T hypodermic thermocouple (Omega®) was embedded in the adsorbent bed to measure the adsorbent temperature directly. Temperatures were output and recorded each second to an Omega data acquisition system on a personal computer. The series of valves needed to switch between adsorption and desorption cycles (Figure 1) were controlled manually. (An upgrade to an electronically controlled valve system is in progress.) Water, fed from separate constant-temperature hot and cold reservoirs, was used as the heat-exchange fluid. During desorption, gas was evolved at essentially ambient pressure through a tube to the head space of an inverted graduated cylinder which was partially filled with water and whose opening was submerged in a room-temperature water reservoir. The water displaced from the cylinder provided the volume of evolved gas. To monitor gas evolution as a function of time, the water displacement from the cylinder was video taped for subsequent evaluation. (Electronic mass flow meters are available for incorporation in the next generation system.) Ideal gas law assumptions were applied to determine the equivalent mass of CO_2 released for comparison to the theoretical working capacity.

(a) Isotherms provided by zeolite suppliers such as Zeochem®.

Figure 2 demonstrates the rapid thermal-swing capability for an all-metal microscale adsorber in a series of 1-minute cycle heating and cooling curves. (In separate tests, it was determined that the heat-exchange surface-measured temperatures depicted in the figure are representative of the zeolite bed temperature to within 1 to 2°C.) As the heat-exchange fluid flow rate was increased from 20 to 80 mL/min, the maximum and minimum adsorber temperatures approached the hot (70°C) and cold (5°C) reservoir temperatures. A larger temperature differential between adsorption and desorption cycles increases the zeolite working capacity, and therefore a higher adsorbent working capacity is expected as the water flow rate is increased. This was verified experimentally. Figure 2 also shows that the approach to the maximum (or minimum) temperatures is faster with increasing heat-exchange fluid flow rate. The heating curves were fit to exponential decay functions, and the exponential time constants were estimated. The time constants were approximately 6, 9, and 19 seconds for water flow rates of 80, 40, and 20 mL/min, respectively. These data validate, from a heat transfer perspective, the potential for rapid thermal cycling in microscale adsorbers.

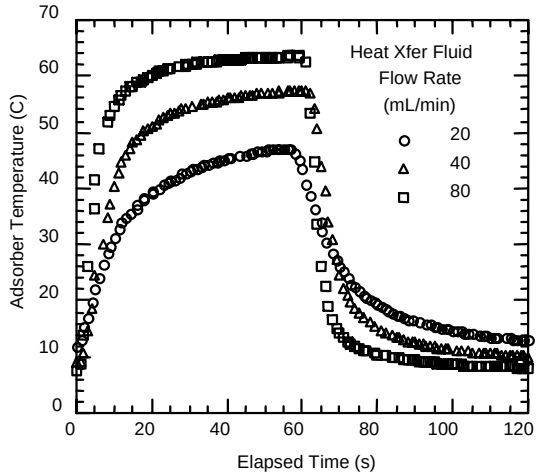

Figure 2. Effect of heat exchange fluid flow rate on temperature profiles for a metal microscale adsorber in 1-minute adsorption and desorption cycles

Both heat and mass transfer must be effective for rapid adsorption/desorption cycles to work well. Figures 3 and 4 demonstrate the simultaneous heat and mass transfer effectiveness for metal, plastic, and metal-plastic composite microscale adsorbers. Figure 3 shows measured bed temperatures in an all-metal device for a series of 0.5-, 1-, 3-, and 5-minute adsorption/desorption cycles. The figure also shows the volume of gas measured at the end of each desorption cycle (open circles). In the tests, water flowed through the heat exchanger at 80 mL/min, and the hot and cold reservoirs were set to 90° and 5°C, respectively. Pure CO_2 was fed to the zeolite at the rate of 50 mL/min during the cooling cycles, and the feed stream bypassed the adsorber bed during desorption cycles (Figure 1). The desorbed CO_2 volume consistently reached 46 mL for longer cycle times, fell slightly (~42 mL) in 1-minute cycles, and dropped significantly (~22 mL) in 0.5-minute cycles. The recovered volumes in the faster cycles were limited, at least in part, because of the lower temperature differentials attained in the cycles. A primary limitation for the 0.5-minute cycles was the feed gas flow rate; only ~25 mL CO_2 was delivered to the bed during the adsorption swing. (Tests with higher feed flow rates resulted in larger recovered gas volumes for 0.5-minute cycles.) The theoretical working capacities, based on measured temperature differentials, were ~52 mL for the 3- and 5-minute cycles and ~47 mL for the 1-minute cycle. Therefore, better than 80% of the theoretical working capacity was achieved in each of these cycles. Factors affecting the actual working capacity are discussed later in this section. Figure 3 also indicates excellent cycle-to-cycle consistency—for example, volumes evolved in 3- and 5-minute cycles late in the sequence were identical to those measured early on.

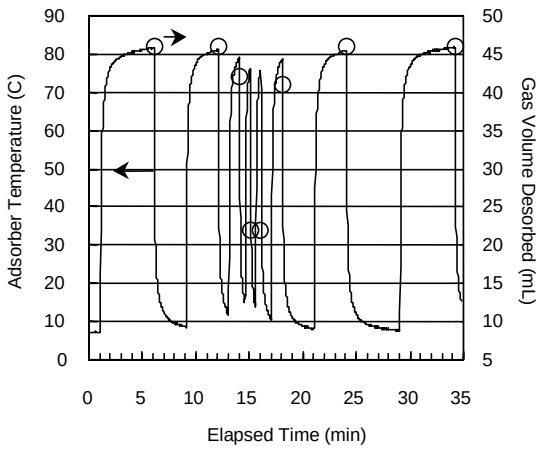

Figure 3. Temperature profile and desorbed gas volumes (open circles) for a metal microscale adsorber in a series of adsorption and desorption cycles

Figure 4 compares the thermal and mass transfer performance of three different microscale adsorption devices during desorption cycles. In all cases, water was delivered to the adsorber heat exchangers from a 90°C reservoir at 80 mL/min. Figure 4a indicates a somewhat lower rate of temperature change in the all-plastic device than in the all-metal and metal-plastic composite devices. However, after ~70 seconds the temperatures in the all-plastic device match those in the all-metal device, and at longer times the temperatures in the all-plastic device

exceed those in the all-metal device by a few degrees. This may be due to the lower thermal mass and lower heat loss associated with the plastic unit. The metal-plastic composite adsorber combines the superior qualities of each of the other units. The temperature profile shows rapid heat transfer to the adsorber bed, the rate of temperature change exceeding the all-metal device after ~15 seconds. The metal-plastic composite also attained a slightly higher maximum temperature than the all-metal device, suggesting relatively low heat loss. The profiles of gas evolution from these three devices (Figure 4b) show similar trends. Gas desorption was fastest in the metal-plastic device and slowest in the all-plastic unit. The results suggest that heat transfer rather than mass transfer is the primary limitation in the regeneration process of these microscale adsorbers.

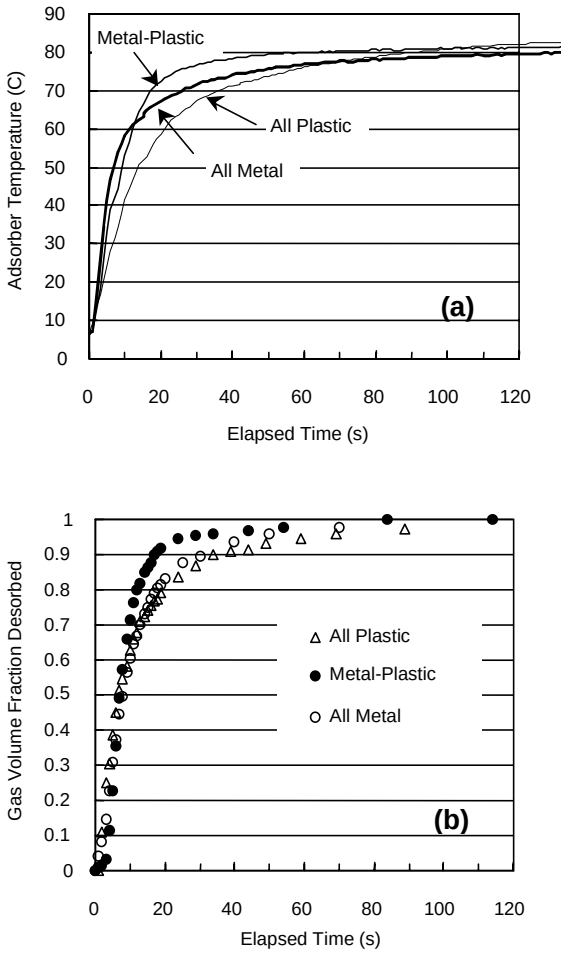

Figure 4. (a) Thermal and (b) mass transfer performance of three microscale adsorber assemblies during desorption

In Figure 4b, the gas volume fractions represent the absolute gas volumes normalized by the total volume desorbed. In general, we observed that the absolute volume of CO_2 desorbed per cycle, the working capacity, was higher in all-metal adsorbers (up to 93% of theoretical) than in devices containing plastic (maximum of 62% of theoretical). We believe this is due primarily to lower device conditioning temperatures used with plastic-bearing units (~125°C) compared with all-metal devices (~195°C). Water vapor, which is sorbed on zeolite 13X during assembly of adsorbers exposed to atmospheric conditions, is difficult to strip from the adsorbent at low temperatures because of the strong affinity of zeolite for water. Even at 195°C some water is strongly adhered to zeolite. The working capacity for an all-metal device (Figure 3) conditioned in a 195°C oven was ~81% of theoretical. Additional conditioning of the zeolite-filled adsorber at 195°C, including treatment in a nitrogen purged vacuum oven, resulted in a working capacity increase to ~93% of theoretical. These CO_2 recovery results are very promising but also indicate precautions that must be taken against water poisoning for low-temperature operations with zeolite sorbents. Of course, the adsorption devices developed here are not specific to zeolite adsorbents (or CO_2 processing), and other adsorbents that are less sensitive to water may be available.

Summary and Conclusions

Microscale adsorbers were successfully designed, fabricated, and tested in rapid thermal-swing adsorption experiments. The single-channel devices, using conventional zeolite 13X adsorbent, were effective at scrubbing CO_2. Multichannel devices of similar design should provide equivalent performance (cycle time and relative working capacity) and increased absolute gas-scrubbing capacity. Because of the rapid cycling and continual regeneration of the sorbent in the microscale adsorbers, the mass of sorbent needed to treat a given volume of feed gas is reduced from conventional processing schemes. The important findings include

- effective adsorption/desorption cycles on the order of 1 minute were readily attained with current device designs
- devices can be fabricated from plastic and metal-plastic composites to reduce adsorber mass relative to all-metal units
- the adsorbent in the metal-plastic adsorbers heated (and cooled) more quickly than the metal devices, and metal-plastic devices provide reduced thermal mass much like the all-plastic units

- adsorption/desorption cycle frequency appears to be heat-transfer limited, not mass-transfer limited

- working capacities of all-metal units were somewhat better (up to about 93% of theoretical) than plastic-containing units (maximum about 62% of theoretical), most likely due to differences in preconditioning and water uptake.

References

Kohl AL and RB Nielsen. 1997. *Gas purification*, 5th Edition. Gulf Publishing Company, Houston.

Reichle D et al. 1999. *Separation and capture of carbon dioxide, in carbon sequestration, state of the science.* Draft, U.S. Department of Energy, Washington, D.C.

Trent RE. 1995. *Fundamentals of adsorption.* Proceedings of Gas Conditioning Conference, Zeochem, Norman, Oklahoma.

Presentation

Rassat SD, DP Mendoza, DD Caldwell, WE TeGrotenhuis, and RS Wegeng. 2000. "Microchemical and thermal sorption systems for gas purification." Poster presented at the DOE-OTT Program Review, Richland, Washington.

Nanoscale Fabrication for Enhanced Properties[(a)]

Don R. Baer, Yong Liang

Study Control Number: PN97048/1189

This project focuses on development of functional nanometer components that can be integrated with smart micro-technology for chemical processes.

Project Description

This research project investigated the formation and properties of nanoscale functional structures with the ultimate objective of integrating active nanometer-sized components into smart microtechnology. The specific research effort has been focused on establishing the ability to create arrays of uniform-sized metal clusters on oxide surfaces with possible catalytic application. The ability to control and stabilize particle size provides the opportunity to influence catalytic properties such as selectivity and efficiency and may provide ways to deal with poisoning. Two of the challenges in our research have been preparing suitable oxide substrate surfaces for control and measurement of particles and adequately stabilizing nanodimensional particles on these surfaces. Having established methods of preparing well-defined and stable platinum clusters on titanium oxide surfaces, the current efforts have focused on examining the chemical properties of these particles.

Results and Accomplishments

This research on nanoscale component development uses a range of new experimental tools recently made available in the Environmental Molecular Sciences Laboratory. These tools enhance our ability to work in the nanometer sizes. We have demonstrated the general ability to create the desired types of surfaces and to form organized strings of platinum nanoclusters on these surfaces using self-assembled processes. By controlling the nature of the surface, the size, distribution, and stability of the clusters can be altered. Scanning tunneling microscopy and temperature-programmed desorption studies show that the physical and chemical properties of the platinum clusters are altered with size, offering the possibility of greater control of reactivity and catalytic behavior.

Platinum Cluster Sizes and Stability

Titanium oxide (anatase or TiO_2) is an important catalyst support material. A flat, well-defined surface is needed to enable detailed characterization of the properties of metal clusters attached to this surface. It is well established that the TiO_2 (110) surface can form two different structures, i.e., (1x1) and (1x2). However, recent work using the scanning tunneling microscopy has shown that these structures can exist in different domains on a single surface. Because of their different geometric and electronic structures, one would expect that these two domains exhibit different interactions with metal clusters (supported metal catalysts) and thus result in different catalyst formations. The ability to control the surface structure of TiO_2 surfaces was established in previous years. This work is the subject of a recent publication and provides the basis for the current work.

The different sizes and distributions of platinum clusters formed when platinum was evaporated onto three different TiO_2 surfaces are demonstrated in Figures 1, 2, and 3. The number and size distribution of the clusters depends upon the amount of platinum, the temperature, and the structure of the substrate. Figures 1, 2, and 3 show platinum clusters on a rutile (110) 1x1 surface, a rutile (110) 1x2 (reconstructed) surface, and an anatase (001) surface, respectively.

Table 1 shows the cluster size and distribution for 0.5 mL or less of platinum deposited on each surface. Based on the observed size and growth, clusters on the reconstructed rutile 1x2 surface are most stable and those

(a) Project was formerly called "High Functionality Surfaces and Structures in Microchannels."

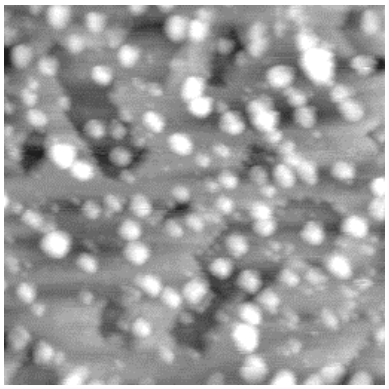

0 nm 50 nm

Figure 1. Scanning tunneling microscopy image of platinum clusters formed by deposition of 0.5 mL of platinum on a rutile (110) 1x1 surface

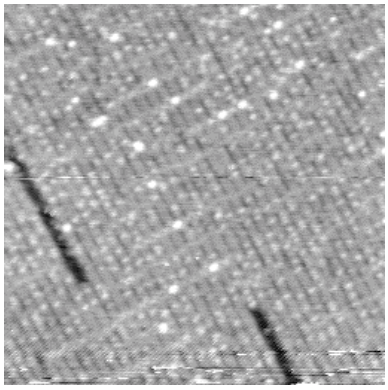

0 nm 40 nm

Figure 2. Scanning tunneling microscopy image showing platinum nanoclusters formed on a rutile (110) 1x2 surface. The clusters are attached primarily to the top of 1x2 atomic rows and appear to have higher thermal stability and smaller size than clusters on the 1x1 surface.

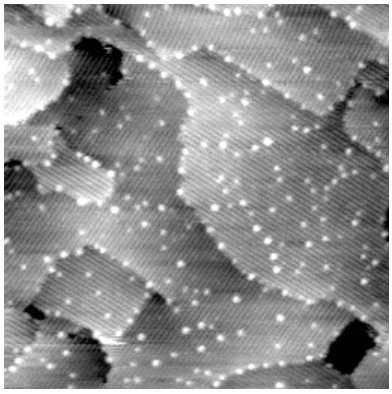

0 nm 120 nm

Figure 3. Scanning tunneling microscopy images of platinum clusters on the anatase (001) surface

Table 1. Platinum cluster size for three different TiO_2 surfaces as a function of deposition or process temperature

Surface	Process Temp	Size nm	FWHM nm
Rutile (110) 1x1	300 K	1.4	1
	600 K	1.6	0.7
	650 K	2.0	0.8
Rutile (110) 1x2	300 K	0.84	0.12
	600 K	0.84	0.12
Anatase (001)	420 K	1.5	0.5
	520 K	1.73	0.23
	670 K	1.77	0.22

on the anatase surface are only slightly less stable. Both are significantly smaller and more stable than clusters on the unreconstructed rutile surface.

Variations in Cluster Properties

Temperature programmed desorption measurements for carbon monoxide sorbed onto the oxide and platinum clusters show significant differences dependent on the size of the cluster as shown in Figure 4. The small clusters on either a 1x1 or 1x2 surface show a significantly higher CO desorption temperature than do the larger clusters. The desorption behavior of the larger clusters is similar to that for bulk platinum.

Differences in the electronic properties of platinum clusters as a function of size are also apparent in scanning tunneling spectra, as shown in Figure 5. Curve I is for the substrate [TiO_2 (110) 1x1] showing an apparent 3-volt band gap. Clusters of 0.8 and 1.4 nm have an apparent but smaller band gap, while 4.5 nm clusters show typical metallic behavior.

Summary and Conclusions

We have demonstrated our ability to form self-organized platinum nanoclusters on TiO_2 surfaces. Our results suggested that on the TiO_2-(1x2) surface, these nanoclusters had enhanced thermal stability. Furthermore, they exhibited unusual chemical activities at size less than 2 nm. These results demonstrated that desired functional structures could be formed through nano-structuring and self-assembly.

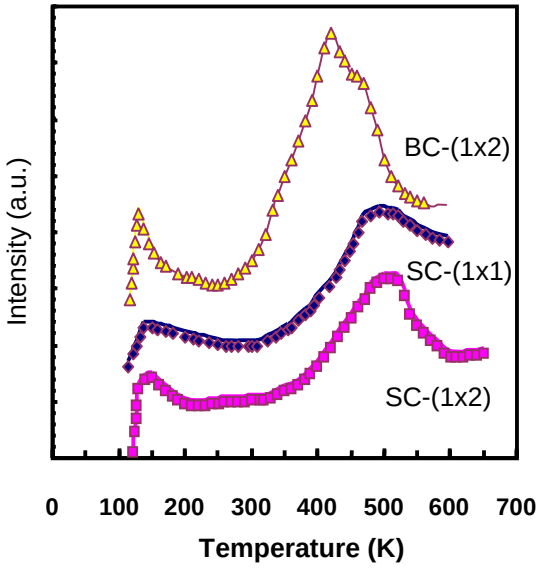

Figure 4. Temperature programmed desorption measurements of CO desorption from platinum clusters on rutile (110) 1x1 and 1x2 surfaces. CO desorbes from small clusters at higher temperatures than from larger clusters or from bulk platinum. These results show that some aspects of surface chemistry can be altered by controlling platinum cluster size.

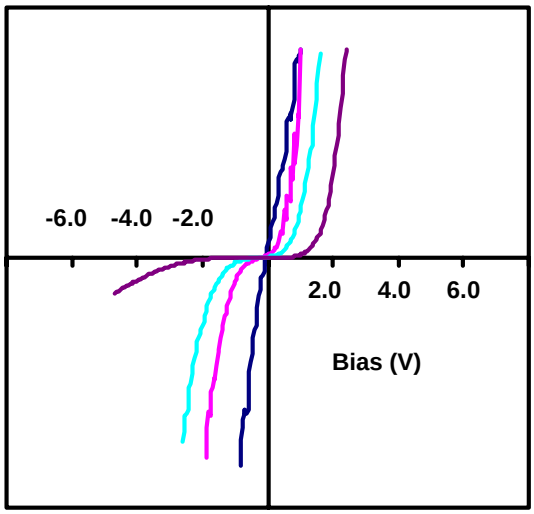

Figure 5. Scanning tunneling spectroscopy curves obtained from clusters of different sizes and a clean surface. Curve I is for the rutile surface and show expected large band-gap behavior. Curves II and III are for 0.8 and 1.4 nm platinum clusters and show nonmetallic behavior. Clusters with a diameter of 4.5 nm appear metallic.

Publications and Presentations

Gan S, Y Liang, and DR Baer. 2000. "Atomic control of TiO2(110) surface by Oxygen Plasma Treatment." *Surface Science* 459:L498-L502.

Baer DR, Y Liang, S Gan, and A Grant. 2000. "Formation and stabilization of nano-sized Pt clusters on TiO_2 surfaces." *In Proceedings of AIChE 2000 Spring National Meeting,* Atlanta, Georgia.

Gan S, Y Liang, DR Baer, and AW Grant. September 2000. "Effects of titania surface structure on the nucleation and growth of Pt nanoclusters on rutile TiO_2 (110)." *Physical Review B* (submitted).

Gan S, Y Liang, DR Baer, MR Sievers, GS Herman, and CHF Peden. August 2000. "The effect of Pt nanocluster size and surface structure upon CO desorption chemistry on Pt supported TiO_2 (110). *J. Chem. Phys. Lett.* (submitted).

Gan S, DR Baer, MR Sievers, GS Herman, C Peden, and Y Liang. September 2000. "Effects of titania surface structure on Pt nanoclusters on TiO_2 (110): nucleation, growth, and chemisorption." Pacific Northwest American Vacuum Society Meeting, Portland, Oregon.

Liang Y, A Grant, D Baer, and S Gan. October 1999. "Formation and properties of Pt on TiO_2 rutile and anatase surfaces." AVS meeting, Seattle.

Liang Y, S Gan, TT Tran, SA Chambers, and DE McCready. December 1999. "Characterization of TiO_2 anatase thin films." Materials Research Society Fall Meeting, Boston.

Liang Y, S Gan, DR Baer, MR Sievers, GS Herman, and C Peden. October 2000. "Nano-sized Pt clusters on TiO_2 rutile surfaces: growth, self-organization, and chemisorption." 2000 National Lab Catalysis Conference, Argonne, Illinois.

Optothermal Nanosensor

Tom Autrey

Study Control Number: PN00071/1478

Instruments are needed for characterizing extremely small quantities of a sample. This project is developing an optothermal nano-scale sensor for special-purpose applications, such as characterizing the constituents in blood (glucose, hemoglobin, or protein), industrial monitoring of lubricant breakdown or fuel oxidation, and detectors for capillary electrophoresis or supercritical fluids.

Project Description

A fundamental understanding of the properties that dictate the absorption of light and subsequent release of heat to generate a transient pressure wave was used to develop a multi-wavelength photoacoustic detector. A flash lamp that emits a broad spectrum over the ultraviolet and visible region is used as an excitation source to detect trace quantities of metals in aqueous solution using photoacoustic detection. Calculation of the mechanical to electrical conversion efficiencies of piezoelectric transducers shows absorbed energies of microjoules per milliliter (typical of flash lamps) are sufficient to provide measurable photoacoustic signals. This work demonstrates that monochromatic lasers are not necessary for photoacoustic spectroscopy and can be replaced with relatively inexpensive flash lamps.

Introduction

In previous work, we investigated the detection limits of chromium (VI) in aqueous solutions using laser spectroscopy. Although a significant enhancement in detection limits was obtained compared with traditional spectroscopic methods, the technique was limited by availability of a tunable laser and a fast transient digitizer resulting in a sensitive but expensive analytical technique. In subsequent work, we investigated the fundamental properties describing the conversion of the absorbed electromagnetic energy to the transient pressure change detected with a piezoelectric element. Several important findings from our fundamental studies provide a direct bearing on the current work. First, only minute absorbed energy densities (nanojoules/μL) are required to obtain a measurable piezoelectric signal given the sensitivity of piezoelectric transducers (-60dB ref 1V/μbar). Second, an understanding of the mechanical to electrical efficiency of a piezoelectric element predicts that it is advantageous to use low frequency transducers. In addition to the predicted increase in sensitivity, a low frequency transducer can be adequately sampled with commercially available Ms/s data acquisition boards housed in common laboratory personal computers, eliminating the need for expensive fast transient digitizing oscilloscopes. Energies of dozens of microjoules that are readily available with commercially available flash lamps should provide a suitable (and less expensive) alternative to solid-state or gas lasers. In addition, if we can devise a method to select wavelengths of interest, not only will we have tunability but the possibility of monitoring several wavelengths simultaneously to provide an enhancement in detector selectivity.

Results and Accomplishments

Analysis of the fundamental parameters that describe the conversion of absorbed electromagnetic energy to a transient pressure gradient shows that the intensity provided by flash lamps provides acoustic pressures that can be readily detected with low frequency ultrasonic transducers.

Combining a flash lamp and personal computer data acquisition of low frequency transducers provides simultaneous multiple wavelength detection for enhanced selectivity and faster data analysis with comparable sensitivity at a fraction of the cost and space of conventional photoacoustic methods that use lasers and expensive transient recorders. This work continues on optimizing detector response and lower noise issues to achieve even better detection limits. The current configuration cost of a photoacoustic detector can be reduced significantly using a broadband lamp source and a data acquisition board circumventing the use of a laser and a fast transient digitizer.

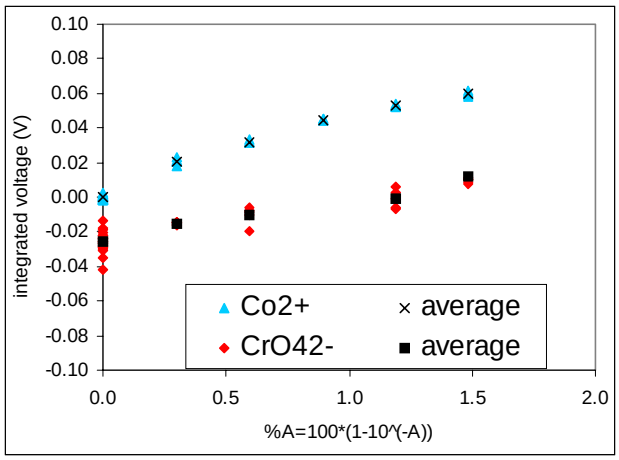

Figure 1. Standard addition of analyte to aqueous solution in sample cell. Co^{2+} detected at 532 nm, CrO_4^{2-} detected at 355 nm. The signal is linear with absorbance providing a detection limit for % absorbance ~ 0.15% (A=0.00065/cm).

References

Autrey T, N Foster, and K Klepzig. 1999. Nanojoules, nanoliters and nanosecond calorimetry; A nanoscale quartz capillary photoacoustic cell for time-resolved calorimetric investigations." *J. Photochem. Photobio. A: Chem. 125:*13-19.

Autrey T, N Foster, K Klepzig, J Amonette, and J Daschbach. 1998. "A new angle into time-resolved photoacoustic spectroscopy: A layered prism cell increases experimental flexibility." *Review of Scientific Instruments*. *69(6):*2246-2258.

Foster N, J Amonette, and T Autrey. 1999. "In-situ detection of chromate using photoacoustic spectroscopy." *Applied Spectroscopy. 53(6):*735-740.

Presentation

Autrey T, N Foster-Mills, D Hopkins, and J Price. June 2000. "Fast, cheap and in control. Towards the design of a photoacoustic spectrometer in a shoe box." Presented at EMSL users meeting.

Simulation of Reactions in Thermal Multiphase Flows for Microchannel Reactors

David R. Rector, Bruce J. Palmer

Study Control Number: PN00082/1489

Miniature energy and chemical devices have been developed for special microtechnology applications. One example is a microchannel reactor that features fast heat and mass transfer, increased process efficiency, and process miniaturization without sacrificing productivity. In this project, computation methods have been developed to simulate gas phase and liquid solution chemistry in microchannel reactors.

Project Description

Recent developments in microreactor technology at the Laboratory have created a significant number of opportunities for project development. A major obstacle to microreactor development is that the transport and reaction processes that occur within these systems are not well understood. The primary objective of this project is to develop a simulation capability that accurately models the transport and reaction of chemical species in microreactor systems.

Introduction

This capability is based on the lattice Boltzmann algorithms and codes for simulating multiphase thermal flows and multicomponent flows that were developed in a previous project (Palmer and Rector 2000). The modifications to the lattice Boltzmann method required for simulating chemical reactions include the creation and destruction of chemical species, inclusion of heat generation in the energy equation, and developing a procedure for solving the chemical kinetics equations. This unique capability will be used for both design and optimization of microreactor components and systems.

Results and Accomplishments

Microreactor chemical reactions of interest include gas phase and liquid solution chemistry and systems in both that involve intervening liquid, gas, or solid phases. A general chemical reaction capability must include methods for modeling systems in all of these categories.

CHEMKIN and SURFACE CHEMKIN (Kee et al. 1996) are the standard chemical kinetic tools for the gas phase case. We have incorporated both the CHEMKIN and SURFACE CHEMKIN chemical reaction packages into the multiphase, multicomponent lattice Boltzmann computer program developed at the Laboratory. The chemical species and energy equations were modified to account for species creation and destruction. The time step sequencing was modified to allow operator splitting. The modified lattice Boltzmann program was tested using simple bulk gas mixture model systems.

For liquid solutions, the same de-facto standard does not exist. If restricted to aqueous phase chemistry, there are a number of geochemistry codes in use. The KEMOD (Yeh and Iskra 1995) (mixed chemical kinetic and equilibrium model) chemistry package has been incorporated into our lattice Boltzmann program under a separate project. The usefulness of this approach for modeling microreactor systems was evaluated by simulating a simple bulk solution system of practical interest.

The sample case chosen to demonstrate reacting flow simulation capability is an aqueous solution of amine and CO_2. This system is of enormous importance in industry for removing CO_2 and sour gas from natural gas. It is also important to our Laboratory's research efforts in microchemical reactors for gas cleanup, specifically for CO_2 removal from room air (Kohl and Reisenfeld 1985). In this application we are most interested in diethanolamine.

A literature search was conducted for chemical mechanisms and kinetic data. Others have debated specific mechanisms that lead to observed behavior, but some consensus has been reached on the role of the zwitterion intermediate (see Danckwerts 1979).

In our model, we elected to follow the detailed mechanism and use data referenced in Rinker (1996). Rinker's model includes 11 species in 8 reactions; 4 are equilibrium reactions, and 4 are kinetic. Missing specific kinetic data required assumptions on our part, so results presented here are preliminary and are shown for demonstration purposes only.

The first step was to implement this system as a perfectly mixed batch chemistry model using KEMOD by itself. Next, the model was coupled with the lattice Boltzmann model to simulate spatial effects for a gas-liquid contactor, including diffusion and advection. In the results to date on the batch chemistry model, two cases were considered:

- Case 1 - ambient water/CO_2 mixed with amine and evolved without added CO_2
- Case 2 - same system as Case 1 but with high concentration of initial CO_2.

The first case examines CO_2 absorption when the amine is mixed with water while sealed from additional atmospheric CO_2. Initial CO_2 in the water was typical of surface water, 1E-5 M (moles per liter of solution). Amine was added to produce a 2.2-M solution. The second case has a 1-M initial CO_2 concentration and is more typical of a gas-liquid interface in an absorption process. The same 2.2-M amine concentration was used for this case. Both cases begin with instantaneous combination/mixing of the reactants at time zero, and the chemical species evolve over the 65-msec time period. Results are presented in Figures 1 and 2.

Summary and Conclusions

Chemical reaction capabilities for both gas phase and solution chemistry have been incorporated into our lattice Boltzmann computer program. Both capabilities were tested and the usefulness of the solution chemistry package has been demonstrated by application to a CO_2 removal system based on an amine solution.

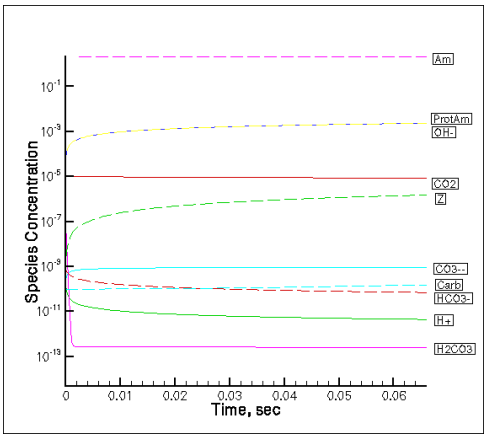

Figure 1. Species concentration in moles per liter after mixing for Case 1 (Am is diethanolamine, ProtAm is protonated amine, Z is zwitterion)

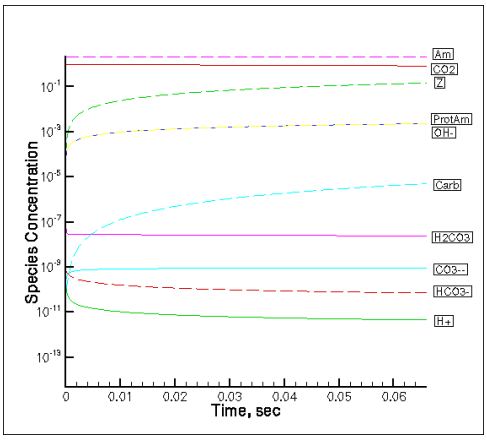

Figure 2. Species concentration in (moles per liter) after mixing for Case 2

References

Danckwerts PV. 1979. "The reaction of CO_2 with ethanolamines." *Chemical Engineering Science* 34:443-446.

Kee RJ, RM Rupley, E Meeks, and JA Miller. 1996. *CHEMKIN-III: A Fortran Chemical Kinetics Package for the Analysis of Gas-Phase Chemical and Plasma Kinetics.* SAND96-8216, Sandia National Laboratories, Albuquerque, New Mexico.

Kohl A and Riesenfeld. 1985. *Gas Purification*, 4th edition. Gulf Publishing, Houston, Texas.

Palmer BJ and DR Rector. 2000. "Lattice-Boltzmann algorithm for simulating thermal two-phase flow." *Phys. Rev*. E 61:5295-5306.

Rinker EB. 1996. "Kinetics and modeling of carbon dioxide absorption into aqueous solutions of diethanolamine." *Ind. Eng. Chem. Res*. 35:1107-1114.

Yeh GT and GA Iskra. 1995. KEMOD*: A Mixed Chemical Kinetic and Equilibrium Model of Aqueous and Solid Phase Geochemical Reactions.* PNNL-10380, Pacific Northwest National Laboratory, Richland, Washington.

Synthesis and Characterization of Interfaced Cu_2O Nanostructures

Yong Liang, Scott A. Chambers, H. Luo

Study Control Number: PN00083/1490

Quantum dots are often cited as an exciting new class of nanomaterials for use in optical and photosynthetic applications. In this project, Cu_2O quantum dots are grown on $SrTiO_3$ and their properties are characterized.

Project Description

Three-dimensional structures on a length scale of a few to a few tens of nanometers exhibit properties of a particle-in-zero dimension. Such nanostructures are often referred to as quantum dots or quantum particles. This project is aimed at investigating the properties of self-assembled Cu_2O. Cooper oxide (anatase) is an important material system in energy and environmental research. We use molecular beam epitaxial methods to synthesize Cu_2O quantum dots on $SrTiO_3$ substrates, and characterize the morphological, electronic, and optical properties of these quantum dots using a number of surface, laser spectroscopic, and microscopic techniques.

Results and Accomplishments

We completed all the proposed tasks. These were 1) synthesis of self-assembled Cu_2O quantum dots on $SrTiO_3$ substrates, 2) determining morphological and electronic properties of $Cu_2O/SrTiO_3$ using atomic force microscopy and x-ray photoelectron spectroscopy techniques, and 3) investigation of photoluminescence properties of Cu_2O quantum dots. We also successfully synthesized Cu_2O nano-corrals on $SrTiO_3$ substrates. These results demonstrated our ability to synthesize and characterize these oxide nanostructures, a class of materials of potential significance in energy and environmental research.

Synthesis of Cu_2O Quantum Dots

We successfully synthesized Cu_2O quantum dots on $SrTiO_3$ substrates using molecular beam epitaxial method. Figure 1 is an atomic force microscopy image that shows Cu_2O quantum dots self-assembled on a $SrTiO_3$ substrate. Results show that most of the Cu_2O quantum dots have the same lateral orientations at the surface, suggesting a high degree of crystal graphic coherency among these dots, and an excellent structural registration between the dots and the $SrTiO_3$ substrate. By controlling the copper flux, substrate temperature, and growth time, we have been able to control the average size of these quantum dots with lateral size from less than 10 nm to nearly 100 nm. We have also characterized the quantum dots with x-ray diffraction. Results confirmed that the quantum dots grown on $SrTiO_3$ under appropriate conditions had a Cu_2O crystal structure, as demonstrated in Figure 2.

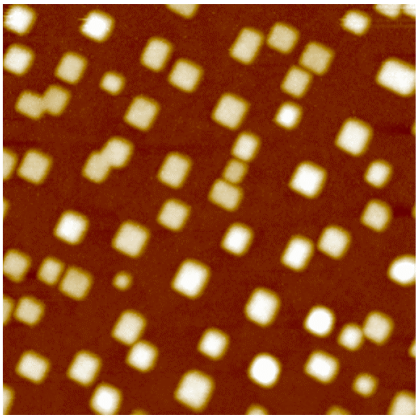

Figure 1. An atomic force microscopy image showing self-assembled Cu_2O quantum dots grown on an $SrTiO_3$ substrate. The size of the image is 1x1 μ.

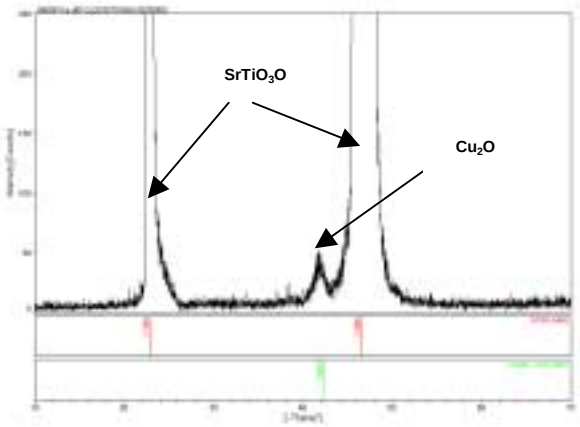

Figure 2. X-ray diffraction showing that quantum dots grown on a $SrTiO_3$ substrate have a Cu_2O crystal structure

Spontaneous Formation of Cu_2O Nano-Corrals

In addition to Cu_2O quantum dots, we have also developed a process for growth of Cu_2O nano-corrals on $SrTiO_3$ substrates. These were grown by first depositing a layer of copper metal on a $SrTiO_3$ substrate, then subsequently annealing the $Cu/SrTiO_3$ in oxygen plasma at elevated temperatures. The resulting surface exhibited corrals with diameters ranging from approximately 50 nm to 80 nm, as shown in Figure 3. The chemical state of copper was examined by x-ray photoelectron spectroscopy. Results confirmed that copper at the surface was copper (I) instead of copper (II), suggesting these corrals consisted of Cu_2O instead of a CuO phase. The importance of this finding is that these nanoscale ring structures can exhibit artificial magnetic and conducting properties, as was predicted by Laudauer et al. (1985) and

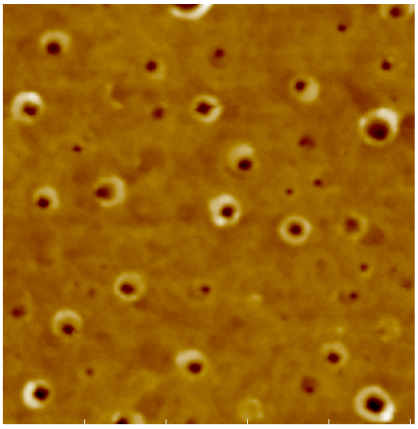

Figure 3. An atomic force microscopy image of Cu_2O nano-corrals formed on a $SrTiO_3$ substrate surface

recently confirmed by Lorke et al. (2000) on InAs. The driving force for the formation of these nano-corrals is currently unclear. We speculate that they are due to stress relaxation and subsequent dislocation formation at the $Cu_2O/SrTiO_3$ interface.

Photoluminescence Behavior of Cu_2O Quantum Dots

One potential application of the $Cu_2O/SrTiO_3$ quantum-dot system is photocatalysis. It is important to characterize the optical properties of this system. We conducted photoluminescence measurements on $Cu_2O/SrTiO_3$. Results are shown in Figure 4. The photoluminescence spectrum shows a broad distribution

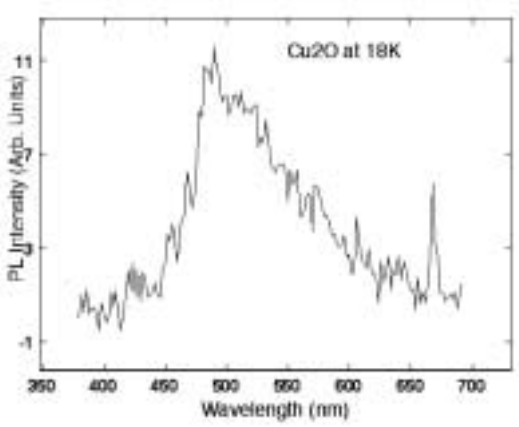

Figure 4. Photoluminescence spectrum of Cu_2O quantum dots showing typical luminescence behavior from quantum dots. The spectrum was taken at 18 K to eliminate photon scattering effects.

with a peak centered around 480 nm. The breadth of the spectrum is due to the size distribution of quantum dots, as has been demonstrated in other quantum dots systems (Bimberg et al. 1999). The fact that these Cu_2O quantum dots exhibit photoluminescence under above-gap irradiation suggests that the defect density of this system is low. It would otherwise show no photoluminescence because of scattering and recombinations mediated by defects.

References

Bimberg D, M Grundmann, and N Ledentsov. 1999. *Quantum dot heterostructure.* John Wiley & Sons, New York.

Laudauer R et al. 1985. *Phys. Lett.* 96A, 365.

Lorke A, RJ Luyken, AO Govorov, and JP Kotthaus. 2000. "Spectroscopy of nanoscopic semiconductor rings." Phys. Rev. Lett. 84, 2223.

Presentation

Liang Y, D McCready, S Lea, S Chambers, and S Gan. November 2000. "A novel stable quantum dot system for electron-hole pair separation: self-assembled Cu_2O quantum dots on $SrTiO_3$(001)." Material Research Society Meeting, Boston.

Nuclear Science and Engineering

Actinide Chemistry at the Aqueous-Mineral Interface by Atomic Force Microscopy

David L. Blanchard Jr., Steven C. Marschman

Study Control Number: PN00002/1409

The interaction of actinides with soil-mineral surfaces affects the migration of contaminants through the vadose zone and aquifers. However, little direct, sub-micron and molecular level data on this interaction have been collected. Such data could help validate models of actinide transport currently in use. This project investigated one aspect of that interaction, the morphology of actinides deposited on a mineral from aqueous solution, using atomic force microscopy.

Project Description

The purpose of this project was to determine the morphology of actinides deposited at mineral surfaces using atomic force microscopy, and to use that to infer the identity of the actinide species present and the mechanism of their attachment to the surface (sorption, precipitation). A neptunium(V) nitrate (NPO_2NO_3) solution was synthesized and deposited on the surface of a single crystal of a mineral, calcite, found in great abundance in soils, particularly at the Hanford Site. Atomic force microscopy was used to record the morphology of the resulting neptunium deposits. This project advanced our expertise in the area of the interaction of actinides with surfaces.

Sorption/desorption and precipitation/dissolution processes at mineral surfaces play a key role in determining the rate of migration of contaminants through soils and groundwater systems, and in the fixing of contaminants in soil minerals. Much empirical work has been performed on the macroscopic scale to determine distribution coefficients between groundwaters (or simulated groundwaters) and minerals. However, as stated succinctly by Liang et al. (1996), any rigorous attempt to understand and control the chemistry of the aqueous-mineral interface must include an explicit model of molecular-scale interactions at that interface. Molecular scale models of sorption/desorption and precipitation/dissolution have been hypothesized to describe the results of the macroscopic experiments and predict contaminant migration in real systems, with varying success.

Atomic force microscopy has been used to study the growth and dissolution of a number of minerals and to study the interaction of solution species with mineral surfaces. References for this large body of work may be found in a number of reviews (Maurice and Lower 1998; Maurice 1998; Hochella et al. 1998; Brady and Zachara 1996; Wicks et al. 1994). However, little molecular-level data exist on the interaction of actinides with mineral surfaces (Combes et al. 1992; Wersin et al. 1994). Three other studies that focus on the interaction of uranium (U) with mineral surfaces have recently appeared as presentation abstracts only (Nitsche et al. 1999; Wasserman et al. 1999; Morris et al. 1997).

Attention is now focused on subsurface radionuclide contamination issues, but little knowledge exists on the fundamental controlling processes for actinides. Investigation of these processes at the molecular level is key to understanding and developing accurate models of subsurface contaminant migration.

Results and Accomplishments

A NpO_2NO_3 solution (10 mg neptunium per mL) was prepared by purifying a solution containing multiple anions (NO_3^-, SO_4^{2-}, PO_4^{3-}, ClO_3^-), and neptunium in multiple oxidation states (+IV, +V, and +VI). Neptunium(V) crystalline deposits were formed by evaporating a 10 μL drop of the neptunium solution on a chip (10 mm x 5 mm x 2 mm) of freshly cleaved calcite. Such a deposition may mimic processes that occur in the vadose zone.

The neptunium deposits covered the calcite surface extensively. Large crystals 50 μm to 200 μm across and over 5 μm thick were observed, as well as dendritic crystals 5 μm to 10 μm wide, hundreds of μm long, and only 100 nm to 150 nm thick. Some ordering of both large crystals and dendrites was observed in the calcite substrate. The crystals covered most of the surface exposed to the solution. A blank sample showed very few crystals, indicating that the crystals are not simply dissolved and recrystallized $CaCO_3$.

A number of optical images (7) and atomic force microscopy scans (57) were collected. Crystalline deposits at the edge of the 10 μL drop coverage are shown

in Figure 1. This optical image (10X) was obtained using an optical microscope built into the atomic force microscopy instrument. The curving lower boundary of the regular crystalline arrays is the boundary of the drop. The edge of the calcite crystal is seen at the bottom of the image. The upper right boundary of the deposit was formed as the drop evaporated (the drop initially covered the bare upper right region). Another 10X optical image of the combination of large crystals and dendrites is shown in Figure 2. The preferred orientation of both crystals and dendrites, from upper left to lower right, is apparent.

Figure 1. 10X optical image of neptunium(V) crystalline deposits at the edge of 10 μL drop coverage

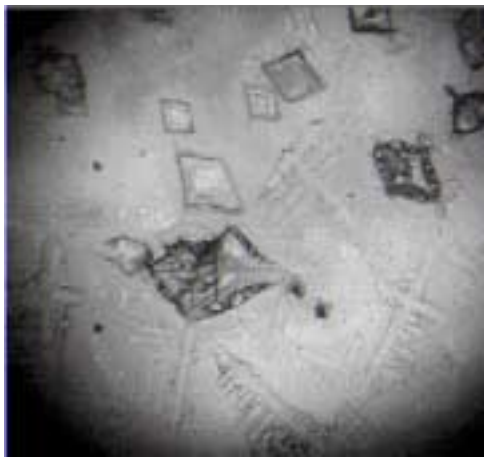

Figure 2. 10X optical image showing combination of Np(V) large crystals and dendrites

Figure 3 is a close-up of Figure 2, showing the dendrites in more detail. Figure 4 is a scan of the tip of the large crystal shown in Figure 3, using the atomic force microscopy scanning tip. This scan provided high spatial resolution in three dimensions. The thickness of this relatively small portion of the crystal was 5 μm, indicating that the total thickness of the large crystals was greater than this. Figure 5 is a closeup atomic force microscopy scan of Figure 4, showing crystalline terraces that form the large crystal. Figure 6 is an atomic force microscopy scan of the dendrites just to the right of the large crystal in Figure 3. The dendrites were 5 μm to 10 μm wide, 50 μm to 100 μm (or more) long, and had many parallel branches arrayed along their long edges. The line analysis capability of the atomic force microscopy software was used to determine the 100 nm to 150 nm thickness of the dendrites. The surface of the dendrites was found to be very flat, as shown in Figure 7. The height variation is less than 0.16 nm, probably within the error of this measurement.

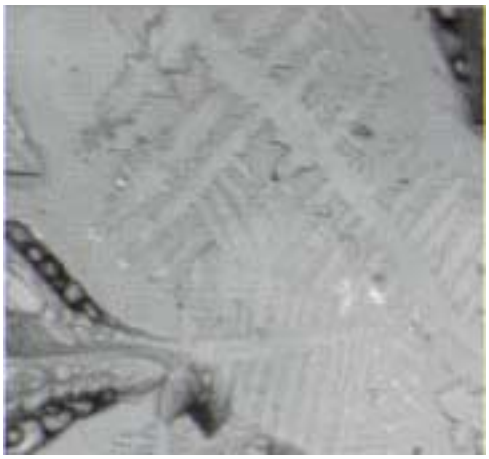

Figure 3. Close-up of Figure 2 (30X total) showing dendrites in more detail

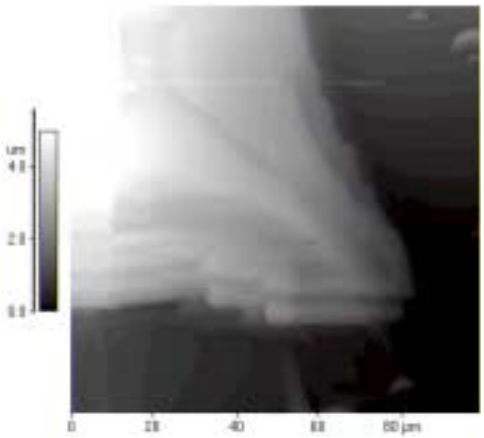

Figure 4. Atomic force microscopy scan of the tip of the large crystal shown in Figure 3. Crystal thickness is over 5 μm.

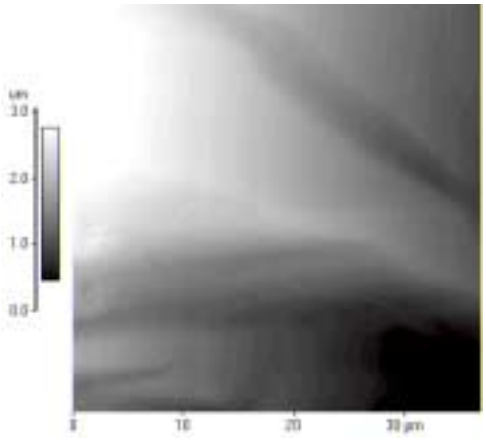

Figure 5. Close-up atomic force microscan scan of Figure 4 showing crystalline terraces that compose the large crystal

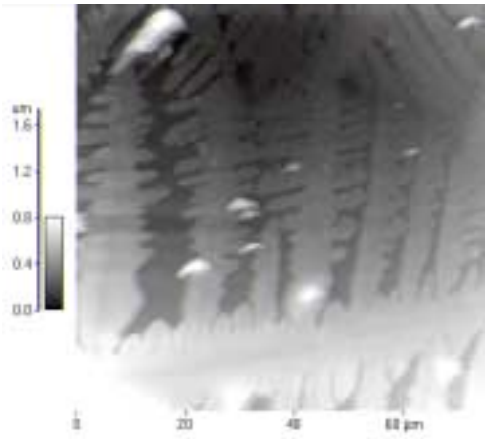

Figure 6. Atomic force microscopy scan of the dendrites just to the right of the large crystal in Figure 3

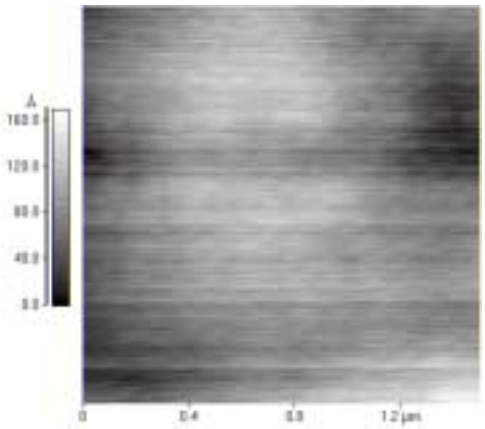

Figure 7. Atomic force microscopy scan of the surface of a dendrite shown in Figure 6

Summary and Conclusions

A sample of Np(V) deposits on the cleavage surface of single crystal calcite was prepared, and the surface imaged both optically and by atomic force microscopy. These images indicated that Np(V) forms both thick crystals and thinner dendrites under a deposition process that may be similar to that found in the vadose zone. Both large crystals and dendrites showed a preferred orientation, suggesting some alignment with the underlying calcite crystal structure. The project demonstrated our ability to collect data relevant to vadose zone and groundwater contaminant transport issues.

References

Brady PV and JM Zachara. 1996. "Geochemical applications of mineral surface science." *In Phys. Chem. Miner. Surf.,* 307-356, CRC, Boca Raton.

Combes JM, CJ Chisolm-Brause, GE Brown Jr., GA Parks, SD Conradson, GP Eller, IR Triay, DE Hobart, and A Miejer. 1992. "EXAFS spectroscopic study of neptunium(V) sorption at the a-iron hydroxide oxide (a-FeOOH)/water interface." *Environ. Sci. Technol.* 26(2):376-382.

Hochella MF Jr., JF Rakovan, KM Rosso, BR Bickmore, and E Rufe. 1998. "New directions in mineral surface geochemical research using scanning probe microscopes." ACS Symp. Ser., 715 *Mineral-Water Interfacial Reactions* 37-56.

Liang Y, DR Baer, JM McCoy, JE Amonette, and JP LaFemina. 1996. "Dissolution kinetics at the calcite-water interface." *Geochemica et Cosmochimica Acta* 60:4883-4887.

Maurice PA. 1998. "Scanning probe microscopy of environmental surfaces." IUPAC Ser. Anal. Phys. Chem. Environ. Syst., 4 *Structure and Surface Reactions of Soil Particles* 109-153.

Maurice PA and SK Lower. 1998. "Using atomic force microscopy to study soil mineral interactions." *Adv. Agron.,* 62:1-43.

Morris DE, JP McKinley, SC Smith, and JM Zachara. 1997. "Uranyl surface complexation on smectites: Combining optical spectroscopic studies with modeling." Book of Abstracts, 213th ACS National Meeting, San Francisco, California. GEOC-136.

Nitsche H, G Bernhard, G Geipel, M Rutsch, K-H Heise, S Pompe, K Schmeide, M Bubner, T Arnold, T Zorn, L Baraniak, A Abraham, B Mack, T Reich, A Rossberg, H Zaenker, P Panak, and S Selenska-Pobell. 1999. "Uranium speciation in the aquatic environment: Convergence between modeling results and laboratory and field measurements." Book of Abstracts, 217th ACS National Meeting, Anaheim, California. NUCL-139.

Wasserman SR, L Soderholm, C Williams, and MR Antonio. 1999. "The structure of actinide ions exchanged into smectite clays." Book of Abstracts, 217th ACS National Meeting, Anaheim, California. NUCL-198.

Wersin P, HF Hochella Jr., P Persson, G Redden, JO Leckie, and D Harris. 1994. "Interaction between aqueous U(VI) and sulfide minerals: Spectroscopic evidence of sorption and reduction." *Geochimica et Cosmochimica Acta,* 58:2829-2843.

Wicks FJ, GS Henderson, and GA Vrdoljak. 1994. "Atomic and molecular scale imaging of layered and other mineral structures." CMS Workshop Lect., 7 *Scanning Probe Microscopy of Clay Minerals* 91-138.

BWR Burnable Absorber Coating

Mikal A. McKinnon, Edward F. Love, David J. Senor

Study Control Number: PN98009/1255

This technology may serve to enhance operations in commercial nuclear facilities and make them more competitive with fossil fuel plants.

Project Description

Previous projects have completed neutronic analysis of a boiling water reactor core containing fuel assemblies with burnable poison in the channels. The results showed enhanced neutronic performance of the core that resulted in a lower pin peaking factor and a potential $500K cost savings per fuel reload (12 to 18 months). In fiscal year 1998, various methods of fabrication were studied including alloying, coating, and laminating. In fiscal year 1999, the development of the most promising fabrication technique was pursued using coupon-sized samples. For fiscal year 2000, several coupons were made and hot rolled. In addition to the hot rolling of the specimens, bending of the specimens was demonstrated. Metallographic analysis was completed to assess the performance of the coupons. Then the process used in developing the most promising coupon was used to demonstrate fabricability of channels at various scales.

Introduction

Three techniques for incorporating burnable absorber material into a boiling water reactor fuel channel were explored. One technique involved coating a zircaloy-4 substrate with erbium to form an intermetallic surface layer, another focused on producing laminates using erbium foil sandwiched between zircaloy-4 sheets, and a third explored zirconium-erbium alloys. We discovered that the foil method for producing laminates was not particularly promising, and a hybrid technique was developed in which erbium-coated zircaloy-4 coupons were used successfully to produce laminates.

Results and Accomplishments

Coating Development

Electrospark deposition was the coating technique selected as most promising. The technique can be easily adapted to provide coatings of different compositions or thickness at different locations on the substrate material.

Two significant modifications to traditional electrospark deposition coating were developed. The first was adapting the technique to use square cross-section electrodes. The second modification was adapting the technique to produce coatings under an inert cover gas rather than in air. Erbium coatings produced in air appeared to oxidize, which led to embrittlement and cracking upon cooling. With an inert cover gas, erbium coatings up to 75 µm thick were successfully produced in a single pass. Metallography of these coatings revealed excellent coverage with no cracks, good uniformity in thickness and a relatively smooth surface. Thicker coatings were produced by producing erbium layers in successive passes. Coatings up to 150 µm thick were successfully fabricated.

Laminate Development

The attractive feature of producing a zircaloy-erbium-zircaloy (Zry/Er/Zry) laminate is that the burnable absorber is not exposed to the primary loop coolant. By placing the erbium within the zircaloy structure of the fuel channel, issues associated with exposure to boiling water reactor primary coolant are avoided. For economic reasons, it is desirable to minimize changes to present fuel channel manufacturing processes. If erbium could be incorporated into zircaloy feedstock early in the manufacturing process, fabrication of fuel channels potentially could proceed with minor additional considerations due to the presence of erbium (welds and heat affected zones, nondestructive evaluation for erbium assay). Therefore, a series of experiments was conducted to evaluate the potential for roll bonding and subsequent cold- or hot-rolling of bonded laminates.

A hybrid technique was developed in which electrospark deposition erbium coatings were sandwiched with zircaloy-4 sheet to produce laminates. A variety of

erbium coatings were applied to zircaloy-4 sheet. The erbium coatings were applied in the pure state and also with Zr overcoats, and a variety of thicknesses and coating parameters were investigated.

Coated coupons (both Er-only and Zr-overcoated Er) were paired with other coated and bare zircaloy-4 coupons, and seal-welded to produce feedstock for hot roll bonding. Prior to welding, the surfaces to be bonded were sanded with SiC paper and swabbed with B-etch for several minutes to remove any oxide film. After preparation, the coupons were rapidly transported to the weld chamber to prevent oxide formation. Coupons were hot roll bonded at 800°C at overall thickness reductions of 10% to 20%. The best results were obtained with either erbium or Zr-overcoated erbium coatings bonded with bare zircaloy-4 coupons.

Coupons seal-welded in a He atmosphere were prevented from completely bonding during hot rolling by the He. Three alternate coupon welding techniques were investigated. These included: 1) electron beam welding in vacuum, 2) TIG welding in He with a brazed Cu tube serving as a vacuum port, and 3) TIG welding in He with a brazed Cu tube serving as a gas bladder to accommodate the He during hot rolling. The TIG welding techniques were unsuccessful because the braze failed during heating to 800°C prior to hot rolling. Although electron beam welding is not suitable for large, manfactured components, it was used for the remainder of the development work due to resource limitations. The TIG welding approach would likely work if Zr or zircaloy tubes were used for the vacuum ports or gas bladders.

Initial efforts to hot roll bond the coupons fabricated by electron beam welding were unsuccessful. The time between surface preparation (sanding and B-etch) and insertion into the vacuum chamber appeared to be unacceptably long, allowing an oxide layer to form. Later efforts were successful when the samples were stored in a dessicator and evacuated to 10^{-6} torr within 10 to 15 minutes after sample preparation. These samples displayed complete bonding across the width of the coupons, with no evidence of failures.

The final objective of the development effort involved a demonstration of the formability of the laminates in a prototypical width (approximately 20 cm). The most common method for producing boiling water reactor fuel channels involves forming the zircaloy-4 sheet into a U-channel, and butt-welding two U-channels to form a continuous square duct. Significant effort was expended to develop a suitable thermomechanical processing schedule to produce laminated U-channels of prototypic width. Difficulties associated with embrittlement of the zircaloy-4 by oxidation during hot rolling and annealing in air occured. To alleviate these problems, the surface oxide picked up during hot rolling was removed prior to further processing, and annealing was done in vacuum or inert gas.

After e-beam welding, the samples were milled on both faces to produce a prototypic thickness of 0.25 cm. They were then hot-rolled. The hot rolling was done in air. The oxide film was mechanically removed prior to annealing. The samples were then annealed and formed into U-channels using a mechanical press.

Experimental work on this study is in its final stages. A prototypic-dimension fuel channel section will be produced from two U-channels produced using the process described above. Some of the U-channels will be hot-rolled and/or annealed at 750°C to evaluate the effect of a lower working temperature. Ideally, a final thermomechanical processing schedule will be established as the starting point for manufacturing scale-up activities that would be conducted as part of a follow-on program.

Summary and Conclusions

To date, the study has demonstrated the feasibility of producing Zry/Er/Zry laminate structures consistently and with reasonably reproducible properties. Laminates and U-channels have been produced in prototypic thicknesses and widths for boiling water reactor fuel channel applications. Significant development work remains to transform the laboratory-scale process to one more suitable for high-throughput production. However, most of the methods used for commercial zircaloy production appear to be applicable to fabricating square ducts fabricated from Zry/Er/Zry laminates.

Bibliography

American Society for Testing and Materials. 1979. S*tandard specification for zirconium and zirconium alloy sheet, strip, and plate for nuclear application*, *ASTM B 352-79*. American Society for Testing and Materials, West Conshohocken, Pennsylvania.

Savitskii EM, VF Terekhova, IV Burov, IA Markova, and OP Maumkin. 1962. "Rare earth alloys." USSR Academy of Sciences, p. 58. Moscow.

Love B and C Kirkpatrick. 1961. "Mechanical properties of rare earth metals" in *Rare Earth Research*, Ed. E.V. Kleber, The Macmillan Company, New York.

Formation Decomposition of Hydrated Phases on Nuclear Fuels

Brady Hanson, Bruce McNamara, John Abrefah, Steve Marshaman

Study Control Number: PN00045/1452

Recent studies at this Laboratory suggest that the presence of small quantities of hydrated uranium oxide can be deleterious to dry storage of spent nuclear fuels. An understanding of the mechanisms and kinetics of formation of these hydrated phases and a technical basis for a drying technique to remove the physisorbed and chemisorbed water from spent fuel is necessary to mitigate these undesirable consequences.

Project Description

The purpose of this project is to determine whether hydrated phases of spent fuel are expected to form under the typical conditions a failed fuel rod would experience in a spent fuel storage pool and to establish the technical basis for a drying technique to remove these phases. The presence of water, even in an absorbed phase, may be detrimental to long-term dry storage of spent fuels. Samples of unirradiated UO_2 and spent fuel were hydrated at various temperatures by placing them in deionized water. The hydration products were observed and identified using x-ray diffractometry. These hydrated phases were then subjected to thermogravimetric analysis under a variety of temperature and atmospheric conditions to observe the decomposition of the hydrates. It appears clear that hydrated phases will form during pool storage and the industry standard vacuum drying techniques are inadequate to remove the absorbed water from the fuel.

Introduction

A fraction of fuel rods are known to fail (via pin-holes in the cladding or larger defects) during in-core operation and storage in spent fuel pools. These failed rods may become waterlogged and allow hydrated phases of the fuel to form. The presence of small quantities of hydrated fuel have been shown to increase the dry-air oxidation rate by up to three orders of magnitude over fuels where no hydration has occurred. This rapid oxidation is important to consider in the event of off-normal or accident scenarios involving the ingress of air during dry-storage, transportation, or repository conditions. In addition, free and absorbed water remaining in a cask may be subjected to radiolytic decomposition and form species that could degrade the fuel, cladding, or system components.

Current industry practices for drying commercial fuel assemblies call for subjecting the assembly to a vacuum of approximately 3 torr for 30 minutes and then repeating. Based on studies of N-Reactor fuel at PNNL, such a vacuum technique without applied heat and a properly controlled atmosphere was inadequate for removal of physisorbed and chemisorbed water from failed rods. The aims of this project were first to determine whether hydrated species are expected to form under the conditions experienced in a spent fuel pool and second, to determine the conditions necessary to remove these phases. Our goal was to develop a simple and economical means by which free and absorbed water could be removed from failed fuel rods and minimize any future degradation associated with the presence of water.

Approach

Approximately 1-gram samples of unirradiated UO_2 fragments and powders were placed in glass vials. The fuel was covered with about 8 mL of water and the vial was then capped. Batches of samples were heated at 25°C, 60°C, 75°C, and 95°C. Each week, the samples were shaken and stirred with a glass stirring rod to provide maximum surface area contact of the fuel with the water. Subsamples (~10 mg) from selected vials were then removed for semi-quantitative analysis using x-ray diffraction. The samples were prepared by combining a known quantity of fuel with a similar, known quantity of Al_2O_3, which served as an internal standard. Duplicate samples were prepared for each of the unirradiated specimens. A similar procedure was followed using spent fuel powders. Samples of the original material had been similarly analyzed to ensure that there were no hydrated species prior to placement in the water.

Subsamples (~250 mg) of those specimens where x-ray diffraction had positively identified hydrated phases were then heated under a controlled atmosphere using a thermogravimetric analysis system. The rate of weight change as a function of time and/or temperature was measured. The decomposition of the hydrated phases was observed at heat ramp rates ranging from 0.2°C min^{-1} to

5°C min^{-1} and at temperatures up to 400°C. During these tests, the fuel was held at a constant temperature of 75°C for 2 hours before the temperature was increased. Tests were conducted under vacuum, and with flowing nitrogen, helium, or hydrogen/argon mixture. When the thermogravimetric analysis tests were completed, the specimens were again analyzed using the semi-quantitative x-ray diffraction procedure to determine the residual phases.

Results and Accomplishments

Hydrated Phase Formation

The results of the hydration experiments clearly indicated that hydrated phases formed rapidly on both unirradiated UO_2 and spent fuel powders. Quantities large enough to be observed using x-ray diffraction formed within 10 days at 95°C and within 6 weeks at 25°C. Two different phases were identified, dehydrated schoepite ($UO_3 \bullet 0.8H_2O$) and, more predominantly, metaschoepite ($UO_3 \bullet 2H_2O$). The relative quantity of hydrated phase increased with time (Figure 1).

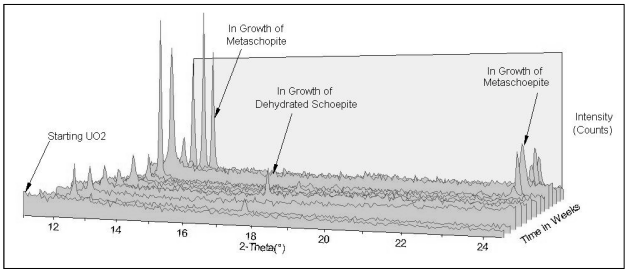

Figure 1. In-growth of hydrated phases as a function of time at 95°C

Metaschoepite was also identified on unirradiated powders that have been left exposed to ambient air for several years (aged fuel). It is not clear whether the dehydrated phase forms prior to the in-growth of the metaschoepite and there is no clear temperature dependence favoring formation of one phase over the other. At all temperatures, we observed a pattern (Figure 2) where the hydrated phases would form and be identified using x-ray diffraction, but the samples taken the following week would exhibit a decrease in relative quantity of hydrated phases. Overall, we saw a trend to higher quantities of hydrated phases being present on the fuel. However, the reason for the intermittent decreases was not known. Future tests must analyze the uranium concentration in the liquid to help understand the mechanisms associated with this observation.

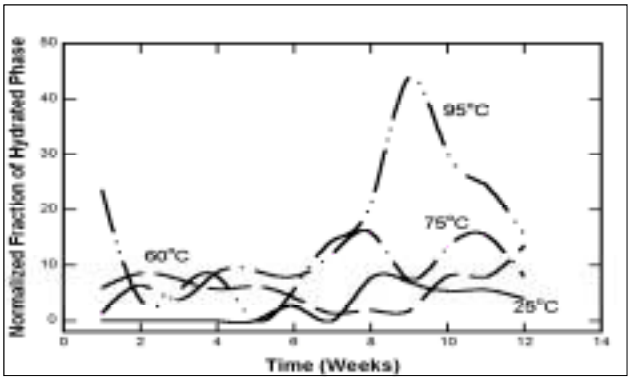

Figure 2. Normalized quantity of hydrated phases as a function of time and temperature

Another interesting observation was that of "floating" phases. With time, increasing amounts of a white, flocculent material (identified as metaschoepite) was observed floating on top of the water. When the aged fuel was placed in water, large black floating material (also identified as metaschoepite) was observed (Figure 3). The implication of these phases on transport and radionuclide release is not known.

Figure 3. "Floating" phase (metaschoepite) on aged fuel

Hydrated phase decomposition

The results of the thermogravimetric analysis tests clearly showed that different waters of hydration were released at different temperatures, with a temperature of about 300°C being required to remove most of the water. Figure 4 illustrates the typical weight loss of a sample and the associated temperature profile for decomposition runs up

to 300°C and 400°C. Unfortunately, the amount of tramp oxygen in the system was enough to allow oxidation of the fuel once the temperature approached 275°C, even with a 3% hydrogen gas mixture flowing through the system.

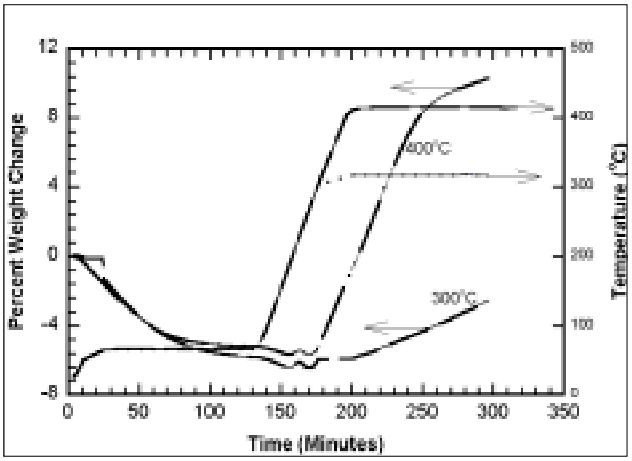

Figure 4. Thermogravimetric analysis decomposition of metaschoepite at 300°C and 400°C

X-ray diffraction of the samples after thermogravimetric analysis testing showed that the metaschoepite had been removed. However, dehydrated schoepite remained. It was not clear if the dehydrated schoepite was a decomposition product of the metaschoepite or if the decomposition product was UO_3, which then readily rehydrates even at ambient conditions. A truly inert environment must be maintained, even for preparation of the x-ray diffraction sample to address this issue. Thermogravimetric analysis testing on the dehydrated schoepite demonstrated that even with temperatures of about 300°C for over 10 hours, this phase was not completely removed. Testing under more controlled conditions and under different atmospheres is necessary to optimize the method for removal of the hydrated phases.

Summary and Conclusions

Testing on unirradiated UO_2 and spent fuel powders clearly demonstrated that hydrated phases formed rapidly under conditions expected under spent fuel pool storage. While the large surface area of the samples tested was a factor, the time in storage for spent fuel supported the conclusion that hydrates will form. The week-to-week fluctuations in the relative quantity of hydrated phases are not explained, but they raise the question as to whether hydrated phases are formed by a dissolution/ reprecipitation reaction as assumed or if they are formed through direct reaction with the fuel. The stability of these hydrated phases, especially metaschoepite, in an aqueous environment was unresolved. The observation of floating phases raised questions regarding the expected transport of radionuclides from areas contaminated with uranium.

Standard drying techniques that do not apply heat will not remove the absorbed water. Additional atmospheres must be tested to determine the conditions for removing hydrated phases from failed spent fuel rods.

References

CRWMS M&O. 2000. *Clad Degradation-Dry Unzipping*. ANL-EBS-MD-000013 REV00. Las Vegas, Nevada.

Oliver BM, GS Klinger, J Abrefah, SC Marschman, PJ MacFarlan, and GA Ritter. 1998. *Drying Results of K-Basin Fuel Element 1164M (Run 6)*. PNNL-11896, Pacific Northwest National Laboratory, Richland, Washington.

Proliferation Signatures

Douglas P. Frank, Michael P. Sohn, Richard A. Libby, Michael J. Newman, Robert G. Clemmer

Study Control Number: PN99058/1386

Our Laboratory conducts research needed to identify and thwart the proliferation of weapons of mass destruction. Details of this research are classified.

Project Description

The aim of this project is to analyze, research, and validate a specific nuclear proliferation scenario not previously investigated. Identification of the corresponding signatures for that scenario and design of appropriate response options will also be studied.

The first objective of the project is validation of the specific nuclear proliferation scenario, in terms of technical viability and potential for implementation. The second objective is to identify the signatures associated with the proliferation scenario through analysis of the associated processes and necessary facilities. The third objective is to design response options for the scenario in general, as well as for the specific signatures.

Results and Accomplishments

The project is divided into four phases: 1) technical assessment, 2) technical analysis and design, 3) signature analysis, and 4) response options.

The first and second phases of the project have been successfully completed. The specific nuclear proliferation scenario has been validated as technically viable. The technical analysis and design phase of the project has identified and resolved implementation issues.

Presentations

Presentations of this work were made to the Department of Energy, Office of Intelligence, and to the Defense Intelligence Agency.

Reactor Transmutation of Waste

Rick J. Migilore

Study Control Number: PN00078/1485

Technetium-99 and iodine-129 are long-lived fission products generated during the normal operation of a nuclear reactor. Methods were studied on ways to transmute these radionuclides into nonhazardous forms and thereby eliminate the long-term risks associated with their disposal in a repository.

Project Description

The purpose of this project is to determine the amounts of technetium-99 (Tc-99) and iodine-129 (I-129) that may be transmuted into stable isotopes using existing commercial nuclear reactors. It would be advantageous to destroy these long-lived isotopes, and to mitigate the associated long-term risks of storing and containing them in the Yucca Mountain repository. The computer program Monte Carlo N-Particle (MCNP) transport code was used for the transmutation calculations. We estimated that approximately 63% of the projected Tc-99 inventory and 35% of the projected I-129 inventory could be transmuted during the years 2010 through 2030 using existing light water reactors. This concept appears to be feasible, as commercial nuclear reactors can be designed to burn more of these isotopes than they produce.

Introduction

Reactor transmutation of waste has been studied extensively over the past 25 years using a variety of calculational methods and reactor types (Wachter and Croff 1980; Binney et al. 1990; Wootan et al. 1992; Abrahams et al. 1995). The goal of waste transmutation studies is to demonstrate that reactor waste can be destroyed, thereby circumventing the risks associated with disposing of the waste in an underground repository. The spent fuel repository slated to be built at Yucca Mountain must comply with federal regulations for a period of 10,000 years, although the risks to the public do not end after that time. Reactor transmutation of waste would eliminate the long-lived fission products in the waste stream, leaving only shorter-lived fission products to be disposed. Reactor transmutation of waste would reduce the required repository confinement lifespan to 500 years or less, because after that time the waste would be no more radioactive than the original uranium ore.

Most transmutation studies include transmutation of actinides (heavy metals such as plutonium, neptunium, etc.) in addition to transmutation of fission products such as Tc-99 and I-129. The current study focused only on the transmutation of long half-life fission products Tc-99 and I-129 and assumed that all actinides are recycled.

Tc-99 and I-129 are transmuted to stable isotopes by the following reactions:

$$^{99}Tc + n \rightarrow {}^{100}Tc \rightarrow {}^{100}Ru \text{ (stable) } 16s\ (\beta^-)$$

$$^{129}I + n \rightarrow {}^{130}I \rightarrow {}^{130}Xe \text{ (stable) } 12.4h\ (\beta^-)$$

Further irradiation of Ru-100 and Xe-130 leads only to stable isotopes. Xenon-130 is a gas and that the target must be designed to accommodate the increase in pressure from buildup of radioxenon.

Tc-99 is metallic and may be formed into slugs for irradiation without difficulty. I-129, conversely, is a gas and must be bonded with another material prior to irradiation. For the purposes of this study, solid vanadium iodide (VI_2) was selected as the form to be irradiated. Vanadium iodide was selected for both its high density (5.44 g/cm^3) and high melting temperature (1431°F). The stability of this compound in a true radiation environment is unknown. Iodine compounds may be corrosive to cladding materials.

Approach

The MCNP reactor physics code was used to calculate the instantaneous transmutation rate for each of the nuclides. A simplified 3000 MWt pressurized water reactor core was modeled using 17x17 fuel assemblies. Each fuel assembly has 24 locations that may be used for inserting fission product target rods. To maximize the quantity of fission product targets that may be inserted into the reactor, all of the target locations are filled with target rods. In reality, this would not be possible, as locations must be retained for control rods. Six different cases were executed.

Case 1: Full-density solid targets

Case 2: Full-density thick annular targets (IR=0.2 cm, OR=0.41 cm)

Case 3: Full-density thin annular targets (IR=0.35 cm, OR=0.41 cm)

Case 4: ½ density solid targets

Case 5: $^{1}/_{700}$ density solid targets

Case 6: Target material mixed directly with fuel.

Note that Case 6 is different than the other cases because target rods are not used. In Case 6, the target material is mixed directly with the fuel in a quantity that contains the entire available Tc-99 and I-129 inventories in all available reactors (both pressurized water and boiling water reactors).

We estimated that 73 MT of Tc-99 and 20 MT of I-129 will be generated when all of the current operating light water reactors in this country have been shut down. We assumed for this report that the transmutation effort would begin in the year 2010 and that the inventory of Tc-99 and I-129 available for irradiation in 2010 would be 45 MT and 14.5 MT, respectively.

Results and Accomplishments

Table 1 gives the yearly transmutation percentage per reactor, the number of reactors required to contain the inventory, and the yearly transmutation rate using all necessary reactors for Cases 1 through 6, assuming available inventories of 45 MT Tc-99 and 14.5 MT I-129. Both Tc-99 and I-129 have the highest transmutation rates when present in low concentrations in a reactor. This effect results from the reduced self-shielding when these isotopes are present in low quantities. However, as the quantity per reactor is reduced, the number of reactors required to burn the inventory increases. In particular, Case 5, which has the best overall transmutation rate, has the worst total throughput due to the large number of reactors that would be required to contain the targets. However, Case 5 does demonstrate the importance of self-shielding to this problem, particularly for Tc-99.

These results may be extrapolated through the year 2030 to give an approximate life-cycle analysis, taking into consideration generation of Tc-99 and I-129 in these reactors during this time, and yearly decommissioning of 40-year-old reactors. We estimate that a typical reactor will generate approximately 25 kg/yr of Tc-99 and 5 kg/yr of I-129. For the life-cycle analysis, Case 6 was selected for Tc-99 as it had the highest transmutation rate, while Case 2 was selected for I-129 because the annular design allowed for Xe gas buildup and because of the small number of reactors required. Tc-99, Case 6, gives a total 20-year transmutation of 46.3 MT, or 63% of the total projected inventory destroyed. I-129, Case 2, gives a total 20-year transmutation of 6.9 MT, or 35% of the total projected inventory destroyed.

The effects of adding Tc-99 to the fuel matrix and the implications regarding fabricability are important. Adding Tc-99 to the fuel matrix would result in an additional dose rate of 3 mrem/hr on the surface of a fuel pellet. The contact dose rate of a pellet is a function of both enrichment and age and can exceed an exposure rate of 200 mrem/hr. Therefore, the dose effects of adding an additional 3 mrem/hr from Tc-99 in the fuel matrix appear to be inconsequential.

Table 1. Transmutation rates for Tc-99 and I-129 (year 2010)

	Tc-99			I-129		
	Transmutation Rate Per Reactor	**Approx. Number of Reactors Required**	**Total Annual Transmutation Rate (MT/yr)**	**Transmutation Rate Per Reactor**	**Approx. Number of Reactors Required**	**Total Annual Transmutation Rate (MT/yr)**
Case 1	1.43%	4	0.65	2.12%	5	0.31
Case 2	1.64%	6	0.74	2.21%	7	0.32
Case 3	2.46%	16	1.11	2.71%	19	0.39
Case 4	1.91%	9	0.86	2.50%	10	0.36
Case 5	8.35%	3028	0.09[(a)]	3.05%	3589	0.01[a]
Case 6	5.65%	All (106)	2.54	2.69%	All (106)	0.39

(a) Based on 69 PWRs.

Summary and Conclusions

Transmutation of Tc-99 and I-129 in light water reactors is feasible because reactors are capable of destroying more of these wastes than they produce. These isotopes may be mixed directly with the fuel or fabricated into target pins. In both cases the transmutation rate is highest when the isotopes are mixed directly with the fuel, presumably because self-shielding in the target pins is significant, especially for Tc-99. We therefore recommend mixing small quantities of Tc-99 directly into the fuel matrix.

Because of the potential corrosive nature of iodine on cladding materials in a reactor environment, we do not recommend mixing I-129 into the fuel. Rather, the I-129 should be bonded with vanadium as solid vanadium iodide (VI_2) and should be fabricated into annular target pins. We recommend an annular design to accommodate the pressure increase due to xenon buildup in the I-129 target pin, as xenon gas is a product of I-129 transmutation. We expect that 63% of the projected Tc-99 inventory and 35% of the projected I-129 inventory could be destroyed by 2030 if a transmutation scheme is adopted.

References

Abrahams K et al. 1995. *Recycling and Transmutation of Nuclear Waste*. ECN-RX-95-067. Netherlands Energy Research Foundation (ECN), Petten, Netherlands.

Binney SE et al. 1990. *CURE: Clean Use of Reactor Energy*. WHC-EP-0268. Westinghouse Hanford Company, Richland, Washington.

Wacher JW and AG Croff. 1980. *Actinide Partitioning-Transmutation Program Final Report. III. Transmutation Studies*. ORNL/TM-6983. Oak Ridge National Laboratory, Oak Ridge, Tennessee.

Wootan DW et al. 1992. *A Comparative Assessment of the Destruction of Selected Fission Products in Fast and Thermal Reactors*. WHC-SA-1436. Westinghouse Hanford Company, Richland, Washington.

Policy and Management Sciences

Assessing Vulnerability to Climate Change

Richard H. Moss

Study Control Number: PN99004/1332

Research on global climate change is driven by the increasing levels of carbon dioxide in the atmosphere. Scientific studies on climate change include policy analysis to determine risks and appropriate actions.

Project Description

An important scientific challenge with high relevance to climate-change policy formulation is to identify the potential human consequences to rates and magnitudes of climate change associated with different atmospheric concentrations of greenhouse gases. This project builds on initial proof-of-concept methods for assessing vulnerability and resilience to climate change.

Results and Accomplishments

We performed analyses at the national and global levels, benchmarked against both U.S. and global baselines. We performed an uncertainty analysis that validated the concept of leading indicators. Work on this project was interrupted because the principal investigator was asked by DOE to lead a high-priority project to prepare a long-term strategic science plan for the U.S. Global Change Research Program.

Potential future plans include the following:

- further analysis of potential proxy variables in each of five sectors
- programming and database development, including incorporation of approaches for analysis of uncertainty in the indicator results
- development of qualitative analysis techniques for data interpretation in integrated assessments of vulnerability and adaptation options, including incorporation of effects of climate variability and extreme events
- completing the draft of a research results publication.

Sensors and Electronics

Advanced Calibration/Registration Techniques and Software Agents for New Generation Remote Sensing Systems

George G. He, Louis M. Martucci, Brian D. Moon

Study Control Number: PN99002/1330

Remote sensing is a key national security tool. The availability of remotely sensed images from new generation commercial satellites, along with national technical means, will create opportunities for serving national energy priority (resource exploration) and security interests (nonproliferation and counter-proliferation). This project developed a "random" computing architecture and algorithm in the form of software agents equipped with database-like technology, such as triggers and transaction controls to improve image precision, accuracy, and repeatability.

Project Description

Common imagery artifacts include different scales, resolution, and revisit frequency. For the new generation of remote sensing systems, the multi-modality data collected are large in volume, inconsistent in precision and accuracy, and complex in attributes. Registration and calibration are essential for bringing imagery to a common useful state so that data can be combined and metrics like thresholding applied. The standard approach of carefully controlling the sensor pointing and tracking to allow registration of the data, or manually registering and calibrating the data has proved to be less than optimum. This project advances technical capabilities in performance diagnosis, system analysis, and exploitation of output data from remote sensing imaging systems to support national security decision-making interests.

A typical scenario might be the surveillance of rogue nations attempting to establish nuclear weapons facilities or develop a military infrastructure for aggression against neighboring states. Critical to a successful assessment of such situations would be the use of change detection over a large area where multi-temporal imagery from successive acquisitions is comparatively analyzed. Beyond the observation and tracking of obviously large features of interest would be the detection of smaller details near the resolution limits of imagery, which can be obscured or distorted by uncalibrated or poorly registered data. This project is aimed at uncovering the maximum information content of commercial imaging systems, regardless of the sensor type, and will also offer potential applications for national security systems.

Introduction

This project focused on replicating previous registration and calibration results in earlier planetary science studies conducted by the principal investigator. The new result was mandated so that such replication would be based on an advanced computational technique centered on the use of agent technology and amenable to full automation using ratios rather than auto-correlation or difference. The adopted innovative method is superior to the manual and semi-automatic procedures used in the planetary work, and has potential to encompass a variety of imaging systems and diverse acquisition requirements that are expected in the emerging generation of remote sensing platforms. The goals were demonstrated through the efforts of a multidisciplinary team of scientists from several laboratory technical groups.

Results and Accomplishments

Agent Architecture for Automation

A key project component is the core agent system. This includes a master agency, field office, tasking, display, global registration, local registration, sub-pixel registration, and user interface agents. These agents are designed to communicate, query, and learn from each other to solve a particular registration task requested by the user interface agent. The user initiates a request to perform a task such as to register two images using the user-interface agent. Since the user-interface agent has no registration capability, query is sent to the master agency via the field office asking for an agent that knows registration. Upon receiving the message, the master

agency will query the field offices for agents able to do registration and picks one that can deal with the request. The tasking agent is designed to handle the registration task and picks up the request from the master agency. The tasking agent communicates with the global, local, and sub-pixel registration agents and supplies the appropriate input parameters to each agent upon request. The local registration agent requires knowledge of the general offset between the two images as determined by the global registration agent. The display agent is requested to visualize the processing results for quality control.

Resource Dependency and Triggers

Our agent design uses multiple threads for message receiving, retrieving, forwarding, and processing. The message queue is populated from several threads that impose no restrictions on the order in which messages enter the queue. This could be a major problem if the visualization needed for debugging and quality control is out of sequence with the messages that other agents are sending. The mechanism used to create resource dependencies inside the messages traveling in the system is called a trigger. A message containing a trigger will not be released for processing until the trigger release (required resource) is received. Any message can be dependent on zero or more resources and any resource can be the trigger for zero or more messages waiting to be processed. The concept feasibility demonstration is fully implemented with this trigger and trigger release mechanism.

The agent system assumes that not all the necessary resources and tools to solve a specific request are in place, and the system may have to hold the request until the resource becomes available. This design holds true even during system startup when agents are busy establishing communication links between one another. The trigger and trigger release mechanism enables the randomly initiated and queued up events to be coordinated.

Transaction Controls

Another feature of our agent architecture is the ability to mark messages as being part of a transaction. The transaction controls enable process flow tracking and debugging. In an experimental setting, one can submit many different requests to the agents, analyze the results, and then select and save the process flow that produced the best results. Transaction controls also provide the ability to maintain locks on resources much like the standard database transactions.

Registration Problem Revealed by Galileo Imagery

This research used images of Earth's moon acquired by the Galileo probe en route to Jupiter. Figures 1a and 1b display the image pair located in the Humboldtianum basin on the west limb of the moon, with rotation, scale, and offset differences due to slightly different geometries produced by relative motion between the moon and the spacecraft. To achieve meaningful composition analysis through ratio, precise registration of the image pair was required.

The quality of the registration results is best judged by examining the ratio of the co-registered images. Considering the extensive manual effort employed to establish several dozen registration points in Figure 1c, the results were relatively inadequate for this seemingly simple, but actually very complex, technical task. In contrast, the methodology with limited human intervention establishes computer agents that independently search through the images to find thousands (rather than tens) of registration points. The resulting image (Figure 1d) is much clearer than the manually registered image. When comparing the two results, note the crater in the top left quadrant. Both the crater and the radial arms are more clearly depicted in Figure 1d. The false valley and ridge features of the crater/trajectory region in Figure 1c are eliminated in Figure 1d. Our advanced registration and calibration agent automated and more accurate approach is superior to the manual method.

Calibration Diagnostics Using LANDSAT 7 Imagery

LANDSAT 7 collects its thermal channel with two observations (high and low gains). Because the difference between the two gains lies in gain and offset only, their corrections render the difference between corrected images statistically insignificant. We demonstrated the existence of significant difference by traditional statistics. Subsequently, our advanced registration and calibration agent method was used to reveal calibration diagnostics. The use of ratio and binning provided visual cues for the search of root cause of the calibration errors.

By selecting multiple (5) areas (Table 1) of different ranges of digital number, traditional statistics can be used to model and compare the gain and offset to reveal the consistency for the collected data. In general, the relationship between the low gain and high gain digital number may be expressed as:

$$Hi = offset + slope \times Low \qquad \textit{(Equation 1)}$$

Figure 1a. Violet filter

Figure 1b. Blue filter

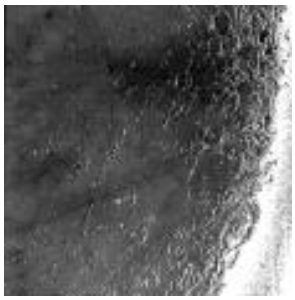

Figure 1c. Ratio using human manual system

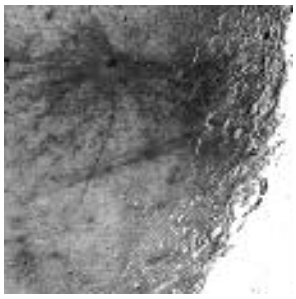

Figure 1d. Ratio using the advanced registration and calibration agent algorithm

The analysis described here incorporates both areas, when one is compared to the other, into one model as:

Hi = offset + incremental offset + slope x Low + incremental slope x Low *(Equation 2)*

Statistically significant values for incremental values of offset and slope reflect a problem of calibration consistency within the original image for the five areas (i.e., relative to each other, they provide a different low/high gain relationship and the difference is likely due to incorrect calibration).

Table 1. Data results summary across the five test areas within LANDSAT image

	Digital Number Range			Regression Estimates	
Area	Low-Gain	High-Gain	Number of Pairs	Intercept	Slope
1	131-172	151-225	223	-84.18	1.797
2	89-165	73-212	392	-89.58	1.830
3	115-164	122-210	277	-86.64	1.807
4	117-158	125-199	232	-86.04	1.802
5	121-163	133-209	203	-84.63	1.793

Equation 2 was used to fit the data selected from five different regions for both high and low gain offsets. Table 1 provides the range of digital numbers for each area, the number of unique pairs in each area, and the absolute regression intercept and slope for each area. The intercepts and slopes are pair-wise statistically significant. The incremental slope and intercept are statistically distinct from zero indicating that the effective calibration across the five areas is different.

The regression intercepts are significantly different. Of particular note is the -89.5819 estimate for area 2—some 5 digital number units different from the intercept estimate for area 1. Care must be taken to appropriately interpret these estimates as an ordered pair (i.e., intercept and slope) and not necessarily as individual entities. The regression lines associated with each area are not parallel (i.e., the slope estimates above are not the same statistically). Therefore, gray-scale pixel value differences between areas will change in magnitude with increasing magnitude of low-gain gray scale. The differences in the gray-scale pixel values for each area are what matters most. Table 2 spans the effective range of low-gain gray-scale values. Table 2 provides the difference between the area estimated high-gain gray-scale value and the smallest high-gain gray-scale value for a given low-gain gray-scale number. For example, column 1 shows differences for a low-gain gray-scale value of 100. The estimated high-gain value for area 2 is 93.4. The same calculation for area 1 is 95.5. The area 2 estimate was the lowest of the five areas (denoted by the '*') for this value of low-gain gray scale. The difference between the two estimates (2.1) is recorded in the table. One can see that area 1 is consistently at least 1 digital number different over the entire range. Areas 2 and 4 share the notoriety of having the minimum high-gain estimates for specific ranges of low-gain values.

Table 2. Extent of estimated high-gain values for specified low-gain values

	Values for low-gain gray scale						
Area	100	110	120	130	140	150	160
1	2.1	1.8	1.5	1.2	1.1	1.0	1.0
2	0*	0*	0*	0.1	0.3	0.6	0.9
3	0.6	0.4	0.3	0	0	0.1	0.1
4	0.8	0.5	0.3	0*	0*	0*	0*
5	1.3	0.9	0.7	0.3	0.1	0.1	0

Figure 2 illustrates use of the ratio binning technique for diagnosing the calibration error revealed by the standard statistical approach for areas 1 and 2. Due to the lack of absolute truth, a relative comparison scenario in which a high digital number region was used as the base data set. For the low-gain offset data set, a linear regression was used to remove the correlation between high- and low-gain offset observations before the ratio-binning technique is calculated. The intensity of the modeled high-gain value based on low-gain observation was then ratioed to the actual high-gain measurement. Next, the

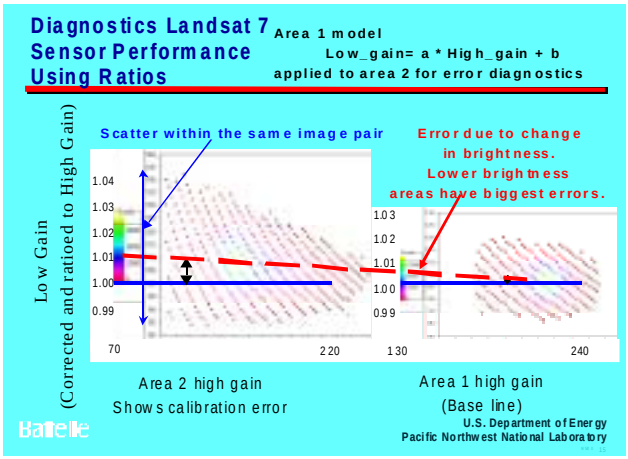

Figure 2. LANDSAT 7 thermal channel calibration error diagnostics using ARCA and CIT methods and technology

ratio was paired with the actual high-gain measurement as input for the ratio-binning plot. The low intensity area was processed in the same manner, with the same regression coefficients and method for calculating ratio and plot as used in higher digital number area. The comparison between the two different regions shows at least 1% difference in ratio with respect to ~70 digital number difference between the selected high and low intensity areas. The error budget for the system should be bigger than 1% given the difference of 1% for a 70 digital number. This dependency will create hidden problems for any automation process if not correctly diagnosed and calibrated. The use of this technology and its fundamental predecessors provides the foundation for error modeling, diagnostics, and production of accurately registered and calibrated images.

Summary and Conclusions

The human brain is our best image-processing tool. As a result, image processing has traditionally required a large amount of manual labor. The automated advanced registration and calibration agent technique developed during this project better employs and optimizes the human element in the process, while still achieving a high level of precision and accuracy.

Autonomous Ultrasonic Probe for Process Measurements

Richard A. Pappas, James A. Fort, James M. Prince, Larry D. Reid, Gerald P. Morgen

Study Control Number: PN00012/1419

Ultrasonic probes can become effective real-time sensors for process monitoring and control. Ultrasonic methods are proven performers for continuous, noninvasive monitoring of fluids during processing and conveyance. The applications of this technology share a common set of measurement parameters, including signal time-of-flight and amplitude.

Project Description

This project applied novel signal processing techniques and automated signal mixing designs to making high-precision measurements of time-of-flight and amplitude. These features were incorporated into the design of an autonomous ultrasonic probe. The end deliverable is a demonstration device that develops and captures the technology necessary for the fabrication of an autonomous ultrasonic probe.

Introduction

Ultrasonic methods are proven performers for continuous, noninvasive monitoring of fluids during processing and conveyance. The myriad of applications share a common set of measurement parameters: signal time-of-flight and amplitude. One, or both, of these two parameters are measured whether the need is to determine liquid fill level, identify liquid contents, or measure fluid flow rates. Technical limitations for many applications in the processing and transporting of hazardous waste and industrial chemical reactor gas-solids include a means to automate ultrasonic time-of-flight and amplitude measurements at lower frequencies (200 kHz to 500 kHz). A prototype ultrasonic probe using advanced signal processing techniques to provide automated time-of-flight and amplitude outputs was the product of this research.

Approach

The prototype device on a single, bench-top electronics board included a custom design for signal mixing and a Texas Instruments, TMS320C31 Floating Point Digital Signal Processor. The device provides two direct current voltage signals and a parallel interface for outputs of the time-of-flight and amplitude. Time gating and amplitude threshold are adjustable by software and electronic potentiometers on the board with subsequent designs providing for remote programmable settings.

Results and Accomplishments

The product of this research was a demonstration device that develops and captures the technology necessary for the fabrication of an autonomous ultrasonic probe. The demonstration probe resides in a bench-top configuration (see Figure 1). The next generation device will be a small device that possesses the application simplicity of a thermocouple or accelerometer. It can be installed on process vessels and transport lines and can be programmed for the specific application needs. Its high degree of automation and low frequency of operation will allow for an extension of noninvasive ultrasonics into difficult and severe environments encountered when dealing with hazardous waste and industrial chemical manufacturing. The probe concept will incorporate advanced communication technologies, such as wireless techniques.

Figure 1. Autonomous ultrasonic probe demonstration prototype device

Cavity-Enhanced Infrared Absorption with Quantum Cascade Lasers

Tanya L. Myers, Richard M. Williams, Matthew S. Taubman, Steven W. Sharpe, Robert L. Sams, James F. Kelly

Study Control Number: PN00018/1425

Laser spectrometers can detect and characterize chemical compounds in the atmosphere. Signals from tunable laser absorption spectrometers can be enhanced with the use of an optical cavity, providing improved sensitivity to trace amounts of key compounds critical to atmospheric processes. An apparatus has been developed under this project and design configurations specific to infrared optical detection are being evaluated.

Project Description

The purpose of this project is to build and test a novel cavity-enhanced, infrared laser absorption spectrometer used to detect molecular compounds in the atmosphere that are relevant to key environmental processes. As our level of understanding about the chemistry of the atmosphere increases, new high-sensitivity instruments are needed to reveal even more subtle details. The instrument under development offers the potential for high-sensitivity and field-portability; which are two key aspects required for next-generation sensors. We built a working in situ measurement instrument and obtained promising initial results. During this initial testing, we found that our instrument yields comparable path-length results to commercially available alternatives (optical multi-path cells). Path-length enhancement provides for a longer interaction length between the interrogating laser and sample under study, thereby improving absolute sensitivity. We have also identified technical issues limiting our present sensitivity. We expect that our instrument will be several times more sensitive than conventional off-the-shelf alternatives. Additionally, we have observed that our instrument benefits from mechanical vibrations; this is truly exciting as it supports instrument deployment on airplanes.

Introduction

Infrared absorption spectroscopy is recognized as an extremely valuable method for chemical detection and identification efforts. In the mid- (3 to 5 micron) and long-wave (8 to 14 micron) infrared regions, molecules exhibit unique absorption features, commonly referred to as molecular finger-print bands, which allow for accurate identification and quantification. Recently, a new infrared laser source, the quantum cascade laser (Capasso et al. 1999), was developed at Bell Laboratories (Lucent Technologies). The quantum cascade laser allows tremendous advances in the field of atmospheric monitoring. Our Laboratory has a strong collaborative arrangement with Bell Labs, and we are developing instrumentation under this project that incorporates the quantum cascade laser.

A tunable laser absorption spectrometer obtains concentration information about specific compounds within a sample cell by measuring the amount of attenuation a laser experiences as it is passed through the sample cell. If very little of the compound is present, then very little of the laser light is attenuated because of absorption by the vapor sample. To observe higher levels of attenuation producing greater signal-to-noise and higher sensitivity, the physical cell is made longer or the laser is passed many times back-and-forth through the cell. Using this technique, path lengths of tens of meters are possible from a cell which is 40 cm in length. An alternative to multi-path cells is the use of optical-resonator-cavities to capture and “store” the light inside the cavity (Engeln et al. 1998; O’Keefe et al. 1999). These new cavity-enhanced techniques can produce effective path lengths in the hundreds to thousands of meters in a cell 40 cm in length. Our goal is to produce a cavity-enhanced spectrometer, operating in the infrared spectral region, with an effective path length of 1 km (roughly an order of magnitude improvement over conventional technology).

Results and Accomplishments

This project is aimed at integrating the necessary components to build an infrared laser absorption spectrometer uses cavity enhancement. The main thrust of the first year has been the successful assembly of a complete apparatus and initial experimentation.

A schematic layout of the experimental apparatus is shown in Figure 1. The experiment consists of an 8.5-micron single-mode quantum cascade laser operating at liquid nitrogen temperatures (77 K), a reference cell

containing nitrous oxide, an optical cavity (with piezo adjustable end mirror), and a digital oscilloscope used for data averaging and export to a computer. Liquid nitrogen cooled HgCdTe photovoltaic detectors are used with custom-built low-noise preamplifiers. The optical cavity used in this work incorporated plano-concave ZnSe mirrors (radius = 100 cm) with a reflectivity of 99.85%. The cavity itself consists of a 40-cm stainless steel tube with vacuum-sealable mirror mounts (incorporating a piezo element used to modify the cavity length). Approximately 4 MW of infrared emission is collimated from the quantum cascade laser, 10% of which is diverted to a reference cell for wavelength calibration prior to the optical cavity.

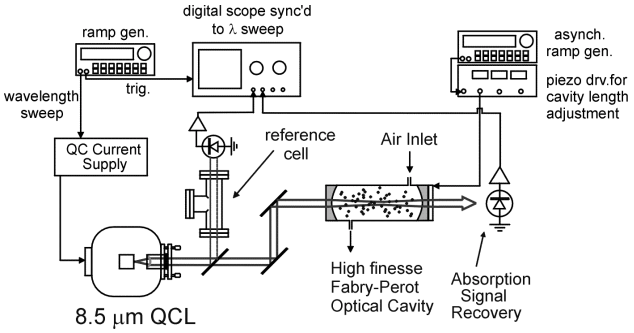

Figure 1. Experimental infrared integrated cavity absorption spectrometer layout

Since the cavity length is 40 cm and the radius of curvature of the resonator mirrors is 100 cm, a myriad of longitudinal modes of the cavity are seen (in transmission) as the wavelength of the quantum cascade laser is scanned. Typical scans (accomplished by applying a sawtooth modulation on the injection current) are up to 0.5 cm^{-1} at a repetition rate of 1 to 10 kHz. At first, this quasi-continuum of transmission modes may seem to be detrimental to the absorption measurement; however, if the optical cavity is being used to increase the effective path length, then the higher number of modes is advantageous. If fact, our apparatus is intentionally misaligned (to reduce back-reflections to the laser) and the spatial mode profile of the quantum cascade laser is non-optimal for coupling to the primary mode of the cavity. These two effects act to increase the number of accessible modes of the cavity. During an experiment, the cavity length is dithered (typically 10 to 100 Hz) using various waveforms that are not synchronized to the wavelength scan of the laser. Therefore, when many cavity transmission scans are averaged on the digital oscilloscope, the resulting spectrum appears as a nearly flat baseline with a small direct current offset, rather than the multitude of sharp cavity resonance peaks. The lower panel in Figure 2 compares a signal-sweep trace and an averaged trace (2500 sweeps) of the cavity transmission with 100 ppmv of nitrous oxide present in cavity. The upper panel in Figure 2 shows an expanded version of the averaged data.

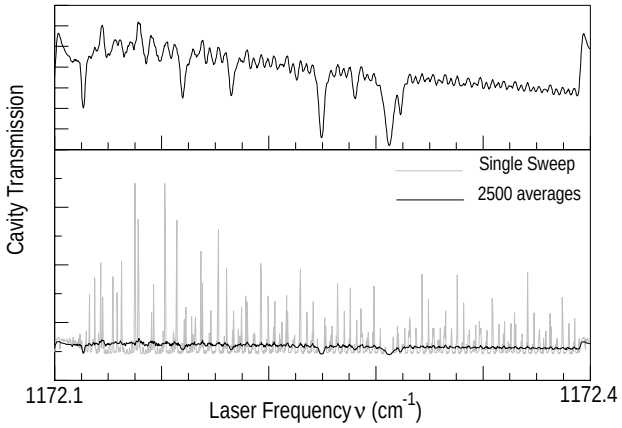

Figure 2. Lower panel depicts a comparison of single (gray) and averaged (black) transmission spectra with approximately 100 ppmv of nitrous oxide present in the cell at 25 torr. Upper panel is an expanded version of the averaged trace.

As can be seen in the upper panel in Figure 2, the noise floor is very regular and is similar to etaloning commonly seen in laser absorption measurements. In this case, the periodicity of the baseline fluctuations results from an incomplete averaging of clusters of cavity modes. Ideally, the cavity modes would be uniformly spaced in the transmission spectra. Conventional cavity modes calculations support this observation and suggest that this effect can be dramatically reduced using a slightly shorter cavity.

The effective path length (i.e., cavity-enhancement factor) of this arrangement was found by multiplying the cavity length by the ratio of cavity-enhanced absorbance to the single-pass absorbance (found by replacing the mirrors with plain windows). The comparison of the cavity-enhanced absorption spectrum with the single-pass absorption is shown in Figures 3a and 3b, respectively. The effective path length in the cavity-enhanced case was found to be 38 meters (cavity-enhancement factor of ~90). This initial effective path length can be improved upon with the use of high reflectivity mirrors; a factor of ten improvement would yield path lengths not easily obtained with multi-pass cells.

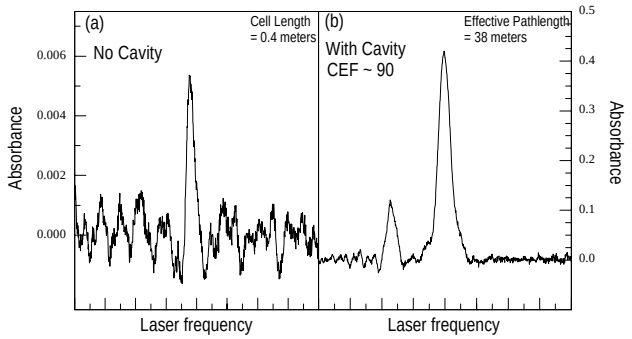

Figure 3. Comparison of single-pass (3a) and cavity-enhanced (3b) absorption spectra for same nitrous oxide line under the same conditions (100 ppmv in 25 torr air). The cavity-enhancement factor (CEF) is given by the ratio of the two measurements.

Summary and Conclusions

The first phase of the instrument development has been accomplished and initial results are very encouraging. Technical milestones that have been reached include

- integration of infrared system components (quantum cascade laser, detectors, optical cavity)
- an effective path length of 38 meters has been obtained from a 40-cm cell
- cavity mode calculations have identified optimal cavity configurations.

Our goal for continuation of this project will be to increase the effective path length of the instrument and to make field atmospheric measurements.

References

Capasso F, C Gmachl, D Sivco, et al. 1999. "Quantum Cascade Lasers." *Physics World* 12:27.

Engeln R, G Berden, R Peeters, et al. 1998. "Cavity enhanced absorption and cavity enhanced magnetic rotation spectroscopy." *Review of Scientific Instruments* 69(11):3763-9.

O'Keefe A, JJ Scherer, and JB Paul. 1999. "CW Integrated Cavity Output Spectroscopy." *Chem. Phys. Lett.* 307:343-349.

Chemical Detection Using Cavity Enhanced Infrared Absorption with Quantum Cascade Lasers

Richard M. Williams, Matthew S. Taubman, James F. Kelly, Steven W. Sharpe, John S. Hartman

Study Control Number: PN00020/1427

Optical cavity enhancement of the signals from a tunable laser absorption spectrometer can provide a tremendous improvement in the ability to detect trace amounts of chemical vapors in the environment. Key technologies are being developed on this project to realize cavity-enhancement techniques combined with the recently invented infrared quantum cascade laser.

Project Description

The purpose of this project is to develop critical technologies necessary to implement an infrared cavity-enhanced chemical sensor capable of detecting extremely low levels of chemical vapors. The critical technologies addressed in this project include the development of infrared optical systems and design/fabrication of advanced electro-optical components. The initial assembly of the laser absorption experiment has been completed, including integration of a high-quality Fabry-Perot optical cavity. Presently, data from the apparatus is guiding the design of electronics necessary for the second phase of the project. Additionally, a collaboration with researchers at the University of Idaho (funded by this project) was initiated to computationally evaluate electro-optic phase modulator concepts. This extremely productive external collaboration has resulted in a modulator design that will be integrated into our system in the next phase of the project.

Introduction

Infrared absorption spectroscopy is recognized as an extremely valuable method for chemical detection and identification efforts. In the mid- (3 to 5 micron) and long-wave (8 to 14 micron) infrared regions, molecules exhibit unique absorption features, commonly referred to as "molecular finger-print bands," which allow for accurate identification and quantification. A recently invented optical absorption concept known as Noise-Immune Cavity-Enhanced Optical Heterodyne Molecular Spectroscopy (NICE-OHMS) has demonstrated inherently high-contrast signals with noise suppression qualities, providing an unprecedented level of sensitivity (Ye et al. 1998). The goal of this project is to develop critical components necessary to realize a mid- or long-wave infrared variant of NICE-OHMS using another recently invented technology, the quantum cascade infrared laser.

Hall and coworkers at the Joint Institute for Laboratory Astrophysics in Boulder, Colorado (a joint institute between the University of Colorado and the National Institute of Standards and Technology) recognized that by introducing a molecular species into a high-quality Fabry-Perot optical cavity, the transmission through the cavity would be extremely sensitive to trace amounts of an absorbing species within the cavity. More importantly, was their realization that by frequency-modulating the laser's output at precisely the resonance frequency of the optical cavity, the technical noise from the laser source would be suppressed. Combining these two ideas, with their thorough knowledge of laser stabilization and control, Hall and coworkers demonstrated optical absorbance sensitivities of 5×10^{-13} cm^{-1} at 1.06 microns using acetylene as their test molecule. For comparison, a very good direct absorption apparatus can measure fractional absorption of 1×10^{-6} cm^{-1}. Including the cavity-enhancement factor alone, other researchers have reported absorbance sensitivities of 1×10^{-9} cm^{-1}. NICE-OHMS immediately surpassed these previous state-of-the-art techniques by nearly four orders of magnitude. Theoretical limits of 10^{-15} cm^{-1} are feasible with continued technical improvements. NICE-OHMS may be capable of detecting as few as 100 molecules per cubic centimeter in such a way that the sample can be retained for further analysis since it is a nondestructive technique.

Results and Accomplishments

This project is aimed at developing the necessary technologies to extend the revolutionary NICE-OHMS concept into the important infrared spectral region. Two main thrusts of the project have been the integration of optical components and the design of an advanced electro-optic phase modulator.

Infrared Optical Integration

We have successfully completed the assembly of the necessary components for the first phase of this project. Figure 1 represents a schematic concept drawing of the final phase assembly expected in FY 2001. Figure 2 is a photograph taken of the working phase-one experiment.

The quantum cascade laser was mounted and thoroughly tested using electronic drive circuits. After laser testing, the next phase of integration involved locking the lasers output wavelength to the center of one of the optical cavity's transmission modes using a technique referred to a Pound-Drever-Hall stabilization (Drever et al. 1983). A significant challenge in meeting this objective involved isolating the laser from back-reflected light from the optical cavity, which was found to cause laser instabilities. This was solved with the use an acousto-optic modulator placed between the laser and the cavity.

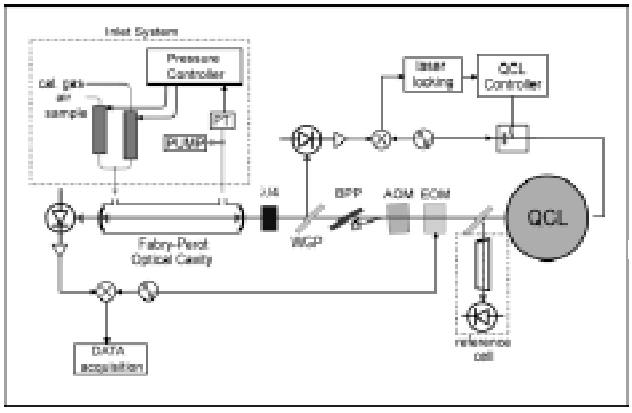

Figure 1. Schematic representation of quantum cascade laser-NICE-OHMS apparatus

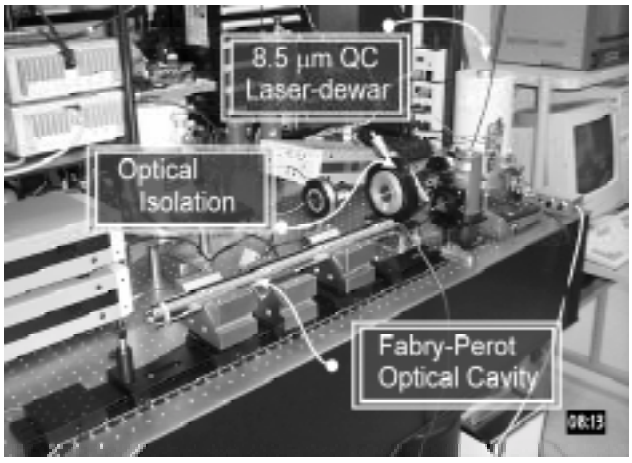

Figure 2. Photograph of completed phase-one assembly of quantum cascade laser-NICE-OHMS apparatus

The acousto-optic modulator shifts the laser's frequency by a fixed amount as the laser passes through it in the forward direction. If any back-reflected light back-propagates through the modulator, it is again shifted by the same amount. Therefore any light reaching the laser will have experienced a significant frequency shift relative to the actual laser output frequency, thereby significantly reducing its negative impact on laser performance.

Electro-Optical Modulator Design

The second thrust of the project during the last year has been the design of a resonant electro-optic phase modulator. The NICE-OHMS concept requires the laser source to be frequency modulated at precisely the separation frequency of the transmission peaks of the Fabry-Perot optical cavity. For our experiment, this means the quantum cascade laser must be modulated at 300 MHz, with sufficient depth to transfer 10 to 20% of the optical power of the main carrier beam into the sidebands. This is accomplished by passing the infrared laser light through a nonlinear crystalline material while an electrical signal at the modulation frequency is applied to the crystal. Several factors make this a challenging task. The first is that crystalline materials suitable for operation in the infrared spectral region have much weaker nonlinear interaction strengths than their counterparts in the visible or near-infrared. Secondly, the amount of applied electrical power needed to obtain a specific interaction magnitude between the optical and applied electrical fields is much higher at infrared wavelengths compared to visible wavelengths. Taking these two factors into account, it can be shown that approximately 500 times more electrical power needs to be applied to an electro-optic modulator operating at 8 microns compared to one operating at 0.8 microns. These inherent processes require that an advanced, highly efficient modulator design be considered.

In order to optimize time and resources, we elected to collaborate with researchers at the University of Idaho (Moscow, Idaho) whose expertise is in the field of computational simulations of propagating electro-magnetic fields within structures. Dr. Jeff Young, (Department of Electrical Engineering and member of the Microelectronic Research and Communications Institute at the University of Idaho) was contracted to provide feedback on several design concepts originating at our Laboratory. Based upon the results of his simulations we have adopted a design that will be fabricated early in the next fiscal year and ultimately integrated into the optical layout.

Figure 3 is a color rendered simulation of the University of Idaho-designed modulator showing the magnitude of the electric field in the region of the nonlinear optical crystal.

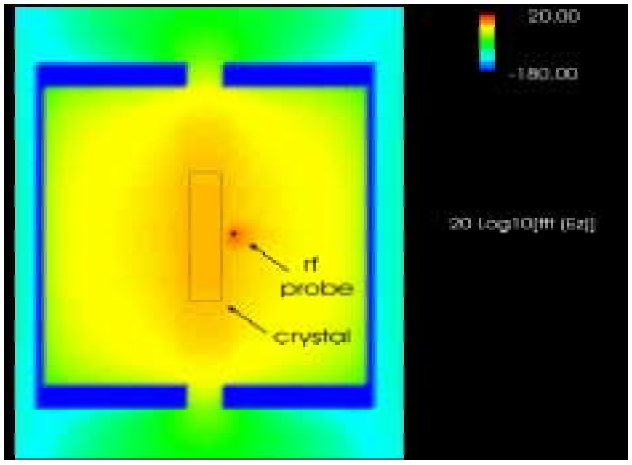

Figure 3. Computational results showing the magnitude of an applied electric field within the concept electro-optic modulator designed jointly between PNNL and the University of Idaho

Precision Pressure Control

Also tested during this fiscal year was a system designed to precisely control the pressure within the optical cavity during analysis. Because the length of the NICE-OHMS optical cavity must be maintained to a high degree during a measurement, a system needed to be developed that allows different gas samples to be added without a significant change in the pressure. A system was procured which incorporates mass-flow controllers, pressure measuring devices and a servo control unit. The system was assembled and tested. Figure 4 is a photograph of the assembled system. Next fiscal year a second mass controller will be added and software written to allow for the gradual transition from an actual sample to a calibration sample.

Summary and Conclusions

The first phase of the development of two key technologies necessary for the realization of an infrared variant of a NICE-OHMS instrument have been successfully completed. Technical milestones that have been reached include

Figure 4. Photograph of phase-one inlet system for a QCL-NICE-OHMS apparatus

- infrared system components (QC laser, detectors, optical cavity) were integrated
- deleterious optical-feedback was reduced using an acousto-optic modulator
- university collaboration successfully generated an electro-optic modulator design
- the feedback-controlled pressure regulation system was tested.

This project will continue with the goal of integrating the advanced electro-optic phase modulator with the optical cavity system and testing of the complete NICE-OHMS signal acquisition process.

References

Drever RWP, JL Hall, FV Kowalski, J Hough, GM Ford, AJ Munley, and H Ward. 1993. "Laser Phase and Frequency Stabilization Using an Optical Resonator." *Applied Physics B* 31:97.

Ye J, M LS Ma, and JL. Hall. 1998. "Ultrasensitive detections in atomic and molecular physics: demonstration in molecular overtone spectroscopy." *J. of the Optical Society of America, B* 15:6.

Development of High-Temperature Sensing Technology for On-Line Ceramic Melter Processing Control

Morris S. Good, Michael J. Schweiger, Pavel R. Hrma, Hong Li, Aaron A. Diaz, Chester L. Shepard, Margaret S. Greenwood

Study Control Number: PN00032/1439

Vitrification of high-level radioactive waste is a major aspect of dealing with the large volumes of legacy waste from nuclear weapons production. The vitrification process is highly temperature-dependent. This project has developed a method to detect the sludge level and formation of crystals that develop when the temperatures drop below the melting point. The ability to more accurately sense temperature and crystal formation will lead to greater control and more efficient vitrification densities.

Project Description

We are developing a new method to quantify the sludge level in a waste melter for process control. High-level radioactive waste melters handle material rich in various metal oxide constituents that precipitate in the form of spinel crystals and settle onto the floor during vitrification. This can cause melter failure. Spinel settling is a primary factor in determining waste loading. Benefits of monitoring spinel settling for process control of melter operation include the following:

- preventing electrical shorting of electrodes
- increasing melter life
- increasing or maintaining the production rate.

The current need to avoid accumulation of noble metals in significant amounts results in considerable conservatism in melter operating life projections and waste loading specifications. A method to mitigate that risk would allow an increase in waste loading by several percent and therefore, could save DOE-EM billions of dollars over the lifetime of the River Protection Project's Waste Treatment Plant at the Hanford Site. One approach is in situ measurement of spinel layer growth; however, measurement techniques must be compatible with high operating temperatures and melter operation. A potential solution is advance ultrasonic sensing technology that was evaluated using room temperature surrogates of molten glass and sludge. We concluded that spinel-layer can be detected and quantified, and we recommended that future work should entail high-temperature tests.

Introduction

Noble metal precipitation and settling in a melter has been observed numerous times and has led to melter failure. Cooper et al. reported in 1994 an occurance during research scale melter tests at Pacific Northwest National Laboratory. Whittington et al. in 1996 reported an accumulation on the melter floor. Mini-melter tests conducted at Savannah River Technology Center revealed noble metal particles dispersed in the glass during mini-melter tests[(a)]. The accumulation of noble metals at the melter floor has caused electrical shorting as was the case at the PAMELA vitrification plant in Mol, Belgium[(b)]. Krause and Luckscheiter reported in 1991 a melter failure attributed to noble metal accumulation and subsequent shorting of the electrode. Electrical shorting occurred since noble metal crystals are electrical conductors. High-level wastes at Hanford have been shown to be rich in iron (Fe_2O_3) with lower quantities of nickel (NiO), chromium (Cr_2O_3), magnesium (MnO), and ruthenium (RuO_2) and these constituents in waste borosilicate glasses can induce crystallization of spinel phases, a solid solution of $(Ni_x, Mn_y, Fe_{1-x-y})(Fe_z, Cr_{1-z})_2O_4$ (Hrma et al. 1994, Vienna et al. 1996).

Acoustic measurements for process control have been made for more than 50 years (Lynnworth 1989) and has been configured to withstand hostile environments. It has also been introduced as a tool for making real-time process analytical measurements (Workman et al. 1999) such as to characterize the degree of mixing (Bond et al. 1998). Ultrasonic technology has been utilized in a wide variety of diagnostic applications. However, no

(a) Nakaoka RK and DM Strachan. 1990. Melter performance evaluation report. Milestone report HWVP-90-1.2.2.04.08B. Pacific Northwest Laboratory, Richland, Washington.

(b) Collantes CE, LK Holton, JM Perez Jr., and BA Wolfe. 1987. Research facilities in the Federal Republic of Germany & the PAMELA facility workshop: "vitrification operational experience." Foreign trip report. Pacific Northwest Laboratory, Richland, Washington.

appropriate study has been performed on determining the settling of crystals in viscous fluids including molten glasses.

Ultrasonic theory has been developed for the study of fundamental properties of a diverse range of two phase systems (Harker and Temple 1988) and the characterization of media using ultrasonic backscatter (Goebbles 1980, Good 1984). Recent studies have shown that ultrasound can be used to characterize complex slurries, such as those at Hanford (Clark and Martin 1994). Other groups have used ultrasound to monitor slurries at elevated temperatures (Soong et al. 1996) and ultrasonic piezoelectric transducers are now available that can operate at temperatures as high as 950ºC (Patel et al. 1990).

Approach

This work consisted of room temperature, proof-of-concept tests by employing liquids that had properties at room temperature that mimicked material properties of molten glass and sludge contained within a high-level radioactive waste melter. Information of interest included the optimized frequency for ultrasonic measurement and the sensitivity to detect the sludge-glass interface.

Glycerin-citric acid is the room temperature simulant of the molten glass. Viscosity can be well controlled between 0.4 and 37 Poise depending on the concentration of citric acid (Stanek 1977). The sludge simulant was the same liquid loaded with small particles of alumina, to simulate spinel crystals in the melt.

Rapid forming of a sludge layer would be used for future high-temperature tests. Initially, the temperature of the molten glass mixture is raised above its liquidus temperature to dissolve spinel in the melt. Subsequently, the temperature is lowered to a level sufficiently below the liquidus. While holding the mixture at this temperature, spinel crystals nucleate, grow, and settle due to their higher density (Mika et al. 1997).

Results and Accomplishments

Three proof-of-concept tests were successfully performed and a laboratory scale melter cell was fabricated for future high-temperature tests. Ultrasonic techniques 1 and 2 as illustrated in Figure 1 utilized ultrasonic sensors that were external to the melter cavity. These were viewed as more robust since transducers would be removed from the higher temperature of the molten glass and isolated from the caustic mixture. Ultrasonic technique 3 would house transducers in an envelope of refractory material for protection against the caustic melt. A small laboratory refractory cell was designed and fabricated to permit an economical means of performing high-temperature tests (Figure 2).

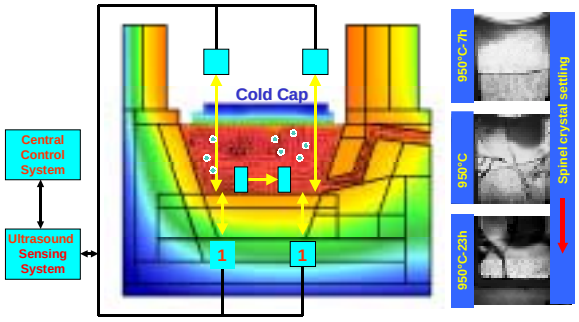

Figure 1. Real time monitoring of noble metal and spinel crystal settling accumulation at the bottom of the melter by advance ultrasonic sensing technology

Figure 2. Small-scale refractory cell prepared for laboratory high-temperature test

Summary and Conclusions

Three proof-of-concept tests were successfully performed with room temperature, nonradioactive surrogates of molten waste and sludge. Two of the three techniques used ultrasonic transducers external to the melter cavity. Our data showed that the sludge-glass interface is detectable for quantifying the spinel-layer depth. Small-scale crucibles have been fabricated and are ready for use in high-temperature laboratory tests.

References

Bond LJ, M Meenaksh, and HO Matthiesen. 1998. "Ultrasonic methods for the on-line real-time characterization of state of mixing." *In Proceedings 16th ICA and 135th Meeting Acoustical Society of America,* Eds. PK Kuhl and LA Crum, pp. 1161-1162.

Clark MA and DM Martin. 1994. "Acoustic properties of underground storage tank simulant wastes." *In Review of Progress in Quantitative Nondestructive Evaluation,* vol. 13, Eds. DO Thompson and DE Chimenti, pp. 1075-1081, Plenum Press, New York.

Cooper MF, ML Elliott, LL Eyler, CF Freeman, JJ Higginson, LA Mahoney, and MR Powell. 1994. *Research-scale melter test report.* PNL-9428, Pacific Northwest Laboratory, Richland, Washington.

Goebbels K. 1980. "Structure analysis by scattered ultrasonic radiation." Chapter 4 in *Research Techniques in Nondestructive Testing,* vol. IV, Ed. RS Sharpe. Academic Press, New York.

Good MS. 1984. "Effective case depth measurement by an ultrasonic backscatter technique." in *1984 ASM Metals/Materials Technology Series* paper 8408-003, pp. 1-6, American Society for Metals, Metals Park, Ohio.

Harker AH and JAG Temple. 1988. "Velocity and attenuation of ultrasound in suspensions of particles in fluids." *Journal of Physics D: Applied Physics* 21:1576-1588.

Hrma P, GF Piepel, MJ Schweiger, DE Smith, DS Kim, PE Redgate, JD Vienna, CA LoPresti, DB Simpson, DK Peeler, and MH Langowski. 1994. *Property/ composition relationships for Hanford high-level waste glasses melting at 1150°C.* PNL-10359, Pacific Northwest Laboratory, Richland, Washington.

Krause C and B Luckscheiter. 1991. "Properties and behavior of the platinum group metals in the glass resulting from the vitrification of simulated nuclear fuel reprocessing waste." *J. Mater. Res.,* 6:2535-2546.

Lynnworth LC. 1989. *Ultrasonic measurement for process control: theory, techniques, applications.* Academic Press, Inc., San Diego, California.

Mika M, MJ Schweiger, and P Hrma. 1997. "Liquidus temperature of spinel precipitating high-level waste glass." *In Scientific Basis for Nuclear Waste Management XX, MRS Sym. Proc.,* vol. 465, Eds. W Gray and I Triay, Proc. Mat. Res. Soc. Symp, MRS, Pittsburgh, Pennsylvania.

Patel ND, WX Fulford, and PS Nicholson. 1990. "High frequency-high temperature ultrasonic transducers." *In Review of Progress in Quantitative Nondestructive Evaluation,* vol. 9, Eds. DO Thompson and DE Chimenti, pp. 823-828. Plenum Press, New York.

Soong Y, IK Gamwo, AG Blackwell, FW Harke, RR Schehl, and MF Zarochak. 1996. "Ultrasonic characterization of slurries in an autoclave reactor at elevated temperature." *Ind. Eng. Chem. Res.,* 35:1807-1812.

Stanek J. 1977. "Electric melting of glass." *Glass Science and Technology 1,* Elsevier Scientific Publishing Company, Amsterdam, p. 169.

Vienna VD, PR Hrma, MJ Schweiger, MH Langowski, PE Redgate, DS Kim, GF Peipel, DE Smith, CY Chang, DE Rinerhart, SE Palmer, and H Li. 1996. *Effect of composition and temperature on the properties of high-level waste (HLW) glass melting above 1200°C.* PNNL-10987, Pacific Northwest National Laboratory, Richland, Washington.

Whittington KF, DK Seiler, J Luey, JD Vienna, and WA Sliger. 1996. *Feed process studies - research-scale melter.* PNNL-11333. Pacific Northwest National Laboratory, Richland, Washington.

Workman J Jr., DJ Veltkamp, S Doherty, BB Anderson, KE Creasy, M Koch, JF Tatera, AL Robinson, L Bond, LW Burgess, GN Bokerman, AH Ullman, GP Darsey, F Mozayeni, JA Bamberger, and MS Greewood. 1999. *Process Analytical Chemistry,* 71(12)121R-180R.

Exploitation of Conventional Chemical Sensing Data

Michael G. Foley, Timothy J. Johnson, Bruce A. Roberts, Steven W. Sharpe, Marie V. Whyatt

Study Control Number: PN00043/1450

Pacific Northwest National Laboratory is developing "remote" methods to detect and characterize chemical species in air as part of a larger national security effort. Since few chemicals provide stand-alone signatures for components of weapons of mass destruction, innovative sensing technologies are being developed for the analysis of suspected weapons-production facilities.

Project Description

This project will integrate chemical with spatial and other types of intelligence information in the context of proliferation detection. We are developing methods to streamline this site functional-analysis process by automating the reverse-engineering of three-dimensional site infrastructure from overhead imagery, placing the chemical information in that spatial context, and correlating the chemicals, plumbing, and site infrastructure with all other sources of information relevant to candidate weapons-production processes. The first year's work focused on fusing remotely sensed chemical data with time-sequenced three-dimensional imaging of the site. During the second year, existing information-visualization and correlation approaches will be expanded to include correlation of spatial/object-oriented site characterization derived from imagery and chemical information with similar process-based data from other sources. Third-year efforts will focus on developing software agents that will enhance the use of updated information-visualization technology to correlate imagery with databases for retrieval of information.

We also developed improved chemical ground-truth data collection and analysis techniques and technology to ensure the Laboratory's participation in future field test campaigns, and thus access to conventional chemical sensing data. We integrated a graphical user interface to spectral databases (to improve the user-friendliness of ground-truth data analysis techniques) with a trailer-mounted passive infrared sensor. The sensor, coupled with the new software, was then used to demonstrate our ground-truth capabilities during field tests of an airborne DOE sensor.

Introduction

While chemical information brings a new dimension to analysis of suspected weapons of mass destruction production facilities, few chemicals are "smoking guns" that provide stand-alone proof of proliferation, as is true of most other types of proliferation information. Correlating chemical information with other site- or process-related data is therefore critical, and we hope to build a larger share of the eventual data analysis market by pioneering techniques for facilitating and exploiting these correlations. Correlations between chemical, process/ facility-requirement, and imagery information are particularly important; in this project we are evaluating approaches for creating three-dimensional computer aided design site models from close-range photogrammetry of simulated and actual weapons production site imagery. Our objective is to explore faster, better, and more robust semiautomated approaches for generating object-based site and engineered-facility computer aided design models. Expansion of our STARLIGHT, SPIRE, and other data correlation and visualization software to include object-based three-dimensional site infrastructure derived from time-transgressive imagery would allow comparison with three-dimensional site "templates" specific to particular countries' chemical, nuclear, and biological weapons production practices. Such country and weapons-type specific three-dimensional conceptual models are developed by, for example, S-Tech analytical software. Incorporation of three-dimensional site infrastructure as a data type for correlation with chemical plume and other intelligence information would provide an exceptionally useful platform for conducting intelligence analyses of suspected weapons installations if they can be provided in a timely, labor-conservative manner.

Results and Accomplishments

We used the HAZMAT Spill Center facility (Figure 1) at the Remote Sensing Test Range on Frenchman Flat at the Nevada Test Site for the test area both for the site-modeling development effort and the ground-truth sensor demonstration.

Figure 1. Oblique photograph of HAZMAT Spill Center at the Nevada Test Site—the test case for applications of close-range photogrammetry and the field-sampling studies

Correlation of Chemical and Other Information

For the site-modeling part of this project, we explored two approaches to site modeling: 1) geometry-based systems and 2) a hybrid geometry-based/image-based system (Figure 2). Our intention was to simulate the use of imagery expected to be available for arbitrary weapons sites with analytical approaches developed for reverse-engineering facilities or making architectural renderings to advance the state-of-the-art for weapons site and facility characterization. Our criteria for evaluating these site-modeling approaches were:

- **Visualization versus functional characterization**—Current technology used in the national technical means imagery community, (such as RapidScene) generates simulated three-dimensional scenes using imagery-texture-mapped bumps on topography for semi-photorealistic virtual-reality walkthroughs, and fly-bys. However, a functional characterization is a three-dimensional association of virtual physical objects. This association includes individual shapes and textures (and internal structure where appropriate), spatial arrangement, and physical connections (pipes, trenches, etc.).

- **Object-locked texture mapping for functional understanding and to communicate functional understanding**—Three-dimensional scene visualization texture maps, such as those described above, represent a static association of objects. Multiple images are used to get the best map image for each surface. To move virtual objects around in a site model, they must be individual three-dimensional objects and must be individually texture mapped.

- **Association of virtual objects with weapons processes**—We start with a suite of objects and shapes (pipe, prism/cylinder, sphere, tanks of various compound shapes, etc.) generated for a site to build the virtual site from imagery, then hyperlink the site objects to a database by their primitives, and hyperlink weapons site templates to the same database to provide associations/arrangements of objects indicative of proliferation activities.

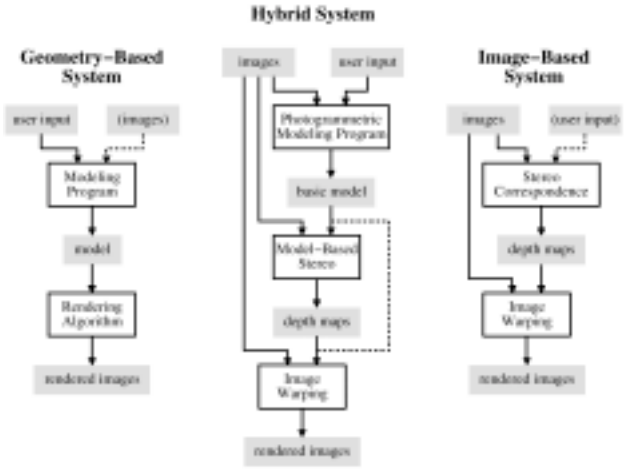

Figure 2. Schematic (Debevec et al. 1996) relating hybrid site-modeling approach to geometry-based and image-based approaches

For raw imagery data, we obtained 4-inch by 5-inch color contact prints of aerial photographs of the HAZMAT Spill Center from the Remote Sensing Laboratory in Las Vegas. We scanned these prints to create uncontrolled digital images for use in close-range photogrammetric analyses; such images represent the lowest-level data we expect to obtain for arbitrary sites.

Geometry-Based Systems. We acquired two commercial off-the-shelf close-range photogrammetry software packages; Eos Systems, Inc. PhotoModeler® Pro 3.1, and Vexcel Corporation FotoG-FMS™ 5.1. Both of these programs allow the user to use multiple, overlapping photographs to reconstruct object geometry by calculating camera positions and relative orientations of pairs of stereographic images from tie points common to the images, and to place those objects in an absolute coordinate system using surveyed control points visible in the images. Creation and linking of tie and control points between images can be performed manually in both systems.

Figures 3 and 4 illustrate the impact of that uncertainty on modeled geometry. We observed severe distortion in the PhotoModeler and FotoG objects. A biased elevation distortion was evident in the FotoG site model that has objects either under (southwest end) or above (northeast end) the surface of what in actuality is a very flat dry lake bed. This feature, using a geometric primitive to constrain the photogrammetrically derived geometry, is the core of the hybrid geometry- and image-based site-modeling approach described below.

Figure 3. Partial three-dimensional model of the HAZMAT Spill Center constructed and photo-rendered with PhotoModeler Pro—although line/face continuity for constructing objects is easily maintained during on-screen construction, geometric distortion cannot be controled. Model geometry can be exported to computer aided design.

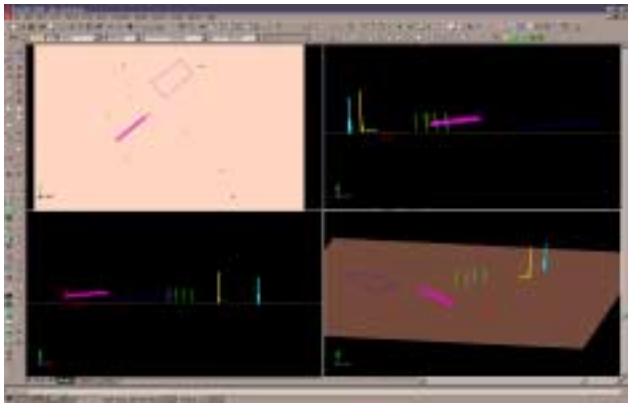

Figure 4. Partial three-dimensional model of the HAZMAT Spill Center constructed and rendered in AutoCAD from linked FotoG-FMS—geometry can be constructed only from points, single lines (not polylines), and cylinders, so construction of faces and objects must be done in AutoCAD after point/line/cylinder generation from the imagery. Geometry here again is distorted; the ground surface is effectively flat, so the features should "sit" on it, the trailer should be rectangular and square, etc. Rendering of this model with photographs must be done in a separate visualization program such as 3D Studio.

Hybrid Geometry- and Image-Based System. Debevec (1996) and Debevec et al. (1996) described a hybrid geometry- and image-based approach to "creating realistic synthetic views of existing architectural scenes from a sparse set of still photographs." This approach, similar in principle (but much more sophisticated) to that used by RapidScene for National Technical Means imagery, depends on fitting geometric primitives (rectangular planes, boxes, pyramids, etc.) to features in the photographs, and using knowledge of those shapes to assist in photogrammetric calculations and determining overall site geometry.

Expansion of this approach to use genetically meaningful primitives representing weapons process components, and to allow creation in computer aided design of site features similar to the geometry-based approaches, would make it the system-of-choice for site-modeling applications. This object-based approach would provide a basis for hyperlinking (e.g., Feiner et al. 1995) with object-based site three-dimensional computer aided design templates and all other sources of information.

Ground-Truth Sensor Development and Demonstration

We developed and demonstrated an improved ground-truth chemical sensor, as well as the associated analysis software for determination of nuclear, biological, chemical-type weapons. To this end, a commercial Fourier-transform infrared spectroscopy was obtained and employed for proliferation determination using passive infrared sensing. We transported its spectrometer and ancillary detection equipment to the Nevada test site for data measurement and acquisition, and have subsequently analyzed the data via introduction of a graphical user interface software package for data reduction.

The Owl 2000 campaign for remote detection of chemical signatures was carried out at the test range under the auspices of LLNL. The campaign consisted of monitoring a number of controlled releases from the HAZMAT Spill Center and test range stacks (see Figure 1) by several ground-sensing techniques as well as from two airborne platforms (General Dynamics H-57 "Canberra" and DeHavilland DHC-6 "Twin Otter" aircraft). Our Laboratory's chemical remote sensing system consisted primarily of a Midac model M2401-C emission interferometer; the Midac FTIR was equipped with ZnSe optics and a mercury-cadmium-telluride detector with spectral response to 16 μm in the long-wave infrared. The infrared data were augmented by meteorological data from the test site, as well as stack and background temperatures and estimated flow release rates for the release species under investigation.

In addition to the measurement campaign, the software for chemical retrieval information has been under development and continues to undergo further refinement.

Summary and Conclusions

Correlation of Chemical and Other Information

We explored two approaches to quantitative three-dimensional site modeling using three commercial, off-the-shelf software systems: two were optimized for computer aided design-based site geometric reconstruction, and one was optimed for hybrid, object-based site virtual-reality representation and visualization. All require extensive manual intervention from the analyst, and the two geometry-based computer aided design systems further require precise knowledge of camera parameters, full-frame images, and substantial effort to create computer aided design objects representing the site. Geometric primitives used by the hybrid system are too limited for application to National Technical Means facilities, and the entire system does not obviously support computer aided design-based feature-building in addition to the general geometric reconstruction for visualization purposes. This latter observation is preliminary, because the software is currently unavailable and testing was done with what may be an obsolete demonstration package. For the purposes of creating a three-dimensional computer aided design model of a weapons facility, none of these systems was a complete solution. However, by combining the two approaches with the mensuration capabilities innate in National Technical Means imagery, a basis can be hypothesized for object-based site modeling and functional characterization. Such a hybrid site modeling system, built on a hybrid geometry- and image-based approach derived from Debevec et al. (1996), augmented with geometry-based computer aided design-modeling capability and weapons-object relevant primitives hyperlinked to their physical-world counterparts for information-correlation purposes as discussed by Feiner et al. (1995), and geospatially controlled by the inherent National Technical Means mensuration capability, would become a valuable asset in the site functional analysis community.

Ground-Truth Sensor Development and Demonstration

We also developed and demonstrated an improved ground-truth chemical sensor, as well as the associated analysis software and graphical user interface for determining chemical identity. We obtained a commercial Fourier-transform infrared spectroscopy and evaluated it, the analysis software, and the graphical user interface for use in proliferation determination using passive infrared sensing in field tests at the OWL 2000 initiative. The Laboratory team acquired data at the Nevada Test Site, and subsequently analyzed them using the new software system and graphical user interface. Results agreed well with known test conditions, with noted differences; the result of predictable and expected effects of variations between test conditions and geometry and assumed database conditions. The result of this software and hardware development and field evaluation was a robust ground-truth measurement system that will provide participation in and data from future community infrared-spectroscopy field-experiment campaigns.

References

Debevec PE. 1996. *Modeling and Rendering Architecture from Photographs*. Ph.D. Dissertation, University of California at Berkeley, Berkeley, California, 140 pp.

Debevec PE, CJ Taylor, and J Malik. 1996. *Modeling and Rendering Architecture from Photographs: A Hybrid Geometry- and Image-Based Approach.* Technical Report UCB//CSD-96-893, Computer Science Division, University of California at Berkeley, Berkeley, California, 33 pp.

Feiner SK, AC Webster, TE Krueger III, B MacIntyre, and EJ Keller. 1995. "Architectural Anatomy." *Presence: Teleoperators and Virtual Environments* 4(3): 318-326.

Infrared Chemical Sensor Development

David M. Sheen, Bret D. Cannon, Jim F. Kelly

Study Control Number: PN00056/1463

Detecting and characterizing chemical vapors is important for detecting the proliferation of weapons of mass destruction. Coherent lidars or ladars can provide substantially enhanced sensitivity for detecting chemical vapors with narrow-band absorptions, or phase information that contains velocity, vibration, and turbulence parameters, associated with scattering targets.

Project Description

This project developed sensitive, non-cryogenic technologies for detecting important effluents such as HF, HCl, and HCN, which constitute a class of compounds analyzed in the mid-infrared (optical wavelengths from 3 to 18 microns). These are difficult effluents to detect because their absorption features are very narrow, so traditional methods of hyperspectral imaging cannot be exploited to do wide-area plume detection and sensitive identification.

The objectives of this project included: 1) developing coherent spread-spectrum lidars, such as frequency modulated differential absorption lidar, for detecting/identifying vent plumes and characterizing the phase properties of the plumes (velocity, vibrational spectrum, turbulence; etc.); and 2) mating the lidar with a passive imaging spectrograph to enhance the plume imaging capability of hyperspectral imaging passive sensors.

Introduction

Detecting the phase information is relevant to vent location, targeting, and other functions. The short-wave infrared (optical wavelengths between 1 and 3.5 microns) atmospheric transmission windows are especially useful for detecting halogenated-acids and -hydrocarbons, and this wavelength region also offers excellent reflectance returns from the Earth's surfaces that make remote sensing practical. We are studying the application of short-wave infrared technologies, first developed for fiber communications to make high-duty cycle, narrow-band coherent lidar and ladars for applications in wide-area vent location. We are also studying the suitability of mating these lidars with passive dispersive sensors to perform hybridized vent imaging and identification of important halogen acids and cyanogens.

Initially, this research had three distinctive tasks that have relevance to infrared chemical sensing:

1. **system concept development,** consisting of numerical model development and use of the models to identify promising system concepts

2. **quantum cascade laser heterodyne chemical sensing,** in which signals from frequency modulation formatted infrared quantum cascade lasers were studied for efficient signal recovery after scattering from rough surfaces

3. **short-wave infrared chemical sensing instrumentation,** which involved development of suitable short-wave infrared lidars and passive sensor platforms to detect halogen-acids, in the lower troposphere.

We decided to involve many other laser architectures and avoid possible collateral technology channeling effects should the supply of quantum cascade lasers become a critical impasse. We also decided to study the effects of propagation and scattering under realistic field conditions. The instrumentation developed in the third task was to be studied to confirm theoretical and bench-scale measurements in the first two tasks.

Results and Accomplishments

System Concept Development

An extensive numerical model for remote infrared chemical sensing using frequency modulation spectroscopy was developed (Sheen 2000). This model is a mathematical tool for predicting the performance of laboratory and field prototype frequency modulation chemical detection systems as applied in various detection scenarios. Components of the model include: modulation source, transmitter laser, transmitter optics, atmosphere, target, receiver optics, detector and preamplifier, and

output signal processing. The initial modeling effort focused on the mathematical modeling of the frequency modulation system. Formulas and mathematical techniques have been developed to predict the detected frequency modulation harmonic amplitudes as a function of wavelength, modulation frequency, modulation index, and absorption line shape. A direct detection numerical model for the detector and preamplifier has been developed and implemented that incorporates the effects of thermal background induced photo-current, dark current, signal current, and Johnson noise. Initial modeling calculations at medium ranges (5 km to 30 km) indicated that very high detection sensitivity is required. Therefore, a heterodyne detection model was implemented to detect near the signal shot noise limit.

Conventional differential absorption lidar systems developed using pulsed CO_2 lasers are performance limited by the effects of target-induced speckle. A numerical model predicting the effects of speckle for frequency modulation systems has been developed. frequency modulation-based systems differ significantly from conventional differential absorption lidar systems because the laser is continuously modulated in frequency rather than jumping between two discrete frequencies. One-dimensional and three-dimensional numerical simulations are used to develop formulas predicting the signal-to-noise ratio performance of a frequency modulation system due to target-induced speckle. These formulas predict that speckle can be mitigated by using a small illuminated spot (at close range) which maintains the speckle pattern as common-mode, or by using a large illuminated spot (at medium to long ranges) that allows for significant speckle averaging. The frequency modulation-based system will have additional averaging due to the de-correlation of the speckle pattern as the laser frequency is modulated. This may represent a significant advantage over conventional lidar systems.

The atmospheric model includes the effects of atmospheric turbulence and absorption. Turbulence causes small index of refraction variations that induce a finite transverse coherence length, additional beam divergence, and intensity scintillation. Formulas predicting these effects have been obtained through the technical literature and have been incorporated into the model. Extensive models of atmospheric absorption have been developed by the U.S. Air Force. This software (FASCODE/HITRAN) is available and has been implemented at our Laboratory to predict the atmospheric background transmission spectrum.

The models developed under this project were used to predict detection limits for two unmanned airborne vehicle scenarios. A medium range Predator scenario was assumed to operate at a range of 6.5 kilometers with 10 cm diameter optics, and a long-range Global Hawk scenario was assumed to operate at 30 km with 20 cm diameter optics. The modeling predicted that sensitive chemical detection for both scenarios would require heterodyne detection coupled with speckle mitigation. Efficient heterodyne detection required that the returned light have a relatively uniform phase-front. Speckle mitigation through averaging required a highly speckled (nonuniform) phase-front. Therefore, a speckled wavefront would not be detected efficiently using a heterodyne detection system. One solution may be to use small two-dimensional coherent arrays for detection. The phase-front can be made relatively uniform over each array element if the element has a size comparable to the diameter of a speckle lobe at the focal plane, and would allow simultaneous speckle mitigation and sensitive heterodyne detection.

Experiments were conducted using short-wave infrared optics to determine possible heterodyne detection architectures. A frequency offset homodyne architecture was constructed for bench-scale experiments (Figure 1). This setup used an acousto-optic modulator to frequency shift a local-oscillator beam relative to the transmitted beam to perform the heterodyne mixing. Experiments were conducted with heterodyne beat detection limits approaching theoretical levels.

Figure 1. Shown is a bench-scale system to study different frequency modulation-formatting schemes. Also included is a short-wave infrared lasers imaging camera and monitor used to help align the heterodyne beams to high precision.

Heterodyne Chemical Sensing

Self-referenced homodyne offset detection was used to enhance signal recovery of weak signals due to the specular component of scattering. We postulated several

benefits of using a modified spread-spectrum local oscillator to enhance the signal recovery of narrow-band chemical absorption. The frequency modulation heterodyne detection scheme offers some benefits over a homodyne scheme that may lead to higher dynamic range signal recovery that mitigates amplitude noise effects of the laser or effects that may result from multi-path propagation errors. The quantum cascade lasers make fairly good frequency modulation-formatted lasers, but existing commercial, off-the-shelf-based infrared detectors, especially the long-wave infrared mercury-cadmium-telluride detectors, are problematic because they have considerable harmonic and intermodulation distortion that mask the effects theorized in the models.

Subsequently, our bench-scale efforts switched to the short-wave infrared where better detectors are available to do a wide dynamic range of heterodyne studies. Unfortunately, most of our laser diodes were not useful to test this new technique. The proposed heterodyne experiments need two very low noise, phase stable lasers to effect the best measurements. A setup was finally crafted as shown in Figure 2 using more stable external cavity-based lasers. These lasers have better short-term phase stability but exhibit periodic slow perturbations (due to mechanical vibrations) in their center frequency that caused aliasing of the effects we had hoped to confirm. To date, we see a modest 6 dB improvement of the carrier-to-noise ratio as opposed to potential theoretical carrier-to-noise ratio improvements of > 30 dB.

Short-Wave Infrared Chemical Sensing Instrumentation

We are working toward the development of brass-board sensor systems that can yield good field data for all aspects of this task. The work involves both the development of short-wave infrared lidars based on fiber communications lasers, and potential dispersive spectrographs that enable better active signal recovery (by rejecting background light), but which permit imaging. Initial work has led to several bench-scale prototype systems that can be used to test different formatting ideas that have been developed under the first two tasks. Figure 2, for example, shows a setup that tests concepts of a fully coaxial lidar configuration wherein the telescope is used in a common mode transceiver arrangement, typical of radars. The transmit and receive signals are multiplexed with a polarization switch so that the outgoing beam is not coupled to the receiver. This design could afford the simplest matching of the beam shapes for best heterodyne signal recovery from glints, however it puts a premium on the polarization fidelity of our optics.

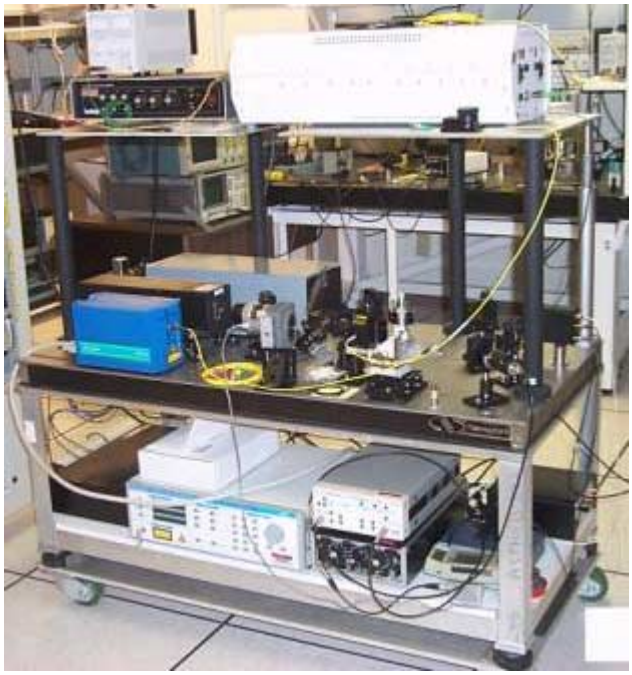

Figure 2. Portable lidar system using two different short-wave infrared lasers to affect a heterodyne signal recovery of back-scattered signals

As shown in Figure 2, we can utilize two separate short-wave infrared lasers, to effect formatting options other than simple homodyne offsets of the transmit laser. The transmitted laser is projected through a two-mirror afocal telescope with a beam offset, so that diffraction effects of the secondary mirror are not added into the beam. We are currently studying specular glints using a retro mirror to return the free-space propagated laser without significant speckle distortion. The telescope we are using has a small primary aperture of 10 cm, so it is not ideal for recovering signals from diffusively scattering rough surfaces. A much larger aperture all-reflective telescope using an offset afocal design has now been thoroughly ray-traced and validated for low aberrations. The newly designed telescope also has much better aberration corrections, so it should perform very well for planned monostatically scattered transceiver path-loss experiments that might simulate conceptual systems modeled in the first task.

We also prepared a system to simulate the returns from frequency modulation-differential absorption lidar concepts where the return signal is not filtered or amplified with a heterodyne local oscillator Figure 3. We are preparing this system to recover the direct signal of an frequency modulation-formatted laser using a much bigger and better throughput telescope design.

Figure 3. This portable system is being developed to recover signals from rough surface back scattering. The use of a commercially tunable cavity enhanced laser diode permits coverage over many available absorption lines of gases.

There is a possibility of exploiting frequency modulation spectroscopy at low frequencies if the laser beam has a small target depth so that the return rays are embodied in one or a few imaged speckles. In short-range applications, the multi-path distortions are common-mode when the pixels are matched to the telescope's angular resolution. This scheme is being static tested for possible application on low-flying craft or where static platforms can make use of returns from ~100 meters. The common-mode rejection of multi-path distortions could allow more sensitive signal recovery of narrow absorption lines. To date, we have only tested results over ~50 meters indoors with single pixel detectors, but the path-loss ratios bode reasonable signal return for sensitive absorption measurements in the short-wave infrared against low reflective rough surfaces (R< 2%). Using a multiplexed detector array with optimal filtering for coherent signal addition should produce substantial improvements. We are also studying this setup for use with optical amplification using commercial short-wave infrared amplifiers for fiber communications. The noise performance and gain of existing erbium doped fiber amplifiers suggest that low-noise optical preamplifiers could be used to help recover weak signals nearly as well as a heterodyne receiver design. Optical alignment to the fiber will require development of properly tapered multi-mode fibers, but this alignment scheme may be easier to effect in the field than heterodyne alignments which need much better absolute angular match of two beams.

Summary and Conclusions

New and significant areas of coherent and frequency modulation-differential absorption lidar research were identified to optimize remote sensing strategies of our lidar concepts. The development of the instrumentation slowed due to our desire to understand the modeling results. Nevertheless, three bench-scale systems have been developed. The systems shown in Figures 2 and 3 can be applied against outdoor targets at ranges useful for low-flying unmanned aerial vehicles and micro-airborne-vehicles. The latter could be used to position sensitive short-wave infrared detectors for bistatic reception. Multiple lidar architectures, using heterodyne or optical amplification techniques will be studied next year in order to provide a parametric basis for comparison. This field work should provide valuable insights on atmospheric and rough surface scattering properties.

Reference

Sheen DM. 2000. *Frequency modulation spectroscopy modeling for remote chemical detection.* Pacific Northwest National Laboratory, Richland, Washington.

Infrared Polarization Signatures

Thomas A. Blake, John F. Schultz

Study Control Number: PN00057/1464

This project will produce a laboratory database of infrared reflectance and polarization spectra of liquid phase chemical compounds coated onto terrestrial surfaces such as rocks, minerals, sands, clays, etc. The database will be indispensable in understanding remote sensing data of the terrain surrounding suspected weapons of mass destruction proliferation sites. Such a database could also be extended to detecting changes in soil salinity and moisture as well as surface pollution such as petroleum spills.

Project Description

The purpose of this project is to set up a Fourier transform infrared spectrometer that can then be used to record reflectance spectra of low volatility organic and organophosphorous compounds coated onto terrestrial surfaces. In the second year, the spectrometer will be modified to include an ellipsometry capability, so that changes in the state of polarization as light reflects off these coated surfaces can be measured. The database of infrared reflectance and polarization spectra of a select group of compounds on a select group of surfaces will be invaluable in interpreting remote sensing data of soils surrounding suspected proliferation sites. To date, we have set up the Fourier transform spectrometer, and a reflectance accessory for holding our samples and recording spectra at variable reflectance and detection angles. We have begun recording reflectance spectra of several surfaces such as rough cut quartz crystal, and quartz and feldspar sands. The spectra agree nicely with reflectance spectra recorded for geological spectral databases, and we are now coating quartz and feldspar sands with dimethyl methylphosphonate, which is a benign simulant of the G class of chemical weapon compounds, and recording reflectance spectra of these coated surfaces. The spectra show that there is a significant change in the spectra in going from the uncoated to coated surface. Such changes will provide a "smoking gun" signature of the presence of this compound. This work is now expanding to other compounds and other surfaces.

Introduction

The objective of this project is to explore unpolarized and polarization-resolved reflectance spectra for detecting the presence of liquids and particulates related to the production of weapons of mass destruction on surfaces around suspected facilities. It will be possible to detect changes in the reflectance spectra as a surface is coated with liquids, thus providing information about the operational status of a facility and likely locations for physical sampling. By comparing how the reflectance spectra change as a compound accumulates and ages on a surface, it may also be possible to identify classes of compounds, and perhaps even specific chemicals. We will determine whether such spectral features can be found for each compound-substrate combination and if the signatures will be pronounced enough to detect from a remote sensing platform. If this work indicates that the polarization-resolved reflectance spectra can be used to detect weapons-related compounds on surfaces, we see immediate extension to a number of important battlefield chemical warfare and environmental applications.

Field data will be collected using multispectral passive remote sensing systems similar to NASA's Airborne Visible and InfraRed Image Spectrometer (wavelength coverage 0.4 to 2.45 μm) or Thermal Infrared Multispectral Scanner (wavelength coverage 8 to 12 μm). These instruments operate from NASA's ER-2 and Lear Jet aircraft, respectively, and have instantaneous ground fields of view of about 10 meters. As an example of sensitivity, the Thermal Infrared Multispectral Scanner uses liquid nitrogen cooled HgCdTe detectors and has a noise equivalent temperature difference of 0.1 K at 300 K. This figure of merit can be related to a noise equivalent reflectance difference of 0.002 at a wavelength of 8 μm. Since most terrestrial materials have a reflectance between 0.2 and 0 the instruments are sensitive to reflectance changes of 1 part in 100. The laboratory measurements will allow us to quantify reflectance changes with amounts of coverage of our target compounds (Asrar 1989; Wolfe and Zissis 1985).

Tailings and effluents pumped from mines (Barettino et al. 1999), petroleum ground spills (Brodskii and Savchuk

1998), and soil salinity changes (Mikati 1997) have been monitored using remote sensing reflectance spectroscopy. One long-term outgrowth of this project could be an expanded database of industrial chemicals on a variety of surfaces for detecting soil pollution.

Approach

We have chosen an empirical approach to exploring the utility of these phenomena. Theoretical predictions would require an immense expenditure of time and money to model the complex chemisorption and physisorption processes and to carry out optical calculations for rough, inhomogeneous surfaces. Our approach is to use substrate materials that simulate weapons of mass destruction production sites and to coat the substrate material with a known amount of the compound of interest and then collect diffuse and specular reflectance spectra in the laboratory using a Fourier transform infrared spectrometer. Recording spectra in the laboratory is a viable alternative to field collections. We should be able to reproduce field conditions in the laboratory as well as control relevant conditions such as temperature, humidity, and quantity of sorbed compound.

The spectroscopic work performed for this project will be done in a "source on" mode. We will use an infrared light source in the spectrometer to record spectra. We will study spectra of new and aged compounds. Environmental chambers will be used to simulate weathering (hydrolysis, ultraviolet photolysis) of the compounds on the substrates.

Results and Accomplishments

We obtained a Bruker Instruments Fourier transform infrared spectrometer with a specular reflectance accessory (Figure 1). The reflectance accessory is shown in Figure 2. The spectrometer is capable of eighth wavenumber resolution. Four wavenumber resolution is typically used in our work. The spectrometer covers the infrared spectral range from 400 to 14,000 cm^{-1}. The reflectance accessory has been modified to hold the sand samples. The accessory takes light from the spectrometer in through a side port and, through a set of mirrors, reflects the incident light up to a movable mirror which in turn reflects light down onto the sample. Light reflecting off the sample is collected by a second movable mirror. The light is then directed by another set of mirrors onto a liquid nitrogen cooled detector. In this way we can collect spectra at variable incident and detection angles.

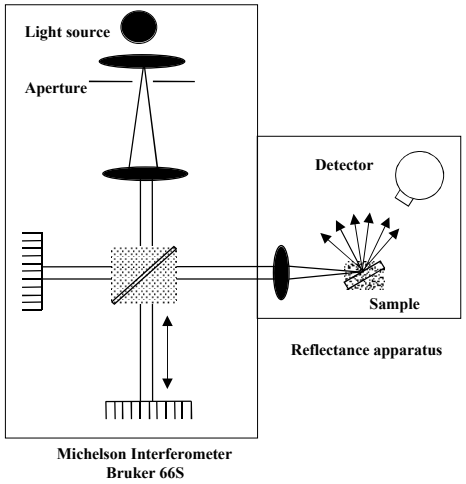

Figure 1. Schematic of Fourier transform infrared reflectance spectrometer

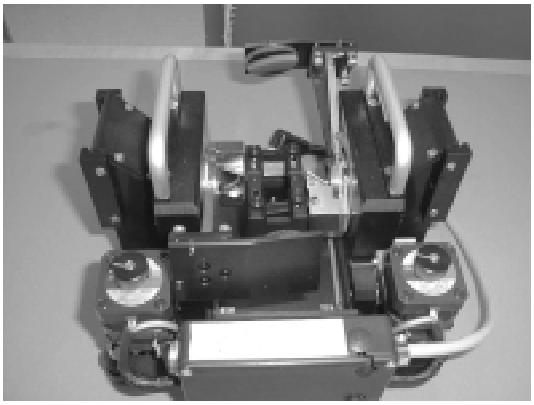

Figure 2. Photograph of the reflectance accessory

Figure 3 shows a reflectance spectrum of dry quartz sand at a spectral resolution of 4 cm^{-1} and a reflectance angle of 63°. The grain size of the sand is 200 to 290 μm (50 to 70 mesh). The spectrum shows the silicon-oxygen stretch band centered at 1200 cm^{-1} and silicon-oxygen bending bands at lower frequencies. When the sand is coated with dimethyl methylphosphonate, the band at 1200 cm^{-1} changes its shape, and a significant change occurs on the high frequency side of the band. The ratio of the coated sand spectrum to that of the dry sand spectrum is shown as the solid line in the plot. The sharp feature at 1350 cm^{-1} will be useful as a signature for organophosphorous compounds. Present remote sensing technology is sensitive enough to detect such a feature in field data. To give a sense of the relative reflective losses in going from a specular reflector such as a mirror to a quartz crystal to the quartz sand a spectrum of all three is shown in Figure 4 (the ordinate units on each spectrum in Figure 4 are the same). The plot shows that there is a loss of approximately a factor of 100 in reflected light in going from the quartz slab to the quartz sand.

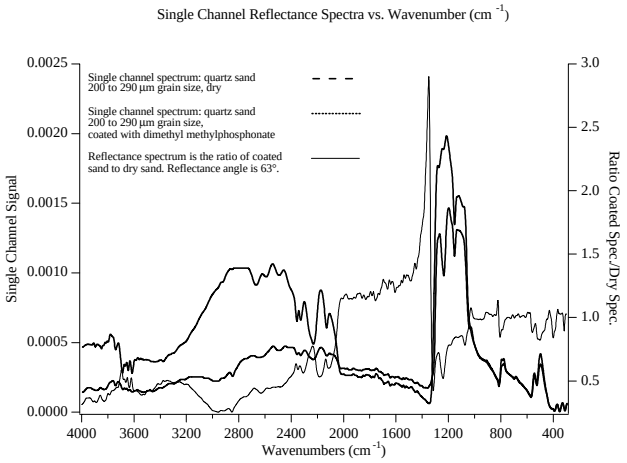

Figure 3. Infrared spectra of dimethyl methylphosphonate on quartz sand

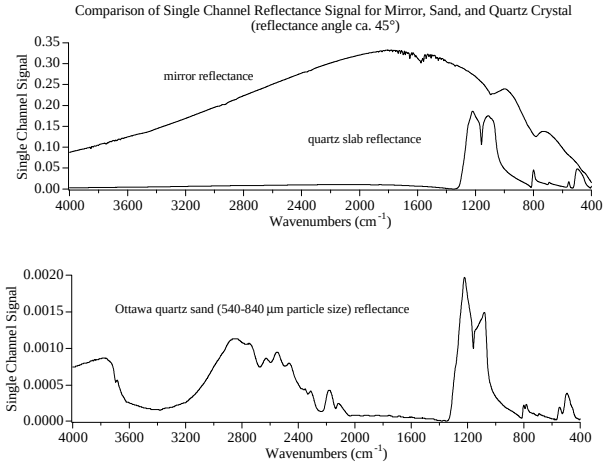

Figure 4. Comparison of reflectance signal strength for a flat mirror, a quartz slab, and quartz sand

We found that for the same compound, dimethyl methylphosphonate for example, its evaporation rate off of metal surfaces is extremely slow compared to that off of quartz crystal, and is different than that off the quartz sand. Research into this would provide invaluable information to modelers calculating the accumulation of effluent compounds on surfaces surrounding proliferation sites.

Summary and Conclusions

We established a spectroscopic facility for recording reflectance spectra of chemical compounds coated onto terrestrial surfaces. Prominent spectral feature changes take place when these surfaces are coated. The continued research will provide a database of compounds and surfaces that should prove valuable to the intelligence community for evaluating possible weapons of mass destruction proliferation sites.

References

Asrar G. 1989. *Theory and Applications of Optical Remote Sensing.* Chapter 12, John Wiley & Sons, New York.

Barettino EL-PD, C Anton-Pacheco, G Ortiz, JC Arranz, JC Gumiel, B Martinez-Pledel, M Aparicio, and O Montouto. 1999. "The Extent of the Aznalcollar Pyritic Sludge Spill and its Effects on Soils." *Sci. Tot. Environ*. 242:57-88.

Brodskii ES, SA Savchuk. 1998. "Determination of Petroleum Products in the Environment." *J. Anal. Chem*. 53:1070-1082.

Mikati GOF. 1997. *Temporal Analysis of Multispectral Video/Satellite Imagery for the Detection and Monitoring of Salinity on Agricultural Lands.* Dissertation, Utah State University, UMI order no. DA9822024.

Wolfe WL, GJ Zissis, eds.. 1985. *The Infrared Handbook.* pp 19-10 – 19-17. ERIM, Ann Arbor, Michigan.

In Situ Real-Time Through-the-Wall Measurements of the Density and Viscosity of a Liquid or Slurry

Margaret S. Greenwood, Judith Ann Bamberger, Richard A. Pappas

Study Control Number: PN00058/1465

New methods are needed to characterize liquids and slurries. These methods must involve real-time, nonintrusive sensors. A new approach has been found to characterize fluid density and viscosity by transmitting an ultrasonic signal through the wall of the pipe or vessel.

Project Description

The objective of the research is to demonstrate the feasibility of an ultrasonic sensor to measure the density and viscosity of a liquid or slurry through the wall of a pipe or tank. The experiments considered the optimum frequency of the ultrasound for a given wall thickness, as well as the bonding of the transducers to the pipeline material.

Introduction

The need has developed to identify and demonstrate sensors and instrumentation that provide on-line real-time capabilities for characterizing liquids and slurries. Such techniques are important during retrieval operation and for characterizing the contents of tanks at Hanford and other DOE sites. The density and viscosity of a liquid or slurry are two important properties and such measurements have many applications. We developed a density and viscosity sensor in which the base of the sensor is in contact with the fluid to be measured. It would be advantageous if a sensor could be developed that operated through the wall of the pipeline or tank. Figure 1 shows a schematic diagram for through-wall measurement of viscosity and density.

This research seeks to demonstrate that the density and viscosity of a liquid can be determined by mounting longitudinal and shear wave transducers on the wall of a pipeline or tank. Our objective is to distinguish small changes in density and viscosity. A longitudinal wave transducer determines the product of the density and speed of sound in the liquid, while a shear wave transducer determines the product of the viscosity and density. A low frequency ultrasonic beam from another longitudinal wave transducer, traveling through the liquid, will measure the speed of sound through the liquid. The combination of these three measurements yields the density and viscosity of the liquid or slurry, as well as the speed of sound through it.

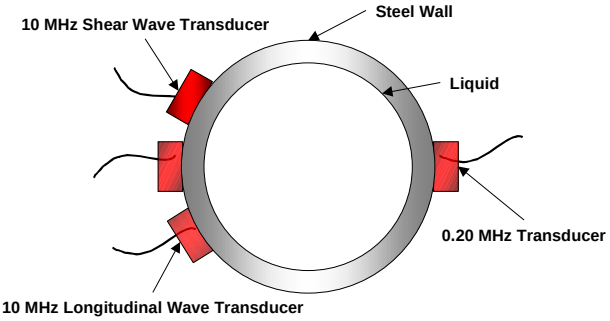

Figure 1. Transducer configuration for through-wall measurements

Viscosity Measurement

The viscosity measurement uses a high-frequency shear wave transducer (about 5 to 10 MHz), producing vibrations in the wall that are perpendicular to the direction of motion of the wave. When the shear waves strike the wall-liquid interface, only a small amount of the energy of the shear waves is transmitted into the liquid. Liquids cannot easily support a shear wave and the (large) remainder of the energy is reflected back to the transducer. However, as the viscosity increases, the liquid can support the shear wave more easily and the amount of energy returning to the shear wave transducer decreases. Then, the reflection coefficient, defined as the ratio of reflected ultrasound to incident ultrasound, is a measure of the viscosity. As the viscosity increases, the reflection coefficient decreases. In order to obtain the viscosity, it is necessary to compare the voltage measurement to some standard, usually water, where the viscosity and density at a given temperature are known. The theory shows that the reflection coefficient is dependent upon the product of density and viscosity.

Therefore, in order to extract the viscosity, one also needs to measure the density.

Acoustic Impedance Measurement (Density-Speed of Sound Product)

The acoustic impedance of a material is defined as the product of the density and speed of sound in the material. For a perpendicular reflection, the reflection coefficient is dependent upon the acoustic impedance of the wall material and the acoustic impedance of the liquid.

Speed of Sound in the Liquid

Figure 1 shows 0.2 MHz transducers on opposite sides of a tank. It also might be possible to use a single transducer operating as both the sender and receiver of the ultrasonic wave, i.e., the pulse-echo mode of operation. The time of flight of the pulse can be used to determine the speed of sound.

The combination of these three types of measurements can yield the density, viscosity, and speed of sound in the liquid.

Approach

To evaluate the feasibility of through-wall measurements, we conducted a series of experiments varying the transducer frequency and bandwidth and type of pulse for both shear and longitudinal waves to investigate the types of responses that met the criteria that the succeeding echoes do not overlap. The properties of the transducers were determined. Design parameters include the frequency of the transducer and its bandwidth, because the frequency determines the period of the pulse while the bandwidth determines the shape of the pulse. The bonding of the transducer to the wall is another important aspect, which may be accomplished using epoxy. The time length of the pulse is determined by the pulse that is sent to the transducer and the bandwidth of the transducer. For these investigations, a square-wave pulser provided a high voltage pulse of short duration to the transducer. Data were obtained using a digital oscilloscope that has the capability to obtain fast Fourier transforms and save the information to disk. Also investigated were the use of toneburst signals of approximately 6 cycles. Both methods were equivalent. An experimental apparatus was designed and constructed, and experiments were conducted to measure the acoustic impedance of a liquid.

Results and Accomplishments

Shear wave transducers produced vibrations that were perpendicular to the direction of the wave and that traveled easily in solids. While longitudinal waves travel easily in liquids, shear waves penetrate the liquid only very slightly. This penetration depends upon the viscosity and increases with an increasing viscosity. The acoustic impedance of stainless steel was large compared to most liquids; therefore, the change in viscosity was not significant enough to be readily observed in our experiments. However, experiments with a machinable glass allowed us to differentiate between a range of water and sugar water samples with differing viscosities. The results showed that differences in voltages can be seen for 30% sugar water and 50% sugar water, compared to water.

Summary and Conclusions

A new approach was developed to characterize fluid density and viscosity by transmitting an ultrasonic signal through the wall of the pipe or vessel. Experiments were conducted to evaluate configurations for successful measurement. These experiments showed the potential to measure the density through the wall of pipes or vessels. Experiments showed that the measurement of viscosity using machinable glass is feasible.

References

Bamberger JA, and MS Greenwood. 2000. "Measuring slurry density and viscosity in-situ in real time during pipeline transport using an ultrasonic sensor." FEDSM00-11121. *Proceedings of the ASME 2000 Fluids Engineering Division Summer Meeting,* June 11-15, 2000, Boston, Massachusetts. American Society of Mechanical Engineers, New York.

Bamberger JA, LJ Bond, and MS Greenwood. 1999. "Ultrasonic measurements for on-line real-time food process monitoring." *In Proceedings of the Sixth Conference on Food Engineering,* 1999 AIChE Annual Meeting, Dallas, Texas. PNNL-SA-32024, Pacific Northwest National Laboratory, Richland, Washington.

Greenwood MS, JR Skorpik, and JA Bamberger. 1999. "On-line sensor for density and viscosity measurement of a liquid or slurry for process control in the food industry." *In Proceeding of the Sixth Conference on Food Engineering,* 1999 AIChE Annual Meeting, Dallas, Texas. PNNL-SA-32025, Pacific Northwest National Laboratory, Richland, Washington.

Plutonium Mass Estimation via Gamma-Ray Spectrometry

Walter K. Hensley, Anthony J. Peurrung, Debra S. Barnett, Dale N. Anderson

Study Control Number: PN00074/1481

The measurement of plutonium mass is a critical requirement in nuclear arms control applications. A computational algorithm is being developed and optimized for the estimation of plutonium mass with sufficient accuracy, while alleviating the drawbacks of traditional neutron-based methods of coincidence counting, for use in a variety of arms control applications.

Project Description

The purpose of this project is to demonstrate that gamma-ray based plutonium mass estimation offers sufficient accuracy to mandate its use for a variety of arms control applications, including those now using neutron coincidence counting. The information contained in a full gamma-ray spectrum can be used to obtain an estimation of plutonium mass because of the different attenuation to which gamma rays of different energies are subjected. These differential attenuations allow considerable inference to be drawn about the shielding external to any plutonium and about the plutonium itself. This information, in turn, can be used to formulate a mass estimate along with an associated error. This project is exploring this process in detail, developing an optimal algorithm, determining the various errors associated with mass estimates, and demonstrating mass estimation using a variety of relevant spectra. The potential savings in time and money that would result from the use of spectral mass estimation are sufficient to significantly accelerate progress toward current and future arms control objectives.

Introduction

Currently, plutonium mass measurements are performed almost entirely using the neutron-based method of coincidence counting. Although the neutron-based method is capable of accurate mass measurements, it suffers from a number of drawbacks which are completely alleviated with gamma-ray based plutonium mass measurements. Table 1 compares the features of neutron-based and gamma-ray spectrometry methods for estimating plutonium mass in a nuclear weapon.

While gamma-ray estimation of plutonium mass does have the disadvantage of reduced accuracy, this is readily tolerable for arms control applications. Frequently, arms control measurements entail demonstration that an item or component merely exceeds a threshold amount of plutonium. The thresholds are typically set so low that any conceivably valid item or component will pass inspection.

Table 1. Comparison of spectrometric methods for assessing plutonium mass

Issue	Neutron-based Methods	Gamma-ray Methods
Cost/unit	Roughly one million dollars. Long lead times commonly required for new application system development.	Post-development cost is nearly zero. Existing software, computers, and sensors can be used.
Portability	Large number of rigid moderators required leads to high weight and devices often best suited to fixed installations.	Laptop computer and hand-held High Purity Germanium (HPGe) sensor required.
Geometry	Inflexible, each counting system is limited to particular item geometry. Nuclear weapons vary in shape and size.	Accommodates any size or shape.
Evasion	Although fully calibrated systems are hard to evade, issues with confusion by alternate neutron sources such as ^{252}Cf, AmLi, and PuBe exist.	No issue of spoofability. The method directly quantifies ^{239}Pu, *the* isotope of interest for arms control applications.
Matrix effects	Strange or unknown geometries in arms control measurements, especially those involving moderator, can seriously affect accuracy.	An issue of this research.
Criticality Safety	Substantial amounts of required moderator precludes some plutonium measurements.	No moderator required.

A next-generation technology is needed to address the problem of plutonium mass measurement in arms control applications. Despite the tremendous inertia behind the established technique of coincidence counting, there is a growing acknowledgment of the general failure of neutron-based methods to properly support the United States arms control objectives. Further, it is likely that a simple but effective technology such as this could actually accelerate progress in negotiations such as START III, START III+, and Mayak. The amount of necessary measurement hardware would be greatly reduced, with a single measurement involving a single detector and single information barrier potentially being sufficient. The timeline for development and testing of measurement systems would be greatly accelerated.

Approach

The approach to this problem necessarily involves the development of a model for the plutonium configuration, with subsequent evaluation of the errors resulting from the use of the model. Two major simplifications are necessary for such a model to proceed. First, the set of shielding materials can be reduced to three basic types with quantifiable properties. High-Z shielding accounts for substances such as lead and uranium, medium-Z shielding accounts for substances such as iron, low-Z shielding accounts for all hydrogenous substances and materials with atomic numbers below roughly aluminum. A plot of mass attenuation coefficients (as a function of energy) for the simplified model is shown in Figure 1.

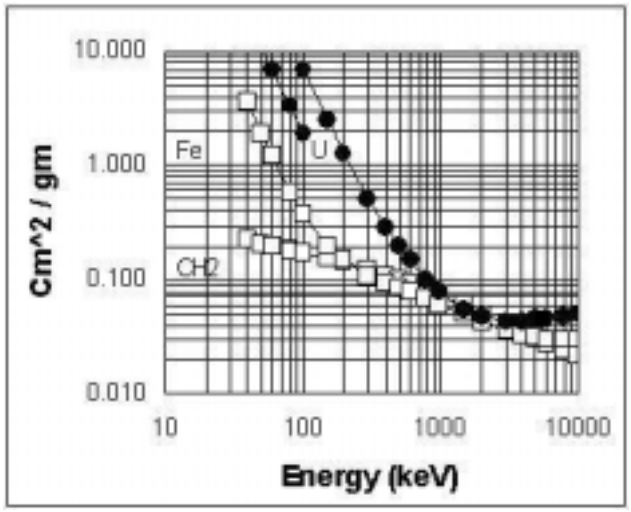

Figure 1. Mass attenuation coefficients for selected materials as a function of photon energy

The second major simplification involves object geometry. Calculations are most easily completed for slab (planar) geometries, while real components incorporate more complex geometries. Our initial algorithm assumes slab geometry. Future work will assess improvements, if any, from incorporating a non-slab geometry. Perfectly accurate geometries are not possible because nuclear weapons are constructed in a variety of shapes, sizes, and designs. We anticipate that the uncertainties associated with using this simplification will be small. Estimates accurate to within 25 to 50% may be more than satisfactory for arms control applications.

This work complements and extends the Sandia National Laboratory algorithm work, called "Minimum Mass Estimate (MME)" (Mitchell and Marlow 2000), by the use of a larger part of the gamma-ray spectrum, an elaborate shielding and geometric model, and sophisticated statistical methods.

Results and Accomplishments

Our approach to development and testing of the initial mass estimate algorithms was based on the use of increasingly complicated gamma-ray spectra. Initially, simplified spectra were generated using the SYNTH gamma-ray generating software, followed by spectra collected in the laboratory from a small (~100 gram) weapons grade plutonium source. A wide variety of absorbers (that spanned a broad range of atomic number and density) were then used to attenuate the gamma-rays from the plutonium both individually and in combinations with other absorber materials. Measurements were made using both short and long acquisition times so that we could determine the sensitivity of the algorithms to the statistics of the input spectra.

The key to the probabilistic approach to this problem is that the expected (average) gamma-ray signals, as a function of energy, are completely determined by known physics. Under the absorber and geometric assumptions discussed above, the expected gamma-ray signal at a spectrometer has been described mathematically using first-order effects.

The current algorithm assumes known thickness of the low, medium, and high barriers. This assumption will be relaxed in future development and the mathematics of mass estimation in the presence of absorber-thickness-uncertainty is developed.

Summary and Conclusions

The first round of algorithm development has yielded very promising results. We were able to successfully calculate an accurate plutonium mass from experimental data given the composition of a combination of

attenuation materials (but unknown thickness), as well as calculate the attenuation material thickness given plutonium mass and attenuation material. Thus, we have been able to show that the individual pieces of the underlying algorithm appear to be well behaved in the regions of the parameter space examined. We have also seen some early indications that the method may be somewhat insensitive to the poor statistics associated with short data acquisition times.

The success of this year's research indicates improvement can be made through additional testing and refinements to the algorithm.

Reference

Mitchell DJ and KW Marlow. 2000. *Minimum Mass Estimates for Plutonium Based on the Peak Intensities and Scattered Radiation in HPGe Spectra* SAND2000-0383, Sandia National Laboratories, Albuquerque, New Mexico.

Radiation Detection at 50 km

Randy Hansen, Anthony Peurrung, Theodore Bowyer

Study Control Number: PN99060/1388

This project seeks to begin development of a long-range radiation detection technology that exploits regions of elevated ionization in air. A variety of recent results published in the literature has indicated that detection of radioactivity from as far as 50 km may be possible via three fundamentally different approaches. This project studied the underlying premises of the three approaches and assessed their capability for long-range radiation detection.

Project Description

The background level of ionization in the lower atmosphere arises primarily from natural radiation. Consequently, any radioactivity release or strong radioactive source would be expected to lead to elevated levels of ionization in the atmosphere. Possible long-range radiation detection techniques were divided into three categories. The first approach, using microwave reflection to locate regions where the index of refraction is substantially altered by high concentrations of free ions, and the second approach that looks for changes in the lower ionosphere caused by local alteration of the earth's circuit were shown to be physically impractical. The third basic approach looks directly for altered ionization levels, space charge levels, or electric fields in the downwind plume. Analysis of this approach indicated radiation sources should be detectable from more than 100 meters.

Results and Accomplishments

With relatively inexpensive instruments, experiments were conducted to demonstrate the feasibility of detecting radiation via altered ionization levels downwind from a source. In the first phase, the instrumentation was selected and purchased. Learning the intricacies of the instruments and their ability to measure changes in atmospheric electrostatics composed the second phase. The third phase was the proof-of-principle experiment where we attempted to detect a real radiation source using the suite of commercially available instruments.

Due to budgetary constraints, most of the testing was conducted using an ion generator. We were able to detect ions from the generator at 100 meters with a handheld instrument that cost less than $600. The final test we conducted was to detect an Ir-192 gamma-ray source. Although we clearly saw a change in the ion flux at 40 meters and arguably at 80 meters, a number of research issues were identified. A radiation source can be detected using atmospheric electrostatic measurements, but a number of questions need to be answered before the viability of this technique is determined.

Suite of Instruments

The suite of instruments was composed of two ion meters used to measure the concentration of both positive and negative ions, an electric field meter used to measure the earth's electric field, and a set of weather monitoring instruments. A data acquisition system was engineered to facilitate in the acquisition, analyses, and display of real-time data.

The commercial ion meters are constructed of a stack of three parallel plates with small air gaps between them. The two outside plates are the opposite polarity of the middle plate. A fan on the end draws air (200 cc/s) between the plates. The ions of the opposite polarity of the center plate are repelled from the outer plates and attracted to the inner plate. The charge collected on the inner plate is measured and converted to the number of ions per cubic centimeter contained in the incoming air. The units have a collection efficiency of 65%, and an accuracy of ± 25%. They were modified so the data acquisition system could directly read the value of the charge collected on the inner plate. One meter measured the concentration of positive ions, and the other meter measured the concentration of negative ions. The space charge was calculated from the difference between these values.

The electric field meter (electric field mill) is composed of a motor and two vanes. One vane is stationary, the stator, and the other rotates at a given frequency, the rotor. The vanes look like a pie cut into six pieces with every other piece removed (a trifoil). When the three lobes of the rotor are out of phase with the three lobes of the stator, the earth's electric field produces a potential that causes a current to flow. As the lobes come into

phase, less of the earth's electric field lines contact the lobes of the stator and therefore the current flow decreases. This cycle is repeated hundreds of times per second and an alternating current signal is produced. The amplitude of this signal is proportional to the earth's electric field. During normal atmospheric conditions, the earth's potential is around 100 volts per meter.

Instrument Optimization and Testing

Our approach involved three steps: 1) examination of the instruments in a controlled atmosphere to ensure a robust setup, 2) brief examination of the environmental factors that influence atmospheric electrostatics, and 3) direct detection of an ion source.

Numerous modifications were made to optimize the instruments and the data acquisition system to make them more robust. To minimize the variability of external factors on the ion detectors during this testing, they were placed in a cardboard box and the air was ionized by the radiation from an external Co-60 source. The results in Figure 1 show the dramatic increase in the negative ion concentration created by the ionizing radiation.

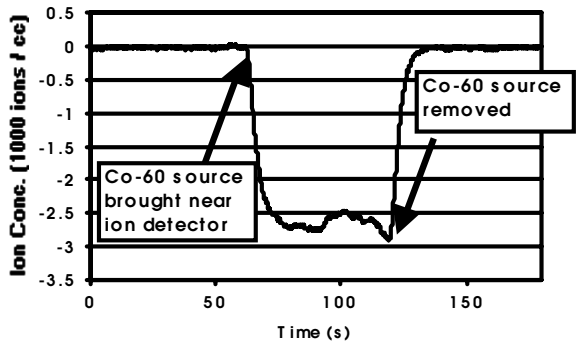

Figure 1. Ion concentration in a box as a function of time as an ionizing radiation source is brought near the box and then removed

The second step was to try to determine whether environmental factors other than radiation would contribute significantly to the normal ion population. Most of the ions found in the environment are the direct result of radiation, but open flames, electrical arcs, and combustion engines can also produce ions. We verified that these effects were minimal. We set up the instruments in interesting locations and found an effect from passing vehicles, but the effect was minimal. It is not clear whether the effect of the passing vehicle is due to the ions produced during combustion or more likely due to the charge it acquires while gliding through the air. The net result was that there was an effect that will not have an important impact on sensitivity.

Once the instruments and the environmental factors were characterized to some degree, experiments were conducted to see how well the system would be able to detect an ion source set some distance upwind. We chose an ion generator for this set of experiments. The goal was to become familiar with the dynamics of making electrostatic measurements so only a small subset of measurements would have to be made with an actual radiation source. The experimental setup consisted of placing two ion detectors, one detecting positive ions and one detecting negative ions, and an electric field mill downwind from the ion generator. An anemometer was placed along with these instruments to record the wind direction and speed. The data from these instruments were fed into a data acquisition system where a polar plot was produced. The angular coordinate represented the wind direction and the radial coordinate was the magnitude of the instrument response.

Three separate measurements were made: the negative ion concentration, the positive ion concentration, and the electric field. The space charge was calculated from the difference between the positive and negative ion concentrations. The negative ion concentration measurement was the most sensitive for determining the presence of an ion source. An example of the data for an ion generator located 50 meters upwind is shown in Figure 2. Data were collected for 30 minutes and the magnitude of the response was averaged for each angular coordinate. This shows that with inexpensive equipment and without sophisticated techniques, we were able to easily detect an ion source at 50 meters.

The data in Figure 2 correlates very well with the ideal case, but at greater distances or lower wind speeds the variability increases significantly. One solution that was investigated was the use of sophisticated data analysis algorithms with the aim of improving the signal to noise ratio. Although these techniques were partially successful, the fact that the wind direction can vary dramatically and the ions can take between 30 to 60 seconds to reach the detector made polar plots a difficult system to implement. Further testing was conducted by simply obtaining a background with the ion generator turned off, then looking for significant deviations when the generator was operating, and then correlating this data with the wind direction. Under these conditions the ion generators were detected from 100 meters away. Figure 3 shows the results of this test. The peaks occurred when the wind direction was optimal for transporting the ions to the detectors.

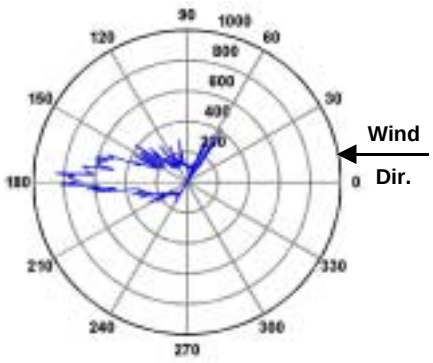

Figure 2. Negative ion concentration for an ion generator located 50 meters upwind and at approximately 180° with respect to the instrument suite

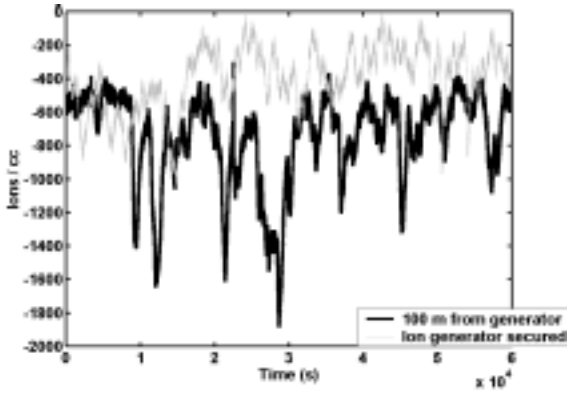

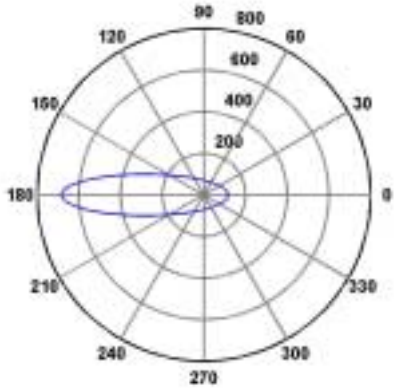

Figure 3. Negative ion concentration for an ion generator located 100 meters upwind from the instrument suite

Looking for correlations between the negative ion concentration and electric field measurements was another effective tool to reduce the variability. Although this technique is not as sensitive as knowing the background a priori, it may be a more viable method for actual field measurements.

Detection of a Radiation Source

The final set of tests was conducted using a 52 Ci Ir-192 radiographer's source in a shielded, hermetically sealed container.

During the transfer between the lead box and storage container, the source was not shielded and a spike in the ion density resulted from the increased flux. The presence of the source in the lidless lead box produced a measurable difference in the ion flux at a distance of 40 meters downwind from the source (Figure 4).

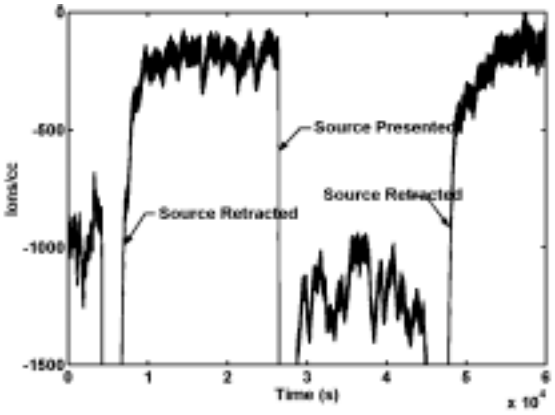

Figure 4. Negative ion concentrations observed 40 meters downwind from a 52 Ci Ir-192 source as it was transferred between a shipping container and a lead box that did not have a top

A response was also observed 40 meters upwind, but it was of lesser magnitude. One possible explanation is that the instrument was measuring ions created near the detector by the increased flux of radiation from the source. The goal of these tests was to measure an ionization plume as it blew by the suite of instruments. From the tests conducted using the ion generator, we anticipated a spike in the number of ions detected when a favorable wind direction and speed were observed. Unfortunately, only small spikes were observed when the instruments were 20 and 40 meters downwind from the source. Due to the variability of the wind and time and resource constraints, we were not able to perform the test under optimal conditions. These tests did, however, identify three areas requiring further research to enhance the viability of this technique for radiation detection.

Summary and Conclusions

If this work continues, three recurring issues will need to be addressed:

1. The detection equipment needs to be more robust and optimized for these tests.

2. A more controlled set of experiments needs to be conducted. A key factor is the ability to control the wind direction and wind speed.

3. The phenomenon of ion transport, as it relates to this method of detecting radiation sources, needs to be studied and these results experimentally verified. As discussed previously, it is difficult to determine the proper location to place the instrumentation to maximize signal collection.

Real-Time Direct Surface Ultrasonic Holography

Robert Vail Harris, Jr., Byron B. Brenden, Gerald J. Posakony

Study Control Number: PN99061/1389

Ultrasonic techniques are inherently well suited to nondestructive testing and characterizing the composition of materials. Real-time ultrasonic images, or holograms, may be processed to show flaws and discontinuities in materials. This technology has many practical applications in a variety of sciences.

Project Description

This project provided a basis for revolutionizing the technology for ultrasonic nondestructive inspection of metals and composite materials. By combining technology from Pacific Northwest National Laboratory and Idaho National Engineering and Environmental Laboratory (INEEL), a new ultrasonic imaging system could be developed capable of real-time imaging of internal features of materials directly on the surface, without the need for a water tank or bath and without the use of radiation. This would dramatically enhance the ability to detect and image flaws and discontinuities in materials. It also has the potential for greatly enhancing medical diagnostic imaging in the human body.

Results and Accomplishments

We determined that high-frequency ultrasonic wavefronts and lower-frequency reflections from internal discontinuities can be imaged, but presently attainable levels of ultrasonic power and optical sensitivity are insufficient to provide direct-surface ultrasonic imaging of internal defects in bulk metals.

Solid Surface Imaging

The overall objective of this project is to produce real-time ultrasonic images (ultrasonic holograms) of internal features of an object by viewing its surface. We produced images of ultrasound as it impinged on the surface of the object. The next step was to make a block with suitable internal discontinuities (artificial defects) and demonstrate that the external surface images could be further processed to reconstruct images of the internal discontinuities. No work on liquid surface imaging was planned or performed.

Higher Frequency

To obtain a resolution adequate to produce images of internal defects in metal, the ultrasonic frequency had to be increased by a factor of three. This entailed changes in equipment for both transmission and detection.

Test Block Design

Two test blocks were fabricated of aluminum. Both had a 60 degree face to which the ultrasound transmitter was clamped, 30-degree flat-bottomed holes to reflect the ultrasound, and flat surfaces on which to observe the transmitted and reflected ultrasound. One block had a single hole, and the other had nine holes in an “F” pattern.

Transmission Results

Transmitted ultrasound was imaged on both blocks (“F” block image, Figure 1). The spacing of the wavefronts was consistent with the frequency, velocity, and insonification angle. The transmitted waves did not show evidence of interaction with the drilled holes. However, the signal-to-noise ratio in the best images was 1:1, so the effects of the interaction may have been masked by noise.

Reflection Results

No reflected high-frequency ultrasound was imaged, although the presence of reflected ultrasound had been detected using conventional ultrasonic receivers. For the single hole, a bright or dark reflected circular spot should have been observed, surrounded by contrasting diffraction rings (Figure 2).

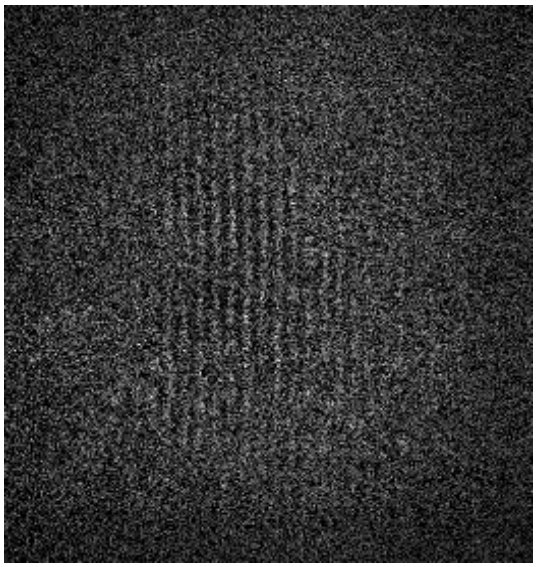

Figure 1. Image of high-frequency ultrasonic bulk waves arriving at the surface of an aluminum block, from data taken at INEEL. The vertical bands are the primary wavefronts from the transducer. Shadowing by internal defects is theoretically present, but is not observable.

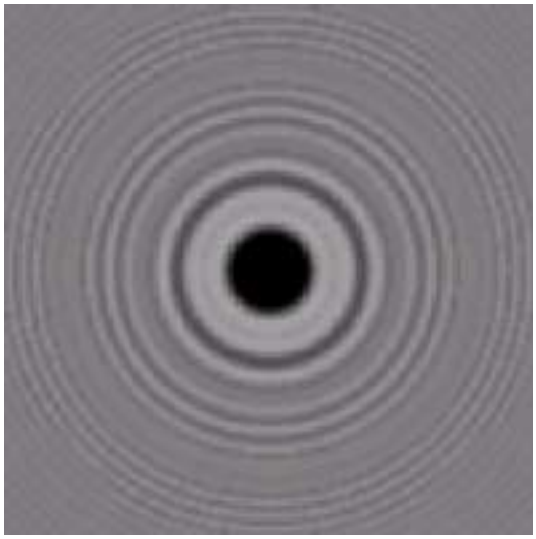

Figure 2. Theoretical image reflected from single hole, with alternating light and dark circular regions

A hazy spot was observed corresponding to the optical illumination. No perturbations attributable to the ultrasonic energy could be detected. However, at a lower frequency and slightly different geometry, others (INEEL) were able to obtain a surface image of an internal reflector (Figure 3).

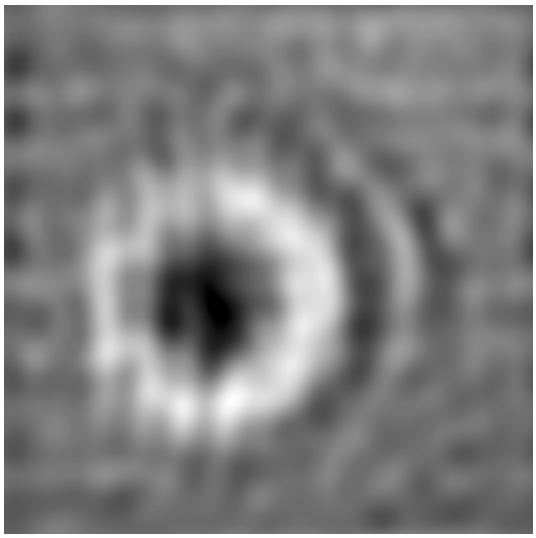

Figure 3. Actual image reflected from single hole, lower frequency

Summary and Conclusions

Full-field ultrasonic imaging of transmitted ultrasound on a solid surface at a high ultrasonic frequency was obtained. An image from an internal reflector was observed at a lower frequency.

Acknowledgments

Imaging on the solid surfaces was carried out at INEEL under the direction of Vance Deason and Kenneth Telschow. Image conversion and enhancement were performed at this Laboratory by Charles Batishko. Frequency-domain analyses were conducted by David Sheen.

Volumetric Imaging of Materials by Advanced, High Resolution Pulse-Echo Ultrasound

Morris S. Good, Leonard J. Bond, Peter M. Martin, Gerry J. Posakony, James R. Skorpik

Study Control Number: PN98081/1327

Ultrasound is a useful, nondestructive analytical tool for imaging structures that cannot be examined visually by other means. The advanced capabilities of high-resolution, pulse-echo ultrasound are being extended to very high frequencies using improved electronics and tranducers. It is now possible using high-resolution ultrasound to examine the characteristics of living cells, the structure of cell nuclei, the integrity of cell membranes, and the response of cells to environmental stresses.

Project Description

High resolution, volumetric acoustic microscopy imaging has evolved into 1) an invaluable tool in establishing the quality of critical parts and 2) an analysis tool for biological cells. Ultrasound offers a noninvasive means of imaging sub-surface structures on the order of 0.5 microns and larger (Bereiter-Hahn 1996). Applications of interest include intercellular imaging in support of the cellular observatory, imaging of ceramic materials at the microstructural level to aid in material design and life prediction, and the inspection of small solder connections of the next generation of integrated circuits [(a,b)]. To achieve the desired resolution, ultrasonic, pulse-echo systems must operate at frequencies ranging from 200 MHz to 800 MHz, however restrictions exist in the ability to fabricate transducers in this range. Two technologies have been used to fabricate pulse-echo transducers. Lapping of bulk piezoelectric material to fabricate a thin wafer has an upper frequency limit in the range of 200 MHz due to material damage incurred during lapping. Deposition of piezoelectric material has traditionally had a lower frequency limit of 1 GHz due to difficulties in maintaining a proper microstructure of the piezoelectric. This effort leveraged the world-class deposition skills at Pacific Northwest National Laboratory to overcome this problem and in fiscal year 1999, fabricated a film thickness several orders of magnitude greater than typically deposited and evaluated the resulting ultrasonic transducers as reported earlier. Due to budget restrictions in FY 2000, work centered on resolution enhancement utilizing an existing 50-MHz transducer.

(a) Private communication with Pacific Northwest National Laboratory staff.

(b) Private communication with a major integrated circuit manufacturer.

Introduction

Future work should address three fundamental issues that still hinder imaging at a resolution representative of milestone frequencies of 100 MHz and 200 MHz. Two are related to improved material deposition while the third is improved electronics to achieve adequate signal-to-noise values. Improving the deposition process to maintain a (002) columnar orientation within a 2° tolerance and thickness uniformity across the transducer diameter are the first two issues. Issue 1: The (002) columnar microstructure of the Pacific Northwest National Laboratory piezoelectric film has been observed at an orientation ranging from 0° to 15° relative to the surface normal. Inclinations greater than 2° degraded signal quality by generating shear waves. Shear waves formed an upper noise baseline and leached energy away from the primary longitudinal wave. Although several transducers with a 2° inclination have been obtained, most microstructures at the end of FY 1999 were inclined at approximately 10° and therefore resulted in a strong shear wave component. Issue 2: Thickness uniformity of the deposited film is needed to ensure a good focus and generation of the desired frequency. A mild thickness taper (30% thickness change) was observed across the transducer face. Thickness uniformity within 5% should be obtained with changes in the presentation of the substrate to the sputtering electrode. Issue 3: Refinement of tone-burst electronics should also continue. A low voltage (10 Volts peak-to-peak) prototype was demonstrated, however an order of magnitude improvement is desired to permit adequate penetration in both materials of interest and fluids such as water that are used to couple ultrasound between transducer and part.

Results and Accomplishments

Two experiments were performed; one imaged living cells and the second evaluated acoustic attenuation in water as a function of temperature.

Xenopus oocytes were selected for imaging living cells since the National Institute of Health recognizes them as a reference system, their large size makes them attractive for imaging internal features, and their opaqueness hinders imaging by optical confocal techniques. Images acquired from stage 6 Xenopus oocytes in media at 20°C are illustrated in Figure 1. An amplitude-color bar was placed in the far right-hand side of the images. The top of the bar denoted amplitude saturation while the bottom of the bar denoted no signal and a linear relation between them. The wave passed through the oocyte, reflected off the slide, and passed a second time through the oocyte as it returned to the transducer for Figure 1A. The false color was signal amplitude modulated by an integrated attenuation (scattering and absorption). Signal saturation was set to black to provide a dark background. Red denoted a high but unsaturated signal level (minimal attenuation). Yellow, green, and blue were decreasing values of amplitude (increasing attenuation). Gray was the lowest amplitude values (highest attenuation in a cell). The nucleus was clearly observed, and the animal pole was the circumferential position of the cell membrane closest to the nucleus. The nucleus was less attenuative than other regions within the oocyte. If we employ a simple model and assume that lipids are more attenuative than water, data indicated that the nucleus has a higher concentration of water, as expected. The animal pole also

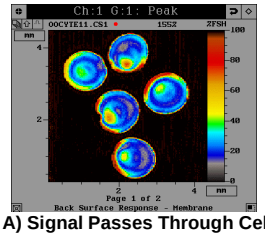

A) Signal Passes Through Cell and is Reflected off a Glass Plate

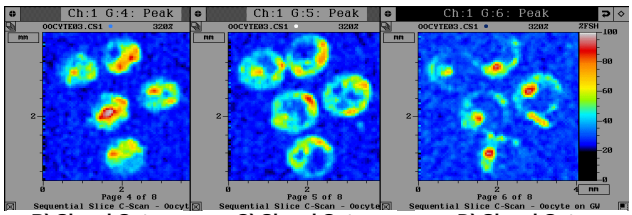

B) Signal Gate Positioned at Top **C) Signal Gate Positioned at Middle** **D) Signal Gate Positioned at Bottom**

Figure 1. Integrated through-transmission image and pulse-echo images at selected depths

was higher amplitude (less attenuation), as evident from the reds and yellows about the periphery.

Because acoustic velocity was relatively constant, a time gate was shifted to successively later values to image features at a constant depth within the oocyte. Four planes were digitized simultaneously. The images of the lower portion of Figure 1 were the top, middle, and bottom of the oocytes. These were digitized by gates 1 through 3 and were placed side-by-side from left to right, respectively. Each gate had a duration that roughly corresponded to one quarter of the oocyte. Note the color-amplitude bar to the far right-hand side. A reflection or backscatter occurred at each localized change in density and stiffness—the greater the change, the higher the signal amplitude. Organelle membranes were expected to be reasonably strong signal sources since cytoplasm existed to either side of a stretched membrane between the two regions. The top and bottom of the nucleus were of high amplitude since the membrane was specular and an efficient reflector of ultrasound. The middle image gives a well-rounded image of the oocyte since it cut through the central axis, and internal features within the nucleus and within the oocyte were observed. Examination of the acoustic signal traversing through the nucleus revealed a complex series of internal responses. We concluded that more work is needed to identify these responses. Gate 4 was set to digitize the surface that the oocytes rested against and was described above (Figure 1A). All four gates were digitized simultaneously from a train of responses with the transducer at one location. The transducer was moved to the next adjacent (x, y) coordinate, and the process was repeated in milliseconds, assigning an amplitude value to each of the four gates. Thus, the picture was painted in as the transducer was moved back and forth along the scanning axis (x-axis) and incremented along the y-axis at each pass. The entire scan took 5 minutes, although it was not optimized for speed. The result was the four images shown. Two false-color relations were assigned, as indicated by amplitude-color bars to the right side of the images, Figure 1A and Figure 1B-1D, respectively. Both were selected to highlight the internal structures of the oocyte.

Acoustic attenuation in water was evaluated as a function of temperature. Amplitude and peak frequency were monitored for a pulse-echo response from a 50-MHz transducer oriented normal to a glass plate that was placed at the focal length, i.e., 13 mm. A heater-chiller permitted a temperature swing from 20°C to 40°C. As temperature increased, a 6 dB increase (factor or 2) was observed in

amplitude and peak frequency changed from 42 MHz to 65 MHz. The attenuation coefficient for water was reported to change from 0.191 to 0.086 dB μm^{-1} GHz^{-2} for water at 25°C and 40°C, respectively (Briggs 1992). This indicates further enhancement might be obtained by increasing water temperature to 60°C.

Finally, greater design progress was achieved toward development of 70-MHz tone-burst electronics.

Summary and Conclusions

Imaging of living cells was demonstrated using Xenopus oocytes in media at 20°C. The images reveal detail of internal structures such as the nucleus and provide insight to water-lipid distribution within the cell. Use of higher frequency (higher resolution) transducers should permit observation of greater detail. One application is real time imaging of living cells during simultaneous application of stress. This could be used in environmental studies to evaluate reaction to and recovery from selected stressors at the cellular level.

Imaging of materials may be improved by employing warm water as the couplant. Decreased attenuation permits passage of higher frequency (higher resolution) responses.

References

Bereiter-Hahn J. 1996. "Probing biological cells and tissues with acoustic microscopy." Chapter 3 in *Advances in Acoustic Microscopy,* Vol. 1, eds. A Briggs and W Arnold, pp. 79-115. Plenum Press, New York.

Briggs A. 1992. *Acoustic Microscopy.* p. 32. Oxford University Press, New York.

Publication

Martin, PM, MS Good, JW Johnston, GJ Posakony, LJ Bond, and SL Crawford. 2000. "Piezoelectric films for 100-MHz ultrasonic transducers." *Thin Solid Films* 379(1-2): 253-258.

Separations and Conversions

Fiber Hydrolysis Capability Development[(a)]

James A. Franz, Todd A. Werpy, Douglas C. Elliott

Study Control Number: PN99070/1398

Vast U.S. resources of low-cost sugars from agricultural-derived products and byproducts are readily available for conversion to chemicals, fuels, and neutraceuticals. In particlar, the fiber byproducts of corn processing that are currently used as livestock feed are a major potential source of sugars, and the fiber-derived oils are also potential sources of important nutraceutical substances, such as cholesterol-reducing sitosterols and tocopherols. Efficient extraction of sugars and neutraceuticals from grain fiber will have significant economic impact to U.S. agriculture and will make available substantial amounts of new feedstock for fuels and chemical production. Developing new approaches to selective sugar and neutraceuticals extraction from fiber requires use of modern approaches in structural chemistry and kinetics. This project applies modern kinetic and spectroscopic methods to develop new sugar and oil separation methods that will enable use of a substantial fraction of corn fiber produced by U.S. agriculture and will result in improved economics for biomass-derived chemicals and fuels.

Project Description

New processing capabilities will be supported by the development of hydrolysis process information for use in the production of value-added products from agricultural-derived feedstocks. The processing capability will be based upon laboratory testing, including chemical mechanisms and chemical analytical procedure development, that was conducted as part of this project.

The project used liquid and solid-state nuclear magnetic resonance spectroscopy and chromatographic methods to determine hydrolysis kinetics of cellulose, hemicellulose, oligermic sugars, and starch with specific feedstock targets of corn fiber and wheat shorts. Further, a method was developed for detecting components in oil fractions of grain fiber hydrolysate products. Procedures for the measurement of tocopherols and related lipid-like components were developed and applied to assess conditions for separation of fiber components.

Introduction

This project examined kinetics of sugar production from corn fiber and related materials. Potential economic benefits to be derived from a detailed understanding of fiber hydrolysis kinetics included

- reduced sugar cost (by as much as 75%) by enabling use of abundant, low-cost biomass feedstocks
- tailored feedstock streams for each application based on 5- and 6-carbon sugars
- reduced overall cost of fermentation and catalysis products.

The identified benefits for DOE include a strong understanding of hydrolysis and an expanded capability in processing biomass-derived feedstocks.

Approach

We previously characterized oligomeric and monosaccharide sugars derived from corn fiber. In that project, sugar production from batch autoclave hydrolysis experiments at a variety of temperatures and acidities was examined. Because of limitations in heating rates and contact times with the batch (as opposed to flow reactor) equipment available, results were basically limited to long exposure times that resulted in substantial conversion to unwanted sugar dehydration products. Nevertheless, the study identified major sugar decomposition products and identified upper limits of conditions for fiber processing. In order to provide realistic processing data, an improved kinetic procedure was needed to develop accurate time profiles for sugar production. Initial scouting studies were carried out on model disaccharide compounds and complete kinetic hydrolysis curves were derived for the model compounds. Several different acids and conditions were tested to evaluate the kinetics.

(a) Project started in FY 1999 as a task under the project entitled, “Sustainable Production of Value Added Chemicals and Products/Fiber Hydrolysis.”

In the current project, improved kinetic methods using rapid-heating micro-cell reactors were introduced with the goal of producing accurate kinetic measurement of hydrolysis rates of sugar precursors. Experiments were carried out in micro-reactors using quantitative ^{13}C nuclear magnetic resonance (NMR). The purpose of using NMR to monitor products was primarily to be able to selectively detect monosaccharides in the presence of aldehydic byproducts that may interfere with sugar quantitation using conventional chromatography. Micro-cell kinetic studies were carried out for a series of oligomeric sugars using NMR and chromatographic methods.

The key goal of fiber hydrolysis was to maximize the rate of acid-catalyzed hydrolysis of starch, hemicellulose, and cellulose with minimum or no ketone byproduct formation. Byproduct ketones such as furfural and 2-hydroxymethylfurfural are produced by acid-catalyzed dehydration of 5- and 6-carbon sugars, if excessive conditions of acidity or temperature are employed. Thus, a series of conditions of varying temperature and acidity were examined using wet-milled corn fiber as well as a series of disaccharide model structures. Near-optimal hydrolysis conditions were applied to wet-milled corn fiber and quantitative rates of sugar formation were determined under conditions inducing no more than trace formation of aldehydic dehydrations products. Analytical procedures for carbohydrate products and for grain fiber oils were refined.

Results and Accomplishments

Optimal conditions for hydrolysis of corn fiber were identified and kinetics of formation of arabinose, xylose, glucose, and galactose were determined. These conditions allow precise sugar extraction to be designed. Under optimal conditions (120°C, 0.2% v/v H_2SO_4), arabinose is most rapidly formed, followed by xylose, glucose, and galactose. Figure 1 shows about 25% conversion of corn fiber by dry weight to monosaccharides, with an additional 25% soluble additional 25% soluble oligosaccharides produced (not shown in Figure 1), corresponding primarily to hemicellulose. Examination by NMR and chromatography confirmed very low production of aldehydic products under the identified conditions.

Kinetics of hydrolysis of disaccharide structures, arabinobiose (Ab), xylobiose (Xb), cellobiose (Cb), and lactose (L) were examined under optimal fiber conversion conditions, as shown in Figure 2 for the hydrolysis of xylobiose to xylose. Pseudo-first-order rate constants

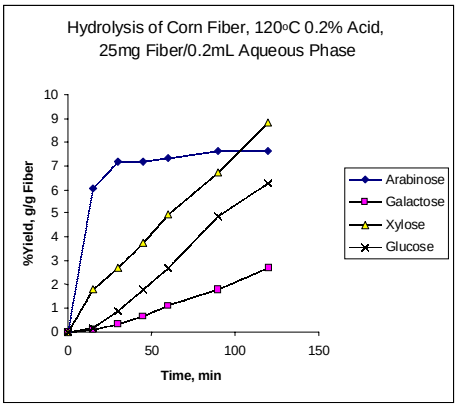

Figure 1. Hydrolysis of wet-milled corn fiber. Hydrolysis of hemicellulose leads to early formation of arabinose.

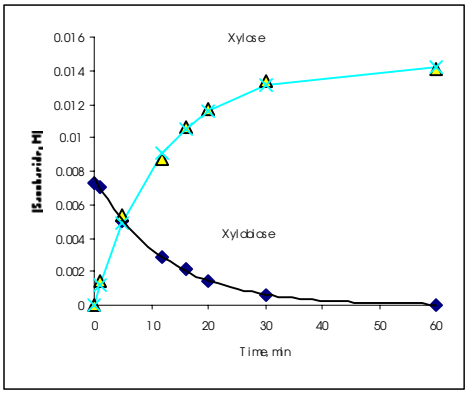

Figure 2. Kinetics of hydrolysis of xylobiose. At 120°C and 0.2%v/v H_2SO_4, xylobiose exhibits clean pseudo-first-order disappearance with a rate constant 0.08 min^{-1}.

were found to be Ab < 0.1 min^{-1}, Xb 0.08 min^{-1}, Cb 0.01 min^{-1}, and L 0.03 min^{-1}. The kinetic methods used here are now available for more exhaustive studies of the response of fibers to selective hydrolysis conditions. A typical ^{13}C NMR spectra of liquid corn fiber hydrolysate is shown in Figure 3. Further work to determine the kinetics of reaction of hemicellulose and xylan and arabinan is in progress.

Finally, conditions for the analytical separation of neutraceutical products (tocopherols, sitosterols) were examined. Collection of ^{13}C NMR data for the subject materials was begun, and chromatographic methods for separation of the neutraceuticals were examined. Procedures for isolation of neutraceuticals include alkaline treatment of the wet-milled corn fiber to dissolve hemicellulose and oils. Neutralization of this fraction followed by ethanol extraction removes neutraceutical-containing oils and yields isolated hemicellulose. Characterization of parent corn fiber and hemicellulose by solid-state ^{13}C NMR was carried out as a function of

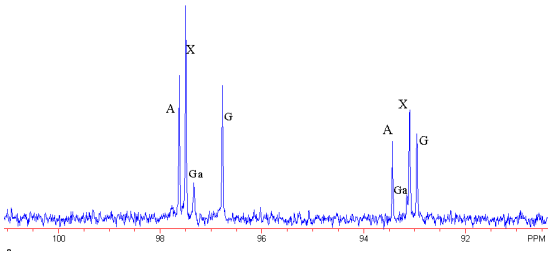

Figure 3. ^{13}C NMR spectrum of corn fiber hydrolysate, showing α- and β-anomeric mixtures of arabinose (A), galactose (Ga), xylose (X), and glucose (G)

magnetic field. The hemicellulose was found to contain no detectable sterol/lipid oil components as expected, but did contain detectable carboxyl groups. The solid-state NMR spectroscopic method is useful for direct analysis of residual protein in the mixtures, and for analysis of residual carbohydrate in the extracted source corn fiber. The results of this study include the successful measurement of fiber hydrolysis rates and byproduct formation, the identification of optimal hydrolysis conditions, and measurement of kinetics of both corn fiber and model disaccharide systems. This capability development provides the starting point for the development of economical sugar and neutraceutical production.

Summary and Conclusions

Kinetics of hydolysis of a series of oligomeric sugars were carried out to optimize reaction conditions for minimal byproduct and maximum monomeric sugar yields. Accurate corn fiber hydrolysis kinetics demonstrated clean sugar production. The relative rate of production of sugars followed the trend arabinose >> xylose >> glucose >> galactose, and the rates of hydrolysis of disaccharides demonstrated the trend arabinobiose >> xylobiose > > cellobiose. Since the homogeneous liquid phase hydrolysis of cellobiose is relatively rapid, the very slow rate of hydrolysis of cellulose reflects the well-known structural inaccessibility of this material. The kinetic methods developed here for disaccharides, and applied to wet milled corn fiber provide support for scale-up design of commercial carbohydrate extraction.

The results of the work serve to define the response of categories of saccharide bonds to hydrolysis. Solid-state NMR spectroscopy was also used to determine the components of corn fiber derived hemicellulose, as well as wet milled corn fiber.

Instrumented Test Loop for Evaluation of In Situ Real-Time Physical and Rheological Properties

Judith A. Bamberger, James A. Fort, Margaret S. Greenwood, Leonard J. Bond, Richard A. Pappas

Study Control Number: PN00059/1466

Many processes, including radioactive waste transfer operations, and several industrial processes, require real-time instrumentation to measure physical, rheological, and constituent properties of slurries and multiphase flows to quantify the state of mixing and solids concentration and particle size distribution, detect solids settling and stratification, and to identify changes in rheology and phase by measuring colloid agglomeration and gelation. Previous experience at the Hanford Site has provided ample evidence of the adverse effects that result from pipeline plugging. To support ultrasonic instrument development and deployment, two flow testing systems, one operating in the laminar flow regime and one operating over a higher flow rate range, were developed. These flow "loops" provide a flexible test system equipped with a suite of unique nonintrusive ultrasonic sensing systems to characterize slurry physical and rheological properties in situ in real time in pipelines and vessels under prototypic operating conditions.

Project Description

The purpose of this project was to increase our capability for evaluating fluid and slurry physical and rheological properties in situ, in real-time over a broad range of simulated Hanford Site and industrial process conditions. These testing systems require only small quantities of fluids, slurries, or suspensions to operate while evaluating fluid properties using ultrasonic instruments that are being developed to characterize physical and rheological properties. The instruments used included sensors to measure flow velocity and rheological profiles, density, viscosity, solids concentration, particle size, speed of sound through the mixture, and the ability to detect interfaces. The loops are co-located with the Food Science and Process Measurement Laboratory to provide access to complementary fluid mixing and characterization equipment. To provide flexibility to evaluate a range of sensors, the loops include penetrations for spool pieces housing the unique instrumentation. This capability permits analysis and evaluation of the physical and rheological properties of fluids, slurries, and colloidal suspensions under flowing conditions that are similar to those obtained during transport during production. The lamina flow loop and equipment were successfully used to evaluate instrument capability to characterize thick paste-like slurries and viscous fluids. They can also operate using simulants to model radioactive waste slurries and typical intermediate process stages encountered during food production.

Introduction

Many industrial processes in the oil and gas, chemical, food, forest product, and mineral processing industries could benefit from real-time quantification of physical, rheological, and constituent properties. This need is also prevalent at the DOE Hanford Site and other DOE sites where radioactive waste transport characterization needs include quantifying the state of mixing, solids concentration and particle size distribution, detection of settling and stratification, and identifying changes in rheology and phase through colloid agglomeration and gelation. Previous experience at the Hanford Site has provided ample evidence of the adverse effects that result from pipeline plugging. In general, two groups of particulate commonly exist within the Hanford tanks as well as in the petrochemical industries. These are insoluble solids that are subject to settling, saltation and bed formation, and soluble species that in addition to settling, could lead to precipitation on the walls (scaling or fouling) and bulk precipitation which could form plugs due to compaction. The pulp and paper industry faces challenges similar to those at Hanford. Pulp fibers tend to flocculate into clumps as they are processed in the headbox. These clumps deposit on the wire used to form the paper sheet resulting in poor paper formation. The pulp and paper industry also implements dilution to reduce flocculation. Our Laboratory developed ultrasonic sensors that can be used to nonintrusively characterize physical and rheological properties of these processes. Several large flow loops at our Laboratory require significant (190 to 568 L [50 to 150 gal]) quantities of simulant. To support rapid evaluation of sensor applicability to support DOE and Hanford Site characterization needs, a reduced-volume system was developed to evaluate the feasibility of ultrasonic characterization of the physical and rheological properties of unique process streams.

Approach

Two flow loops, one that operates in the laminar flow regime, and one that operates over a higher flow rate range, were developed to provide a flexible system for sensor evaluation. The laminar flow loop, shown in Figure 1 was designed especially for evaluating applications for ultrasonic doppler velocimetry and pressure drop, a technique to provide rheological profiles across the pipe. Based on conservation of linear momentum for steady pressure-driven flow, the pressure drop in the pipe provides the local shear rate distribution.

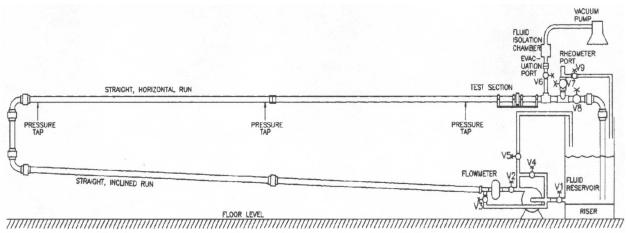

Figure 1. Laminar flow loop instrumented with an ultrasonic doppler velocimetry sensing system for in-line velocity and viscosity profile measurements

Evaluating the shear rate and the shear stress at points along the pipe yields the shear stress shear rate relation, which is equivalent to the shear viscosity shear rate relationship. This information and attenuation profiles can provide both rheological and concentration profiles of the fluid flowing in the 5-cm- (2-in.-) diameter loop. A Moyno pump provides flow rates of up to 40 L/min. The flow rate range and piping configuration were designed to provide fully developed laminar pipe flow and pressure drop measurements (the theory and operation of the sensing system are described in Powell et al. [2000]). Laminar flow loop support instrumentation includes measurement of temperature, flow rate, and pressure drop.

The second loop, shown in Figure 2, is powered by a centrifugal pump that provides a flow rate from 114 to 568 L/min (30 to 150 gal/min). This flexible configuration includes two pipelines, a 2.5-cm- (1-in.-) diameter and 5-cm- (2-in.-) diameter. These lines can be operated either singly or in parallel. The lines include penetrations to permit integration of spool pieces housing several existing ultrasonic sensors, shown in Figure 3. These ultrasonic densimeters measure the density at the sensor-fluid interface based on the amount of reflected ultrasonic signal (Greenwood et al. 1999). In addition to density, by making measurements at multiple orientations, the sensors can be used to characterize sedimentation, the presence of bubble layers, and detect density gradients.

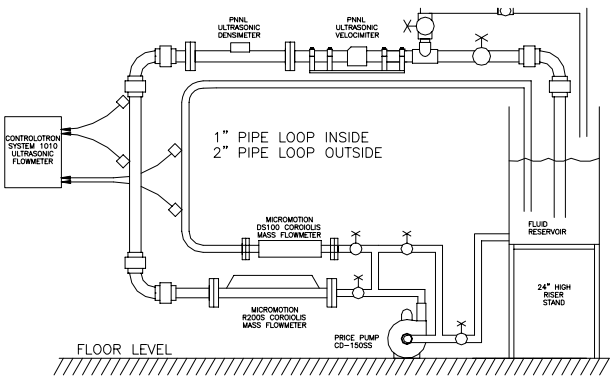

Figure 2. Variable-flow rate, low-volume flow loop for slurry process evaluation using multiple ultrasonic sensing systems

Figure 3. a) Prototype ultrasonic densimeter spool piece, b) Ultrasonic densimeter spool piece for deployment at Hanford to support radioactive waste transfers

Instrumentation in each line to support loop operation includes temperature measurement; Micromotion coriolus mass flow meters to measure mass flow rate, density, and temperature; and Controlotron clamp on ultrasonic flow meters to measure volumetric flow and velocity. The process sensors are integrated into a data acquisition computer.

In addition to fluid evaluation during pipeline transport, sensors such as the immersion densimeter (shown in Figure 4a) and the concentration and particle sizing sensor (shown in Figure 4b) can be installed into the fluid

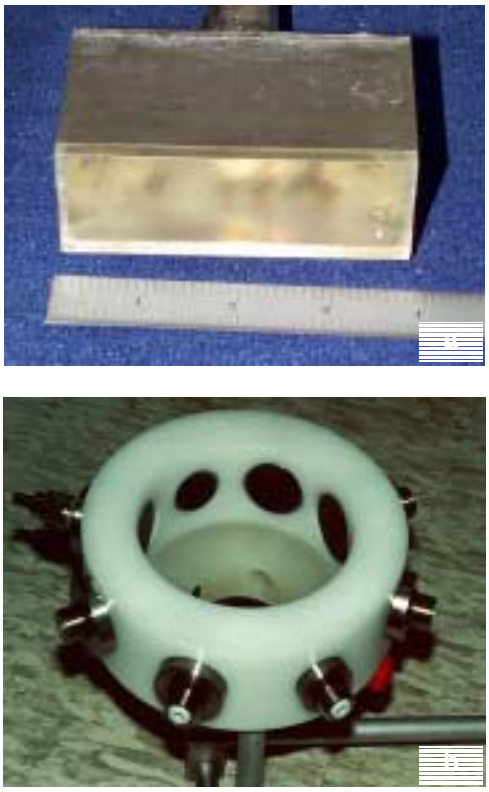

Figure 4. a) Immersion ultrasonic densimeter for characterization of density and stratification in vessels, b) Prototype ultrasonic signal attenuation sensor for characterization of slurry concentration, particle size distribution, sedimentation, stratification, and resuspension in vessels

accumulation tanks to make measurements under batch mixing or settling operations. The particle sizing and concentration sensor uses ultrasonic signal attenuation and speed of sound in the fluid to characterize the particulate phase in the slurry (Bamberger et al. 1998). By making measurements at multiple levels, sedimentation, settling, and resuspension as well as particle size distribution and concentration can be characterized in real time.

Results and Accomplishments

Two flow loops, one that operates in the laminar flow regime and one that operates over a higher flow rate range, were developed to provide a flexible test system for evaluation of fluid and slurry properties under prototypic operating conditions using a suite of nonintrusive ultrasonic sensing systems to characterize slurry physical and rheological properties in situ in real time.

The integrated instrumentation, when deployed with a suitable suite of transducers will be applicable to both vessel and pipeline applications. Vessel applications include characterization, mixing, blending, settling, and separations. Pipeline applications include transport and detection of conditions that could cause fouling or plugging.

An expected focus of future research will be to characterize radioactive waste simulants and colloidal systems that can be subject to flocculation, initiation of gelation and phase change associated with pipe plugging as well as slurry settling, resuspension, and state of mixing.

References

Bamberger, JA, MS Greenwood, and HK Kytomaa. 1998. *"Ultrasonic characterization of slurry density and particle size."* FEDSM98-5075, *In proceeding of the American Society of Mechanical Engineers,* New York.

Greenwood, MS, JR Skorpik, JA Bamberger, and RV Harris. 1999. "On-line ultrasonic density sensor for process control of liquids and slurries." *Ultrasonics 37:*159-171.

Powell, RL, Y Uludag, MJ McCarthy, JA Fort, DM Pfund, DM Sheen. 2000. "Development of devices for in-line viscosity measurements of wastes." PNNL-SA-32644, Pacific Northwest National Laboratory, Richland, Washington.

Publications and Presentations

Bamberger JA and MS Greenwood. 2000. "Measuring slurry density and viscosity in-situ in real time during pipeline transport using an ultrasonic sensor." FEDSM00-11121, *Proceedings of the ASME 2000 Fluids Engineering Division Summer Meeting,* June 11-15, 2000, Boston, Massachusetts. American Society of Mechanical Engineers, New York. PNNL-SA-32925, Pacific Northwest National Laboratory, Richland, Washington.

Powell RL, Y Uludag, MJ McCarthy, JA Fort, DM Pfund, and DM Sheen. 2000. "Development of devices for in-line viscosity measurements of wastes." *Waste Management* '00, February 27-March 2, 2000, Tucson, Arizona.

Microchannel Distillation

Ward E. TeGrotenhuis, V. Susie Stenkamp

Study Control Number: PN00065/1472

The Department of Energy has established goals for the chemical industry to reduce by 30% material use, energy consumption, water consumption, toxic dispersion, and pollution dispersion. Advances in distillation technology are critical for achieving these goals, because distillation is the most often used technology for separations in the chemical process industry. Microchannel distillation may substantially reduce the size of equipment and improve energy efficiency.

Project Description

The objective of this project was to evaluate the feasibility of microchannel distillation devices using proof-of-concept testing and predictive modeling. These devices have the potential to significantly reduce the energy and the size of equipment needed to produce a wide array of chemicals and fuel. A test device was built and charged with a mixture of acetone and methanol and operated in total reflux mode. The temperature profile along the length of the heat pipe and the operating pressure were measured and used to determine composition profiles at different heat inputs. Vapor and liquid equilibrium curves were subsequently used to calculate the number of theoretical stages and the height equivalent of a theoretical plate. Results indicate a substantial reduction in the height equivalent of a theoretical plate over commercially available advanced structured packings. Progress was also made in developing a predictive model and initial designs were developed for incorporating the concepts into high interfacial area, multi-channel microchannel devices.

Introduction

For several years, Pacific Northwest National Laboratory has been developing microchemical and thermal systems that are compact and efficient in comparison to conventional process technology.

The typical order of magnitude or more reduction in hardware volume and mass over conventional technology is achieved through rapid heat and mass transfer rates that can be accomplished in microchannel devices. The potential for reduced capital and operating costs over conventional distillation technologies due to reduction in equipment size and improved thermal efficiency would have a dramatic impact on the petrochemical industry.

The key aspects for demonstrating microchannel distillation capability are to achieve high mass transfer efficiency between counter-flowing gas and liquid streams while providing means for condensation and reboiling.

Results and Accomplishments

Distillation was successfully demonstrated within the heat pipe configurations that were built and tested, thereby establishing the capability for microchannel distillation. Axial temperature profiles are shown in Figure 1 for a range of heat inputs. The starting composition was 5 mol% acetone in a mixture of acetone and methanol and the device was operated in total reflux mode. Assuming constant pressure along the length of the device and assuming the gas and liquid are at equilibrium at the measured temperatures, composition profiles are constructed from the vapor-liquid equilibrium curve. Composition profiles are shown in Figure 2 for the temperature profiles shown in Figure 1. Finally, the degree of separation, as determined from the composition profile, is used to calculate the number of theoretical stages that when divided into the length gives the height equivalence of a theoretical plate. Figure 3 gives the number of theoretical stages and the height equivalence as a function of heat input.

The results indicate there exists optimal heat input where the maximum separation of components is achieved. Values achieved for height equivalence within the devices tested as represented by Figure 3 are 4 to 10 times smaller than commercially available advanced structured packed columns (Humphrey and Keller 1997) shown in Table 1.

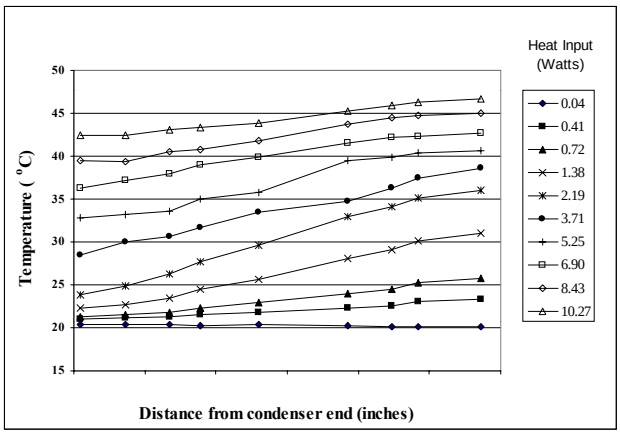

Figure 1. Temperature profiles at varying heat input for starting composition of 5-mole percent acetone in a 2-component mixture of acetone and methanol

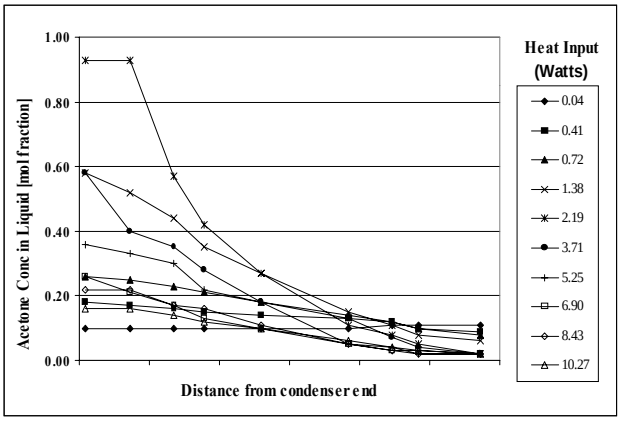

Figure 2. Composition profiles at varying heat input for starting composition of 5-mole percent acetone in a 2-component mixture of acetone and methanol

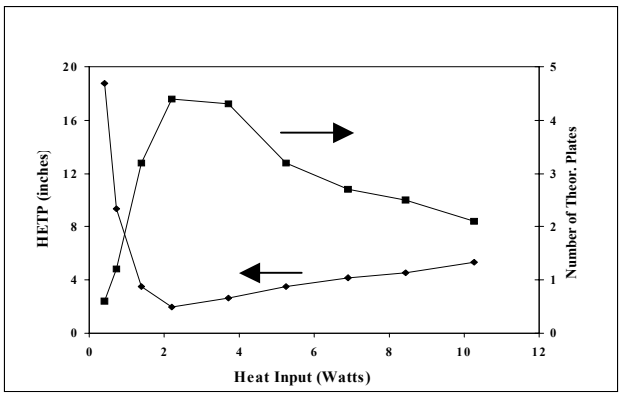

Figure 3. Height equivalence of a theoretical plate and number of theoretical plates as a function of heat input in the separation of acetone and methanol

Table 1. Height equivalence of a theoretical plate for advanced structure packings based on n-heptane/ cyclohexane separation

Packing	HETP, in.
Flexipac 2 (Koch)	12-16
Gempak 2AT (Glitsch)	16-20
Gempak 2A (Glitsch)	12-16
Sulzer BX (Koch)	8-12
Flexeramic 48 (ceramic)[(a)]	10-15

(a) Based on chemical system of ammonia/air/water

The other measure of the potential for microchannel concepts to reduce hardware size is comparisons of the flow capacity per unit cross-sectional area. Because this metric has not been fully explored, the interfacial surface area to equipment volume, a related metric for capacity, is used for comparison. Commercial advanced structured packings achieve interfacial areas from 50 to 160 ft^2/ft^3. Devices designed, built, and tested under this project also ranged from 60 to 160 ft^2/ft^3. Designs for multi-channel microchannel devices that employ the concepts developed here are projected to achieve interfacial areas exceeding 500 ft^2/ft^3.

Summary and Conclusions

Concepts for microchannel distillation where mass transfer occurs between counter-flowing gas and liquid streams have been demonstrated. Height equivalence values achieved were 4 to 6 times smaller than commercial advanced structured packings with similar interfacial contact area per unit hardware volume. This was demonstrated in total reflux mode. Initial designs of multi-channel microchannel devices are predicted to achieve 3 to 10 times higher interfacial contact areas. The combination of reduced height equivalence and increased interfacial area per unit hardware volume is expected to result in microchannel distillation technology that is at least an order of magnitude more compact than existing technologies.

Future directions include demonstration of the concepts with flow through—adding a feed and producing two product streams, detailed design and construction of a multi-channel device, incorporation of integral heat exchange for high energy efficiency, and reactive distillation.

Reference

Humphrey JL and GE Keller II. 1997. *Separation Process Technology*, McGraw-Hill, San Francisco.

Modification of Ion Exchange Resins for Removal of Soluble Sulfate from Hanford Tank Wastes

Shas V. Mattigod, Jun Liu

Study Control Number: PN00069/1476

There is a need for an effective technology for removing sulfate from Hanford tank wastes. This is a crucial process because vitrification has been chosen as the technology for immobilizing tank wastes in the form of low activity waste glass, and it has been recognized that high sulfate levels are detrimental to the vitrification process. Commercially available ion exchange resins are unable to effectively remove this sulfate and therefore separation systems are needed.

Project Description

The goal of this project was to develop modified ion exchange resins to remove sulfate from Hanford tank wastes. We modified six different types of commercial ion exchange resins and tested their efficiencies for removing sulfate from a simulated envelope C (containing very high sulfate concentrations) Hanford tank waste. The results from these tests showed that sulfate removal goals for envelope C wastes can be achieved using our modified resin technology.

Introduction

The privatization contractor for treatment of Hanford wastes has chosen vitrification as the treatment technology for making low activity waste glass. Their melter design focuses on low temperature glass compositions, which retain only very low levels of sulfate. Therefore, there is a crucial need for a technology to pretreat and effectively remove high concentrations of sulfate from the Hanford tank wastes. Many Hanford waste tanks contain high levels of sulfate in a matrix of a very complex mixture of chemicals that renders conventional ion exchange technologies practically useless. Typically, the tank wastes have very high salt concentrations, high pH, very high competing anion concentrations (nitrate, phosphate, etc.) and radiolytic conditions generated by radionuclides. Commercial ion exchange resins do not have the required selectivity for removing sulfate from such a matrix in the presence of other competing anions. Precipitation of sulfate has been proposed as a pretreatment step, but it is difficult to implement, because of stringent solid/liquid separation requirements. Specially designed resins that use ion-pair interactions are very expensive and the effectiveness of these resins has yet to be demonstrated. The goal of our project was to develop and refine an effective sulfate removal technology that could be deployed to pretreat the Hanford tank wastes.

Approach

The approach was to modify cation exchange resins to increase their affinity for sulfate ions. There are several advantages to this approach: 1) the process uses commercial resins and raw materials making the cost of sulfate treatment very low; 2) the commercial resins are available in appropriate engineered form and can be readily deployed in column operation; 3) the modified resin is stable and effective in removing sulfate from high pH solutions that are typical of tank wastes; and 4) the treatment process is very effective. Batch studies were conducted to evaluate the effectiveness of a number of modified exchange resins (Table 1) in removing SO_4 from AN-107 waste simulants (Table 2).

Table 1. Ion exchange resins modified for sulfate removal

Resin	Matrix/Functional Group	Exch Capacity (meq/mL)
AG 50W-12	Styrene divinylbenzene/sulfonate	2.1
AG 50W-8	Styrene divinylbenzene/sulfonate	1.7
Biorex 70	Acrylic/carboxylic	2.4
IRC 86	Polyacrylic copolymer/carboxylic	4.1
IMAC HP 333	Polyacrylic copolymer/carboxylic	3.8
CNP 80 WS	Acrylic/carboxylic	4.3

Table 2. AN-107 waste tank simulants used in batch experiments

Component	15% Res. CO_3 Simulant (mM)	0% Res. CO_3 Simulant (mM)
Na_2SO_4	45	45
Na_2CO_3	100	0
$NaNO_3$	3160	3160
$NaNO_2$	960	960
NaOH	800	800

Results and Accomplishments

The data indicated that modified resins differed in their capacity to remove sulfate from AN-107 tank simulants (Figures 1 and 2). The results showed that all the modified resins were capable of removing sulfate from the waste tank simulants; however, three of the modified resins performed better than the others. Tests showed that better performing modified resins could be used to process a larger number of bed volumes of waste solutions to meet the 73 to 85% sulfate removal goal for envelope C type Hanford tank wastes. The data also showed that decreasing carbonate concentration engendered more effective sulfate removal and that the sulfate removal efficiency of these modified resins were unrelated to their exchange capacities.

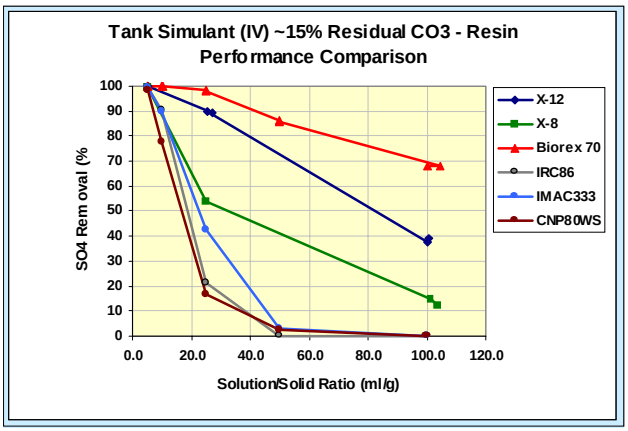

Figure 1. Performance comparison of modified resins for sulfate removal from tank simulant with 15% residual carbonate

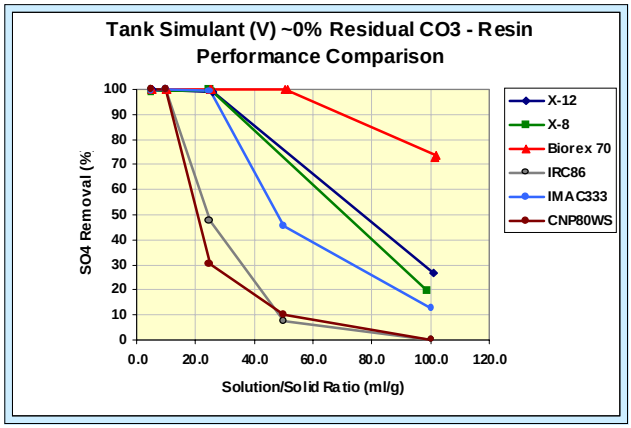

Figure 2. Performance comparison of modified resins for sulfate removal from tank simulant with 0% residual carbonate

Summary and Conclusions

Modified resins are effective for removing sulfate from high pH solutions that are typical of Hanford envelope C tank wastes.

Modified resin technology can be used to reach 73 to 85% sulfate removal goal for AN-107 (envelope C) waste. There were no increases in treated waste volume. The sulfate removed by the modified resins could be easily separated from the resin matrix indicating potential ease of resin regeneration.

Permanganate Treatment for the Decontamination of Radioactive Contaminated Wastes

Richard T. Hallen, Michael A. Lilga, Amber M. Gauger

Study Control Number: PN00073/1480

The Department of Energy has radioactive waste and contaminated equipment and facilities that must be treated as part of the nuclear defense legacy cleanup. High-level radioactive wastes, such as those stored at Hanford, Idaho, Oak Ridge, and Savannah River, present one of the major challenges because of the complex mixture of chemicals that have been used and disposed of to storage tanks. Fundamental unit operations such as solid/liquid separations are a challenge for processing radioactive wastes stored at Hanford. Pretreatment will likely be required for many of the wastes prior to solidification and final disposal.

Project Description

High-level wastes stored at Hanford and other DOE sites contain a large variety of organic compounds. At Hanford, the majority of the organic compounds disposed of to the tanks include glycolate, citrate, EDTA, HEDTA, and a few other organic complexants. These original compounds have degraded over time to lower molecular weight organics such as formate, oxalate, acetate, and various amine-containing compounds. The complexant concentrate wastes contain the highest concentration of organic compounds and present additional challenges to treatment and disposal. The organic complexants increase the solubility of radioactive strontium and transuranic wastes, and prevent the treatment by more conventional separation processes. Permanganate, a chemical oxidant, can destroy organic compounds which complex radioactive ions, allowing them to precipitate from solution. Permanganate reduction in solution under basic conditions results in formation of dense, manganese dioxide solids which co-precipitate/flocculate transuranics and act as an aid to solid/liquid separations. Adding manganese dioxide as a solid does not provide the benefits of permanganate addition. So the permanganate reduction chemistry and in situ solids formation are very important.

The potential use of permanganate to decontaminate tank waste was first demonstrated by Orth et al. (1995). Actual waste from tank SY-101 was treated with permanganate, and decontamination factors for strontium were greater than 140 and for plutonium were 12 to 140. More conventional treatment schemes did not work because this waste contained significant concentrations of organic complexants. Permanganate was found to be a selective oxidant, solubilizing chromium first, then reducing the total organic carbon concentration, and lastly, nitrite oxidation to nitrate. However, permanganate was never seriously considered for pretreatment of tank wastes because it had been used in quite high concentration (>0.1M) and increased the volume of high activity glass produced.

Results and Accomplishments

The reaction of permanganate with various organic compounds, formate, oxalate, glycolate, and glycine, was studied under basic conditions. Formate and oxalate are the major aging products from the complexants and are present in relatively high concentrations in tank wastes. Glycolate was added to the tanks and is also similar to citrate in structure. Glycine was studied as a model compound for the amine-based complexants, EDTA and HEDTA, as well as the aging products from these compounds. Reactions were conducted at various concentrations of permanganate (oxidant) and organic (reductant). Permanganate reaction with nitrite was also studied at one concentration for comparison to the reactions of the organic compounds.

Upon reaction with a reductant, permanganate undergoes a series of reactions and oxidation changes from Mn(VII) to Mn(VI), Mn(V), and Mn(IV) which precipitates in hydroxide solution. Permanganate, Mn(VII), and manganate, Mn(VI), are highly colored allowing the use of UV-VIS spectroscopy to monitor the reduction chemistry of manganese. Mn(VII) is characterized by strong absorption at 546, 526, and 311 nm. Mn(VI) is characterized by strong absorption at 606, 439, 347, and 299 nm. At treatment concentrations of 0.03 to 0.05M permanganate and with an excess of reductant such as formate, complete reduction of Mn(VII), purple solution, to Mn(IV), clear solution and dark brown/black solids, occurs in less than 5 minutes. The characteristic green color of Mn(VI) is observed for a few minutes while the reaction is occurring. Conducting the experiments at lower concentrations of permanganate and stiochiometric or lower levels of reductant, the reactions slow down so

the stepwise reduction can be observed. Figure 1 shows spectra at various times for the reduction of 0.01M Mn(VII) to Mn(VI) with 0.005M formate. The Mn(VI) concentration reaches a maximum around 15 minutes before it begins decreases as it disproportionates to Mn(VII) and Mn(V). The Mn(VII) concentration increases with time as shown in Figure 2 because the formate had been entirely consumed in the initial oxidation. The Mn(V) reacts with Mn(VI) producing more Mn(VII) and Mn(IV) which precipitates from solution.

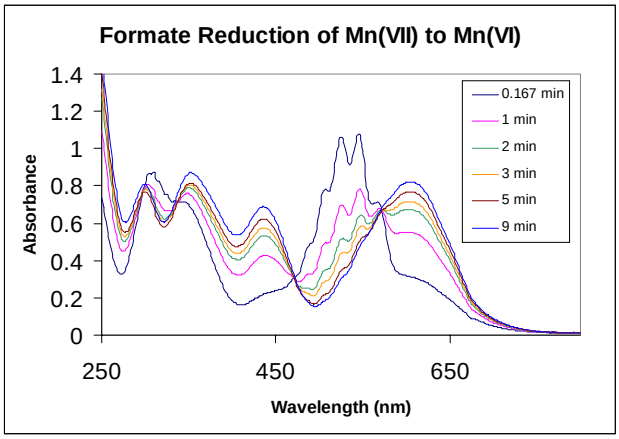

Figure 1. Spectral change on reduction of Mn(VII) to Mn(VI) with formate

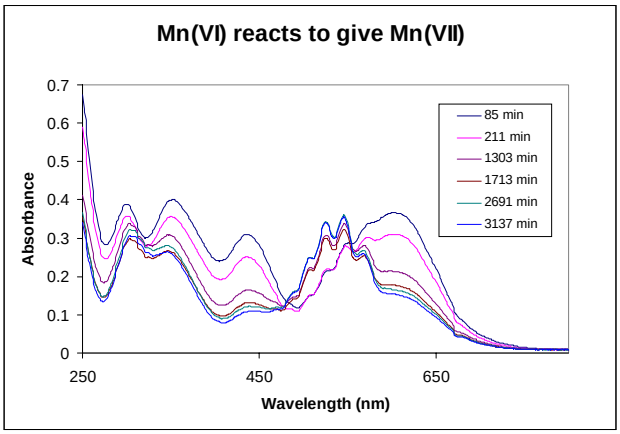

Figure 2. Spectral change as Mn(VI) disproportionates to Mn(VII)

Using extinction coefficients calculated from Mn(VII) and Mn(VI) solutions of known concentrations, concentrations at various reaction times can be determined and used to examine the kinetics of the reactions. The reaction kinetics is very complex, with many concurrent and competing reactions. To compare the rates of reactions of the various reductants, reactions were carried out under the same conditions, and the initial rate of Mn(VII) disappearance was calculated under psuedo-first-order conditions. The analysis revealed that formate reacts 40 times faster than glycolate and glycine, which react at similar rates. Oxalate and nitrite did not react with permanganate under the conditions studied.

Reactions were allowed to go to completion and the final products analyzed. Permanganate oxidation of formate yields carbonate. Both glycolate and glycine yield oxalate on oxidation, and glycine also yields ammonia. The permanganate (Mn(VII) is reduced to Mn(IV) which precipitates from solution. The pH of the solution is higher then the isoelectric point of manganese dioxide, so hydroxide is consumed by deprotanation of the precipitated solids. The dark brown/black solids are dense and settle to the bottom of the reaction vessel, resulting in a clear supernatant solution.

Summary and Conclusions

Permanganate reacts rapidly with organic compounds present in radioactive wastes resulting in a manganese dioxide precipitate that removes radioactive elements from solution. The amount of complexant destruction will be low when significant concentration of formate is present, since formate reacts much faster. Permanganate does not react directly with oxalate or nitrite under typical treatment conditions. A reduction in total organic carbon will be seen for the oxidation of formate to carbonate, but glycolate and glycine oxidation yields oxalate, which would still be included in the total organic carbon analysis.

Sensors for On-Line Technetium-99 Monitoring

Yuehe Lin, Oleg Egorov, Dean Kurath

Study Control Number: PN00080/1487

The portable analyzer developed in this project can be used in process control for nuclear waste processing and for groundwater monitoring.

Project Description

The goal of this project is to develop a novel flow injection/electrochemical sensor system for on-line, on-site monitoring of technetium (Tc) in nuclear waste processing streams and in complex environmental matrices. To reduce the cost, rhenium was used as a nonradioactive surrogate for technetium. Technetium and rhenium have similar electrochemical properties. The electrochemical behavior of rhenium on electrode surfaces was studied as necessary for the sensor development. The parameters affecting the analytical performance of the flow injection/square wave anodic stripping voltammetry were also investigated. Results from this work will provide the proof-of-principle for further construction of an automated and efficient technetium analyzer for on-line, on-site monitoring.

Introduction

Technetium, because of long life and mobility, is one of the major radionuclides of concern found in the nuclear waste storage tanks. Analysis of technetium is usually carried out in central laboratories using inductively coupled plasma-mass spectrometry, radiochemical methods, and inductively coupled plasma-atomic emission spectrometry. However, in view of the huge labor and analytical costs or time delays associated with centralized laboratory analyses, there are immediate needs for developing portable analytical systems for on-site, on-line monitoring. A portable, on-line compatible technetium sensor instrument would be valuable for groundwater monitoring programs and is required for process control during nuclear waste processing.

Electrochemical detection is sensitive, compact, and easily integrated into a small size (Wang 1995; Lin et al. 1999). One advantage of an electrochemical sensor approach is that both Tc (VII) and Tc (IV) can be preconcentrated on the electrode surface by applying a reduction potential and then detected by stripping voltammetry. Speciation information of Tc (VII) and Tc (IV) can be obtained by selecting an appropriate reduction potential. The technique is potentially sensitive enough for both process and environmental monitoring applications. Unlike radiochemical techniques, electrochemical detection does not require a rigorous chemical separation step. In addition, the sample oxidation step, which is required for radiochemical methods, may not be needed with an electrochemical detection approach.

Results and Accomplishments

A portable analytical system based on a simple flow injection/square wave anodic stripping voltammetry concept was developed. Figure 1 shows a schematic diagram of the analytical system. The portable analytical system could be used for on-line Tc monitoring by connecting a sample injection valve with the waste stream through a sampling pump. For initial testing, a standard solution was injected into the flow stream through a manual injection mode. The system consists of a low-flow-rate solution delivery module (syringe pump), a low-dead-volume six-port injection valve (with a 30 μL sample loop), and a miniaturized flow-onto thin-layer electrochemical cell. Square wave voltammetry is used as a rapid and sensitive detection method for flow stripping voltammetry. The microelectrochemical flow cell, which integrates three electrodes, was based on a wall-jet design and was fabricated on polymer substrates. The microelectrochemical flow cell has a wall-jet (flow-onto) configuration similar to that in the BAS (BAS, West Lafayette, Indiana) UniJet cell design. Instead of a stainless steel block in the BAS UniJet radial flow cell design, a polyetherketone block with a groove of small volume (about 5 μL) was used in order to eliminate the potential trace metal contamination due to the corrosion of stainless steel. A laser-cut Teflon gasket was sandwiched between two polyetherketone blocks to form a radial flow cell. The auxiliary electrode was a 1-mm diameter Pt disk and the reference electrode was an Ag/AgCl electrode. The solution flowed onto the glassy carbon working electrode and exited through the groove from the outlet that was positioned directly across the platinum auxiliary electrode.

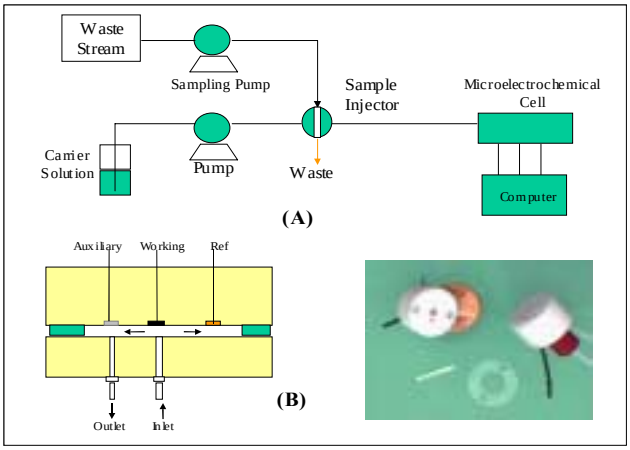

Figure 1. (A) Flow diagram of the flow injection/anodic stripping analysis system. (B) Microelectrochemical cell based on wall-jet design.

In this preliminary study, rhenium was used as a non-radioactive surrogate for technetium. The potential of the working electrode was poised at -1.40 V for a 5-minute deposition period after a 30 µL ReO_4^- sample was injected into the flow stream (0.1M NaAc, 0.1 M NaCl, pH 4.4, flow rate 10 µL/min). Thirty seconds before the deposition had elapsed, the flow stream was stopped to allow the solution to become quiescent. Square wave voltammetry was used for the anodic stripping step.

During the preconcentration step, ReO_4^- was reduced to rhenium oxide(s) and deposited on an electrode surface according to the following process:

$$ReO_4^- + 4\,H^+ + 3\,e^- \rightarrow ReO_2\,(s) + 2\,H_2O$$
$$(1)\quad E_{applied} = 1.40\ V$$

During the anodic stripping step, potential was scanned from -1.40 V to + 0.60 V. A typical anodic stripping voltammogram in 0.1 M, pH 4.4 acetate buffer from a square wave positive potential scan is shown in Figure 2A. There are three stripping waves, the first at -0.25 V (peak 1), the second at -0.05 V (peak 2), and the third at 0.10V (peak 3). Peak 1 corresponds to the stripping wave of copper. Copper was introduced from chemicals as impurity. Our inductively coupled plasma-mass spectrometry analysis results confirmed the presence of copper impurity. Peak 2 is probably due to the formation of a copper-rhenium compound. Therefore, the presence of copper interferes the detection of rhenium. To eliminate the copper interference, a three-step stripping voltammetry procedure was developed:

1. Accumulation step: E = -1.40 V. At this step, Cu^{2+} was reduced to Cu(s) and ReO_4^- was reduced to ReO_2 (s) :

$$Cu^{2+} + 2\,e^- \rightarrow Cu(s)$$
$$ReO_4^- \rightarrow ReO_2(s)$$

2. Stripping out of Cu(s): E= -0.10V, 10 seconds. During this step, Cu(s) was oxidized and removed from the electrode surface, leaving ReO_2 (s) on the electrode surface:

$$Cu\,(s) \rightarrow Cu^{2+} + 2\,e^-$$

3. Stripping analysis of Re:

$$ReO_2\,(s) + 2\,H_2O \rightarrow ReO_4^- + 4\,H^+ + 3\,e^-\ (2)$$

A typical anodic stripping voltammogram obtained from a three-step stripping voltammetry is shown in Figure 2B. As can be seen from Figure 2B, the interference of copper on rhenium analysis was completely eliminated.

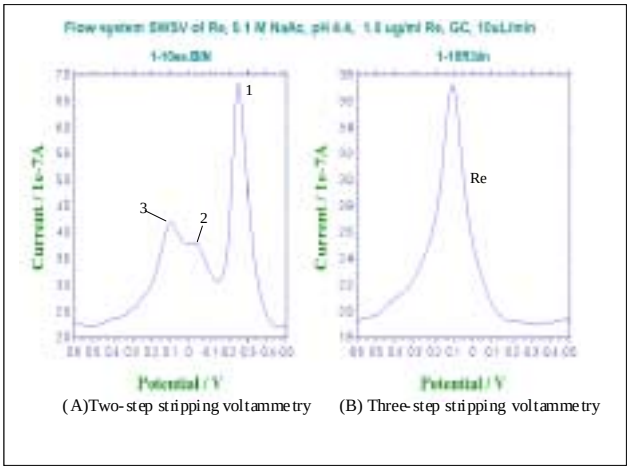

(A)Two-step stripping voltammetry (B) Three-step stripping voltammetry

Figure 2. Stripping voltammograms of 1.0 ppm ReO_4^- in 0.1 M, pH 4.4 acetate buffer

We also examined the parameters affecting the analytical performance of the flow injection/square wave anodic stripping voltammetry. Applied potential during the accumulation step was evaluated from -0.8V to -1.50 V. The results indicate that higher peak current was observed at a more negative potential. The calibration curve for Re has a linear range from 0.10 ppm to 100 ppm with a detection limit of 0.1 ppm. The sample frequency was 8 minutes per sample.

One potential advantage for the combination of flow injection with square wave anodic stripping voltammetry is that the system allows the automatic replacement of the solution matrix for the stripping step. Stripping analysis is sensitive to sample matrix during the stripping measurement step. In a flow system, matrix effect can be

minimized by medium exchange. After the preconcentration step, the complex sample matrix was replaced by a clean electrolyte solution (carrier solution) and the stripping step was conducted in the same electrolyte solution as the standard. This makes the FI/SWASV system suitable for analysis of Tc in complex sample matrices (i.e., nuclear waste).

In the future, the electrochemical detection approach will be compared and combined with the automated radiochemical monitoring technique that is currently being developed at Pacific Northwest National Laboratory.

References

Wang J. 1995. "Electrochemical sensors for environmental monitoring: A review of recent technology." In *Recommendations on the Development of Chemical Sensors and Field Deployable Instrumentation for DOE Needs.* http://www.cmst.org

Yuehe L, R Zhao, KD Thrall, CA Timchalk, WD Bennett, and DW Matson. 1999. "Integration of microfluidics/ electrochemical system for trace metal analysis by stripping voltammetrey." *In Proceedings of SPIE, Microfluidic Devices and Systems,* Vol 3877, pp 248-256.

Thermochemical Methods for Measuring Ligand-Actinide Ion Binding Strength

Gregg J. Lumetta, Richard L. Sell, Bruce K. McNamara

Study Control Number: PN00087/1494

Safe management and disposal of highly radioactive spent fuel is a major problem threatening the future viability of nuclear energy. Chemical processing to separate and remove long-lived radionuclides before disposing of the spent nuclear fuel in geologic repositories would significantly improve the post-closure performance of these repositories. The results of this project expand the tools available for developing highly specific separating agents for actinide ions.

Project Description

Thermochemical methods are being employed to quantitatively determine the binding enthalpy for ML_n complexes, where M is a lanthanide or actinide element and L is a ligand of the type that might form the basis of an extractant (an amide). The key tools employed in this study are differential thermal analysis and thermogravimetric analysis. Complementary spectroscopic measurements are conducted to fully characterize the chemical systems being examined.

Introduction

Actinide separations is an important scientific and technological research area because spent nuclear fuel contains dangerous levels of long-lived radionuclides.

Coordination chemistry forms the basis for the development of efficient metal ion separations, and quantum leaps in efficient separation will hinge on understanding structure-function relationships central to coordination chemistry. This is especially true for the actinide ions. The results of this project expand the tools available for developing highly specific separating agents for actinide ions. The work has focused on applying direct thermochemical methods for measuring the thermodynamics of binding for ligands to actinide and other metal ions.

Approach

In this work, we applied thermochemical methods to quantitatively determine the binding enthalpy for ML_n complexes, where M is a lanthanide or actinide element, and L is a ligand of the type that might form the basis of an extractant (an amide). The enthalpy of the following type of reaction is measured.

$$MX_zL_n \rightarrow MX_z + nL$$

The key tools employed in this study have been differential thermal analysis and thermogravimetric analysis (TGA). Complementary spectroscopic measurements have been be conducted to fully characterize the chemical systems being examined.

Results and Accomplishments

The decomposition of $NdCl_3L$ (L = N,N-dimethylformamide [DMF] or N,N-dimethylacetamide [DMA]) compounds has been investigated by thermogravimetric analysis and differential thermal analysis, coupled with Fourier transform infrared (FTIR) spectroscopy.

When heated in air, the $NdCl_3{\cdot}L$ (L = DMF or DMA) compounds decompose by a mechanism involving the oxidation of the amide ligand. Figure 1 presents the TGA data for the thermal decomposition of $NdCl_3{\cdot}$DMF in air and the species identified by Fourier transform infrared in the off-gas. When $NdCl_3{\cdot}$DMF is heated from 80 to 150°C, TGA indicates a complex series of weight losses. Fourier transform infrared analysis of the off-gas indicates that these mass losses are from the release of water and methanol. Release of DMF becomes evident at ~155°C, although the DMF release is gradual from 155 to 270°C. From 270 to 340°C, a more rapid mass loss occurs. All of the DMF is released by the time the sample is heated to 340°C. Gas evolution becomes more complex during the accelerated mass loss between 270 and 340°C. In addition to DMF, HCl and CO_2 are evident in the off-gas, indicating combustion of DMF.

Similar to $NdCl_3{\cdot}$DMF, water and methanol are released in a complicated series of steps when $NdCl_3{\cdot}$DMA is heated to 165°C in air. DMA is first evident in the off-gas at about 200°C. The DMA loss occurs primarily in two regimes. The first occurs from 270 to 310°C. In this regime, free DMA and a small amount of CO_2 and H_2O are evident in the off-gas. However, as the temperature is

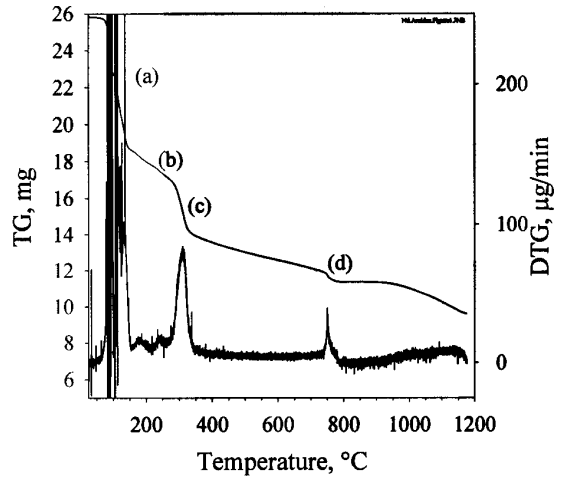

Figure 1. Thermogravimetric analysis of $NdC1_3$·DMF in air. The chemical species identified in the off-gas by FTIR spectroscopy were: (a) H_2O + MeOH, (b) DMF, (c) DMF + HC1 + CO_2, (d) HC1.

increased above 310°C, CO_2 and H_2O become more dominant. Between 340 and 370°C, little free DMA is present in the off-gas, HCl, CO_2, and H_2O are the dominant species evolved. Unlike that observed for $NdCl_3$·DMF, CO_2 continues to evolve as the DMA complex is heated to about 700°C. HCl is also released as the sample is heated to about 700°C. Above 700°C, the CO_2 and HCl release become diminished, and water becomes a dominant feature in the off-gas. HCl becomes evident again at 900°C.

Because of the concurrent combustion of the amides during the decomposition of the $NdCl_3L$ complexes in air, the enthalpy of the amide release cannot be obtained by differential thermal analysis when air is used as the purge gas. However, when nitrogen is used as the purge gas, the amide is cleanly released from $NdCl_3$·DMF. The DMF release can be divided into two regimes (Figure 2a). First, there is a gradual release of 0.4 mole DMF/mole Nd between 160 and 280°C. The differential thermal analysis indicates little enthalpy associated with this initial loss. Second, there is a sharp loss of 0.6 mole DMF/mole Nd between 280 and 320°C. The enthalpy for the latter endothermic DMF release can be determined by differential thermal analysis.

Similarly, DMA is released from $NdCl_3$·DMA in two events when heated under nitrogen (Figure 2b). As was the case with $NdCl_3$·DMF, little enthalpy is associated with the first DMA release (from 260 to 305°C). This release corresponds to 0.3 mole DMA/mole Nd, and this event is accompanied by evolution of a small amount of CO_2. The second amide release between 305 and 340°C (0.7 mole DMA/mole Nd) resembles that seen with $NdCl_3$·DMF; that is, the off-gas indicates predominantly DMA during this endothermic event. Analyzing these endothermic amide releases, the enthalpy of binding can be obtained by differential thermal analysis.

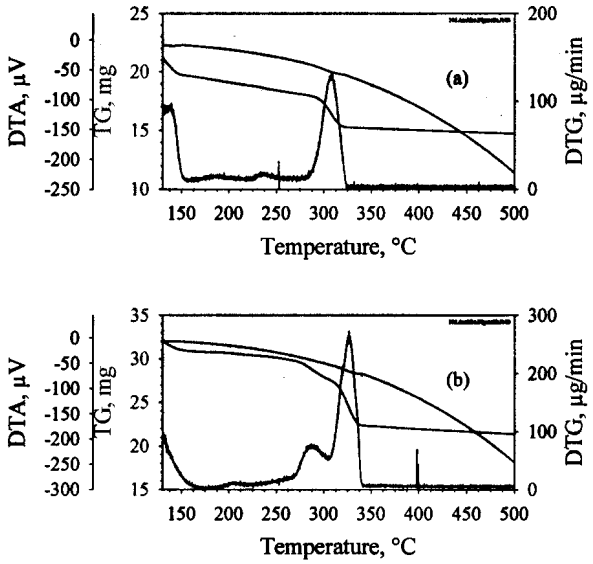

Figure 2. Thermogravimetric analysis of $NdC1_3$·DMF (a) and $NdC1_3$·DMA (b) under nitrogen

Table 1 presents the enthalpy binding data for the $NdCl_2$·L compounds. The values presented are the mean values from triplicate measurements, and the uncertainties are the standard deviation from the mean. The results suggest that DMF binds more strongly to Nd(III) than does DMA. This result is surprising because it is the opposite of what would be expected based on the basicity of the ligands. The gas-phase proton affinities for DMF and DMA are 887.5 kJ/mole and 908.0 kJ/mole, respectively (NIST 2000). Thus, DMA is more basic than DMF, yet the latter amide more strongly binds Nd(III). The reason for the stronger DMF binding compared to DMA might be the steric congestion caused by the additional methyl group in DMA. Steric effects have been observed in the solid-state structures of trivalent lanthanide amide complexes by the increase in the average M-O-C bond angles from 134 degrees for DMF complexes to 152 degrees for DMA complexes (Clement et al. 1998).

Table 1. Binding enthalpies for $NdC1_3L$ compounds

	Reaction Temperature, °C			
L	Start	Center	End	ΔH, kJ/mole[(a)]
DMF	280	307	320	53.1 ± 3.8
DMA	305	325	340	40.9 ± 1.1

(a) Per mole of amide released

A series of $ThCl_4$·L complexes has been prepared. The complexation of the amide to the Th(IV) ion has been confirmed by FTIR spectroscopy. Table 2 lists the positions of the carbonyl bands in the Th complexes, along with those for the free amide ligands.

Table 2. Summary of amide carbonyl stretching frequencies for $ThC1_4L$ compounds

	ν(C+O), cm^{-1}		
	Complex	**Free Amide**	**Δν(C+O), cm^{-1}**
$ThC1_4$(DMF)	1651	1673	22
$ThC1_4$(DMA)	1614	1643	29
$ThC1_4$(MF)	1645	1663	18
$ThC1_4$(TBF)	1654	1668	14
$ThC1_4$(TMP)	1600	1646	46

DMF = N,N-dimethylformamide
DMA = N,N-dimethylacetamide
MF = N-methylformamide
TBF = N-t-butylformamide
TMP = N,N,2-trimethylpropionamide

Summary and Conclusions

The complexes $NdCl_3$·L (L = DMF or DMA) were examined by thermogravimetric analysis/differential thermal analysis techniques and by Fourier transform infrared spectroscopy. The Fourier transform infrared spectra suggest that dehydration of the complexes yields no significant change in the amide-Nd binding. When heated, a portion (from 30 to 40%) of the amide is initially released with little or no associated enthalpy as measured by differential thermal analysis. As the temperature is increased further, the remaining 60 to 70% of the amide is released via an endothermic process. The results suggest that DMF binds more strongly to Nd(III) than does DMA.

This work demonstrated the potential application of TGA/differential thermal analysis to determine the binding enthalpy of neutral ligands to f-block actinide elements.

References

Clement O, BM Rapko, and BP Hay. 1998. *Coord. Chem. Reviews* 170, 203.

U.S. Department of Commerce. 2000. *NIST Chemistry WebBook, NIST Standard Reference Database Number 69 - February 2000 Release.* http://webbook.nist.gov/chemistry/, U.S. Department of Commerce, Washington, D.C.

Publication

Lumetta GJ, RL Sell, and BK McNamara. "Thermal decomposition of neodymium amide complexes," *Journal of Coordination Chemistry* (submitted).

Validation and Scale-Up of Monosaccharide Production from Grain Fiber

Andrew J. Schmidt, Rick J. Orth

Study Control Number: PN00092/1499

Renewable feedstocks, such as grain fiber, are a potential source for end products that would otherwise be produced from fossil fuels. A key to using these renewable feedstocks is to economically break down the carbohydrate fractions to soluble monosaccharides for further processing to the value-added chemicals. This project investigated various pathways, methods, and operating conditions of using acid and enzyme hydrolysis to produce the monosaccharides from grain fiber, in this case, corn fiber.

Project Description

The purpose of this project was to evaluate processing options and operating conditions for breaking down the carbohydrate fractions present in corn fiber to soluble monosaccharides. This project also developed an apparatus for continuous processing at a future date. Acid and enzyme hydrolysis processes were investigated with the main focus being on the breakdown of the hemicellulose fraction in corn fiber to 5-carbon monosaccharides (e.g., xylose and arabinose). Acid hydrolysis conditions were identified where a significant fraction of the corn fiber was solubilized, resulting in the formation of soluble monosaccharides and oligosaccharides. This acid hydrolysis work was conducted in close collaboration with another LDRD project ("Kinetics of Formation of Monosaccharides for Grain Fiber and Related Constituents," James A. Franz, principal investigator). In addition, a variety of commercially available enzymes was evaluated. Some of the enzymes evaluated showed promise for breaking down the hemicellulose fraction to monosaccharides. The results from this project have provided valuable information and capabilities that can be used to develop and evaluate flowsheets using acid hydrolysis, enzyme hydrolysis, or a combination for breaking down hemicellulose in corn fiber to monosaccharides.

Introduction

The United States annually produces 13.9 billion pounds of corn fiber from corn wet milling. This fiber is mixed with protein to create a 21% protein feed for livestock, and is sold primarily in Europe. However, the low value of this byproduct and a recent boycott of genetically modified food products in Europe creates a need to generate a higher market value for corn fiber.

Hemicellulose, one of the major components of corn fiber (Figure 1) is primarily composed of polymeric 5-carbon sugars (e.g., arabinose and xylose). These monosaccharides can be used as feedstocks for downstream processing via catalytic processing to produce chemicals such as polyols (e.g., ethylene glycol, propylene glycol or glycerol), or via fermentation to produce ethanol. To successfully use the hemicellulosic fraction of corn fiber, the monosaccharides must be recovered economically and without the production of degradation products, such as furfurals, that can be detrimental to downstream processing.

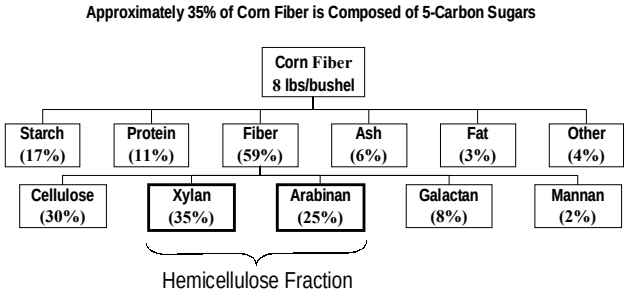

Figure 1. Major components in corn fiber

Acid and enzyme hydrolysis processes were investigated during this project to evaluate hydrolysis conditions for breaking down the hemicellulosic fraction to soluble monosaccharides. The yield of xylose, arabinose, oligomers, and detection of detrimental breakdown products were tracked during the testing. In addition, the filterability and pumpability of the slurries were noted for processing considerations.

Results and Accomplishments

A literature review was conducted at the beginning of the project to evaluate earlier work on corn fiber hydrolysis. Many approaches used complete hydrolysis followed by extensive downstream separations and purification of the 5-carbon and 6-carbon sugars. In most of the past work, the goal was to recover all or nearly all of the

carbohydrate value from the corn fiber, including the glucose from hydrolysis of the cellulose fraction. In this project, selective hydrolysis was evaluated to recover monosaccharides from the hemicellulosic component.

Development of Novel and Simple Processing Strategies

Based in part on the literature and on testing both under this project and under a separate LDRD project led by James Franz, three hydrolysis processing strategies were developed, and portions of the processing strategies were further tested (see Figure 2).

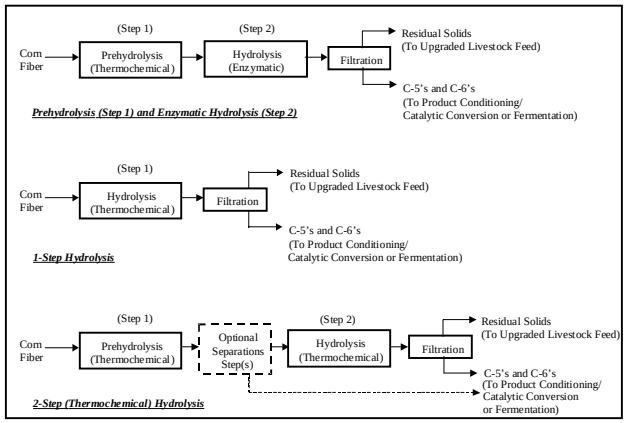

Figure 2. Hydrolysis processing strategies

The first approach included both acid and enzyme hydrolysis. The fiber was first subjected to selective acid hydrolysis to solubilize the hemicellulosic fraction of the corn fiber. Next, enzymes were added to further break down the solubilized hemicellulosic fraction to the monomers. (An alternative to this flowsheet is to conduct two acid hydrolysis steps, the first to solubilize the hemicellulosic fraction, with a filtration to remove the solids, and the second hydrolysis to convert the oligosaccharides in solution to monosaccharides. With this approach, however, the conditions of the second hydrolysis were needed to control and prevent the formation of degradation products.)

The second approach involved a one-step acid hydrolysis at selected conditions. This approach was simpler than the first; however, if the conditions were not right, total conversion to the monosaccharides did not occur, or degradation products could form.

The third approach used a two-step thermochemical method. In the first step, the hemicellulose component was solubilized, and an optional polishing step was employed to remove the monosaccharides (e.g., ultrafiltration), then the slurry was subjected to further hydrolysis to break down the oligosaccharides to the monomers. By removing the monosaccharides after the first hydrolysis, the formation of degradation products was minimized, while monosaccharide production is maximized.

Acid Hydrolysis Testing

During evaluation of some of the acid hydrolysis conditions, significant solubilization was observed without the formation of degradation products. This testing was conducted at the micro-scale and bench-scale. The bench-scale results illustrated in Figure 3 were obtained by operation at elevated temperatures without acid addition. Even without acid addition, approximately 25% solubilization took place, with the solubilized fraction mainly consisting of oligomers. At higher temperatures, significantly more solubilization took place, but degradation products also formed. The micro-scale testing (Figure 3) was conducted under selective hydrolysis conditions with the addition of acid. Approximately 50% solubilization took place, and no degradation products (e.g., furfural) were detected. Approximately half of the solubilized fraction was monosaccharides, and the remainder was oligosaccharides.

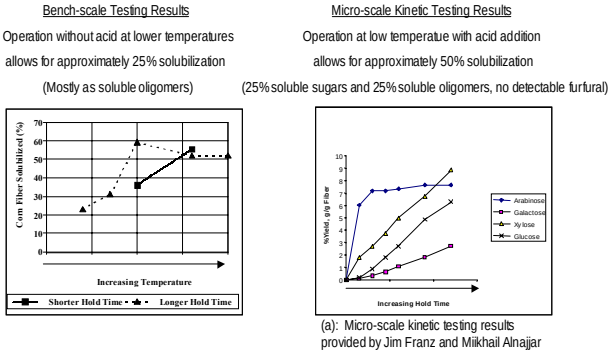

Figure 3. Acid/thermochemical hydrolysis of corn fiber

Enzyme Hydrolysis Testing

Enzyme hydrolysis testing was conducted, using several commercially available enzymes. These enzymes are relatively inexpensive and readily available. As can be seen in Figure 4, three of the enzymes tested showed promise for converting hemicellulose to the monomer sugars (xylose and arabinose). In these tests, the corn fiber itself was treated with the enzymes. If the corn fiber were first treated via selective thermochemical (with or

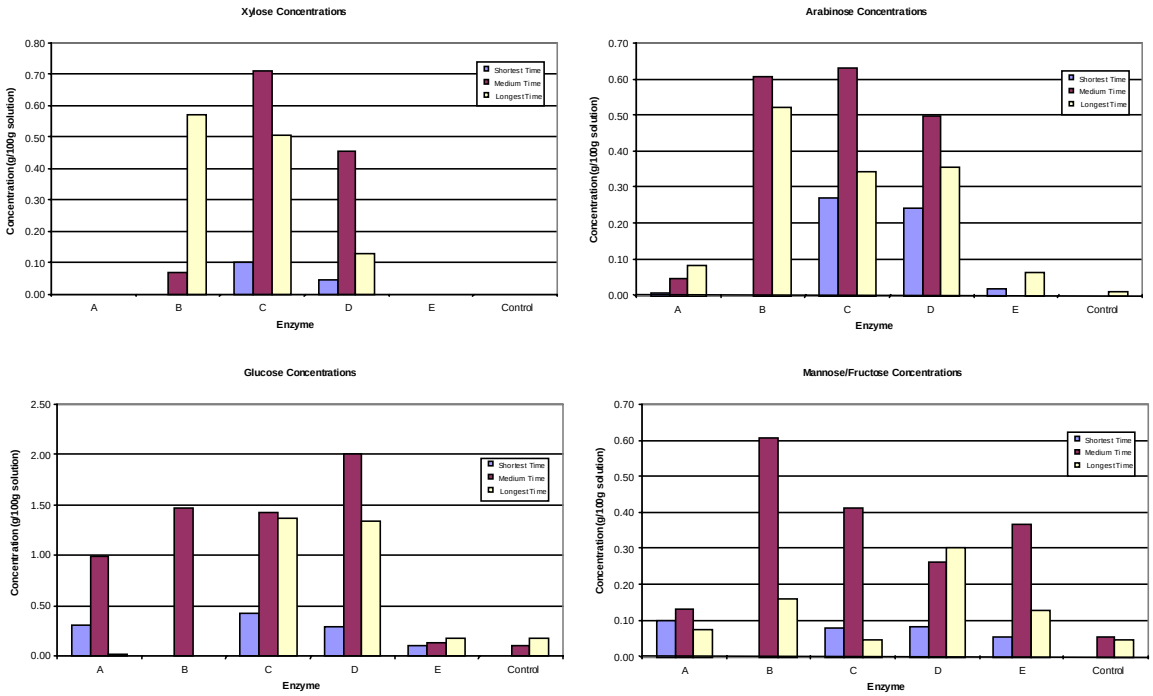

Figure 4. Enzyme hydrolysis of corn fiber

without acid) hydrolysis (i.e., as in Figure 3), and the hydrolysate were subjected to enzymatic treatment, the enzymes would likely be even more effective because mass transfer limitations and accessibility to the hemicellulosic fraction would be minimized.

Processing Equipment

Based on observations during testing and filtration, and the characteristics of the feed slurry, bench-scale processing equipment was developed and modification of an existing continuous flow system was initiated. A Moyno feed pump, capable of pumping the feed slurry at the conditions evaluated was also acquired. In addition, since the acid hydrolysis was conducted at slightly elevated pressure (to keep the reaction mixture in the liquid phase), pressure letdown was required for the continuous system. It has been observed, however, that if the pressure is reduced through a small orifice or instantaneously, the fiber particles break apart and are more difficult to filter. Thus, a more amenable pressure letdown system has been designed, and the hardware for the system has been acquired.

Summary and Conclusions

The hemicellulosic fraction of corn fiber is a promising source for providing 5-carbon sugars that can be converted to value-added products. Observations from the tests using acid and enzyme hydrolysis to recover the hemicellulosic fraction are summarized below:

- Some hydrolysis options have been developed from literature and test results. Based on the data to date, one of the most attractive approaches is a two-step process, using acid and enzyme hydrolysis. The data suggest that this approach will result in high yields of monosaccharides while minimizing formation of degradation products.

- Thermochemical (with and without acid addition) hydrolysis conditions have been identified, where significant corn fiber solubilization takes place and little or no degradation products are formed.

- Commercially available and relatively inexpensive enzymes have been identified that are effective in converting corn fiber hemicellulose to xylose and arabinose.

- Bench-scale equipment was developed for continuous thermochemical processing. The equipment was selected based on observations made during the testing.

Statistics

Analysis of High-Volume, Hyper-Dimensional Mixed Data: NMR Spectra and Confocal Image Ensembles

Don Simone Daly

Study Control Number: PN00009/1416

New research tools for advanced biological studies generate highly complex, large volume, and multi-dimensional data. Often, these datasets represent mixed media, such as spectra, picture images, and scalars.

Project Description

Scientific research often generates complex, large volume, or hyper-dimensional datasets. Analyzing complex, multi-dimensional datasets can be highly challenging. The object of this project was to provide the tools, techniques, and expertise to analyze ensembles of spectra and images as an ensemble. Making the step from characteristics of a single object (such as an NMR spectrum) to the characteristics of the ensemble (i.e., an NMR spectral time series) provides new opportunities to unravel complex associations. We investigated the tools, techniques, and expertise necessary for the analysis of mixed sets of NMR spectra and optical images.

Results and Accomplishments

The primary accomplishments of this project are 1) the introduction of a new perspective from which to view the collection and analysis of NMR and optical datasets, and 2) the development of new analysis methods made possible by this perspective. Our new perspective emphasizes the data ensemble over the individual measurements. The new methods are geared to the collection and analysis of the ensemble.

We reexamined the NMR phenomenon and its subsequent measurement. Our examination produced a stochastic model of this spectral measurement that is true to the physics and includes the measuring uncertainties. Our model suggested a graphical method to view an NMR quadrature spectrum and an NMR spectral ensemble.

Our stochastic model describes an NMR-quadrature free-induction-decay measurement as a complex-valued time series. This model suggested that a phase-space graph plotting the real component of the measured time series against the imaginary component would provide not only information about the phenomenon under study, but also about the effects of measuring this phenomenon using NMR (Figure 1).

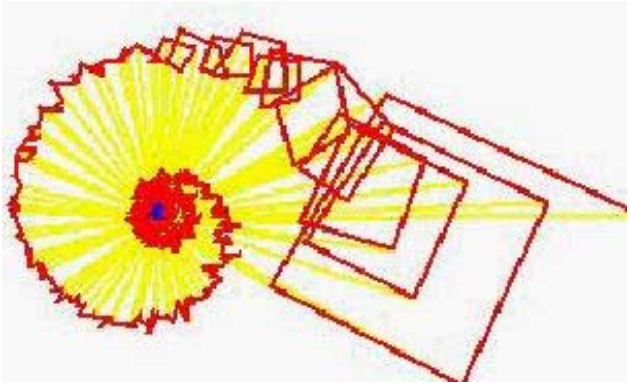

Figure 1. Phase space representation of a complex-valued NMR free induction decay of a sample featuring two dominant NM environments

A quick assessment of an ensemble of NMR measurements is gained by using the phase-space graph as a glyph to represent one NMR free induction decay on a graph of the ensemble (Figure 2). In this figure, the variation in the glyph over the underlying image hints at the varying spatial distribution of chemicals within the sample. The corner glyphs, where no signal is present, indicate that the measuring noise is random and uncorrelated between the two components of the complex-valued free induction decay measurements.

Under this project, APEX, a set of spectral feature extraction algorithms developed for MALDI-mass spectrometry was extended to extract features from an NMR spectrum. The extended algorithms automatically extract objective, robust estimates of peak locations, heights, and other peak characteristics with associated standard errors. The collection of estimates for each spectrum was then analyzed further.

We also explored the analysis of original and extracted spectral collections using spectral mixing models and spectral unmixing algorithms. Under a spectral mixing

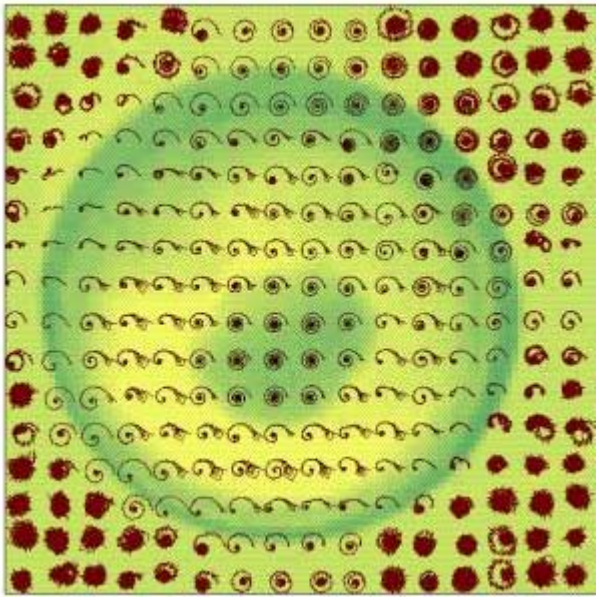

Figure 2. Display of an NMR dataset with NMR free induction decay phase glyphs overlaid on MRI of an amphibian oocyte

model, each observed spectrum in a collection is modeled as a mixture of pure spectra which may or may not be known. The objectives of spectral unmixing are to 1) estimate the number of pure spectra, 2) estimate the pure spectra, and 3) estimate the contributions of each pure spectra to each observed spectrum.

The spectral unmixing literature proposes a number of algorithms to estimate the parameters in the spectral mixing model. We found these algorithms to be less inadequate. We are presently developing new approaches, deriving new estimators, and developing new algorithms that will, hopefully, generate improved solutions.

Ongoing studies being conducted will benefit from spectral enhancement and unmixing.

Life Extension Analysis and Prognostic (LEAP) Architectures

Frank L. Greitzer

Study Control Number: PN99038/1366

This project is developing robust analytic methods for predicting the remaining life of mechanical systems. This research is relevant to a diverse set of challenges facing aging equipment in government (such as military air, land, and ships) and industry (power generators for industrial applications; large equipment for mining, farming, or earth moving; aircraft). While advancements in sensor technologies are making it feasible to install sensors on equipment for health monitoring, reliable methods for analyzing system status and predicting system life expectancy need to be developed.

Project Description

This research focuses on defining the constituents, and developing a method for predicting the remaining useful life of systems (and predicting the cause of system failure). The goal of this work is to specify a dynamic system that can be used to change the operating envelope of the target system. We investigated advanced statistical methods for characterizing and predicting various types of degradation using a generalized strategy capable of targeting diverse mechanical systems.

Introduction

A pervasive problem in both government and industry is the need to extend the useful life of systems. Economic pressures to maintain aging fleets of military and commercial equipment and vehicles (both ground and aircraft) are very real. Even with relatively new equipment, there is a tremendous cost-benefit of extending the time between overhauls, reducing the probability of a failure in the field and preventive repairs. A major predictor of the need for maintenance is the type of use and operating conditions that the product has experienced—such as environmental factors, duty factors, and service history. Keys to extending the useful life of each of these "systems" are 1) the capability to record "operational experience," and 2) the capability of integrating and analyzing the recorded data to produce reliable diagnostics and prognostics about the state of the system and its remaining useful life.

Prognostics is the process of predicting the future state of a system. Prognostics systems are composed of sensors, a data acquisition system, and microprocessor-based software to perform sensor fusion, analysis, and reporting and interpreting results with little or no human intervention in real-time or near real-time. Prognostics offer the promise of minimizing failures in the field, extending the time between maintenance overhauls, and reducing life-cycle costs. Implementing prognostics is a challenging task on several levels: 1) identifying appropriate hardware and sensor technologies, 2) analytically effective predictive methods, and 3) organization changes to capture the logistical benefits made possible by effective prognostic information. The benefits of the effective prognostics are substantial.

The objectives of this project are to define the architecture of a dynamic prognostic system for enhancing the operating envelope of target systems and to develop a generalized methodology for predicting the remaining useful life of systems.

Approach

To predict a failure (the inability of the operating system to perform its intended function), it is typically necessary to have three things: 1) knowledge of the system's current degree of fault; 2) a theory about the progression of the fault, so as to postulate the system's degree of fault at a particular point in time in the future; and 3) if that level of fault will produce a failure of the operating system. This last item is the threshold of a specified system parameter or figure of merit that corresponds to system failure. Archived manufacturer's data, historical data, engineering judgment, and real-time data collected from the system contribute to the assessment of these factors.

The approach employed in the life extension analysis and prognostic research was to identify and investigate different statistical methods and analytic techniques for improving the ability to predict future states of a system. Candidate statistical methods include multivariate regression, Bayesian regression methods, time-series analysis, and discrimination or clustering analysis. Analysis may focus on a single parameter or multiple

parameters. For single parameter prognostics, statistical analyses may be performed simultaneously on each real-time data source. As data are collected, regression models are applied to the data to determine trends in figures of merit. These figures of merit are compared, in real-time, to metric failure limits that are established off-line. The point of predicted failure is calculated as the intersection of these two lines (see Figure 1). Uncertainty intervals (dashed lines surrounding the trend lines) may also be derived to incorporate confidence estimates into the prediction.

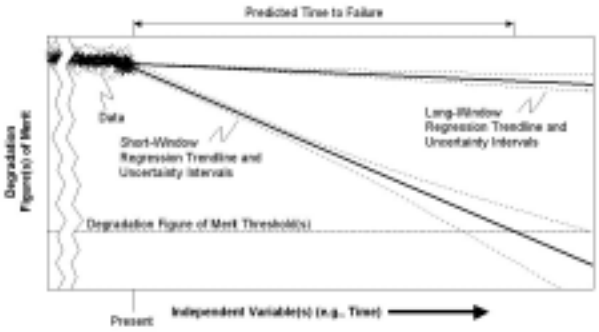

Figure 1. Regression trend lines that intersect degradation figure of merit threshold indicate predicted time to failure

The ability to predict, possibly in real time, the future state of a system based on sensor data collected from an operating system requires analytical methods that must overcome inherent problems with dynamic data—namely, dynamic variation and independent variable selection.

Dynamic Variation—Normal variation in sensor values must be distinguished from degradation. There is an inevitable tradeoff between using a large set of data to reduce the consequence of noisy sensor values and inherent system variability and using a smaller set of data to be responsive to change system characteristics that may occur when a system health problem begins to manifest itself.

Independent Variables—A second challenge relates to the selection of independent variables to be used for prediction. Prediction, by definition, implies the estimation of a parameter at some future point in time. Here, the use of the term "time" may be misleading, as it is clear that elapsed time or calendar time is a poor unit of measure for a mechanical system. Better manifestations of the independent variable "time" might be "running time" or "cycles" or a measure of "work" produced (e.g., joules or torque-time).

A comparison of alternative methods for prediction was conducted to choose the most effective techniques. To conduct this comparison, performance of alternative methods was assessed using simulated data and real data collected from the field.

Results and Accomplishments

Architecture. To address the problem of defining a framework for using prognostics, this project developed a prognostics architecture concept that helped to communicate logistics and organizational requirements that are fundamental to establishing capabilities for anticipatory logistics that exploit prognostics analyses (Greitzer 2000; Greitzer et al. 1999). Because of this work, several major programs have resulted or are being pursued using the LEAP Architecture as a foundation.

Prognostic Methods. The basis for prediction was to conduct trend analyses for each possible fault. The life extension prognostics method uses the value of the current figure of merit for each fault, the rate of change in that figure of merit, and the threshold, to compute the operating system's remaining life. Exploration of different trending concepts has produced a method that appears to have promise in improving prognostics for dynamic systems. The overall method, which is called "LEAP-Frog" regression, may be combined with any of a number of alternative statistical trending methods. The choice among trending methods is dependent upon the specific application. Further research in this area is required.

LEAP-Frog Technique. A novel technique for trending the figures of merit has been developed to meet the objective of improving predictive performance of the statistical method: the "LEAP-Frog" technique. For each figure of merit the analysis computes a plurality of regression lines that differ in the amount of past data that are included in the analysis (i.e., the size of the "window"). The regression lines may differ in slope and amount of error (such as extent of the uncertainty intervals) because they reflect differing window sizes. In general, regression lines built from longer windows will be more reliable (lower uncertainty), except when the operating system conditions are changing. In such cases, shorter windows (based on more recent data) will produce more accurate and reliable predictions. The basis of this methodology is to select from among the plurality of regression lines the regression line for a given figures of merit that exhibits a realistic compatibility with the most

recent figure of merit values. Should a recent set of figure of merit values be unrealistically high or low, a shorter window (i.e., one more responsive to changes in trends) is tested for realistic compatibility. In this way, the selected regression line for each analysis cycle may jump from one line to another (hence the term "leap"). This method attempts to maximize the responsiveness to changes in the trend line, as would occur if the system health began to degrade, without allowing wildly varying predictions that would be characteristics of a regression based on a small amount of noisy data.

Figure 2 summarizes and compares the performance of four standard or typical prognostic methods with that of the LEAP-Frog method. The four standard methods predict future performance based on 1) the last value of the figure of merit, 2) the average value of the figure of merit since the start of data collection, 3) the regression of the figure of merit on all the data since the start of data collection, or 4) the regression of the figure of merit on the last 1000 records. The LEAP-Frog method illustrated in these figures uses 5) a linear independent variable (such as time), and 6) a nonlinear independent variable (such as distance driven).

Figure 2 shows the results with simulated data that exhibit a slow degradation with a sudden change to a rapid degradation (as might happen with a catastrophic engine problem). The simulated data are shown in the left side of the figure; prediction errors of the alternative methods are shown in the graph on the right side of the figure. Similar results were obtained using simulated data that exhibits a constant, slow degradation; and simulated data with an increasing rate of degradation (as might happen with a problem that is building up to catastrophic). As one might suspect from the figure, there is a statistically significant difference among the average prediction errors for the six methods. In particular, the difference between the LEAP-Frog methods and the others is statistically significant ($p<0.05$).

Other more sophisticated mathematical techniques such as regression analysis, Bayesian analysis, time series analysis, linear/nonlinear analyses, and Kalman Filtering can provide an estimate of the future condition of the operating system. The Leap-Frog technique requires very little coding, data processing time, or data storage. This prediction can be based on past maintenance and repair data, data from similar operating systems, modeling and simulation data of the system, prior beliefs, or past sensor data. The techniques may perform a prediction alone or a prediction with uncertainty limits.

Summary and Conclusions

Following are the major accomplishments of this research:

- A high-level architecture or framework for prognostics was developed and described. This helped to communicate logistics requirements and organizational concepts that are fundamental to establishing capabilities for anticipatory logistics.

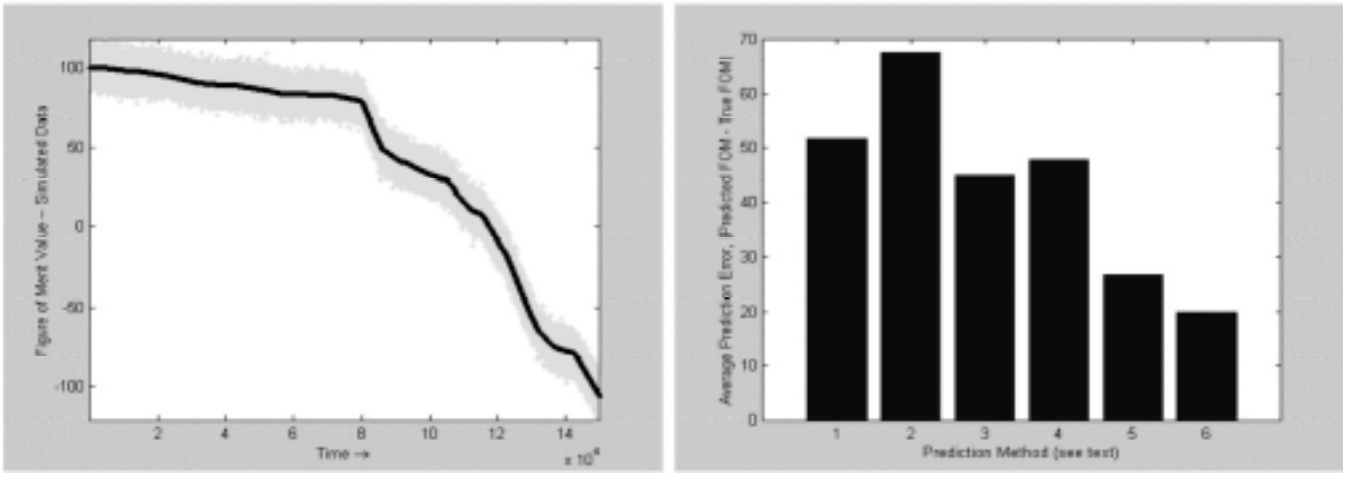

Figure 2. Comparison of regression methods for predicting future performance of simulated data that follows a slow linear degradation followed by a sharper linear degradation (simulated degradation data shown on the left). Chart on the right shows average prediction errors for six alternative regression methods. The LEAP-Frog method (method 6) yields the lowest prediction errors.

- A novel, LEAP-Frog regression technique was developed to provide more adaptive predictions of future performance from dynamic data. An early version of the LEAP-Frog technique is being incorporated in a prototype prognostics system for the U.S. Army.

- The high-level LEAP architecture and the LEAP-Frog analytic technique are applicable to a wide variety of prognostic problems.

References

Greitzer FL. 2000. "Life Extension Analysis and Prognostics (LEAP) Architectures." *In Laboratory Directed Research and Development Annual Report, Fiscal Year 1999.* PNNL-13203, pp. 85-88, Pacific Northwest National Laboratory, Richland, Washington.

Greitzer FL, EJ Stahlman, TA Ferryman, BW Wilson, LJ Kangas, and DR Sisk. 1999. "Development of a Framework for Predicting Life of Mechanical Systems: Life Extension Analysis and Prognostics (LEAP)." *SOLE '99 Symposium*, August 31- September 2, 1999, Las Vegas, Nevada.

Presentation

Greitzer FL, EJ Stahlman, TA Ferryman, BW Wilson, LJ Kangas, and DR Sisk. 1999. "Development of a framework for predicting life of mechanical systems: Life Extension Analysis and Prognostics (LEAP)." *SOLE '99 Symposium,* Las Vegas, Nevada.

Probabilistic Methods Development for Comprehensive Analysis of Complex Spectral and Chromatographic Data

Kristin H. Jarman, Alan R. Willse, Karen L. Wahl, Jon H. Wahl

Study Control Number: PN00076/1483

Techniques such as chromatography, spectrometry, and spectroscopy are being used in both basic research to improve understanding of biological and biochemical processes, and in field portable instrumentation to perform rapid, on-site chemical analysis in a complex environment. Under this project, new data analysis methods are being developed for spectral and chromatographic data, providing algorithms that are automated, scientifically interpretable, and versatile enough to analyze spectral or chromatographic data under complex backgrounds or varying experimental conditions.

Project Description

The purpose of this project was to develop new methods for analysis of spectral or chromatographic data that apply to a wide variety of instrumentation, and can be readily adapted to either laboratory or field application. This research draws from modern probabilistic reasoning and statistics, where similarities between two data sets are quantified based on the properties of the peaks within the sets. The goal of this research was to advance the state of the art by providing data analysis methods that are automated, scientifically interpretable, and versatile enough to analyze spectral or chromatographic data under complex backgrounds or varying experimental conditions. Methods developed are initially being applied to and tested on specific problems in the area of matrix-assisted laser desorption/ionization (MALDI) spectrometry and gas chromatography.

Introduction

Analytical instrumentation techniques are evolving rapidly. Various techniques are being developed for basic research, while at the same time many of these techniques are being developed and deployed into field portable chemical or biological analysis tools. The tremendous potential of new and existing analytical techniques has resulted in rapid progress in the area of hardware and methods development. In a research setting, it is now possible to analyze sophisticated biochemical or physical processes. In a field development setting, it is possible to analyze samples in environments that generate complex, nonhomogeneous background signals. In both cases, the result is a complex spectrum and/or chromatogram.

Current data analysis methods, such as principal-components-based methods (Seber 1984; Johnson and Wichern 1992) tend to place nearly all of their emphasis on peak intensities. This is appropriate for some applications but not others. For example, intensity-based methods are appropriate in gas chromatography, where quantitation of analytes is often of interest. On the other hand, mass spectrometry is often used to identify analytes present in a sample based on the locations of the peaks that appear. In this case, it can be difficult to obtain reproducible relative peak intensities, and therefore the presence or absence of peaks is of more interest than peak heights. In this case, intensity-based data analysis methods such as principal components analysis do not reliably capture the features of interest in a spectrum and a more subjective, manual interpretation tends to be used.

Under this project, we developed a unified statistical framework through which many different types of analytical data can be interpreted. This approach incorporates recent research in both discrete and continuous multivariate statistical methods. This model is general enough to handle different types of analytical data, where different spectral features are of interest. In the first year of this project, methods for hypothesis testing and process control of spectral data were developed based on this model. A comparison against the more traditional methods demonstrates that this approach improved upon existing approaches.

Approach

The research under this project draws from a unique mathematical model for spectral and chromatographic data. The exact form of this multi-stage model is specified by the spectral features of interest for a particular application. Therefore, it is general enough to handle mass spectral data, where peak locations are of primary interest but intensities are not. It can also handle chromatographic data, where both peak locations and relative intensities may be of interest. In addition, this

model is designed to handle other types of data where additional peak properties such as width and shape may be important.

Results and Accomplishments

Model Construction and Hypothesis Testing Procedure

The multi-stage model for spectral and chromatographic data was constructed. The model is currently able to handle data types where peak presence, location, and intensity are important. A hypothesis testing algorithm was developed based on this model. The hypothesis testing algorithm is a likelihood ratio based test for simple or composite hypotheses.

Process Control Procedure

A multivariate cumulative sum procedure for control of analytical processes based on the model presented here was developed. We assume the process follows some prescribed nominal behavior until time $k>1$, called the change point, at which time the process behavior changes. This multivariate approach considers the sequence $Z_i = g(X_i) - c$, where c is some constant, and $g(\cdot)$ is a function of the incoming spectra constructed from the spectral model. We let $S_n = \sum_{1 \le j \le n} Z_j$, and define the test statistic to be $C_n = S_n - \min_{1 \le j \le n} \{S_j\}$ for $n \ge 1$ with $C_0 = 0$. Then C_n can be formulated recursively by the relation $C_{n+1} = \max\{0, C_n + Z_{n+1}\}$. This process is repeated for incoming observations until $C_n \ge A$ for some constant A, at which time the process is declared to be out of control.

Comparison to Existing Methods

A comparison of our process control technique to the more traditional method proposed in Nijhuis et al. (1997) was made for two application areas. The first application area involves control of routine analysis in gas chromatography, where peak presence, location, and intensity are important. In this case, both the traditional approach and the new approach identified an out-of-control gas chromatography process. The second application area involves bacterial analysis using MALDI mass spectrometry, where peak presence and location are of interest. In this case, the new approach performed much better than the traditional approach. The results of the MALDI mass spectrometry comparison are provided here.

The goal was to determine if the new approach could better detect contamination of an *E. coli* bacterial culture by *Shewanella alga* (*S. alga*) using MALDI mass spectrometry than the existing method. Contamination was simulated by using a mixture of the two bacteria. Figure 1 plots MALDI mass spectra for a pure *E. coli* culture and for a mixture of *E. coli* and *S. alga*. Figure 2 compares the two different process control procedures, where the first 29 samples are of pure *E. coli* and the last 30 samples contain a mixture of the two bacteria.

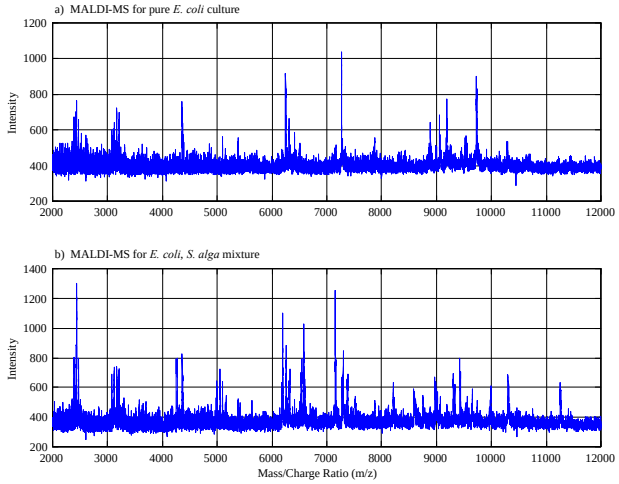

Figure 1. Typical MALDI mass spectra for bacterial cultures

Figure 2a shows the results of the traditional method, where the process control test statistic is plotted. Test statistic values that lie above the threshold (horizontal bold line at 0.1) result in a conclusion that the culture is pure. Test statistic values that fall below the horizontal line result in a conclusion that contamination is present. Figure 2b shows the results of new approach developed under this project. In this case, the test statistic is plotted and compared to an upper threshold marked by the bold horizontal line at 4.6. Test statistic values that remain below the threshold result in a conclusion that the culture is pure, whereas values that hit the threshold result in the conclusion that the culture is contaminated. Figure 2 clearly shows that the new approach developed under this project detects the bacterial contamination whereas the more traditional approach fails to identify any of the contaminated samples.

Summary and Conclusions

A novel mathematical model for spectral/ chromatographic data was developed. Methods for hypothesis testing and process control of analytical instrumentation were developed based on this model. Comparison with more traditional methods indicates that this approach performs as well as or better than the traditional methods for the applications tested here. A more complete comparison using different applications

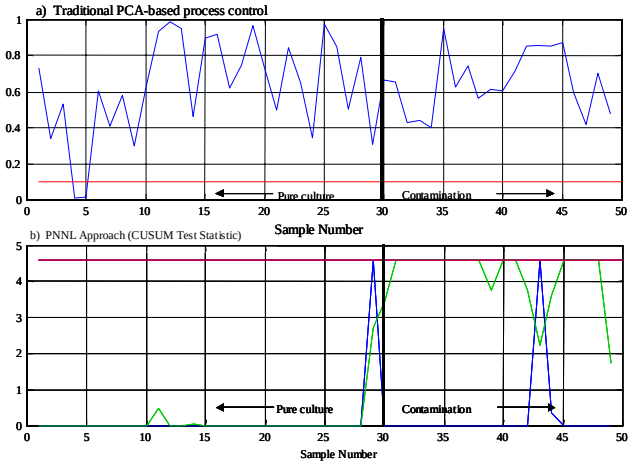

Figure 2. PNNL developed quality control of mass spectral data. The approach (b) detects simulated sample contamination where the traditional approach (a) fails.

and a wider variety of data types, along with the extension of this probabilistic model to multi-dimensional analytical instrumentation needs to be investigated.

References

Johnson RA and DW Wichern. 1992. *Applied Multivariate Statistical Analysis.* 3rd ed.; Prentice Hall, Englewood Cliffs, New Jersey.

Nijhuis A, SD Jong, and BGM Vandegiste. 1997. "Multivariate process control in chromatography." *Chemometrics and Intelligent Laboratory Systems*, 38:51-62.

Seber GAF. 1984. *Multivariate Observations.* John Wiley & Sons, Inc., New York.

Acronyms and Abbreviations

Acronyms and Abbreviations

2-D	two-dimensional
2-D PAGE	two-dimensional polyacrylamide gel electrophoresis
AR-MSRI	angle-resolved mass spectroscopy of recoiled ions
CaR	calcium-sensing receptor
CRADA	Cooperative Research and Development Agreement
DoD	U.S. Department of Defense
DOE	U.S. Department of Energy
EMSL	William R. Wiley Environmental Molecular Sciences Laboratory
EPA	U.S. Environmental Protection Agency
ESI	electrospray ionization
FTICR	Fourier-transform ion cyclotron resonance
GAP	GTPase activating protein
GPCR	G-protein coupled receptor
GTP	guanosine triphosphate
HEPA	high-efficiency particulate air
ICP-MS	inductively coupled plasma mass spectrometry
LDRD	Laboratory Directed Research and Development
MALDI	matrix-assisted laser desorption ionization
MS/MS	tandem mass spectrometry
NMR	nuclear magnetic resonance
PAGE	polyacrylamide gel electrophoresis
PBPK/PD	physiologically based pharmacokinetic/pharmacodynamic
PCR	polymerase chain reaction
PM	particulate matter
SEM	scanning electron microscopy
SIMS	secondary ion mass spectrometry
TNFα	tumor necrosis factor alpha
TNT	trinitrotoluene
TOFMS	time-of-flight mass spectrometry